ACTA MECHANICA ET AUTOMATICA

2025 volume 19 no. 3

quarterly

ISSN 1898-4088 (printed)
ISSN 2300-5319 (online)

THE EDITORIAL BOARD:

EDITOR-IN-CHIEF:

Michał Kuciej (Białystok, Poland)
(m.kuciej@pb.edu.pl)

V-CE EDITOR-IN-CHIEF:

Bogdan Sapiński (Kraków, Poland)
(deep@agh.edu.pl)

TOPIC EDITORS:

mechatronics and machine design
Norbert Krüger (Odense, Denmark)
(norbert@mmmi.sdu.dk)

automatic control and robotics
Jerzy T. Sawicki (Cleveland, USA)
(j.sawicki@csuohio.edu)

mechanics
Gennady Mishuris (Aberystwyth, UK)
(ggm@aber.ac.uk)

biocybernetics and biomedical engineering
Jozef Živčák (Kosice, Slovakia)
(jozef.zivcak@tuke.sk)

THE SCIENTIFIC BOARD:

Manuel Ruiz de Adana Santiago (Spain)
Yunus Z. Arslan (Turkey)
Jerzy Bajkowski (Poland)
Vladimir G. Barsukov (Belarus)
Wojciech M. Batko (Poland)
Filippo Berto (Italy)
Romuald Będziński (Poland)
Pavel Bogdanovich (Belarus)
Tadeusz Burczyński (Poland)
Ömer Civalek (Turkey)
Leszek Demkowicz (USA)
André Dragon (France)
Nicholas Fantuzzi (Italy)
Miguel A. Ferrer (Spain)
Xin-Lin Gao (USA)
Giancarlo Genta (Italy)
Grzegorz Glinka (Canada)
Riza Gürbüz (Turkey)
Radovan Hudak (Slovakia)
Satoshi Ikezawa (Japan)
Sergii A. Ischenko (Ukraine)
Oleksandr Jewtuszenko (Poland)
Mark Kachanov (USA)
Tadeusz Kaczorek (Poland)
Julius Kaplunov (UK)
Laszlo Keviczky (Hungary)
Jerzy Klamka (Poland)
Ülle Kotta (Estonia)
Janusz Kowal (Poland)
Józef Kubik (Poland)
Prafulla Kumar Jha (India)
Roman Kushnir (Ukraine)
Chee W. Lim (China)
Arkadiusz Mężyk (Poland)
Krzysztof Marchelek (Poland)
Jan J. Marciniak (Poland)
Andrejus Marcinkevičius (Lithuania)
Stanisław J. Matysiak (Poland)
Romuald P. Mosdorf (Poland)
Zenon Mróz (Poland)
Agnes Muszynska (USA)
Wiesław Ostachowicz (Poland)
Martin Ostoja-Starzewski (USA)
Marek Penhaker (Czech Republic)
Ernian Pan (USA)
Volodymyr Panasyuk (Ukraine)
Timon Rabczuk (Germany)
Igor Sevostianov (USA)
Anatolii I. Sviridenok (Belarus)
Rymantas T. Tolocka (Lithuania)
Francesco Tornabene (Italy)
Delfim F. M. Torres (Portugal)
František Trebuňa (Slovakia)
Tomasz Wierzbicki (USA)
Vladas Vekteris (Lithuania)
Ehrenfried Zschech (Germany)
Krzysztof K. Żur (Poland)

TECHNICAL EDITOR:

Małgorzata Zdrodowska
(m.zdrodowska@pb.edu.pl)

Katarzyna Szymul
(k.szymul@pb.edu.pl)

Oleksii Nosko
(oleksii.nosko@pg.edu.pl)

The articles published in „Acta Mechanica et Automatica"
have been given a favourable opinion by reviewers designated by Editorial/Scientific Board

Acta Mechanica et Automatica is covered by the following services: Web of Science - Emerging Sources Citation Index, SCOPUS, DOAJ (Directory of Open Access Journals), BazTech, Google Scholar, Arianta, Baidu Scholar, CNKI Scholar (China National Knowledge Infrastructure, CNPIEC - cnpLINKer, Dimensions, EBSCO (relevant databases), EBSCO Discovery Service, Genamics JournalSeek, Index Copernicus, Japan Science and Technology Agency (JST), J-Gate, JournalGuide, JournalTOCs, KESLI-NDSL (Korean National Discovery for Science Leaders, Microsoft Academic, MyScienceWork, Naver Academic, Naviga (Softweco), POL-index, Primo Central (ExLibris), Publons, QOAM (Quality Open Access Market), ReadCube, Semantic Scholar, Sherpa/RoMEO, Summon (ProQuest), TDNet, TEMA Technik und Management, Ulrich's Periodicals Directory/ulrichsweb, WanFang Data, WorldCat (OCLC).

© 2025 Bialystok University of Technology
This work is licensed under the Creative Commons BY-NC-ND 4.0 License (CC BY-NC-ND 4.0)

ISSN 1898-4088 (printed) **ISSN 2300-5319 (online)**

The original version of the journal is a printed version

THE ADDRESS FOR THE CORRESPONDENCE:
„Acta Mechanica et Automatica"
Faculty of Mechanical Engineering, Bialystok University of Technology
ul. Wiejska 45C, 15-351 Białystok, Poland
tel. +48 85 746 9206, fax +48 85 746 92 10
e-mail: acta.mechanica@pb.edu.pl
https://www.amajournal.com/

Guidlines for the authors and conditions of subscription you can find on website https://www.amajournal.com/

Project of the cover: Marcin Dominów
Published by: Bialystok University of Technology
Edition: 200 copies

acta mechanica et automatica

vol. 19, no. 3 (73)

Bialystok University of Technology

Białystok 2025

CONTENTS

BENDING AND VIBRATION ANALYSIS OF MAGNETO-ELECTRO BILATERALLY COATED QUASI-3D MICROBEAM VIA DQ-FEM

Besma KHOUANI*, Ahmed SAIMI, Ismail BENSAID***

*"IS2M Laboratory, Mechanical engineering Department, Faculty of Technology, University Abou Beckr Beklaid, Tlemcen, Algeria
**"Mechanical engineering Department, Faculty of Science and Technology, University Belhadj Bouchaib, Ain Temouchent, Algeria

besma.khouani@univ-tlemcen.dz, ahmed.saimi@univ-temouchent.edu.dz, ismail.bensaid@univ-tlemcen.dz

received 26 December 2024, revised 09 April 2025, accepted 10 April 2025

Abstract: In this study, the static bending and free vibration of a bilaterally coated magneto electro elastic (MEE) functionally graded (FG) microbeam is analysed by using a high order quasi-3D beam theory, along with a Differential Quadrature Finite Element Method (DQ-FEM). The power formulation for FG gradation through the thickness direction is considered. The microbeam consists of two materials, one possessing piezo-magneto-electric characteristics and the other without them. The material characteristics are progressively graded from the outermost surfaces to the innermost core. In order to localize the microstructural effect of the beam, the modified couple stress theory (MCST) is incorporated. By the application of Lagrange's theorem and Gauss-Lobato node scheme, the general governing equation are established. Through the implementation of the established model, "the static bending and free vibration" analysis are determined. To illustrate the effectiveness and accuracy of this particular numerical resolution method, the obtained results are validated with similar outcomes in existing literature. The effects of the material gradation volume fraction index, and the length-thickness ratio on the natural frequencies and static bending are investigated. The results reveal that the material distribution plays a significant role in influencing both static bending and free vibration behavior. Material composition plays a critical role, with higher proportions of MEE material enhancing the piezoelectric effect and magnetostrictive response, respecting the material gradation with optimized combinations of MEE material for higher deflection and optimal electric and magnetic potentials. This study provides a comprehensive framework for optimizing MEE microbeams in applications requiring precise control of mechanical, electrical, and magnetic responses.

Key words: higher-order Q3D beam theory, magneto-electro-elastic microbeam, MCST, DQ-FEM, FGM

1. INTRODUCTION

Magneto-electro-elastic materials have sparked widespread attention due to their multifunctional features, which integrate mechanical, electrical, and magnetic forces. These materials are commonly employed in sophisticated engineering applications such as sensors, actuators, and energy harvesters. Understanding these materials' mechanical behavior, particularly in microbeam structures, is critical for maximizing their performance and dependability in practical applications [1-4]. "In addition, functionally graded materials (FGM) exhibit continuous changes in properties through various direction. FGM offer several benefits, including temperature protection, sound insulation, and energy and electromagnetic wave absorption [5-7]. Currently, scientists have been interested in evaluating the mechanical behavior of laminated-surface- piezoelectric in host structures [8]. Research into multilayer magneto-electro-elastic functionally graded materials (MEE-FGMs) on thin beams and plates has gained popularity in recent years. [9] investigated the free vibration behavior of both anisotropic and linear MEE-FGM plates. [10] suggested a meshless approach for analyzing the bending of circular MEE-FGM plates. [11] conducted an inquiry into the implications of porosity on the nonlinear deformation characteristics exhibited by functionally graded magneto-electro-elastic smart shells in the context of simultaneous application of loads. [12] analyzed the static bending and the free vibration of a transversely isotropic magneto-electro-elastic beam including microstructure and foundation effects. [13] studied the bending and vibration of FG MEE Timoshenko Microbeams and added wave propagation analysis [14]. [15] developed a microstructure-dependent anisotropic magneto-electro-elastic Mindlin plate model via a modified couple stress theory. Notably, [16] introduced an isogeometric model to study size-dependent effects in magneto-electro-elastic microbeams. Their work highlights the role of gradient index variations in tailoring MEE responses. Similarly, [17] conducted nonlinear bending analysis on nonlocal MEE laminated nanobeams and emphasized the influence of boundary conditions and external electric/magnetic potentials. The thermal buckling behavior of MEE nanobeams has also been explored by [18] who employed von Kármán's nonlinear equations to examine the impact of temperature gradients and electrical/magnetic fields. Further, [19] investigated the nonlinear vibrations of flexoelectric functionally graded nanoplates under the influence of a magnetic field, demonstrating the importance of electromechanical interactions at the nanoscale. [20] extended this research by analyzing nonlinear deformations of MEE nanobeams resting on an elastic foundation, using a modified couple stress theory to accurately capture nonlocal effects. Additionally, [21] investigated the free vibration characteristics of MEE nanobeams in a thermal environment, revealing the dependency of natural frequencies on length and thickness variations. In the context of buckling analysis, [22] focused on size-dependent magneto-electromechanical buckling using strain gradient theory, showing how mechanical and electrical fields affect stability conditions. Nonlinear postbuckling behavior has been studied by [23], who analyzed magneto-electro-thermo-elastic laminated microbeams incorporating the modified couple stress theory and Reddy's shear deformation theory. Their results provide key insights into the combined effects of temperature, magneto-electric potential, and slenderness ratio on postbuckling performance. [24] introduced a continuum-based model for functionally graded conical nano/microshells, demonstrating how flexoelectric effects influence static and vibrational behaviors. [25] presented a nonlinear dynamic model for geometrically imperfect functionally graded MEE nanobeams, which is essential for understanding real-world imperfections in nanostructures. Recent models, such as the axially functionally graded (AFG) micro-beam based on strain gradient elasticity theory (RSGET), incorporate size effects and material inhomogeneity to analyze the static and dynamic responses at the microscale [26]. Similarly, isogeometric analysis (IGA) has been applied to magneto-electro-elastic functionally graded microplates, highlighting the impact of microstructure effects on mechanical and electromagnetic behaviors [27]. Additionally, a new IGA model for magneto-electro-elastic curved microbeams, considering size effects and the modified couple stress theory (MCST), offers insights into the bending and vibration behaviors of functionally graded structures [16]. These models are essential for optimizing the performance of micro-sensors, actuators, and other micro-scale devices. "Numerous investigations [28, 29] have demonstrated that thin beams and plates typically display size effects. Classical theories at the micro/nano scale cannot account for non-local interactions of material particles at such small scales due to a lack of material length scale parameters. To anticipate size effects, a variety of theories with extra material properties have been developed, including couple stress theories [30-32], strain gradient theories [33-35]. These concepts were effectively used to generate size-dependent structural models at extremely tiny scales. For example, based on nonlocal theories, a variety of MEE beam and plate models have been created to capture non-local size effects [36-39], in which a non-local medium with long-range material interactions is used. [40] suggested a non-local strain gradient theory that incorporates both non-local and strain gradient effects, and the bending, buckling, and free variation issues of FGM beams have been resolved [41, 42]." "Researchers frequently employ 1st "order shear deformable beam theory", (HSBT) "higher-order shear deformable beam theory", and shear and "normal deformable beam theory", commonly known as Q3D theory. The FSBT is the simplest model, but it necessitates a shear correction factor as it does not fulfil the zero traction boundary criterion at the top and bottom surfaces of the beam [43],[44]. The "HSBT" theories were suggested, that enhanced the "transverse shear stress distribution" and, as a result, removed the need for a "shear correction factor" (SCF) [45]. However, HSBT theories do not take into consideration the usual strain as well as stretch effect, which then becomes highly relevant and should be considered for thick typical FGBs. As a consequence, Q3D theories [46], [47] that take shear and stretching effects into account are created by employing the idea of higher order variation in both transverse and axial displacements". In recent decades, numerical and semi-numerical methods, such as the finite element method (FEM) and the generalized differential quadrature method (GDQM), have gained popularity for their efficiency, flexibility, and adaptability in solving differential equations related to structural elements with complex effects, including geometries, shapes, interactions, boundary conditions, and more, with precise results. Since then, other investigations have been conducted using these numerical approaches. [48] investigated the dynamic behavior of functionally graded porous beams sitting on a viscoelastic foundation using GDQM. Dahmane et.al studied the influence of crack on the dynamic behavior of bidirectional imperfect FG beams on an elastic basis via FEM. [49] used the DQFEM to investigate the dynamic behavior of on-board shafts. [50] investigated the vibration and buckling characteristics of nano-composite beams reinforced with agglomerated carbon nanotubes using the DQFEM. A combined study between DQFEM and MCST to analyze the dynamic behaviors of microbeams was used in several works [51, 52].

The present paper uses the extended modified couple stress theory to develop a bilaterally coated MEE microbeam model via the refined high order beam theory combined with the DQFEM for the first time to solve the static bending and free vibration.

The proposed bilaterally coated magneto-electro-elastic (MEE) microbeam, analyzed using a quasi-3D beam theory and DQ-FEM, has potential applications in various engineering fields. The unique electromechanical coupling behavior enables its use in microelectromechanical systems (MEMS) such as high-sensitivity sensors, actuators, and vibration-based energy harvesters. In biomedical engineering, it can be employed in micro-pumps, biosensors, and drug delivery systems. Additionally, the tailored functionally graded composition makes it suitable for aerospace applications, including adaptive structures and damping mechanisms. These diverse applications highlight the significance of the proposed model in advancing smart material-based technologies.

2. FORMULATION

2.1. MEE FG microbeam model

This study considers a microbeam of length L, width b, and thickness h, as shown in figure 1, from which the material characteristics are progressively graded from the outer surfaces to the inner core.

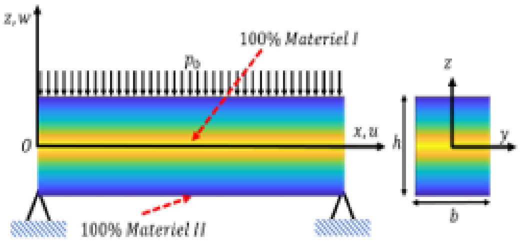

Fig. 1. Piezo- bilaterally FG microbeam model

The material characteristics are considered to change continuously in two opposite direction throughout the thickness (z-axis) based on the power-law distribution [52]. The following equations describe the distribution of material characteristics in FG materials:

$$P(z) = (P_1 - P_2)\left(\left|\left|\frac{2z}{h}\right| - 1\right|\right)^{k_z} + P_2 \qquad (1)$$

Where $P(z)$ represent "elastic stiffness, couple stress stiffness, piezoelectric constant, piezomagnetic constant, dielectric constant, magnetic permeability constant, magneto-dielectric constant and density".

The total strain energy in this particular situation is as follow.

$$U = \frac{1}{2}\int_0^L \int_A \left(\sigma_{ij}\varepsilon_{ij} + m_{ij}\chi_{ij} - D_iE_i - B_iH_i\right) dA\, dx \qquad (2)$$

The equations representing “transversely isotropic magneto-electro-elastic materials” are provided in accordance with the extended MCST[12]. Where σ_{ij}, m_{ij}, D_i, B_i represent the “Cauchy stress tensor, deviatoric couple stress tensor, electric displacements, and magnetic fluxes:

$$\begin{Bmatrix}\sigma_{xx}\\ \sigma_{zz}\\ \sigma_{zx}\end{Bmatrix}=\begin{bmatrix}C_{11} & C_{13} & 0\\ C_{13} & C_{33} & 0\\ 0 & 0 & C_{55}\end{bmatrix}\begin{Bmatrix}\varepsilon_{xx}\\ \varepsilon_{zz}\\ 2\varepsilon_{xz}\end{Bmatrix}-\begin{bmatrix}0 & q_{31}\\ 0 & q_{33}\\ q_{15} & 0\end{bmatrix}\begin{Bmatrix}H_x\\ H_z\end{Bmatrix}-\begin{bmatrix}0 & e_{31}\\ 0 & e_{33}\\ e_{15} & 0\end{bmatrix}\begin{Bmatrix}E_x\\ E_z\end{Bmatrix} \tag{3}$$

$$\begin{Bmatrix}m_{yz}\\ m_{xy}\end{Bmatrix}=\begin{bmatrix}A_{44} & 0\\ 0 & A_{66}\end{bmatrix}\begin{Bmatrix}2\chi_{yz}\\ 2\chi_{xy}\end{Bmatrix} \tag{4}$$

$$\begin{Bmatrix}D_x\\ D_z\end{Bmatrix}=\begin{bmatrix}0 & 0 & e_{15}\\ e_{31} & e_{33} & 0\end{bmatrix}\begin{Bmatrix}\varepsilon_{xx}\\ \varepsilon_{zz}\\ 2\varepsilon_{zx}\end{Bmatrix}+\begin{bmatrix}s_{11} & 0\\ 0 & s_{33}\end{bmatrix}\begin{Bmatrix}E_x\\ E_z\end{Bmatrix}+\begin{bmatrix}d_{11} & 0\\ 0 & d_{33}\end{bmatrix}\begin{Bmatrix}H_x\\ H_z\end{Bmatrix} \tag{5}$$

$$\begin{Bmatrix}B_x\\ B_z\end{Bmatrix}=\begin{bmatrix}0 & 0 & q_{15}\\ q_{31} & q_{33} & 0\end{bmatrix}\begin{Bmatrix}\varepsilon_{xx}\\ \varepsilon_{zz}\\ 2\varepsilon_{zx}\end{Bmatrix}+\begin{bmatrix}\mu_{11} & 0\\ 0 & \mu_{33}\end{bmatrix}\begin{Bmatrix}H_x\\ H_z\end{Bmatrix}+\begin{bmatrix}d_{11} & 0\\ 0 & d_{33}\end{bmatrix}\begin{Bmatrix}E_x\\ E_z\end{Bmatrix} \tag{6}$$

The parameters (C_{11}, C_{13}, C_{55}) , (A_{44}, A_{66}) describe the elastic stiffness tensor and the couple stress tensor, with:

$$A_{\alpha\beta}=C_{\alpha\beta}l^2 \tag{7}$$

where l is the material length scale parameter (MLSP).

$q_{i\alpha}$, $e_{i\alpha}$, s_{ij}, μ_{ij}, d_{ij} are the piezomagnetic tensor, the piezoelectric tensor, the dielectric tensor, the magnetic permeability tensor, and the magneto-dielectric tensor respectively. And ε_{ij}, χ_{xx} are “the strain tensor and the rotationally symmetric gradient tensor”, which are described by the following equations: [53]

$$\varepsilon_{ij}=\frac{1}{2}\left(u_{i,j}+u_{j,i}\right) \tag{8}$$

$$\chi_{ij}^{s}=\frac{1}{2}\left(\theta_{i,j}+\theta_{j,i}\right) \tag{9}$$

$$\theta_i=\frac{1}{2}e_{ijk}u_{k,j} \tag{10}$$

The variables u_i and θ_i represent the components of the displacement vector and rotation vectors, respectively. e_{ijk} is the permutation symbol. Also, E_i and H_i represent the electric field and magnetic field intensities, respectively. [15]

$$E_i=-\Phi_{,i} \quad , \quad H_i=-M_{,i} \tag{11}$$

Φ and M represent the “electric and magnetic potentials, respectively.

In accordance with the higher order quasi-3D beam theory [50], The current study posits that the field of displacement at any random spot on the microbeam can be expressed as follows:

$$\begin{cases} u(x,z,t)=u_0(x,t)-z\frac{dw_b}{dx}+f(z)\frac{dw_s}{dx}\\ w(x,z,t)=w_b(x,t)+w_s(x,t)+g(z)w_z(x,t)\end{cases} \tag{12}$$

The transversal displacement is divided into two components, notably w_b, w_s and w_z, following this method. Where u, w_b, w_s and w_z represents the displacement in the x-direction, the bending component, the shear components and the stretching components of the transverse displacement of the points on the neutral axis of the beam, respectively. The selection of our function $f(z)$ is governed by the shear function provided by Reddy in equation (15).

$$f(z)=z-\left(1-\left(\frac{4z^2}{3h^2}\right)\right), \ g(z)=\left(1-\frac{df}{dz}\right) \tag{13}$$

The distribution of electric and magnetic potentials in the thickness direction of the piezoelectric inner layer (core) is provided by [13]:

$$\begin{cases}\Phi(x,z,t)=-\cos\left(\frac{\pi}{h}z\right)\gamma(x,t)+\frac{2z}{h}\gamma_0\\ M(x,z,t)=-\cos\left(\frac{\pi}{h}z\right)\zeta(x,t)+\frac{2z}{h}\zeta_0\end{cases} \tag{14}$$

The spatial variations of electric potential in the x-direction are represented by γ, while the external electric potential is denoted as γ_0. ζ and ζ_0 represent the spatial variations of the magnetic potential in the x-direction and the external magnetic potential, respectively. Several studies used uniform distribution in the longitudinal direction and linear distribution [54, 55]. Works donne by Gopinathan [56] and Wang and Quek [57] demonstrated that a quadratic or half-cosine distribution provides a more accurate representation, as it better satisfies Maxwell’s static electricity equation. The electric and megnitic potential distribution we adopted follows this approach. The choice of electric and magnetic potential distributions directly affects the coupling terms in the strain energy expression. A different assumption, such as a purely linear distribution, would result in different governing equations, potentially missing key coupling effects. By considering a half-cosine and linear variation, the proposed model ensures that the strain energy formulation incorporates essential electro-magnetic coupling effects without neglecting significant terms.

By substituting equation (12) into equation (8), the non-zero components of the deformation tensor are extracted as:

$$\begin{cases}\varepsilon_{xx}=\frac{du}{dx}-z\frac{d^2w_b}{dx^2}-f\frac{d^2w_s}{dx^2}\\ \varepsilon_{zz}=\frac{dg}{dz}w_z\\ \varepsilon_{xz}=\frac{1}{2}g\left(\frac{dw_s}{dx}+\frac{dw_z}{dx}\right)\end{cases} \tag{15}$$

Replacing equation (12) into (10) and (9) gives:

$$\begin{cases}\chi_{yz}=\chi_{zy}=-\frac{1}{4}\left(\frac{d^2f}{dz^2}\frac{dw_s}{dx}+\frac{dg}{dz}\frac{dw_z}{dx}\right)\\ \chi_{xy}=\chi_{yx}=-\frac{1}{4}\left(2\frac{d^2w_b}{dx^2}+\left(\frac{df}{dz}+1\right)\frac{d^2w_s}{dx^2}+g\frac{d^2w_z}{dx^2}\right)\end{cases} \tag{16}$$

Introducing equation (14) into (11) yields:

$$\begin{cases}H_x=\left(\cos\left(\frac{\pi}{h}z\right)\frac{d\zeta}{dx}\right)\\ H_z=\left(-\frac{\pi}{h}\sin\left(\frac{\pi z}{h}\right)\zeta-\frac{2}{h}\zeta_0\right)\\ E_x=\left(\cos\left(\frac{\pi}{h}z\right)\frac{d\gamma}{dx}\right)\\ E_z=\left(-\frac{\pi}{h}\sin\left(\frac{\pi z}{h}\right)\gamma-\frac{2}{h}\gamma_0\right)\end{cases} \tag{17}$$

Given Equations (8)-(11), the constitutive equation (2) is derived as follows:

$$\begin{cases} \{I_{1:6}\} = \int \mathrm{C}_{11}(1,z,f,zf,z^2,f^2)dzdy\,, \\ \{I_{8:10}\} = \int \mathrm{C}_{13}\frac{dg}{dz}(1,z,f)dz\,dy\,, \\ \{I_{12:14}\} = \int e_{31}\frac{\pi}{h}\sin\left(\frac{\pi z}{h}\right)(1,z,f)dz\,dy \\ \{I_{18:19}\} = \int g\frac{\pi}{h}\cos\left(\frac{\pi z}{h}\right)(e_{15},q_{15})dz\,dy \\ \{I_{22:24}\} = \int \left(\frac{\pi}{h}\cos\left(\frac{\pi z}{h}\right)\right)^2(s_{11},\mu_{11},d_{11})dz\,dy \\ \{I_7\} = \int \mathrm{C}_{33}\left(\frac{dg}{dz}\right)^2 dzdy\,, \{I_{11}\} = \int C_{55}g^2dz\,dy \\ \{I_{15:17}\} = \int q_{31}\frac{\pi}{h}\sin\left(\frac{\pi z}{h}\right)(1,z,f)dz\,dy \\ \{I_{20:21}\} = \int \frac{dg}{dz}\frac{\pi}{h}\sin\left(\frac{\pi z}{h}\right)(e_{33},q_{33})dz\,dy \\ \{I_{25:27}\} = \int \left(\frac{\pi}{h}\sin\left(\frac{\pi z}{h}\right)\right)^2(s_{33},\mu_{33},d_{33})dz\,dy \end{cases} \tag{18}$$

$$\begin{cases} \{D_{1:3}\} = \int \frac{1}{4}A_{44}\left(\left(\frac{d^2f}{dz^2}\right)^2, \left(\frac{dg}{dz}\right)^2, \frac{d^2f}{dz^2}\frac{dg}{dz}\right)dzdy \\ \{D_{4:9}\} = \int \frac{1}{4}A_{66}\left(1, \left(\frac{df}{dz}+1\right), g, g\left(\frac{df}{dz}+1\right), \left(\frac{df}{dz}+1\right)^2, g^2\right)dzdy \end{cases} \tag{19}$$

$$\begin{aligned} U = \frac{1}{2}\int_0^l \Bigg(& I_1\left(\frac{du}{dx}\right)^2 - 2I_2\frac{du}{dx}\frac{d^2w_b}{dx^2} - 2I_3\frac{du}{dx}\frac{d^2w_s}{dx^2} + \\ & 2I_4\frac{d^2w_b}{dx^2}\frac{d^2w_s}{dx^2} + I_5\left(\frac{d^2w_b}{dx^2}\right)^2 + I_6\left(\frac{d^2w_s}{dx^2}\right)^2 + I_7{w_z}^2 + \\ & 2I_8\frac{du}{dx}w_z - 2I_9\frac{d^2w_b}{dx^2}w_z - 2I_{10}\frac{d^2w_s}{dx^2}w_z + I_{11}\left(\left(\frac{dw_s}{dx}\right)^2 + \right. \\ & \left.\left(\frac{dw_z}{dx}\right)^2 + 2\frac{dw_s}{dx}\frac{dw_z}{dx}\right) + 2I_{12}\frac{du}{dx}\gamma - 2I_{13}\frac{d^2w_b}{dx^2}\gamma - \\ & 2I_{14}\frac{d^2w_s}{dx^2}\gamma + 2I_{15}\frac{du}{dx}\zeta - 2I_{16}\frac{d^2w_b}{dx^2}\zeta - 2I_{17}\frac{d^2w_s}{dx^2}\zeta - \\ & 2I_{18}\left(\frac{dw_s}{dx}\frac{d\gamma}{dx} - \frac{dw_z}{dx}\frac{d\gamma}{dx}\right) - 2I_{19}\left(\frac{dw_s}{dx}\frac{d\zeta}{dx} - \frac{dw_z}{dx}\frac{d\zeta}{dx}\right) + \\ & 2I_{20}w_z\gamma + 2I_{21}w_z\zeta - I_{22}\left(\frac{d\gamma}{dx}\right)^2 - I_{23}\left(\frac{d\zeta}{dx}\right)^2 - 2I_{24}\frac{d\zeta}{dx}\frac{d\gamma}{dx} - \\ & I_{25}\gamma^2 - I_{26}\zeta^2 - 2I_{27}\gamma\zeta + D_1\left(\frac{dw_s}{dx}\right)^2 + D_2\left(\frac{dw_z}{dx}\right)^2 + \\ & 2D_3\frac{dw_s}{dx}\frac{dw_z}{dx} + 4D_4\left(\frac{d^2w_b}{dx^2}\right)^2 + 4D_5\frac{d^2w_b}{dx^2}\frac{d^2w_s}{dx^2} + \\ & 4D_6\frac{d^2w_b}{dx^2}\frac{d^2w_z}{dx^2} + 2D_7\frac{d^2w_s}{dx^2}\frac{d^2w_z}{dx^2} + D_8\left(\frac{d^2w_s}{dx^2}\right)^2 + \\ & D_9\left(\frac{d^2w_z}{dx^2}\right)^2\Bigg)dx \end{aligned} \tag{20}$$

The Kinetic Energy can be written as:

$$\begin{aligned} T = \frac{1}{2}\int_0^l \Bigg[& J_1\left(\dot{u}^2 + {\dot{w}_b}^2 + {\dot{w}_s}^2 + 2\dot{w}_b\dot{w}_s\right) - 2J_2\dot{u}\frac{d\dot{w}_b}{dx} - \\ & 2J_3\dot{u}\frac{d\dot{w}_s}{dx} + 2J_4\frac{d\dot{w}_b}{dx}\frac{d\dot{w}_s}{dx} + J_5\left(\frac{d\dot{w}_b}{dx}\right)^2 + J_6\left(\frac{d\dot{w}_s}{dx}\right)^2 + J_7{\dot{w}_z}^2 + \\ & 2J_8\left(\dot{w}_b\dot{w}_z + \dot{w}_s\dot{w}_z\right)\Bigg]dx \end{aligned} \tag{21}$$

with:

$$\{J_1, J_2, J_3, J_4, J_5, J_6, J_7, J_8\} = \int \rho(1,z,f,zf,z^2,f^2,g^2,g)dz\,dy \tag{22}$$

Furthermore, the virtual work performed by the applied loades acting on the current quasi-3D microbeam can be written as:

$$\int_0^L \left[q_0\left(w_b(x,t) + w_s(x,t) + g(z)w_z(x,t)\right)\right]dx \tag{23}$$

3. DQ-FEM

This approach combines the “generalized differential quadrature method” (GDQM) with the traditional finite element method (FEM).

In order to simulate our beam, we assume that the shape functions take the following form: [49]

$$q[x] = \sum_{i=1}^{N} L_i(x)q_i \tag{24}$$

With $\mathrm{L_i}$ is the Lagrange polynomial, $\mathrm{q_i} = \mathrm{q(x_i)}$, $q = u, \mathrm{w_b}, \mathrm{w_s}, \mathrm{w_z}, \gamma, \zeta$ are the displacements the spatial variations of the electric potential and $\zeta_i = \zeta(\mathrm{x_i})$ the spatial variations of the magnetic potential of the Gauss Lobato quadrature points where the nodal displacements DQ of the finite element of the beam.

The derivative of order n at a discrete point $\mathrm{x_i}$ of a field variable f (x) is expressed by”: [49]

$$\left.\frac{\partial^n F(x,t)}{\partial x^n}\right|_{x_i} = \sum_{j=1}^{N} A_{ij}^{(n)} F(x_j,t) \quad (i = 1,2,3,\ldots\ldots,N) \tag{25}$$

Where $\mathrm{A_{ij}^{(n)}}$ is the weighting coefficient, which is related to the derivative of order n. “The Gaussian - Lobato quadrature rule with a degree of precision (2n-3) for the function F(x) defined in the interval [-1, 1] is:” [49]

$$\int_{-1}^{1} F(x)dx = \sum_{j=1}^{N} C_j F(x_j) \tag{26}$$

$\mathrm{C_j}$ is the weighting coefficient of Gauss-Lobatto integration: [58]

$$C_1 = C_N = \frac{2}{N(N-1)},$$

$$C_j = \frac{2}{N(N-1)[P_{N-1}(x_j)]^2} \quad (j \neq 1, N) \tag{27}$$

$\mathrm{x_j}$ represents the (j-1) zero of the first derivative of Legendre polynomials $\mathrm{P_{N-1}(x)}$. To achieve rapid convergence and high accuracy, a denser population near the boundaries is essential. Sampling points are selected based on the distribution of the grid of Gauss-Lobato nodes.

$$x_j = -\cos\left(\frac{j-1}{N-1}\pi\right) \tag{28}$$

Gauss-Lobatto nodes are determined using the Newton-Raphson iteration method. The relationship between u and $\bar{u}$, as well as , w and $\bar{w}$, is established according to rule DQ.

$$u = Q\bar{u},\quad w_b = Q\bar{w}_b,\ w_s = Q\bar{w}_s,\ \gamma = Q\bar{\gamma},\ \zeta = Q\bar{\zeta} \tag{29}$$

where

$$Q = \begin{bmatrix} 1 & 0 & 0 & \cdots & 0 & 0 \\ A_{1,1}^{(1)} & A_{1,2}^{(1)} & A_{1,3}^{(1)} & \cdots & A_{1,N-1}^{(1)} & A_{1,N}^{(1)} \\ 0 & 0 & 1 & \cdots & 0 & 0 \\ \vdots & \vdots & \vdots & \ddots & \vdots & \vdots \\ 0 & 0 & 0 & \cdots & 0 & 1 \\ A_{N,1}^{(1)} & A_{N,2}^{(1)} & A_{N,3}^{(1)} & \cdots & A_{N,N-1}^{(1)} & A_{N,N}^{(1)} \end{bmatrix} \tag{30}$$

Utilizing the DQ-FEM, the principles of motion are derived by substituting equations (24-30) into the energy equations (18, 21). Subsequently, by substituting the resulting expressions and applying Lagrange’s principle, the following system of equations is obtained. The elementary mass and stiffness matrixs and external loads vector derived using DQ-FEM.

$$[M^e]=\begin{bmatrix} [M^e]_{11} & [M^e]_{12} & [M^e]_{13} & [0] & [0] & [0] \\ & [M^e]_{22} & [M^e]_{23} & [M^e]_{24} & [0] & [0] \\ & & [M^e]_{33} & [M^e]_{34} & [0] & [0] \\ & & & [M^e]_{44} & [0] & [0] \\ & & & & [0] & [0] \\ sym & & & & & [0] \end{bmatrix} \quad (31)$$

$$[K^e]=\begin{bmatrix} [K^e]_{11} & [K^e]_{12} & [K^e]_{13} & [K^e]_{14} & [K^e]_{15} & [K^e]_{16} \\ & [K^e]_{22} & [K^e]_{23} & [K^e]_{24} & [K^e]_{25} & [K^e]_{26} \\ & & [K^e]_{33} & [K^e]_{34} & [K^e]_{35} & [K^e]_{36} \\ & & & [K^e]_{44} & [K^e]_{45} & [K^e]_{46} \\ sym & & & & [K^e]_{55} & [K^e]_{56} \\ & & & & & [K^e]_{66} \end{bmatrix} \quad (32)$$

$$[F]=\begin{Bmatrix} [0] \\ [F^e]_{22} \\ [F^e]_{33} \\ [F^e]_{44} \\ [0] \\ [0] \end{Bmatrix} \quad (33)$$

Hence the components of the elementary stiffness matrice and mass matrix are detailed in the appendix. The “matrices for the whole system are derived applying the MEF principles for constructing elementary matrices,

$$([K]-\omega^2[M])(\bar{u} \quad \bar{w}_b \quad \bar{w}_s \quad \bar{w}_z \quad \bar{\gamma} \quad \bar{\zeta})^{\mathrm{T}}=\{\mathrm{F}\} \quad (34)$$

Since the Differential Quadrature Finite Element Method (DQFEM) follows a similar approach to the Finite Element Method (FEM), the electrical and magnetic boundary conditions are applied in the same manner as the displacement boundary conditions. Specifically, for clamped (C), simply supported (S), and free (F) beams, the electric and magnetic boundary conditions. At clamped and simply supported ends the electrical potential $\gamma=0$ and also the magnitic potential $\zeta=0$.

In the Differential Quadrature Finite Element Method (DQFEM), boundary conditions are imposed by modifying the elementary matrices through the elimination of specific rows and columns associated with the constrained generalized coordinates. For the Simply Supported Case: The first and penultimate rows and columns are eliminated from the elementary matrices to enforce the boundary conditions. This ensures that the displacement at the supports is constrained while allowing rotation. For Clamped (Fixed) Case: The first, second, penultimate, and last rows and columns are eliminated. This fully constrains both displacement and rotational degrees of freedom, ensuring a rigid connection at the clamped boundary. This approach effectively reduces the system's degrees of freedom, ensuring that the boundary conditions are properly enforced in the numerical model while maintaining accuracy and stability in the solution process.

Numerical results and validation

In this work, the $\mathrm{BaTiO_3}-\mathrm{CoFe_2O_4}$ [12, 15, 59] is chosen as inner core material (Table 1). For the upper and bottom outer surfaces, epoxy [60] is used, from which this mixture is controlled by the power law of FG materials in equation (1). The physical characteristics of these materials are listed in Table 1. A uniform continuous load $q_0=1/2000h\ N/m$ is applied along the microbeam along the Oz axis. In the first step, a comparison with literature works is made, where the model used is a simply supported (S-S) microbeam assumed to be composed of 50%-50% $\mathrm{BaTiO_3}-\mathrm{CoFe_2O_4}$ [12]. The shape cross section is taken as $b=2h$ and $L=20h$, and $h=14.42\ \mu m$. In the second step, a parametrical study is elaborated to observe the behavior of the static bending and the free vibration with different geometrical parameters, and various upper and bottom outer surfaces materials.

The units in table 1 are as follow: the piezoelectric constants are given in $e_{ij}\ (C/m^2)$, the dielectric constants are given in $s_{ij}(10^{-9}C^2/(N.m^2))$, the piezomagnetic constants are given in $q_{ij}(N/(A.m))$, the magnetoelectric constants are given in $d_{ij}(10^{-12}Ns/(V.C))$, the magnetic constants are given in $\mu_{ij}(10^{-6}Ns^2/C^2)$, and the density is given in $\rho(kg/m^3)$. The material length scale parameter is given in $l\ (\mu m)$.

To validate our model, we computed the semi-analytical model presented in reference [12] and compared it with our method. As shown in Figures 2-4, the results of our current model closely align in midspan with the semi-analytical results from [12]. Our model give the exact shape of the bending , electrical potential and magnetic potential, on the other hand the literature semi analytical model give only the sinusoidal midspan value shape. This comparison supports the validity of the existing model and demonstrates that the DQFEM, in conjunction with the refined high-order beam theory, provides more accurate results at all locations, in contrast to analytical methods, which only provide data at the midline. Table 2 presents a comparison of the first and second frequencies, as well as the midspan deflection, electric potential, and magnetic potential. The results in Table 2 further confirm the effectiveness and validity of our model.

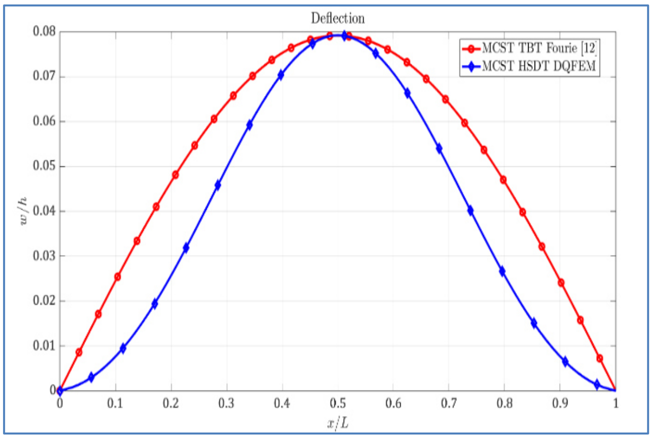

Fig. 2. Comparative analysis of the bending of a doubly S-S microbeam exposed to an even distribution of load

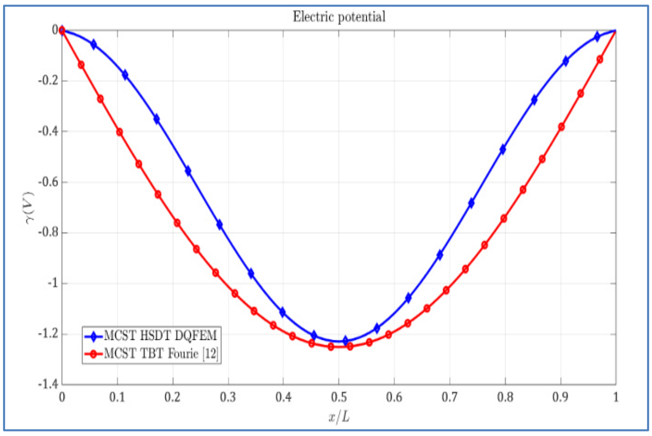

Fig. 3. Comparative analysis of electrical potential of a doubly S-S microbeam exposed to an even distribution of load

DOI 10.2478/ama-2025-0041

Tab. 1. Materials Properties of the mixture ($\mathrm{BaTiO_3-CoFe_2O_4}$)

	$\mathbf{BaTiO_3-CoFe_2O_4}$							**epoxy**
	0%-100%	**20%-80%**	**40%-60%**	**50%-50%**	**60%-40%**	**80%-20%**	**100%-0%**	
C_{11}	286	262	238	226	214	190	166	4.889
C_{13}	170	151.6	133.2	124	114.8	96.4	78	2.407
C_{33}	269.5	248	226.5	215.75	205	183.5	162	4.889
C_{55}	45.3	44.84	44.38	44.15	43.92	43.46	43	1.241
q_{31}	580.3	464.24	348.18	290.15	232.12	116.06	0	0
q_{33}	699.7	559.76	419.82	349.85	279.88	139.94	0	0
q_{15}	550	440	330	275	220	110	0	0
e_{31}	0	-0.88	-1.76	-2.2	-2.64	-3.52	-4.4	0
e_{33}	0	3.72	7.44	9.3	11.16	14.88	18.6	0
e_{15}	0	2.32	4.64	5.8	6.96	9.28	11.6	0
s_{11}	0.08	2.3	4.53	5.64	6.75	8.98	11.2	0
s_{33}	0.093	2.59	5.10	6.35	7.6	10.10	12.6	0
d_{11}	0	2.6	4.58	5.38	6.02	7.04	0	0
d_{33}	0	2020	2760	2740	2520	1550	0	0
μ_{11}	590	473	356	297.5	239	122	5	0
μ_{33}	157	127.6	98	83.5	68.8	39.4	10	0
ρ	5300	5400	5500	5550	5600	5700	5800	1180
$MLSP\ \ l$	7.33	7.29	7.24	7.21	7.18	7.10	7	16.93

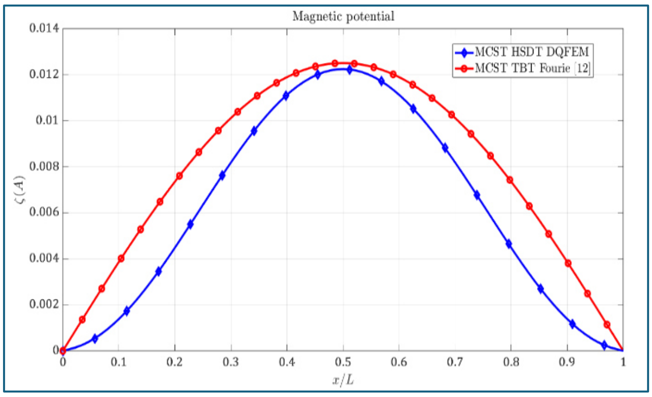

Fig. 4. Comparative analysis of magnetic potential of a doubly S-S microbeam exposed to an even distribution of load

Tab. 2. Comparison of numerical results ($b = 2h, L = 20h$), 50%-50% $\mathrm{BaTiO_3-CoFe_2O_4}$

$h(\mu m)$	Frequency (MHz)					
	1st mode		2nd mode		3rd mode	
	[12]	present	[12]	present	[12]	present
14.42	4.097	4.069	16.811	16.228	39.647	34.853
28.84	1.710	1.701	7.007	6.784	16.466	14.796

$h(\mu m)$	Midspan Deflection w/h		Midspan Electric potential $\gamma(V)$		Midspan Magnetic potential $\zeta(A)$	
	[12]	present	[12]	present	[12]	present
14.42	0.0792	0.0793	-1.251	-1.229	0.0125	0.0122
28.84	0.0284	0.0283	-0.896	-0.877	0.0090	0.0087

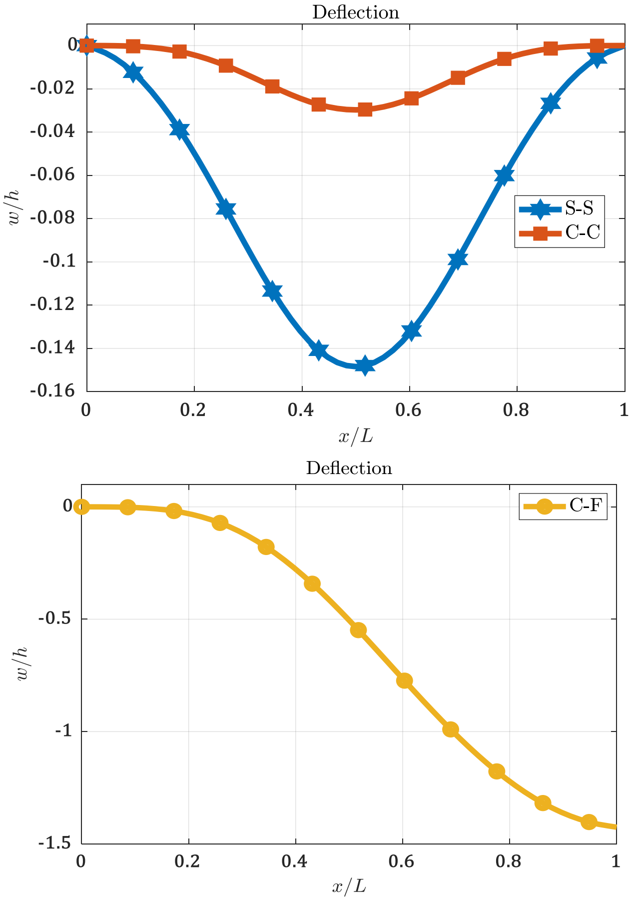

Fig. 5. Deflection of MEE bilaterally microbeam with various boundary conditions $\left(k_z = 1,\ h = 20\mu m,\ b = 2h,\ L = 20h,\ \mathrm{BaTiO_3(50\%)-CoFe_2O_4(50\%)}\right)$

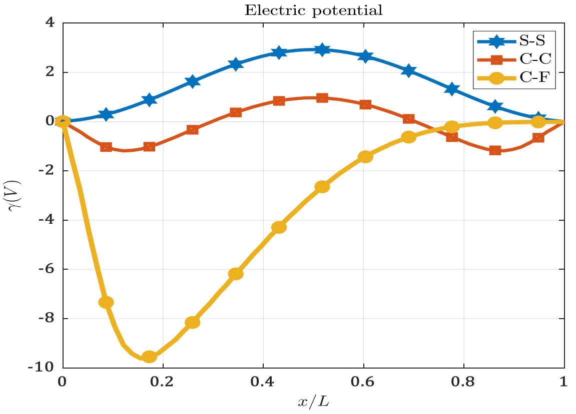

Fig. 6. Electric potential of MEE bilaterally microbeam with various boundary conditions $\left(k_z = 1,\ h = 20\mu m,\ b = 2h,\ L = 20h,\ \mathrm{BaTiO_3(50\%) - CoFe_2O_4(50\%)}\right)$

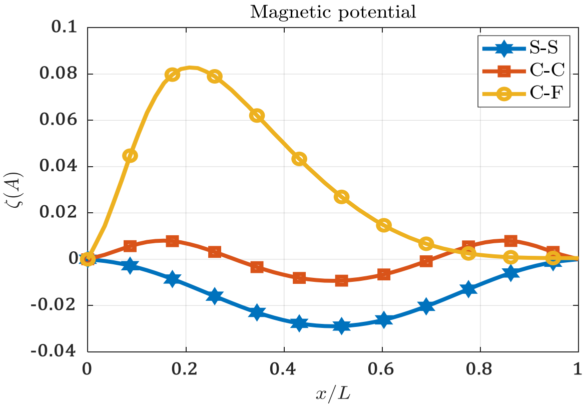

Fig. 7. Magnetic potential of MEE bilaterally microbeam with various boundary conditions $\left(k_z = 1,\ h = 20\mu m,\ b = 2h,\ L = 20h,\ \mathrm{BaTiO_3(50\%) - CoFe_2O_4(50\%)}\right)$

In Figure 5, we demonstrated the bending response of the magneto-electro-elastic (MEE) bilaterally supported microbeam under different boundary conditions (simply supported, clamped, and clamped-free). The observed variations in deflection arise due to differences in constraint stiffness. The simply supported beam experiences the highest deflection as it lacks rotational constraints at the ends, whereas the clamped beam exhibits reduced deflection due to restricted end rotations.

The clamped-free (cantilever) configuration shows the highest deflection at the free end due to the absence of support at one end. This deflection pattern influences the distribution of electric and magnetic potentials along the beam length, as illustrated in Figures 6 and 7.

The electromechanical coupling in the system arises due to the piezoelectric and piezomagnetic effects. When the beam undergoes bending, the induced strain leads to charge polarization. The regions experiencing compression generate a positive electric charge (due to the direct piezoelectric effect) and a negative magnetic charge (due to the piezomagnetic effect), whereas the tensioned regions exhibit the opposite effect.

This explains why, in the simply supported case, the electric potential (V) is uniformly positive (Figures 6), while in the clamped-free case, it is uniformly negative. The clamped configuration results in a more complex charge distribution due to localized constraint effects at the boundaries.

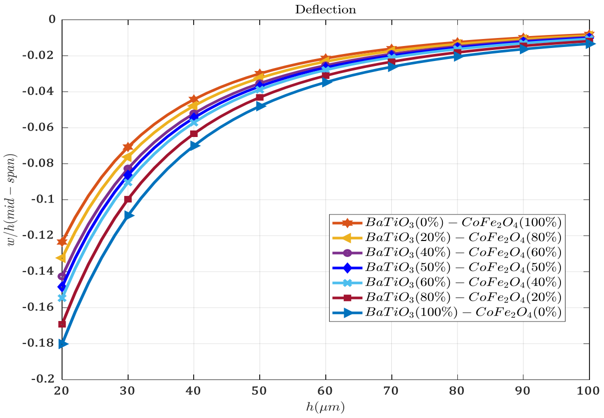

Fig. 8. Simply supported microbeam midspan deflection with various thickness and MEE inner material mixture percentage $\mathrm{BaTiO_3 - CoFe_2O_4}$ $(k_z = 1,\ b = 2h,\ L = 20h,)$

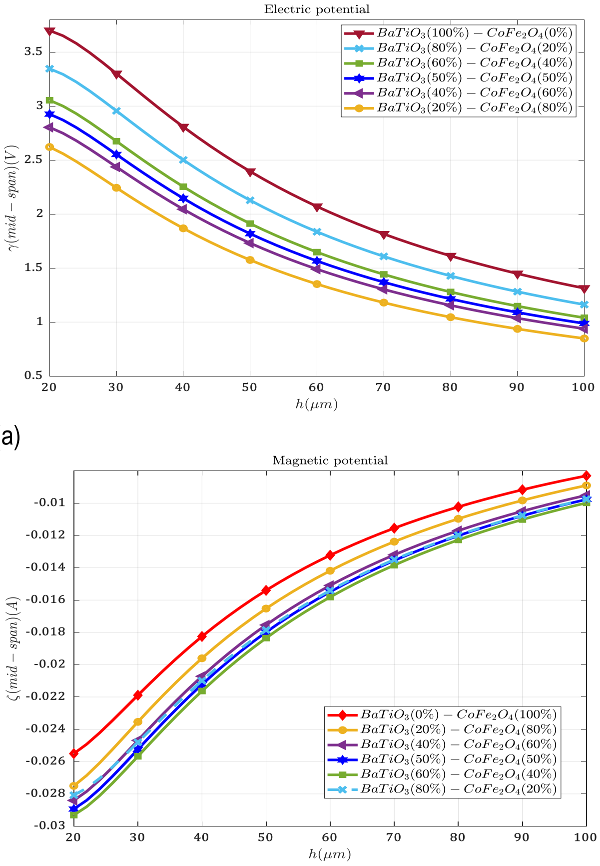

(a)

(b)

Fig. 9. Electric (a) and magnetic (b) potentials at simply supported microbeam midspan with various thickness and MEE inner material mixture percentage $\mathrm{BaTiO_3 - CoFe_2O_4}$ $(k_z = 1,\ b = 2h,\ L = 20h,)$

Figures 8 and 9 illustrate the midspan deflection, electric potential, and magnetic potential as functions of beam thickness and inner material composition. The inverse relationship between thickness and deflection is expected, as thicker beams possess higher flexural rigidity, making them more resistant to deformation under the same applied load. Regarding electromechanical behavior, increasing the proportion of $\mathrm{BaTiO_3}$ enhances the piezoelectric response, leading to higher electric potential generation. This occurs because $\mathrm{BaTiO_3}$ is a piezoelectric ceramic with a high electromechanical coupling coefficient, meaning it efficiently converts mechanical deformation into electrical energy. Conversely, $\mathrm{CoFe_2O_4}$ exhibits strong piezomagnetic properties, leading to higher magnetic potential generation. However, as the beam thickness increases, both electric and magnetic potentials decrease because strain distribution becomes more uniform, reducing localized stress concentrations that drive charge generation. This behavior aligns with the fundamental principles of piezoelectric and piezomagnetic materials, where mechanical strain directly affects charge separation and potential generation.

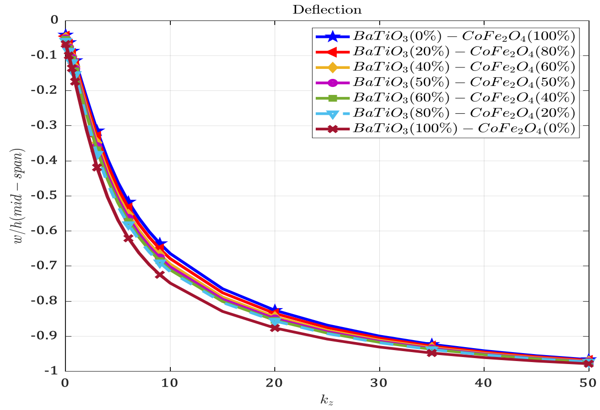

Fig. 10. Simply supported microbeam midspan deflection with various FG fraction index and MEE inner material mixture percentage $\mathrm{BaTiO_3-CoFe_2O_4}$ $(h=20\mu m,\ b=2h,\ L=20h,)$

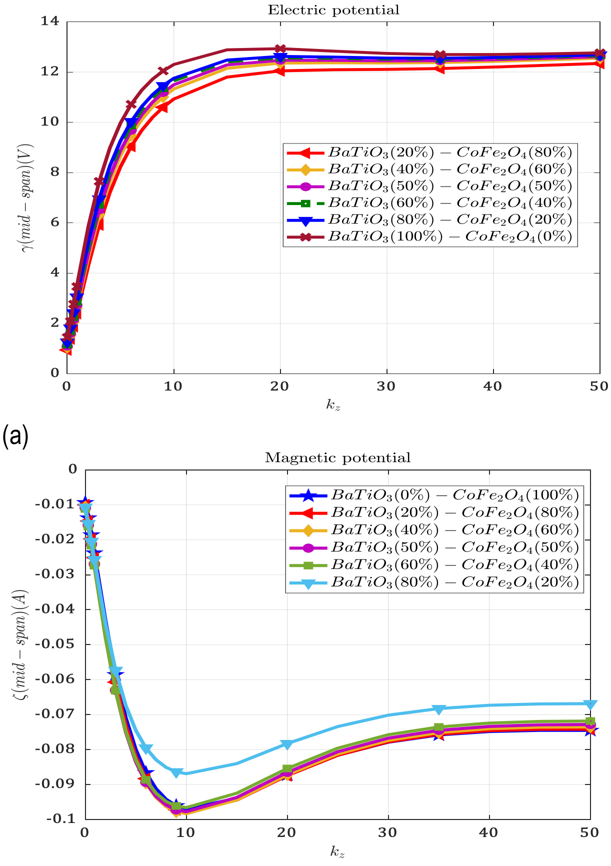

(a)

(b)

Fig. 11. Electric (a) and magnetic (b) potentials at simply supported microbeam midspan with various FG fraction index and MEE inner material mixture percentage $\mathrm{BaTiO_3-CoFe_2O_4}$ $(h=20\mu m,\ b=2h,\ L=20h,)$

Figures 10 and 11 depict the influence of the functionally graded (FG) material gradation index on the midspan deflection and electromechanical potentials. As the gradation index k_z increases, the beam composition transitions from a fully magneto-electro-elastic core $(\mathrm{BaTiO_3-CoFe_2O_4})$ to an outer epoxy-rich composition. Given that epoxy is significantly more flexible and less dense than the ceramic phases, the beam exhibits increased deflection due to reduced overall stiffness.

The electrical and magnetic potentials initially increase with the FG index, peaking at a critical range $(k_z=[6{:}\,20])$, before stabilizing. This behavior suggests that an optimal material gradation exists where electromechanical efficiency is maximized. The increasing deflection enhances charge generation up to a certain threshold, beyond which further material gradation reduces effective coupling due to the dominance of the epoxy phase. This insight is crucial for optimizing FG microbeam designs to balance mechanical flexibility and electromechanical efficiency.

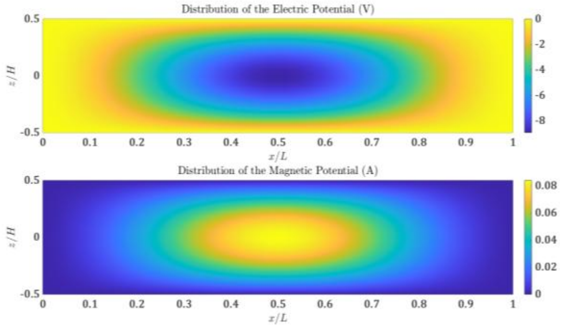

Fig. 12. Electric and magnetic potentials distribution of simply supported microbeam with $k_z=5,\ h=20\mu m,\ b=2h,$ $L=20h,\ \mathrm{BaTiO_3(50\%)-CoFe_2O_4(50\%)}$

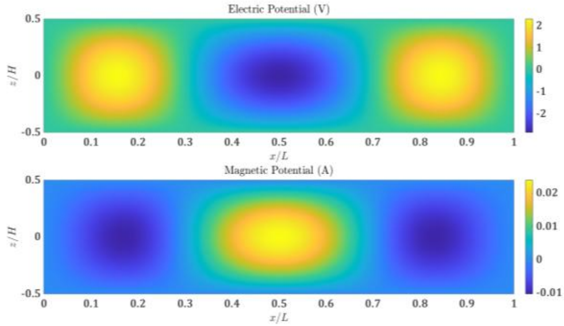

Fig. 13. Electric and magnetic potentials distribution of clamped microbeam with $k_z=5,\ h=20\mu m,\ b=2h,\ L=20h,$ $\mathrm{BaTiO_3(50\%)-CoFe_2O_4(50\%)}$

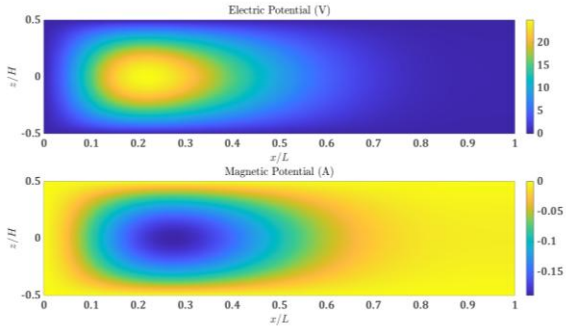

Fig. 14. Electric and magnetic potentials distribution of clamped free microbeam with $k_z=5,\ h=20\mu m,\ b=2h,\ L=20h,$ $\mathrm{BaTiO_3(50\%)-CoFe_2O_4(50\%)}$

Figures 12-14 illustrate the distribution of electric and magnetic potentials across the xOz surface of a magneto-electro-elastic microbeam under different boundary conditions: simply supported (Figure 12), clamped (Figure 13), and clamped-free (Figure 14).

It is evident that the electric and magnetic potential distributions for the simply supported (Figure 12) and clamped (Figure 13) beams exhibit central symmetry.

For the simply supported beam, the maximum values of both electric and magnetic potentials occur at the center. In contrast, for the clamped beam, the highest potentials are found at three locations: near the embedding points and in the center.

In the case of the clamped-free beam, the electric and magnetic potentials are primarily concentrated near the embedding location. In conclusion, the high values of electric and magnetic potentials correspond to areas where bending-induced deformations are most significant.

Figures 15-18 presents the variations in deflection, electrical potential, magnetic potential, and natural frequency respectively for different microbeam thicknesses, considering the length-to-thickness ratio in both the current (MCST) and classical models.

With $\mathrm{BaTiO_3(50\%) - CoFe_2O_4(50\%)}$. In the numerical analysis, the current model accounts for the couple stress effect, which is incorporated using the Modified Length Scale Parameter (MLSP) $l \neq 0$ (as defined in Equation (7)).

Conversely, the classical model is derived using the same governing equation but with $l = 0$, meaning that it does not consider the microstructural effects introduced by MCST.

The results indicate that the deflection, electrical potential, and magnetic potential predicted by the current model are consistently lower than those obtained using the classical model across all tested cases.

This discrepancy arises due to the inclusion of the couple stress effect in the MCST model, which introduces additional material stiffness at the microscale. As expected, the difference between the two models becomes more pronounced as the microbeam thickness decreases.

This behavior is due to the fact that size-dependent effects become more significant at smaller scales, where the influence of microstructural mechanics cannot be neglected.

In other words, the classical model, which disregards these effects, tends to overestimate the response of the microbeam in comparison to the MCST-based model.

The increasing stiffness introduced by the couple stress theory results in reduced deflection and altered electrical/magnetic responses, as well as higher natural frequencies.

Additionally, it is observed that as the length-to-thickness ratio increases, the microbeam becomes more flexible, leading to a greater deflection. This increase in deflection consequently enhances both the electrical and magnetic potentials.

On the other hand, the natural frequencies exhibit an inverse relationship with the length-to-thickness ratio, decreasing as the microbeam becomes thinner.

This trend is attributed to the reduced stiffness associated with higher length-to-thickness ratios, which lowers the beam's resistance to dynamic vibrations.

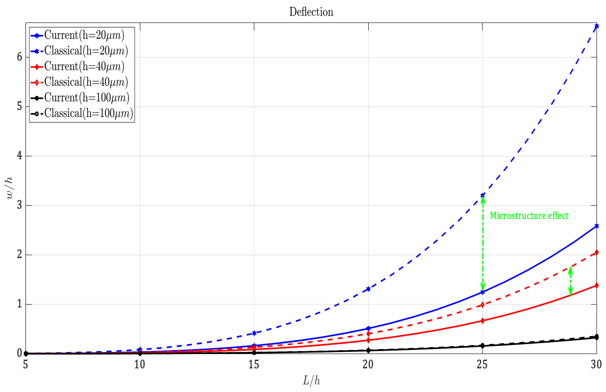

Fig. 15. Deflection with respect to length-thickness ratio of simply supported microbeam with $k_z = 5, b = 2h$

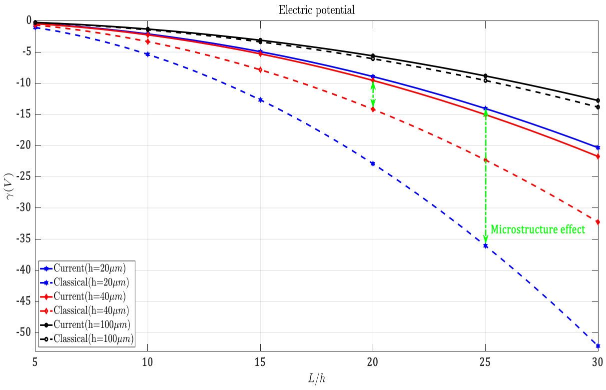

Fig. 16. Electric potential with respect to length-thickness ratio of simply supported microbeam with $k_z = 5, b = 2h$

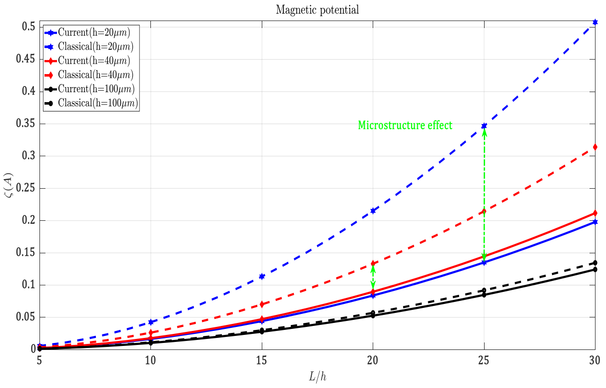

Fig. 17. Magnetic potential with respect to length-thickness ratio of simply supported microbeam with $k_z = 5, b = 2h$

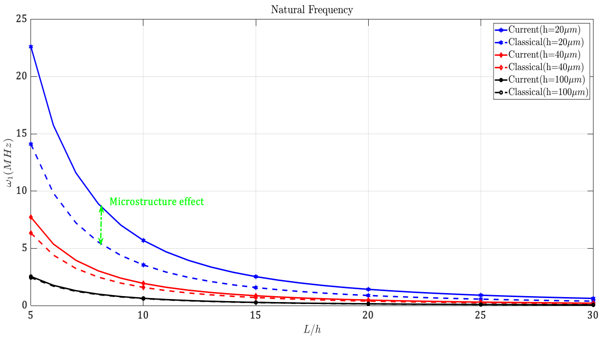

Fig. 18. Natural frequencies with respect to length-thickness ratio of simply supported microbeam with $k_z = 5, b = 2h$

DOI 10.2478/ama-2025-0041

Tab. 3. Natural frequency (MHz) of simply supported MEE FG microbeam ($(b = 2h,\ L = 20h,)$)

		$\mathbf{BaTiO_3 - CoFe_2O_4}$						
$h(\mu m)$	k_z	**0%-100%**	**20%-80%**	**40%-60%**	**50%-50%**	**60%-40%**	**80%-20%**	**100%-0%**
20	0	3.0009	2.8571	2.7108	2.6363	2.5613	2.4071	2.2472
	0.5	2.5250	2.4124	2.2975	2.2391	2.1802	2.0589	1.9332
	1	2.2200	2.1283	2.0348	1.9872	1.9393	1.8404	1.7380
	5	1.5182	1.4840	1.4491	1.4313	1.4135	1.3766	1.3386
	10	1.3919	1.3731	1.3539	1.3441	1.3344	1.3141	1.2932
	15	1.3538	1.3411	1.3282	1.3216	1.3150	1.3013	1.2872
	20	1.3352	1.3260	1.3166	1.3118	1.3070	1.2970	1.2867
40	0	1.3578	1.2891	1.2191	1.1836	1.1476	1.0739	0.9974
	0.5	1.0979	1.0449	0.9909	0.9634	0.9356	0.8786	0.8194
	1	0.9270	0.8847	0.8415	0.8196	0.7973	0.7518	0.7045
	5	0.5204	0.5078	0.4950	0.4885	0.4820	0.4687	0.4550
	10	0.4603	0.4548	0.4492	0.4464	0.4436	0.4378	0.4318
	15	0.4502	0.4469	0.4435	0.4418	0.4401	0.4366	0.4330
	20	0.4481	0.4458	0.4435	0.4423	0.4411	0.4387	0.4362
100	0	0.5260	0.4989	0.4713	0.4572	0.4430	0.4139	0.3836
	0.5	0.4189	0.3980	0.3768	0.3660	0.3550	0.3326	0.3092
	1	0.3475	0.3310	0.3141	0.3055	0.2968	0.2789	0.2604
	5	0.1722	0.1677	0.1633	0.1610	0.1587	0.1541	0.1494
	10	0.1473	0.1458	0.1442	0.1434	0.1427	0.1411	0.1395
	15	0.1449	0.1441	0.1433	0.1429	0.1425	0.1417	0.1408
	20	0.1455	0.1450	0.1445	0.1442	0.1440	0.1434	0.1429

Table 3 shows the natural frequencies of a simply supported magneto-electro functionally graded microbeam made of $\mathrm{BaTiO_3 - CoFe_2O_4}$ and epoxy composite material. Here, natural frequencies are influenced by the thickness $h(\mu m)$ and the power-law compositional gradient index k_z, with different percentages of $\mathrm{BaTiO_3}$ and $\mathrm{CoFe_2O_4}$. As the thickness $h(\mu m)$ increases from 20 µm to 100 µm, the natural frequencies decrease across all material distributions and power-law indices. This is expected as thicker beams generally have lower resonant frequencies due to increased mass and flexibility. The material $\mathrm{BaTiO_3 - CoFe_2O_4}$ distribution percentages (ranging from 0%-100% to 100%-0%) also impact the natural frequencies. Generally, as the proportion of $\mathrm{BaTiO_3}$ increases, the natural frequency decreases. For instance, at $h = 20\mu m$ and $k_z = 0$, the natural frequency changes from 3.0009 MHz (0%-100%) to 2.2472 MHz (100%-0%). This suggests that a higher content of $\mathrm{BaTiO_3}$ (0%-100%) corresponds to higher stiffness and thus higher natural frequency, while increasing $\mathrm{CoFe_2O_4}$ content (100%-0%) reduces the stiffness, lowering the natural frequency. For each thickness $h(\mu m)$, as k_z increases from 0 to 20, there is a notable decline in natural frequency, regardless of the $\mathrm{BaTiO_3 - CoFe_2O_4}$ distribution. For instance, at $h = 20\mu m$, with a 0%-100% distribution, natural frequency decreases from 3.0009 MHz at $k_z = 0$ to 1.3352 MHz at $k_z = 20$. Higher k_z values indicate a more percentage of epoxy in material gradation composition, which lowers stiffness and thus reduces the natural frequency. In summary, increasing thickness h, higher content of $\mathrm{CoFe_2O_4}$, and larger power-law index k_z all contribute to lower natural frequencies. These parameters offer tunability in the design of microbeam resonators by adjusting stiffness through material composition and geometric factors.

4. CONCLUSION

In this study, we investigated the static bending and free vibration behavior of a bilaterally coated magneto-electro-elastic (MEE) microbeam using a quasi-3D high-order beam theory in conjunction with the Differential Quadrature Finite Element Method (DQ-FEM). The incorporation of the modified couple stress theory (MCST) effectively accounted for the microstructural effects within the beam. Our model, validated against existing literature, demonstrated a high degree of accuracy in predicting both the deflection and vibrational behavior of the microbeam under various loading and boundary conditions.

Beam thickness plays a significant role in reducing both mid-span deflection and the magnitudes of electric and magnetic potentials, as thicker beams are stiffer and resist deformation.

Material composition influences the beam's response significantly. Higher proportions of $\mathrm{BaTiO_3}$ increase the piezoelectric effect, enhancing both deflection and electric potential, while increased $\mathrm{CoFe_2O_4}$ improves the magnetostrictive response, raising the magnetic potential.

Material gradation affects the mechanical and electromechanical responses, with optimized combinations of $\mathrm{BaTiO_3 - CoFe_2O_4}$ and epoxy producing the highest electric and magnetic potentials.

Natural frequency decreases with both increasing beam thickness and the gradation index, indicating that the mechanical and vibrational properties are highly sensitive to material distribution.

These results highlight the importance of beam geometry and material composition in the design and optimization of MEE microbeams for applications that require precise control of mechanical, electrical, and magnetic responses. The developed model and numerical approach provide a robust framework for further exploration of functionally graded materials in micro-scale systems.

A comparative analysis between the MCST-based model and the classical model revealed that the couple stress effect introduces additional material stiffness at the microscale, leading to consistently lower deflections and energy potentials in the current model. The discrepancy between the two models becomes more pronounced as beam thickness decreases, emphasizing the significance of size-dependent effects in micro-scale systems. The results also show that increasing the length-to-thickness ratio enhances deflection, thereby increasing both electrical and magnetic potentials. However, this increase in flexibility also leads to a reduction in natural frequencies due to the lower stiffness of thinner microbeams.

These results highlight the importance of beam geometry and material composition in the design and optimization of MEE microbeams for applications requiring precise control of mechanical, electrical, and magnetic responses. The developed model and numerical approach provide a robust framework for further exploration of functionally graded materials in micro-scale systems.

5. ANNEX

$$\begin{cases} [K^e]_{11} = I_1\left[Q^T {A^1}^T C A^1 Q\right] \quad [K^e]_{12} = -I_2\left[Q^T {A^1}^T C A^2 Q\right] \\ [K^e]_{13} = -I_3\left[Q^T {A^1}^T C A^2 Q\right] \quad [K^e]_{14} = I_8\left[Q^T {A^1}^T C Q\right] \\ [K^e]_{15} = I_{14}\left[Q^T {A^1}^T C Q\right] \quad [K^e]_{16} = I_{17}\left[Q^T {A^1}^T C Q\right] \\ [K^e]_{22} = (I_5 + 4D_4)\left[Q^T {A^2}^T C A^2 Q\right] \\ [K^e]_{23} = (I_4 + 2D_5)\left[Q^T {A^2}^T C A^2 Q\right] \\ [K^e]_{24} = -I_9\left[Q^T {A^2}^T C Q\right] + 2D_6\left[Q^T {A^2}^T C A^2 Q\right] \\ [K^e]_{25} = -I_{15}\left[Q^T {A^2}^T C Q\right] \\ [K^e]_{26} = -I_{18}\left[Q^T {A^2}^T C Q\right] \\ [K^e]_{33} = (I_6 + D_8)\left[Q^T {A^2}^T C A^2 Q\right] + (I_{11} + D_1)\left[Q^T {A^1}^T C A^1 Q\right] \\ [K^e]_{34} = -I_{10}\left[Q^T {A^2}^T C Q\right] + (I_{13} + D_3)\left[Q^T {A^1}^T C A^1 Q\right] + D_7\left[Q^T {A^2}^T C A^2 Q\right] \\ [K^e]_{35} = -I_{16}\left[Q^T {A^2}^T C Q\right] - I_{20}\left[Q^T {A^1}^T C A^1 Q\right] \\ [K^e]_{36} = -I_{19}\left[Q^T {A^2}^T C Q\right] - I_{21}\left[Q^T {A^1}^T C A^1 Q\right] \\ [K^e]_{44} = I_7[Q^T C Q] + (I_{12} + D_2)\left[Q^T {A^1}^T C A^1 Q\right] + D_9\left[Q^T {A^2}^T C A^2 Q\right] \\ [K^e]_{45} = -I_{22}\left[Q^T {A^1}^T C A^1 Q\right] + I_{24}[Q^T C Q] \\ [K^e]_{37} = -I_{23}\left[Q^T {A^1}^T C A^1 Q\right] + I_{25}[Q^T C Q] \\ [K^e]_{55} = -I_{26}\left[Q^T {A^1}^T C A^1 Q\right] - I_{29}[Q^T C Q] \\ [K^e]_{56} = -I_{28}\left[Q^T {A^1}^T C A^1 Q\right] - I_{31}[Q^T C Q] \\ [K^e]_{66} = -I_{27}\left[Q^T {A^1}^T C A^1 Q\right] - I_{30}[Q^T C Q] \end{cases} \tag{35}$$

$$\begin{cases} [M^e]_{11} = J_1[Q^T \bar{C} Q] \quad [M^e]_{12} = -J_2[Q^T \bar{C} \bar{A}^1 Q] \\ [M^e]_{13} = -J_3[Q^T \bar{C} \bar{A}^1 Q] \\ [M^e]_{22} = J_1[Q^T \bar{C} Q] + J_5[Q^T {\bar{A}^1}{}^T \bar{C} \bar{A}^1 Q] \\ [M^e]_{23} = J_1[Q^T \bar{C} Q] + J_4[Q^T {\bar{A}^1}{}^T \bar{C} \bar{A}^1 Q] \\ [M^e]_{24} = J_8[Q^T C Q] \\ [M^e]_{33} = J_1[Q^T \bar{C} Q] + J_6[Q^T {\bar{A}^1}{}^T \bar{C} \bar{A}^1 Q] \\ [M^e]_{34} = J_8[Q^T C Q] \\ [M^e]_{44} = J_7[Q^T C Q] \end{cases} \tag{36}$$

$$\begin{cases} [F^e]_{22} = q_0[Q^T \bar{C}] \\ [F^e]_{33} = q_0[Q^T \bar{C}] \\ [F^e]_{44} = q_0[Q^T \bar{C}] \end{cases} \tag{37}$$

All types of nodal arrangement for differentiation and quadrature reside inside the interval [-1, 1]. Consequently, to implement them in practice, the subsequent adjustments must be applied to the differential and quadrature matrices,

$$\bar{C} = \frac{l_e}{2} C, \quad \bar{A}^1 = \frac{2}{l_e} A^1, \quad \bar{A}^2 = \frac{4}{{l_e}^2} A^2 \tag{38}$$

Were l_e is the length of the microbeam element.

REFERENCES

1. Sahmani S, Aghdam MM. Nonlocal strain gradient shell model for axial buckling and postbuckling analysis of magneto-electro-elastic composite nanoshells. Composites Part B: Engineering. 2018;132:258-74. Available from: https://www.sciencedirect.com/science/article/pii/S1359836817312209.
2. Farajpour MR, Shahidi AR, Hadi A, Farajpour A. Influence of initial edge displacement on the nonlinear vibration, electrical and magnetic instabilities of magneto-electro-elastic nanofilms. Mechanics of Advanced Materials and Structures. 2019;26(17):1469-81. Available from: https://doi.org/10.1080/15376494.2018.1432820
3. Yakhno VG. An explicit formula for modeling wave propagation in magneto-electro-elastic materials. Journal of Electromagnetic Waves and Applications. 2018;32(7):899-912. Available from: https://doi.org/10.1080/09205071.2017.1410076
4. Haghgoo M, Hassanzadeh-Aghdam M-K, Ansari R. Effect of piezoelectric interphase on the effective magneto-electro-elastic properties of three-phase smart composites: A micromechanical study. Mechanics of Advanced Materials and Structures. 2019;26(23):1935-50. Available from: https://doi.org/10.1080/15376494.2018.1455932
5. Chen W, Yan Z, Wang L. On mechanics of functionally graded hard-magnetic soft beams. International Journal of Engineering Science. 2020;157:103391. Available from: https://www.sciencedirect.com/science/article/pii/S0020722520301786
6. Taati E. On buckling and post-buckling behavior of functionally graded micro-beams in thermal environment. International Journal of Engineering Science. 2018;128:63-78. Available from: https://www.sciencedirect.com/science/article/pii/S0020722518302489
7. Dahmane M, Benadouda M, Fellah A, Saimi A, Hassen AA, Bensaid I. Porosities-dependent wave propagation in bi-directional functionally graded cantilever beam with higher-order shear model. Mechanics of Advanced Materials and Structures. Available from: https://doi.org/10.1080/15376494.2023.2253546
8. Khaje Khabaz M, Eftekhari SA, Hashemian M, Toghraie D. Optimal vibration control of multi-layer micro-beams actuated by piezoelectric layer based on modified couple stress and surface stress elasticity theories. Physica A: Statistical Mechanics and its Applications. 2020;546:123998. Available from: https://www.sciencedirect.com/science/article/pii/S0378437119322137
9. Bhangale RK, Ganesan N. Free vibration of simply supported functionally graded and layered magneto-electro-elastic plates by finite element method. Journal of Sound and Vibration. 2006;294(4):1016-38. Available from: https://www.sciencedirect.com/science/article/pii/S0022460X06000320
10. Sladek J, Sladek V, Krahulec S, Chen CS, Young DL. Analyses of Circular Magnetoelectroelastic Plates with Functionally Graded Material Properties. Mechanics of Advanced Materials and Structures. 2015;22(6):479-89. Available from: https://doi.org/10.1080/15376494.2013.807448
11. Mahesh V. Porosity effect on the nonlinear deflection of functionally graded magneto-electro-elastic smart shells under combined loading. Mechanics of Advanced Materials and Structures. 2022;29(19):2707-25. Available from: https://doi.org/10.1080/15376494.2021.1875086
12. Zhang GY, Qu YL, Gao XL, Jin F. A transversely isotropic magneto-electro-elastic Timoshenko beam model incorporating microstructure and foundation effects. Mechanics of Materials. 2020;149:103412. Available from: https://www.sciencedirect.com/science/article/pii/S0167663620301137
13. Hong J, Wang S, Zhang G, Mi C. On the Bending and Vibration Analysis of Functionally Graded Magneto-Electro-Elastic Timoshenko Microbeams. Crystals. 2021;11(10):1206. Available from: https://www.mdpi.com/2073-4352/11/10/1206
14. Hong J, Wang S, Qiu X, Zhang G. Bending and Wave Propagation Analysis of Magneto-Electro-Elastic Functionally Graded Porous Microbeams. Crystals. 2022;12(5):732. Available from: https://doi.org/10.3390/cryst12050732
15. Qu YL, Li P, Zhang GY, Jin F, Gao XL. A microstructure-dependent

anisotropic magneto-electro-elastic Mindlin plate model based on an extended modified couple stress theory. Acta Mechanica. 2020;231(10):4323-50.
Available from: https://doi.org/10.1007/s00707-020-02745-0

16. Wang S, Hong J, Gu S, Xiao Z, Zhang G. A size-dependent isogeometric model for magneto-electro-elastic graded curved beams in advanced structures. Composite Structures. 2025;358:118877. Available from: https://doi.org/10.1016/j.compstruct.2025.118877
17. Zheng Y-f, Qu D-y, Liu L-c, Chen C-p. Size-dependent nonlinear bending analysis of nonlocal magneto-electro-elastic laminated nanobeams resting on elastic foundation. International Journal of Non-Linear Mechanics. 2023;148:104255. Available from: https://www.sciencedirect.com/science/article/pii/S0020746222002256.
18. Alibeigi B, Tadi Beni Y, Mehralian F. On the thermal buckling of magneto-electro-elastic piezoelectric nanobeams. The European Physical Journal Plus. 2018;133(3):133.
Available from: https://doi.org/10.1140/epjp/i2018-11954-7
19. Ghobadi A, Beni YT, Golestanian H. Nonlinear thermo-electromechanical vibration analysis of size-dependent functionally graded flexoelectric nano-plate exposed magnetic field. Archive of Applied Mechanics. 2020;90(9):2025-70. Available from: https://doi.org/10.1007/s00419-020-01708-0
20. Zheng Y-f, Zhou Y, Wang F, Chen C-p. Nonlinear deformation analysis of magneto-electro-elastic nanobeams resting on elastic foundation by using nonlocal modified couple stress theory. European Journal of Mechanics - A/Solids. 2024;103:105158. Available from: https://www.sciencedirect.com/science/article/pii/S0997753823002504
21. Habibi B, Beni YT, Mehralian F. Free vibration of magneto-electro-elastic nanobeams based on modified couple stress theory in thermal environment. Mechanics of Advanced Materials and Structures. 2019;26(7):601-13.
Available from: https://doi.org/10.1080/15376494.2017.1410902
22. Alibeigi B, Tadi Beni Y. On the size-dependent magneto/electromechanical buckling of nanobeams. The European Physical Journal Plus. 2018;133(10):398. Available from: https://doi.org/10.1140/epjp/i2018-12208-6
23. Zheng Y-f, Liu L-C, Qu D-y, Chen C-p. Nonlinear postbuckling analysis of magneto-electro-thermo-elastic laminated microbeams based on modified couple stress theory. Applied Mathematical Modelling. 2023;118:89-106. Available from: https://www.sciencedirect.com/science/article/pii/S0307904X23000227
24. Fattaheian Dehkordi S, Tadi Beni Y. Size-dependent continuum-based model of a truncated flexoelectric/flexomagnetic functionally graded conical nano/microshells. Applied Physics A. 2022;128(4):320. Available from: https://doi.org/10.1007/s00339-022-05386-3
25. Lyu Z, Ma M. Nonlinear dynamic modeling of geometrically imperfect magneto-electro-elastic nanobeam made of functionally graded material. Thin-Walled Structures. 2023;191:111004. Available from: https://www.sciencedirect.com/science/article/pii/S0263823123004822
26. Wang S, Hong J, Wei D, Zhang G. Bending and wave propagation analysis of axially functionally graded beams based on a reformulated strain gradient elasticity theory. Applied Mathematics and Mechanics. 2023;44(10):1803-20. Available from: https://doi.org/10.1007/s10483-023-3042-6.
27. Wang S, Hong J, Yin S, Zhang G. Isogeometric analysis of magneto-electro-elastic functionally graded Mindlin microplates. Thin-Walled Structures. 2024;198:111740. Available from: https://www.sciencedirect.com/science/article/pii/S0263823124001836
28. Lam DCC, Yang F, Chong ACM, Wang J, Tong P. Experiments and theory in strain gradient elasticity. Journal of the Mechanics and Physics of Solids. 2003;51(8):1477-508. Available from: https://www.sciencedirect.com/science/article/pii/S002250960300053X
29. McFarland AW, Colton JS. Role of material microstructure in plate stiffness with relevance to microcantilever sensors. Journal of Micromechanics and Microengineering. 2005;15(5):1060. Available from: https://dx.doi.org/10.1088/0960-1317/15/5/024
30. Toupin RA. Elastic materials with couple-stresses. Archive for Rational Mechanics and Analysis. 1962;11(1):385-414.
Available from: https://doi.org/10.1007/BF00253945
31. Mindlin RD. Influence of couple-stresses on stress concentrations. Experimental Mechanics. 1963;3(1):1-7.
Available from: https://doi.org/10.1007/BF02327219
32. Mindlin RD. Micro-structure in linear elasticity. Archive for Rational Mechanics and Analysis. 1964;16(1):51-78.
Available from: https://doi.org/10.1007/BF00248490
33. Mindlin RD, Eshel NN. On first strain-gradient theories in linear elasticity. International Journal of Solids and Structures. 1968;4(1):109-24. Available from: https://www.sciencedirect.com/science/article/pii/002076836890036X
34. Polizzotto C. A hierarchy of simplified constitutive models within isotropic strain gradient elasticity. European Journal of Mechanics - A/Solids. 2017;61:92-109. Available from: https://www.sciencedirect.com/science/article/pii/S0997753816302145
35. B.S. Altan, E.C. Aifantis. On Some Aspects in the Special Theory of Gradient Elasticity. Journal of the Mechanical Behavior of Materials. 1997;8(3):231-82.
Available from: https://doi.org/10.1515/JMBM.1997.8.3.231
36. Ebrahimi F, Barati MR. Vibration analysis of embedded biaxially loaded magneto-electrically actuated inhomogeneous nanoscale plates. Journal of Vibration and Control. 2018;24(16):3587-607.
Available from: https://journals.sagepub.com/doi/abs/10.1177/1077546317708105
37. Kiani A, Sheikhkhoshkar M, Jamalpoor A, Khanzadi M. Free vibration problem of embedded magneto-electro-thermo-elastic nanoplate made of functionally graded materials via nonlocal third-order shear deformation theory. Journal of Intelligent Material Systems and Structures. 2018;29(5):741-63.
Available from: https://journals.sagepub.com/doi/abs/10.1177/1045389X17721034
38. Liu H, Lv Z. Vibration performance evaluation of smart magneto-electro-elastic nanobeam with consideration of nanomaterial uncertainties. Journal of Intelligent Material Systems and Structures. 2019;30(18-19):2932-52.
Available from: https://journals.sagepub.com/doi/abs/10.1177/1045389X19873418
39. Xiao W-s, Gao Y, Zhu H. Buckling and post-buckling of magneto-electro-thermo-elastic functionally graded porous nanobeams. Microsystem Technologies. 2019;25(6):2451-70.
Available from: https://doi.org/10.1007/s00542-018-4145-2
40. Lim CW, Zhang G, Reddy JN. A higher-order nonlocal elasticity and strain gradient theory and its applications in wave propagation. Journal of the Mechanics and Physics of Solids. 2015;78:298-313.
Available from: https://www.sciencedirect.com/science/article/pii/S0022509615000320
41. Şimşek M. Nonlinear free vibration of a functionally graded nanobeam using nonlocal strain gradient theory and a novel Hamiltonian approach. International Journal of Engineering Science. 2016;105:12-27. Available from: https://www.sciencedirect.com/science/article/pii/S0020722516300520
42. Li X, Li L, Hu Y, Ding Z, Deng W. Bending, buckling and vibration of axially functionally graded beams based on nonlocal strain gradient theory. Composite Structures. 2017;165:250-65. Available from: https://www.sciencedirect.com/science/article/pii/S0263822316304974
43. Nguyen T-K, Vo TP, Thai H-T. Static and free vibration of axially loaded functionally graded beams based on the first-order shear deformation theory. Composites Part B: Engineering. 2013;55:147-57. Available from: https://www.sciencedirect.com/science/article/pii/S1359836813003223
44. Li S-R, Batra RC. Relations between buckling loads of functionally graded Timoshenko and homogeneous Euler–Bernoulli beams. Composite Structures. 2013;95:5-9. Available from: https://www.sciencedirect.com/science/article/pii/S0263822312003558
45. Nguyen T-K, Nguyen B-D. A new higher-order shear deformation theory for static, buckling and free vibration analysis of functionally graded

sandwich beams. Journal of Sandwich Structures & Materials. 2015;17(6):613-31.
Available from: https://journals.sagepub.com/doi/abs/10.1177/1099636215589237

46. Van Vinh P. Deflections, stresses and free vibration analysis of bi-functionally graded sandwich plates resting on Pasternak's elastic foundations via a hybrid quasi-3D theory. Mechanics Based Design of Structures and Machines. 2021:1-32.
Available from: https://doi.org/10.1080/15397734.2021.1894948
47. Adhikari B, Singh BN. Dynamic response of functionally graded plates resting on two-parameter-based elastic foundation model using a quasi-3D theory. Mechanics Based Design of Structures and Machines. 2019;47(4):399-429.
Available from: https://doi.org/10.1080/15397734.2018.1555965
48. Bensaid I, Saimi A. Dynamic investigation of functionally graded porous beams resting on viscoelastic foundation using generalised differential quadrature method. Australian Journal of Mechanical Engineering. 2022:1-20.
Available from: https://doi.org/10.1080/14484846.2021.2017115
49. Ahmed S, Abdelhamid H, Ismail B, Ahmed F. An Differential Quadrature Finite Element and the Differential Quadrature Hierarchical Finite Element Methods for the Dynamics Analysis of on Board Shaft. European Journal of Computational Mechanics. 2021;29(4-6):303–44.
Available from: https://journals.riverpublishers.com/index.php/EJCM/article/view/5999
50. Houalef IE, Bensaid I, Saimi A, Cheikh A. An analysis of vibration and buckling behaviors of nano-composite beams reinforced with agglomerated carbon nanotubes via differential quadrature finite element method. Mechanics of Advanced Materials and Structures. 2023:1-19.
Available from: https://doi.org/10.1080/15376494.2023.2185706
51. Saimi A, Bensaid I, Houalef IE. Dynamic analysis of a porous microbeam model based on refined beam strain gradient theory via differential quadrature hierarchical finite element method. Advances in Materials Research. 2023;12(2):133-59.
52. Saimi A, Bensaid I, Civalek Ö. A study on the crack presence effect on dynamical behaviour of bi-directional compositionally imperfect material graded micro beams. Composite Structures. 2023;316:117032.
Available from: https://www.sciencedirect.com/science/article/pii/S0263822323003768
53. Saimi A, Bensaid I, Khouani B, Mazari MY, Houalef IE, Cheikh A. A Novel Differential Quadrature Galerkin Method for Dynamic and Stability Behaviour of Bi-directional Functionally Graded Porous Micro Beams. European Journal of Computational Mechanics. 2023;32(04):393-440. Available from: https://journals.riverpublishers.com/index.php/EJCM/article/view/23191
54. Tadi Beni Y. Size-dependent electromechanical bending, buckling, and free vibration analysis of functionally graded piezoelectric nanobeams. Journal of Intelligent Material Systems and Structures. 2016;27(16):2199-215.
Available from: https://journals.sagepub.com/doi/abs/10.1177/1045389X15624798
55. Tadi Beni Y. Size-dependent analysis of piezoelectric nanobeams including electro-mechanical coupling. Mechanics Research Communications. 2016;75:67-80. Available from: https://www.sciencedirect.com/science/article/pii/S0093641316300477
56. Senthil VG, Vasundara VV, Vijay KV. A review and critique of theories for piezoelectric laminates. Smart Materials and Structures. 2000;9(1):24. Available from: https://dx.doi.org/10.1088/0964-1726/9/1/304
57. Wang Q, Quek ST, Sun CT, Liu X. Analysis of piezoelectric coupled circular plate. Smart Materials and Structures. 2001;10(2):229. Available from: https://dx.doi.org/10.1088/0964-1726/10/2/308
58. Liu C, Liu B, Zhao L, Xing Y, Ma C, Li H. A differential quadrature hierarchical finite element method and its applications to vibration and bending of Mindlin plates with curvilinear domains. International Journal for Numerical Methods in Engineering. 2017;109(2):174-97. Available from: https://onlinelibrary.wiley.com/doi/abs/10.1002/nme.5277
59. Li JY. Magnetoelectroelastic multi-inclusion and inhomogeneity problems and their applications in composite materials. International Journal of Engineering Science. 2000;38(18):1993-2011. Available from: https://www.sciencedirect.com/science/article/pii/S0020722500000148
60. Zhang GY, Gao XL. Elastic wave propagation in 3-D periodic composites: Band gaps incorporating microstructure effects. Composite Structures. 2018;204:920-32. Available from: https://www.sciencedirect.com/science/article/pii/S0263822318318270

Besma Khouani: https://orcid.org/0009-0008-3096-2995

Ahmed Saimi: https://orcid.org/0000-0002-3722-2526

Ismail Bensaid: https://orcid.org/0000-0003-4316-0648

INFLUENCE OF COMMERCIAL ADDITIVES AND y-IRRADIATION ON STRUCTURAL AND MECHANICAL PROPERTIES OF RHDPE/RGFRP

Maciej Jan SPYCHAŁA*, Danuta MIEDZIŃSKA*, Grzegorz SŁAWIŃSKI*, Dorota GAJDA,**
Paulina LATKO-DURAŁEK*, Anna CZAJKA-WAROWNA***, Tomasz SZREDER******

*Faculty of Mechanical Engineering, Institute of Mechanics and Computational Science, Military University of Technology in Warsaw,
gen. Sylwestra Kaliskiego 2, 00-908 Warsaw, Poland
**Military Institute of Chemistry and Radiometry, Al. gen. Antoniego Chruściela "Montera" 105, 00-910 Warsaw, Poland
***Faculty of Materials Science and Engineering, Warsaw University of Technology, Wołoska 141, 02-507, Warsaw, Poland
****Institute of Applied Radiation Chemistry, Lodz University of Technology, Wroblewskiego 15, 93-590 Lodz, Poland
Institute of Nuclear Chemistry and Technology, Dorodna 16, 03-195 Warsaw, Poland

maciej.spychala@wat.edu.pl, danuta.miedzinska@wat.edu.pl, grzegorz.slawinski@wat.edu.pl, d.gajda@wichir.waw.pl,
paulina.latko@pw.edu.pl, anna.czajka2.dokt@pw.edu.pl, tomasz.szreder@p.lodz.pl

received 17 February 2025, revised 04 June 2025, accepted 06 June 2025

Abstract: In response to environmental regulations, particularly within the European Union, there is an urgent need to implement new, sustainable materials derived from recycling processes. This study investigates the potential for modifying and predicting the mechanical properties of composites made from recycled high-density polyethylene (rHDPE) and recycled glass fiber-reinforced polymer (rGFRP). Specifically, it examines tensile strength parameters and structure changes in rHDPE/rGFRP treated with three different chemical additives, including a silica-based agent (S) and maleic-anhydride polyethylene (MAH) compatibilizers; and a thermal stabilizer dedicated for the recycled polyolefins. The findings reveal that these additives do not significantly change the mechanical properties of the composite. All additives increase elastic modulus (compared to rHDPE/rGFRP for max. 3% - S), tensile strength (max. for 14%, MAH), and offset yield strength (max. 16%, MAH). Moreover, the strength of the composite can be enhanced through γ-irradiation, which was found to affect the stress-strain characteristics of the rHDPE/rGFRP blend. Notable differences were observed in the strength and elongation behavior of the composite (for rHDPE increased to 0.58 for 40 kGy and decreased for 100 kGy dose to 0.35, which is very close to the non-irradiated sample), suggesting that irradiation could be a viable method for modifying the properties of recycled composites for specific applications.

Key words: circular economy, recycled polyethylene, post-consumer GFRP, γ-irradiated polymers, tensile properties, microstructure

1. INTRODUCTION

The main types of fiber-reinforced polymers are those based on carbon or glass fibers impregnated with epoxy or polyester resin. Those based on glass fibers and polyester resin (GFRP) are widely used in low-demanding applications mainly due to the lower cost compared to carbon fibers and epoxy resin. Nevertheless, GFRP characterizes relatively high strength and stiffness, ease of shaping, and good resistance to environmental conditions. Their popularity on the market is also driven by their low-cost manufacturing [1].

In our previous paper we demonstrated that milled GFRP can be used directly as a filler for recycled high-density polyethylene (rHDPE) [2]. We observed that the adhesion between recycled GFRP (rGFRP) and rHDPE is too low, leading to insufficient improvement in mechanical properties. Therefore, our intention was to examine if the addition of chemical compatibilizers and stabilizers will positively affect the mechanical performance of rHDPE mixed with rGFRP. Potential applications for such a composite include products like patio boards, pipes, and casings [3].

Mineral and organic fillers are crucial in modifying polymers to obtain required properties such as mechanical strength, thermal stability, and price. The most popular are: talc, calcium carbonate, carbon black, and organics like wood powder [4] or grape leaves fiber [5]. The final material's properties can be changed utilizing different particle sizes of filler, shape, and mass share [6,7]. Many efforts have been made to increase the strength of PE while not affecting the non-bioactivity [8,9].

Poor adhesion between fibers and thermosetting matrix results from low matrix wettability and high surface energy of the fibers. This leads to defective composites with poor mechanical properties due to insufficient stress transferring from the matrix to the reinforcing. To improve the interphase between fractions, various modification methods are used [10]. Commercially used glass fibers are mostly modified by sizing. Sizing is a coating modification method consisting of dipped-in slurry using coupling agents (silane coupling agent), film formers, and other additives. Sized fibers present a good adhesion to the polymer matrix and have higher resistance to damage, moisture, and environmental damage [11]. Unfortunately, after recycling, sizing can be damaged by milling and other recycling operations. Mechanical damage and fibers shortening caused by milling, resin residues, and sizing damage cause reduced mechanical properties compared to composites with virgin fibers. One of the methods to prevent this is the use of compatibilizers. These substances act as a binder between materials with different polarities, through polar interaction or covalent bonding [12].

Chemical compatibilizers can be divided into two main groups proposed by A. Ghosh [13]: low-molecular-weight coupling agents and polymeric compatibilizers. The first group includes chemical compounds with reactive groups such as anhydride, isocyanate, epoxide, peroxide, etc., and they are able to produce covalent bonding. One of the most popular is the silane coupling agent. Similar to sizing, they increase adhesion between reinforcement and matrix. Ch. Tselios et al. [14] used γ-methacryloxy propyltrimethoxy silane for glass fibers compatibilization in low-density polyethylene/polypropylene (LDPE/PP) blend. They found out that coupled fibers have better adhesion to LDPE [14]. Polymeric compatibilizers are high-molecular-weight coupling agents that can improve interfacial adhesion but also act as an impact modifier. One is commercially available functionalized polyolefins obtained via the free-radical grafting process during melt extrusion. The multitude of their types is significant, depending on the matrix and filler used, like polymer-graft-glycidyl methacrylate, polymer-graft-ethyl acrylate, or polymer-graft-butyl acrylate [14]. One of the most popular for polyolefins compatibilization is grafted maleic anhydride on polypropylene (PP-g-MA) or polyethylene (PE-g-MA). PP-g-MA and PE-g-MA are commonly used for increasing adhesion between natural fibers and the hydrophobic polymeric matrix. I. Noranizan and I. Ahmad [15] used PE-g-MA in kenaf fiber/HDPE composites. They deduced that MA could react with the hydroxyl group of natural fiber, and PE chains diffuse into the HDPE matrix through interchain entanglements, which increase the dispersion of the fibers [15]. Compatibilization of GFRP with maleic anhydride is also a common way of obtaining better phase interaction. The anhydrite groups of the grafted polyolefins can react with sized (amino groups of silane) glass fibers [16], but also with silanol groups of the fibers [17]. Many scientists have reported using maleic anhydride for composites with glass fibers and polyolefins [17,10]. R. Watanabe et al. obtained an increase in tensile strength from 38.5 MPa to 87.0 MPa after introducing PP-g-MA to GF/PP composites, thanks to enhancement in the interfacial adhesion between components [17].

Filler affects polymer resistance to γ radiation. Mineral fillers increase while organic fillers decrease [18]. To improve coupling, and strength properties several studies have also investigated other coupling agents, including isocyanates [19,20] and silanes [21]. Overall, coupling agents have been used to increase the mechanical properties of composites.

Improving the polymer matrix through crosslinking can effectively reduce creep under long-term loading [22]. Various techniques for obtaining crosslinked polyethylene have been developed, such as peroxide crosslinking, irradiation techniques, and silane crosslinking. However, both peroxide and irradiation methods involve high investment costs [23].

γ-irradiation stimulates the crosslinking process; however, when it is done under inert atmosphere, irradiated in air, oxidative degradation becomes dominant. Singh [24] summarized the observation that the effects of irradiation on PE highlight several potential processes that seem to have received limited attention in previous research, specifically: a) during irradiation in air, superoxide anions, hydroperoxyl radicals, and hydrogen peroxide are likely to form in the amorphous regions; b) cationic condensation reactions involving sites of unsaturation may result in crosslinking in both the crystalline and amorphous regions; c) the transfer of excitation energy to peroxides and hydroperoxides, along with their reactions with radiolytically produced electrons, could lead to the formation of alkoxy radicals, which, in turn, may form ether linkages (PEOPE) and encourage crosslinking; and d) cationic and excited molecule reactions are likely the primary pathways for the formation of trans-vinylene.

In this study, two approaches to modifying rHDPE/rGFRP composites were explored: one involves using additives such as compatibilizers and stabilizers to enhance the adhesion between the fibers and matrix, while the other utilizes γ-irradiation. The influence of both on the mechanical properties (uniaxial tension test), structure (SEM and optical microscopy) and thermal properties (DSC) was investigated.

2. MATERIALS

As the starting material the composite of rHDPE containing 40 wt% of rGFRP was used. rHDPE was bought from POLCHEM Sp. z o.o. company. Both components were delivered from the industry with rGFRP from post-consumer bus bumpers. The composite pellets were produced by the extrusion method by TMBK Partners Sp. z o.o. from Warsaw, Poland and the whole procedure was described deeply in [5]. To improve the mechanical properties of the composite rHDPE/rGFRP the following commercial additives in the form of granulate were used:

- IrgaCycle PS032G (BASF, Germany) - is a stabilizer solution designed to improve the processing and long-term thermal stability of recycled polyolefins that have been degraded or contaminated due to exposure to aggressive substances such as acids or metal ions [25].
- Licocene® PE MS 431 (Clariant Plastics and Coatings Ltd) - stabilized maleic anhydride grafted polyethylene wax [26].
- SilmaLink AX2292 (Silma S.L) - acts as a compatibilizer or/and crosslinker in many reactive applications to build a network copolymerization between organic CH groups and organic/inorganic OH groups. It is a vinyl functional silane with methoxy groups [27].

Tab. 1. Sample description with commercial additives names and mass shares

Additive	Sample name rHDPE/rGFRP/x%abbrv.	Additive concentration (wt%)
none	rHDPE/rGFRP	0
IrgaCycle PS 032 G	0.2P	0.2
	0.5P	0.5
Licocene® PE MS 431	1MAH	1.0
	2MAH	2.0
	3MAH	3.0
SilmaLink AX2292	0.3S	0.3
	1S	1.0
	2S	2.0

Before compatibilization of the material rHDPE/rGFRP with additives, rHDPE/rGFRP pellets were dried in a vacuum, at 80 °C for 12 h. Then, the pellets were mixed with each additive at various concentrations recommended by the producers (Table 1), and then extruded with a co-rotational two-screw extruder Haake MiniLab (Thermo Fisher Scientific, Massachusetts, USA). Extruding parameters were as follows: temperature 190 °C and screws velocity 25 rpm. The extruded profile was cut and once again extruded to improve homogenization between components

The produced composite pellets were then injection molded into the form of dog bones (version 5A [28]) and rounds with a diameter of 25 mm and thickness of 1 mm using a HAAKE Mini Jet

Piston Injection Molding System (ThermoFischer Scientific, Massachusetts, USA), Figure 1. The parameters of the injection molding were as follows: 220 °C - the temperature of the barrel, 40 °C - the mold temperature, 700 bars and 7 seconds injection pressure and time, and 600 bars and 5 seconds the post-processing injection pressure and time.

Fig. 1. Geometry of injected specimens to mechanical and radiation tests

3. METHODS

3.1. Mechanical properties

The mentioned bone-shaped specimens were used for the uniaxial tensile test. Tensile strength was determined as the engineers' stress. The test was conducted on a Zwick/Roell Kappa 50 DS machine (ZwickRoell, Ulm, Germany) with a speed of 5 mm/min in speed and 20 Hz of sampling under 20 °C and 1010 hPa. The test was conducted in accordance with ASTM D638-14 [29].

Tensile modulus was determined based on the inclination of 24 consecutive measurements of the stress-strain test with the beginning at $\varepsilon = 0.002$. $Re_{0.2}$ was considered as offset yield strength, when elongation at maximum strength. The results were averaged according to normal distribution. In every series 8 samples were tested with additives and 4 specimens of irradiated ones.

In every series, 8 samples with additives were tested and 4 irradiated specimens.

3.2. Microstructure

Microstructure images were captured using the Keyence VHX-1000 microscope (Keyence, Osaka, Japan). Images were taken on cross-sections of bone-shaped specimens [30]. The cut was done 10 mm from the outer edge of the holder location SEM analysis was done with Hitachi Su-70 (Hitachi, Tokyo, Japan), 15 kV.

3.3. Irradiation test

Irradiation was carried out at the Institute of Nuclear Chemistry and Technology in Warsaw. Bone-shaped specimens of rHDPE and rHDPE/rGFRP were irradiated using ^{60}Co Gamma Chanber 5000 (BRIT, India) source, Figure 2 a. The average dose rate was ~1.4 kGy/h. Dose was determined by standard Fricke dosimeter [31,32] using radiation yield of Fe^{3+} equal to 1.61 μmol J^{-1}, molar absorption coefficient of Fe^{3+} at 303 nm 2174 M^{-1} cm^{-1} and mass density of dosimetric solution 1.023 g cm^{-3}, The test was conducted at 30 °C. During the process, specimens were fixed in a holder that was rotating to ensure homogeneous distribution of radiation dose in specimen volume. Dose absorbed by the samples were in range: 0 – 100 kGy. This range was taken into consideration of previous results published by Cota [33]. Tensile modulus, strain at tensile strength, and tensile strength were determined.

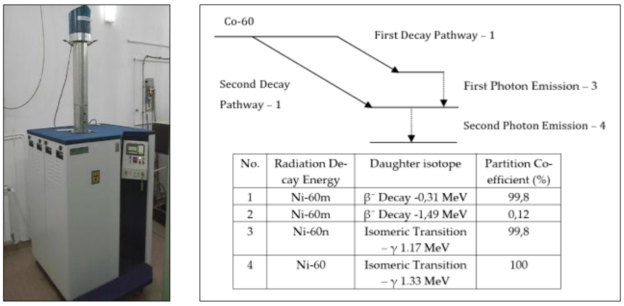

No.	Radiation Decay Energy	Daughter isotope	Partition Coefficient (%)
1	Ni-60m	β^- Decay -0,31 MeV	99,8
2	Ni-60m	β^- Decay -1,49 MeV	0,12
3	Ni-60n	Isomeric Transition – γ 1.17 MeV	99,8
4	Ni-60	Isomeric Transition – γ 1.33 MeV	100

a) b)

Fig. 2. a) Gamma Chamber 5000 equipment; b) schematic of radioactive decay of ^{60}Co

Irradiated specimen names correspond to doses, as listed in Table 2.

Tab. 2. Radiation test samples names.

Material/Absorbed dose	0 kGy	40 kGy	60 kGy	80 kGy	100 kGy
rHDPE/rGFRP 40%	A0	A40	A60	A80	A100
rHDPE	B0	B40	B60	B80	B100

3.4. Thermal properties

Differential scanning calorimetry (DSC) was carried out using DSC Q1000 (TA Instruments, New Castle, PA, USA). Samples of 8 g were placed in the aluminum hermetic pan. Then it was heated from -80 °C to 200 °C (1st heating cycle), next cooled from 200 °C to -80 °C (cooling cycle), and then heated again to 200 °C was repeated (2nd heating cycle). Processes were conducted at a rate of 10 °C/min in a nitrogen atmosphere. Based on the experiment following parameters were determined: melting temperature (T_m), melting enthalpy (ΔH_m, 2nd heating curve), crystallization temperature (T_c) and crystallinity degree (X_c) using formula (1):

$$X_c[\%] = \frac{\Delta H_m}{\Delta H_m^0 * \omega_{HDPE}} * 100 \quad (1)$$

where: ΔH_m - melting enthalpy (from 2nd heating cycle), $\Delta H_m^0 = 288\ \mathrm{J/g}$ [34] –, ω_{HDPE} - weight fraction of HDPE in composites.

4. RESULTS AND DISSCUSION

4.1. Mechanical properties

The sample containing 1 wt% S (AX2292) shows the highest tensile modulus, 1.91 GPa, which is 3% higher than the reference material (rHDPE/rGFRP) 1.82 GPa. The relative standard deviation does not exceed 8.5%, Figure 3 a. There are no significant differences in parameters when studying additives content, Figure 3 b,c.

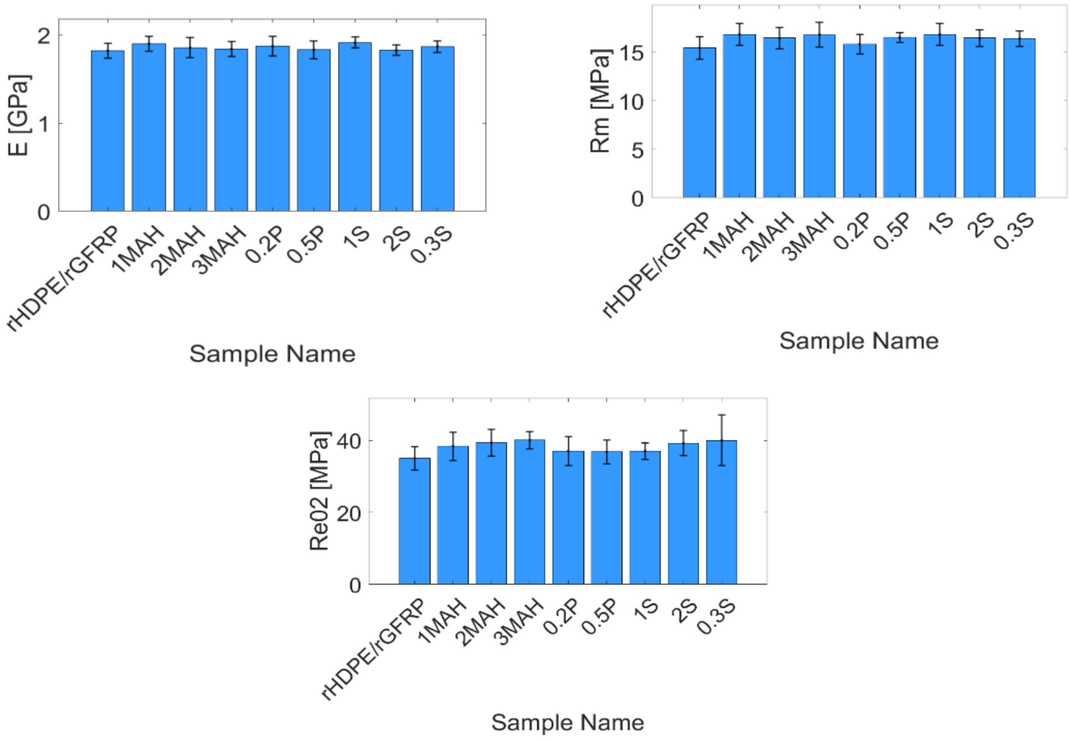

Fig. 3. Mechanical parameters of rHDPE/rGFRP material with additives described below the chart: a) tensile modulus; b) tensile strength; c) offset yield strength

The highest strength is exhibited by material with maleic anhydrate additive which equals 40.08±0.14 MPa. 1 wt% of of this additive translates to a 10% strength increase, respectively 2 wt% to 12% and 3 wt% to 14%. Such a relation is not observed considering silane-based additives. The maximum relative standard deviation was 9.5%.

Offset yield strength is also highest for samples with maleic anhydrate additive, which is 16% higher than the reference sample. The maximum relative standard deviation reaches 7.6%.

S. da Silva and JRM d/Almeida [35] investigated the influence of 0, 2, and 3 wt% HDPE-alt-MAH on HDPE/PA12 blends. They reported that the addition of 2 wt% of the additive significantly improved tensile modulus by over 40%, while the 3 wt% addition led to a smaller increase. Similarly, tensile strength increased for 2 wt% content of compatibilizer and decreased for 3 wt%.

4.2. Microstructure of the material rHDPE/rGFRP with additives

Figure 4 presents the microstructure of the composites. The non-modified composite does not exhibit higher porosity than the modified.

The brighter and more colorful particles are fragments of the filler.

In some areas, there are significantly more chaotic, non-linear regions, as shown in Figure 4b.

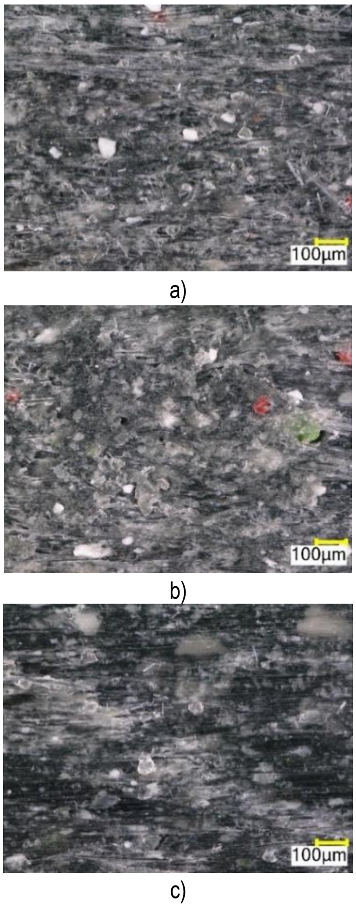

Fig. 4. Surface of the materials rHDPE/rGFRP 40%: a) without additives; b) 3S; c) 3MAH

Figures 5 a-i shows the SEM images of a cross-sections of the composites. Pores are formed in the matrix around the resin and fiber elements, which can be observed as brighter areas. The cross-section surfaces do not exhibit any significant differences compared to the reference material (rHDPE/rGFRP), Figure 5 b. However, when studying a close-up view of fibers, Figure 6, shows that pores form around the fibers, suggesting that the matrix and filler create a homogeneous microstructure. The fibers in Figure 6 h-I, the sample with MAH additive, are covered with a thin polymer layer that was not picked up during grinding.

Analyzing failure zones, it can be concluded that composite failure was brittle. Fibers protrude from the matrix in every sample and in the vast majority are oriented in line with the stretching axis. It can be seen that MAH samples present a much more perpendicular character of structure, which is convergent with the direction of tensile test force direction. This pattern is also seen in the 2S sample, which exhibits almost comparable durability to MAH samples.

Yu S. et al. [36] examined a BF/PLA/PLA-g-MAH composition and it's tensile strength and observed that system does not show interfacial void channels among inter-filament threads; thus, the microstructure formed a single matrix composite system when some other tested polymeric compositions do. Poor wettability can be observed, as it was reported in several previous studies on thermoplastics filled with rigid bodies [37].

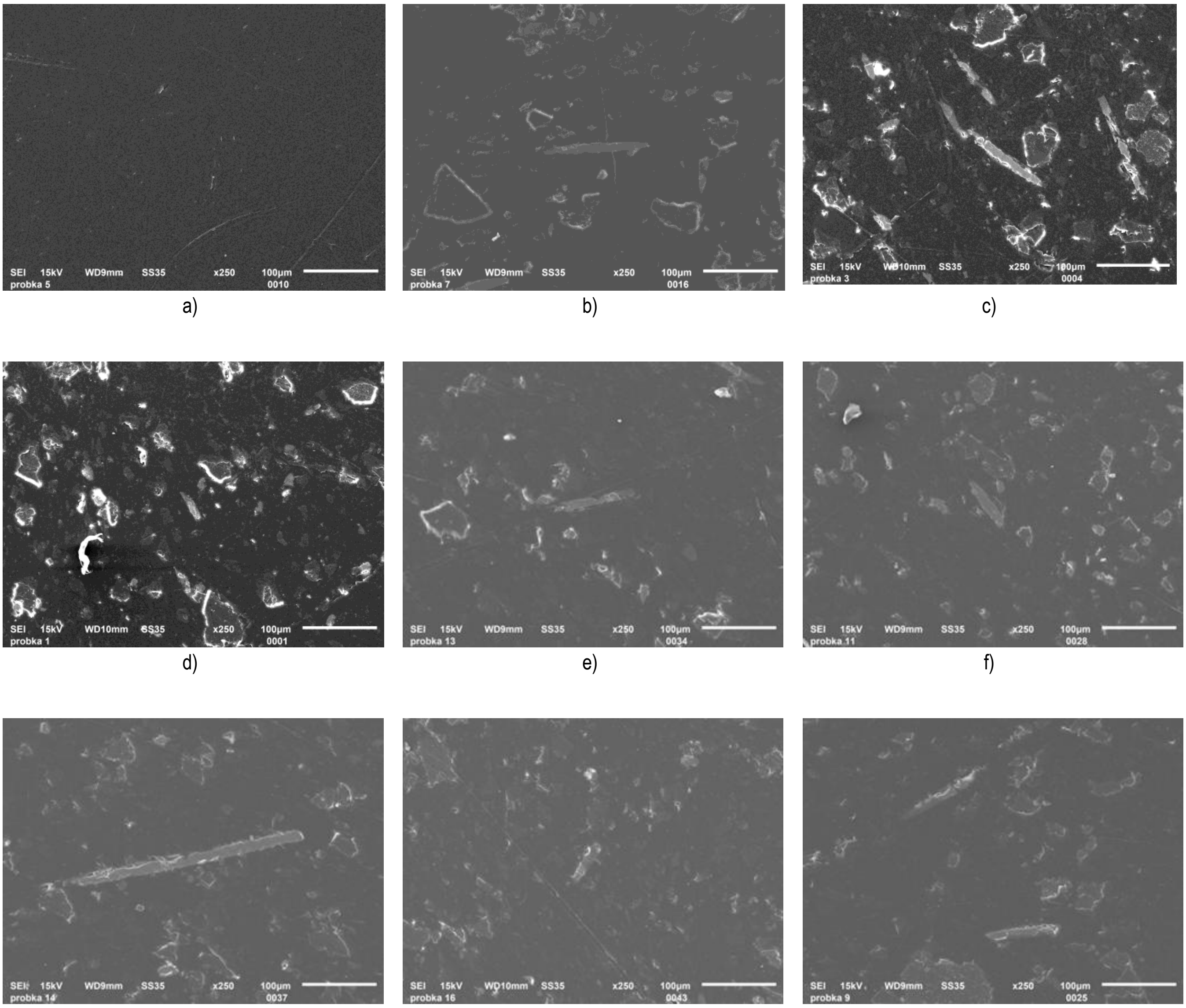

a) b) c)

d) e) f)

g) h) i)

Fig. 5. SEM images of the composite material with additives: a) rHDPE; b) rHDPE/rGFRP; c) 0.2P; d) 0.5P; e) 1S; f) 2S; g) 1MAH; h) 2MAH; i) 3MAH

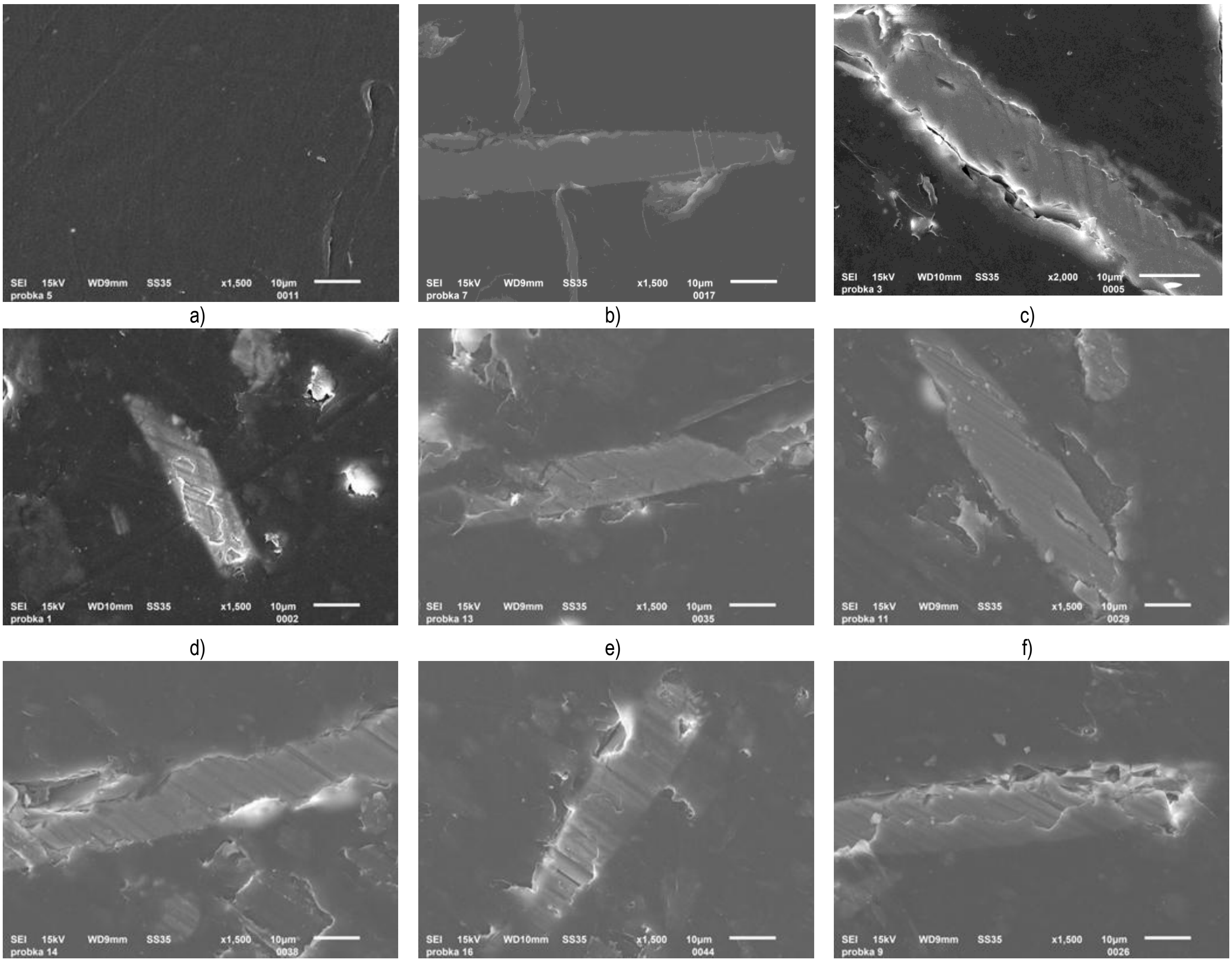

a) b) c)

d) e) f)

g) h) i)

Fig. 6. SEM images of the composite material with additives close-up view on fibre: a) rHDPE; b) rHDPE/rGFRP; c) 0.2P; d) 0.5P; e) 1S; f) 2S; g) 1MAH; h) 2MAH; i) 3MAH

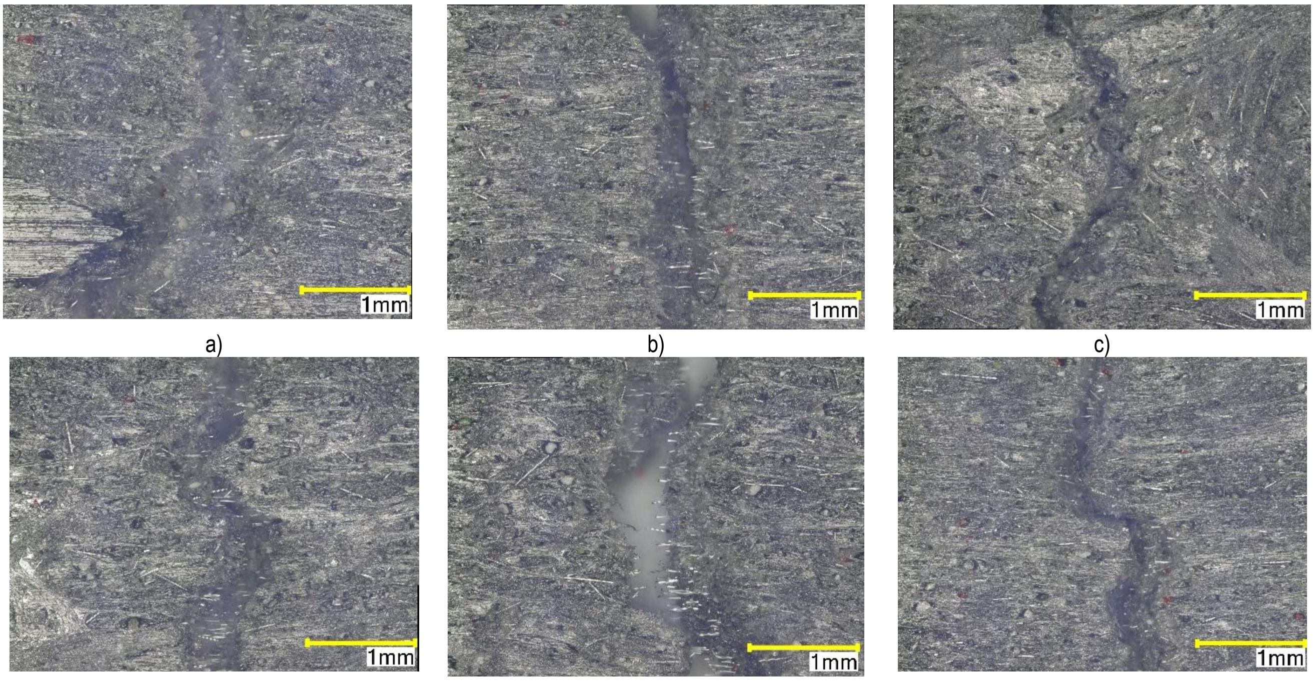

a) b) c)

d) e) f)

g) h) i)

Fig. 7. Optical microscope images of the composite material: a) rHDPE/rGFRP; b) 0.2P; c)0.5P; d) 0.3S; e) 1S; f) 2S; g) 1MAH; h) 2MAH; i) 3MAH

4.3. Mechanical properties of irradiated materials

Tensile modulus increases with increasing absorbed dose, no matter which material (with filler or without) it was, Figure 8a. A similar relation can be observed for both materials – the modulus is higher for the material with filler, which could be predicted and was tested before. Offset yield strength values do not change in such a clear way, as shown in Figure 8 b. The highest strain at maximum stress (ε_{Rm}) presents specimens with the lowest absorbed dose. Further, the proportional relation can be observed between ε_{Rm} and absorbed dose, Figure 8 c.

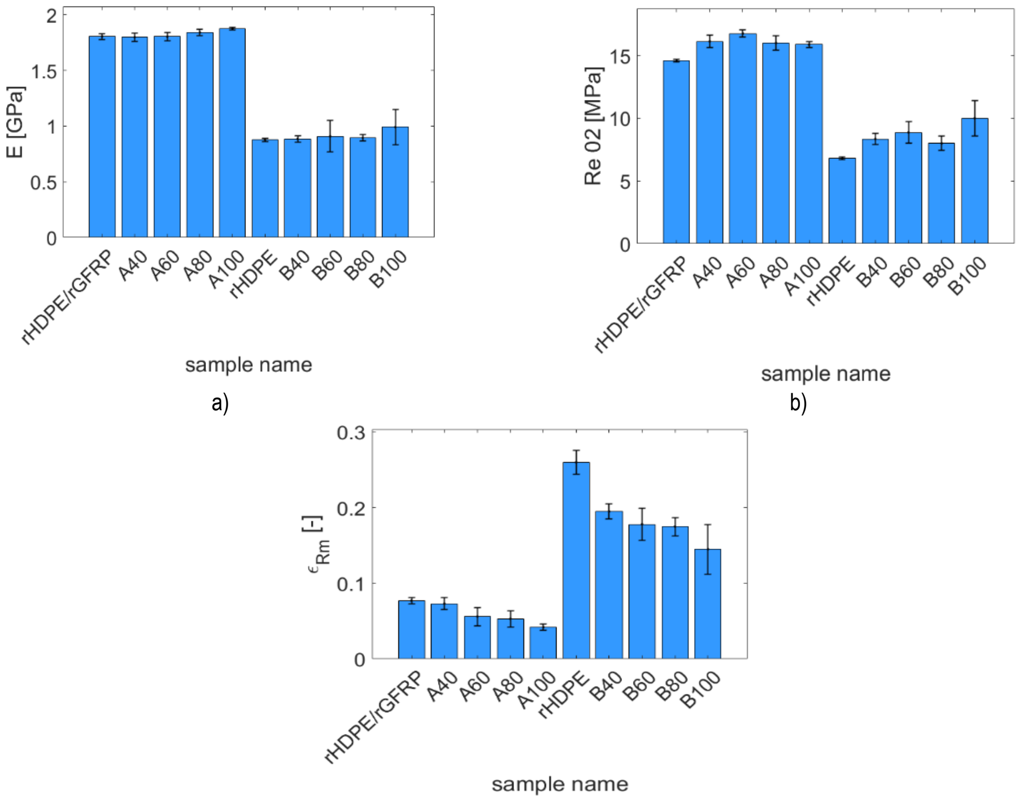

a) b) c)

Fig. 8. Mechanical parameters of irradiated specimens: a) tensile modulus of irradiated materials; b) offset yield strength; c) strain at tensile strength

When analyzing stress-strain curves, Figure 9, significant differences can be observed. γ-irradiation does not influence the tensile modulus (similar results in this dose range are presented by Cota [33]). However, it changes the character of $\sigma(\epsilon)$ relation and tensile strength. For A material (rHDPE/rGFRP – black curve on Figure 9, it can be seen that the offset yield strength is lower. A Linear decreasing character of strain at tensile strength can be observed, in Figure 9, when the strain at break parameter rises with higher irradiation dose. Further, there is a plateau fragment for ε=0.02-0,08 (A40). For a raw material, rHDPE, the relation changes even more. The slope of the function descends softly. Considering all B series, single curves behave differently. $R_{m\_rHDPE}=36.5\pm0.3$ MPa, when the average maximum strength for irradiated samples equals $R_{m\_B40\text{-}B100}=33.5\pm2$ MPa. The decrease is not significant. Absorbed doses 40-100 kGy do not impact tensile strength. However, ε_{Rm} transfers to lower values, when elongation at break is increasing for B40 and under the influence of increasing γ-irradiation dose, decreasing from 0.6 to 0.35. Partially the same results were reported by M. Zayat et al. [38] who studied HDPE/modified sugarcane bagasse. The tensile modulus increased by over 25%

for neat HDPE, and tensile strength improved at 100 kGy by circa 15%. However, there is a discrepancy when analyzing elongation at break (for doses 0-100 kGy), as it increased in this study, but decreased in the mentioned paper (by 15%).

Shershneva et. all. [39] were investigating the influence of γ-irradiation on LDPE/GF and concluded that at irradiation doses up to 60 kGy, the process of gel formation proceeded with a greater speed than destruction. They also tested the simultaneous effects of nitrile butadiene filler rubber and radiation on strength, consequently reaching similar conclusions that the material with filler has higher stiffness [39]. The presence of filler changes the rHDPE degradation mechanism, which was observed by Valandez Gonzalez [40] when studying UV irradiation influence on HDPE and HDPE/CaCO3. In our study, irradiation of the material decreases tensile strength but increases yield strength. In the mentioned studies, UV irradiation increased gel content and crystallization. Normally, the oxidation starts from the outer layers since the process takes place in the air atmosphere. There is a directed structure of the matrix that is coaxial with the direction of tensile test axial force. The cross-linking process occurred in the whole sample, hence the entire sample stretched much more evenly.

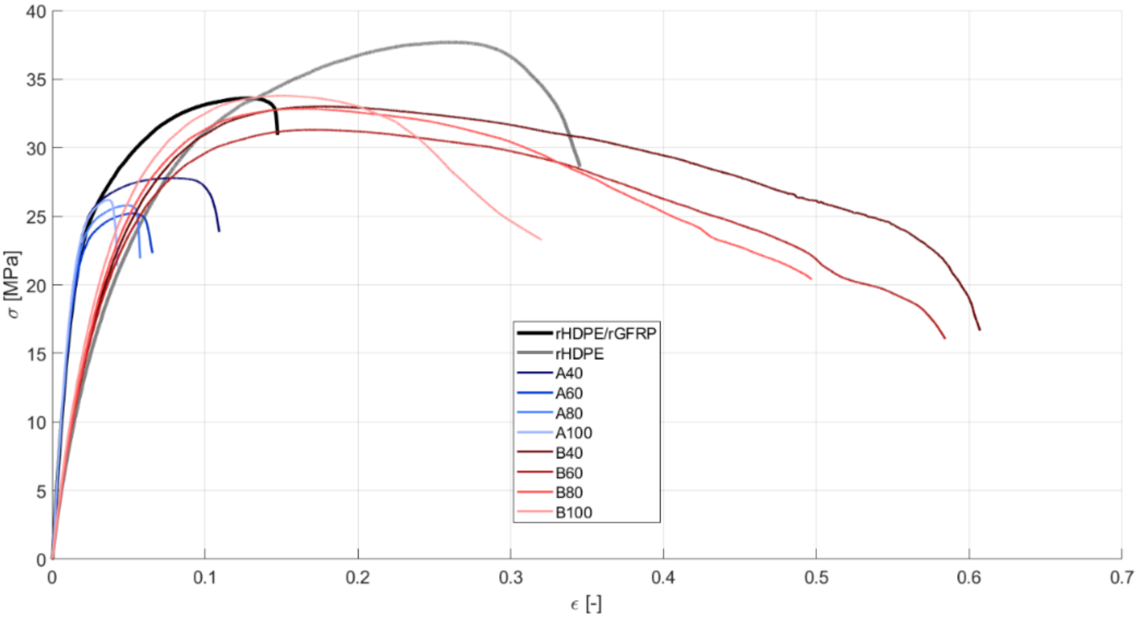

Fig. 9. Engineering stress-strain relationship for non-irradiated (rHDPE/rGFRP and rHDPE) and irradiated samples (A40-A100 and B40-B100).

The microstructure images of the failure location show that external layers of specimens are stiffened when the core is more flexible, Figure 10, which is a consequence of receiving higher dose of radiation. Material failure starts near the resin and fibre fragments where pores are created, Figure 10 b-c. However, the comparing results to samples modified with additives, the fracture zone is more homogenous.

Failure sections of the rHDPE/rGFRP irrigated composite. The inner layers are more ductile as shown in Figure 11 b-d. Fracture of the A series samples is much more brittle than B series. A significant difference can be observed when comparing B80 and B100 samples. The surface of the B80 sample does not detach as it does for the B100 sample.

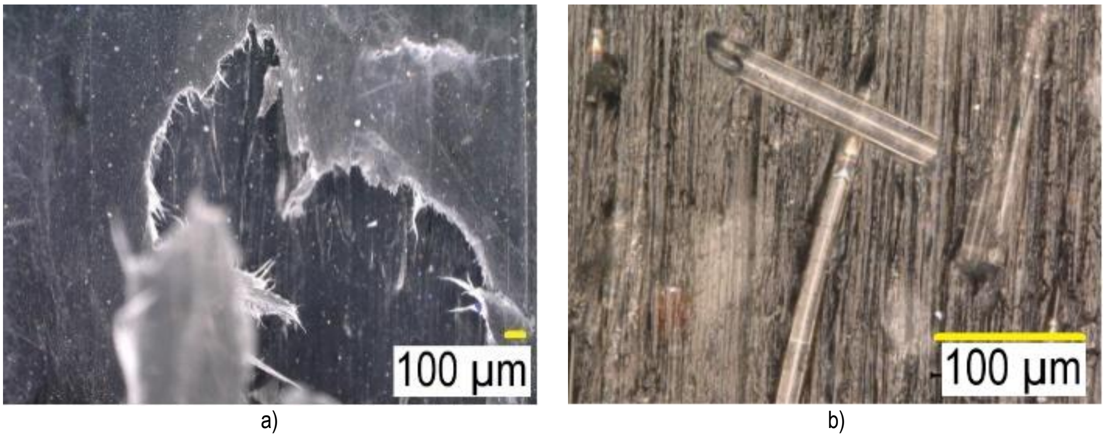

a)

b)

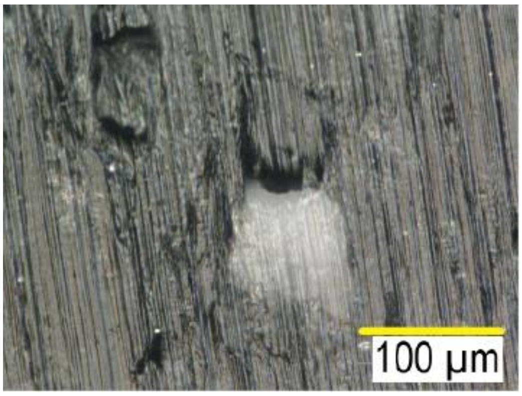

c)

Fig. 10. The surface of irradiated specimens after the tensile test: a) macro view on the degraded surface; b) close-up view on fibres; c) close-up view on resin fragment on the surface of the rHDPE/rGFRP sample after the tensile test

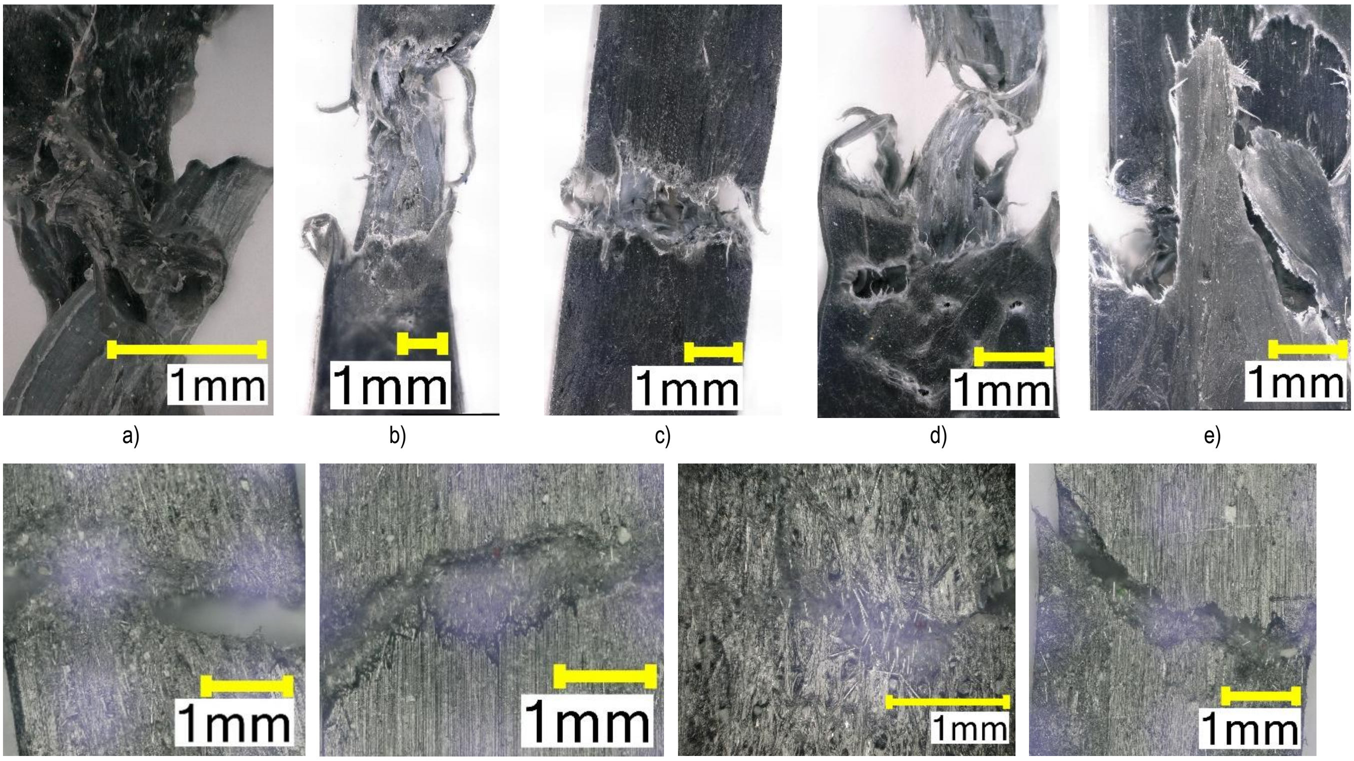

a) b) c) d) e)

(f) g) h) i)

Fig. 11. Failure locations of specimens after the tensile test: a) rHDPE; b) B40; c) B60; d) B80; e) B100; f) A40; g) A60; h) A80; i) A100

4.4. Thermal properties

The results of the DSC analysis of the composites modified with commercial additives before the irradiation test are shown in Figure 12 and collected in Table 3. The 2nd heating curves (Figure 12a) for all materials have single melting peak corresponds to melting of the crystal phase. It occured at 136 °C for the reference composite rHDPE/rGFRP, and it does not change after modification with additives. Similarly, the crystallization curves presented in Figure 12b have the same shape with narrow peak occur between 113-115°C for all composites. In the case of crystallinity content, a slight increase is observed for composites containing silica-based compatibilizer; however the highest increase is reached for composites modified by 3 wt% of MAH, from 61.1% up to 68.3%. It suggests that MAH increase the nucleation capacity of rHDPE or enhance the crystallization rate.

Similar conclusions were reached by A. Hassan et al. [41], who used PP-g-MA for compatibilization of the glass fibres with polypropylene. These results are consistent with the mechanical properties, which are the highest for the composite modified with 3 wt% MAH. More crystal phase in the material results in better mechanical performance. The shift of T_c towards higher temperatures usually indicates faster crystallization associated with increased mobility of the polymer matrix chains [42]. Such an increase would be expected for the 3MAH sample. However, the observed rise is insignificant (only 1 °C higher compared to the reference sample).

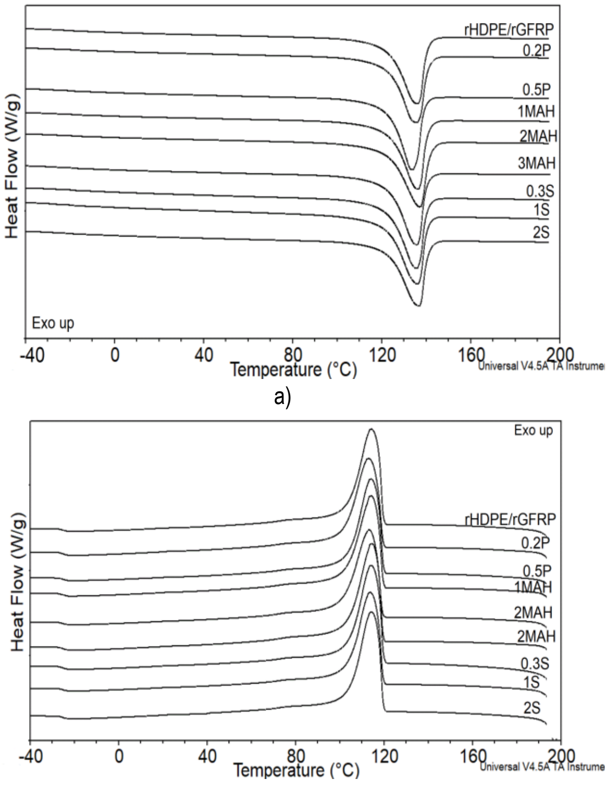

a)

b)

Fig.12. a) 2nd heating curves and b) cooling curve for analyzing composites before irradiation test

The result of the DSC analysis of irradiated composite samples is is presented in Figure 13 and in Table 4. There are no effect or changes about maximum up to 4 °C on the melting and crystallization temperature of the irradiation doses used. However, some changes are observed in the crystallinity content due to the applied irradiation. After exposure to 60 kGy dose the crystallinity content decreases from 61.1% to 56.7%. Similarly, H. Ahmad et al., investigated HDPE cross-linking with dicumyl peroxide (2.5 wt%), thus reducing the crystallinity content by almost half. They explained this phenomenon by creating a three-dimensional crystalline lattice and lower mobility of chains, which was previously mentioned, making it more difficult for crystallization and increasing the time required to form crystallites and the crystal network [43].

Tab. 3. DSC parameters determined for the rHDPE/rGFRP modified with various additives

Sample name	T_m, °C	T_c, °C	X_c, %
rHDPE/rGFRP	136	114	61.1
0.2P	135	114	61.0
0.5P	137	113	62.2
1MAH	136	114	63.3
2MAH	137	113	62.4
3MAH	135	115	68.3
0.3S	136	114	63.9
1S	136	114	64.0
2S	136	114	61.4

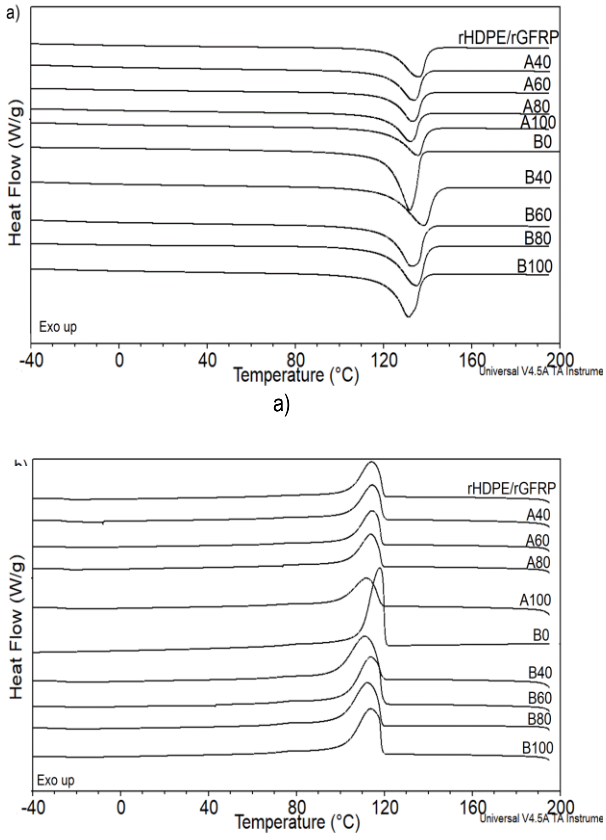

a)

b)

Fig. 13. a) 2nd heating curves and b) cooling curve for analyzing composites after irradiation test

Tab. 4. DSC parameters of irradiated samples

Sample name	T_m, °C	T_c, °C	X_c, %
rHDPE/rGFRP	136	114	61.1
A40	134	114	61.2
A60	133	114	56.7
A80	132	114	57.7
A100	135	112	58.2
B0	132	118	64.1
B40	138	111	55.8
B60	133	114	55.5
B80	135	112	53.7
B100	131	114	53.9

5. CONCLUSIONS

Investigation of modifying tensile strength of rHDPE containing 40 wt%rGFRP indicated that it can be improved by mixing material with commercially available compatibilizers (Licocene® PE MS 431 and SilmaLink AX2292), and by γ-irradiation by selecting appropriate dose. The paper also includes results of DSC, SEM, and optical microscopy studies.

Summarizing:

- Maleic anhydride additive (3MAH) increases the tensile strength of rHDPR/rGFRP by 14% and offset yield strength by 16%. Silan-based additive (2S) also increases the material’s tensile strength (by 12%).

- Tested additives do not significantly impact on elastic modulus of the composite, max. enhancement for sample 2S equals 3%.
- Mechanical characteristics of rHDPE and filled rHDPE with rGFRP can be modified with γ-irradiation and stimulate internal polymerization of the material. The elastic modulus is increasing slightly. Irradiated rHDPE characterizes a higher offset yield than irradiated GFPR (as predicted by Wondrich [24]). On the other hand, the tensile strength is lower for irradiated rHDPE. This parameter increases only for the 100 kGy dose sample. Moreover, there is a constitutive relationship between irradiation dose and elongation at maximum strength, which decreases with higher doses.

During the tensile test, when the sample is subjected to tension, pores are formed at the matrix-filling boundary. Similar results were reported by Wang et al. that γ-irradiation can improve PE and PP blend strength and compounding properties [44].

- γ-irradiation can modify the mechanical characteristics and structure of rHDPE/rGFRP material. The modification level depends on the polymer composition and absorbed dose. A similar modification of structure was observed for the 3MAH sample and irradiated-smooth, shining with parallel patterns. Both also exhibit higher elastic modulus and offset yield strength than the reference samples. This can be a consequence of longer polymeric chains. Both approaches of modifying polymeric composition stimulate cross-linking when not significantly affecting melting temperature, crystallite temperature nor crystallite degree.
- DSC analysis exhibits that the chosen additives and their shares do not significantly influence the crystallization temperature, melting temperature, and crystallite degree. Only MAH 3 wt% additive increases for the crystallinity content of about 11.7% what means that it improves nucleation capacity or increases the crystallization rate.

As demonstrated El-Zyat et. al. [41], further investigation into the impact of gamma irradiation on the additive-enhanced material would be of value. Authors studied bio-composite rHDPE with sugarcan bagasse chemicaly modified with acetic anhydrate. In results gamma irradiation (50-250 kGy absorbed dose range) improves water resistance and shows higher thermal stability of composite modified by mentioned additive.

This paper is a further step towards a better understandingthe behavior of recycled polyethylene blends with compatibilizers. It presents the possibility of modifying rHDPE/rGFRP composite blend with γ-irradiation.

REFERENCES

1. ICT Fibers. Available online: https://ictfibers.com/ (accessed on 2024-11-05).
2. Spychala MJ, Latko-Durałek P, Miedzińska D, Sałasińska K, Cetnar I, Popławski A, Boczkowska A. Structural and mechanical properties of recycled HDPE with milled GFRP as a filler. Materials. 2022; 15: 5302. https://doi.org/10.3390/ma15155302
3. Spychała MJ, Miedzińska D. Potencjalne kierunki wdrożenia nowego materiału kompozytowego z recyklatów HDPE i LPS. Projektowanie, Budowa i Eksploatacja Maszyn – cz. III. 2024.
4. Rahayu Y, Wahyu S. Physical Behaviour of Wood Plastic Composite Made of Recycled High-Density Polyethylene (HDPE). Jurnal Kehutanan Papuasia. 2023;9: 229–237. https://doi.org/10.46703
5. Dorra H, Khlif M, Tounsi F, Bradai C. Effect of Maleic Anhydride–Grafted Polypropylene Coupling Agent on Mechanical Properties of HDPE Composites Filled with Grape Leaves Fiber. Biomass Conversion and Biorefinery. 2024;14(14):15251–1563. https://doi.org/10.1007/s13399-023-03963-x
6. Long Y, Shanks RA. The use of additives in the processing of biodegradable polyesters. Journal of Applied Polymer Science. 1996;61:1877.
7. Misra RKD, Nerikar P, Bertrand K, Murphy D. Nanocrystalline filler induced changes in electrical and stability properties of a polymer nanocomposite electrolyte based on amorphous matrix. Journal of Materials Science. 2004;384:284.
8. Li Q, Matuana LM. Effectiveness of maleated and acrylic acid-functionalized polyolefin coupling agents for HDPE-wood-flour composites. Journal of Thermoplastic Composite Materials. 2003;16(6): 551–564. https://doi.org/10.1177/089270503033340
9. Abad MJ, Ares A, Barral-Losada LF, Ramirez CR. Effects of a mixture of stabilizers on the structure and mechanical properties of polyethylene during reprocessing. Journal of Applied Polymers Science. 2004;92(6). https://doi.org/10.1002/app.20420
10. Delli E, Gkiliopoulos D, Vouvoudi E, Bikiaris D, Chrissafis K. Defining the Effect of a Polymeric Compatibilizer on the Properties of Random Polypropylene/Glass Fibre Composites. Journal of Composites Science. 2024 ; 8:44. https://doi.org/10.3390/jcs8020044
11. Wu Y, Song Y, Wu D, Mao X, Yang X, Jiang S, Zhang C, Guo R. Recent Progress in Modifications, Properties, and Practical Applications of Glass Fiber. Molecules. 2023;28:2466. https://doi.org/10.3390/molecules28062466
12. Vachon J, Assad-Alkhateb D, de Araujo Hsia L, Lora JH, Baumberger S. Effect of compatibilizers on polyethylene-eucalyptus lignin blends. Journal of Applied Polymers Science. 2023;140:e53695. https://doi.org/10.1002/app.53695
13. Ghosh A. Performance modifying techniques for recycled thermoplastics. Resources, Conservation and Recycling. 2021;175. https://doi.org/10.1016/j.resconrec.2021.105887
14. Tselios C, Bikiaris D, Savidis P, Panayiotou C, Larena AJ. Glass-fiber reinforcement of in situ compatibilized polypropylene/ polyethylene blends. Journal of Material Science. 1999;34:385–394. https://doi.org/10.1023/A:1004434412273
15. Noranizan IA, Ahmad I. Effect of fiber loading and compatibilizer on rheological, mechanical, and morphological behaviors. Open Journal of Polymer Chemistry. 2012;2(2). https://doi.org/10.4236/ojpchem.2012.22005
16. Zheng A, Wang H, Zhu X, Masuda S. Studies on the interface of glass fiber-reinforced polypropylene composite. Composite Interfaces. 2002;9:319–333. https://doi.org/10.1163/156855402760194683
17. Watanabe R, Sugahara A, Hagihara H, Mizukado J, Shinzawa H. Insight into interfacial compatibilization of glass-fiber-reinforced polypropylene (PP) using maleic-anhydride modified PP employing infrared spectroscopic imaging. Composites Science and Technology. 2020;199. https://doi.org/10.1016/j.compcitech.2020.108379
18. Wündrich K. A review of radiation resistance for plastic and elastomeric materials. Physics, Materials Science. 1985;24:503–510.
19. Kokta BV, Raj RG, Daneault C. Use of wood flour as filler in polypropylene: studies on mechanical properties. Polymer Plastic Technology and Engineering. 1989;28(3).
20. Raj RG, Kokta BV, Maldas D, Daneault C. Use of wood fibers in thermoplastics. VII. The effect of coupling agents in polyethylene-wood fiber composites. Journal of Applied Polymer Science 1989;37(4).
21. Kuan HC, Huang JM, Ma CCM, Wang FY. Processability, morphology, and mechanical properties of wood-reinforced high-density polyethylene composites. Plastics Rubber and Composites. 2003;32.
22. Bengtsson M, Gatenholm P, Oksman K. The effect of crosslinking on the properties of polyethylene/wood flour composites. Compos Science Technology 2005;65(10):1468–79.
23. Liu NC, Yao GP, Huang H. Influences of grafting formulations and processing conditions on properties of silane grafted moisture crosslinked polypropylenes. Polymers. 2000;41.
24. Singh A. Irradiation of polyethylene: Some aspects of crosslinking and oxidative degradation. Radiation Physics and Chemistry.

1999;56:375–380.

25. Polymer-Additives. https://polymer-additives.specialchem.com/product/a-basf-irgacycle-ps-032-g
26. Mengeloglu F, Karakus K. Thermal degradation, mechanical properties, and morphology of wheat straw flour-filled recycled thermoplastic composites. Sensors. 2008;8:500–519. https://doi.org/10.3390/s8010500
27. Polymer-Additives. https://polymer-additives.specialchem.com/product/a-silma-silmalink-pro-453
28. PN-EN ISO 527-2. Plastics. Determination of Tensile Properties. Part 2: Test Conditions for Moulding and Extrusion Plastics. Polski Komitet Normalizacyjny: Warsaw. Poland; 2012.
29. ASTM D638-14; Standard Test Method for Tensile Properties of Plastics. ASM International: Novelty OH USA; 2014.
30. Wojnar L, Kurzydłowski KJ, Szala J. Praktyka Analizy Obrazu. Polskie Towarzystwo Stereologiczne; 2002.
31. Ross CK, Klassen NV, Shortt KR, Smith GD. A Direct Comparison of Water Calorimetry and Fricke Dosimetry. Physics in Medicine & Biology. 1989;34. https://doi.org/10.1088/0031-9155/34/1/003
32. Klassen NV, Shortt KR, Seuntjens J, Ross CK. Fricke dosimetry: The difference between $G(Fe^{3+})$ for Co-60 gamma-rays and high-energy x-rays. Physics in Medicine & Biology. 1999;44:1609–1624. https://doi.org/10.1088/0031-9155/44/7/303
33. Cota SS, Vasconcelos V, Senne Jr M, Carvalho LL, Rezende DB, Côrrea RF. Changes in mechanical properties due to gamma irradiation of high-density polyethylene (HDPE). Brazilian Journal of Chemical Engineering. 2007;24:259–265. https://doi.org/10.1590/S0104-66322007000200010
34. Hejna A, Barczewski M., Kosmela P., Ani´sko J., Mysiukiewicz, O., Mar´c M. Mandarin peel as an auspicious functional filler for polymer composites. Macedonian Journal of Chemistry and Chemical Engineering. 2021;40: 89–106.
35. da Silva GdA, d'Almeida JRM. Mechanical properties and morphology of HDPE/PA12 blends compatibilized with HDPE-alt-MAH. Polymers and Polymer Composites. 2022;30:1–13. https://doi.org/10.1177/09673911211064049
36. Yu S, Hwang YH, Lee KT, Kim SO, Hwang JY, Hong SH. Outstanding strengthening and toughening behavior of 3D-printed fiber-reinforced composites designed by biomimetic interfacial heterogeneity. Advanced Science. 2022;9, 2103561. https://10.1002/advs.202103561.
37. Fazli A, Stevanovic T, Rodrigue D. Recycled HDPE/Natural Fiber Composites Modified with Waste Tire Rubber: A Comparison between Injection and Compression Molding. Polymers. 2022;14(15):3197. https://doi.org/10.3390/polym14153197
38. EL-Zayat MM, Abdel-Hakim A, Maysa AM. Effect of gamma radiation on the physico mechanical properties of recycled HDPE/modified sugarcane bagasse composite. Journal of Macromolecular Science. 2019, Part A. https://doi.org/10.1080/10601325.2018.1549949
39. Shershneva IN, Shershnev VA, Bubnova ML, Lesnichaya VA, Kolesnikova AM, Rabinskiy LN, Kydralieva KA, Dzhardimalieva GI. Fiber-Matrix-Coupling Agent Interactions in Glass-Fiber-Reinforced Polyethylene Composites Under Gamma Irradiation. Mechanics of Composite Materials. 2019;55. https://doi.org/10.1007/s11029-019-09836-7
40. Valadez-Gonzalez A, Cervantes-Uc JM, Veleva L. Mineral filler influence on the photo-oxidation of high density polyethylene: I. Accelerated UV chamber exposure test. Polymer Degradation and Stability.1999;63(2):253–260. https://doi.org/10.1016/S01413910(98)00102-5
41. Hassan A, Abd. Rahman N, Yahya R. Extrusion and injection-molding of glass fiber/MAPP/polypropylene: effect of coupling agent on DSC, DMA, and mechanical properties. Journal of Reinforced Plastics and Composites. 2011;30(14):1223–1232. https://doi.org/10.1177/0731684411417916
42. Kang KS, Lee SI, Lee TJ, Narayan R, Shin BY. Effect of biobased and biodegradable nucleating agent on the isothermal crystallization of poly(lactic acid). Korean Journal of Chemical Engineering. 2008;25(3):599–608. https://doi.org/10.1007/s11814-008-0101-7
43. Ahmad H, Rostami-Tapeh-Esmaeil E, Rodrigue D. The effect of chemical crosslinking on the properties of rotomolded high density polyethylene. Applied Polymer Science. 2023; 141(1): e54744. https://doi.org/10.1002/app.54744.46
44. Wang W, Xiaochao Z, Zongyuan M, Weiquan Z. Effects of Gamma Radiation on the Impact Strength of Polypropylene (PP)/High Density Polyethylene (HDPE) Blends. Results in Physics. 2019;12:2169–2174. https://doi.org/10.1016/j.rinp.2019.02.020

The work has been accomplished under the research project No. 22-873 financed by the Military University of Technology.

Maciej Jan Spychała: https://orcid.org/0000-0002-4612-1639

Danuta Miedzińska: https://orcid.org/0000-0003-2503-6600

Grzegorz Sławiński: https://orcid.org/0000-0003-0411-0955

Dorota Gajda: https://orcid.org/0000-0002-6335-4792

Paulina Latko-Durałek: https://orcid.org/0000-0002-1568-5431

Anna Czajka-Warowna: https://orcid.org/0000-0003-0121-1996

Tomasz Szreder: https://orcid.org/0000-0003-0074-6315

DOI 10.2478/ama-2025-0043

USING COMPUTER SIMULATION TO EFFECTIVELY SOLVE POWER TRANSMISSION PROBLEMS FOR NON-SINUSOIDAL WAVEFORMS

Maciej KLEBBA* , **Arkadiusz FRĄCZ*** , **Michał BRODZICKI*** , **Adrianna RZEPKOWSKA****

*Faculty of Mechanical and Electrical Engineering, Polish Naval Academy, Śmidowicza 69 Street 81-127 Gdynia, Poland
**Doctoral School of GMU, Gdynia Maritime University, 81-87 Morska Street, 81-225 Gdynia, Poland

m.klebba@amw.gdynia.pl, a.fracz@amw.gdynia.pl, m.brodzicki@amw.gdynia.pl, a.rzepkowska@sd.umg.edu.pl

received 07 February 2025, revised 06 June 2025, accepted 10 June 2025

Abstract: Nonlinear and periodically switched receivers can cause distortions in current and voltage waveforms within power systems. The growing use of renewable energy sources introduces electrical energy into the system through power converters, which often produce voltages that approximate a sinusoidal waveform rather than being perfectly sinusoidal. This trend poses increasing challenges in designing new systems and managing existing ones. A proper description and interpretation of the physical phenomena associated with non-sinusoidal waveforms have become increasingly important. This paper presents simulation models of power circuits using non-sinusoidal signals and discusses the energy transfer that occurs within them. It also outlines current computational methods based on circuit theories as they apply to these systems. The results from the calculations and simulations in various configurations are compared with data obtained from real objects. The findings highlight fundamental inaccuracies in the methods used and potential errors arising from computer simulations.

Key words: energy transfer, non-sinusoidal waveforms, distortion, simulation, reactive power, power factor

1. INTRODUCTION

To describe the transmission of electrical energy in circuits, various physical quantities known as powers are utilized, particularly in systems designed for specific purposes. In the context of single-phase circuits with sinusoidal current and voltage waveforms, three key types of power are defined: active power *P*, reactive power *Q*, and apparent power *S*. Understanding these individual powers is crucial for both design and operational purposes. Active power, consumed by businesses, public institutions, or individual households, forms the basis for financial settlements between energy suppliers and consumers. Apparent power is equally important, as it is needed for the proper design of electricity-generating devices and transmission equipment, including transformers, transmission lines, and circuit breakers. Reactive power emerges in the system alongside active power when the load is not purely resistive, leading to a phase shift between the current flowing through the circuit and the supply voltage. The concepts of active, reactive, and apparent power in single-phase circuits with sinusoidal voltage *u(t)* and current *i(t)* waveforms were thoroughly described in the 19th century.

Active power [1]:

$$P = \frac{1}{T}\int_0^T u(t)i(t)\,dt = UIcos\varphi \qquad (1)$$

Reactive power [1]:

$$\text{Q}= \frac{1}{T}\int_0^T u(t)i\left(t-\frac{T}{4}\right)dt = UIsin\varphi \qquad (2)$$

Apparent power [1]:

$$S = \sqrt{\frac{1}{T}\int_0^T u^2(t)\,dt}\sqrt{\frac{1}{T}\int_0^T i^2(t)\,dt} = UI \qquad (3)$$

where:
U – voltage effective value,
I – current effective value,
φ – phase shift angle of current relative to voltage.

The relation that connects all types of power is called the power equation and for sinusoidal waveforms takes the form [1]:

$$S^2 = P^2 + Q^2 \qquad (4)$$

Power devices designed for the transmission of electrical energy are developed with the maximum apparent power in consideration. The energy supplied to and consumed by the end user is characterized by active power. In situations where there is a phase shift, the active power is less than the apparent power. Consequently, the transmission capacity of devices optimized for apparent power is not fully utilized. This results in higher effective supply current values, which consequently lead to increased transmission losses. The parameter that indicates the efficiency with which the energy source's transmission capacity is utilized by the receiver is referred to as the Power Factor [1]:

$$PF = \frac{P}{S} = \frac{P}{\sqrt{P^2+Q^2}} \qquad (5)$$

This factor equals 1 when there is no reactive power present, meaning the receiver does not induce a phase shift between current and voltage. For purely sinusoidal waveforms, the Power Factor (PF) is represented by $cos\varphi$.

In 1892, Charles Proteus Steinmetz conducted an experiment with an electric arc [2]. In the arrangement shown in Figure 1.

Steinmetz noticed that in a circuit with an arc lamp, despite the lack of phase shift, i.e. in the absence of reactive power defined classically according to equation (2), the apparent power is greater than the active power [2]:

$$S > P \tag{6}$$

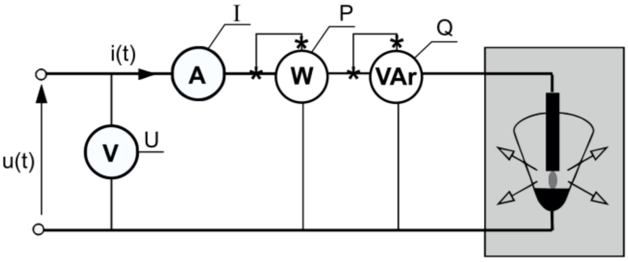

Fig. 1. Arc lamp circuit [16]

This means that according to equation (5), the power factor of the arc lamp is less than 1. The difference between equations (5) and (6) is due to the presence of a non-sinusoidal current in the circuit with the arc.

Currently, nonlinear and periodically switched receivers cause current and voltage waveform distortions in power systems. The increasingly widespread use of renewable energy sources introduces electricity into the system generated using power converters that provide voltages that have only an approximate sinusoidal waveform. Designing new systems and operating current ones is an increasing challenge. Proper description and interpretation of physical phenomena in non-sinusoidal waveforms is becoming increasingly important.

Steinmetz's observation initiated a discussion on the energy properties of circuits with non-sinusoidal waveforms. The debate, doubts and research continue to this day. The problem is to provide an unambiguous and universal description of the energy transfer phenomenon and to define individual powers. The description of these properties and the set of interpretations of energy phenomena is called power theory.

2. REACTIVE POWER THEORIES

As a result of work over a hundred years, many power theories have been developed. Many of them are considered imperfect. In the literature, we can find many works questioning the validity of individual theories.

The most widespread theory describing energy phenomena occurring in circuits with non-sinusoidal waveforms is the theory presented by a professor at the Polytechnic University of Bucharest, C.I. Budeanu [3]. Since the reactive power Q in circuits with sinusoidal current and voltage waveforms is calculated from formula (2) and this power is the amplitude of the oscillating component of the instantaneous power *p(t)*, i.e. the speed of energy flow between the power source and the receiver:

$$p(t) \overset{\mathrm{def}}{=} \frac{dW(t)}{dt} = u(t)i(t) \tag{7}$$

According to the assumptions of Budeanu's theory, active and reactive powers for non-sinusoidal waveforms are the sum of the powers of individual harmonics. So, for active power the definition is as follows:

$$P = \sum_n U_n I_n cos\varphi_n = \sum_n P_n \tag{8}$$

For reactive power:

$$Q_B = \sum_n U_n I_n sin\varphi_n = \sum_n Q_{Bn} \tag{9}$$

The B index at reactive power Q_B means reactive power according to Budeanu's theory. The sum of the squares of the active power and reactive power is less than the square of the apparent power, therefore the power equation has been supplemented with the distortion power:

$$D \overset{\mathrm{def}}{=} \sqrt{S^2 - (P^2 + Q_B^2)} \tag{10}$$

The concept of distortion power is relevant only when dealing with non-sinusoidal currents and is often used to interpret physical phenomena in these types of circuits. Despite the widespread acceptance of Budeanu's theory, there are several doubts regarding its overall accuracy and applicability. Many authors have analytically demonstrated that Budeanu's interpretation of distortion power lacks a solid physical basis. In some instances, there is no correlation between the distortion power *(D)* and the actual distortion of the waveform. Furthermore, the issue of power compensation remains unresolved within the framework of this theory.

The second most widespread power theory is presented by Professor Fryze. He was sceptical of Budeanu's theory and the analysis that involves decomposing signals through Fourier series. Professor Fryze argued that it is possible to describe phenomena in non-sinusoidal circuits without breaking down the signal into individual harmonics. The foundation of his theory is the assertion that the receiver with the best energy properties, when viewed from the power supply side, is one that has no susceptance. This type of receiver can be represented using conductance G_e [4].

$$G_e = \frac{P}{||u||^2} \tag{11}$$

where $||u||$ is the effective value of the voltage, which in the case of harmonic excitation is equal to the square root of the sum of the squares of the effective values of the individual harmonics, that is:

$$||u|| = \sqrt{\sum_n ||u_n||^2} \tag{12}$$

The current flowing between the source and the receiver with the conductance G_e has the same course as the supply voltage. It is called the *active current* and has the value:

$$i_a(t) = G_e \cdot u(t) \tag{13}$$

This current flows in the circuit if the receiver consumes active power *P*. Since the effective value of this current depends on the active power drawn by the receiver, therefore:

$$||i_a|| = ||u|| G_e = \frac{P}{||u||} \tag{14}$$

The remaining part of the current flowing through the receiver is harmful because it increases the effective value of the supply current and does not give any useful effects in return. This current is called *reactive current*:

$$i_{rF}(t) = i(t) - i_a(t) \tag{15}$$

The index F in the equations means quantities according to the Fryze theory. The receiver current has only two components: active and reactive:

$$i(t) = i_a(t) + i_{rF}(t) \tag{16}$$

The author of the theory showed that the reactive current is orthogonal to the active current. Therefore, the effective values of the

DOI 10.2478/ama-2025-0043

current components satisfy the relation:

$$\|i\|^2 = \|i_a\|^2 + \|i_{rF}\|^2 \tag{17}$$

By multiplying both sides of the equation by the square of the effective voltage value we obtain the Fryze power equation:

$$S^2 = P^2 + {Q_f}^2 \tag{18}$$

And the reactive power itself is defined as:

$$Q_F = \|u\| * \|i_{rF}\| \tag{19}$$

The author of the method successfully determined the system's energy parameters without relying on Fourier series.

In 1972, W. Shepard and P. Zakikhani [5] published another theory, which proposed that current as a function of time can be divided into two components: the resistive current $i_R(t)$ and the reactive current $i_r(t)$. These components are treated as harmonic spectra and are orthogonal to each other.

$$i_R(t) = \sqrt{2}\sum_{n=1}^{\infty} I_n cos\varphi_n \cos\,(n\omega_1 - \alpha_n) \tag{20}$$

$$i_r(t) = \sqrt{2}\sum_{n=1}^{\infty} I_n sin\varphi_n \sin\,(n\omega_1 - \beta_n) \tag{21}$$

where:
φ_n – phase shift between current and voltage harmonics,
α_n – initial phase of n-harmonic current,
β_n – initial phase of n-harmonic voltage,

As a consequence, the dependence of the expressed power was obtained by the formula:

$$S^2 = S_R^2 + Q^2 \tag{22}$$

The equation mentioned above does not account for active power, which is a primary reason for the criticism of this theory. Nevertheless, it offers a practical advantage by enabling the determination of the optimal compensation capacity for inductive load currents. In subsequent years, the equation was enhanced with the concept of complementary reactive power, as described by the relationship in reference [6]:

$$S_c = \sqrt{S_R^2 - P^2} \tag{23}$$

Therefore

$$S^2 = P^2 + Q^2 + S_c^2 \tag{24}$$

Many theories of electric power have been published to date, including Buchholz [7], Curtis [8], Depenbrock [9], Kusters and Moore [10], A. Nabae, H. Akagi, Y. Kanazaway [11] and Czarnecki [12]. Despite so many theories and such a long time that has passed in research, we still do not have an answer to the question of what reactive power is and what it is responsible for. Therefore, after almost 100 years, Budeanu's and Fryze's definitions of power and Illovici's concept of currents and voltages [13] have reappeared in the circle of interest. The works of many researchers show the imperfections of individual theories and go towards finding a universal description of phenomena occurring in systems with non-sinusoidal waveforms [14,15,16].

This article explores the potential of using simulation techniques to analyse circuits with non-sinusoidal voltage and current waveforms. To validate the proposed solutions, both arithmetic calculations and simulation results will be compared against tests conducted on real components. Additionally, the article will examine the application of Budeanu's theory to a circuit where the current waveform does not exist throughout the entire period T.

2.1. Analytical interpretation

As mentioned in the introduction, many theories are supposed to clearly describe the transfer of energy in both sinusoidal and non-sinusoidal waveforms. Scientists worldwide are trying to confirm or disprove the validity of individual theories. In this article, the authors will try to check the usefulness of simulation methods for verifying specific examples that are supposed to confirm or disprove individual theories.

The first example under study is the circuit cited by Professor Czarnecki in his article [17]. In this article, the author analytically solves a circuit consisting of a sinusoidal power source with zero impedance, a triac, and a purely resistive load. The circuit is shown in Figure 1.

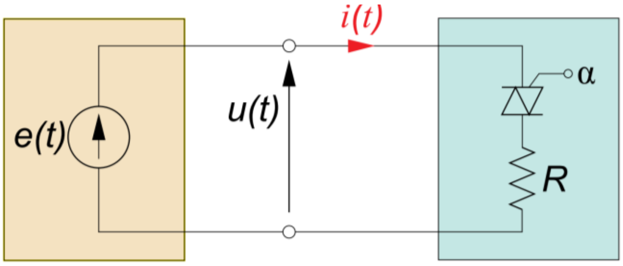

Fig. 1. Purely resistive circuit with TRIAC [17]

Based on the mathematical proof presented, which relies on Budeanu's power theory, it can be concluded that in a purely resistive system, reactive power is observed. However, this situation does not reflect reality, as a purely resistive load cannot store energy. Consequently, there can be no oscillation of energy between the source and the load, meaning that reactive power cannot occur. The current waveform in the circuit, assuming a sinusoidal supply voltage waveform, is illustrated in Figure 2.

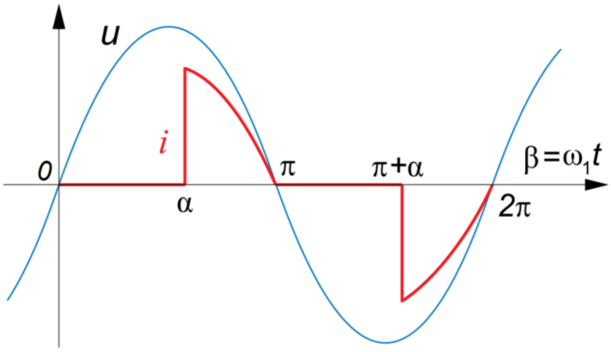

Fig. 2. Current waveform in the circuit with TRIAC [17]

From the current waveform graph it is clear that the instantaneous power of the receiver calculated from formula (25):

$$p(t) = u(t)i(t) \tag{25}$$

where:
$u(t)$ – instantaneous voltage value,
$i(t)$ – instantaneous current value,
always takes a positive value, so there is no energy oscillation in the system.

Continuing the calculations according to Budeanu's theory, the author calculated the first harmonic of the current signal in the case of a typical mains voltage supply $u = 220\sqrt{2}sin\omega t\ [V]$. Assuming the triac firing angle at $\alpha = 135°$, the fundamental harmonic of the current has the value:

$$i_1(t) = \sqrt{2}I_1 sin(\omega t - \varphi_1) \tag{26}$$

$$i_1(t) = 40.32\sqrt{2}sin(\omega t - 60.28°)\ [A] \tag{27}$$

there

$$Q = UI_1 sin\varphi_1 = 7.7\ [kVar] \tag{28}$$

The result obtained from arithmetic calculations should be interpreted in such a way that energy oscillations between the source and the receiver are not necessary for the occurrence of reactive power. Such a result does not agree with the physical interpretation of reactive power.

The first problem we encounter in this situation is the inconsistency of the physical interpretation of reactive power with the analytical results obtained.

The second problem is the correct application of Budeanu's power theory. Indeed, the first harmonic of the current in this circuit will be shifted relative to the supply voltage, but it should be mentioned here that the total reactive power and active power should be calculated as the sum of the powers of the individual harmonics:

$$P = U_1 I_1 cos\varphi_1 \tag{29}$$

$$Q = U_1 I_1 sin\varphi_1 \tag{30}$$

If we assume for power calculations in the circuit that the current waveform is distributed into individual harmonics, and leave the supply voltage in the shape of a pure sinusoid, the results obtained in the article [16] will be confirmed and we will be able to show the imperfection of the theory. However, if we recall that energy transfer occurs only when energy is drawn by the receiver, i.e. only in those time periods in which the current flows, then only these time periods should be taken into account for the calculations of the supply voltage. In the case under consideration, it would also be necessary to analyse the load voltage into individual harmonics using the Fourier series. With such an application of the power theory, it turns out that there is no phase shift angle between the first harmonic of the current and the first harmonic of the voltage - $cos\varphi_1 = 1$. In such an interpretation of the power theory, we will not deal with the occurrence of reactive power.

As you can see, algebraic calculations carry many problems and ambiguities regarding the interpretation of individual issues. Hence the authors' proposal to try to use simulation tools to verify the calculations and confirm the results in relation to real physical phenomena occurring in circuits.

2.2. Simulation studies

Simulation studies were conducted in the MATLAB–Simulink environment. The circuit depicted in Figure 1 was assembled, with all component parameters selected according to the analytical calculations. Measurements were taken using a voltmeter and an ammeter, while power measurements were based on the principles of Budeanu's theory. The circuit diagram is presented in Figure 3.

The system was built using blocks from the specialized power systems library. The library allows you to build basic electrical circuits and perform calculations using three selectable methods:

- Continuous, which uses a variable-step solver from Simulink®;
- Discretization of the electrical system for a solution at fixed time steps;
- Continuous or discrete phasor solution.

The powergui block also opens tools for steady-state and simulation results analysis and for advanced parameter design.

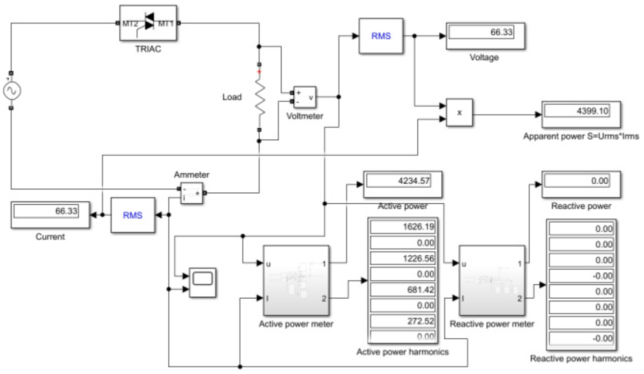

Fig. 3. Circuit diagram in MATLAB-Simulink application

As can be seen in the diagram, in addition to the standard blocks from the "specialized power systems" library, it contains the "Active power meter" and "Reactive power meter" blocks. These are elements created for the needs of the simulations carried out. Their task is to calculate active and reactive power by the assumptions of the Budean theory. The functional diagram of these blocks is shown in Figure 4. Block -C- is a constant with the value of √2

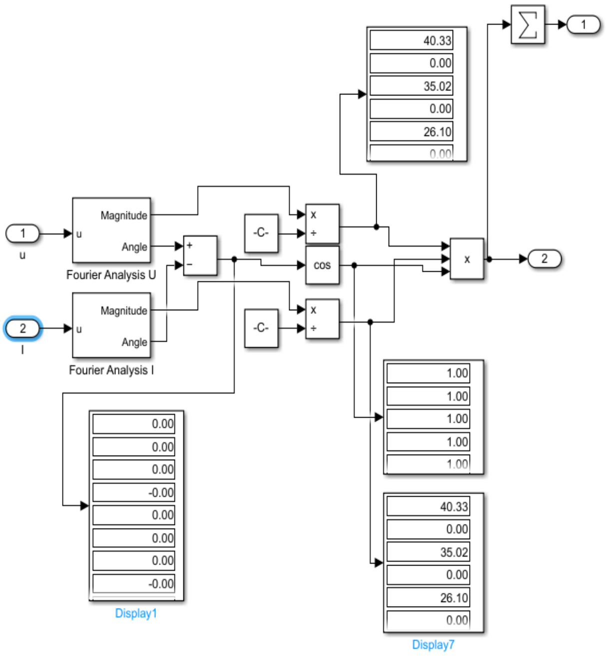

Fig. 4. MATLAB-Simulink active power meter diagram

The tests were carried out in two variants. In the first, the wattmeter, consisting of a voltmeter and an ammeter, was connected in such a way as to measure the source voltage and the current flowing in the circuit (Figure 5a). In the second variant, the voltmeter was connected to the system in such a way as to measure the voltage directly at the receiver (Figure 5b). The use of both variants is intended to verify whether the theoretical description is universal enough so that regardless of the connection, the power consumed by the only receiver in the system is the same.

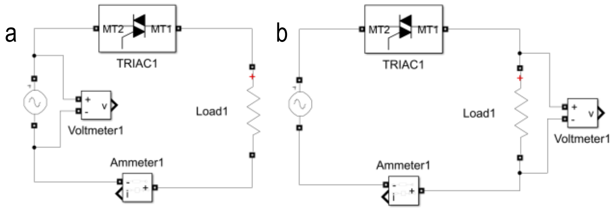

Fig. 5. Connection diagrams a) supply voltage measurement b) voltage measurement at the receiver

The tests were carried out for 3 different triac ignition angles:

- $\alpha = 0^{\circ}$ - fully sinusoidal waveform,
- $\alpha = 90^{\circ}$ - a waveform in which half of the time passed without energy transfer
- $\alpha = 135^{\circ}$ - waveform with parameters from the article [16]

The simulations at different ignition angles were conducted to verify the correctness of the simulation operation under different conditions. At the same time, it was possible to confirm the results obtained for well-known conditions such as a pure sinusoidal waveform. The results of the simulations are presented in Table 1.

Tab. 1. Simulation results table

Circuit type	TRIAC firing angle	Active power	Reactive power	Apparent power	power factor	Voltage	Current
	°	kW	kVar	kVA		V	A
a	0	48.4	0	48.4	1	220	220
b	0	48.4	0	48.4	1	220	220
a	90	24.2	15.4	34.2	0.71	220	155.6
b	90	23.8	0	24.2	1	155.6	155.6
a	135	4.4	7.7	14.6	0.3	220	66.3
b	135	4.23	0	4.4	1	66.3	66.3

The results presented in the table highlight several key observations: The method of connecting the voltmeter impacts the calculation of power consumed by the receiver, even when only a single purely resistive receiver is present in the system. Since a purely resistive receiver cannot generate reactive power in the circuit, the simulation results may be inaccurate in certain cases. This issue arises from a misunderstanding of how to calculate apparent power and reactive power, particularly when relying on the first harmonic of the current, as outlined in equation (28). When the wattmeter is connected as shown in Figure 5(a)—the conventional method used for energy meters in both residential and industrial settings—the first harmonic of the current will indeed be phase-shifted relative to the first harmonic of the total supply voltage. The variations in voltages and currents for this setup are illustrated in Figure 6.

This text presents a simplified application of Budeanu's circuit theory, focusing on the total supply voltage waveform for calculations. It is important to remember that energy transfer takes place only during the moments when both voltage and electric current are present. Therefore, if current flow does not occur throughout the entire duration of the supply voltage signal, we should not use the full supply voltage signal for calculations. Instead, we should only consider the time intervals in which actual energy transfer occurs. For example, this situation occurs when we connect a voltmeter directly to the load. In this case, we will observe both the voltage and current waveforms during energy transfer (see Figure 7).

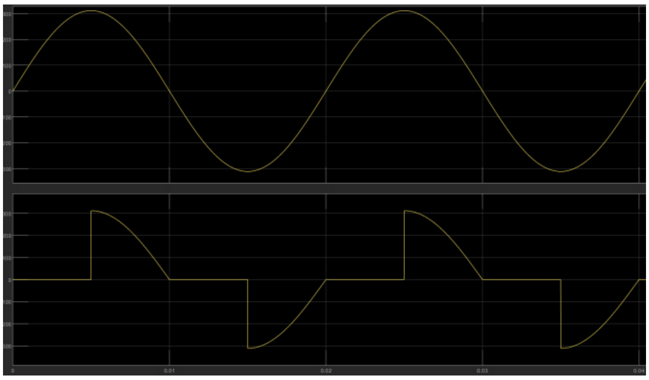

Fig. 6. Voltage and current waveform for the TRIAC firing angle of 90° incircuit a)

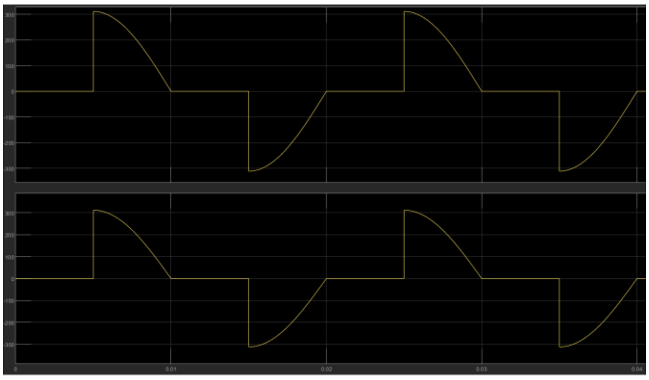

Fig. 7. Voltage and current waveform for the TRIAC firing angle of 90° in circuit b)

As can be seen in the graph, the voltage waveform on the receiver is different from the supply voltage. In this case, if we apply formulas (29) and (30) to the calculations, we will obtain a result that is confirmed by physical phenomena. In a circuit with a purely resistive receiver, there is no reactive power, regardless of the triac ignition angle. In such a circuit, there is also no phase shift between individual voltage and current harmonics.

Repeating the calculations from the article in a simulation manner confirmed the results obtained algebraically, provided that the full supply voltage signal is accepted for calculations. In the case of using the voltage waveform resulting from the load current waveform, the simulation results agree with the physical interpretation of energy transfer with a resistive load.

In Table 1, slight differences can be observed between active and apparent power in system b when measuring signals that are not full sinusoids. At a Triac firing angle of 90°, the apparent power is 24.2 kVA, while the active power is 23.8 kW, with no reactive power measured. Similarly, at a firing angle of 135°, the apparent power is 4.4 kVA and the active power is 4.23 kW, again with no reactive power. These differences do not stem from any physical phenomena; rather, they are not errors resulting from the calculation method used. Instead, these discrepancies arise from the limited number of harmonics included in the simulation calculations. In this case, the authors restricted the number of harmonics to 30 to reduce computation time. These errors can be minimized by increasing the number of harmonics, and they do not indicate that the method is incorrect but rather highlight its limitations.

As can be seen from the simulation results presented above, it is possible to perform calculations using the specialized power systems library and obtain results consistent with theoretical assumptions. Another problem is the selection of the appropriate mathematical apparatus and the proper interpretation of its assumptions.

2.3. Research on a real object

In order to confirm the correctness of the results obtained by simulation, the real circuit was tested based on the circuit from Figure 1. Due to the high current values used for algebraic calculations and simulation studies, of the order of over 200A, the system for testing the real object was built with a load of higher resistance in order to limit the current in the circuit. The scale used does not affect the possibility of confirming the results obtained analytically in practice. The experiment parameters were selected as follows:

- Supply Voltage 103V RMS,
- Triac firing angles $0^\circ, 90^\circ, 135^\circ$,
- Load Resistance 235Ω,

As part of the tested circuit, Gwinstek GPM-8213 wattmeter were connected, enabling the simultaneous measurement of voltage, current, active power, reactive power, apparent power, total harmonic distortion (THD), and power factor (PF). The results from the tests conducted on the real object are presented in Table 2.

Tab. 2. Real object results table

Circuit type	TRIAC firing angle	Active power	Reactive power	Apparent power	power factor	Voltage	Current
	∘	W	Var	VA		V	mA
a	0	43.1	0	43.1	1	103	420
b	0	43.1	0	43.1	1	103	420
a	90	20.9	21.1	29.7	0.71	102.8	288.9
b	90	19.4	0	19.4	1	67.6	286.3
a	135	4.2	12.9	13.5	0.31	102.8	131.6
b	135	4	0	4	1	30.7	129.9

Fig. 8. Real object test results: a) power and power factor measurement, b) signal waveform on a resistive load

By comparing the results obtained from the simulation in Table 1 with those from the real object in Table 2, we can conclude that the simulation studies accurately reflect the nature of physical phenomena. The measurements taken demonstrate that current measuring devices, which operate based on established theories, can sometimes indicate values that do not correspond to real-world situations. For instance, in the case of a discontinuous signal throughout the period of changes, a wattmeter may suggest the presence of reactive power in a circuit that is purely resistive (see Figure 8).

3. CONCLUSION

The research presented in this article makes several fundamental observations.

Theories of power, which have been studied and developed for over a century, are not completely unambiguous. Researchers worldwide are attempting to mathematically describe the phenomena occurring in electrical circuits. While this has been successfully achieved for direct current (DC) and alternating current (AC) with purely sinusoidal waveforms, there are several challenges when dealing with non-sinusoidal waveforms. Applying theoretical principles without considering the specific characteristics of a given circuit and separating calculations from physical interpretations can lead to erroneous conclusions, such as the appearance of reactive power in a circuit with a resistive load.

Simulation studies facilitate a significant simplification and acceleration of circuit analysis compared to analytical methods. However, it is crucial to ensure that, similar to theoretical considerations, the research reflects the real physical phenomena occurring in the circuit being studied.

In both methods of solving circuits, a key condition is that energy transfer occurs only during the flow of electric current. Therefore, with discontinuous signals, the effective value of the supply voltage cannot simply be used; instead, the actual effective value of the voltage must be calculated based on instantaneous values. In this context, the RMS value of the supply voltage does not equal the effective value of the voltage at the load.

Currently manufactured digital measuring instruments calculate the apparent power as the product of the RMS supply voltage and the RMS current flowing through the circuit. This can lead to incorrect calculations of reactive power and power factor (PF) values, especially when the signals are not purely sinusoidal.

In the next phase of research, the authors aim to develop an analytical approach to describe the phenomena occurring in electrical circuits while addressing the identified imperfections.

REFERENCES

1. Bartman J. Analysis of voltages, currents and powers in systems with periodically distorted waveforms. Rzeszów: Wydawnictwo Uniwersytetu Rzeszowskiego; 2019.
2. Steinmetz CP. Does the phase displacement occur in the current of electric arcs? ETZ. 1892;587.
3. Budeanu CI. Puissances reactives et flictives. Inst Romain I Energ. 1927.
4. Fryze S. Moc rzeczywista, urojona i pozorna w obwodach elektrycznych o przebiegach odkształconych prądu i napięcia. Przegląd Elektrotechniczny. 1932;7.
5. Nedelcu VN, Shepherd W, Zakikhani P. Suggested definition of reactive power for nonsinusoidal systems. Proc Inst Electr Eng [Internet].

1974;121(5):389. https://doi.org/10.1049/piee.1974.0086
6. Shepherd W, Zakikhani P, Sharon D. Reactive-power definitions and power-factor improvement in nonlinear systems. Proc Inst Electr Eng [Internet]. 1974 ;121(5):390. https://doi.org/10.1049/piee.1974.0087
7. Buchholz F. Die Drehstrom-Scheileistung bei ungleichmabiger Belastung der drei Zweige. Lich Und Kraft. 1922;2.
8. Curtis H, Silsbee F. Definitions of power and related quantities. AIEE. 1935;54.
9. Depenbrock M. Wirk und Blindleistung. ETG-Fachtagung, Aachen. 1979.
10. Kusters NL, Moore WJ. On the Definition of Reactive Power Under Non-Sinusoidal Conditions. IEEE Trans Power Appar Syst [Internet]. 1980;PAS-99(5):1845-54. https://doi.org/10.1109/tpas.1980.319833.
11. Akagi H, Kanazawa Y, Fujita K, Nabae A. Generalized theory of instantaneous reactive power and its application. Electr Eng JPN [Internet]. Jun 1983;103(4):58-66. https://doi.org/10.1002/eej.4391030409.
12. Czarnecki LS. Moce w obwodach elektrycznych z niesinusoidalnymi przebiegami prądów i napięć. Warszawa: Oficyna Wydawnicza Politechniki Warszawskiej; 2005.
13. Illovici M. Definition et mesure de la puissance et de l'energie reactives. Bull. Soc. Franc. Electric.1925.
14. Hartman MT, Hashad M. A few remarks on the analysis of energy transfer through any periodic current and voltage waveforms. Przegląd Elektrotechniczny. 2008;11. https://doi.org//10.1109/ISNCC.2008.4627486
15. Hartman MT. A Few Remarks on the Energy Transfer Analyses During a Time Less than Period T for Voltage and Current Waveforms in Electrical Circuits. Sci J Gdyn Marit Univ. 2022;123:32-9. Available from: https://doi.org/10.26408/123.03
16. Czarnecki LS. Development History of the Currents' Physical Components (CPC)-Based Power Theory. Autom Elektr Zakłocenia. 2016;7 nr 4(26):6-19. https://doi.org/10.17274/aez.2016.26.01
17. Czarnecki LS. Powers and compensation in circuits with nonsinusoidal and asymmetrical voltages and currents part 1 problems review. Autom Elektr Zakłocenia. 2015;6(3). https://doi.org/10.17274/AEZ.2015.21.01

The authors of the article give special thanks to Professor Marek Hartman for inspiration and substantive support during the research work.

Maciej Klebba: https://orcid.org/0000-0003-1099-577X

Arkadiusz Frącz: https://orcid.org/0009-0004-5499-2559

Michał Brodzicki: https://orcid.org/0000-0002-0366-6292

Adrianna Rzepkowska: https://orcid.org/0009-0005-2593-8542

DOI 10.2478/ama-2025-0044

E-FUEL BLEND OPERATION OF SMALL INDUSTRIAL SI-ENGINES WITH CARBURETORS

Leander MARQUARDT*, Heiner-Joachim KATKE*, Maik HABECK*, Andreas REINKE*, Lena TEUBNER*

*Fakultät Maschinenbau, Hochschule Stralsund, Zur Schwedenschanze 15, D-18435 Stralsund

leander.marquardt@hochschule-stralsund.de, heiner.katke@hochschule-stralsund.de, maik.habeck@hochschule-stralsund.de,
andreas.reinke@hochschule-stralsund.de, lena.teubner@hochschule-stralsund.de

received 12 February 2025, revised 14 May 2025, accepted 16 June 2025

Abstract: Intentions for replacing small SI-engines in motor-equipment for professional gardening and forestry by battery-electric solutions are limited by requested disposability and tolerable power-to-weight ratio. Due to this fact experimental investigations for using methanol/ gasoline fuel-blends and pure methanol in a small air-cooled industrial SI-engine (4 kW @ 3600 rpm) were carried out. At a first step (only) for these experiments, the serial mechanical carburetor was additionally equipped with a self-developed electronic lambda-control, to enable tests for different fuel-blends (Super E5, M30, M60, M100) with constant boundary conditions during engine operation without exchange of carburetor jets. This concept of control will be presented. Special needs for these SI-engines (exhaust-gas temperature, non-electric start) require a permanent sub-stoichiometric operation. For serial applications free of electronic components, the size of jets would have to be adapted as well as the use of standardized fuel-mixtures will be necessary. In addition to reference tests on different days in operation with gasoline ´Super E5´ to check repeatability, operating values and emissions will be presented for operation with the fuel-blends described. Pressure indications allow statements for changes in heat release and - additionally to acoustical perception - evaluations of combustion stability. Following inspection of engine components showed consequences of sub-stoichiometric combustion of methanol-fuel-blends and resulting recommendation. Lube-oil analysis, afterwards carried out by ATR spectroscopy shows possible contamination inside crankcase. Optical inspections and material measurements at normally used serial components of fuel system (float, housing, sealings, hoses) showed possible incompatibilities with this alcoholic fuel-blends as well as necessary alternative materials.

Key words: SI-engine, gasoline Super E5, e-fuel, fuel blend, methanol, electronic carburetor, chemical resistance

1. PROJECT MOTIVATION

The currently favorized electrification of all kinds of power drives, mainly caused by CO_2/climate-discussions reaches its technical limit in all economic sectors with restricted time frames, such as construction, agriculture, commercial gardening or forestry. The reasonably energy reservoir, stored in available accumulator technologies (e.g. 35 min for Husqvarna 120i) as well as their necessary time for re-charging (e.g.130 min for Husqvarna 120i) are no meaningful alternatives compared to the small, air-cooled SI-engines, used up to now.

The difficulties regarding manageable power-to-weight ratios, especially for hand-operated working equipment (chain saws, brush cutters, concrete cutters) and their influences on labor physiology are rarely discussed. Even well working and fuel-economy attractive 4-stroke engines with mix-lubrication [1] [2] failed inside professional market due to enlarged weight ratio of approx. 20 % compared to power-equivalent 2-stroke engines. This example significantly shows the extreme sensibility of professional customers regarding mass of their power equipment, which often must be handled in piece-rate contracts over a time of 8 hours per day.

Fig. 1a shows the nominal power rating versus the mass of commercially available chain saws in model year 2023. Data were collected from different websites (www.vergleich.org, www.amazon.de, www.baywa.de). Power rating for accumulator operated devices is often given with ‘depending on accu-level’, so that a reasonable evaluation becomes difficult. But even with the comparison of masses of cable-electric and 2-stroke saws it is obviously, that the available margin for the additional masses of accumulators is quite small.

Diagrammed in Fig. 1b are the outputs and times for use and recharging commercially available accumulator-powered lawn mowers of a Swedish supplier (www.husqvarna.com). For these times given in Fig. 1b the accumulators with the highest available capacity and the strongest re-charger were used. Power rating and usable time are not sufficient for objects with more than 1000 m^2. Comparable models of competitor Stihl are suggested for lawn areas of approx. 300 m^2… 800 m^2, so that even for ambitious hobby gardeners these devices are no meaningful options.

Alternative fuels for the existing SI-engine technology can be a wise solution for the conflict of politically driven CO_2-demands and applicability in real life. Beside biological-based alcohols with all their problems regarding monocultures electrical power-based synthetic fuels are discussed. The often favorized use of hydrogen or ammonium for energy storage fails in that case even by practical considerations regarding pressurized storage tanks and its necessary thickness of housing, so that the use of fuels, which are liquid at normal pressure and ambient temperatures, is inescapable. Even in case of a restricted volumetric energy content refilling can be executed fast, nearly everywhere without special equipment and with respect to normal safety instructions without any special knowledge.

Meaningful options can be short-chain alcohol or their blends with conventional crude oil-based gasolines or synthetic ones. For health effects as well as its specific energy content the use of longer-chain alcohol would be wise. But its production requires much electrical power, so that the focus is currently on methanol, which lower heating values is as half as for gasoline and its high toxicity occurred by resorption via respiration, eupepsia and skin-surface.

As a result of these preliminary consideration, the focus of a research project was set to experimental investigations on a typical small industrial SI-engine regarding the use of methanol/gasoline-blends. With special respect to financial limits and staff-potentials of a small university it was decided, to carry out these experiments for fuels with only 3 special volumetric methanol-fractions of 30 %, 60 % and 100 % (M30, M60, M100). For reference measurements and for blending component a commercial gasoline with 5 vol.% ethanol (Jet- Super E5 acc. DIN EN 228) was used.

Beside the operation and relevant operational values, the exhaust gas emissions were considered as well as the influence on the dilution of lubrication oil and material compatibility with plastics, used for standard tanks, carburetor-components and fuel lines. Cylinder-liner and sparkplug were inspected after the experiments. Practical relevance for the commercial use of these e-fuel blends relates to questions of evaporation rates of fuel inside the tanks, its possible component separation and changes in blend-ratio, occurred by the partly vaporization.

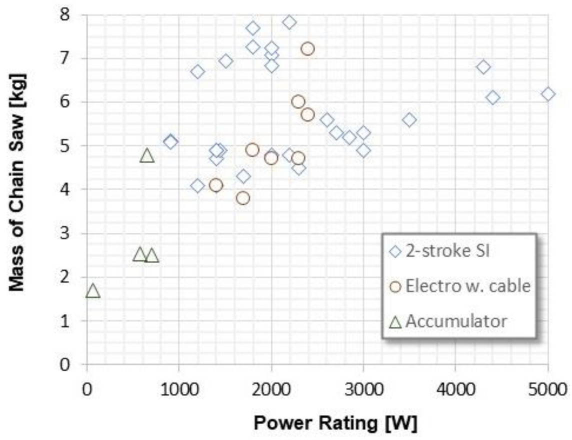

Fig. 1a. Power and mass of chain saws

Fig. 1b. Time for use/recharging of lawn mowers

2. THEORETICAL CONSIDERATIONS

2.1. Calculation of Fuel Specifications

To consider the effects of blending gasoline by methanol the relevant specifications were calculated. Due to the quite similar density of gasoline and methanol varied the values for the blends by max. 5 %, so that for dimensioning the fuel tanks the mass-related lower heating value Δh_u gives a good approximation for the volume-related energy content, too (Tab. 1). For combustion calculation the elementary analyses of all fuel-blends used, had to be calculated by mass-related superposition of both single fuels. For these calculations the fuel data for gasoline Super E5 were taken from [3]. The elementary analysis of pure methanol M100 was calculated by its molecular formula and the relevant molar masses of carbon, hydrogen and oxygen.

Tab. 1. Analysis of Gasoline (E5) and Blends with 30, 60 and 100 vol.% CH_3OH (M30, M60, M100)

Fuel	Elementary Analysis			Atomic Fraction	RON
	c_K [m%]	h_K [m%]	o_K [m%]	C : H : O	(approx.)
Super E5	88.307	11.329	0.364	1 : 1.53 : 0.00	95
M30	72.497	11.714	15.750	1 : 1.93 : 0.16	99
M60	57.167	12.087	30.668	1 : 2.52 : 0.40	103
M100	37.437	12.567	49.869	1 : 4.00 : 1.00	109

Actually, for measurement of air/fuel-ratio λ the atomic fractions C : H : O for the blends used had to be known. As well as it is very time-consuming to change these values during the measurements in lambda-meter and in exhaust-gas analysis, it was decided to leave the mass-fraction of gasoline in both measuring device and calculate the exact air/fuel-ratio for lean and sub-stoichiometric combustions by methods, usable for fuels containing important rates of oxygen, while evaluating the experiments afterwards. Simultaneously, the knowledge of the composition of fuels is basic precondition for interpretation of exhaust-gas consistency.

Due to the half energy content of methanol related to gasoline the lower heating value Δh_u decreases linearly by increasing its fraction in fuel blends (Fig. 2a, top). Furthermore, the low heating value limits its energetic shares in the blended fuels. Even with a volumetric rate of 60 % methanol its energetic portion in lower heating value is below 45 % (Fig. 2b, top). With perfect combustion the energy-specific CO_2-emission decreases by only 13 %. If the methanol is partly produced by regenerative energy and/or the necessary CO_2 for production is captured from industrial exhaust-gases or ambient air the effective CO_2-emissions are more reduced. Dependent of the literature used the values for research octane-number of methanol vary between RON = 106 [4] … 108.6 [5] … 114 [6, p. 475].

From literature there is no save numeric relation for RON of fuel-blends known. An approximation with volume-share related superposition of the properties of all single components is given by [7]. To check this approximation, the resulting RON a gasoline 'DEA-Super' was calculated this way. In [8] its composition (butane 3.8 vol.%, reformate 48,4 vol.%, light crack gasoline 27.6 vol.%, heavy crack gasoline 6.9 vol.%, tertiary butyl alcohol 1.4 vol.%, methyl-tertiary butylether 11.9 vol.%), the RON of all single components with RON = 76 … 116 and the resulting RON = 97.7 of the mixture were published. The result of the volume related superposition is calculated to RON = 98.0, so that the use of this approximation for the fuel blends used seemed to be useful. Based on [7] the RON of the blends M30 and M60 were estimated and shown in Table 1.

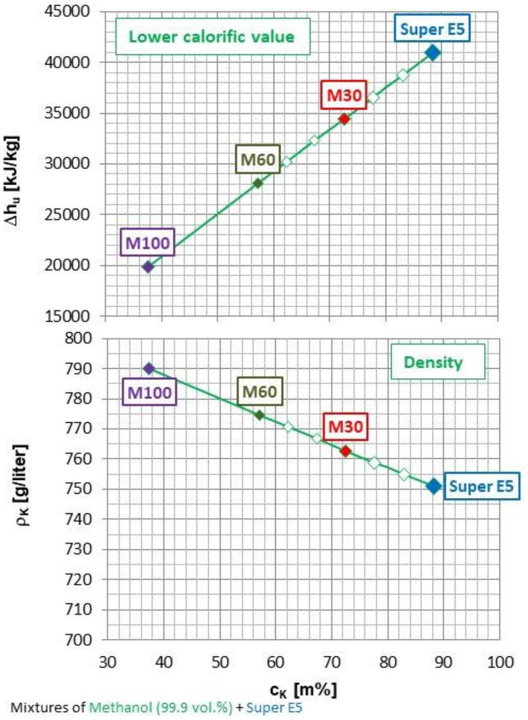

Fig. 2a. Relevant fuel specifications for blends with 0 … 100 vol.% CH_3OH

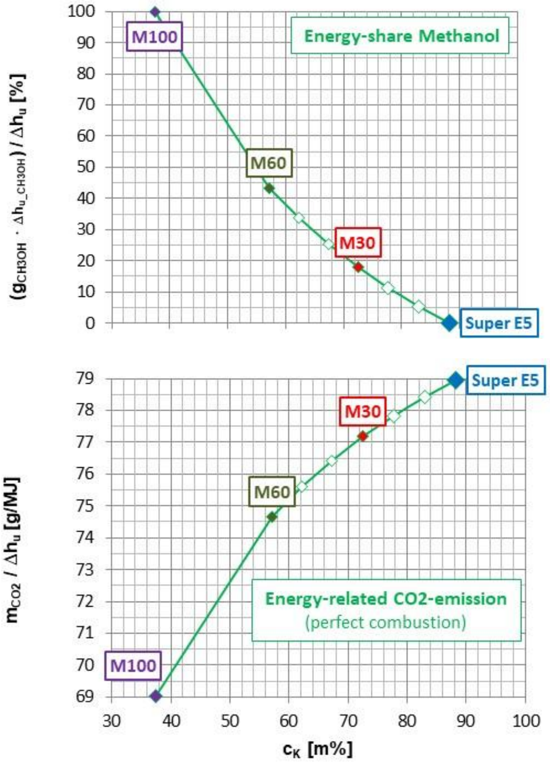

Fig. 2b. Relevant fuel specifications for blends with 0 … 100 vol.% CH_3OH

With respect to the RON = 95 of gasoline Super E5 it can be proposed that the knocking resistance of all blends will be raised. Beside this assumption the knocking resistance is irrelevant for small industrial engines, as well as the indicated mean effective pressure is quite low and this way the thermal load, too. Occurred by the special demands for starting by hand (e.g. guarantees by Briggs&Stratton) and the worldwide operation with dubious fuel qualities, hot ambient temperatures / high altitudes and inadequate maintenance at site all important suppliers (Briggs&Stratton, Honda) work with low compression ratios of ε_C = 7.5 … 8.5. Briggs&Stratton requires at least RON = 91 for their engines [9], so that every blend of gasoline Super E5 and methanol fullfills this demand.

2.2. Calculation of Water-Content in Exhaust-gas

For calculative conversion of concentrations in exhaust-gas for components measured by physical techniques according to ISO8178 in dry gas, generally for CO, CO_2, SO_2, O_2 and depending for NO_x, into output-specific mass-flows the coefficient K_{Exh} as relation between concentrations ϕ_{Exh_dry} in dry and ϕ_{Exh_wet} in wet exhaust-gas is necessary. As well as the water-steam concentration in exhaust-gas is not measured, K_{Exh} must be determined by combustion calculations, separately for lean (perfect combustion) and sub-stoichiometric conditions.

While combustion calculations for oxygen-rich mixtures are quite easy, the calculation of sub-stoichiometric exhaust-gas components becomes more complex (Fig. 3a). In these investigations the possible components in exhaust-gas were defined by only 5 components (reaction products CO_2, CO, H_2O, H_2 and inert N_2). The available content of oxygen was defined by fuel composition $C_xH_yO_z$ and air/fuel-ration λ. With 3 atomic balances for carbon, hydrogen and oxygen and a nominal oxygen-share of 21 vol.% in dry air the relevant reaction equations were formed.

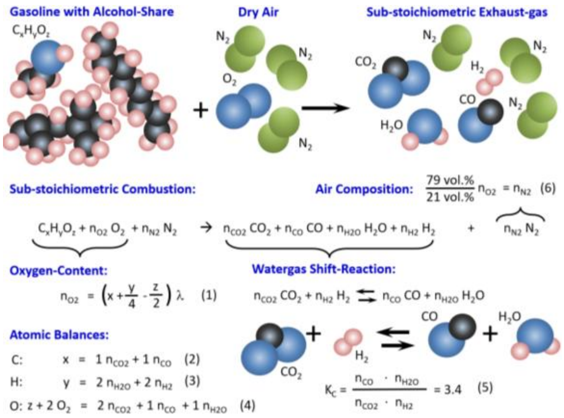

Fig. 3a. Calculation of sub-stoichiometric combustion

Watergas-shift reaction with balance factor K_C = 3.4 for frozen conditions [10] delivered the proportion of reaction products in wet exhaust-gas. A system of 6 linear equations for 6 unknown variables is the result (Fig. 3a, down), which was solved analytically. Related operations were carried out with different air/fuel-ratios λ for all fuels and blends used and diagramed in Fig. 3b.

To avoid these complex calculations for each operational point measured, a regression for operation with normal gasoline Super E5 was developed. As carried out equivalently in former investigations with gasoline/ethanol-mixtures [11] the influence of rising methanol fractions in fuels were considered by an additive regression-correction ΔK_{Exh} = f (volume-fraction ϕ_{CH3OH}, λ) to K_{Exh} for combustion of gasoline Super E5 according to Eq. 1 … Eq. 3.

For post-processing of the experimental data the λ -formular by Brettschneider [12] was used, which is also already available in the exhaust-gas analysis equipment.

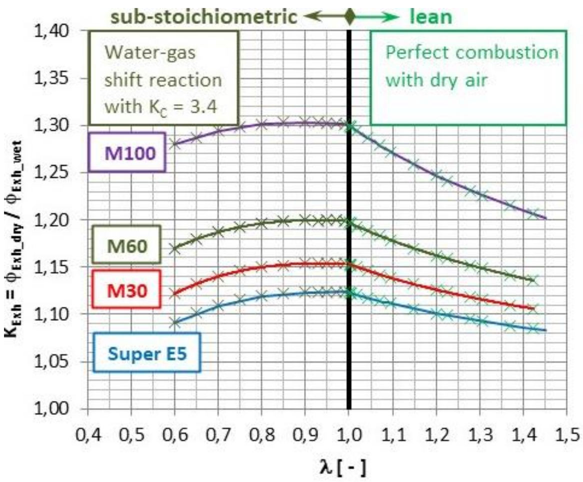

Fig. 3b. Conversion of exhaust-gas concentration

For engine operation with gasoline Super E5:

$$K_{Exh\_E5} = \begin{cases} +0.3837\,\lambda^3 - 1.2195\,\lambda^2 + 1.2797\,\lambda^1 + 0.6796 & for \quad 0.6 \leq \lambda < 1.0 \\ -0.1364\,\lambda^3 + 0.5788\,\lambda^2 - 0.8866\,\lambda^1 + 1.5675 & for \quad 1.0 \leq \lambda \leq 1.4 \end{cases} \tag{1}$$

Additive regression-correction for operation with methanol-shares:

$$K_{Exh_{Mxx}} = K_{Exh_{E5}} + 0.12192 \cdot \left({\phi_{CH3OH}\,[vol.\%]}/{100} \right)^2 + 0.0547 \cdot \left({\phi_{CH3OH}\,[vol.\%]}/{100} \right)^1 + 0.008 + \Delta K_{Exh}(\lambda) \tag{2}$$

with λ -correction:

$$\Delta K_{Exh}(\lambda) \begin{cases} 0 & for \quad 0.6 \leq \lambda < 1.0 \\ (\lambda - 1)^{0.7} \cdot \left({\phi_{CH3OH}\,[vol.\%]}/{100} \right)^2 & for \quad 1.0 \leq \lambda \leq 1.5 \end{cases} \tag{3}$$

3. EQUIPMENT FOR EXPERIMENTAL INVESTIGATIONS

3.1. Basic Test-Engine

Testbed was originally concepted for output tests of two-stroke engines [13]. Continuous problems with stability of combustion processes occurred by membrane-type carburetor while temporary operation, vibration damages at the ridged mounted engine housing and hazard for emission measurement devices avoided reasonable operation. Further the clutch supplier did not ensure the operational safety of its chosen model at engine speeds of 9300 rpm. A cage for containment safety in case of clutch failure had to be installed.

That's why the testbed was converted to performance-tests of small 4-stroke SI-engines as used for snow-throwers, portable generators, cleaning equipment or water-pumps. With the engine the exchange of clutch was necessary, too. With respect of output, spare part supply and price a Briggs&Stratton engine Intek Pro 206 was chosen (Fig. 4a). Main engine data were collected from the website of a supplier. Length of con-rod was measured at an engine grabbed out. Compression ratio was investigated while installing the sensor for cylinder-pressure indication [14].

Valve timing was measured with inductive lift-sensors several times while turning the engine by hand and averaged (Fig. 4b, down). Remarkably is the second opening of exhaust-valve during compression-stroke for de-compression in hand-start operation. After engine-start this device is disabled automatically by a mechanical ball-head-switch.

As well as the engines performance was given by manufacturer as gross-output (= brutto) according to SAE standard J1940 without attached auxiliary devices (silencer, cooling fan, ignition magnet and generator) no reliable rating value for practical use was known. Due to that fact own performance tests were carried out at testbed (Fig. 4b, top).

Model Series:	123337-0182B2
Engine No.:	070 803 888 3840
Bore:	D_B = 68.3 mm
Stroke:	s_H = 55.8 mm
Length of Con-rod:	l_{Con} = 83.1 mm
Compression ratio:	ε_c = 7.81
Valve-Timing:	ϕ_{IC} = BDC+100 °CA ϕ_{IO} = TDC - 80 °CA ϕ_{EC} = TDC + 72 °CA ϕ_{EO} = BDC -112 °CA

Fig. 4a. Test-engine Briggs & Stratton Intek Pro 206

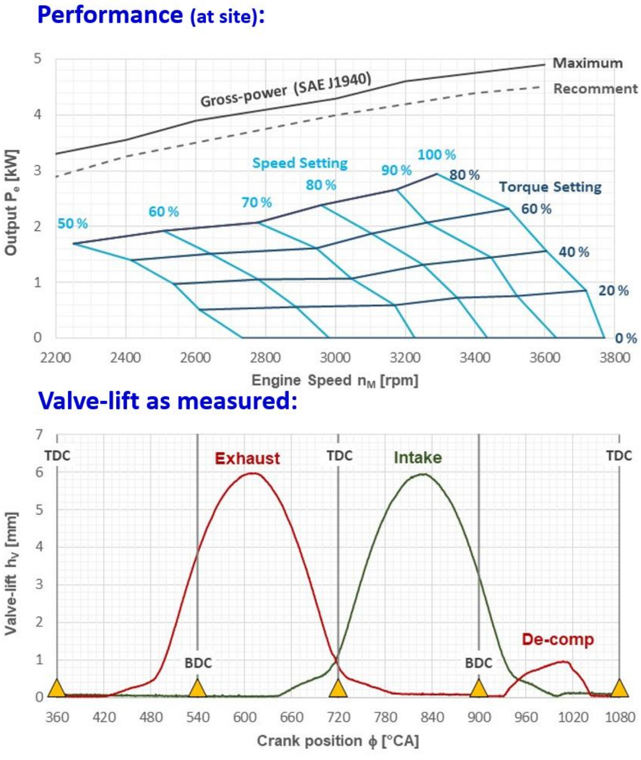

Fig. 4b. Performance at site and valve lift of test-engine

Engine performance was considered at site (approx. 22 deg C/1000 mbar) with all auxiliary devices necessary [15]. Output measured at testbed is not necessarily performance-maximum of this engine type as well as the supply voltage for the electric retarder was limited to BES = 29 V. Torque setting of the retarder was interrupted at 80 % of maximum because with settings of the speed-governor lower than 70 % no stable engine operation was possible anymore.

Remarkable is the strong speed droop, the mechanical speed-governor provides. While a speed drop of $\Delta n/n_M$ = +3 % between full and zero load is standard for large diesel-gensets this SI-engine does not reach its nominal speed n_N = 3600 rpm already at torque settings of 40 %.

3.2. Conceptions for Adjustable Air/Fuel-Mixtures

Even without any experimental investigations in methanol operation and with the experiences in ethanol-operation [11] it became clear, that mechanical carburetors must be adapted for the use of oxygen-rich fuels, as well as the air/fuel-ratio λ would reach the lean limit for misfiring. Already in earlier projects concepts for adjusting the air/fuel-ratio for SI-engines with mechanical carburetor were investigated.

Based on the basic layout four different strategies were identified. Without changing the sub-stoichiometric sizing of the fuel's main-jet (= calibrated main fuel metering orifice [16]) the easiest way seem to be systematic addition of secondary air ("fault-air") after throttle of the carburetor (Fig. 5a, top).

Pressure in intake manifold of natural aspirated SI-engines is below ambient pressure, so that no flow-supporting device would be necessary. With an easy metering-valve the amount of secondary air can be adjusted from basic air/fuel-ratio λ = 0.7 to the lean limit of ignition. Experimental considerations showed that the pressure p_{Intake} in intake manifold is not sufficiently negative for acceptable range of λ -variation [14].

A second way for in-operation variation of air/fuel-ratio with sub-stoichiometric basic layout would be the use of a pulsed solenoid valve in fuel line before carburetor (Fig. 5a, down). Due to the non-available solenoid valve and its electronic amplifier for pulsing this option was refused. An alternative way was found while continued literature studies [17] with injecting air bubbles into the fuel line before carburetor [18]. This idea was rejected due to apprehension regarding save fuel supply for engines with fuel delivery by gravity as normally used for small SI-engines.

With lean basic layout the idea of a booster fuel-pump was tested. Even with a booster-pressure of 730 mbar no relevant change in air/fuel-ratio was measured (Fig. 5b, top). The addition of this fuel pump did not influence the operation of the float chamber.

With these preliminary studies [14] [17] [19] [20] the old idea of combining lean basic layout by diameter-reduced fuel-jets and adjustable choking device for combustion air [21] [22] was reanimated (Fig. 5b, down). Based on the diameter in standard main jet, several jets were manufactured with smaller diameters and tested.

Oxygen content in exhaust-gas is measured by a separate lambda-sensor Bosch LSU4.9. Its signal is converted into an analogue voltage of 0 … 5 V and transmitted to a microcontroller, which compares the measured I with the given target value. According to this control deviation the necessary position of choke (Pos_Choke) is calculated by the self-developed PID-controller software of microcontroller and adjusted by a small servomotor, driving the shaft of the choke plate.

With the finally chosen setup of main jet and flow area of choke lambda-variation in the range of λ = 0.7 … 1.2 became possible in gasoline-operation.

With a test of fuel-switch from normal gasoline Super E5 to fuel-blend M60 with a content of 60 vol.% methanol the assumption of necessary in-operation adaptation of carburetor setting was confirmed experimentally (Fig. 6a). Air/fuel-ratio raised from λ = 0.75 to λ = 1.1. In combination of a carburetor layout of $\lambda \approx 0.85$ for gasoline-use and higher methanol additions a faultless operation was not ensured anymore.

Fig. 6b shows a fuel-switch from gasoline Super E5 to methanol-blend M30 with enabled lambda-control. Air/fuel ratio is set to a value of λ = 0.86, which is normal for these industrial SI-engines at part load. As shown in Fig. 6a there is a time delay of approx. 60 s of entering the blend into the float chamber in relevant quantity. Choke position increases immediately because of the lower stoichiometric air requirements of the methanol content. Air/fuel ratio is quite constant with tolerances lower than $\Delta\lambda$ = 0.05, occurred by instabilities in combustion. Because of higher evaporation enthalpy the exhaust gas temperature becomes with Δt_{Exh} = -10 K slightly lower than in gasoline combustion. With constant sub-stoichiometric air/fuel ratio the lambda-effect of hotter combustion while converging to λ = 1 is excluded.

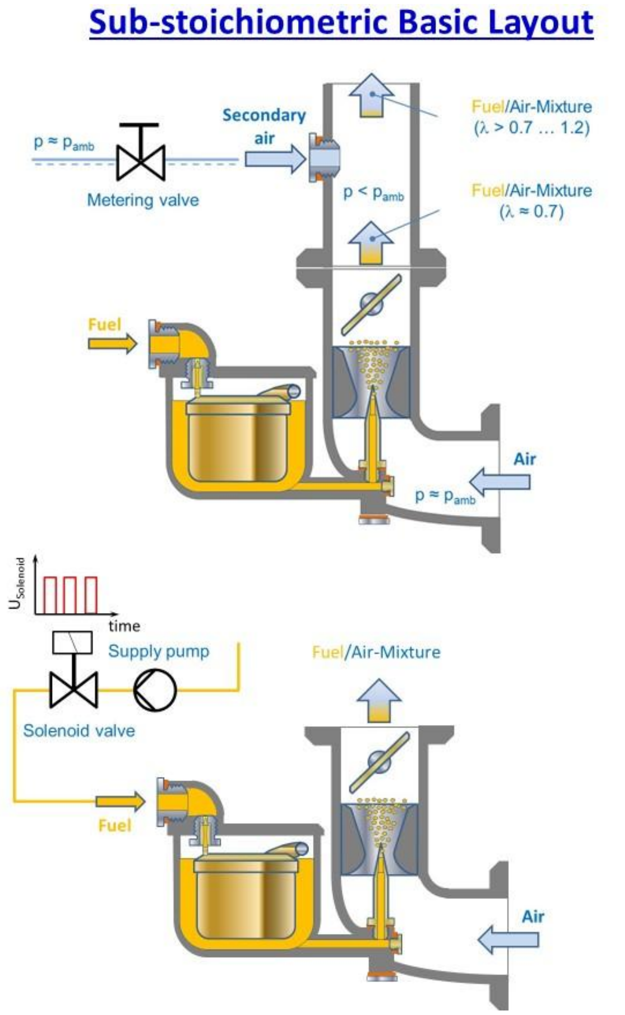

Fig. 5a. Strategies for λ-adjustment with sub-stoichiometric basic layout

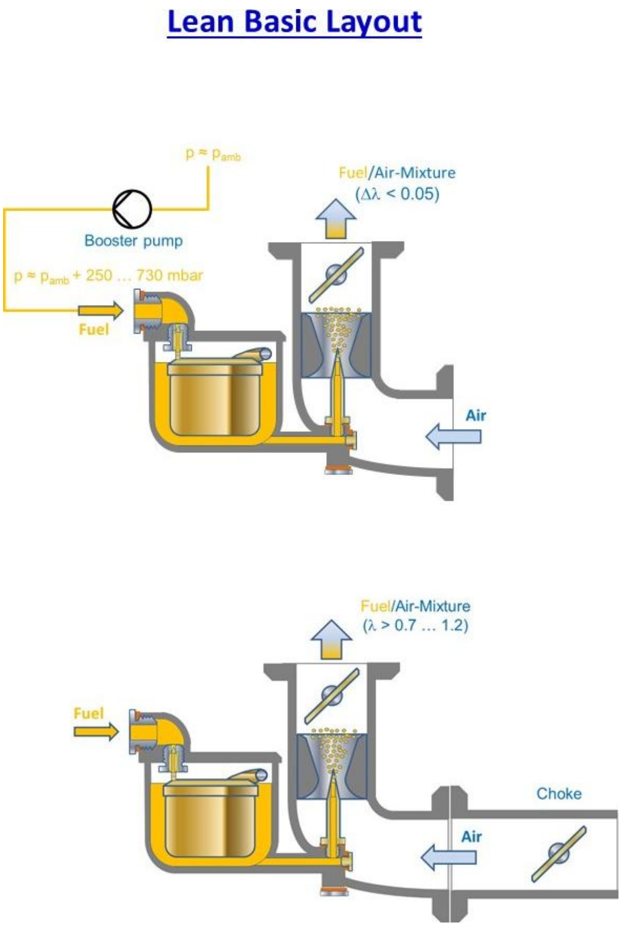

Fig. 5b. Strategies for λ-adjustment with lean basic layout

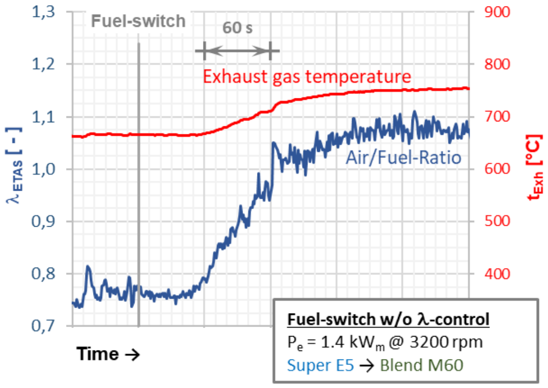

Fig. 6a. Fuel-switch without adaptations of carburetor

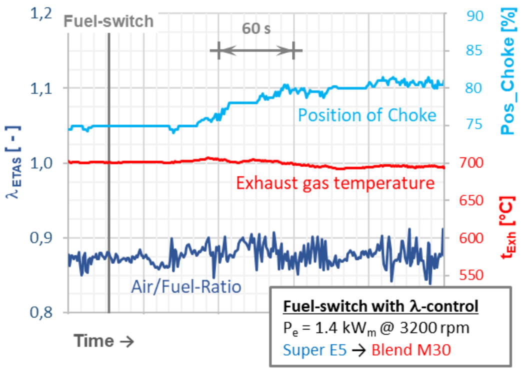

Fig. 6b. Fuel-switch with enabled λ-control

3.3. Relevant Test Equipment

Testbed is equipped with standard pressure sensors and temperature probes (NiCr-Ni, Pt100) for integral operation values of the engine and all necessary monitoring sensors for safe operation. Selection of relevant test equipment is displayed in Fig. 7.

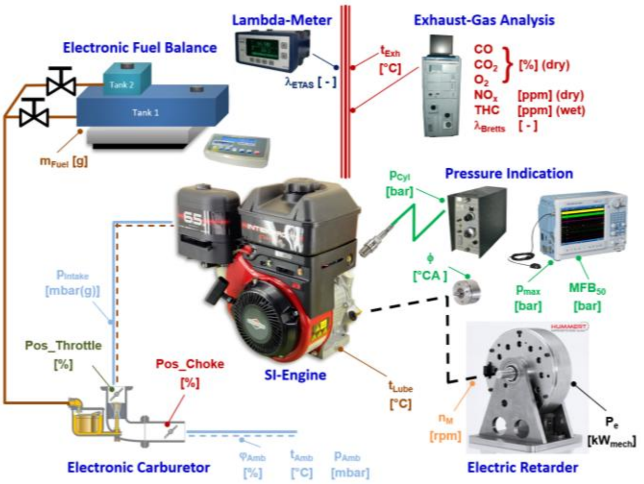

Fig. 7. Relevant test equipment

Engine itself is equipped with a mechanical speed-governor for engine speed n_M acting the throttle of carburetor. Engine speed n_M is detected by an optical sensor, observing a reflecting mark at the surface of the clutch. Position of throttle Pos_Throttle is detected by rotary potentiometer as well as the setting of choke Pos_Choke.

Tab. 2. Relevant test equipment and measuring devices

Value	Measuring principle	Type
Output P_e	Electric retarder (eddy-current)	Hummert HAT WWB C1
Engine speed n_M	Optical reflection sensor	Alborn FUA 9192
Fuel mass m_{Fuel}	Laboratory balance	Kern ITB35K1IP
Fuel/air-ratio λ_{ETAS}	ZrO_2-sensor	Lambda-Meter ETAS ES630.1 / BOSCH LSU4.2
Exhaust gas CO CO_2 O_2 NO_x THC	 NDIR NDIR MPA CLA (dry / cold) FIA	Horiba EXSA-1500
Cyl. indication $p_{Cyl} = f(f)$	Piezo-electric transducer Charge amplifier Optical encoder ScopeCorder	KIAG 6051B KIAG 5007 Hohner Serie 27 Yokogawa DL850

Additionally, the pressure inside intake manifold p_{Intake} was taken to exclude influences of fluctuating ambient pressures.

Ambient conditions (t_{Amb}, p_{Amb}, f_{Amb}) were measured inside an air-container, which can be supplied by an aircondition.

4. EXPERIMENTAL INVESTIGATIONS

4.1. Engine Tests

Engine tests were carried out on 3 different days within 4 weeks. Fuel-mixtures were prepared with pure methanol (99.9 vol. %) and commercial gasoline Super E5 (JET) with an ethanol content of max. 5 vol.%. Mixtures were blended according to calculated mass fractions and filled for the tests into tank 2 while pure gasoline was stored in tank 1. For all measurements a standard output P_e = 1.4 kW @ 3200 rpm (break torque M_d = 4.12 Nm) was used. The engine was started in gasoline operation and driven up to normal lube-oil temperatures t_{Lube} = 91 °C. After the heating-up procedure tests with variations of fuel started. Not consumed fuel-blends were removed from tank 2, while the engine was re-switched to gasoline operation from tank 1 and replaced by the next blend for testing. On each testing day reference measurements in gasoline operation (Super E5, Ref. 1 and Ref. 2 in Fig. 8, Fig. 9a-c) were carried out.

Each testing-day was ended by long-term gasoline operation from tank 2 for purging whole fuel system, as compatibility with materials of tank 2, fuel-line, sealings, jets, needle-valve, float and its chamber was not clear and became subject of additional considerations.

4.2. Experimental Results of Engine Tests

Relevant results of experimental investigations with the gasoline Super E5, the blends M30 and M60 as well as pure Methanol M100 are shown in Fig. 9a … c. Diagrammed in Fig. 9a are the operational values fuel consumption m'_{Fuel}, the specific fuel consumption $b_{e42.7}$ related to standard lower heat value of Δh_u = 42.7 MJ/kg and that way reciprocal to the efficiency and the exhaust-gas temperature t_{Exh} versus the air/fuel-ratio λ.

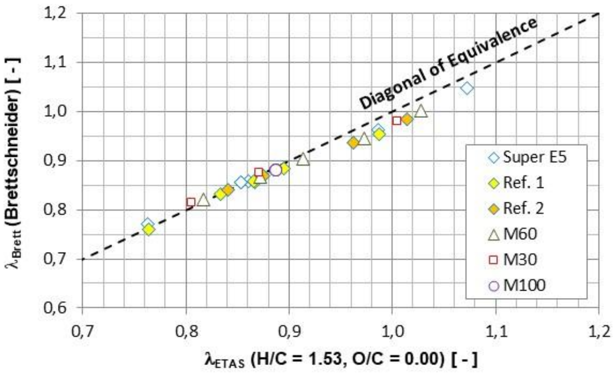

Fig. 8. Fault of Lambda-Meter without adjusting fuel-parameters

Air/fuel-ratio was measured with the lambda-meter by ETAS. Values of fuel composition H/C and O/C were set constant to the values for Super E5 and not changed during engine operation. Afterwards the results of lambda-meter were counterchecked by values calculated from complete exhaust-gas emissions by Brettschneider-regression, usable also for oxygen-rich fuels [12], with real fuel-composition. For single measured points additionally analytical calculation with all components in sub-stoichiometric combustion were carried out according to watergas-shift reaction with the balance constant K_C = 3.4. The failure of ETAS-device was approx. 1 %, related to Brettschneider-regression (Fig. 8) and 2 % related to combustion calculation within the interval of λ = 0.7 … 1.0. Diagramming versus ETAS display without changing fuel-parameters seemed to be acceptable.

Fuel consumption m'_{Fuel} rises by using e-fuels due to poor energy content compared to standard hydrocarbon-fuels. Tank volume capacity must be enlarged by approx. 75 % to ensure same operating range (Fig. 9a). Surprising is the energy content-related specific fuel consumption $b_{e42.7}$. As long as the methanol volume-share is below 30 % (M30) the efficiency is the same as for gasoline operation. This result can be explained by cylinder-indication (Fig. 10). Up to methanol volume-share to 30 % (M30) the heat release is nearly unchanged compared to standard operation with gasoline Super E5.

With higher methanol contents efficiency increases by three effects. First, even at same global air/fuel-ratio the oxygen content in fuel blends leads to more complete combustion due to local O_2-concentration, provided by the methanol. Concentration of unburnt components CO and THC in exhaust-gas decreases significantly (Fig. 9b). Second, due to higher local O_2-content in cylinder gas the combustion gets faster, what will be demonstrated by the cylinder-indications in Fig. 10, too. Oxygen contents in fuels enlarge the velocity of the flames during combustion [23]. The combustion process is significantly advanced by approx. 4 °CA in operation with M60 and M100. The same effect was already observed by the tests with ethanol-shares in gasoline [11].

Third, the higher evaporation enthalpie of methanol leads to lower gas temperatures inside the cylinder, what lowers the specific isochoric heat capacity of the cylinder-gases. The influence of this third effect is quite small. Cycle calculations with completly constant heat capacities at a large dual-fuel engine S.E.M.T. Pielstick 18PC2-5 DFC showed efficiency improvements lower than 5 % [24]. With pure methanol M100 the advantage in energy consumption is approx. 20 %, what does not compensate the lower content of chemical energy.

Exhaust-gas temperature becomes lower with raising methanol shares according to the standard evaporation enthalpy of Δh_{V_CH3OH} = 1100 kJ/kg @ 1013 mbar [25]. The cylinder gas mass is cooled in inlet manifold and inside the cylinder during intake stroke. Additionally, the fuel-mass burnt per cycle is approx. 75 % higher in methanol-operation, so that the temperature at the start of compression is lower than with gasoline ($\Delta h_{V\_Gasoline}$ = 380… 500 kJ/kg @ 1013 mbar [25]). The whole temperature level of the engine's process is dominated by the gas temperature at the start of compression stroke. This way exhaust-gas temperature decreases in e-fuel operation.

With lower gas temperatures inside the cylinder instable combustions were suspected. Fig. 9b shows the standard deviation of indicated peak pressures inside the cylinder. Up to volumic shares in fuel of 100 % methanol the standard deviations in peak pressures are within the tolerance of operation with pure gasoline, measured at the 3 different test-days (Super E5, Ref. 1 and Ref. 2).

Diagrammed in Fig. 9c are the mass-related specific emissions for carbon-monoxide CO, residual hydrocarbons THC from unburnt fuel and Nitrous oxides NO_x. As well as the concentrations for NO_x and CO were measured in dry exhaust gas, the measured values had to be corrected to wet conditions in un-cooled exhaust-gas by factor K_{Exh} according to Fig. 3b. Additionally, the specific NO_x

emissions must be corrected depending on the water-content inside the combustion air at site according to ISO 8178.

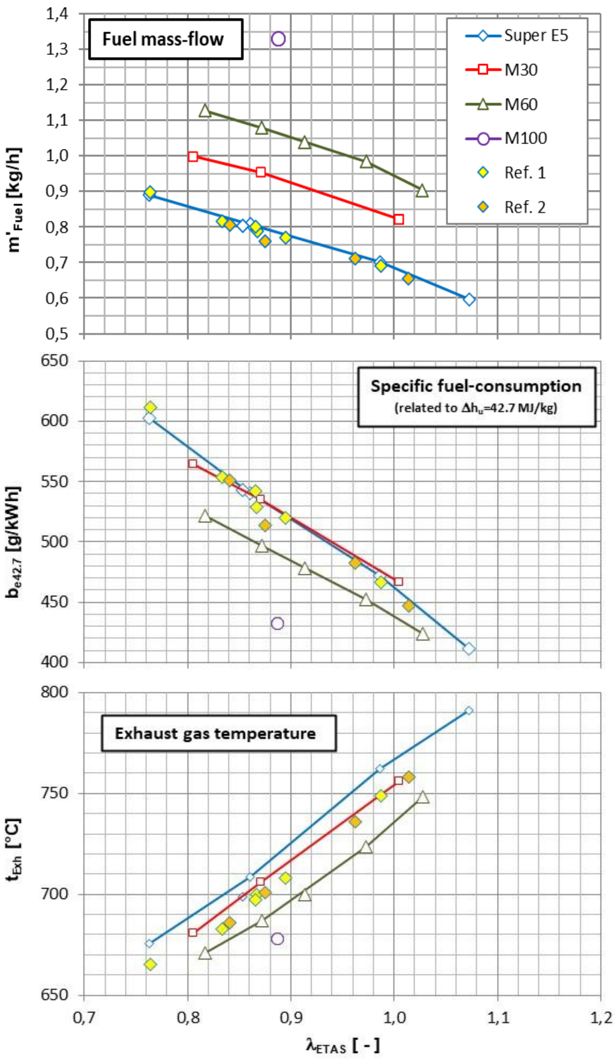

Fig. 9a. Test results – Operational values

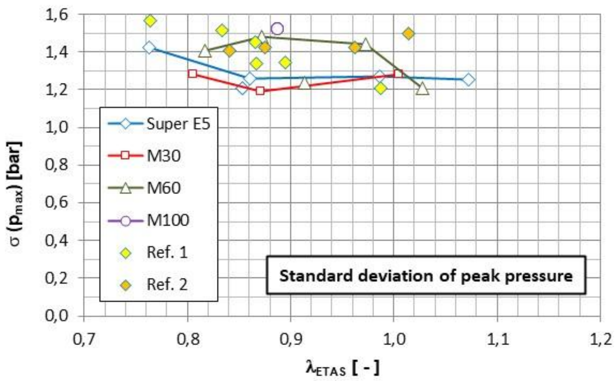

Fig. 9b. Test results – Standard deviation of peak pressure

As mentioned above, the local availability of O_2 close to the flame during combustion decreases the content of unburned components CO and THC in exhaust-gas. Significantly is the influence on specific NO_x emissions. For the formation of NO_x are high local gas-temperatures, sufficient local concentration of O_2 and time are necessary.

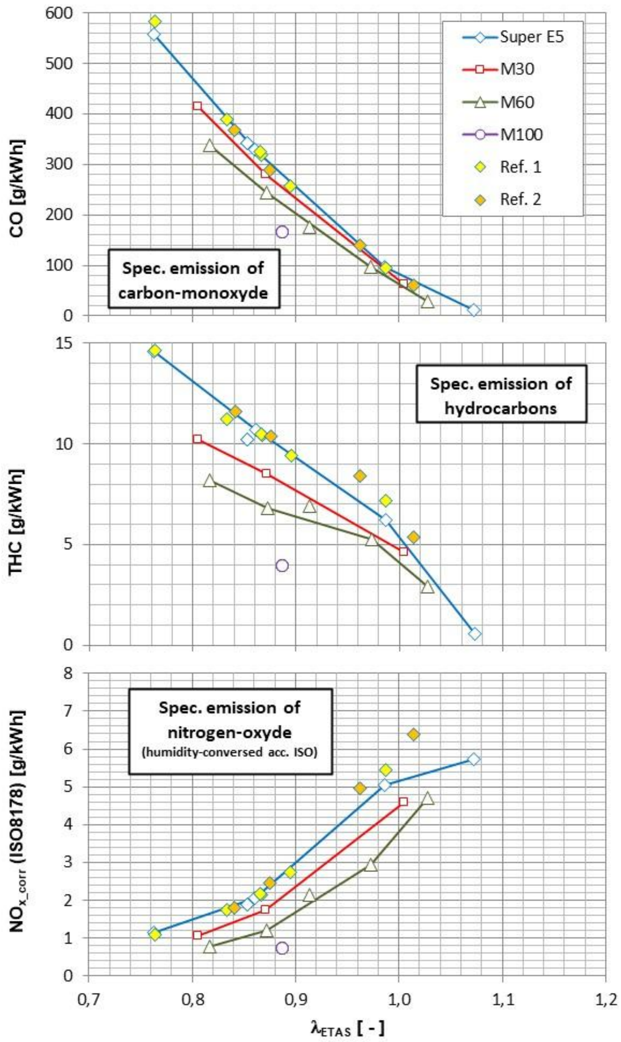

Fig. 9c. Test results – Specific exhaust gas emissions

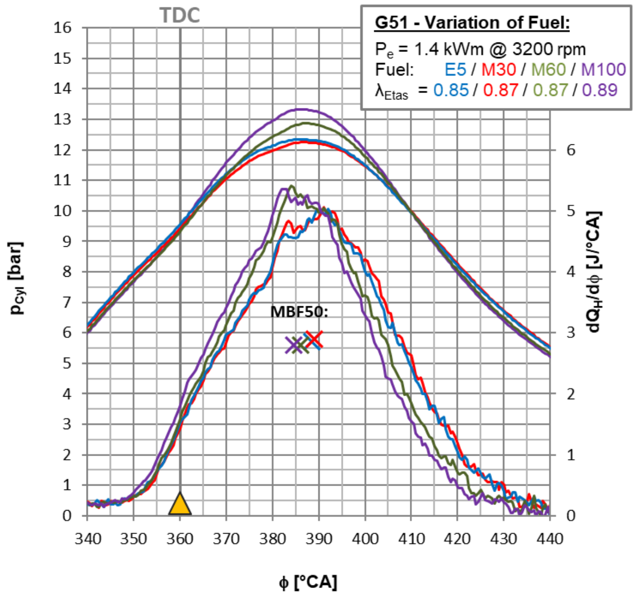

Fig. 10. Test results – Pressure indications at λ ≈ 0.85

At the same operating point of the engine the influence of time is excluded. With constant rating and engine speed in that operating point a shift in ignition timing can be excluded, too. While higher O_2-concentration leads to higher NO_x-level the formation of thermal NO_x would be decreased by lower gas-temperatures. It becomes clear that the low gas-temperatures in blend-operation and with pure methanol dominate this effect as well as the level for NO_x-emissions is decreased significantly.

Cylinder indication was carried out with 100 cycles per measuring point. While post-processing it became clear, that especially at higher air/fuel-ratios with unstable combustions the recording of more cycle would have improved the results.

Based on the pressure indications carried out a slight influence on the cylinder peak pressure p_{max} can be detected (Fig. 10). Due to advanced combustion detected by the crank-angle MBF_{50} of half chemical energy released the cylinder peak pressure p_{max} was enlarged by less than 1 bar. Compared to the cycle-to-cycle deviation of more than 6 bar this small increase is irrelevant for the stability of crank-drive and cylinder unit.

5. ASPECTS OF OPERATION AND MAINTANANCE

5.1. Inspections of Engine Components

Heat rating of the sparkplug was not changed for operation with methanol/gasoline-blends. Despite concerns regarding the lower gas-temperature inside the combustion chamber and that way forming of deposits at the electrodes the original sparkplug was not replaced. Even in operation with pure methanol no anomalies in combustion cycles were detected.

Despite the lower gas temperatures inside the cylinder at compression start due to the high enthalpy for evaporation of methanol no abnormal deposits were found during the optical inspection at the electrodes of the sparkplug (Fig. 11a, photo). No changes of sparkplug configuration seemed to be necessary.

Fig. 11a. Sparkplug after methanol operation

Combustion chamber was inspected after the tests by endoscope (Fig. 11b). Deposits of lube-oil coke were detected at piston head. No cleaning effect of methanol could be observed. The upper flank of first piston ring seemed to be corroded, what is a possible effect of sub-stoichiometric combustion of alcohols, forming formic acid. In consequence to avoid further damage, sparkplug was removed after every day's test-run, cylinder was filled by fresh lube-oil and engine was turned by hand to distribute the lube-oil at the liners surface.

Fig. 11b. Endoscopy of combustion chamber [26]

5.2. Lube-oil Contamination

Fresh and used lube-oil after operation with blends and pure methanol were analyzed by ATR-spectroscopy (Fig. 12). Both spectra seemed to be quite equal. Methanol could not be detected in the ATR-spectrum. The characteristic band of the C-O stretching vibration and the OH deformation vibration at 1021 cm^{-1} is not present in the spectrum of the used lube oil. But the engine was operated after all tests with gasoline over a time-period of approx. 1 hr. for purging all fuel equipment. Possibly in this way the contamination of lube-oil with methanol could be eliminated by evaporation.

As a hint for carbonyl groups differences in spectrum were detected at the band of 1739 cm^{-1}. The carbonyl groups can be occurred by formaldehyde or formic acid. Formaldehyde seems to be implausible due to its evaporation behavior, so that probably formic acid, produced in sub-stoichiometric combustion of methanol, contaminated the lube-oil.

Additionally X-ray fluorescence examinations showed contamination with the element iron, what could be occurred by the influence of acid at cylinder liner and piston rings as described above. This observation supports the theory of acid input into crankcase. No TBN were investigated.

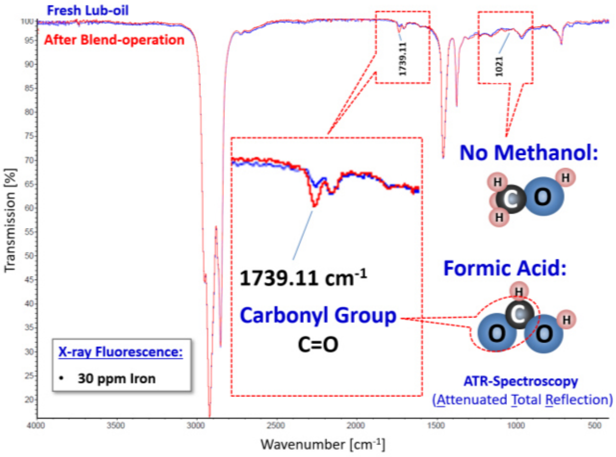

Fig. 12. Results of analysis of lubrication-oil

5.3. Chemical Resistance of Materials

Chemical resistance of different materials used in engine components were tested with pure methanol and its blends with gasoline. Besides optical evaluations mechanical tests were carried out, too. In fact, all materials tested and used in components of the engine were chemically attacked by these fuels (Fig. 13).

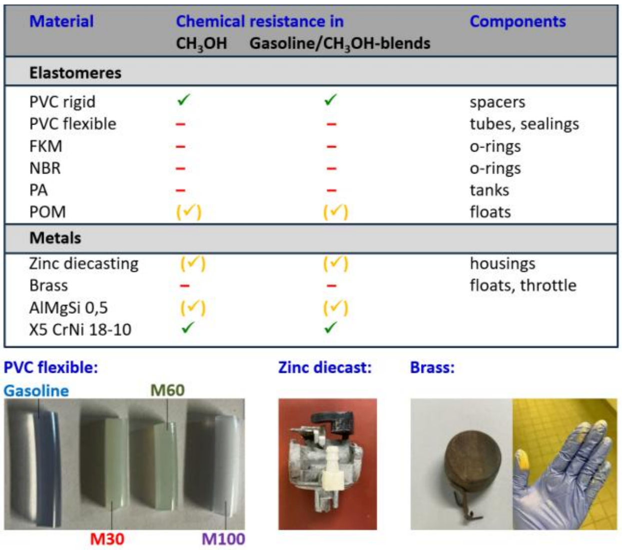

Material	Chemical resistance in CH_3OH	Gasoline/CH_3OH-blends	Components
Elastomeres			
PVC rigid	✓	✓	spacers
PVC flexible	–	–	tubes, sealings
FKM	–	–	o-rings
NBR	–	–	o-rings
PA	–	–	tanks
POM	(✓)	(✓)	floats
Metals			
Zinc diecasting	(✓)	(✓)	housings
Brass	–	–	floats, throttle
AlMgSi 0,5	(✓)	(✓)	
X5 CrNi 18-10	✓	✓	

Fig. 13. Results of material tests [26]

6. CONCLUSIONS

The influence of fuel-blends of gasoline and methanol on the operational values and emissions of small industrial gasoline SI-engines was considered for one part-load operation point with constant output P_e = 1.4 kW @ 3200 rpm. Conclusions were found as follows.

Sub-stoichiometric operation of small industrial SI-engines was stable up to 100 % methanol content in fuel. No significant differences in standard deviation of indicated peak pressure were observed.

The simple exchange of conventional hydrocarbon fuel without adaption of carburetors is not possible. With respect to the oxygen-content of alcoholic share larger main-jet areas are necessary to achieve same air/fuel-ratio.

Based on the lower calorific value of methanol fuel consumption is rising nearly the same relation. Larger tanks will be necessary. Oxygen content accelerates the heat release. Efficiency at typical air/fuel-ratio λ = 0.9 is rising by approx. 7 % in operation with M60 and 17 % with pure methanol M100.

At same air/fuel-ratio λ = 0.9 emissions of carbon monoxide CO are lowered by 27 % in M60-operation and by 45 % with pure methanol M100. Due to enlarged evaporation enthalpy of methanol the NO_x-emissions are improved by 38 % and 74 %.

Sub-stoichiometric combustion of alcoholic fuels leads to formation of acids. Carbonyl groups as hint for formic acid were detected in lube-oil by ATR-spectroscopy. Optical inspection of liner and piston rings showed corrosion.

All tested elastomers and metals used normally in fuel lines of conventional carburetors were attacked chemically by methanol and its fuel blends.

REFERENCES

1. Auler B, Rodenbeck J, Lügger J, Gorenflo E. Gemischgeschmierter Einzylinder-Viertaktmotor für Motorsägen. MTZ 66. 2005;452-456.
2. Dobler H. Leichter Viertaktmotor mit Gemischschmierung. MTZ 65. 2004;680-682.
3. v. Basshuysen R, Schäfer F. www.motorlexikon.de. 11.11.2010.
4. Reed TB, Lerner RM. Methanol: A Versatile Fuel for Immediate Use. Science. 1973;182(4119):1299-1304.
5. May H, Hattingen U, Wiedenhöft D. Klopf- und Abgasverhalten von Alkohol-Mischkraftstoffen. MTZ 51.1990;210-219.
6. Pischinger R, Kraßnig G, Taucar G, Sams T. Thermodynamik der Verbrennungskraftmaschine. Wien: Springer-Verlag; 1989.
7. Marder M. Motorkraftstoffe/Erster Band: Kraftstoffe aus Erdöl und Naturgas. Berlin: Springer-Verlag;1942:459.
8. Hansen U. DEA-Kraftstoffe für Ottomotoren. Firmenschrift DEA Mineralöl AG. Hamburg;1992:36.
9. NN. Operator's Manual – Model 120000 Intekt I/C®. Briggs & Stratton Corporation. Milwaukee; 2014:7.
10. Betz A. Rechnerische Untersuchung des stationären und transienten Betriebsverhaltens ein- und zweistufig aufgeladener Viertakt-Dieselmotoren. Dissertation TU München, Lehrstuhl für Verbrennungskraftmaschinen und Kraftfahrzeuge;1985.
11. Teubner L, Mainusch V. Experimentelle Untersuchungen zum Betrieb von luftgekühlten Ottomotoren mit Benzin/Ethanol-Mischungen. Projektarbeit im Bachelorstudiengang „Maschinenbau". Hochschule Stralsund; 2022.
12. Brettschneider J. Berechnung des Luftverhältnisses von Luft-Kraftstoff-Gemischen und des Einflusses von Meßfehlern auf l. BOSCH Technische Berichte. 1979;6:177-183.
13. Habeck M, Schumacher C. Aufbau und Inbetriebnahme eines Leistungsprüfstandes für Kleinmotoren. Projektarbeit im Bachelorstudiengang „Maschinenbau". FH Stralsund; 2012.
14. Rohde E. Experimentelle Voruntersuchungen zur Lambda-Regelung an Vergasermotoren. Abschlussarbeit im Bachelorstudiengang „Maschinenbau", FH Stralsund; 2016.
15. Habeck M, Schulz C. Entwicklung eines modularen Prüfstandes zum automatisierten Ausdauertest von kleinen Industriemotoren. Abschlussarbeit im Masterstudiengang „Maschinenbau", FH Stralsund; 2014.
16. Heywood JB. Internal Combustion Engine Fundamentals. New York: McGrwa-Hill Inc. 1988; 289.
17. Werner K. Gezielte Androsselung des Ansaugluftflusses zur Lambda-Regelung bei Vergasermotoren (Projekt „Gandalf"). Große Projektarbeit im Bachelorstudiengang „Motorsport Engineering", Hochschule Stralsund; 2020.
18. Teramura M. Vorrichtung zur Regelung der Kraftstoffzufuhr zu einem Vergaser. Deutsches Patentamt, Offenlegungsschrift DE000003329860A1. München 31.10.1984.
19. Schmidt MA „Emma". Kraftstoffdruckerfassung am Prüfstand „Briggs & Stratton". Praktikumsbericht im Bachelorstudiengang „Regenerative Energiesysteme". Hochschule Stralsund; 2019.
20. Schmidt MA „Emma". Gezielte Androsselung des Ansaugluftflusses zur Lambda-Regelung bei Vergasermotoren (Projekt „Gandalf"). Abschlussarbeit im Bachelorstudiengang „Regenerative Energiesysteme". Hochschule Stralsund; 2020.
21. Mader R, Troll H. BMW-Vierzylindermotoren mit elektronisch gesteuertem Gemischbildungssystem. MTZ 44. 1983; 325-329.
22. Bahr A. ECOTRONIC Elektronisches Vergasersystem der Zukunft. MTZ 44. 1983; 343-344.
23. Pucher H et al. Gasmotorentechnik: Technologie und Entwicklungstendenzen. Sindelfingen: Expert-Verlag; 1986.
24. Marquardt L. Entwicklung eines Berechnungsprogrammes zur Auslegung der Verbrennung in Großmotoren bei Einsatz unterschiedlicher Brennverfahren und Kraftstoffe. Diplomarbeit im Studiengang „Schiffsmaschinenbau/Thermische Energieanlagen". TU Hamburg; 1997.

25. Bauer H. Kraftfahrtechnisches Taschenbuch/Bosch. 22. Auflage. VDI-Verlag. Düsseldorf 1995; 238.
26. Teubner L. Experimentelle Untersuchungen zum Betrieb von kleinen luftgekühlten Industrie-Ottomotoren mit Benzin/Methanol-Mischungen. Abschlussarbeit im Bachelorstudiengang „Maschinenbau“. Hochschule Stralsund; 2023.

Internal Research Funding 2023 (Account 12110901)

GHS16-0027 „Messkette Rest-O2“, GHS16-0028 „ScopeCorder“
GHS16-0033 „Messsystem für Druckschwingungen“

Lube-oil Analysis

Thanks for cooperation.

Leander Marquardt: https://orcid.org/0000-0003-0600-6166

Heiner-J. Katke: https://orcid.org/0000-0001-7137-8244

Maik Habeck: https://orcid.org/0009-0009-6787-9869

Andreas Reinke: https://orcid.org/0000-0002-3011-2762

Lena Teubner: https://orcid.org/0009-0001-2450-0531

DOI 10.2478/ama-2025-0045

IMPROVEMENT AND CONTROL TRAJECTORY TRACKING OF A THREE-AXIS MANIPULATOR FOR NEW TRAINING STRATEGIES

Patryk MIETLIŃSKI*, Michał JAKUBOWICZ*, Lidia MARCINIAK-PODSADNA*, Michał WIECZOROWSKI*

*Faculty of Mechanical Engineering, Division of Metrology and Measurement Systems,
Poznan University of Technology, M. Skłodowskiej-Curie 5, 60-965 Poznań

patryk.mietlinski@put.poznan.pl, michal.jakubowicz@put.poznan.pl, lidia.marciniak-podsadna@put.poznan.pl, michal.wieczorowski@put.poznan.pl

received 04 April 2024, revised 21 May 2025, accepted 16 June 2025

Abstract: This study discusses the development of training strategies for RRR (3 revolute joints) triaxial manipulators. Two robot structures and a control phantom were constructed using incremental technology. An universal algorithm was developed to process and autonomously repeat the trajectories of robot movements by imitation and learning. The coordinates of the model articulated positions were then saved as coordinates of the manipulator position. For validation purposes, the newly developed training strategies and the repeatability of robot movements were tested in stages. After the first stage of testing in terms of positioning accuracy, structural changes were introduced in the robot by mechanical engineering to improve its manipulation quality. Next, another training strategy for the improved robot version was developed for the same movement algorithm. This demonstrates the applicability of the developed control system in applications with different structures and requirement for high control-command quality (possibility of using the developed algorithm in various robot designs). Experimental results showed that the function of the developed RRR manipulator algorithm enabling the imitation of phantom trajectories and their learning and memorization, along with the consideration of individual training strategies, can be applied to differing structures, achieving positioning accuracy comparable to that of high-class motion equipment, and facilitating navigation of individual robot members. The system composed of the simplified physical model and the manipulator can directly simplify and globalize the control of the robot over significant distances. Additionally, the positioning accuracy was tested using the photogrammetric method, which is a complete novelty in robot positioning research. Furthermore, it was demonstrated that for the first construction of the robot, it is possible to achieve an accuracy of ±1 mm in the automatic replay mode. Moreover, a construction accuracy of ±0.52 mm at a maximum speed of 0.025 s/1° can also be accomplished after manual repeat of the different model movements, i.e., after a learning procedure.

Key words: three-axis manipulator, RRR robot, training strategies, 3D scanners, robot programming, positioning accuracy

1. INTRODUCTION

In recent years, there has been a continuous and dynamic development of industry, resulting in the Fourth Industrial Revolution or Industry 4.0. The revolution aims to automate production and increase the mobility of individual elements of the product chain [1, 2]. Gradually, companies are introducing autonomous solutions to their factories that enable virtually maintenance-free work on production stands [3, 4]. The human factor is definitely being replaced by manipulators and both automatic production [5] and transport devices [6], leaving only supervisory and control roles [7] for humans. However, such autonomous solutions are required to be universal and have high implementation precision, as described by Jermak Cz. J. et al [8], and Jakubowicz M. et al. [9]. Such solutions require substantial financial outlays, the profitability of which is achieved only after a prescribed, usually long, period of time.

Existing methods for manipulating components and subassemblies involved in the overall production process are of key importance for assembly and internal aspects of interstate handling [10, 11]. Some of the first studies that raised issues regarding the need to automate manipulation operations in order to improve industrial operations related to the control and quality of unattended manufacturing of elements; they were published in 1973 by Häuschen H. [12] and Warnecke H. J. et al. [13]. Moreover, many contemporary authors have emphasized the importance of automating manipulation processes and problems related to their implementation [14, 15]. Furthermore, additional considerations related to the results of control accuracy that enable the determination of the potential quality of positioning.

Quality requirements are constantly growing and production technologies keep developing; hence, more accurate and universal measurement systems and methods [16, 17, 18] as well as diagnostics have to be applied [19]. Articulated robots that enable numerical control along several axes are currently the most frequently used manipulating machines, enabling dimensional and geometric control. The universality of 3D scanner solutions was evidenced by Andrzejewski J. [20]. In most cases, their programming is based on the online programming procedure described by Chen X. et al. [21] and Maini P. et al. [22]. Offline programming is also possible, as reported by Mitsi S. et al. [23] and Larkin N. et al. [24]. In all the above cases, the developer stays far from the operation site. This creates the problem of lack of intuitive programming.

There are also reports of hybrid methods using offline and online programming [25, 26]. However, such solutions have limited applicability and are dedicated to specific purposes. In this respect, it may be helpful to develop a robot operation mode by tracking the trajectory of motion of a simplified physical model used for innovative programming of manipulators in accordance with the guiding principle of Industry 4.0 [27].

In industrial applications related to working machines, manipulators, and their drives, the main criterion to determine their suitability for a particular use is to obtain the best possible positioning accuracy [28]. The operation algorithm is based on obtaining the closest position to the original set position in each pass and cycle of device operation. The main objective for the control system, mechanical structure, and developed program, which are collaboratively responsible for realizing the manipulator movement, is to obtain maximum precision while maintaining the basic motion conditions of the manipulator displacement trajectory. Hybrid methods allowing offline and master-slave robot programming are commonly used [29-31]. Research on such solutions has also been carried out [32-34]. However, a constant limitation is the inability to apply one universal algorithm to various mechanical manipulator designs. It is necessary to create separate control programs for separate mechanical solutions of robots. None of the authors have previously attempted to apply the same control algorithm to two completely different robots.

It is important to note that autonomous solutions are gradually being introduced, enabling nearly maintenance-free operation of production workstations. The human factor is being replaced by manipulators and automatic production and transport devices, leaving only supervisory and control functions to humans. These solutions must be universal and characterized by high implementation precision, which involves significant financial investments that typically pay off only after a longer period of time.

In the context of Industry 4.0, the application of artificial intelligence (AI) techniques plays a key role in optimizing production processes. Azizi et al. [35] presented a hybrid AI algorithm for optimizing RFID network planning, which is significant for efficient resource management in modern production systems. In another study, Azizi [36] proposed the use of artificial neural networks to optimize the dynamic behavior of robotic arms, contributing to increased sustainability in Industry 4.0. Moreover, Latifi-Navid et al. [37] developed an autonomous robot for collecting tennis balls, using LiDAR for environmental mapping and a camera for ball detection, demonstrating the practical application of AI in mobile robotics. In the field of mechanical systems control, the use of a Ring Probabilistic Logic Neural Network (RPLNN) to design an active vehicle suspension controller was presented by Azizi et al. [38], showcasing AI's potential in improving the mechanical stability of structures.

All these studies emphasize the importance of integrating AI techniques into various aspects of industrial automation, from network planning to the control of robots and mechanical systems. However, despite the advances in this field, there remains a need for further research into universal control algorithms that could be applied to different manipulator designs. In response to this need, the present study focuses on the development and implementation of a universal control program that is not dedicated to a single type of manipulator but can be directly applied to various structures.

Therefore, the authors decided to create a universal control program that would not be dedicated only to one type of manipulator but could be directly applied to separate structures. For this purpose, it was decided to design and build two different manipulators from scratch. Then it was decided to apply the same control algorithm to them, based on master-slave programming using a control phantom (the ability of the manipulator to repeat the phantom's movements and then recreate them as faithfully as possible). Next, it was decided to perform an appropriate learning procedure usinga control phantom for each structure and then recreate the same trajectories for each robot. Then, in order to verify the quality of positioning, it was decided to perform positioning quality tests using the photogrammetric method. None of the authors attempted to investigate positioning accuracy using structured light scanners. According to the authors of the article, considering the measurement accuracy of such a measurement system, it is a reliable source of obtaining measurement information for the required positioning quality measurements. This metrological approach is another novelty when testing the accuracy of manipulator positions. Previous studies focused on the optimization of manipulators to obtain better metrological properties [39, 40]. However, the complex design and implementation of a universal, intuitive control algorithm using a robotic phantom that enables its application in various types of automatic manipulation structures, allowing for the development of specific training strategies for specific tasks, have not been described in the literature yet. Therefore, in this study, a research stand was prepared in a configuration that enables the analysis of training strategies using the developed phantom-manipulator control algorithm on various types of structures. In addition, the accuracy of the manipulability for specific robots was evaluated. Thus, a novel analysis is proposed that provides data for a clear comparison of the positioning quality performance of two articulated manipulators with significant design differences.

Previous scientific publications have not undertaken a comprehensive analysis of the issues related to the evaluation of positioning accuracy in three-axis manipulators in the context of the developed control algorithms. There has also been a lack of comparative approaches that would include real-world verification of trajectory reproduction quality in reference to programmed motion paths.

In response to this research gap, the authors of this study are the first to propose a method for verifying and assessing the positioning accuracy of manipulators using advanced, previously unused measurement technologies in this area—namely, a structured light scanner and a multisensor coordinate measuring machine (CMM).

The application of these advanced metrological tools enables precise reproduction and evaluation of deviations from the predefined trajectory, allowing for an objective assessment of the effectiveness of the designed control algorithms. Similar approaches to the assessment of manipulator positioning accuracy have previously been explored by Wang et al. [41], who utilized 3D scanning techniques to evaluate the precision of industrial robots, and by Chen et al. [42], who employed multisensor measurement systems for analyzing positioning accuracy in robotics.

Furthermore, research conducted by Li et al. [43] demonstrated that integrating structured light scanning with robot control significantly enhances the quality of trajectory reproduction. However, these authors did not validate or compare their methods using different metrological systems, nor did they attempt to adapt their solutions to various types of manipulators.

Therefore, the present study aimed to address this gap by comparing two distinct measurement systems in the context of positioning accuracy testing and evaluating the adaptability of the developed control algorithm to different robotic structures.

The proposed approach represents an innovative contribution to the development of methods for evaluating the performance of industrial manipulators, particularly in terms of their adaptability to diverse applications within the Industry 4.0 environment, where precision and flexibility of control are of paramount importance.

2. CONSTRUCTION AND CONTROL ALGORITHM

2.1. Concept of manipulator constructions

Two different manipulators were used to compare the usefulness and universality of the devel-oped control system based on serial motion kinematics. In this concept, the link with the attached force performing the kinematic transfer is a unit of motion of the kinematic set. A kinematic diagram must be defined to specify the basic position of the members, their interconnections and positions, and dimen-sional and geometric descriptions. Therefore, the manipulator structure is designed to integrate robot elements and realize the relationship between sub-assemblies for the selected system. A kinematic diagram of the compiled RRR robot is shown in Fig. 1. Each member moves along a particular axis and is connected to the rest of the system in an articulated manner. The integrated movement of each axle enables the manipulator to be controlled in the working space and realization of the assigned tasks.

To implement the actual design of the manipulator, a non-additive manufacturing method was employed. This gave rise to the expected behavior of the components required for their realization while maintaining a relatively short manufacturing time (printing speed of approximately 50 mm/s). A biodegradable polylactide called PLA was used as the manufacturing material. This material is charac-terized by a small processing cramp resulting from the ease of FDM printing.

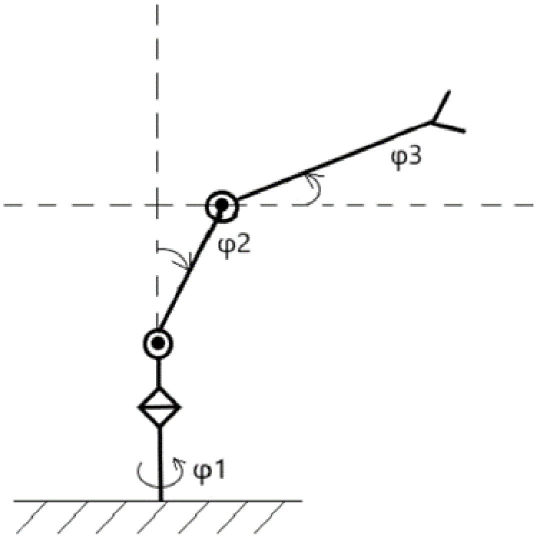

Fig. 1. Kinematic diagram of the RRR serial robot

In addition, pilot kinematic simulations of planned structures were performed for pilot purposes, assuming conditions associated with the type of manipulation of RRR robots. These simulations enabled the analysis of the Denavita–Hartenberg methodology used by Qingbing Ch. et al. [44] and Li H. el. al. [32]. In the case of the manipulator, RRR holds all the rotating connectors. For such a combination, the angle of rotation θ^i is always variable, the linear displacement d_i is always constant, and each connector has only one degree of freedom. Therefore, to determine the location of the individual components of the manipulator in space, the local coordinate systems at each joint must be defined:

$$ROT\,(X,\theta^i)\begin{bmatrix} cos\theta^i & -sin\theta^i cos\alpha^i & sin\theta^i sin\alpha^i & a_i cos\theta^i \\ sin\theta^i & cos\theta^i cos\alpha^i & -cos\theta^i sin\alpha^i & a_i sin\theta^i \\ 0 & sin\alpha^i & cos\alpha^i & d_i \\ 0 & 0 & 0 & 1 \end{bmatrix} \quad (1)$$

The simulations aimed to obtain information on the marginal positions and trajectories of robot movements to develop an initial strategy for the control algorithm. The resulting information enabled us to focus on specific problematic aspects of robot control. Therefore, by recasting the parameters related to the movement of the joints themselves and the homogeneous transformation matrix (Equation 1), a matrix defining the individual marginal positions of the joints and end-end elements of the manipulator (Fig. 2) was obtained. Analyses, calculations, and simulations were performed using the RoboAnalyzer v. 7.5 software (Mechatronics Lab, India).

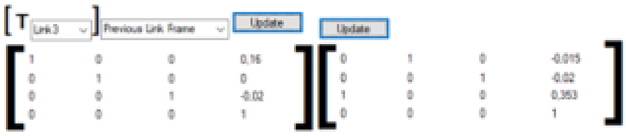

$$\begin{bmatrix} 1 & 0 & 0 & 0.16 \\ 0 & 1 & 0 & 0 \\ 0 & 0 & 1 & -0.02 \\ 0 & 0 & 0 & 1 \end{bmatrix}\begin{bmatrix} 0 & 1 & 0 & -0.015 \\ 0 & 0 & 1 & -0.02 \\ 1 & 0 & 0 & 0.353 \\ 0 & 0 & 0 & 1 \end{bmatrix}$$

Fig. 2. Form of the homogeneous transformation matrix; from the left to the right: form of the third joint relative to the robot arm end; form of the arm end relative to the base coordinate system (source: RoboAnalyzer)

Based on these matrices, the trajectory of robot movements could be simulated. These included the coordinates of the initial points from which the movement of the robot arm was started, and the marginal coordinates of the reference point for the extreme position. Thus, it was possible to delineate and visualize both the working space and nature of the kinema-magnetic manipulation system (Fig. 3).

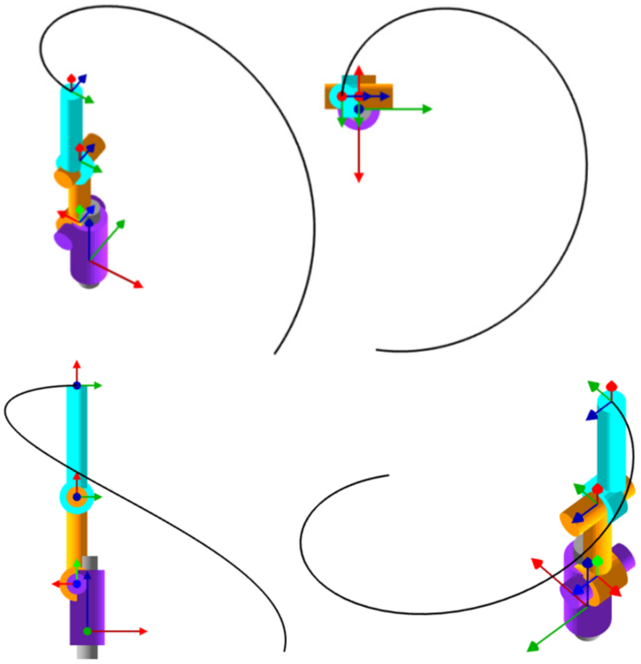

Fig. 3. View of the drawn manipulator trajectory for the maximum extreme position of the robot arm (source: RoboAnalyzer)

2.2. Construction of the first manipulator

The design concept is based on a structure consisting of four modules (Fig. 4). The first segment is the base and fixation of the entire robot on the ground. This is an element of a structure that cannot be moved when the manipulator is in operation. Moreover, it acts as a support for the first motor that rotates in the first direction. The next module considers movement along the x-axis. It was attached directly to the shaft of the first drive and located directly above the base module, allowing eccentric movement with respect to the shape of the bases. Another module was attached in a direction perpendicular to the segment, allowing movement along the x-axis. This enables the next movement along the y-axis. This is realized by means of a motor fixed to the previous component at an angle of 90° in the relation shaft – i.e., the base. The last arm, which is an extension of the previous subassembly moving along the z-axis, was subsequently installed. The beginning of this module was mounted on the shaft of the third motor, which was attached to the end of the previous segment. These arms were connected parallel to the base and previous module. At the end of the last segment, it was possible to rigidly fix the robot tool with possibility of articulation. In the described structure, individual shafts of servos responsible for specific movements are connected directly to movable modules without additional connecting elements. Thus, it was possible to eliminate the additional play on the movable joints. Locating the motors in series with each member successively increased the forces and moments as the number of segments increased with respect to the distance from the attachment point. As a result, the engine that was farthest from the point where the tool was connected to the manipulator was loaded the most. Such a structure reduced the stiffness of the machine, thereby reducing the positioning accuracy. However, it enabled a quick and dynamic response to changes during control.

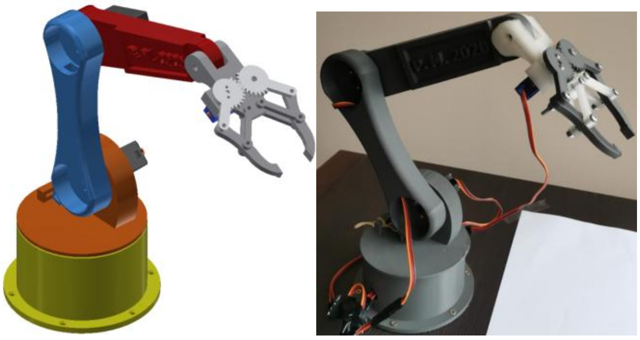
Fig. 4. Model view of the first manipulator (left side) and view of the finished construction of the first manipulator (right side)

2.3. Construction of the second manipulator

After the first construction was completed, some changes were introduced. These changes ad-dressed two aspects. First, the influence of mechanical modifications of individual robot members on the quality of positioning was considered. Second, the feasibility of applying the same algorithm to two different RRR robot constructions was verified. Thus, the usefulness of the executed program and the possibility of introducing and correcting the operation for different manipulators could be evaluated.

The design of the second robot was based on a modular structure with serial kinematics (Fig. 5). A fixed base was made to support the entire robot. Then, through the use of a bolt and nut, bearings, and small spherical balls, the first movable module realizing the movement along the x-axis was mounted. An important aspect was the additional use of a reduction gear on the servo and the component carry-ing out the movement along the x-axis. This allowed for the reduction of the forces and moments on the shaft-first engine. On the first movable module, there were two servos that moved along the y- and z-axes. In this way, additional moments arising on individual parts of the arm due to the mass of the motors themselves were reduced. Because all servos were mounted at a considerable distance from the end of the arm, transmitting the drive to the individual joints became a problem. Therefore, the arm was moved along the y- and z-axes by connecting the individual elements of the movement mecha-nisms by attaching rigid tendons to them. Thus, it was possible to coordinate the movement of the arm along both the y- and z-axes. Owing to the use of this type of drive ratio, it was possible to reduce the weight of the arm and control the stiffness of the manipulator's movement at the expense of the dy-namics of its reaction. Unfortunately, such a solution introduced the possibility of creating additional play in the entire system and the necessity to control the condition of the connection

in the movement areas of the main joints and connection points of the tendons with individual movable elements of the arm.

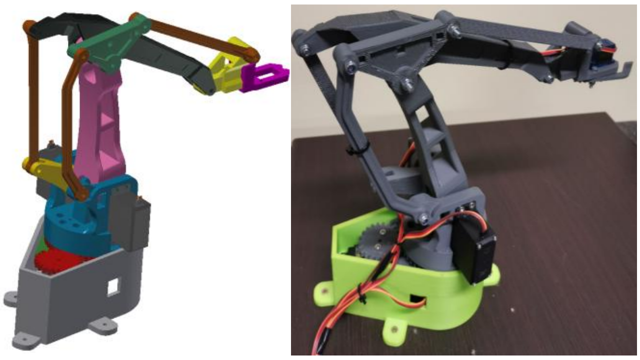
Fig. 5. Model view of the second manipulator (left side) and view of the finished construction of the second manipulator (right side)

2.4. Control algorithm

We decided to combine several types of control, creating an original method for designing the tra-jectory of the manipulator's movements. Through the activation of potentiometers in the form of a simplified physical model and the separation of the electronic system of the robot and phantom, the manipulator became a completely independent device. This enabled online robot programming exactly where it was supposed to work – a phantom connected directly to the manipulator – and offline pro-gramming such that on the basis of the model's movements, positions could be saved in the electronic system. Then, by connecting the system to the robot, the saved program was recreated. These two methods for planning movements are related to teach-in programming, except that the trainer need not be in front of the machine. In addition, with the appropriate use of specific data transfer, it is possi-ble to train the robot in teleconference mode. Therefore, the developed solutions enabled the combi-nation of all types of control: direct, indirect, and the use of direct programming languages. Additional-ly, PTP (point-to-point) control was used. This allowed the manipulator to move smoothly from point to point (stored in memory) according to the set motion trajectories by moving the phantom. In addition, by writing program code, the trajectories of the robot's movement could be manually entered and set. In addition, it is possible to determine the "home" position of the manipulator, from which it always starts the execution of the stored program, and the speed of the motor movement, thereby adjusting the positioning accuracy.The logic diagram of the algorithm is shown in Figure 6.

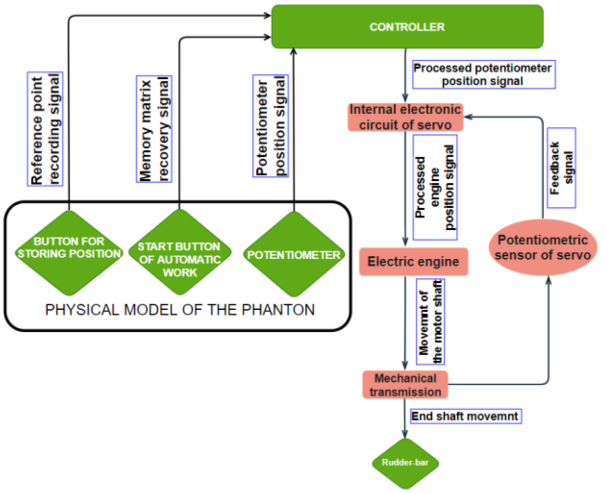

Fig. 6. Control algorithm diagram

The value given at the input in the transmitter is read by the receiver and compared with the output signal changed by the converter. This is how errors arise. They are fed to the corrective element and amplifier. The amplified signal goes to the actuator, that is, the DC electric motor. Its rotation value is the output value of the entire system. The servomechanism is a follow-up system that eliminates the displacement error. It does not control the entire object but only its drive, i.e., the engine. Consequently, the execution track is improved. The integral nature of the servo practically ensures zero static error while maintaining a high gain in the main path, improving the system's ability to follow changes in the input signal. Depending on the difference between the current and defined positions, the motor is driven by a signal with a greater or lesser duty cycle. The running motor, which drives the mechanical transmission, also rotates the potentiometer, which is permanently connected to the transmission. The movement of the potentiometer causes a change in resistance, which is read by the internal system; if it reaches an appropriate defined value for a given input signal, the motor stops working because the servo has reached the prescribed position.

3. RESEARCH METHODOLOGY

3.1. Research methodology of first construction

Stage I

The key movements of the manipulator implementing the trajectories are the reconstruction of straight lines and one angle. Therefore, we decided to execute a pattern printed on paper (Fig. 7). The geometry of five pairs of parallel lines was prepared with distances of 10, 15, 20, 25, and 30 mm and a right angle.

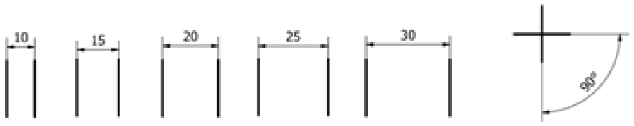

Fig. 7. Reference geometric view

In the first phase, the robot imitated the movements of the phantom at a distance of 500 mm from the manipulator. Additionally, when imitating the movements, the robot marked the developed geometry (one of the six drawn) on a reference sheet attached to its arm with a marker. During the movements, the learning process took place, and the reference points were recorded in the memory of the manipulator. After the learning process, the drawn geometry was repeated 30 times with independent (automatic mode) execution of the developed training strategies to recreate the memorized trajectories. The speed of the movement of the manipulator reached 0,025 s/1°. A blank white sheet of paper was placed at the base of the robot before each cycle was performed in playback mode. During the implementation of the learned trajectories, the manipulator marked the remembered key movement for a given strategy in accordance with the pattern for a given geometric case. After each cycle, the page was changed.

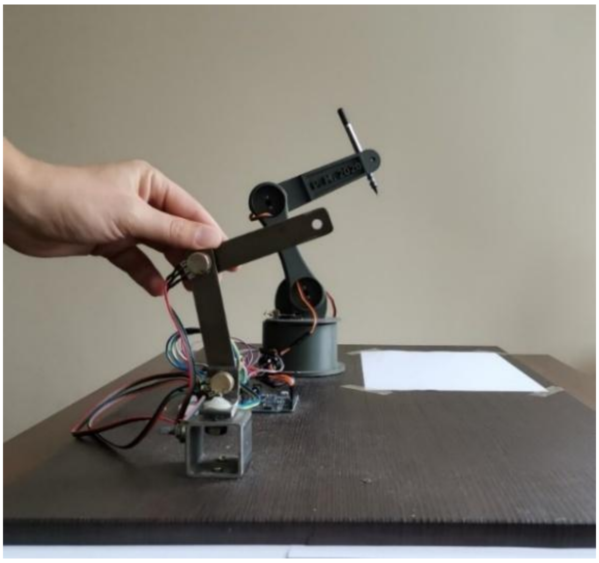

Fig. 8. View of the robot's workstation when executing predetermined geometries

Stage I

After the completion of Stage I, the quality of the developed training strategies had to be verified. Therefore, positioning accuracy was checked by examining the quality of the marked geometries. The dimensions of the printed standard were measured. Additionally, all the geometries marked on the sheet by the manipulator were realized in accordance with the printed standard. Hence, it was necessary to verify the created shapes using the actual dimensions obtained after printing.

For the above analysis, a test was carried out on the Baty Venture XT multisensory measuring device (Fig. 9) equipped with a self-calibrating zoom lens with a magnification of up to 12× and an auto-focus system. This device enables measurements with a resolution of 0.5 μm. The measurement structure was based on optimization using the finite element method.

The test consisted in measuring the distance between two parallel lines or an angle. The center of each line was determined. The points of geometry were then detected and displayed in the measuring system of the machine. Thus, it was possible to create lines from the selected points and measure the distance between them. To ensure the test reliability, each geometry was measured 30 times.

After conducting research on the dimensions, it was necessary to verify the positioning accuracy of the manipulator itself. To this end, we analyzed the dimensions of the geometry created in automatic mode by the robot after performing the learning procedure. Each sample was tested. Thus, a set of 30 measurements was obtained for each geometry. The samples were measured in the same manner as the standard dimensions were checked. The results of the analysis were saved after each measurement.

Fig. 9. Test stand including the Baty Venture XT measuring machine

3.2. Research methodology of second construction

Analysis of the first structure led to consideration of the second structure. In this case, we intro-duced an application aspect to the study. The manipulator was supposed to transfer the designed element from one place to another. Three separate sequences were analyzed. In each of them, the ma-nipulator took the object from the same place and then transferred it to a given distance.

Each se-quence was preceded by a trajectory-learning procedure in which the transfer distance was directly defined. The manipulator performed three sequences. In each of them, the element was moved to a different distance successively: 84.0 mm, 121.2 mm, and 204.2 mm.

An important issue, as in the first construction case, was to start the sequence operation always from the same place – i.e., the home position. This guaranteed the closest similarity of movement and hence, the most reliable mapping of the trajectory and displacement of the transferred element. In each sequence, the manipulator per-formed 30 repetitions (cycles) in accordance with previously learned trajectories (in total, 90 element movements were performed).

A 3D scanner, Atos Core 300, was used to test the accuracy, together with the dedicated Atos software that enables measurement with a resolution of up to 0.182 mm. 3D scanning uses digitization, which is the process of applying data from real objects to digital ones. The measurements provide a spatial cloud of points that can be polygonized into a mesh of triangles.

Based on the scanned data, a CAD model of the real station was developed, and the starting point of movement was fixed. Then, the real object displacement was analyzed in relation to the fixed start and end points of the movement, and it was possible to measure a real object in relation to its nominal values.

A view of the test stand during the examination of the second structure from GOM INSPECT 2018 Professional software (GOM GmbH, Germany) is presented in Fig. 10.

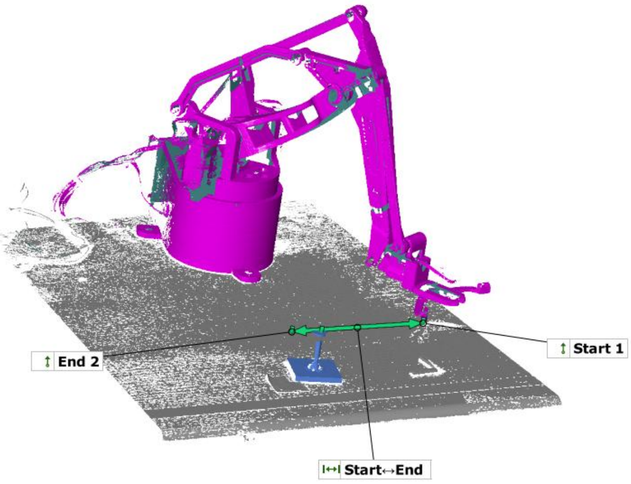

Fig. 10. View of the test stand during the examination of the second structure using GOM software

After each implementation of the trajectory cycle in each sequence, the actual distance of object displacement was measured using a 3D scanner. The original position of the item and position of the item after transfer were measured. Both measurements in the cycle were taken against the previously determined reference points. The relative difference between both positions resulted in a distance displacement in the three axes, and thus, the corresponding total displacement. Consequently, it was possible to determine how the position of the transferred object in relation to its initial position changed in individual cycles for each sequence. The difference between the value of the set distance during the learning procedure and the value obtained in a particular cycle resulted in deviation from the original value. Accuracy analysis was conducted based on the obtained data.

4. RESULTS AND DISCUSSION

4.1. Results of first construction

The results of the measurements of the proposed standard are presented in Table 1. The results are listed for all the considered geometries and calculations on the basis of the obtained values. Table 1 includes drawing distances of 10, 15, 20, 25, and 30 mm, and an angle of 90°. Similar to a previous study [45], for the analysis of results, statistical parameters were used, such as standard deviation σ, skewness A, and kurtosis K.

The standard deviation can be determined from the following expression:

$$\sigma = \sqrt{\frac{1}{(n-1)}\sum_{i=1}^{n}(x_i - \bar{x})^2} \tag{2}$$

where $\bar{x}$ is mean value calculated from the following formula:

$$\bar{x} = \frac{1}{n}\sum_{i=1}^{n} x_i \tag{3}$$

where *xi* is a measurement result
n denotes the number of repetitions.

Properties were determined using a series of 30 repetitions (n = 30).

Skewness A was determined as follows:

$$A = \frac{n}{(n-1)(n-2)}\sum_{i=1}^{n}\left(\frac{x_i-\bar{x}}{\sigma}\right)^3 \tag{4}$$

Kurtosis K was determined from the following expression:

$$K = \left\{\frac{n(n+1)}{(n-1)(n-2)(n-3)}\sum_{i=1}^{n}\left(\frac{x_i-\bar{x}}{\sigma}\right)^4\right\} - \frac{3(n-1)^2}{(n-2)(n-3)} \tag{5}$$

To evaluate the measurement uncertainty of the determined parameters, the type-A method for estimating the uncertainty was used.

Extended uncertainty U0,95 is obtained by multiplying the standard deviation by the appropriate factor:

$$U_{0,95} = k \cdot \frac{\sigma}{\sqrt{n}} \tag{6}$$

For the calculations, k = 1.960 was applied, which corresponds to the quantile of the Gaussian distribution. If there are less than 30 repetitions, the coverage factor assumes the value of the Student's quantile distribution. For example, for a confidence level P = 95%, the quantile of the Student's distribution is tα = 2,262. To check the normality of the random variable, the χ2 compliance test was used; N indicates the number of repetitions [45, 46].

Results for R were calculated as the difference between maximum and minimum values.

Based on the obtained results and calculations, an analysis was conducted; exemplary results are presented in Fig. 11.

Tab. 1. Results of the reference measurements and their calculations

	10 mm	15 mm	20 mm	25 mm	30 mm	90°
Mean	9.125	14.356	19.284	24.068	28.904	89.876
Max	9.398	14.604	19.683	24.315	29.148	89.938
Min	8.746	14.148	18.851	23.733	28.624	89.803
R	0.652	0.456	0.832	0.582	0.524	0.135
σ	0.178	0.140	0.189	0.177	0.132	0.034
A	-0.589	0.342	-0.093	-0.114	0.104	0.012
K	-0.197	-0.743	-0.042	-1.230	-0.120	-0.412
$U_{0.95}$	0.064	0.050	0.068	0.063	0.047	0.012

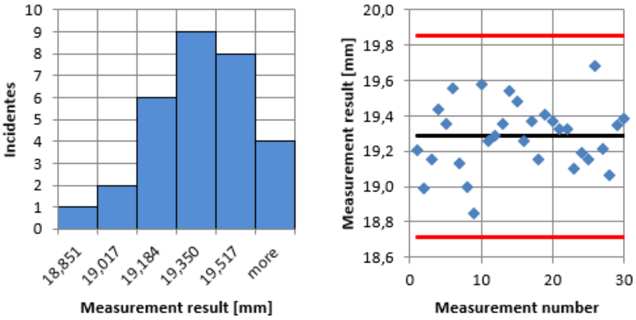

Fig. 11. Value distribution histogram (left side) and distribution of the result values ±3σ (right side) for parallel lines 20 mm apart

The above histogram (Fig. 11) for parallel lines 20 mm apart takes an asymmetric form close to the normal distribution, with a clear peak reached for the values in the range of 19.350 mm. On this basis, it can be concluded that the mean value (19.284 mm) was recorded on one side of the distribution. This proves that the lower limit of the results and density of the measurements are close to the mean values. Additionally, Fig. 11 shows that most of the measurement points oscillate around the mean value. This was confirmed by the distribution of results. Note that most measurements were at or above the mean value. Additionally, all values were within the range (+ 3σ; -3σ). The difference between the maximum and minimum values was 0.832 mm. The skewness coefficient is negative, but remains at a very low level (-0.093), with little scattering. The kurtosis was negative for all measurements, which means scattering around the calculated mean of measurements. However, kurtosis values relatively close to zero indicate that the concentration of results is close to the average distribution. The quality of manipulator positioning was analyzed on the basis of the measurement results of the actual pattern.

For all geometries, calculations were made on the basis of the obtained values presented in Table 2 for the original structure geometries. The same parameters were used for analysis. Moreover, the same graphs were created as in the case of reference.

Tab. 2. Results of geometric measurements made by the robot and their calculations

	10 mm	15 mm	20 mm	25 mm	30 mm	90°
Mean	9.711	14.614	19.004	24.448	29.174	90.100
Max	9.911	14.895	19.280	24.794	29.371	91.253
Min	9.450	14.200	18.680	23.825	28.940	88.048
R	0.461	0.695	0.600	0.969	0.431	3.205
σ	0.130	0.191	0.177	0.274	0.135	0.819
A	-0.166	-0.171	-0.122	-0.470	-0.381	-0.530
K	-0.884	-0.888	-1.127	-0.790	-1.240	-0.336
$U_{0.95}$	0.047	0.068	0.063	0.098	0.048	0.293

Concerning the analysis of the geometry performed by the manipulator, it can be concluded that the average values of the results for each case are very close to the reference ones. Kurtosis values for all cases, similar to the pattern analysis, were below zero. Its mean value is greater than the values of all reference values; therefore, it can be concluded that the dispersion is also greater. This is justified because it is difficult to obtain a high level of a small range of results using the teaching machine.

Then, the results had to be interpreted and compared in the form of a relative error:

$$\delta = \left|\frac{\bar{x_i} - W}{W}\right| \cdot 100\% \tag{7}$$

where $\bar{x}$ is the mean value
W denotes the reference value.

For the calculations using Equation 7, a graph was plotted (Fig. 12) showing the distribution of the relative error for the selected geometry made by the robot in relation to the standard.

Note that the geometries created by the manipulator against the real measurement pattern show that the highest standard error was obtained for parallel lines spaced 10 mm (6.4%). Thereafter, there was a significant decrease in the error for the 15-mm distance (1.8%). Increasing the distance led to similar errors, reaching 1.8%, 1.5%, 1.6%, and 0.9%, respectively. The error for the largest gap was twice that of the previous three. Regarding the mapping of the right angle, an error of 0.2% can be observed. As in the case of measurements of the standard itself, it can be stated that the implementation of the geometric real dimensions became more accurate with the increase in the distance between the created geometries. The relative error did not exceed 7.0% in any case, reaching a maximum of 6.4% for the smallest geometry, and decreasing by a factor of 5 for the largest distances.

A plot was constructed to illustrate the distribution of the standard deviation (Fig. 13).

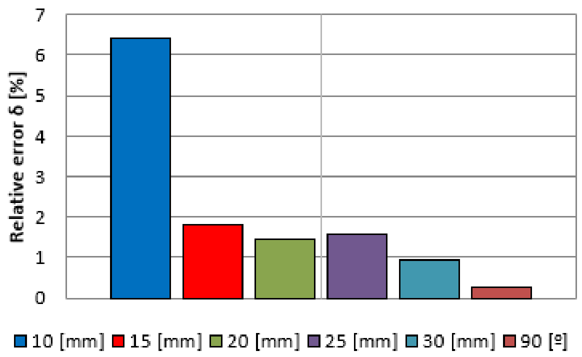

Fig. 12. Relative error robot – reference

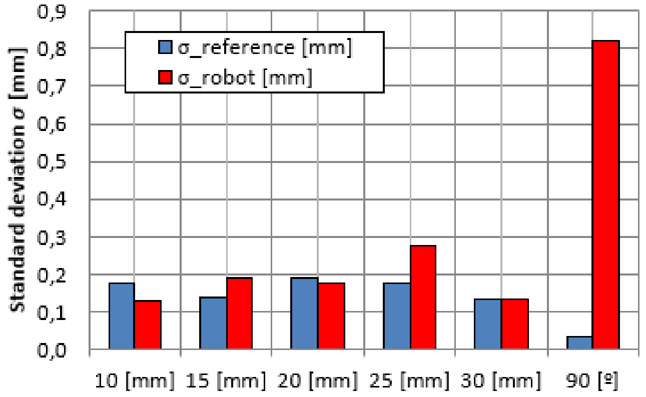

Fig. 13. Standard deviation distribution

Standard deviation is the usual criterion to determine the variability of results. It provides information about spreading and its distribution for the results obtained around the mean of measurements. In accordance with the distributions shown in Fig. 13, it can be concluded that the standard deviations for real standard measurements as well as for geometry measurements made by the robot related to the parallel lines are similar. The standard deviation did not exceed 0.2 except for lines 25 mm apart. However, this increase was small (0.274) and did not affect the overall analysis. A larger standard deviation can be observed for the measurements at 90° (0.819°). Despite the smallest relative error, the volatility of the results around the average is notably high (it remains low compared to the global results).

Additionally, Fig. 14 shows the mean values of each geometry with the corresponding error range and resolution – the maximum and minimum values for both the measurement pattern and geometry made by the manipulator.

Thus, it is possible to determine the range in which the obtained values fell. As emphasized in the previous analysis, the values of the pattern and geometry intervals made by the manipulator are similar, which proves that the measurements were properly made, and the positioning accuracy was high. With respect to the dispersion of the reference values, a greater dispersion was registered for the value at 90° – a difference of 3,2° that, given the size of the angle, it is insignificant and acceptable.

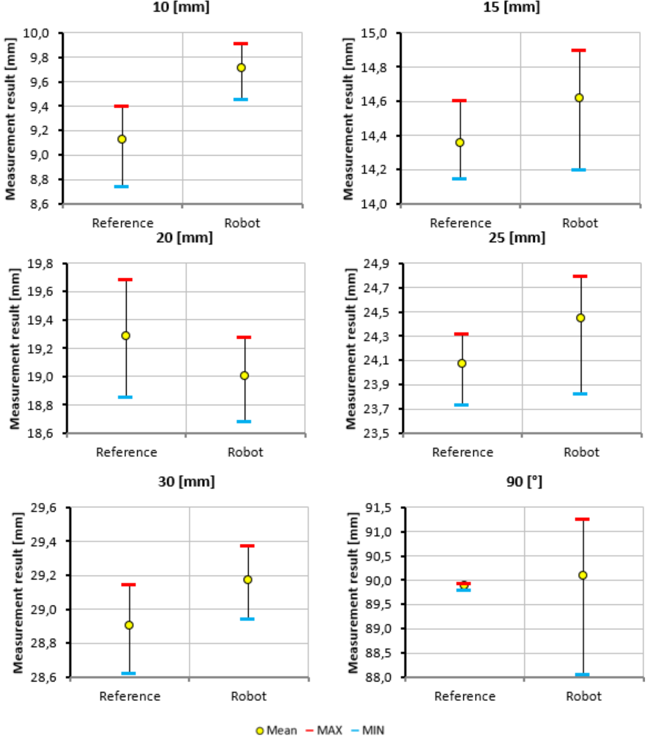

Fig. 14. Variability of measurement results for the analyzed geometries

4.2. Results of second construction

The displacement results obtained from the robot are listed in Table 3. These results include all the displacements performed in individual distance cycles and calculations made on the basis of obtained values. In addition, statistical parameters were again considered, such as standard deviation, skewness, and kurtosis. The experimental results are presented in Fig. 15. Before starting the execution of the individual cycle in automatic mode, the distance of the element transferred during the learning procedure was measured. Table 3 considers the above carrying lengths: 84.0, 121.2, and 204.2 mm.

Tab. 3. Calculations of measurement results of element displacement by the robot

	Distance 1	Distance 2	Distance 3
	84.0 mm	**121.2 mm**	**204.2 mm**
Mean	83.883	121.393	204.587
Max	84.518	121.446	204.763
Min	83.490	121.352	204.400
R	1.027	0.094	0.363
σ	0.378	0.027	0.117
A	0.642	0.861	-0.165
K	-1.060	-0.526	-1.270
$U_{0.95}$	0.135	0.010	0.042

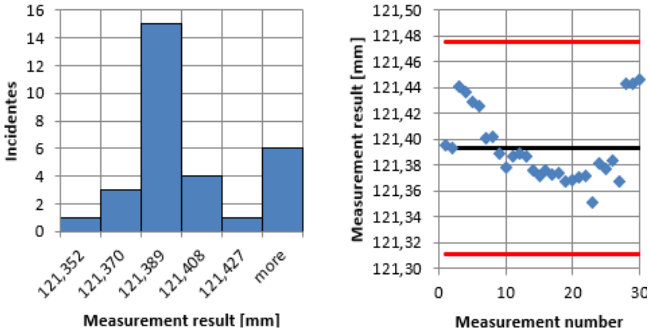

Fig. 15. Value distribution histogram (left side) and distribution of the result values ±3σ (right side) for a displacement of 121.2 mm

According to Table 3, the average values for the second and third items were above the set value, whereas for the first item, they were below the set value. The deviations from the set value were $84.0^{+0.518}_{-0.510}$; $121.2\,^{+0.246}_{+0.152}$, $204.2^{+0.563}_{+0.200}$. The lowest values for both the maximum and minimum deviations were recorded at 121.2 mm. The positioning tolerance for the obtained results was also smallest for the middle distance (0.094 mm). The worst result was recorded for the smallest distance, 84.0 mm; it was 1.027 mm. For extreme maximum distance, that is, 204.2 mm, a tolerance of 0.117 mm was obtained. The difference between the mean and set values was the smallest for the minimum considered distance; this difference was 0.117 mm. These are similar results to the first case, but with a positive value for 121.2 mm: 0.193 mm. The worst distance in this comparison was the maximum one, for which the result was 0.387 mm.

The smallest skewness, as a parameter defining the nature of the dispersion of data distribution from the resulting samples, was recorded successively for 204.2 mm, 84.0 mm, and 121.2 mm. For the third distance, the skewness is left-handed, indicating a slight dispersion of the results above the average. For the first and second items, right-handed dispersion of results below the average was obtained. The histogram (Fig. 15) for the second item takes an asymmetric form, close to the normal distribution, with a clear peak reached for the values in the range 121,389 mm. Accordingly, it can be concluded that the mean value (121.393 mm) was recorded on one side of the distribution. This proves that the lower limit of the results and the density of the measurements close to the average values were maintained. Additionally, it can be observed in Fig. 15 that most of the measurement points revolve around the mean value. Importantly, for all items and trials, no single result exceeding ±3σ was observed. This was confirmed by the distribution of the values. It can be clearly observed that most of the measurements were at or below the mean value.

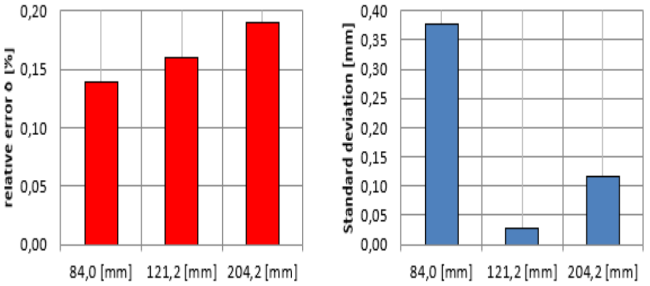

Fig. 16. Distribution of the relative error (left side) and standard deviation (right side)

As shown in Fig. 16, the lowest variability of the observed results was recorded successively for displacements of 121.2 mm, 204.2 mm, and 84.0 mm. The standard deviations were 0.027 mm, 0.117 mm, and 0.378 mm, respectively. An important fact is the increasing nature of the relative error (Fig. 16). For distance 1 (84.0 mm), distance 2 (121.2 mm), and distance 3 (204,2 mm), the errors were 0.14%, 0.16%, and 0.19%, respectively.

5. CONCLUSIONS

This paper presents possibilities of applying a proprietary control algorithm to two different de-signs of RRR manipulators. Correlations were found between the implementation of the distance between the start and end points of individual trajectories and the actual implementation of the manipu-lator's movements.

Analysis of the first proposed structure shows that the worst standard deviation results were ob-tained for a distance in the middle of the interval. However, a relative error was observed for the shortest distance. Owing to the design changes introduced, it was possible to reduce the standard devi-ation in the middle range of the working area at the expense of that in the upper range. Comparing the second structure with the first one, the relative error in the lower range of the working area was signif-icantly reduced, reaching its lowest value for all the displacements.

For both structures, a negative kurtosis was maintained for all the displacements. Thus, it was pos-sible to determine both the distribution and concentration of the results. Negative kurtosis values indi-cate a platykurtic distribution and a lack of outliers, which strongly proves the clustering of results around the mean value.

An important parameter in a distribution is skewness. A skewness coefficient below 0 indicates left-handed asymmetry of the distribution. This means that most of the results are above the average. In case of coefficient values above 0 (right-handed distribution), most results are below the mean. For both structures, negative values of skewness were obtained for all trajectories (except for the positions of the first and second structures, which remained close to 0). The difference in the results for the 84.0-mm and 121.2-mm trajectories was due to a structural change and deliberate change in the standard deviation and relative error by a design change at the expense of other parameters. For both designs, the individual positioning tests were inside the mean ±3σ interval. According to this analysis, a high level of repeatability and concentration of results was confirmed.

The algorithm for the first construction enabled the learning process to be maintained and repro-duced in automatic mode below ±1.0 mm, taking into account the measurement of the pattern itself as well as the measurement of the implementation of the marker trajectory. However, for the second structure, the results were below ±0.6 mm.

The research conducted using all the applications, advanced multisensory equipment, measure-ment methods, and statistical analysis, has proven that the application of the same algorithm to two different designs does not have to negatively affect the resulting positioning quality. By respecting the calculation rules of both the trajectory of movements and geometric dimensions of the manipulator as well as the working area, with the same program executing the manipulator's movement, it is possible to improve positioning parameters by interfering only with the mechanical structure. The statistical calculations used during the analysis of the results confirmed the assumptions related to the analysis of positioning quality and repeatability of the manipulator movement trajectory in automatic mode.

In the subsequent stages of research, particular emphasis will be placed on two key issues that may significantly influence the further optimization of accuracy and reliability in the operation of robotic manipulators in advanced industrial environments.

First, the application of a photogrammetric system is planned for the precise determination of the spatial positions of individual nodes within the manipulator's kinematic structure. This approach will enable high-resolution reconstruction of the robot's geometry and accurate mapping of its actual motion trajectory, thereby allowing for a detailed analysis of deviations from the pre-programmed paths. Photogrammetry, as a non-contact and high-precision measurement method, will be essential for evaluating spatial relationships and identifying potential kinematic discontinuities under real operating conditions.

Second, the impact of the payload mass on positioning accuracy will be examined. This factor is of crucial importance in real-world industrial applications, where variations in the carried load can cause structural deflections and inertial effects, which in turn negatively affect trajectory tracking accuracy. The planned studies will include manipulation tests under various payload conditions to assess the extent to which load mass affects the stability and precision of positioning. These analyses will be conducted using two independent measurement systems: a multisensor coordinate measuring machine (CMM) and a photogrammetric system. This dual-approach will allow for cross-verification of results and provide a comprehensive evaluation of the applicability and accuracy of both methods in the context of dynamic and spatial measurements.

The findings obtained from this research will make a significant contribution to the development of universal and adaptive control algorithms capable of compensating for structural deformations and trajectory disturbances caused by variable load conditions. The ultimate goal of these activities is to enhance the precision, flexibility, and reliability of robotic systems used within the framework of Industry 4.0.

REFERENCES

1. Fromhold-Eisebith M, Marschall P, Peters R, Thomes P. Torn between digitized future and context dependent past – How implementing 'Industry 4.0' production technologies could transform the German textile industry. Technological Forecasting and Social Change. 2021;166:120620. https://doi.org/10.1016/j.techfore.2021.120620
2. Müller JM, Buliga O, Voigt K-I. Fortune favors the prepared: How SMEs approach business model innovations in Industry 4.0. Technological Forecasting and Social Change. 2018;132:2–17. https://doi.org/10.1016/j.techfore.2017.12.019
3. Engemann H, Du S, Kallweit S, Cönen P, Dawar H. OMNIVIL—An Autonomous Mobile Manipulator for Flexible Production. Sensors. 2020;20(24):7249. https://doi.org/10.3390/s20247249
4. Hanh LD, Tu HB. Computer Vision for Industrial Robot in Planar Bin Picking Application. Advances in Science, Technology and Engineering Systems Journal. 2020;5(6):1244–9. https://doi.org/10.25046/aj0506148
5. Bedaka AK, Mahmoud AM, Lee S-C, Lin C-Y. Autonomous Robot-Guided Inspection System Based on Offline Programming and RGB-D Model. Sensors. 2018;18(11):4008. https://doi.org/10.3390/s18114008
6. Engemann H, Wiesen P, Kallweit S, Deshpande H, Schleupen J. Autonomous Mobile Manipulation Using ROS. In: Advances in Service and Industrial Robotics. Cham: Springer International Publishing; 2017. p. 389–401. [accessed 4 Apr 2024] https://doi.org/10.1007/978-3-319-61276-8_43
7. Bedaka AK, Vidal J, Lin C-Y. Automatic robot path integration using three-dimensional vision and offline programming. The International Journal of Advanced Manufacturing Technology. 2019;102(5–8):1935–50. https://doi.org/10.1007/s00170-018-03282-w
8. Jermak CzJ, Jakubowicz M, Dereżyński J, Rucki M. Air Gauge Characteristics Linearity Improvement. Journal of Control Science and Engineering. 2016;2016:1–7. https://doi.org/10.1155/2016/8701238
9. Jakubowicz M, Rucki M, Varga G, Majchrowski R. Influence of the Inlet Nozzle Diameter on the Air Gauge Dynamics. In: Lecture Notes in Mechanical Engineering. Cham: Springer International Publishing. 2017; 733–42. [accessed 2024] https://doi.org/10.1007/978-3-319-68619-6_71
10. Arnarson H, Solvang B. Reconfigurable autonomous industrial mobile manipulator system. In: 2022 IEEE/SICE International Symposium on System Integration (SII). IEEE; 2022. [accessed 4 Apr 2024] https://doi.org/10.1109/sii52469.2022.9708887
11. Teixeira FM, Silva MF. Simulation of a Robotic Co-transport System. In: 2021 IEEE International Conference on Autonomous Robot Systems and Competitions (ICARSC). IEEE; 2021. [accessed 4 Apr 2024] https://doi.org/10.1109/icarsc52212.2021.9429776
12. Häuschen H. Der Bauksten . Industieroboter im praktischen Einsatz. Proc 3rd ISIR. 1973;83–93.
13. Warnecke H, Schraft R. Einlegegeräte zur automatischen. Mainz : Krausskopf-verlag; 1973.
14. Feix T, Romero J, Schmiedmayer H-B, Dollar AM, Kragic D. The GRASP Taxonomy of Human Grasp Types. IEEE Transactions on Human-Machine Systems. 2016 Feb;46(1):66–77. https://doi.org/10.1109/thms.2015.2470657
15. Hua J, Zeng L, Li G, Ju Z. Learning for a Robot: Deep Reinforcement Learning, Imitation Learning, Transfer Learning. Sensors. 2021;21(4):1278. https://doi.org/10.3390/s21041278
16. Rękas A, Kaczmarek T, Wieczorowski M, Gapiński B, Jakubowicz M, Grochalski K, et al. Analysis of Tool Geometry for the Stamping Process of Large-Size Car Body Components Using a 3D Optical Measurement System. Materials. 2021;14(24):7608. https://doi.org/10.3390/ma14247608
17. Swojak N, Wieczorowski M, Jakubowicz M. Assessment of selected metrological properties of laser triangulation sensors. Measurement. 2021;176:109190. https://doi.org/10.1016/j.measurement.2021.109190
18. Grochalski K, Wieczorowski M, Jakubek B. Influence of thermal disturbances on profilometric measurements of surface asperities. Measurement. 2022 Feb;190:110694. https://doi.org/10.1016/j.measurement.2021.110694
19. Jakubek B, Barczewski R, Jakubowicz M. The influence of the lubrication on the vibroacoustic signal generated by rolling bearings. Vibrations in Physical Systems . 2017;28:1–9.
20. Andrzejewski J, Marciniak-Podsadna L. Development of Thermal Resistant FDM Printed Blends. The Preparation of GPET/PC Blends and Evaluation of Material Performance. Materials. 2020;13(9):2057. https://doi.org/10.3390/ma13092057
21. Chen X, Huang Z, Sun Y, Zhong Y, Gu R, Bai L. Online on-Road Motion Planning Based on Hybrid Potential Field Model for Car-Like Robot. Journal of Intelligent & Robotic Systems. 2022;105(1). https://doi.org/10.1007/s10846-022-01620-5
22. Maini P, Gonultas BM, Isler V. Online Coverage Planning for an Autonomous Weed Mowing Robot With Curvature Constraints. IEEE Robotics and Automation Letters. 2022 Apr;7(2):5445–52. https://doi.org/10.1109/lra.2022.3154006
23. Mitsi S, Bouzakis K-D, Mansour G, Sagris D, Maliaris G. Off-line programming of an industrial robot for manufacturing. The International Journal of Advanced Manufacturing Technology. 2004;26(3):262–7. https://doi.org/10.1007/s00170-003-1728-5
24. Larkin N, Milojevic A, Pan Z, Polden J, Norrish J. Offline programming for short batch robotic welding. In: 16th joining of materials (JOM) conference. 2011.
25. Wang C, Zhang Y, Zhang X, Wu Z, Zhu X, Jin S, et al. Offline-Online Learning of Deformation Model for Cable Manipulation With Graph Neural Networks. IEEE Robotics and Automation Letters.

2022;7(2):5544–51. https://doi.org/10.1109/lra.2022.3158376
26. Wang Z, Tian G. Hybrid offline and online task planning for service robot using object-level semantic map and probabilistic inference. Information Sciences. 2022;593:78–98. https://doi.org/10.1016/j.ins.2022.01.058
27. Javaid M, Haleem A, Singh RP, Suman R, Gonzalez ES. Understanding the adoption of Industry 4.0 technologies in improving environmental sustainability. Sustainable Operations and Computers. 2022;3:203–17. https://doi.org/10.1016/j.susoc.2022.01.008
28. Tipary B, Erdős G. Tolerance analysis for robotic pick-and-place operations. The International Journal of Advanced Manufacturing Technology. 2021;117(5–6):1405–26. https://doi.org/10.1007/s00170-021-07672-5
29. Mohsen M, Mohamed AM, Ahmed SM, Ibrahim K. Bilateral Control Of A 2-Dof Teleoperated Manipulator Using Udp Scheme. Ain Shams Engineering Journal. 2023;14(9):102065. https://doi.org/10.1016/j.asej.2022.102065
30. Sun Y, Wan Y, Ma H, Liang X. Workspace Description and Evaluation of Master-Slave Dual Hydraulic Manipulators. Actuators. 2022;12(1):9. https://doi.org/10.3390/act12010009
31. Li Z, Zhang E, Zhai B, Li B. Master-Slave Arm Heterogeneous Mapping With Link Pose Constraint in Teleoperation System. IEEE Access. 2022;10:107202–13. https://doi.org/10.1109/access.2022.3213054
32. Wang J, Li H, Meng F, Ma R, Lai Q, Li J, et al. Control Strategy of Master-Slave Manipulator Based on Force Feedback for Decommissioning of Nuclear Facilities. Mathematical Problems in Engineering. 2022;2022:1–9. https://doi.org/10.1155/2022/9945758
33. Jin X, Guo S, Guo J, Shi P, Kawanishi M, Hirata H. Active Suppression Method of Dangerous Behaviors for Robot-Assisted Vascular Interventional Surgery. IEEE Transactions on Instrumentation and Measurement. 2022;71:1–9. https://doi.org/10.1109/tim.2022.3170997
34. Shi H, Zhang B, Mei X, Song Q. Realization of Force Detection and Feedback Control for Slave Manipulator of Master/Slave Surgical Robot. Sensors. 2021;21(22):7489. https://doi.org/10.3390/s21227489
35. Azizi A, Latifinavid M. Hybrid Artificial Intelligence Algorithm for Optimizing RFID Network Planning in Smart Manufacturing. Journal of Robotics. 2020;2020:1–14. https://doi.org/10.1155/2020/8564140
36. Azizi A, Latifinavid M. Artificial Neural Network Approach for Dynamic Behavior Optimization of Robotic Arms in Industry 4.0. Journal of Robotics. 2017;2017:1–10. https://doi.org/10.1155/2017/8728209
37. Latifinavid M, Azizi A. Development of a Vision-Based Unmanned Ground Vehicle for Mapping and Tennis Ball Collection: A Fuzzy Logic Approach. Future Internet. 2023;15(2):84. https://doi.org/10.3390/fi15020084
38. Azizi A, Latifinavid M. Ring Probabilistic Logic Neural Network for Active Suspension Control in Vehicles. In: Ahram T, Taiar R, Colson S, Choplin A eds. Advances in Intelligent Systems and Computing. Singapore: Springer. 2019;943:35–45. https://doi.org/10.1007/978-981-13-2640-0_4
39. Kim Y-S, Dagalakis NG, Marvel J, Cheok G. Design and Testing of Wireless Motion Gauges for Two Collaborative Robot Arms. Measurement Science Review. 2022;22(2):84–91. https://doi.org/10.2478/msr-2022-0011
40. Liu Q, Guo H, Ma Y, Tian W, Zhang Z, Li B. Real-time error compensation of a 5-axis machining robot using externally mounted encoder systems. The International Journal of Advanced Manufacturing Technology. 2022;120(3–4):2793–802. https://doi.org/10.1007/s00170-022-08867-0
41. Wang X, Li H, Zhang Y. 3D Scanning Based Precision Evaluation of Industrial Robots. Robotics and Computer-Integrated Manufacturing. 2019; 56; 123–130. https://doi.org/10.1016/j.rcim.2018.10.007
42. Chen J, Zhou F, Wu X. Multisensor Measurement System for Robot Positioning Accuracy Assessment. Sensors. 2020;20(4);1015. https://doi.org/10.3390/s20041015
43. Li M, Xu W, Chen L. (2018). Integration of Structured Light scanning in Robot Trajectory Control for Enhanced Precision. IEEE Transactions on Industrial Electronics. 20188; 65(8): 6712–6720. https://doi.org/10.1109/TIE.2017.2787563
44. Chang Q, Gao X, Liu Y, Deng J, Zhang S, Chen W. Development of a cross-scale 6-DOF piezoelectric stage and its application in assisted puncture. Mechanical Systems and Signal Processing. 2022;174:109072. https://doi.org/10.1016/j.ymssp.2022.109072
45. LI H, Xu Y, Zhang C, Yang H. Kinematic modeling and control of a novel pneumatic soft robotic arm. Chinese Journal of Aeronautics. 2022;35(7):310–9. https://doi.org/10.1016/j.cja.2021.07.015
46. Jakubowicz M. Accuracy of roundness assessment using air gauge with the slot-shaped measuring nozzle. Measurement. 2020 Apr;155:107558. https://doi.org/10.1016/j.measurement.2020.107558
46. Dietrich E, Schulze A. Statistical Procedures for Machine and Process Qualification. 1st ed. Munich: Hanser Publications; 2010.

This study, conducted under subject No. 0614/SBAD/1586, was funded by grants for education allocated by the Ministry of Education and Science in Poland.

Patryk Mietliński: https://orcid.org/0000-0002-2300-0834

Michał Jakubowicz: https://orcid.org/0000-0002-6350-0411

Lidia Marciniak-Podsadna: https://orcid.org/0000-0002-4444-0724

Michał Wieczorowski: https://orcid.org/0000-0001-7526-8368

DOI 10.2478/ama-2025-0046

acta mechanica et automatica, vol.19 no.3 (2025)
Special Issue "Techniki Komputerowe w Inżynierii TKI2024"

ANALYSIS OF SELECTED MODELS OF BODY IMPEDANCE IN THE ASSESSMENT OF ELECTRIC SHOCK POSSIBILITY IN THE SHIP'S POWER SUPPLY GRIDS

Arkadiusz FRĄCZ*

*Faculty of Mechanical and Electrical Engineering, Polish Naval Academy, Śmidowicza 69 Street 81-127 Gdynia, Poland

a.fracz@amw.gdynia.pl

received 07 February 2025, revised 10 June 2025, accepted 22 June 2025

Abstract: Ship's low voltage power supply grids with isolated neutral point of the power source are widely used in marine engineering. They can form a potential shock hazard in some specific operational state, when grid capacitance measured against ship's hull exceed critical value. This paper presents analysis of selected models of body impedance in the assessment of electric shock possibility in the ship's power supply grids. Main goal of the analysis is to find a relation between ground capacitance and potential shock current in onboard electrical grids with isolated neutral point of power source, using different body impedance models. The results from the simulations in various configurations are presented and analysed. The findings highlight possibility of electrical shock in isolated neutral point networks with high ground capacitance.

Key words: human body impedance, electric shock protection, ship's power supply network

1. INTRODUCTION

An analysis of documented events [1,2,3,4,5,6] causing injuries to persons following contact with electricity shows that a still significant share (nearly 60%) in all such cases has a human factor, and the most common sources of shocks, indicated by Polish statistics from previous years (in the period 2016-2022 analysed on the basis of available sources), are:

- Incorrect behaviour of the employee,
- The involuntary behaviour of the employee,
- Incorrect use of protective equipment by the employee,
- The improper use of the material factor by the employee.

A smaller share in electric shocks has a directly incorrect condition of the material factor or improper use of it and improper organization of work and workstation. The material factor referred to in the statistics [1,2,3,4,5,6] is to be understood here as the whole of the machines, devices, equipment, apparatus and technical solutions for protection and protection against electric shock.

The available statistical data do not distinguish between the type of electrical grid and the values of the voltages present. However, they illustrate an important thing: it is necessary to use effective shock protection measures to limit the human factor. Due to the fact that the use of electrical appliances is so common at the moment, it seems that cases of shock are becoming, after all, inevitable. Although it seems impossible to completely eliminate the human factor, actions in the field of shock protection should aim at such selection, implementation and protection of the network to limit or prevent the effects of shocks.

In the light of the data cited, it should be considered that – regardless of the area of use of electricity – there may be a risk of electric shock wherever it is used. A special case of an industrial facility in which all elements of the power system (production, transmission, distribution, loads) are simultaneously present is, among others, a ship. In addition to its own electrical power plant, transmission lines, switchboards, in each of the compartments and rooms of the vessel there is a significant accumulation of machinery, apparatus and electrical equipment that potentially pose a risk of electric shock. Limited space, tightened work and service areas, increased humidity, as well as a special mode of work performed by service personnel are an additional risk factor in the operation of ship power grids.

2. SHIP'S ELECTRICAL GRID

In order to describe the area of the study, the following part of the article presents the architecture of a power ship network with an isolated neutral point, in which human body conditions will be simulated using selected body impedance models. The following description of the construction of the network is an introduction to the definition of the research environment to be taken under consideration.

Ship power grids used nowadays are most often networks with an isolated neutral point (in the Polish national nomenclature marked as IT network systems [7], where I: the neutral point is either not connected to the ground/ship's hull or is connected to an intermediate ground, T: each load (device) is separately connected directly to the ground/ship's hull). The diagram of the network of this type with the marking of the insulation condition control device (UKSI) and three-phase loads with individual grounding of the conductive parts available shows the Figure 1.

IT networks have many advantages:

- Long-term work possibility with one phase directly grounded (it should be noted that the time of removal of a single earth fault is not defined) [8]. Operation in the conditions of a single-phase ground fault allows to increase the power supply certainty of loads powered in the grid by ensuring the continuity of

electricity supply to the load even in conditions that should be considered as fault conditions.
- Low ground current values, resulting in increased fire safety.
- Limiting the value of the shock current in the case of contact of the body with the cable of one phase while maintaining high insulation impedance values of the remaining phases (e.g. the provisions of the Polish Register of Shipping provide for circuits with a supply voltage in the range of 125-500 V the minimum value of insulation resistance of electrical network cable circuits 1,0 MΩ [9]).
- The ability to control the state of insulation resistance and the use of control and measurement devices with the function of alarming and switching off the power supply in the case of detection of ground faults of single-phase or exceeding the minimum permissible values of insulation resistance of monitored circuits.

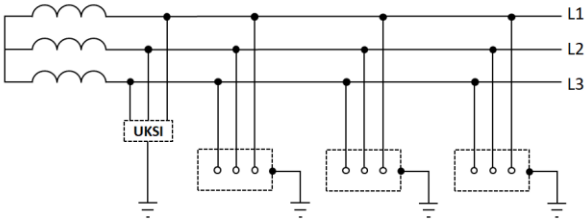

Fig. 1. Typical ship's electric network [12]

At the same time, these grids are characterized by certain disadvantages, the most important of which are:
- Lack of possibility of precise location of the place of occurrence of earth faults. In practice, the place of occurrence of a single-phase ground fault is detected by selective disconnection of loads, what – with an extensive grid and a large number of loads – relatively extends the duration of the earth fault and causes the need to temporarily turn off the power for some loads.
- The possibility of damage to grid elements and loads with the increase in voltage caused by ground short circuit.
- The necessity to ensure high service standards, especially in the field of constant control of the insulation condition and good level of training and operational awareness of personnel.

Although the regulations on vessels allow the use of other network systems in the area of low-voltage [9,10] grids, as well as non-standard and atypical solutions, their occurrence is sporadic and, in practice, a typical ship's power grid is considered to be a system with an isolated neutral point of the power source.

The use of IT network systems is limited to areas and objects where high system availability and the ability to ensure continuity of power supply in the event of network damage is required, as well as in systems, where a high level of protection against electrical shock is indispensable. For this reason, networks with an isolated neutral source point are used onboard ships, in addition to health care facilities (hospitals), in the mining and chemical industries, in aviation as well as in the construction of temporary field power systems, for example for fire-fighting purposes.

Due to the characteristic structure of the grid with an isolated neutral point, it is necessary to use the aforementioned devices for controlling the insulation condition, whose task is to measure, monitoring and informing the user about the possibility of single-phase ground faults and about the reduction of insulation resistance.

3. GROUND FAULTS IN SHIP'S ELECTRICAL POWER GRIDS

The occurrence of a single insulation damage and the formation of a single-phase ground short circuit (short circuit to the ship's hull – in the case of vessels with conductive hulls) is associated with the emission of energy by short-circuit current. With single-phase short-circuits, the short-circuit current does not stimulate the protection devices, guaranteeing continuity of power supply. The insulation condition control system shall signal such a situation so as to prevent the formation of a second short circuit, leading consequently to the black-out condition (power off). Unlike land networks, where there is not always the possibility of a quick response to network damage states, in ship networks, the service should be able to detect, locate and remove a single-phase ground short circuit relatively faster [11,12].

The diagram of a typical insulation status control system is shown in the Figure 2.

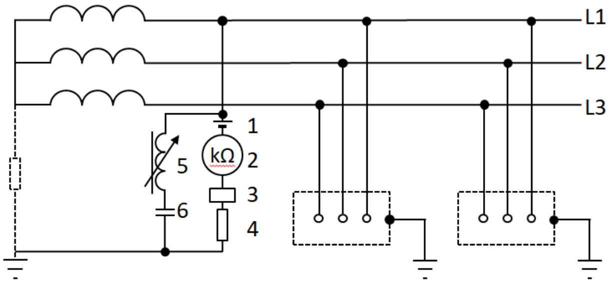

Fig. 2. Typical ship's electrical grid insulation status control system [12]. 1 – DC voltage source, 2 – Insulation resistance meter (Megohmmeter), 3 – singal relay, 4 – limiting resistor, 5 – inductor (suppressor), 6 – DC component blocking capacitor

It is worth noting that the commonly used solutions of insulation condition control systems do not allow to determine the value of the grid capacitance relative to the ship's hull. Therefore, it is not possible to directly determine the value of earth fault currents of the capacitive type. The capacitance of the network depends, among others, on the capacitance of cable networks (treated as a distributed parameter) and on the capacitance between the loads and the hull and other local capacitances (treated as lumped parameters) – e.g. derived from the anti-interference filters used.

The Figure 3 shows the flow paths of short-circuit currents in the case of a single-phase ground short circuit to the hull of the ship, indicating the closing path of the short-circuit both through the insulation resistance and through the grid capacitance. Insulation impedance is represented by RC parallel branches marked in the drawing.

The issue of continuous operational on-line measurement of ground capacitance during ship's electrical grid operation (analogous to measurements of cable network insulation resistance by UKSI systems) has been undertaken many times, for example, for the construction and implementation of Capacitance Current Compensation Systems on Polish ships, or in mines [17,18,19,20,22]. Research and analysis of the possibility of wider use of compensation systems using earth-fault compensation with adjustable inductors [17,21], or using signal processor-controlled current sources [18] are still being conducted.

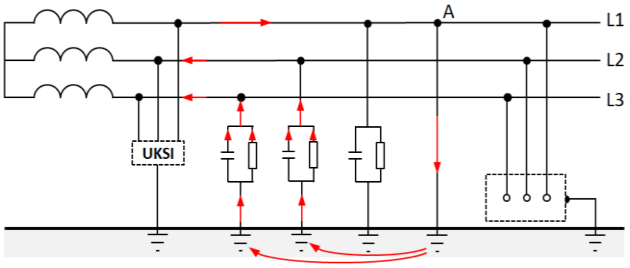

Fig. 3. Single phase earth-fault in ship's electrical network with neutral point isolated. A – earth-fault point [13]

Existing legal regulations for the design and construction of marine power grids and guidelines for the introduction of mandatory shock protection measures on ships [9,10,23] do not include the use of systems for lowering ground currents derived from the capacitance of the electrical grid, arguing that there are no effective and proven measures in this area. Therefore, there is still a need to look for technical and organizational possibilities in the area of electrical shock protection of people.

In the further part of the article, selected models of impedance of the human body were analysed in the assessment of the possibility of electric shock in a ship's network with an isolated neutral point when a ground short circuit of one phase occurred. The purpose of this analysis is to verify and evaluate the parameters of electric shock and critical network parameters given in the available literature (voltage and frequency value, insulation impedance – with particular attention to the network capacitance).

4. EXPERIMENTAL SECTION

In order to build a model of human electrical shock circuit, a simplified ship power grid with an isolated neutral point of the power source network structure was considered (Figure 4). It was assumed that the shock is of tactile type, which is the most common case of shocks during the operation of ship equipment and electrical networks, and the flow of electricity occurs on the hand-hand path, in the absence of additional resistance, e.g. derived from complementary means of shock protection, and the impedance in the path of the shock current consists only of the impedance of the human body Z_{cz}.

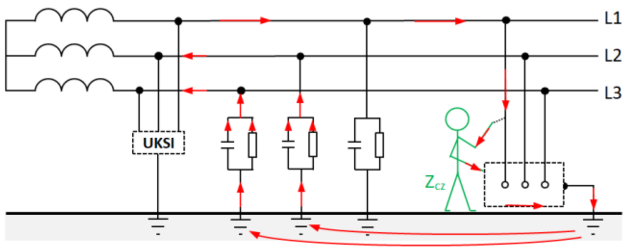

Fig. 4. Human body electrical shock circuit in the ship's electrical grid

4.1. Human body impedance models

Modelling of the human body impedance Z_{cz} is associated with the need to apply a number of simplifications, resulting from the available data from research in the field of electropathology of electrical shocks. Previous studies on the effects of electricity on the human body included both comparative methods and direct methods involving living organisms (people, animals) [16]. The created models of the human body impedance take into account, among others, such parameters as:

- Resistance and capacitance of the epidermis,
- Resistance and capacitance of the keratinized layer of the epidermis,
- Resistance of tissues and internal organs on the electrical shock path,
- Psychophysical status and age of the electrocuted person,
- The hydration state of the body.

For the purposes of the analysis carried out in the article, four model methods of estimating the impedance of the human body were adopted:

- Resistive model (A), often used in the literature for simplified determination of the values of shock currents. A contractual resistance value of 1000 Ω [24,25] has been adopted (Figure 5).
- Model (B) in accordance with IEC 60990 [14] (Figure 6).
- Model (C) proposed by V. De Santis [15] (Figure 7).
- Freiberger model (D), in which a touch surface of 0.01 m2, body resistance and epidermal resistivity according to Biegelmeier [16] were assumed (Figure 8).

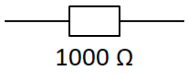

Fig. 5. Simplified resistive Model (A) of human body impedance [24,25]

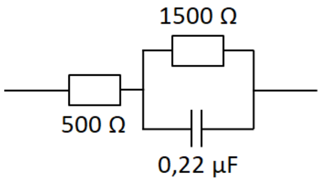

Fig. 6. IEC 60990 Model (B) of human body impedance [14]

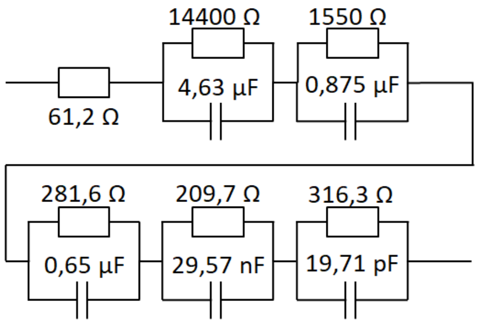

Fig. 7. V. De Santis Model (C) of human body impedance [15]

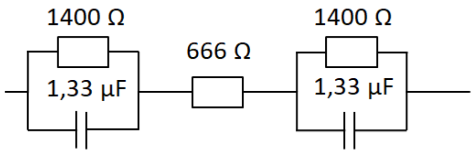

Fig. 8. Freiberger Model (D) of human body impedance [16]

The consideration of several impedance models aims to determine whether the models available in literature sources can be used in research on shock circuits in the network – as an alternative method to research on real objects that is impossible to implement from the ethical point of view.

4.2. Simulation studies

In the assessment of the possibility of electric shock in the electrical grid adopted for consideration, a model study was carried out in the MATLAB-Simulink environment. A simplified network model with an isolated neutral point (Figure 9) was built, in which the initial parameters were assumed:

- 400 VAC voltage and 50 Hz frequency of power source.
- Active symmetrical power load (the Three-Phase Parallel RLC Load module of the Specialized Power Systems library was used). The analysis covered the unloaded network in the quasi-idle mode, in which situation the expected shock current takes maximum values.
- Isolation impedance (coloured blue) composed of 1 MΩ resistance (minimum allowable value of insulation resistance according to [9]) and 0.14 μF capacitance (critical value of network capacitance according to [20]).
- Human body impedance Zcz models (coloured yellow) marked with indices A, B, C, D [24,25,14,15,16].

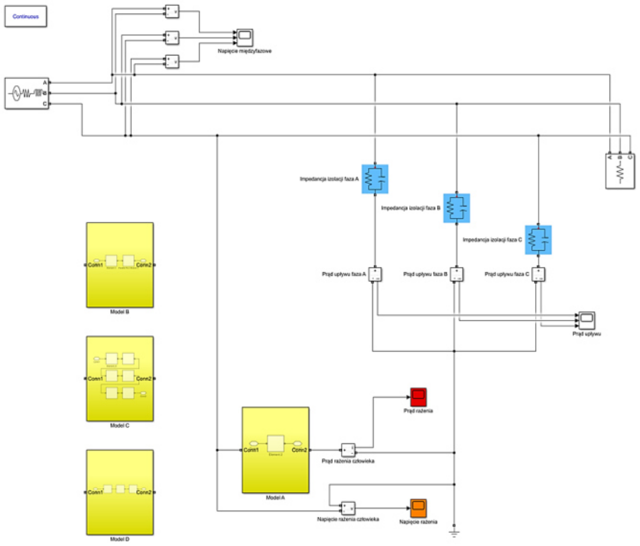

Fig. 9. MATLAB-Simulink model utilized for analysis

In the first phase of the experiment, the operation of the network model was checked assuming that for the limit parameters given in the literature [9] [20] (insulation resistance 1 MΩ, ground capacitance 0,14 μF) a ground fault current of a value exceeding the assumed dangerous current of 30 mA [16] would not occur. This assumption is also directly related to the approximate method of calculating the ground fault current I_R in a grid with an isolated neutral point [26]:

$$I_R \approx \sqrt{3} \cdot U_Z \cdot \omega \cdot C_E \qquad (1)$$

where:

I_R – ground fault current,
U_Z – supply voltage,
$\omega = 2\pi f$ – angular frequency,
C_E – ground capacitance.

Assuming U_Z = 400 V, f = 50 Hz, C_E = 0,14 μF, expected ground fault current $I_R \approx$ 0,03 A. This value is obviously greater than the self-releasing current, but it was taken as a reference value due to the fact that with an electric shock of this value fibrillation for human heart already occurs.

Therefore, it should be assumed that the current flowing through the additional impedance included in the short circuit, for example the impedance of the body, will not take a greater value. For the tested models, the results of the check presented in the Figure 10 were obtained.

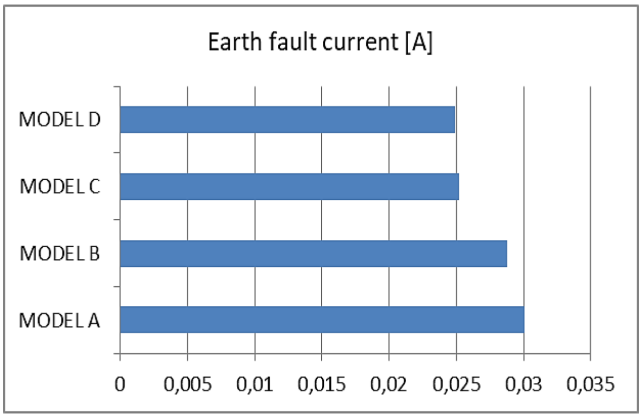

Fig. 10. Earth fault current obtained for tested models

The highest value of the earth fault current was obtained for the simplified model A, but it does not exceed the assumed value of 30 mA. It should be considered that current models A, B, C, D meet the condition of the above check.

In the next part, the model response to the change of power supply parameters was examined. A constant value of the insulation resistance of the network to the hull 1 MΩ and the value of the ground capacitance of the network equal to the critical value of 14 μF were assumed. The range of changes in the supply voltage was selected to include at least the permissible deviations of the voltage value for ship's power supply source in accordance with [9]. Figure 11 shows the dependence of the I_R shock current on changes in the supply voltage value while maintaining its constant frequency of 50 Hz.

Tab. 1. Analysis of the impact of changes in the supply voltage Uz on the value of the shock current IR – selected points

		Supply voltage U_Z [V]						
		360	**370**	**380**	**390**	**400**	**410**	**420**
Shock current I_R [A]	**A**	0,0271	0,0279	0,0286	0,0293	0,0301	0,0308	0,0316
	B	0,0259	0,0266	0,0273	0,0280	0,0288	0,0295	0,0302
	C	0,0215	0,0231	0,0239	0,0243	0,0252	0,0259	0,0264
	D	0,0224	0,0230	0,0236	0,0243	0,025	0,0255	0,0261

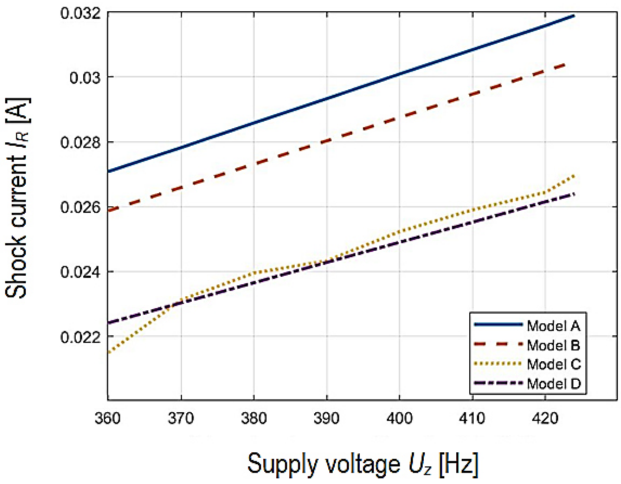

Fig. 11. Impact of changes in the supply voltage *Uz* on the value of the shock current I_R

There is a visible increase in the value of the shock current with an increase in the supply voltage. This relationship is important because it affects the option of designing areas of the grid with reduced voltage.

Simulation analysis was also subjected to the impact of changing the frequency of supply voltage on the value of the shock current. Frequency changes in the range covering at least the permissible frequency deviations in accordance with [9] allowed to formulate a conclusion analogous to the change in the value of the supply voltage: change in the frequency of the supply voltage, which is equal to changing the operating characteristics of the frequency controller, affect the value of the shock current.

The different character of the waveform for Model C (noticeable already in the analysis of changes in the supply voltage) results probably from the impedance parameters of RC branches assumed by the model authors [15] and is related to the way of solving this model by the MATLAB-Simulink package using blocks offered in the Specialized Power Systems library.

In order to analyze the impact of changes in insulation impedance parameters, separate simulations were carried out for changes in the insulation resistance R_{iso} of the grid measured in relation to the hull of the ship and for changes in the ground capacitance C_E of the grid for all models of body impedance considered.

The change of insulation resistance R_{iso} in the simulation was performed for values from 1 kΩ 1 MΩ. The results are shown in Table 3 and in Figure 13.

Tab. 2. Analysis of the impact of changes in the supply voltage frequency f on the value of the shock current IR – selected points

		Supply voltage frequency *f* [Hz]						
		48,5	**48,5**	**48,5**	**48,5**	**48,5**	**48,5**	**48,5**
Shock current I_R [A]	**A**	0,0296	0,0298	0,0299	0,0301	0,0303	0,0306	0,0296
	B	0,0283	0,0285	0,0286	0,0288	0,0289	0,0292	0,0283
	C	0,0245	0,0245	0,0245	0,0252	0,0244	0,0254	0,0245
	D	0,0246	0,0248	0,0248	0,0249	0,0250	0,0252	0,0246

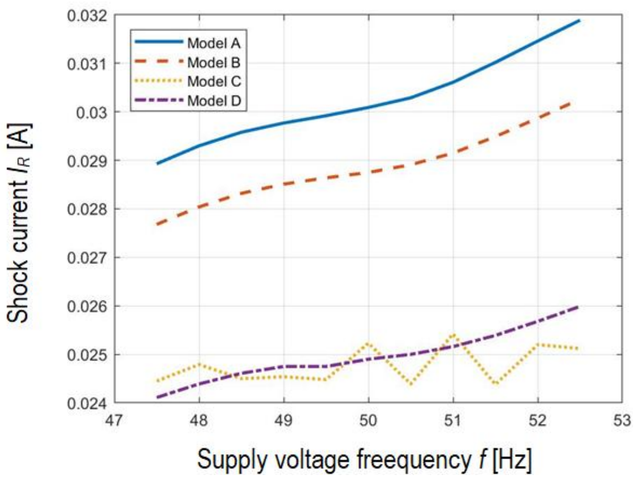

Fig. 12. Impact of changes in the supply voltage frequency *f* on the value of the shock current I_R

The different character of the waveform for Model C (noticeable already in the analysis of changes in the supply voltage) results probably from the impedance parameters of RC branches assumed by the model authors [15] and is related to the way of solving this model by the MATLAB-Simulink package using blocks offered in the Specialized Power Systems library.

In order to analyze the impact of changes in insulation impedance parameters, separate simulations were carried out for changes in the insulation resistance R_{iso} of the grid measured in relation to the hull of the ship and for changes in the ground capacitance C_E of the grid for all models of body impedance considered.

The change of insulation resistance R_{iso} in the simulation was performed for values from 1 kΩ 1 MΩ. The results are shown in Table 3 and in Figure 13.

Tab. 3. Analysis of the impact of changes in insulation resistance Riso on the value of shock current IR – selected points

		Insulation resistance R_{iso} [kΩ]						
		1000	**800**	**600**	**500**	**400**	**300**	**200**
Shock current I_R [A]	**A**	0,0300	0,0301	0,0301	0,0301	0,0300	0,0299	0,0299
	B	0,0288	0,0287	0,0287	0,0286	0,0286	0,0285	0,0284
	C	0,0244	0,02522	0,0233	0,0253	0,0237	0,0240	0,0249
	D	0,0249	0,0249	0,0248	0,0248	0,0247	0,0247	0,0245
		Insulation resistance R_{iso} [kΩ]						
		100	**50**	**40**	**30**	**20**	**10**	**1**
Shock current I_R [A]	**A**	0,0301	0,0314	0,0324	0,0346	0,0399	0,0580	0,173
	B	0,0282	0,0286	0,0294	0,03083	0,0345	0,0465	0,0995
	C	0,0245	0,0253	0,0265	0,0269	0,0304	0,0386	0,0780
	D	0,0243	0,0247	0,0252	0,0263	0,0292	0,0382	0,0695

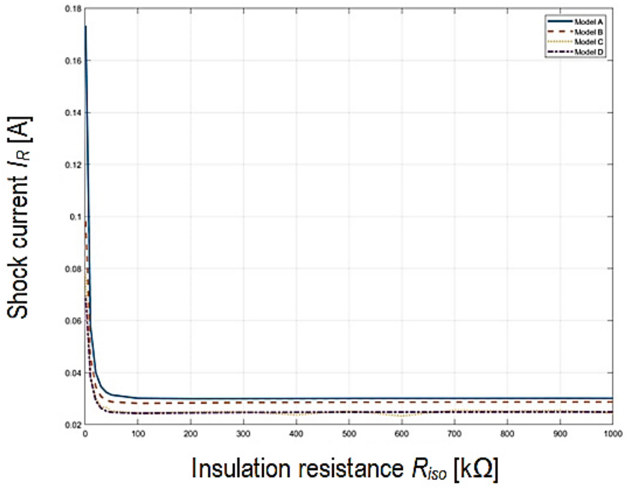

Fig. 13. Impact of changes in the insulation resistance R_{iso} on the value of the shock current I_R

The simulation shows that the change in the insulation resistance of the grid, even below the minimum safe value, does not cause a significant increase in the firing current, and such an increase is observed only at values indicating significant damage to the insulation. Therefore, the minimum value 1 MΩ adopted by the regulations should be considered highly safe, and the control of the insulation resistance status should create conditions sufficient to ensure shock safety.

The change of the ground capacitance C_E in the simulation was performed for values from 0.05 μF to 30 μF. The results are shown in Table 4 and in Figure14.

The simulation revealed that the increase in the expected shock current above the critical capacitance value of 0.14 μF is significant, which may create hazardous conditions for humans. It can also be noted that individual models of body impedance give a different response to changes in the value of ground capacitance, which results from the nature of the construction of each model. The answer of the simplified resistance model allows to obtain the highest values of the shock current, which - for the accepted resistance value - allows to conclude, that its use in further research will allow for quick detection of dangerous values of the shock current in analysed circuits. Assuming that the actual values of the capacitance onboard ships are greater than the critical one [17,23] it can be concluded that the shock protection measures adopted and applied in shipbuilding are becoming insufficient.

Tab. 4. Analysis of the impact of changes in ground capacitance CE on the value of shock current IR – selected points

		Ground capacitance C_E [μF]						
		0,05	**0,1**	**0,14**	**0,5**	**1**	**2**	**3**
Shock current I_R [A]	**A**	0,0109	0,0216	0,0301	0,0982	0,1583	0,2037	0,2177
	B	0,0107	0,0210	0,0288	0,0764	0,0994	0,1101	0,1130
	C	0,00973	0,0189	0,0244	0,0519	0,0726	0,0812	0,0782
	D	0,0102	0,0189	0,0249	0,0534	0,0647	0,0709	0,0728
		Ground capacitance C_E [μF]						
		4	**5**	**6**	**8**	**10**	**20**	**30**
	A	0,2234	0,2260	0,2278	0,2296	0,2304	0,2311	0,2316
	B	0,1140	0,1148	0,1151	0,1155	0,1157	0,1160	0,1162
	C	0,0864	0,0874	0,0876	0,0884	0,0890	0,0901	0,0899
	D	0,0739	0,0746	0,0750	0,0754	0,0756	0,0761	0,0763

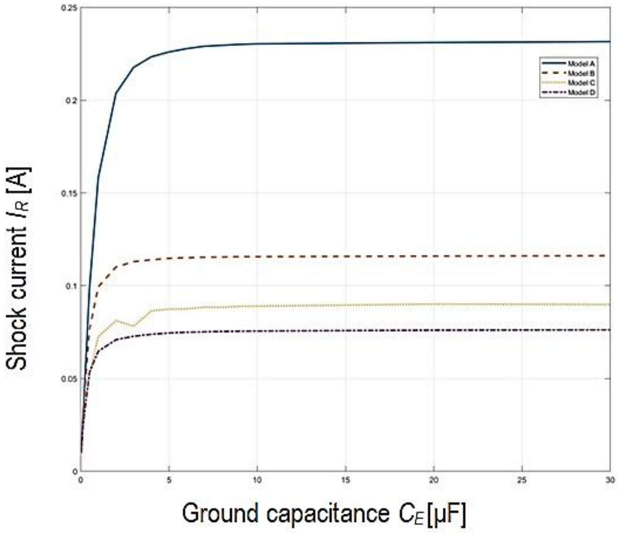

Fig. 14. Impact of changes in Ground capacitance C_E on the value of the shock current I_R

5. CONCLUSION

In the course of the analyses and simulations, the behaviour of body impedance models in cases of shock in a ship IT grid was checked. The work of the constructed model of the shock circuit was checked for cases of changes in power supply voltage parameters and a simulation study of changes in the insulation resistance of the grid to the ship hull and ground capacitance was carried out to determine their impact on the value of the shock current.

The simulation studies showed that:

For the proposed in the literature methods of modelling the impedance of the body, different values of the shock currents are obtained. At the same time, all models show a similar nature of the response to changes in network power supply parameters and network insulation resistance parameters as well as the ground capacitance.

The simplified simulation model A allows for a safe estimation of the expected shock current due to the results obtained. At the same time, it should be noted that the value of body resistance 1000 Ω assumed in the model is an undervalued value in relation to real values.

All models presented in the article provide an answer consistent with the obvious results provided in the cited sources. Due to the simplification of the calculation method and maintaining a significant safety margin, the obvious choice for modeling is the simplified model A, however, the model suggested for use by IEC (Model B) provides a system response adequate to the currently applicable legal provisions and should be primarily used in simulation studies.

There is a relationship between the reduction in the value of the insulation resistance of the grid and the increase in ground capacitance and the possibility of dangerous shock currents when touched by one phase. It is absolutely necessary to use additional shock protection measures in the ship's electrical grid when working near voltage and working under voltage condition.

It is necessary to apply measures limiting ground capacitance. The use of compensation systems for this capacitance is still problematic due to the fact that some of the proposed methods [17,21,23] make it necessary to include additional devices in the circuit, which could affect the effective isolation of the neutral point of the power source. Solutions should be sought to reduce the length of cable lines, for example by separating network sections or lowering the supply voltage in selected circuits.

Further work is planned by the author to find alternative methods of determining the value of ground capacitance in on-line mode and to look for structural and organizational solutions that can exclude the occurrence of expected dangerous values of shock currents resulting from the occurrence of capacitance grounding in marine networks with an isolated neutral point of the power source.

REFERENCES

1. Główny Urząd Statystyczny, Informacje Statystyczne. Wypadki przy pracy w 2021 r. Warszawa: GUS; 2021.
2. Główny Urząd Statystyczny, Informacje Statystyczne. Wypadki przy pracy w 2020 r. Warszawa: GUS; 2020.
3. Główny Urząd Statystyczny, Informacje Statystyczne. Wypadki przy pracy w 2019 r. Warszawa: GUS; 2019.
4. Główny Urząd Statystyczny, Informacje Statystyczne. Wypadki przy pracy w 2018 r. Warszawa: GUS; 2018.
5. Główny Urząd Statystyczny, Informacje Statystyczne. Wypadki przy pracy w 2017 r. Warszawa: GUS; 2017.
6. Główny Urząd Statystyczny, Informacje Statystyczne. Wypadki przy pracy w 2016 r. Warszawa: GUS; 2016.
7. PN-HD 60364-1:2010 Instalacje elektryczne niskiego napięcia. Część 1: Wymagania podstawowe, ustalanie ogólnych charakterystyk, definicje. Warszawa: PKN; 2010.
8. Stanisławski W. Ochrona przeciwporażeniowa w lądowych i morskich sieciach elektroenergetycznych niskiego napięcia, Gdynia: Zeszyty Naukowe AMW 157/2004: 135-148. Available from: https://bibliotekanauki.pl/articles/222372.pdf
9. Przepisy Klasyfikacji i Budowy Statków Morskich. Cz. VIII. Instalacje elektryczne i systemy sterowania. Polski Rejestr Statków. Gdańsk: PRS; 2024.
10. Rules and Regulations for the Classification of Ships. London: Published by Lloyd's Register Group Limited; 2023.
11. Wiatr J. Ochrona przeciwporażeniowa w sieci o układzie zasilania IT, elektro.info, 3/2020, Warszawa: Grupa Medium Sp. z o.o.; 2023.
12. Nowak T. Wybrane zagadnienia dotyczące sieci IT oraz TT w świetle użytkowania w okrętowych systemach elektroenergetycznych, Gdynia: Zeszyty Naukowe Akademii Morskiej w Gdyni. 2018: 43-56. Available from: https://bibliotekanauki.pl/articles/947656.pdf
13. Kacejko P, Machowski J, Pijarski P, Smolarczyk A. Zwarcia w systemach elektroenergetycznych, Warszawa: Wydawnictwo WNT; 2022.
14. IEC 60990:2016. Methods of measurement of touch current and protective conductor current, Geneva: IEC Central Office; 2016.
15. De Santis V, Beeckman PA, Lampasi DA, Feliziani M. Assessment of human body impedance for safety requirements against contact currents for frequencies up to 110MHz. IEEE Transactions on Biomedical Engineering. 2011;58(2):390–396. Available from: https://pubmed.ncbi.nlm.nih.gov/20709636
16. Gierlotka S. Elektropatologia porażeń prądem elektrycznym oraz bezpieczeństwo przy urządzeniach elektrycznych. Warszawa: Zeszyty dla elektryków nr 12; 2015.
17. Czernecki L, Hrynkiewicz J, Sojka J. Kompensacja prądów pojemnościowych w okrętowych sieciach elektrycznych z izolowanym punktem zerowym, Szczecin: Zeszyty Naukowe nr 38 Wyższej Szkoły Morskiej; 1990: 51-67. Available from: https://repository.am. szczecin.pl/handle/123456789/1731
18. Tarnapowicz D. A new active method of protection against electrical shock in low voltage ship networks: experimental results, Problemy Eksploatacji 1-2008: 137-145. Radom: WNITE-PIB; 2008: Available from: https://yadda.icm.edu.pl/baztech/element/bwmeta1.element. baztech-article-BAR0-0036-0012
19. Fedorowa SV, Utegulov BV, Utegulov AB, Koshkin IV, Kurabayev IK. Experimental studies of a developed method for determining the insulation parameters in a network with isolated neutral voltage up to 1000V. Astana: Вестник науки Казахского агротехнического университета им. С.Сейфуллина (междисциплинарный). 2019;1 (100):230-238.
20. Nowak T. Opis wybranych zagadnień związanych z zagrożeniami podczas eksploatacji sieci z izolowanym punktem neutralnym, Gdynia: Zeszyty Naukowe Akademii Morskiej w Gdyni; 2018.
21. Czernecki L, Hrynkiewicz J. Analiza możliwości ograniczenia prądów rażenia człowieka w sieciach okrętowych prądu przemiennego. Szczecin: Zeszyty Naukowe nr 38 Wyższej Szkoły Morskiej. Szczecin: WSM; 1990.
22. Utegulov BB, Utegulov AB, Uakhitova AB. Modeling Method for Measuring the Admittance of Insulation in a Network with an Isolated Neutral Voltage up to 1000 V in Mines Using Matlab/Simulink. Journal of Mining Science. 2017;53(2): 282-290. Available from: https://link.springer.com/article/10.1134/S1062739117022128
23. Hrynkiewicz J, Kozak M. Zagrożenia porażeniowe występujące na statkach, Zeszyty Naukowe nr 66 Wyższej Szkoły Morskiej w Szczecinie, Explo-Ship. Szczecin: WSM; 2002. Available from: https://repository.am.szczecin.pl/handle/123456789/2057
24. Fish RM, Leslie A. Geddes Conduction of Electrical Current to and Through the Human Body: A Review, Eplasty (published online) 2009;9. Available from: https://www.ncbi.nlm.nih.gov/pmc/
25. Dalziel CF. Effects of electric shock on man, University of California Berkeley. California PGME 1956.
26. Ponce P, Molina A, Mata O, Ibarra L, MacCleery B. Power systems fundamentals, CRC Press Taylor&Francis Group. Boca Raton 2017.

Arkadiusz Frącz: https://orcid.org/0009-0004-5499-2559

DOI 10.2478/ama-2025-0047

DEVELOPING A PREDICTIVE WEAR MODEL FOR INTELLIGENT TOOL CHANGE SYSTEMS

Anna ZAWADA-TOMKIEWICZ*, Łukasz GĄSIEWICZ, Jarosław STRELKE****

*Faculty of Mechanical and Energy Engineering, Koszalin University of Technology, Sniadeckich 2, Koszalin 75-466, Poland
**D&H Innovations Ltd, Perłowa 13, 77-132 Niezabyszewo, Poland

anna.zawada-tomkiewicz@tu.koszalin.pl, lukasz.gasiewicz@dhi.com.pl, jaroslaw.strelke@dhe.home.pl

received 09 December 2024, revised 16 June 2025, accepted 10 July 2025

Abstract: The article addresses the challenge of reducing machining errors under tight tolerances, which can negatively affect workpiece quality. It highlights the need for modelling and compensating individual error types, particularly those caused by tool wear. Traditionally, tool wear compensation relies on experimentally determined absolute wear values, but nonlinearity in wear introduces discrepancies between modelled and actual machining processes. To address this, the article introduces a novel tool wear model integrated into an Intelligent Tool Change System. The model represents changes in tool edge reduction over time, allowing for tool position correction relative to the workpiece and signalling alarm states. It incorporates a first-order inertial adaptive model, enabling accurate forecasting of tool wear. These predictions are based on real-time geometric measurements collected during cutting by an Automatic Measurement Unit. The measurements are analyzed in the time domain to provide current process corrections and determine the tool lifecycle. A key feature of the model is its self-tuning capability, which adjusts parameters dynamically to handle limited data availability, improving prediction accuracy and reducing the complexity of parameter settings. The model's predictions were validated by comparing predicted wear values against actual measurements. Additionally, the integrated model was compared with a linear prediction model, demonstrating superior accuracy. To evaluate the model's performance, the article uses the normalized root mean square error (NRMSE) as the assessment metric. Results confirm that the first-order inertial adaptive model not only enhances accuracy over adaptive linear model but also provides reliable wear predictions, supporting effective tool change strategies in machining processes. This innovative approach offers significant improvements in managing machining errors and optimizing tool usage.

Key words: tool wear; prediction model; Intelligent Tool Change System

1. INTRODUCTION

1.1. Tool wear and its symptoms

With the development of smart manufacturing technologies, managing materials, workforce, and equipment in machining processes has become crucial to ensure the reliability of key components. Tool wear, as the weakest and most damage-prone element in the OUPN system, affects both product quality and machining efficiency, and is unavoidable due to thermodynamic interactions during cutting [1]. Standards such as ISO 3685 [2] provide guidelines for tool performance at constant cutting speeds, while Taylor's equation is essential for predicting tool life and production costs, particularly for hard-to-machine materials [3]. Since variable cutting speeds are common in industrial settings, the study presented in [4] aimed to develop a method for predicting tool life under such conditions.

Predicting tool wear or damage, along with estimating its remaining useful life (RUL), is essential for effective monitoring of the machining process. This can be done by using reliability function models based on tool wear behavior, data-driven models utilizing signals from the process, workpiece, and tool, or hybrid models that combine both approaches [5].

In reliability function models, wear is described statistically by establishing a reliability function from empirical data. These models assume that tool degradation follows a specific probability distribution, with parameters estimated from the full wear dataset. Methods such as Gaussian process regression, hidden Markov models, Bayesian models, and adaptive hidden Markov models are commonly applied. A key step in these approaches is collecting accurate wear data and choosing a suitable distribution.

In evaluating tool surface degradation and reliability related to catastrophic failure, it is crucial to identify when a component of the machining system vector first exceeds a critical level. This is complex due to the system's multidimensional nature. The time to such failure is typically treated as a random variable, with its probabilistic characteristics derived from the system's statistical properties.

Many methods for tool wear assessment have been developed [6], with most focusing on identifying critical wear indicators, as summarized in Tab. 1. The data in Tab. 1 were obtained from research by D&H Innovations Ltd. and D&H Engineering Ltd. between 2021 and 2023. Certain wear types involve accelerated degradation of the cutting blade beyond technologically justified limits. However, such occurrences are rare, happening in less than 1% of all tool changes, a rate even lower than other operational events like retooling. This low incidence highlights the reliability of existing wear patterns and supports the feasibility of developing accurate tool wear models. These models can be confidently implemented in production to improve monitoring, optimize tool usage, and reduce unexpected downtime.

Tab. 1. Critical value of tool wear symptoms

Tool wear symptom	Critical value
maximum width of flank wear VBB (ISO 3685 [4]); crater wear on the rake face	VBB = 0.6 mm in case the wear area is not regular; average wear width VBB = 0.3 mm for a regular wear surface in zone B of the cutting tool flank
intensive wear on the major or minor flank VBN	notch wear VBN exceeding 1 mm when it dominates other tool wear phenomena
chipping, flaking or cracking	excessive chipping, flaking or cracking of the cutting edge
sudden deterioration of the machined surface quality caused by destruction of the minor flank	Ra of the machined surface exceeds 0.4 µm, 0.8 µm, 1.6 µm, 3.2 µm, 6.3 µm, 12.5 µm (ISO 3685 [2]), other roughness or waviness parameters
cutting edge damage	catastrophic failure defined as sudden failure of the cutting edge under the influence of both load and increasing cutting temperature (ISO 3685 [2]).

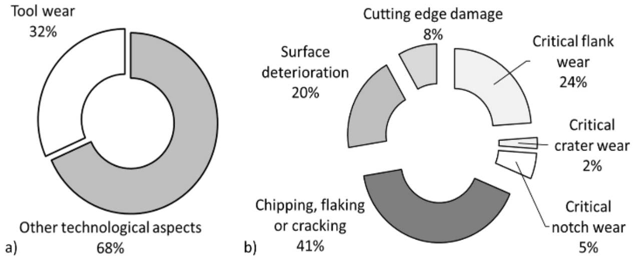

Fig. 1. a) Reasons for premature tool replacement, b) forms of tool wear

1.2. Tool wear prediction in Intelligent Tool Change System

Monitoring and prediction of tool wear has been the subject of many studies, where possible research methods have been indicated. In [7], a literature review is presented on tool wear, its description, monitoring, and RUL prediction in the context of big data. The authors proposed research directions in the area of tool wear. Most often, taking into account the critical value of tool wear, the reference value model was used, which is shown in Fig. 2.

Sensor data can refer to any measured quantity that shows a correlation with the amount of wear [8]. For example, in [9] the development of a wear measurement system based on the AE sensor was developed with an appropriate data processing system adapted to their properties. In works such as [10] and [11], the focus was mainly on developing signal processing for the tool wear inference system. In [12], methods for processing data to obtain the best RUL prediction are discussed in detail. In [13], the authors analyze changes in tool geometry, focusing on wear, design modifications, and operational factors, while presenting methods to describe these changes through measurements and descriptive metrics.

Abrasive wear depends on the physical properties of the interacting material pair – the tool material and the workpiece material, the stereometric features of the cutting edge, and the dynamic properties of the machining system. Changes in these factors over time lead to variations in the wear rate.

By understanding how the wear rate changes over time – that is, the tool wear intensity $I = dVB/dt$ – it is possible to determine the tool life at a given time as the inverse of the tool wear intensity

$$T = \int_0^{VB_{crit}} \frac{1}{I(VB)} dVB \tag{1}$$

VB – tool wear indicator,

VB_{crit} – critical value of the tool wear indicator.

The relationship between tool wear intensity and the actual tool life can be modelled using various functions. For constant tool wear intensity, the simplest and most commonly used approach is a linear model. It works well under stable cutting conditions with wider workpiece tolerance limits and effectively captures the linear portion of the wear curve, based on time or the number of workpieces processed. Tool replacement is then triggered after reaching the defined threshold.

Until the critical value of the tool wear indicator is reached, the tool position is continuously adjusted according to the progressive wear model. However, in cases of accelerated wear – after exceeding the critical value – even corrective measures may fail to keep up with rapid tool degradation. Therefore, to prevent sudden tool failure caused by cumulative cutting effects, the prediction range is intentionally limited to avoid accelerated wear.

The initiation of the tool change process can also occur in the case of a loss of stability in the manufacturing system. Process stability is determined based on measurement results and process stability data. The initiation of the tool change process carried out by the Intelligent Tool Change System, is based on information provided by the management computer, which monitor for any process trends in Statistical Process Control charts. The emergence of such trends signals a potential loss of process stability, leading to the application of artificial intelligence techniques to evaluate the state of the process and tools.

A review of AI integration into CNC systems is provided in [14], while [15] separates the tool wear process into monitoring and prediction phases. An advanced method using deep learning is described in [16].

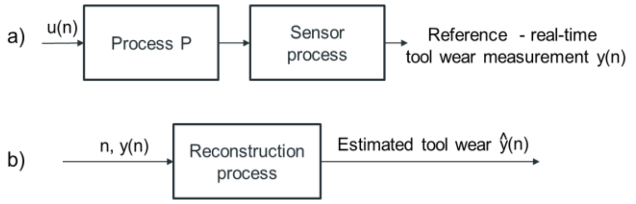

Fig. 2. a) Measuring reference data, b) off-line identification of reference value model

From the analysis conducted, the modelling of wear progression over time in modern systems takes the form of a recursive model, determined according to the scheme presented in Fig. 3. Wear values are predicted recursively based on previous values, considering the measurement data collected from the process.

In the application for tool wear prediction in the Intelligent Tool Change System, the model must be supplied with real-time data from the process. Under these conditions, the recursive model can predict the wear of a cutting tool over time, as tool wear is a gradual process that depends on the number of workpieces processed. Consequently, the model recalculates wear parameters with each new measurement.

The recursive model prediction relies on the quality of the acquired data, as the model update and tool wear prediction primarily depend on new data collected during the machining process. The model evolves with each additional measurement, adapting to real-time changes in the tool's wear state.

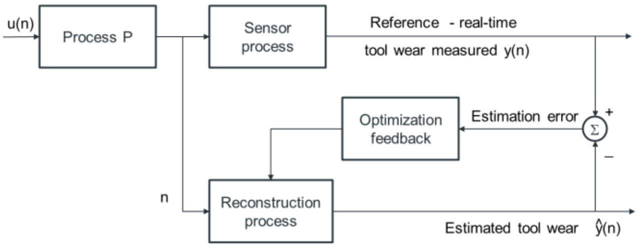

Fig. 3. Recursive model of tool wear

2. STRATEGY FOR DEVELOPING A TOOL WEAR MODEL

The technological problem in machining pertains to the change in the position of the tool tip. Considering the guidelines on the influence of cutting edge reduction on workpiece accuracy, it was found that when the actual reduction of the cutting edge reaches a critical value, the position of the cutting edge should be adjusted by introducing a correction into the CNC program. To implement the strategy and develop the appropriate model, it is essential to create an analytical structure for prediction, continuous data supplementation, and decision support systems. Fig. 4 presents a diagram illustrating the development of the integration prediction model.

The model developed within the intelligent tool change system is subject to integration within the production system. As shown in Fig. 4, for its operation, the system will require a production cell management system along with a database system, a communication and data exchange system, and a measurement system. In the integrated module with the CNC system, the system will collect measurement data and save it in the MES system.

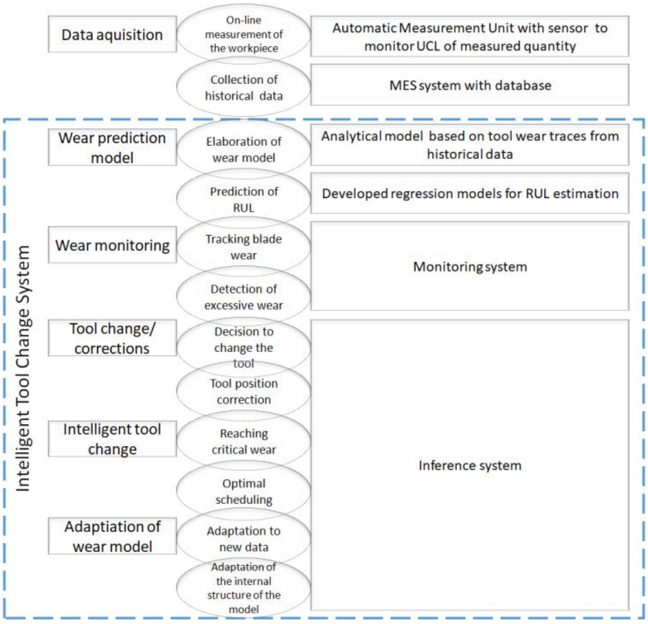

Fig. 4. The strategy for developing wear model useful in Intelligent Tool Change System

The MES data will then be used in the automatic process correction module to adjust the tool position and in the intelligent tool change system for tool change prediction. These actions will enable both the optimization of tool management and the maintenance of product quality at the level of specification compliance.

The model undergoes verification in production conditions. All points were validated by comparing predicted vs. actual tool wear. The strategy has been developed to accurately predict tool wear, optimize tool life, and enhance machining sustainability.

3. MATERIALS AND METHODS

The tests were carried out in industrial conditions, where the blade shortening during cutting was assessed. The maximum cutting time referred to the number of workpieces processed and amounted to 250 pieces. The experimental set-up with the measurement system is shown in Fig. 5

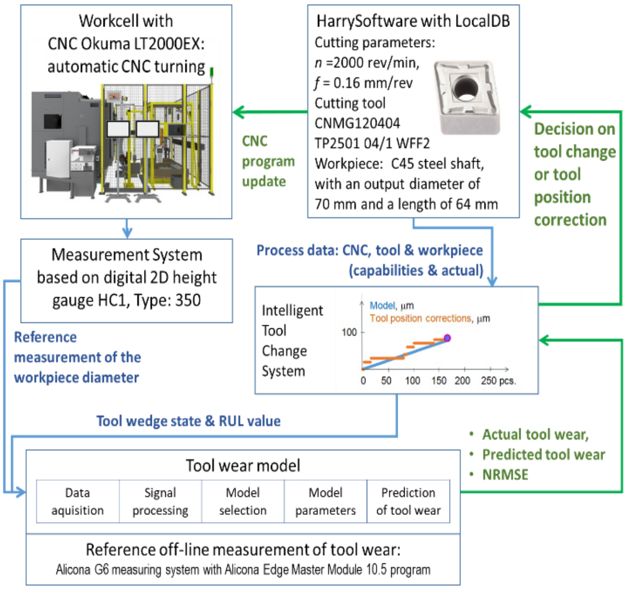

Fig. 5. Schematic diagrams of the cutting experiment and tool wear measurement setup

During cutting, reference measurements were taken and the tool position was corrected relative to the workpiece nominal and measured values. The measurement of the blade geometry in the worn state was verified by the Alicona G6 measuring system using the Advance Focus Variation method [17]. In the Alicona Edge Master Module 10.5 program, the $Ddmax$ parameter values (maximum wear depth along the profile determined on the cutting edge) were determined, which enabled the assessment of the blade shortening (Fig. 6). These values will be used to verify whether the measurements of the workpiece and the total corrections in the process define the tool wear, as determined by the parameter $Ddmax$.

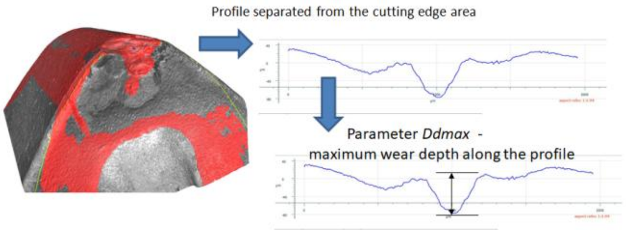

Fig.6. Determination of the blade shortening $KEmax$ using the $Ddmax$ parameter

4. RESULTS AND DISCUSSION

4.1. Assumptions for developing the model

The cutting tool wear model occurs at various levels of the cyber-physical model. The basis for choosing the modelling method is the purpose for which the model is to be developed. The cutting tool wear model is a model of tool deterioration, which consists in the fact that the condition of a cutting tool becomes increasingly worse and gradually causes the tool to lose its ability to perform in line with expectations. However, the wear model is associated with the possibility of developing an inverse model and indicating the usefulness of a given tool, how useful it is in removing machining allowance. The definition of RUL is closely related to the wear model. On the other hand, the tool usefulness model is the possibility of introducing corrections to the process. It follows from the considerations that many basic assumptions should be taken into account when building the model. They are systematically listed in Tab. 2.

The development of models of blade wear over time and determination of RUL were carried out using monotonically changing values of wear indicators, which have a direct impact on the value of blade shortening and surface precision. Determination of the reference value of critical wear enabled the model to be adjusted to the actual values of blade wear in given cutting conditions. The biggest limitation in the use of models with a reference value is the problem of the dispersion of wear intensity and tool life. Studies show the randomness of factors that cause deterioration of cutting properties of tools, where, apart from abrasive wear, other wear mechanisms, such as diffusion or chemical wear, begin to dominate. Defining the tool life in the conditions of randomness of the tool wear process requires determining the time of its reliable operation until the blade blunting criterion (reference value) is achieved. Problems related to determining the time of the first exit of the process from the allowable area were considered in the theory of stochastic processes. Effective solutions can be obtained from the equation of the reliability function, which depends on the physicochemical and strength properties of the blade material. These in turn depend on the temperature and machinability of the processed material. Additionally, the wear of the blade depends on its load and the dynamics of the cutting process.

4.2. Development of the model

The linear wear model of the form as Eq. (2) was analysed

$$y(t) = y(t=0) + At \tag{2}$$

where the parameter A refers to the intensity of tool shortening over time and the first-order inertial model as expressed in Eq. (2)

$$y(t) = y(t=0)exp\left(\frac{-t}{T}\right) + K\left(1 - exp\left(\frac{-t}{T}\right)\right) + C_0 \tag{3}$$

The parameter T in equation (3) for T > 0 can be interpreted as the period where for t=T we reach 63% and for t=3T we reach 95% of the critical value of the wear. The parameter K can be interpreted as the gain, the maximum value in the steady state. Knowing the current value of y(t) and the value of y(t) for t=3T we can estimate the RUL.

Tab. 2. Summary of assumptions for building the cutting tool wear model

Assumptions	RUL	Tool position correction
The model should represent the change in tool edge reduction over time. The output of the model should be the tool edge reduction value KE, and the independent variable should be cutting time.	The edge reduction value over time allows for summing values and comparing them with the critical value.	The edge reduction value over time allows for determining current corrections in the process and predicting corrections for subsequent time units.
The model should enable the determination of the tool infeed, taking into account the tool edge reduction. The infeed value determined on the basis of the model should enable the correction of the position due to the assumed accuracy of the workpiece.	The infeed value determined on the basis of the model enables comparison with the critical infeed value, above which it is not possible to achieve the assumed dimensional and shape accuracy and surface roughness.	The infeed value determined on the basis of the model makes it possible to achieve the assumed accuracy of the workpiece.
The model should reflect the progression of tool wear over time, i.e. a typical S-shaped profile, with rapid initial growth, an almost flat middle region, and a final rapid growth. The model is nonlinear and it should be taken into account that the wear pattern changes with time tA.	The gradient of the S-shaped function determines three areas of wear changes over time: the first area with a decreasing value, the second area of a constant value and the third area of accelerated wear, the value of which increases over time and which allows for the estimation of the RUL.	The gradient of the W-shaped function determines three areas of wear changes over time and thus allows for estimating the correction values for each of the areas.
The model should take into account tool wear mechanisms. Model parameters must be interpretable in terms of tool edge reduction over time. Parameters must enable assessment of the intensity of wear mechanisms over time for different cutting conditions.	Model parameters resulting from the intensity of elementary wear processes can be used to estimate the RUL value.	Model parameters resulting from the intensity of elementary wear processes enable the determination of corrections to tool life based on them.
The model should take into account the constant cutting process load as an input signal. In principle, the undeformed chip thickness for each tool feed has a constant value, which at a constant cutting speed allows the assumption of a constant load (material removal rate), described by a unit stroke function.	The model taking into account the constant cutting load makes it possible to predict RUL.	Assuming a constant cutting load allows the influence of other factors influencing the wear process to be limited and thus the error in predicting corrections in the process to be limited.

The goodness of fit of the models was assessed using the NRMSE index. The goodness of fit values are within the range $\langle -\infty;\ 1 \rangle$, where "0" – perfect fit to the reference data (zero errors) $"-\infty"$ – poor fit, "1" – the model values do not fit better than the fit of the reference value with a linear model. Tab. 3 presents the results for the average NRMSE values for the goodness of fit of the reference data for the linear and first-order inertial models for all experiment points. The results indicate the advantage of the first-order inertial model over the linear model. The fit was significantly better, and the average NRMSE value was half as small.

Tab. 3. Summary of assumptions for building the tool wear model

Cutting edge reduction KE	$NRMSE$	
	Linear model	First order inertial model
10%	1.2	0.17
50%	0.86	0.47
75%	0.75	0.39
100%	0.33	0.43

Fig. 7 shows an example of a single cutting process, in which the collected reference data of the tool wear for 75% of the critical value. The reference data were modelled with a linear model and a first-order inertial model. For this specific cutting case, the linear model seems to be a better fit than the first-order inertial model. The fit was similar for the linear model and the first-order inertial model. However, statistically for the entire experiment, the results for the first-order inertial model indicated its advantage over the linear model.

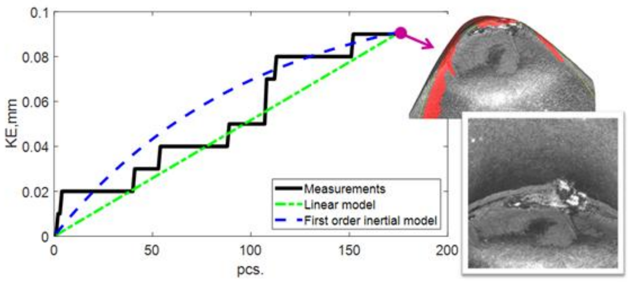

Fig. 7. Example of application of linear and first-order inertial models in the estimation of tool wear

Despite the good fit of the models, it can be observed that the measured values and the values estimated by the models, when compared to the reference value under narrow tolerance conditions, do not ensure complete compliance of the items with the specification. To perform a more comprehensive analysis, Fig. 7 presents the measured value of $Ddmax$ for selected experimental points (10% of the critical wear value) along with the cumulative value of tool position corrections. The value of $Ddmax$ and the cumulative value of the tool position correction, adjusted for the current measurement value, remain in high agreement, which was confirmed by a statistical test for equality of means. The plots in Fig. 8 have been supplemented with estimated cutting edge reduction values for the linear model. The linear model was determined using the least squares method based on all the measured data.

The chart in Fig. 8a indicates that a tool position correction was made for the fifth and seventh workpieces. The corrections were significant, amounting to $10\ \mu\text{m}$ each. Introducing the correction based on the measured dimension values of the workpiece enabled the production of subsequent workpieces in compliance with the specification. Similarly, the situation unfolded in the remaining cutting trials, as shown in Fig. 8b-8d.

In this particular case, all workpieces were measured, and the correction was made in the subsequent step. This is an ideal situation, as statistical process control is used in production, and corrections are applied with a certain delay relative to the current measured value. Therefore, there is a need to predict the tool position correction values for the production of subsequent workpieces.

If the linear model identified based on multiple repetitions of the experiment were applied, it would be evident that its use in production would not guarantee an accurate reflection of the wear progression. The corrections calculated from this model might not ensure the production of workpieces within the specified dimensional tolerance. For example, the intensity of tool wear, according to Fig. 8a and 8c, is much greater than in the case of the experiments shown in Fig. 8b, where tool position corrections were made only for the 14th workpiece. The linear model suggested an earlier correction; however, despite the delay, the intensity of tool wear was small enough that the workpieces remained within the accepted tolerance range.

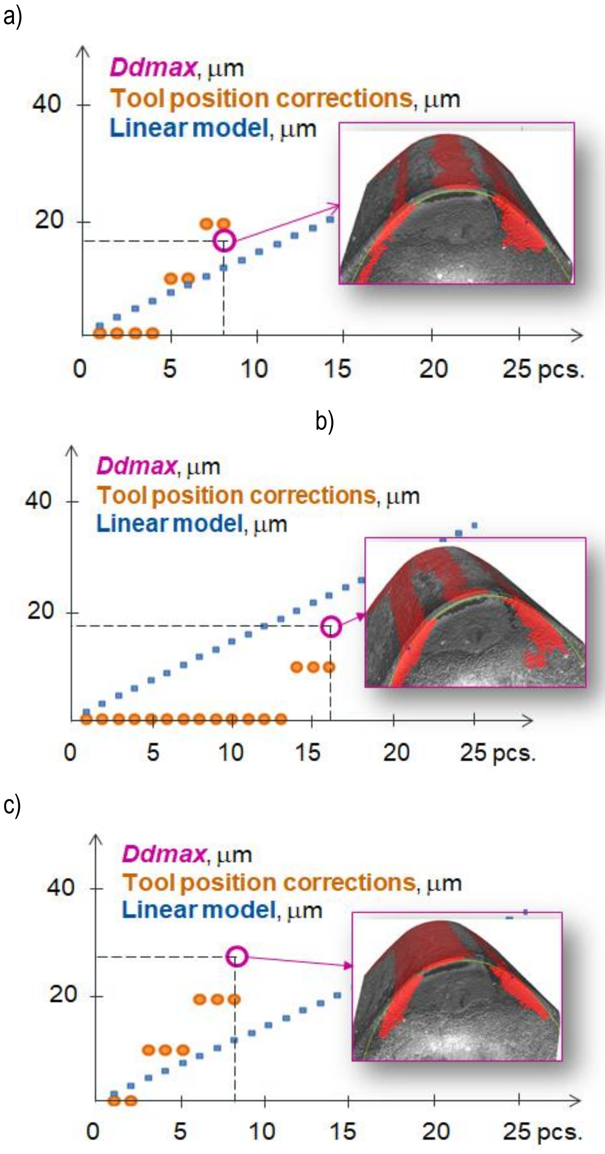

d)

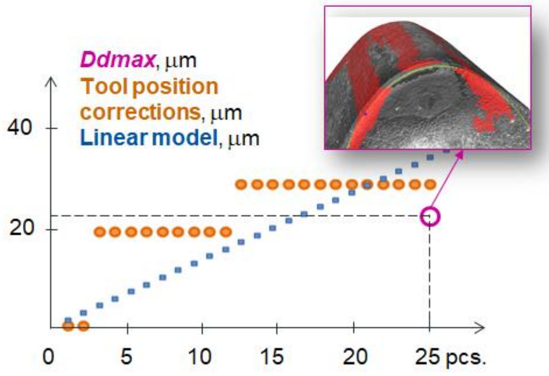

Fig. 8. Tool wear cases as a function of the number of workpieces, highlighting the $Ddmax$ values

The analysis of cases involving tool position corrections and wear progression indicates the need to train the models with reference values during the machining process in order to predict wear values. This, in turn, would enable the effective application of tool position corrections.

4.3. The recursive model with reference value

In the case of the Intelligent Tool Change System, the model is developed based on historical data of the process trace and tool wear. The maximum cutting edge reduction and the number of workpieces machined with the given tool are determined. As indicated in section 4.2, these values do not guarantee achieving the required workpiece accuracy due to the cutting edge reduction but serve as baseline data for developing the appropriate model selection strategy.

The adaptive linear model and first-order inertial adaptive model were developed in two versions, the results of which are shown in Fig. 9 and Fig. 10.

The adaptive linear model (Fig. 9a) and first-order inertial adaptive model (Fig. 9b) more accurately represent the tool position corrections than the linear model. The smoothing of the curves by averaging predictive tool position data from the current and previous models allowed for the model to be smoothed. The use of measured values for model fine-tuning means that the developed recursive model could be applied to predict wear values for subsequent workpieces.

a)

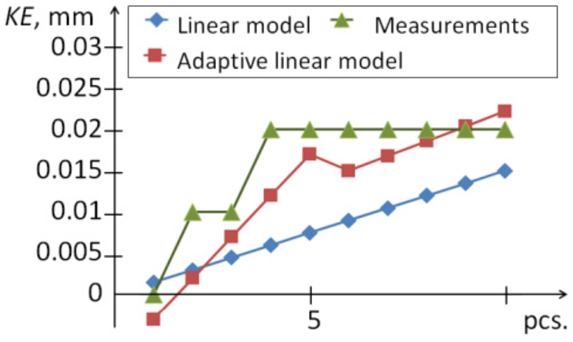

b)

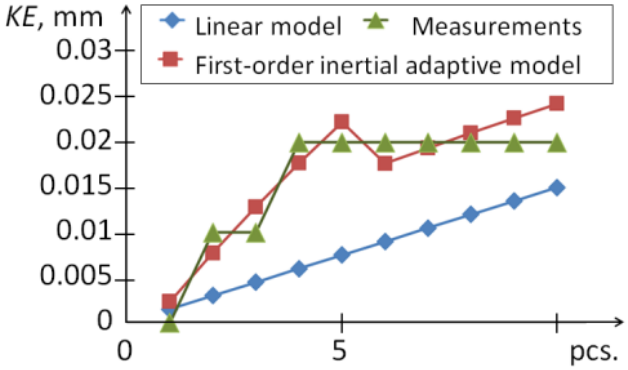

Fig. 9. A comparison of tool wear measurements and data generated using the linear model, as well as the adaptive linear model (a) and first-order inertial adaptive model (b), as reference data for tool position correction for the first 10 pieces

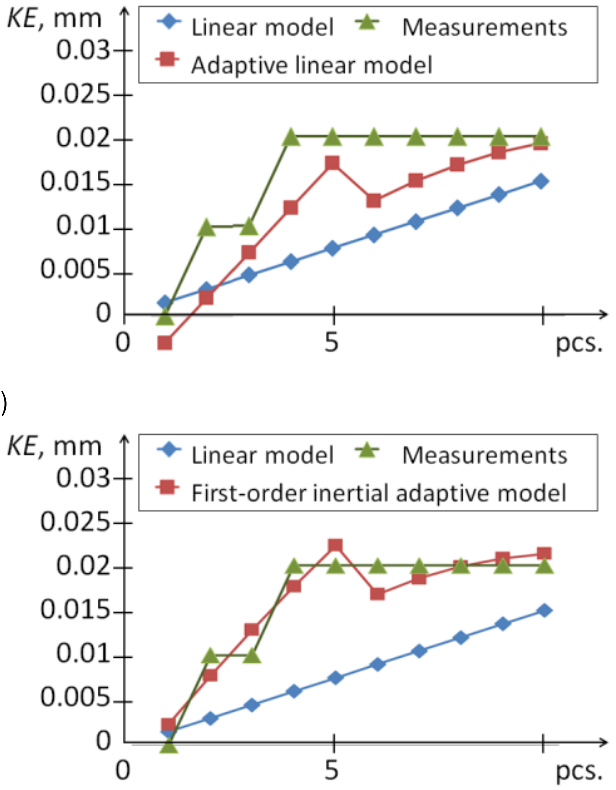
a)

b)

Fig. 10. A comparison of tool wear measurements and data generated using the linear model and the adaptive linear model (a) and first-order inertial adaptive model (b), as reference data for tool position correction, considering a smoothing window for the first 10 pieces

The strategy for determining and fine-tuning the models was verified using experimental data from a real production process in the Intelligent Tool Change System. For the manufacturing process being carried out, based on workpiece measurements taken every 5 pieces, corrections were made using the adaptive linear model. The model was fine-tuned as new measurements were received and predicted the cutting edge reduction values based on a monotonic function model with an increment of 5 µm. The prediction and actual measurements were in high agreement. For the sample data from Figure 7, the goodness of fit index $NRMSE$ for the model was 0.2674, and after averaging, it was 0.2187 (Tab. 4).

Tab. 4. Adaptive linear function models with a 50-piece FIFO buffer

	Recursive model with parameter estimation every 5 pieces	**Averaging recursive model**
Adaptive linear model	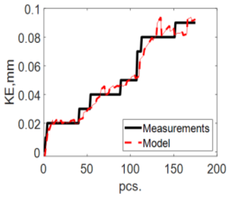 $NRMSE = 0.2087$	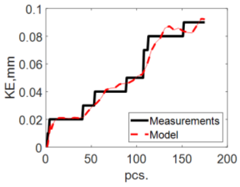 $NRMSE = 0.1964$
Model of the monotonic function	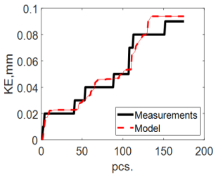 $NRMSE = 0.2350$	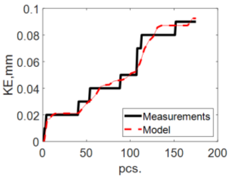 $NRMSE = 0.1884$
Model with a constant increment of 5 µm	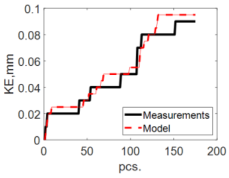 $NRMSE = 0.2674$	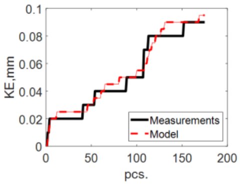 $NRMSE = 0.2187$

Tab. 5. First order inertial adaptive model with a 50-piece FIFO buffer

	Recursive model with parameter estimation every 5 pieces	**Averaging recursive model**
First order inertial adaptive model	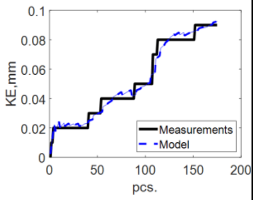 $NRMSE = 0.1515$	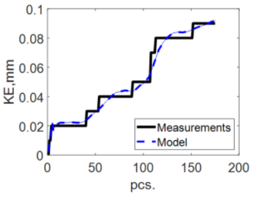 $NRMSE = 0.1527$
Model of the monotonic function	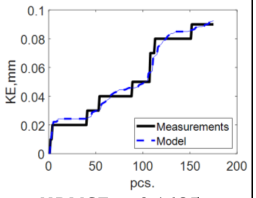 $NRMSE = 0.1685$	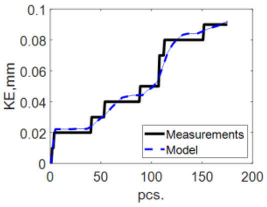 $NRMSE = 0.1543$
Model with a constant increment of 5 µm	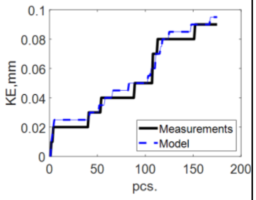 $NRMSE = 0.1890$	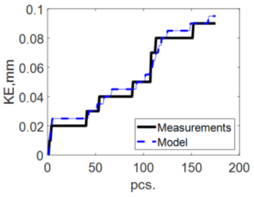 $NRMSE = 0.1783$

The use of the first-order inertial adaptive model for all experiment points yielded better results than the adaptive linear model. For the sample data from Fig. 7, the goodness of fit index NRMSE for the first-order inertial adaptive model was 0.1890, and after averaging, it was 0.1783 (Tab. 5). The prediction allowed for real-time tool position correction, ensuring that all workpieces were produced within the specified dimensional tolerance.

5. CONCLUSIONS

Tool wear during machining negatively affects the dimensional accuracy of the workpiece. In practice, the shortening of the cutting edge is compensated for by applying tool position corrections relative to the workpiece, typically integrated into the production program. These correction values are often based on reference measurements or predefined benchmarks. However, models relying solely on offline-determined parameters often fail to deliver accurate predictions, especially when the tool undergoes rapid wear or when tight dimensional tolerances must be maintained.

To address this limitation, a wear prediction strategy was developed using reference values dynamically adjusted during the machining process. This approach was tested using two model types: an adaptive linear model and a first-order inertial adaptive model. The latter demonstrated superior performance in terms of predictive accuracy and process stability. By fine-tuning model parameters based on real-time tool wear, inferred from measurements of the machined workpieces, it was possible to achieve reliable tool wear prediction. This enabled timely corrections that ensured dimensional compliance across all manufactured parts in a system equipped with the Intelligent Tool Change System.

REFERENCES

1. Grzesik W, Żak K, Zawada-Tomkiewicz A. Analiza i modelowanie powierzchni wytwarzanych w obróbce ubytkowej. PWN Warszawa. 2024; 1–331.
2. ISO 3685:1993 Tool-life testing with single-point turning tools.
3. Abeni A, Metelli A, Attanasio A, Outeiro J, Poulachon G. A Predictive Method for Cumulative Tool Wear in Variable Cutting Speed Turning Operations. Procedia CIRP. 2025;133:454-459.
4. Zhang X, Peng Z, Liu L, Zhang X. A Tool Life Prediction Model Based on Taylor's Equation for High-Speed Ultrasonic Vibration Cutting Ti and Ni Alloys. Coatings. 2022;12(10):1553.
5. Cheng Y, Gai X, Guan R, Jin Y, Lu M, Ding Y. Tool wear intelligent monitoring techniques in cutting: a review. Journal of Mechanical Science and Technology. 2023;37(1):289-303.
6. Wang K, Wang A, Wu L, Xie G. Machine Tool Wear Prediction Technology Based on Multi-Sensor Information Fusion. Sensors. 2024;24: 2652.
7. Zhou Y, Liu C, Yu X, Liu B, Quan Y. Tool wear mechanism, monitoring and remaining useful life (RUL) technology based on big data: A review. SN Applied Sciences. 2022;4:232.
8. Ünal P, Deveci BU, Özbayoğlu AM. A review: Sensors used in tool wear monitoring and prediction. In: Awan I, Younas M, Poniszewska-Marańda A. (Eds.) Mobile Web and Intelligent Information Systems. MobiWIS. 2022. Lecture Notes in Computer Science. 2022;13475.
9. Zhang C, Wang W, Li H. Tool wear prediction method based on symmetrized dot pattern and multi-covariance Gaussian process regression. Measurement. 2022;189:110466.
10. Bombiński S, Kossakowska J, Jemielniak K. Detection of accelerated tool wear in turning. Mechanical Systems and Signal Processing. 2022;162:108021.
11. Zhang X, Gao Y, Guo Z, Zhang W, Yin J, Zhao W. Physical model-based tool wear and breakage monitoring in milling process. Mechanical Systems and Signal Processing. 2023;184:109641.
12. Sayyad S, Kumar S, Bongale A, Kotecha K, Abraham A. Remaining

useful-life prediction of the milling cutting tool using time–frequency-based features and deep learning models. Sensors. 2023;23:5659.

13. Gupta MK, Niesłony P, Sarikaya M, Korkmaz ME, Kuntoğlu M, Królczyk GM. Studies on geometrical features of tool wear and other important machining characteristics in sustainable turning of aluminium alloys. International Journal of Precision Engineering and Manufacturing-Green Technology. 2023;10:943–957.
14. Soori M, Arezoo B, Dastres R. Machine learning and artificial intelligence in CNC machine tools: A review. Sustainable Manufacturing and Service Economics. 2023;100009.
15. Zawada-Tomkiewicz A, Tomkiewicz D. Monitoring System with a Vision Smart Sensor. In: Majewski M, Kacalak W. (eds) Innovations Induced by Research in Technical Systems. IIRTS 2019. Lecture Notes in Mechanical Engineering. 2020.
16. Cheng M, Jiao L, Yan P, Jiang H, Wang R, Qiu T, Wang X. Intelligent tool wear monitoring and multi-step prediction based on deep learning model. Journal of Manufacturing Systems. 2022;62:286–300.
17. https://www.alicona.com/en/technologies/focus-variation.

The authors would like to thank the employees of D&H Innovations Ltd for their assistance during the research, as well as the National Centre for Research and Development for their support under the project POIR.01.01.01-00-1409/20, titled "Implementation of R&D Works Aimed at Developing Solutions Focused on the Automation of Industrial Processes Using CNC Machines."

Anna Zawada-Tomkiewicz: https://orcid.org/0000-0001-6171-8209

Łukasz Gąsiewicz: https://orcid.org/0009-0003-5255-9789

EXPLORING JACOBI ELLIPTIC AND PERIODIC SOLITARY WAVE SOLUTIONS FOR THE FAMILY OF 3-D WBBM EQUATIONS THROUGH THE GENERALIZED APPROACH

Muhammad Ishfaq KHAN*, **Kalim ULLAH****

*College of Mechanics and Engineering Science, Hohai University, Nanjing 211100, P.R. China
**School of Mathematics, Hohai University, Nanjing 211100, P.R. China

m.ishfaqkhan032@gmail.com , kalim6054@gmail.com

received 24 February 2025, revised 08 June 2025, accepted 15 July 2025

Abstract: In this paper, we analyze the family of three-dimensional Wazwaz-Benjamin-Bona-Mahony (3-D WBBM) equations using the generalized Jacobi elliptic function expansion method. Understanding complicated wave patterns is critical, therefore, the family of 3-D WBBM equations is a valuable mathematical model with application in fluid mechanics, plasma dynamics, biomechanics, and engineering sciences. The main objective of this study is to build several new multiple wave form solutions for the nonlinear three-dimensional Wazwaz-Benjamin-Bona-Mahony (3-D WBBM) equations. By first using the travelling wave transformation, the nonlinear partial differential equation is transformed into an ordinary differential equation. Then the generalized Jacobi elliptic function expansion method is used to execute a finite series expansion of degree n. Due to this analytical method, we obtained numerous new exact solutions, including periodic solutions in Jacobi elliptic function forms and their corresponding Solitary and shock wave solutions in a limit convergence sense when the modulus parameter m approaches 1 and 0. These results are particularly useful for nonlinear science and mathematical physics professionals, since they provide important insights into the structure and evolution of nonlinear waves in a variety of physical circumstances. To improve the physical description of the solutions, several typical wave profiles are offered to provide a comprehensive analysis of the wave characteristics of the solutions in 2-D, 3-D, and contour visualizations were generated using accurate parameters value with the help of Mathematica. Moreover, by generating novel and accurate propagating soliton waveform solutions, the generalized Jacobi elliptic function expansion methods highlight its importance in uncovering key aspects of the model behaviours as well as suggesting potential applications in the study of water waves**.**

Key words: Soliton wave solutions, family of 3-D WBBM Equations, Jacobi Elliptic Function Expansion technique, Nonlinear Evaluation Equations

1. INTRODUCTION

Nonlinear phenomena occur in various scientific domains, including applied mathematics, physics, and engineering. Nonlinear evolution equations (NLEEs) are being explored in multiple nonlinear areas, such as nonlinear optics, thermal conductivity, fluid mechanics, optical fiber, electromagnetism, quantum theory, and shallow water wave propagation [1–3]. The research on soliton wave solutions of NLEEs is drawing interest. Because the majority of physical systems are nonlinear, researchers have been encouraged to investigate whether exact solutions exist for NLPDEs, specifically nonlinear evolution equations, or evolution equations (EEs).

Numerous numerical and analytical approaches have been developed to address nonlinear partial differential equations. The researchers prefer analytical approaches over numerical methods because they provide an extensive understanding of physical processes and precise insights into system dynamics. However, analytically solving nonlinear partial differential equations (NLPDEs) can be challenging. For this purpose, in recent decades, much development has been done; many reliable and efficient techniques have been presented to achieve the exact NLEE solutions. Like the exp-function approach [4, 5], (G′/G)-expansion technique [6, 7], F-expansion approach [8, 9], modified extended tanh-function technique [10, 11], the Hirota bilinear technique [12, 13], the extended rational sin-cos and sinh-cosh methods [14], the generalized sine-gordon expansion approach [15], the modified Kudryashov technique [16], Variational Iteration Method [17], Improved (G′/G)-Expansion technique [18, 19], Riccati-Bernoulli Sub ODE approach [20] Generalized Exponential Rational Function approach [21] and so on. These methods have been effectively established and provided to find a precise solution for NLPDEs. Although these approaches have made great progress, but they often fail when used to more complex models, such as a family of 3-D WBBM equations, where more efficient and extended methodologies are needed.

This article uses an efficient and effective strategy to generate different types of periodic and solitary wave solutions for the three-dimensional WBBM equations. The three-dimensional WBBM equation can be stated as follows:

$$v_x + v^2 v_y + v_t - v_{xzt} = 0, \tag{1.1}$$

$$v_y + v^2 v_x + v_t - v_{xyt} = 0, \tag{1.2}$$

$$v_z + v^2 v_z + v_t - v_{xxt} = 0. \tag{1.3}$$

Wazwaz proposed the 3-D Wazwaz-Benjamin-Bona-Mahony (3-D WBBM) equation in 2017 [22]. The 3-D WBBM equation is the modified form of the famous KdV equation, which is used to study the stability and soliton-like properties of fluid waves in various scientific phenomena. The family of Wazwaz- Benjamin-Bona-Mahony (3-D WBBM) equations has attracted much attention because of their mathematical structure and practical applications. This equation is characterized by a scenario that addresses nonlinearity and dispersion, making it valuable for analyzing wave phenomena in a physical setting. In recent years, several successful techniques have been applied to study the WBBM model, such as the first integral method [23], the modified Exp-function approach [24], the Generalized rational exponential function approach for analytical solutions [25], Rational sine-Gordon expansion approach [26], the Sardar-Sub equation approach [27], the Improved Bernoulli Sub-Equation Function technique [28], the extended modified auxiliary equation mapping (EMAEM) approach [29], a new extended direct algebraic technique [30], the Φ6 expansion approach and modified extended direct algebraic [31], the Khater methods [32], and the expanded tanh approach [33].In addition to the existing analytical methods, the generalized Jacobi elliptic function expansion method, previously applied to various nonlinear PDEs and FPDEs [34–42], has not yet been employed for the 3D WBBM model, offering potential for innovative exact solutions.

In this paper, we integrate the generalized Jacobi elliptic function expansion technique for studying the family of 3-D WBBM equations. The generalized JEFE method is more efficient and generalized than the existing methods for solving the 3-D WBBM equations. The generalized JEFE approach makes good use of Jacobi elliptic functions, allowing for a large number of solutions, such as Jacobian elliptic, trigonometric, and hyperbolic trigonometric functions type of solutions, which improves its application to diverse nonlinear wave equations. Furthermore, it is a noteworthy invention that constitutes notable progress. When solving nonlinear partial differential equations (PDEs), the generalized Jacobi elliptic function expansion technique has several advantages and disadvantages. Its ability to provide periodic and exact solutions is one of its primary features. In order to understand complicated nonlinear dynamics, this capacity is crucial. Equations exhibiting specific symmetries and invariants benefit greatly from this method, as it allows for a more thorough examination of the solutions. Its limited application, however, is one of its main drawbacks. The exact solutions demonstrated that our suggested WBBM equations are perfectly suitable for producing innovative traveling wave structures in a wide range of physical scenarios without any problems, in addition, the article contains details 2-D, contour, and 3-D graphical visualizations of the solutions to demonstrate how well the suggested method solves difficult nonlinear equations and to help readers better understand their physical features, to providing useful information for further research in mathematical physics and shallow water waves.

The following is the order of the work in this paper. Section 2 explains how to solve NLPDEs using generalized JEFE techniques. In Section 3, we describe how this approach can be used to solve the nonlinear 3-D WBBM system. This section is divided into three subsections, each of which presents Periodic wave solutions in terms of Jacobi elliptic function expansion, and solitary and shock wave solutions. Section 4 presents a graphical presentation and discussion. Section 5 presents the conclusion of the study.

2. SUMMARY OF THE GENERALIZED JEFE APPROACH

Within this part of the article, we explain the details of the generalized JEFE approach. The following steps will be followed when conducting these types of studies:

Step A: Nonlinear partial differential equations (NPDEs) typically take the mathematical expression

$$N\left(v,\frac{\partial v}{\partial t},\frac{\partial v}{\partial x},\frac{\partial v}{\partial z},\frac{\partial^2 u}{\partial x\partial x},\frac{\partial^2 u}{\partial x\partial t},\frac{\partial^2 u}{\partial x\partial z},\frac{\partial^2 u}{\partial t\partial t},\dots\right)=0. \tag{2.1}$$

Step B: Reformulating Equation (2.1) and utilizing the chain rule, we consider:

$v(x,y,z,t) = v(\psi)$,

where $\psi = px + qy + r\,z - st$, (2.2)

where p, q, r, and s represent constants. We can use equation (2.2) to convert the nonlinear PDEs (2.1) into ordinary differential equations.

$$N\left(v,\frac{\partial v}{\partial \psi},\frac{\partial^2 v}{\partial \psi^2},\dots\right)=0. \tag{2.3}$$

The primary objective of this extended indirect strategy is to maximize the possibility of addressing the derived ordinary differential equation, more especially the initial kind of Jacobian problem that involves three variables, such as $\mathrm{m}_2, \mathrm{m}_1$, and m_0. The goal is to come up with a more comprehensive collection of Jacobi elliptic solutions for the problem that has been presented. It is possible to visually represent the auxiliary equation as follows:

$$(N')^2(\psi) = m_2N^4(\psi) + m_1N^2(\psi) + m_0, \tag{2.4}$$

where

$N' = \frac{dN}{d\psi}, \psi = \psi(x,y,z,t), and\ , \mathrm{m}_2, \mathrm{m}_1, \text{and } \mathrm{m}_0$

are constants.

The mathematical expressions for Jacobi elliptic functions are given by:

$sn(\psi) = sn(\psi,k), cn(\psi) = cn(\psi,k), dn(\psi) = dn(\psi,k)$

Here, the k is used to signify the modulus, and $\mathrm{k} \in (0,1)$.

The solutions of equation (2.4) are presented in Tab.1.

Tab.1. The following table summarizes all the potential solutions to equation (2.3) for the specific m_2, m_1, and m_0 values that have been provided

NO.	m_2	m_1	m_0	N
1	k^2	$-(1+\mathrm{k}^2)$	1	sn
2	k^2	$-(1+\mathrm{k}^2)$	1	cd
3	$-\mathrm{k}^2$	$2\mathrm{k}^2-1$	$1-k^2$	cn
4	-1	$2-k^2$	k^2-1	dn
5	1	$-(1+k^2)$	k^2	ns
6	1	$-(1+k^2)$	k^2	dc
7	$1-k^2$	$2k^2-1$	$-k^2$	nc
8	k^2-1	$2-k^2$	-1	nd
9	$1-k^2$	$2-k^2$	1	sc
10	$-k^2(1-k^2)$	$2k^2-1$	1	sd
11	1	$2-k^2$	$1-k^2$	cs
12	1	$2k^2-1$	-$k^2(1-k^2)$	ds
13	$\frac{-1}{4}$	$\frac{k^2+1}{2}$	$\frac{-(1-k^2)^2}{4}$	$kcn \mp dn$
14	$\frac{1}{4}$	$\frac{-2k^2+1}{2}$	$\frac{1}{4}$	$ns \mp cs$
15	$\frac{1-k^2}{4}$	$\frac{k^2+1}{2}$	$\frac{1-k^2}{4}$	$nc \mp sc$
16	$\frac{1}{4}$	$\frac{k^2-2}{2}$	$\frac{k^4}{4}$	$ns \mp ds$
17	$\frac{k^2}{4}$	$\frac{k^2-2}{2}$	$\frac{k^2}{4}$	$sn \mp icn$
18	$\frac{k^2}{4}$	$\frac{k^2-2}{2}$	$\frac{k^2}{4}$	$\frac{sn}{\sqrt{1-k^2sn\mp cn}}$

DOI 10.2478/ama-2025-0048

19	$\frac{k^2}{4}$	$\frac{k^2-2}{2}$	$\frac{k^2}{4}$	$kcn \pm idn$
20	$\frac{1}{4}$	$\frac{1-2k^2}{2}$	$\frac{1}{4}$	$\frac{sn}{1\mp cn}$
21	$\frac{k^2}{4}$	$\frac{k^2-2}{2}$	$\frac{1}{4}$	$\frac{sn}{1\mp dn}$
22	$\frac{k^2-1}{4}$	$\frac{k^2+1}{2}$	$\frac{k^2-1}{4}$	$\frac{dn}{1\mp ksn}$
23	$\frac{1-k^2}{4}$	$\frac{k^2+1}{2}$	$\frac{-k^2+1}{4}$	$\frac{cn}{1\mp sn}$
24	$\frac{(1-k^2)^2}{4}$	$\frac{k^2+1}{2}$	$\frac{1}{4}$	$\frac{sn}{dn\mp cn}$
25	$\frac{k^4}{4}$	$\frac{k^2-2}{2}$	$\frac{1}{4}$	$\frac{cn}{\sqrt{1-k^2\mp dn}}$

Tab.2. The Jacobi elliptic function exhibit specific limiting behaviour as $k \to 0$ and $k \to 1$

No.	Function	$k \to 1$	$k \to 0$
1	$sn(v)$	$tanh(v)$	$sin(v)$
2	$cn(v)$	$sech(v)$	$cos(v)$
3	$dn(v)$	$sech(v)$	1
4	$cd(v)$	1	$cos(v)$
5	$sd(v)$	$sinh(v)$	$sin(v)$
6	$nd(v)$	$cosh(v)$	1
7	$dc(v)$	1	$sec(v)$
8	$nc(v)$	$cosh(v)$	$sec(v)$
9	$sc(v)$	$sinh(v)$	$tan(v)$
10	$ns(v)$	$coth(v)$	$csc(v)$
11	$ds(v)$	$csch(v)$	$csc(v)$
12	$cs(v)$	$csch(v)$	$cot(v)$

As $k \to 0$ and $k \to 1$, Jacobi elliptic functions, as mentioned in Table. simplify into periodic, trigonometric, and hyperbolic functions. Consequently, soliton solutions and solutions involving trigonometric functions are obtained for the problem. Using the application of the generalized Jacobi elliptic function expansion generalized JEFE technique, $v(\psi)$ is formulated as a finite series of Jacobi elliptic functions

$$v(\psi) = \sum_{i=0}^{n} a_i\, N^i(\psi), i = 0,1,2, \dots n. \tag{2.5}$$

Where $N\ (\psi)$ provides the solution to the nonlinear ODE (2.4) with a_i being constants that will be determined subsequently.

The integer n can be derived from equation (2.5) by considering the maximum order derivative component:

$$O\left(\frac{d^\alpha v}{d\psi^\alpha}\right) = n + \alpha,\ \ \alpha = 0, 1, 2, 3, \dots \tag{2.6}$$

and the nonlinear component with the highest power of the differential equation

$$O\left(\frac{v^\beta d^{\alpha v}}{d\psi^\alpha}\right) = (\beta + 1)n + \alpha,\ \beta = 1,2,3, \tag{2.7}$$

in equation (2.3).

Using equation (2.5) and setting all the coefficients corresponding to powers of N equal to 0, we establish a series of nonlinear algebraic equations corresponding to the coefficient a_i of equation (2.5) Utilising Maple, we resolve this system and substitute all the parameters for $\mathrm{m}_2, \mathrm{m}_1$ from equation (2.4) into Table 1. This approach integrates the value of equation (2.5) with the selected auxiliary equation, allowing for the derivation of accurate solutions for equation (2.1).

3. MATHEMATICAL FORMULATION OF THE GENEERALIZED JEFE APPROACH

3.1. Analysis of the first WBBM equation

Let the first three-dimensional WBBM equation be expressed as:

$$\partial_t u + \partial_x u + \partial_y u^3 - \partial_{xzt}^3 u = 0, \tag{3.1}$$

where ∂ represents partial derivative. Utilizing the wave transformation:

$$v(x, y, z, t) = v(\psi), \tag{3.2}$$

where

$$\psi = p\,x + q\,y + r\,z - s\,t,$$

and substituting into Eq. (3.2) we obtain:

$$(-c + p)v' + q(v^3)' + prcv''' = 0. \tag{3.3}$$

Integrating Equation (3.3) w.r.t ψ yields:

$$(-c + p)v + qv^3 + prcv'' + C = 0. \tag{3.4}$$

Here, the C acts as the arbitrary constant arising from integration. For simplicity, setting $C = 0$, we have:

$$(-c + p)v + qv^3 + prcv'' = 0. \tag{3.5}$$

Considering the homogeneous balancing of the derivative component of maximum order v'' and the nonlinear component v^3 in Eq. (3.5), it is clear that $n = 1$. Thus, the method suggests the following supplementary solution:

$$v(\psi) = b_0 + b_1 N(\psi). \tag{3.6}$$

Differentiating Eq. (3.6) with respect to ψ, we have:

$$v'(\psi) = b_1' N'(\psi). \tag{3.7}$$

Substituting this into the governing equation, we get:

$$v'(\psi) = b_1(\, m_2 N^4(\psi) + m_1 N^2(\psi) + m_0)^{\frac{1}{2}}$$

$$v''(\psi) = b_1 N(\psi)(\, 2\, m_2 N^2(\psi) + m_1). \tag{3.8}$$

Substitute Eq. (3.8) and Eq. (3.7) into the equation

$$-s\, b_0 - sb_1 N(\psi) + pb_0 + pb_1 N(\psi) + qb_0^3 + 3\, qb_0^2 b_1 N(\psi) + 3\, qb_0 b_1^2 N(\psi)^2 + q\, b_1^3 N(\psi)^3 + prs\, b_1 N(\psi) m_0 + 2\, prs\, b_1 N(\psi) m_2 = 0. \tag{3.9}$$

By collecting various powers of $N^i(\psi)$, a subsequent set of algebraic equations is derived:

$$-s\, b_0 + p\, b_0 + q\, b_0^3 = 0, \tag{3.10}$$

$$-s\, b_1 + p\, b_1 + 3\, q\, b_0^2 b_1 + p\, r\, s\, b_1 m_1 = 0, \tag{3.11}$$

$$3\, q\, b_0 b_1^2 = 0, \tag{3.12}$$

$$q\, b_1^3 + 2\, p\, r\, s\, b_1 m_2 = 0. \tag{3.13}$$

The system described above of algebraic equations is calculated through MAPLE, and we derive the roots of the coefficients involved in equation (3.6):

$$b_0 = 0, \tag{3.14}$$

$$b_1 = \pm\sqrt{\frac{2r\,m_2}{-q + q\,p\,r\,m_1}}p, \tag{3.15}$$

$$s = \frac{p}{1 - pr\,m_1}. \tag{3.16}$$

The following solutions for the 3-D WBBM equation can be obtained by inserting the corresponding values into Eq. (3.6):

$$v(x,y,z,t) = \pm\sqrt{\frac{2r\,m_2}{-q + q\,p\,r\,m_1}}p\ N\left(p\,x + q\,y + r\,z - \frac{p}{1 - pr\,m_1}t\right). \tag{3.17}$$

3.2. Analytical periodic solutions in terms of Jacobi elliptic functions (JEF)

Using the data provided in Table 1 and Table 2 and combining the corresponding values as per Eq. (3.6), we may derive the Jacobi elliptic function solutions which are of a periodic nature for Eq. (1.1) as shown below.

$$v_{1,1}(x,y,z,t) = \pm\sqrt{\frac{-2k^2r}{(pr(k^2+1)+q)}}\,psn\left(px + qy + rz - \frac{pt}{1 + pr(k^2+1)}\right), \tag{3.18}$$

$$v_{1,2}(x,y,z,t) = \pm\sqrt{\frac{-2k^2r}{(pr(k^2+1)+q)}}\,pcd\left(px + qy + rz - \frac{pt}{1 + pr(k^2+1)}\right), \tag{3.19}$$

$$v_{1,3}(x,y,z,t) = \pm\sqrt{\frac{-2k^2r}{(pr(2k^2-1)+q)}}\,pcn\left(px + qy + rz - \frac{pt}{pr(2k^2-1)+1}\right), \tag{3.20}$$

$$v_{1,4}(x,y,z,t) = \pm\sqrt{\frac{2r}{(pr(1-k^2)+q)}}\,pdn\left(px + qy + rz - \frac{pt}{pr(2-k^2)+1}\right), \tag{3.21}$$

$$v_{1,5}(x,y,z,t) = \pm\sqrt{\frac{-2r}{(q - pr(k^2+1))}}\,pns\left(px + qy + rz - \frac{pt}{1 - pr(k^2+1)}\right), \tag{3.22}$$

$$v_{1,6}(x,y,z,t) = \pm\sqrt{\frac{-2r}{q(\,pr(k^2+1)+1)}}\,pdc\left(px + qy + rz - \frac{pt}{pr(-k^2-1)+1}\right), \tag{3.23}$$

$$v_{1,7}(x,y,z,t) = \pm\sqrt{\frac{-2r(k^2-1)}{q(pr(2k^2-1)-1)}}\,pnc\left(px + qy + rz - \frac{pt}{pr(2k^2-1)+1}\right), \tag{3.24}$$

$$v_{1,8}(x,y,z,t) = \pm\sqrt{\frac{-2r(k^2-1)}{(prq(2k^2-2)+q)}}\,pnd\left(px + qy + rz - \frac{pt}{pr(2-k^2)+1}\right), \tag{3.25}$$

$$v_{1,9}(x,y,z,t) = \pm\sqrt{\frac{2r(k^2-1)}{(prq(k^2-2)+q)}}\,psc\left(px + qy + rz - \frac{pt}{pr(2-k^2)+1}\right), \tag{3.26}$$

$$v_{1,10}(x,y,z,t) = \pm\sqrt{\frac{2k^2r(k^2-1)}{(prq(2k^2-1)-q)}}\,psd\left(px + qy + rz - \frac{pt}{pr(2k^2-1)+1}\right), \tag{3.27}$$

$$v_{1,11}(x,y,z,t) = \pm\sqrt{\frac{-2r}{(q(pr(k^2-2)+1))}}\,pcs\left(px + qy + rz - \frac{pt}{pr(2-k^2)+1}\right), \tag{3.28}$$

$$v_{1,12}(x,y,z,t) = \pm\sqrt{\frac{2r}{(prq(2k^2-1)-q))}}\,pds\left(px + qy + rz - \frac{pt}{pr(2k^2-1)+1}\right), \tag{3.29}$$

$$v_{1,13}(x,y,z,t) = \pm\sqrt{\frac{-r}{(q(pr(k^2+1)-2))}}\,p\left[kcn\left(px + qy + rz - \frac{pt}{pr\frac{(k^2+1)}{2}+1}\right) \pm dn\left(px + qy + rz - \frac{pt}{pr\frac{(k^2+1)}{2}+1}\right)\right], \tag{3.30}$$

$$v_{1,14}(x,y,z,t) = \pm\sqrt{\frac{-r}{(q(pr(1-2k^2)-2))}}\,p\left[ns\left(px + qy + rz - \frac{pt}{1-\frac{pr(1-2k^2)}{2}}\right) \pm cs\left(px + qy + rz - \frac{pt}{1-\frac{pr(1-2k^2)}{2}}\right)\right], \tag{3.31}$$

$$v_{1,15}(x,y,z,t) = \pm\sqrt{\frac{-r(k^2-1)}{(q(pr(k^2+1)-2))}}\cdot p\left[nc\left(px + qy + rz - \frac{pt}{\left(1-\frac{pr(k^2+1)}{2}\right)}\right) \pm sc\left(px + qy + rz - \frac{pt}{\left(1-\frac{pr(k^2+1)}{2}\right)}\right)\right], \tag{3.32}$$

$$v_{1,16}(x,y,z,t) = \pm\sqrt{\frac{r}{(prq(k^2-2)-2q)}}\,p\left[ns\left(px + qy + rz - \frac{pt}{\left(1-\frac{pr(k^2-2)}{2}\right)}\right) \pm ds\left(px + qy + rz - \frac{pt}{\left(1-\frac{pr(k^2-2)}{2}\right)}\right)\right], \tag{3.33}$$

$$v_{1,17}(x,y,z,t) = \pm\sqrt{\frac{k^2r}{(q(pr(k^2-2)-2))}}\,p\left[sn\left(px + qy + rz - \frac{pt}{\left(1-\frac{pr(k^2-2)}{2}\right)}\right) \pm icn\left(px + qy + rz - \frac{pt}{\left(1-\frac{pr(k^2-2)}{2}\right)}\right)\right], \tag{3.34}$$

$$v_{1,18}(x,y,z,t) = \pm\sqrt{\frac{k^2r}{(q(pr(k^2-2)-2))}}\,p\ \frac{sn\left(px + qy + rz - \frac{pt}{\left(1-\frac{pr(k^2-2)}{2}\right)}\right)}{(\sqrt{(1-k^2)}\pm cn\left(px + qy + rz - \frac{pt}{\left(1-\frac{pr(k^2-2)}{2}\right)}\right)}, \tag{3.35}$$

$$v_{1,19}(x,y,z,t) = \pm\sqrt{\frac{k^2r}{(pqr(2k^2-2)+2q)}}\,p\ \Big[kcn\Big(px +$$

DOI 10.2478/ama-2025-0048

$$qy + rz - \frac{pt}{\left(1-\frac{pr(1-2k^2)}{2}\right)}\Bigg) \pm idn\Bigg(px + qy + rz - \frac{pt}{\left(1-\frac{pr(1-2k^2)}{2}\right)}\Bigg)\Bigg], \tag{3.36}$$

$$v_{1,20}(x,y,z,t) = \pm\sqrt{\frac{-r}{(prq(1 - 2k^2) + 2q)}}\, p\,\frac{sn\left(px+qy+rz-\frac{pt}{\left(1-\frac{pr(1-2k^2)}{2}\right)}\right)}{1\pm cn\left(px+qy+rz-\frac{pt}{\left(1-\frac{pr(1-2k^2)}{2}\right)}\right)}, \tag{3.37}$$

$$v_{1,21}(x,y,z,t) = \pm\sqrt{\frac{k^2r}{(pqr(k^2 - 2) - 2q)}}\,p\,\frac{sn\left(px+qy+rz-\frac{pt}{\left(1-\frac{pr(k^2-2)}{2}\right)}\right)}{(\sqrt{(1-k^2)}\pm d\,n\left(px+qy+rz-\frac{pt}{\left(1-\frac{pr(k^2-2)}{2}\right)}\right)}, \tag{3.38}$$

$$v_{1,22}(x,y,z,t) = \pm\sqrt{\frac{r(k^2-1\,)}{q(pr(k^2+1) - 2)}}\,p\,\frac{dn\left(px+qy+rz-\frac{pt}{\left(1-\frac{pr(k^2+1)}{2}\right)}\right)}{1\pm ksn\left(px+qy+rz-\frac{pt}{\left(1-\frac{pr(k^2+1)}{2}\right)}\right)}, \tag{3.39}$$

$$v_{1,23}(x,y,z,t) = \pm\sqrt{\frac{-(rk^2-r\,)}{(pqr(k^2+1) - 2q)}}\,p\,\frac{cn\left(px+qy+rz-\frac{pt}{\left(1-\frac{pr(k^2+1)}{2}\right)}\right)}{1\pm sn\left(px+qy+rz-\frac{pt}{\left(1-\frac{pr(k^2+1)}{2}\right)}\right)}, \tag{3.40}$$

$$v_{1,24}(x,y,z,t) = \pm\sqrt{\frac{-r(k^2-1\,)^2}{(pqr(k^2+1) - 2q)}}\; p\,\frac{sn\left(px+qy+rz-\frac{pt}{\left(1-\frac{pr(k^2+1)}{2}\right)}\right)}{dn\left(px+qy+rz-\frac{pt}{\left(1-\frac{pr(k^2+1)}{2}\right)}\right)\pm cn\left(px+qy+rz-\frac{pt}{\left(1-\frac{pr(k^2+1)}{2}\right)}\right)}, \tag{3.41}$$

$$v_{1,25}(x,y,z,t) = \pm\sqrt{\frac{k^4r}{\left(q(pr(k^2 - 2) - 2)\right)}}\;p\,\frac{cn\left(px+qy+rz-\frac{pt}{\left(1-\frac{pr(k^2-2)}{2}\right)}\right)}{(\sqrt{(1-k^2)}\pm dn\left(px+qy+rz-\frac{pt}{\left(1-\frac{pr(k^2-2)}{2}\right)}\right)}. \tag{3.42}$$

3.2.1. Solitary wave solutions

When $k \to 1$, in this category, see in table 2, the solutions $v_{1,7}, v_{1,8}, v_{1,9}, v_{1,10}, v_{1,15}, v_{1,22}, v_{1,23}$ and $v_{1,24}$ become zero. The remaining solutions represent solitary wave solutions and can be determined as follows:

$$v_{1,26}(x,y,z,t) = \pm\sqrt{\frac{-2r}{(2prq+q)}}\;p\,tanh\Big(px + qy + rz - \frac{pt}{2\,pr+1}\Big), \tag{3.43}$$

$$v_{1,27}(x,y,z,t) = \pm\sqrt{\frac{-2r}{(prq-q)}}\;p\,sech\Big(px + qy + rz - \frac{pt}{pr+1}\Big), \tag{3.44}$$

$$v_{1,28}(x,y,z,t) = \pm\sqrt{\frac{2r}{(-prq+q)}}\;p\,sech\Big(px + qy + rz - \frac{pt}{pr+1}\Big), \tag{3.45}$$

$$v_{1,29}(x,y,z,t) = \pm\sqrt{\frac{-2r}{(2prq+q)}}\;p\,coth\Big(px + qy + rz - \frac{pt}{-2\,pr+1}\Big), \tag{3.46}$$

$$v_{1,30}(x,y,z,t) = \pm\sqrt{\frac{-2r}{(-prq+q)}}\;p\,csch\Big(px + qy + rz - \frac{pt}{-\,pr+1}\Big), \tag{3.47}$$

$$v_{1,31}(x,y,z,t) = \pm\sqrt{\frac{r}{(prq-q)}}\;p\,csch\Big(px + qy + rz - \frac{pt}{pr+1}\Big), \tag{3.48}$$

$$v_{1,32}(x,y,z,t) = \pm\sqrt{\frac{-r}{(2prq-2q)}}\;p\,\Big[sech\Big(px + qy + rz - \frac{pt}{pr+1}\Big) \pm sech\,\Big(px + qy + rz - \frac{pt}{pr+1}\Big)\Big], \tag{3.49}$$

$$v_{1,33}(x,y,z,t) = \pm\sqrt{\frac{r}{(prq+2q)}}\;p\,\Big[coth\Big(px + qy + rz - \frac{pt}{\frac{1}{2}pr+1}\Big) \pm csch\,\Big(px + qy + rz - \frac{pt}{\frac{1}{2}pr+1}\Big)\Big], \tag{3.50}$$

$$v_{1,34}(x,y,z,t) = \pm\sqrt{\frac{r}{(-prq-2q)}}\;p\,\Big[coth\Big(px + qy + rz - \frac{\mathrm{pt}}{1+\frac{1}{2}\mathrm{pr}}\Big) \pm csch\,\Big(px + qy + rz - \frac{pt}{1+\frac{1}{2}pr}\Big)\Big], \tag{3.51}$$

$$v_{1,35}(x,y,z,t) = \pm\sqrt{\frac{r}{(-prq-2q)}}\; p \left[\tanh\left(px + qy + rz - \frac{\mathrm{pt}}{1+\frac{1}{2}\mathrm{pr}}\right) \pm i\,\mathrm{sech}\left(px + qy + rz - \frac{pt}{1+\frac{1}{2}pr}\right)\right], \tag{3.52}$$

$$v_{1,36}(x,y,z,t) = \pm\sqrt{\frac{r}{(-prq-2q)}}\; p\,\frac{\tanh\left(px+qy+rz-\frac{pt}{1+\frac{1}{2}pr}\right)}{\mathrm{sech}\left(px+qy+rz-\frac{pt}{1+\frac{1}{2}pr}\right)}, \tag{3.53}$$

$$v_{1,37}(x,y,z,t) = \pm\sqrt{\frac{-r}{(prq+2q)}}\; p \left[\mathrm{sech}\left(px + qy + rz - \frac{\mathrm{pt}}{1+\frac{1}{2}\mathrm{pr}}\right) \pm i\,\mathrm{sech}\left(px + qy + rz - \frac{pt}{1+\frac{1}{2}pr}\right)\right], \tag{3.54}$$

$$v_{1,38}(x,y,z,t) = \pm\sqrt{\frac{-r}{(-prq+2q)}}\, p\,\frac{\tanh\left(px+qy+rz-\frac{pt}{1+\frac{1}{2}pr}\right)}{1\pm\mathrm{sech}\left(px+qy+rz-\frac{pt}{1+\frac{1}{2}pr}\right)}, \tag{3.55}$$

$$v_{1,39}(x,y,z,t) = \pm\sqrt{\frac{-r}{(-prq-2q)}}\, p\,\frac{\tanh\left(px+qy+rz-\frac{pt}{1+\frac{1}{2}pr}\right)}{1\pm\mathrm{sech}\left(px+qy+rz-\frac{pt}{1+\frac{1}{2}pr}\right)}, \tag{3.56}$$

$$v_{1,40}(x,y,z,t) = \pm\sqrt{\frac{r}{(-prq-2q)}}\, p\,\frac{\mathrm{sech}\left(px+qy+rz-\frac{pt}{1-\frac{1}{2}pr}\right)}{\mathrm{sech}\left(px+qy+rz-\frac{pt}{1-\frac{1}{2}pr}\right)}. \tag{3.57}$$

3.2.2. Shock wave solutions

When $k \to 0$, in this category see in table 2, the solutions $v_{1,2}$, $v_{1,3}$, $v_{1,10}$, $v_{1,17}$, $v_{1,18}$, $v_{1,21}$, and $v_{1,25}$ become zero. The remaining solutions represent solitary wave solutions and can be determined as follows:

$$v_{1,41}(x,y,z,t) = \pm\sqrt{\frac{-2r}{(prq+q)}}\, p\csc\left(px + qy + rz - \frac{pt}{-pr+1}\right), \tag{3.58}$$

$$v_{1,42}(x,y,z,t) = \pm\sqrt{\frac{-2r}{(prq+q)}}\; p\sec\left(px + qy + rz - \frac{pt}{-pr+1}\right), \tag{3.59}$$

$$v_{1,43}(x,y,z,t) = \pm\sqrt{\frac{-2r}{(prq+q)}}\; p\sec\left(px + qy + rz - \frac{pt}{-pr+1}\right), \tag{3.60}$$

$$v_{1,44}(x,y,z,t) = \pm\sqrt{\frac{r}{(2prq-q)}}\, p\tan\left(px + qy + rz - \frac{pt}{2pr+1}\right), \tag{3.61}$$

$$v_{1,45}(x,y,z,t) = \pm\sqrt{\frac{2r}{(2prq-q)}}\; p\cot\left(px + qy + rz - \frac{pt}{2pr+1}\right), \tag{3.62}$$

$$v_{1,46}(x,y,z,t) = \pm\sqrt{\frac{-2r}{(prq+q)}}\; p\csc\left(px + qy + rz - \frac{pt}{-pr+1}\right), \tag{3.63}$$

$$v_{1,47}(x,y,z,t) = \pm\sqrt{\frac{-r}{(prq-2q)}}\, p\left[\csc\left(px + qy + rz - \frac{\mathrm{pt}}{1-\frac{1}{2}\mathrm{pr}}\right) \pm \cot\left(px + qy + rz - \frac{pt}{1-\frac{1}{2}pr}\right)\right], \tag{3.64}$$

$$v_{1,48}(x,y,z,t) = \pm\sqrt{\frac{-r}{(prq-2q)}}\; p\left[\sec\left(px + qy + rz - \frac{\mathrm{pt}}{1-\frac{1}{2}\mathrm{pr}}\right) \pm \tan\left(px + qy + rz - \frac{pt}{1-\frac{1}{2}pr}\right)\right], \tag{3.65}$$

$$v_{1,49}(x,y,z,t) = \pm\sqrt{\frac{-2r}{(prq+2q)}}\; p\left[\csc\left(px + qy + rz - \frac{\mathrm{pt}}{1+\mathrm{pr}}\right) \pm \csc\left(px + qy + rz - \frac{pt}{1+pr}\right)\right], \tag{3.66}$$

$$\boldsymbol{v_{1,50}(x,y,z,t)} = \pm\sqrt{\frac{\boldsymbol{r}}{(\boldsymbol{prq-2q})}}\; \boldsymbol{p}\,\frac{\boldsymbol{\sin\left(px+qy+rz-\frac{pt}{1-\frac{1}{2}pr}\right)}}{\boldsymbol{1\pm\cos\left(px+qy+rz-\frac{pt}{1-\frac{1}{2}pr}\right)}}, \tag{3.67}$$

$$v_{1,51}(x,y,z,t) = \pm\sqrt{\frac{r}{(prq-2q)}}\; p\,\frac{\cos\left(px+qy+rz-\frac{pt}{1-\frac{1}{2}pr}\right)}{1\pm\sin\left(px+qy+rz-\frac{pt}{1-\frac{1}{2}pr}\right)}, \tag{3.68}$$

$$v_{1,52}(x,y,z,t) = \pm\sqrt{\frac{r}{(prq-2q)}}\; p\,\frac{\sin\left(px+qy+rz-\frac{pt}{1-\frac{1}{2}pr}\right)}{1\pm\cos\left(px+qy+rz-\frac{pt}{1-\frac{1}{2}pr}\right)}. \tag{3.69}$$

3.3. Analysis of the Second WBBM Equation

Using the traveling wave transformation equation (3.2) into equation (1.2), we convert the nonlinear partial differential equation (PDE) to an ordinary differential equation (ODE) of the following form:

$$(-s + r)v' + pv3 + pqsv'' = 0. \tag{3.70}$$

By the balancing procedure, we find the value of $n = 1$. Thus, the ansatz solution has the following simplified form:

$$v(\psi) = c_0 + c_1 N(\psi). \tag{3.71}$$

Substituting equation (3.71) combine with equation (2.4) into

DOI 10.2478/ama-2025-0048

(3.70), we get:

$$-s\,c_0 - s\,c^1N(\psi) + p\,c_0 + p\,c_1N(\psi) + q\,c_0^3 + 3q\,c_0^2\,c_1N(\psi) + 3q\,c_0c_1^2\,N(\psi)^2 + q\,c_1^3\,N(\psi)^3 + p\,r\,s\,c_1N(\psi)m_0 + 2p\,r\,s\,c_1N(\psi)m_2 = 0. \tag{3.72}$$

By collecting various powers of $N^i(\psi)$, a subsequent system of algebraic equations is derived:

$$-sc_0 + pc_0 + qc_0 = 0, \tag{3.73}$$

$$-sc_1 + pc_1 + 3qc_0c_1 + prsc_1m_1 = 0, \tag{3.74}$$

$$3qc_0c_1^2 = 0, \tag{3.75}$$

$$qc_1^3 + 2prs\,c_1m_2 = 0. \tag{3.76}$$

The system described above of algebraic equations is calculated through MAPLE, and we derive the roots of the coefficients involved in equation (3.71):

$$c_0 = 0, \tag{3.77}$$

$$c_1 = \pm\sqrt{\frac{2qr\,m_2}{-1+p\,q\,m_1}}, \tag{3.78}$$

$$s = \frac{r}{1-pq\,m_1}\,. \tag{3.79}$$

The following solutions for the first 3-D WBBM equation can be obtained by inserting the corresponding values into Eq. (3.71):

$$v_{x,y,z,t} = \pm\sqrt{\frac{2qr\,m_2}{-1+p\,q\,m_1}}\;p\,N\left(p\,x + q\,y + r\,z - \sqrt{\frac{2qr\,m_2}{-1+p\,q\,m_1}}\right). \tag{3.80}$$

3.3.1. Analytical periodic solutions in terms of Jacobi elliptic functions (JEF)

Using the data provided in Tables 1 and 2, and combining the corresponding values as per Eq.(3.71), we may derive the Jacobi elliptic function solutions which are periodic for equation (1.3) as shown below.

$$v_{2,1}(x,y,z,t) = \pm\sqrt{\frac{2qr\,k^2}{-1-p\,q(k^2+1)}}p\,sn\left(px + qy + rz - \frac{r}{1+pq\,(k^2+1)}t\right), \tag{3.81}$$

$$v_{2,2}(x,y,z,t) = \pm\sqrt{\frac{2qr\,k^2}{-1-p\,q(k^2+1)}}p\,cd\left(px + qy + rz - \frac{r}{1+pq\,(k^2+1)}t\right), \tag{3.82}$$

$$v_{2,3}(x,y,z,t) = \pm\sqrt{\frac{-2k^2qr}{(pq(2k^2-1)-1)}}p\,cn\left(px + qy + rz - \frac{r}{(1-pq(2k^2-1))}t\right), \tag{3.83}$$

$$v_{2,4}(x,y,z,t) = \pm\sqrt{\frac{-2qr}{(pq(2-k^2)-1)}}pdn\left(px + qy + rz - \frac{r}{(1-pq(2-k^2))}t\right), \tag{3.84}$$

$$v_{2,5}(x,y,z,t) = \pm\sqrt{\frac{2qr}{(-pq(k^2+1)-1)}}pns\left(px + qy + rz - \frac{r}{(1+pq(k^2+1))}t\right), \tag{3.85}$$

$$v_{2,6}(x,y,z,t) = \pm\sqrt{\frac{2qr}{(-pq(k^2+1)-1)}}pdc\left(px + qy + rz - \frac{r}{(1+pq(k^2+1))}t\right), \tag{3.86}$$

$$v_{2,7}(x,y,z,t) = \pm\sqrt{\frac{-2qr(k^2-1)}{(pq(2k^2-1)-1)}}pnc\left(px + qy + rz - \frac{rt}{(1-pq(2k^2-1))}\right), \tag{3.87}$$

$$v_{2,8}(x,y,z,t) = \pm\sqrt{\frac{-2qr(k^2-1)}{(pq(k^2-2)+1)}}p\,nd\left(px + qy + rz - \frac{r}{(1-pq(2-k^2))}t\right), \tag{3.88}$$

$$v_{2,9}(x,y,z,t) = \pm\sqrt{\frac{-2qr(k^2-1)}{(pq(k^2-2)+1)}}p\,sc\left(px + qy + rz - \frac{r}{(1-pq(2-k^2))}t\right), \tag{3.89}$$

$$v_{2,10}(x,y,z,t) = \pm\sqrt{\frac{-2qr(k^2-1)}{(pq(2k^2-1)-1)}}p\,sd\left(px + qy + rz - \frac{r}{(1-pq(2k^2-1))}t\right), \tag{3.90}$$

$$v_{2,11}(x,y,z,t) = \pm\sqrt{\frac{2qr}{(pq(2-k^2)-1)}}p\,cs\left(px + qy + rz - \frac{r}{(1-pq(2-k^2))}t\right), \tag{3.91}$$

$$v_{2,12}(x,y,z,t) = \pm\sqrt{\frac{2qr}{(pq(2k^2-1)-1)}}p\,ds\left(px + qy + rz - \frac{r}{(1-pq(2k^2-1))}t\right), \tag{3.92}$$

$$v_{2,13}(x,y,z,t) = \pm\sqrt{\frac{-qr}{(pq(k^2+1)-2)}}p\left[kcn\left(px + qy + rz - \frac{r}{\left(1-\frac{pq(k^2+1)}{2}\right)}t\right) \pm dn\left(px + qy + rz - \frac{r}{\left(1-\frac{pq(k^2+1)}{2}\right)}t\right)\right], \tag{3.93}$$

$$v_{2,14}(x,y,z,t) = \pm\sqrt{\frac{qr}{(pq(-2k^2+1)-2)}}p\left[ns\left(px + qy + rz - \frac{r}{\left(1-\frac{pq(-2k^2+1)}{2}\right)}t\right) \pm cs\left(px + qy + rz - \frac{r}{\left(1-\frac{pq(-2k^2+1)}{2}\right)}t\right)\right], \tag{3.94}$$

$$v_{2,15}(x,y,z,t) = \pm\sqrt{\frac{(-q\,r\,(k^2-1))}{(p\,q\,(k^2+1)-2)}}p\left[nc\left(px + qy + rz - \frac{r}{\left(1-\frac{pq(k^2+1)}{2}\right)}t\right) \pm sc\left(px + qy + rz - \frac{r}{\left(1-\frac{pq(k^2+1)}{2}\right)}t\right)\right], \tag{3.95}$$

$$v_{2,16}(x,y,z,t) = \pm\sqrt{\frac{q\,r}{(p\,q\,(k^2-2)-2)}}p\left[ns\left(px + qy + rz - \frac{r}{\left(1-\frac{pq(k^2-2)}{2}\right)}t\right) \pm ds\left(px + qy + rz -\right.\right.$$

$$\frac{r}{\left(1-\frac{pq(k^2-2)}{2}\right)}t\Bigg)\Bigg], \tag{3.96}$$

$$v_{2,17}(x,y,z,t)=\pm\sqrt{\frac{k^2qr}{(pq(k^2-2)-2)}}\,p\left[sn\left(px+qy+rz-\frac{r}{\left(1-\frac{pq(k^2-2)}{2}\right)}t\right)\pm icn\left(px+qy+rz-\frac{r}{\left(1-\frac{pq(k^2-2)}{2}\right)}t\right)\right], \tag{3.97}$$

$$v_{2,18}(x,y,z,t)=\pm\sqrt{\frac{k^2qr}{(pq(k^2-2)-2)}}\;p\,\frac{sn\left(px+qy+rz-\frac{pt}{\left(1-\frac{pq(k^2-2)}{2}\right)}\right)}{(\sqrt{(1-k^2)}\pm cn\left(px+qy+rz-\frac{pt}{\left(1-\frac{pq(k^2-2)}{2}\right)}\right)}, \tag{3.98}$$

$$v_{2,19}(x,y,z,t)=\pm\sqrt{\frac{-qr}{(pq(2k^2-1)+2)}}\,p\left[kcn\left(px+qy+rz-\frac{r}{\left(1-\frac{pq(1-2k^2)}{2}\right)}t\right)\pm idn\left(px+qy+rz-\frac{r}{\left(1-\frac{pq(1-2k^2)}{2}\right)}t\right)\right], \tag{3.99}$$

$$v_{2,20}(x,y,z,t)=\pm\sqrt{\frac{-qr}{(pq(2k^2-1)+2)}}\,p\;\frac{sn\left(px+qy+rz-\frac{pt}{\left(1-\frac{pq(1-2k^2)}{2}\right)}\right)}{1\pm cn\left(px+qy+rz-\frac{pt}{\left(1-\frac{pq(1-2k^2)}{2}\right)}\right)}, \tag{3.100}$$

$$v_{2,21}(x,y,z,t)=\pm\sqrt{\frac{-k^2qr}{(pq(k^2-2)-2)}}\;p\,\frac{sn\left(px+qy+rz-\frac{pt}{\left(1-\frac{pq(k^2-2)}{2}\right)}\right)}{1\pm dn\left(px+qy+rz-\frac{pt}{\left(1-\frac{pq(k^2-2)}{2}\right)}\right)}, \tag{3.101}$$

$$v_{2,22}(x,y,z,t)=\pm\sqrt{\frac{qr(k^2-2)}{(pq(k^2+1)-2)}}\;p\,\frac{dn\left(px+qy+rz-\frac{pt}{\left(1-\frac{pq(k^2+1)}{2}\right)}\right)}{1\pm ksn\left(px+qy+rz-\frac{pt}{\left(1-\frac{pq(k^2+1)}{2}\right)}\right)}, \tag{3.102}$$

$$v_{2,23}(x,y,z,t)=\pm\sqrt{\frac{-qr(k^2-2)}{(pq(k^2+1)-2)}}\;p\,\frac{cn\left(px+qy+rz-\frac{pt}{\left(1-\frac{pq(k^2+1)}{2}\right)}\right)}{1\pm sn\left(px+qy+rz-\frac{pt}{\left(1-\frac{pq(k^2+1)}{2}\right)}\right)}, \tag{3.103}$$

$$v_{2,24}(x,y,z,t)=\pm\sqrt{\frac{qr(k^2-2)^2}{(pq(k^2+1)-2)}}\;p\,\frac{sn\left(px+qy+rz-\frac{pt}{\left(1-\frac{pq(k^2+1)}{2}\right)}\right)}{dn\left(px+qy+rz-\frac{pt}{\left(1-\frac{pq(k^2+1)}{2}\right)}\right)\pm cn\left(px+qy+rz-\frac{pt}{\left(1-\frac{pq(k^2+1)}{2}\right)}\right)}, \tag{3.104}$$

$$v_{2,25}(x,y,z,t)=\pm\sqrt{\frac{-k^4qr}{(pq(k^2-2)-2)}}\;p\,\frac{cn\left(px+qy+rz-\frac{pt}{\left(1-\frac{pq(k^2-2)}{2}\right)}\right)}{(\sqrt{(1-k^2)}\pm dn\left(px+qy+rz-\frac{pt}{\left(1-\frac{pq(k^2-2)}{2}\right)}\right)}, \tag{3.105}$$

3.3.2. Solitary wave type solutions

When $k\to 1$, in this category see in table 2, the solution $v_{2,7}$, $v_{2,8}$, $v_{2,9}$, $v_{2,10}$, $v_{2,15}$, $v_{2,22}$, $v_{2,23}$ and $v_{2,24}$ become zero. The remaining solutions represent solitary wave solutions and can be determined as follows:

$$v_{2,26}(x,y,z,t)=\pm\sqrt{\frac{2qr}{-1-2pq}}\,p\,tanh\left(px+qy+rz-\frac{r}{1+2pq}t\right), \tag{3.106}$$

$$v_{2,27}(x,y,z,t)=\pm\sqrt{\frac{-2qr}{pq-1}}\,p\,sech\left(px+qy+rz-\frac{r}{1-pq}t\right), \tag{3.107}$$

$$v_{2,28}(x,y,z,t)=\pm\sqrt{\frac{-2qr}{pq-1}}\,p\,sech\left(px+qy+rz-\frac{r}{1-pq}t\right), \tag{3.108}$$

$$v_{2,29}(x,y,z,t)=\pm\sqrt{\frac{2qr}{-2pq-1}}\,p\,coth\left(px+qy+rz-\frac{r}{1+2pq}t\right), \tag{3.109}$$

$$v_{2,30}(x,y,z,t)=\pm\sqrt{\frac{-2qr}{pq+1}}\,p\,csch\left(px+qy+rz-\frac{r}{1+pq}t\right), \tag{3.110}$$

$$v_{2,31}(x,y,z,t)=\pm\sqrt{\frac{2qr}{-pq-1}}\,p\,csch\left(px+qy+rz-\frac{r}{1+pq}t\right), \tag{3.111}$$

$$v_{2,32}(x,y,z,t) = \pm\sqrt{\frac{-2qr}{2pq-2}}p\left[sech\left(px+qy+rz-\frac{r}{1-pq}t\right) \pm sech\left(px+qy+rz-\frac{r}{1-pq}t\right)\right], \tag{3.112}$$

$$v_{2,33}(x,y,z,t) = \pm\sqrt{\frac{qr}{-pq-2}}p\left[coth\left(px+qy+rz-\frac{r}{1+\frac{1}{2}pq}t\right) \pm csch\left(px+qy+rz-\frac{r}{1+\frac{1}{2}pq}t\right)\right], \tag{3.113}$$

$$v_{2,34}(x,y,z,t) = \pm\sqrt{\frac{qr}{-pq-2}}p\left[coth\left(px+qy+rz+\frac{r}{-1-\frac{1}{2}pq}t\right) \pm csch\left(px+qy+rz+\frac{r}{-1-\frac{1}{2}pq}t\right)\right], \tag{3.114}$$

$$v_{2,35}(x,y,z,t) = \pm\sqrt{\frac{qr}{pq-2}}p\left[tanh\left(px+qy+rz+\frac{r}{-1-\frac{1}{2}pq}t\right) \pm isech\left(px+qy+rz+\frac{r}{-1-\frac{1}{2}pq}t\right)\right], \tag{3.115}$$

$$v_{2,36}(x,y,z,t) = \pm\sqrt{\frac{qr}{-pq-2}}p\,\frac{tanh\left(px+qy+rz+\frac{r}{-1-\frac{1}{2}pq}t\right)}{sech\left(px+qy+rz+\frac{r}{-1-\frac{1}{2}pq}t\right)}, \tag{3.116}$$

$$v_{2,37}(x,y,z,t) = \pm\sqrt{\frac{-qr}{pq+2}}p\left[sech\left(px+qy+rz+\frac{r}{-1-\frac{1}{2}pq}t\right) \pm isech\left(px+qy+rz+\frac{r}{-1-\frac{1}{2}pq}t\right)\right], \tag{3.117}$$

$$v_{2,38}(x,y,z,t) = \pm\sqrt{\frac{qr}{pq+2}}p\,\frac{tanh\left(px+qy+rz+\frac{r}{-1-\frac{1}{2}pq}t\right)}{1\pm sech\left(px+qy+rz+\frac{r}{-1-\frac{1}{2}pq}t\right)}, \tag{3.118}$$

$$v_{2,39}(x,y,z,t) = \pm\sqrt{\frac{qr}{-pq-2}}p\,\frac{tanh\left(px+qy+rz+\frac{r}{-1-\frac{1}{2}pq}t\right)}{1\pm sech\left(px+qy+rz+\frac{r}{-1-\frac{1}{2}pq}t\right)}, \tag{3.119}$$

$$v_{2,40}(x,y,z,t) = \pm\sqrt{\frac{qr}{-pq-2}}p\,\frac{sech\left(px+qy+rz+\frac{r}{-1-\frac{1}{2}pq}t\right)}{sech\left(px+qy+rz+\frac{r}{-1-\frac{1}{2}pq}t\right)}, \tag{3.120}$$

3.3.3. Shock wave solution

When $k \to 0$, in this category see in table 2, the solutions $v_{2,1}, v_{2,2}, v_{2,3}, v_{2,10}, v_{2,17}, v_{2,18}, v_{2,21}$ and $v_{2,25}$ become zero. The remaining solutions represent solitary wave solutions and can be determined as follows:

$$v_{2,41}(x,y,z,t) = \pm\sqrt{\frac{2qr}{-p\,q-1}}p\,csc\left(px+qy+rz-\frac{r}{1+2\,pq}t\right), \tag{3.121}$$

$$v_{2,42}(x,y,z,t) = \pm\sqrt{\frac{2qr}{-p\,q-1}}p\,sec\left(px+qy+rz-\frac{r}{1+2\,pq}t\right), \tag{3.122}$$

$$v_{2,43}(x,y,z,t) = \pm\sqrt{\frac{-2qr(k^2-1)}{-pq-1}}psec\left(px+qy+rz-\frac{r}{1+2\,pq}t\right), \tag{3.123}$$

$$v_{2,44}(x,y,z,t) = \pm\sqrt{\frac{-2qr}{-2\,p\,q+1}}p\,tan\left(px+qy+rz-\frac{r}{1-2\,pq}t\right), \tag{3.124}$$

$$v_{2,45}(x,y,z,t) = \pm\sqrt{\frac{-2qr}{-2\,p\,q+1}}p\,cot\left(px+qy+rz-\frac{r}{1-2\,pq}t\right), \tag{3.125}$$

$$v_{2,46}(x,y,z,t) = \pm\sqrt{\frac{2qr}{-p\,q-1}}p\,csc\left(px+qy+rz-\frac{r}{1+2\,pq}t\right), \tag{3.126}$$

$$v_{2,47}(x,y,z,t) = \pm\sqrt{\frac{qr}{pq-2}}p\left[csc\left(px+qy+rz+\frac{r}{1-\frac{1}{2}pq}t\right) \pm cot\left(px+qy+rz+\frac{r}{1-\frac{1}{2}pq}t\right)\right], \tag{3.127}$$

$$v_{2,48}(x,y,z,t) = \pm\sqrt{\frac{qr}{pq-2}}p\left[sec\left(px+qy+rz+\frac{r}{1-\frac{1}{2}pq}t\right) \pm tan\left(px+qy+rz+\frac{r}{1-\frac{1}{2}pq}t\right)\right], \tag{3.128}$$

$$v_{2,49}(x,y,z,t) = \pm\sqrt{\frac{qr}{-2pq-2}}p\left[csc\left(px+qy+rz+\frac{r}{1+pq}t\right) \pm csc\left(px+qy+rz+\frac{r}{1+pq}t\right)\right], \tag{3.129}$$

$$v_{2,50}(x,y,z,t) = \pm\sqrt{\frac{-qr}{-pq+2}}p\,\frac{sin\left(px+qy+rz-\frac{r}{1-\frac{1}{2}pq}t\right)}{1\pm cos\left(px+qy+rz-\frac{r}{1-\frac{1}{2}pq}t\right)}, \tag{3.130}$$

$$v_{2,51}(x,y,z,t) =$$

$$\pm\sqrt{\frac{qr}{pq-2}}p\frac{cos\left(px+qy+rz-\frac{r}{1-\frac{1}{2}pq}t\right)}{1\pm sin\left(px+qy+rz-\frac{r}{1-\frac{1}{2}pq}t\right)}, \tag{3.131}$$

$$v_{2,52}\,(x,y,z,t)= \pm\sqrt{\frac{qr}{pq-2}}p\frac{sin\left(px+qy+rz-\frac{r}{1-\frac{1}{2}pq}t\right)}{cos\left(px+qy+rz-\frac{r}{1-\frac{1}{2}pq}t\right)}, \tag{3.132}$$

3.4. Analysis of the Third WBBM Equation

Using the traveling wave transformation Equation (3.1) into Equation (1.3), we convert the nonlinear partial differential equation (PDE) to an ordinary differential equation (ODE) of the following form:

$$(-s+r)v'+pv^3+pqsv''=0. \tag{3.133}$$

By the balancing procedure, we find the value of n = 1. Thus, the ansatz solution has the following simplified form:

$$v(\psi)=d_0+d_1N(\psi). \tag{3.134}$$

Substituting Eq. (2.4) in Eq.(3.134) , we get

$$-sd_0-sd_1N(\psi)+pd_0+pd_1N(\psi)+qd_0^3+3qd_0^2d_1N(\psi)+3qd_0c_1^2N(\psi)^2+qd_1^3N(\psi)^3+prsd_1N(\psi)m_0+2prsd_1N(\psi)m_2=0. \tag{3.135}$$

By collecting various powers of Ni(ψ), a subsequent system of algebraic equations is derived:

$$-sd_0+pd_0+qd_0^3=0, \tag{3.136}$$

$$-sd_1+pd_1+3qd_0^2d_1+prsd_1m_1=0, \tag{3.137}$$

$$3qd_0d_1^2=0, \tag{3.138}$$

$$qd_1^3+2prsd_1m_2=0. \tag{3.139}$$

The system described above of algebraic equations is calculated through MAPLE, and we derive the roots of the coefficients involved in equation (3.134):

$$d_0=0, \tag{3.140}$$

$$d_1=\pm\sqrt{\frac{qm_2}{-r+rp^2m_1}}p, \tag{3.141}$$

$$s=-\frac{q}{-1+p^2m_1}. \tag{3.142}$$

The following solutions for the first 3-D WBBM equation can be obtained by inserting the corre- sponding values into Eq. (3.134):

$$v\,(x,y,z,t)=\pm\sqrt{\frac{qm_2}{-r+rp^2m_1}}p\,N\left(px+qy+rz+\frac{q}{p^2m_1-1}t\right). \tag{3.143}$$

3.4.1. Analytical periodic solutions in terms of Jacobi elliptic functions (JEF)

Using the data provided in table 1 and 2, and combining the corresponding values as per Eq. (3.6), we may derive the Jacobi elliptic function solutions which are in a periodic nature for Eq. (3.6) as shown below.

$$v_{3,1}\,(x,y,z,t)=\pm\sqrt{\frac{-k^2q}{(p^2r(k^2+1)+r)}}p\,sn\left(px+qy+rz+\frac{q}{-p^2\,(k^2+1)-1}t\right), \tag{3.144}$$

$$v_{3,2}(x,y,z,t)=\pm\sqrt{\frac{-k^2q}{(p^2r(k^2+1)+r)}}p\,cd\left(px+qy+rz+\frac{q}{-p^2\,(k^2+1)-1}t\right), \tag{3.145}$$

$$v_{3,3}(x,y,z,t)=\pm\sqrt{\frac{-k^2q}{(p^2r(2k^2-1)-r)}}p\,cn\left(px+qy+rz+\frac{q}{p^2\,(2k^2-1)-1}t\right), \tag{3.146}$$

$$v_{3,4}(x,y,z,t)=\pm\sqrt{\frac{-q}{(p^2r(2-k^2)-r)}}p\,dn\left(px+qy+rz+\frac{q}{p^2\,(2-k^2)-1}t\right), \tag{3.147}$$

$$v_{3,5}(x,y,z,t)=\pm\sqrt{\frac{-q}{(p^2r(k^2+1)+r)}}p\,ns\left(px+qy+rz+\frac{q}{-p^2\,(k^2+1)-1}t\right), \tag{3.148}$$

$$v_{3,6}(x,y,z,t)=\pm\sqrt{\frac{-q}{(p^2r(k^2+1)+r)}}p\,dc\left(px+qy+rz+\frac{q}{-p^2\,(k^2+1)-1}t\right), \tag{3.149}$$

$$v_{3,7}(x,y,z,t)=\pm\sqrt{\frac{-q(k^2-1)}{(p^2r(2k^2-1)-r)}}p\,nc\left(px+qy+rz+\frac{q}{p^2\,(2k^2-1)-1}t\right), \tag{3.150}$$

$$v_{3,8}(x,y,z,t)=\pm\sqrt{\frac{-q(k^2-1)}{(p^2r(2k^2-1)+r)}}p\,nd\left(px+qy+rz+\frac{qt}{p^2(2-k^2)-1}\right), \tag{3.151}$$

$$v_{3,9}(x,y,z,t)=\pm\sqrt{\frac{q(k^2-1)}{(p^2r(2k^2-1)+r)}}p\,sc\left(px+qy+rz+\frac{q}{p^2\,(2-k^2)-1}t\right), \tag{3.152}$$

$$v_{3,10}(x,y,z,t)=\pm\sqrt{\frac{k^2\,q(k^2-1)}{(p^2r(2k^2-1)-r)}}p\,sd\left(px+qy+rz+\frac{q}{p^2\,(2k^2-1)-1}t\right), \tag{3.153}$$

$$v_{3,11}(x,y,z,t)=\pm\sqrt{\frac{-q}{(p^2(k^2r-2r)+r)}}p\,cs\left(px+qy+rz+\frac{q}{p^2\,(2-k^2)-1}t\right), \tag{3.154}$$

$$v_{3,12}(x,y,z,t)=\pm\sqrt{\frac{q}{(p^2r(2k^2-1)-r)}}p\,ds\left(px+qy+rz+\frac{q}{p^2\,(2k^2-1)-1}t\right), \tag{3.155}$$

$$v_{3,13}\,(x,y,z,t)=\pm\sqrt{\frac{-q}{(p^2r(k^2+1)-2r)}}p\left[kcn\left(px+qy+rz+\frac{q}{\frac{p^2(k^2+1)}{2}-1}t\right)\pm dn\left(px+qy+rz+\frac{q}{\frac{p^2(k^2+1)}{2}-1}t\right)\right], \tag{3.156}$$

$$v_{3,14}\,(x,y,z,t)=\pm\sqrt{\frac{\frac{1}{2}q}{(p^2r(-2k^2+1)-2r)}}p\left[ns\left(px+\right.\right.$$

$$qy + rz + \frac{q}{\frac{p^2(-2k^2+1)}{2}-1}t\right) \pm cs\left(px + qy + rz + \frac{q}{\frac{p^2(-2k^2+1)}{2}-1}t\right)\right], \tag{3.157}$$

$$v_{3,15}(x,y,z,t) = \pm\sqrt{\frac{\frac{1}{2}q(1-k^2)}{(p^2r(k^2+1)-2r)}}p\left[nc\left(px + qy + rz + \frac{q}{\frac{p^2(k^2+1)}{2}-1}t\right) \pm sc\left(px + qy + rz + \frac{q}{\frac{p^2(k^2+1)}{2}-1}t\right)\right], \tag{3.158}$$

$$v_{3,16}(x,y,z,t) = \pm\sqrt{\frac{\frac{1}{2}q}{(p^2r(k^2-2)-2r)}}p\left[ns\left(px + qy + rz + \frac{q}{\frac{p^2(k^2-2)}{2}-1}t\right) \pm ds\left(px + qy + rz + \frac{q}{\frac{p^2(k^2-2)}{2}-1}t\right)\right], \tag{3.159}$$

$$v_{3,17}(x,y,z,t) = \pm\sqrt{\frac{\frac{1}{2}k^2q}{(p^2r(k^2-2)-2r)}}p\left[sn\left(px + qy + rz + \frac{q}{\frac{p^2(k^2-2)}{2}-1}t\right) \pm icn\left(px + qy + rz + \frac{q}{\frac{p^2(k^2-2)}{2}-1}t\right)\right], \tag{3.160}$$

$$v_{3,18}(x,y,z,t) = \pm\sqrt{\frac{\frac{1}{2}k^2q}{(p^2r(k^2-2)-2r)}}p. \left[\frac{sn\left(px+qy+rz+\frac{q}{\frac{p^2(k^2-2)}{2}-1}t\right)}{\sqrt{1-k^2} \pm cn\left(px+qy+rz+\frac{q}{\frac{p^2(k^2-2)}{2}-1}t\right)}\right], \tag{3.161}$$

$$v_{3,19}(x,y,z,t) = \pm\sqrt{\frac{\frac{1}{2}q}{(p^2r(1-2k^2)-2r)}}p\left[kcn\left(px + qy + rz + \frac{q}{\frac{p^2(2k^2-1)}{2}-1}t\right) \pm idn\left(px + qy + rz + \frac{q}{\frac{p^2(2k^2-1)}{2}-1}t\right)\right], \tag{3.162}$$

$$v_{3,20}(x,y,z,t) = \pm\sqrt{\frac{\frac{1}{2}q}{(p^2r(1-2k^2)-2r)}}p \left[\frac{sn\left(px+qy+rz+\frac{q}{\frac{p^2(2k^2-1)}{2}-1}t\right)}{1 \pm cn\left(px+qy+rz+\frac{q}{\frac{p^2(k^2-1)}{2}-1}t\right)}\right], \tag{3.163}$$

$$v_{3,21}(x,y,z,t) = \pm\sqrt{\frac{\frac{1}{2}k^2q}{(p^2r(k^2-2)-2r)}}p \left[\frac{sn\left(px+qy+rz+\frac{q}{\frac{p^2(k^2-2)}{2}-1}t\right)}{1\pm dn\left(px+qy+rz+\frac{q}{\frac{p^2(k^2-2)}{2}-1}t\right)}\right], \tag{3.164}$$

$$v_{3,22}(x,y,z,t) = \pm\sqrt{\frac{\frac{1}{2}q(k^2-1)}{r(p^2(k^2+1)-2)}}p \left[\frac{dn\left(px+qy+rz+\frac{q}{\frac{p^2(k^2-2)}{2}-1}t\right)}{1\pm ksn\left(px+qy+rz+\frac{q}{\frac{p^2(k^2-2)}{2}-1}t\right)}\right], \tag{3.165}$$

$$v_{3,23}(x,y,z,t) = \pm\sqrt{\frac{q(1-k^2)}{2r(p^2(k^2+1)-1)}}p \left[\frac{cn\left(px+qy+rz+\frac{q}{\frac{p^2(k^2-2)}{2}-1}t\right)}{1\pm sn\left(px+qy+rz+\frac{q}{\frac{p^2(k^2-2)}{2}-1}t\right)}\right], \tag{3.166}$$

$$v_{3,24}(x,y,z,t) = \pm\sqrt{\frac{q(1-k^2)^2}{(p^2r(k^2+1)-2r)}}\cdot p\frac{sn\left(px+qy+rz-\frac{qt}{\left(\frac{p^2(k^2+1)}{2}-1\right)}\right)}{dn\left(px+qy+rz-\frac{qt}{\left(\frac{pq(k^2+1)}{2}-1\right)}\right)\pm cn\left(px+qy+rz-\frac{qt}{\left(\frac{p^2(k^2+1)}{2}-1\right)}\right)}, \tag{3.167}$$

$$v_{3,25}(x,y,z,t) = \pm\sqrt{\frac{\frac{1}{2}k^4q}{(p^2r(k^2-2)-2r)}}p \left[\frac{cn\left(px+qy+rz+\frac{q}{\frac{p^2(k^2-2)}{2}-1}t\right)}{\sqrt{1-k^2}\pm dn\left(px+qy+rz+\frac{q}{\frac{p^2(k^2-2)}{2}-1}t\right)}\right], \tag{3.168}$$

3.4.2 Solitary wave type solutions

When $k \to 1$, in this category see in table 2, the solution $v_{3,7}, v_{3,8}, v_{3,9}, v_{3,10}, v_{3,15}, v_{3,22}, v_{3,23}$ and $v_{3,24}$ become zero. The remaining solutions represent solitary wave solutions and can be determined as follows:

$$v_{3,26}(x,y,z,t) = \pm\sqrt{\frac{-q}{(2p^2r+r)}}p\tanh\left(px + qy + rz + \frac{q}{-2p^2-1}t\right), \tag{3.169}$$

$$v_{3,27}(x,y,z,t) = \pm\sqrt{\frac{-q}{(2p^2r+r)}}p\,\mathrm{sech}\left(px + qy + rz + \frac{q}{-2p^2-1}t\right), \tag{3.170}$$

$$v_{3,28}(x,y,z,t) = \pm\sqrt{\frac{-q}{(p^2r-r)}}p\,\mathrm{sech}\left(px + qy + rz + \frac{q}{p^2-1}t\right), \tag{3.171}$$

$$v_{3,29}(x,y,z,t) = \pm\sqrt{\frac{-q}{2p^2r+r}}p\coth\left(px + qy + rz +\right.$$

$$\frac{q}{-p^2-1}t\Big), \tag{3.172}$$

$$v_{3,30}(x,y,z,t) = \pm\sqrt{\frac{-q}{(-p^2r+r)}}p\, csch\left(px + qy + rz + \frac{q}{p^2-1}t\right), \tag{3.173}$$

$$v_{3,31}(x,y,z,t) = \pm\sqrt{\frac{-q}{(2p^2r-2r)}}p\left[sech\left(px + qy + rz + \frac{q}{p^2-1}t\right) \pm sech\left(px + qy + rz + \frac{q}{p^2-1}t\right)\right], \tag{3.174}$$

$$v_{3,32}(x,y,z,t) = \pm\sqrt{\frac{\frac{1}{2}q}{(-p^2r-2r)}}p\left[coth\left(px + qy + rz + \frac{q}{\frac{-p^2}{2}-1}t\right) \pm csch\left(px + qy + rz + \frac{q}{\frac{-p^2}{2}-1}t\right)\right], \tag{3.175}$$

$$v_{3,33}(x,y,z,t) = \pm\sqrt{\frac{\frac{1}{2}q}{(-p^2r-2r)}}p\left[coth\left(px + qy + rz + \frac{r}{\frac{-p^2}{2}-1}t\right) \pm csch\left(px + qy + rz + \frac{q}{\frac{-p^2}{2}-1}t\right)\right], \tag{3.176}$$

$$v_{3,34}(x,y,z,t) = \pm\sqrt{\frac{\frac{1}{2}q}{(-p^2r-2r)}}p\left[tanh\left(px + qy + rz + \frac{r}{\frac{-p^2}{2}-1}t\right) \pm isech\left(px + qy + rz + \frac{q}{\frac{-p^2}{2}-1}t\right)\right], \tag{3.177}$$

$$v_{3,35}(x,y,z,t) = \pm\sqrt{\frac{q}{\left(-\frac{1}{2}p^2r-r\right)}}p\left[\frac{sn\left(px+qy+rz+\frac{q}{\frac{-p^2}{2}-1}t\right)}{\pm cn\left(px+qy+rz+\frac{q}{\frac{-p^2}{2}-1}t\right)}\right], \tag{3.178}$$

$$v_{3,36}(x,y,z,t) = \pm\sqrt{\frac{\frac{1}{2}q}{(-p^2r-2r)}}p\left[sech\left(px + qy + rz + \frac{q}{\frac{p^2}{2}-1}t\right) \pm isech\left(px + qy + rz + \frac{q}{\frac{p^2}{2}-1}t\right)\right], \tag{3.179}$$

$$v_{3,37}(x,y,z,t) = \pm\sqrt{\frac{\frac{1}{2}q}{(-p^2r-2r)}}p\left[\frac{tanh\left(px+qy+rz+\frac{q}{\frac{p^2}{2}-1}t\right)}{1 \pm sech\left(px+qy+rz+\frac{q}{\frac{p^2}{2}-1}t\right)}\right], \tag{3.180}$$

$$v_{3,38}(x,y,z,t) = \pm\sqrt{\frac{\frac{1}{2}q}{(-p^2r-2r)}}p\left[\frac{tanh\left(px+qy+rz+\frac{q}{\frac{-p^2}{2}-1}t\right)}{1 \pm sech\left(px+qy+rz+\frac{q}{\frac{-p^2}{2}-1}t\right)}\right], \tag{3.181}$$

$$v_{3,39}(x,y,z,t) = \pm\sqrt{\frac{\frac{1}{2}q}{r(-p^2-2)}}p\left[\frac{sech\left(px+qy+rz+\frac{2q}{p^2-2}t\right)}{sech\left(px+qy+rz+\frac{2q}{p^2-2}t\right)}\right]. \tag{3.182}$$

3.4.3. Shock wave solution

When $k \to 0$, in this category see in table 2, the solutions $v_{3,1}, v_{3,2}, v_{3,3}, v_{3,4}, v_{3,10}, v_{3,17}, v_{3,18}, v_{3,21}$ and $v_{3,25}$ become zero. The remaining solutions represent solitary wave solutions and can be determined as follows:

$$v_{3,40}(x,y,z,t) = \pm\sqrt{\frac{-q}{(p^2r+r)}}p\, csc\left(px + qy + rz + \frac{q}{-p^2-1}t\right), \tag{3.183}$$

$$v_{3,41}(x,y,z,t) = \pm\sqrt{\frac{-q}{(p^2r+r)}}psec\left(px + qy + rz + \frac{q}{-p^2-1}t\right), \tag{3.184}$$

$$v_{3,42}(x,y,z,t) = \pm\sqrt{\frac{-q}{(-p^2r-r)}}psec\left(px + qy + rz + \frac{q}{-p^2-1}t\right), \tag{3.185}$$

$$v_{3,43}(x,y,z,t) = \pm\sqrt{\frac{-q}{(-2p^2r+r)}}ptan\left(px + qy + rz + \frac{q}{2p^2-1}t\right), \tag{3.186}$$

$$v_{3,44}(x,y,z,t) = \pm\sqrt{\frac{-q}{(-2p^2r+r)}}pcot\left(px + qy + rz + \frac{q}{2p^2-1}t\right), \tag{3.187}$$

$$v_{3,45}(x,y,z,t) = \pm\sqrt{\frac{q}{(-p^2r-r)}}pcsc\left(px + qy + rz + \frac{q}{-p^2-1}t\right), \tag{3.188}$$

$$v_{3,46}(x,y,z,t) = \pm\sqrt{\frac{\frac{1}{2}q}{(p^2r-2r)}}p\left[csc\left(px + qy + rz + \frac{q}{\frac{p^2}{2}-1}t\right) \pm cot\left(px + qy + rz + \frac{q}{\frac{p^2}{2}-1}t\right)\right], \tag{3.189}$$

$$v_{3,47}(x,y,z,t) = \pm\sqrt{\frac{\frac{1}{2}q}{(p^2r-2r)}}p\left[sec\left(px + qy + rz + \frac{q}{\frac{p^2}{2}-1}t\right) \pm tan\left(px + qy + rz + \frac{q}{\frac{p^2}{2}-1}t\right)\right], \tag{3.190}$$

$$v_{3,48}(x,y,z,t) = \pm\sqrt{\frac{\frac{1}{2}q}{(-2p^2r-2r)}}\,p\left[csc\left(px + qy + rz + \frac{q}{-p^2-1}t\right) \pm csc\left(px + qy + rz + \frac{q}{-p^2-1}t\right)\right], \tag{3.191}$$

$$v_{3,49}(x,y,z,t) = \pm\sqrt{\frac{\frac{1}{2}q}{(p^2r-2r)}}\,p\left[\frac{sin\left(px+qy+rz+\frac{q}{\frac{-p^2}{2}-1}t\right)}{1 \pm cos\left(px+qy+rz+\frac{q}{\frac{-p^2}{2}-1}t\right)}\right], \tag{3.192}$$

$$v_{3,50}(x,y,z,t) = \pm\sqrt{\frac{q}{(2p^2r-2r)}}\,p\left[\frac{cos\left(px+qy+rz+\frac{q}{-p^2-1}t\right)}{1\pm sin\left(px+qy+rz+\frac{q}{-p^2-1}t\right)}\right], \tag{3.193}$$

$$v_{3,51}(x,y,z,t) = \pm\sqrt{\frac{q}{(p^2r-2r)}}\,p\,\frac{sin\left(px+qy+rz-\frac{qt}{\left(\frac{p^2}{2}-2\right)}\right)}{1\pm cos\left(px+qy+rz-\frac{qt}{\left(\frac{p^2}{2}-1\right)}\right)}. \tag{3.194}$$

4. GRAPHICAL RESULTS AND DISCUSSION

In this section, we present several solution figures in 2-D, 3-D, and contour plots. All of the figures were created using Mathematica. The generalized JEFE technique yields novel solutions to the nonlin ear three-dimensional Wazwaz-Benjamin-Bona-Mahony (3-D WBBM) equations, and its periodicity is proved. We illustrated many sorts of soliton structures, including steep kink, kink, peakon, rogue, and periodic soliton. The 2D plots show simplified cross-sections of the wave solutions, focusing on specific directions to highlight their oscillatory and (quasi-)periodic patterns. These views make it easier to observe changes in amplitude, phase, and frequency over time, helping us understand how the waves behave and evolve.

The 3D surface plots clearly display how the wave's height, frequency, and shape vary with different parameters, offering insights that are hard to see just from equations. Contour plots, which map the wave levels onto a flat surface, reveal the internal structure of the solutions, showing areas with steady values or sharp transitions. Together, these 2D, 3D, and contour plots give a fuller picture of the wave behaviors described by the 3D WBBM equations. Subsequently, the generalized JEFE process leads to more consistent results when addressing the WBBM equation, making it an effective tool for generating exact periodic and solitary wave-type soliton solutions.

Additionally, the Φ^6-expansion and modified extended direct algebraic methods [31], and Khater method [32] to compute trigonometric, hyperbolic, Jacobi elliptic, and rational functions. The expanded tanh approach [33] was also applied to the bright, dark, periodic, and single soliton solutions. To differentiate this from the previous efforts. All our founded solutions are depending on the Jacobi elliptic functions and their corresponding hyperbolic and trigonometric functions. Jacobi elliptic function is a more generalized form of the hyperbolic and trigonometric functions.

This work is important for our research because it shows how effective the generalized Jacobi elliptic function expansion method is in analyzing and resolving intricate nonlinear systems. The technique advances our knowledge of the dynamics at play in nonlinear systems by producing precise and physically meaningful solutions as well as making complex wave phenomena like solitons easier to visualize. The Jacobi elliptic function expansion approach is a strong and flexible tool for studying nonlinear wave dynamics.

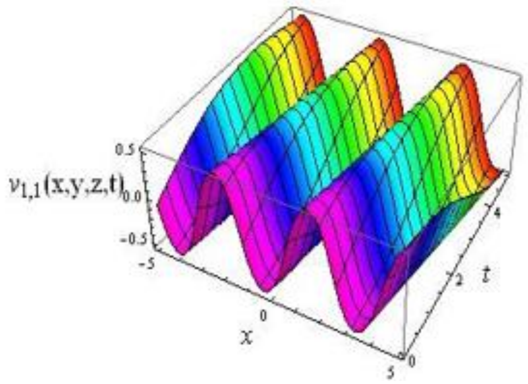

a) 3-D visualization

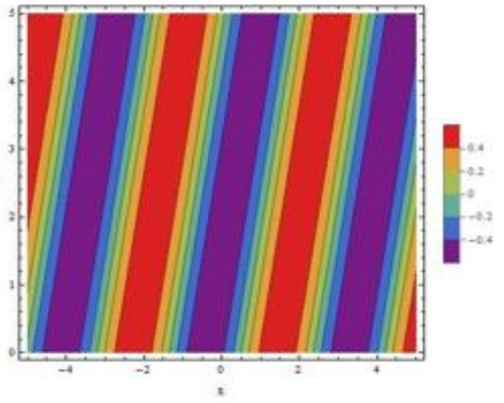

b) Contour figure

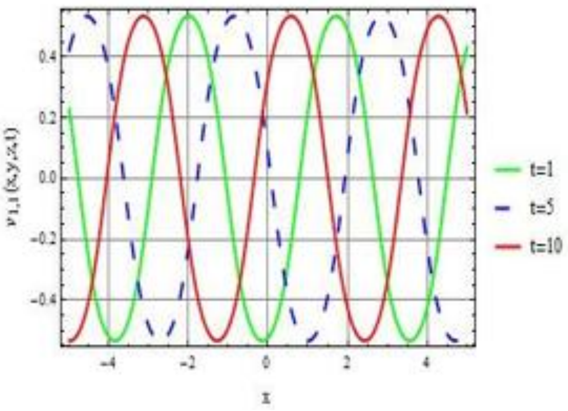

c) The time 2-D plot for t=1,5 and 10

Fig.1. The 3-D visualization, contour plot, and 2-D graphical representation of $v_{1,1}(x, y, z)$ are presented for the parameter values $k = 0.5$, $r = 1$, $p = 2$, $q = -2$, and $y = z = 1$

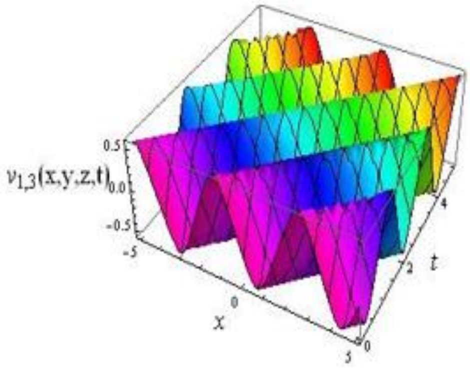

a) 3-D visualization

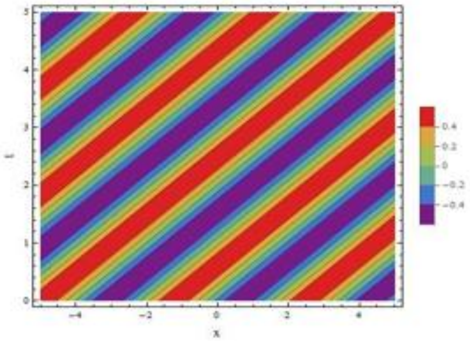

b) contour figure

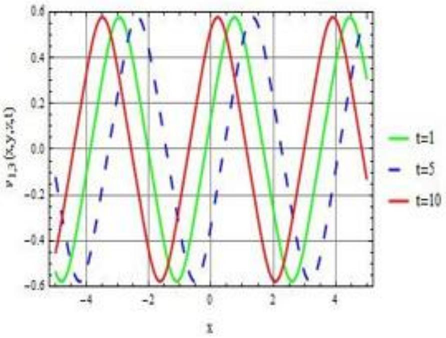

c) the time 2-D plot for t=1,5 and 10

Fig. 2. The 3-D visualization, contour plot, and 2-D graphical representation of v1,3(x, y, z) are presented for the parameter values k = 0.5, r = 0.5, p = 2, q = 2, and y = z = 1

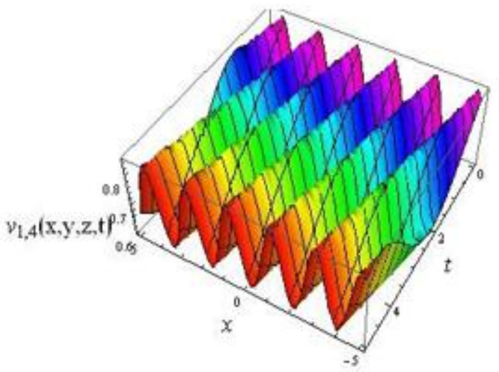

a) 3-D visualization

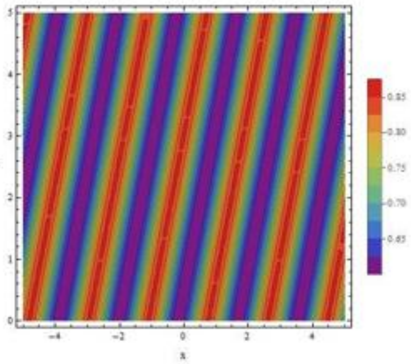

b) contour figure

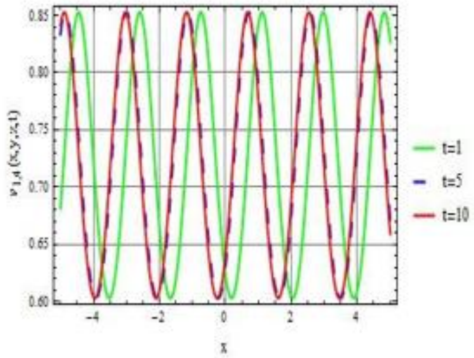

c) the time 2-D plot for t=1,5 and 10

Fig.3. The 3-D visualization, contour plot, and 2-D graphical representation of $v_{1,4}(x, y, z)$ are presented for the parameter values$k = 0.5$, $r = 0.5$, $p = 2$, $q = -2$, and $y = z = 1$

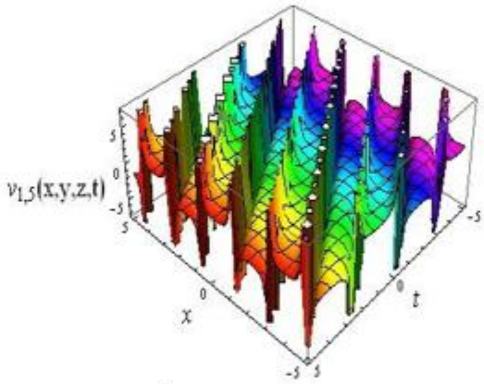

a) 3-D visualization

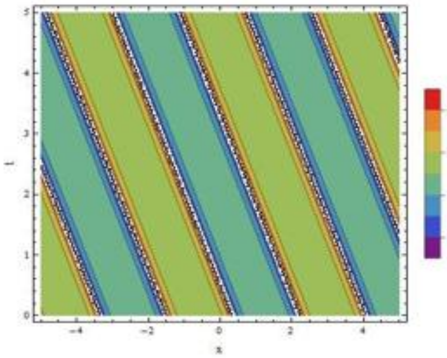

b) contour figure

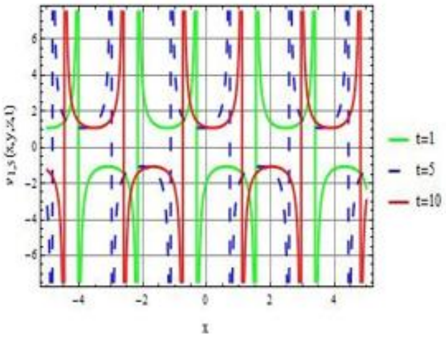

c) the time 2-D plot for t=1,5 and 10

Fig.4. The 3-D visualization, contour plot, and 2-D graphical representation of $v_{1,5}(x,y,z)$ are presented for the parameter values $k = 0.5$, $r = 1$, $p = 2$, $q = 2$, and $y = z = 1$

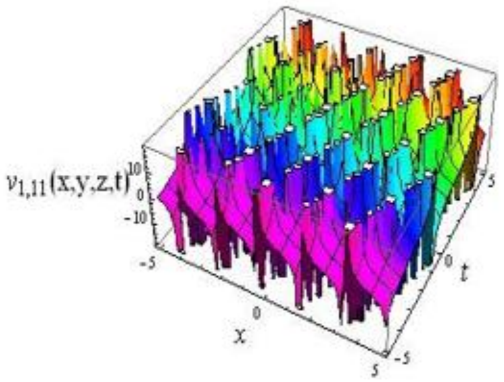

a) 3-D visualization

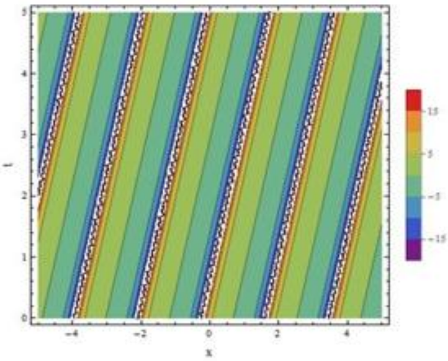

b) contour figure

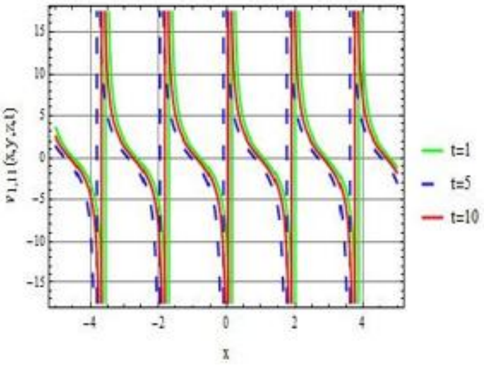

c) the time 2-D plot for t=1,5 and 10

Fig.5. The 3-D visualization, contour plot, and 2-D graphical representation of $v_{1,11}(x,y,z)$ are presented for the parameter values $k = 0.5$, $r = 1.5$, $p = -2$, $q = -2$, and $y = z = 1$

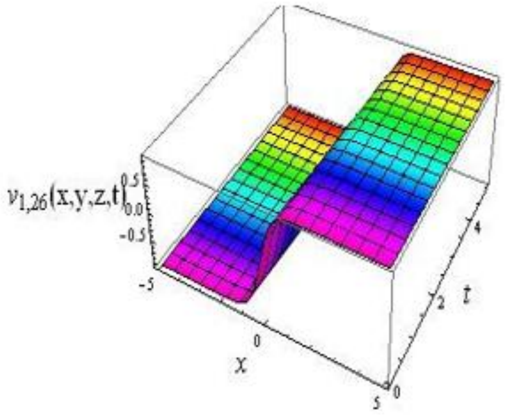

a) 3-D visualization

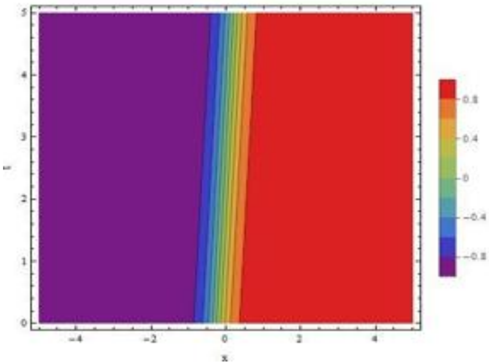

b) contour figure

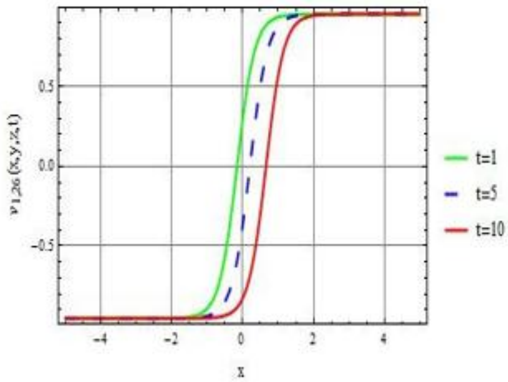

c) the time 2-D plot for t=1,5 and 10

Fig.6. The 3-D visualization, contour plot, and 2-D graphical representation of $v_{1,26}(x,y,z)$ are presented for the parameter values $r = 2.5$, $p = 2$, $q = -2$, and $y = z = 1$

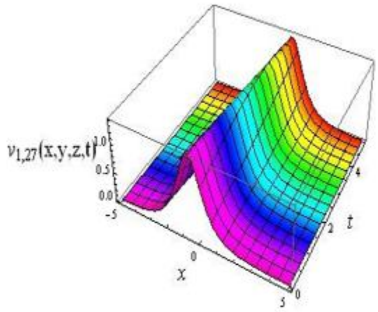

a) 3-D visualization

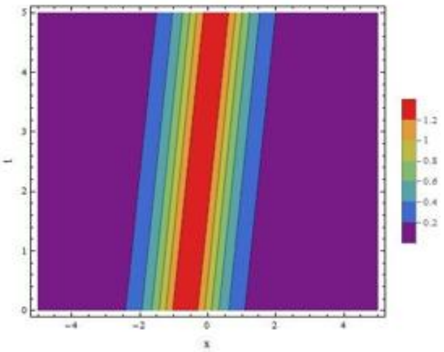

b) contour figure

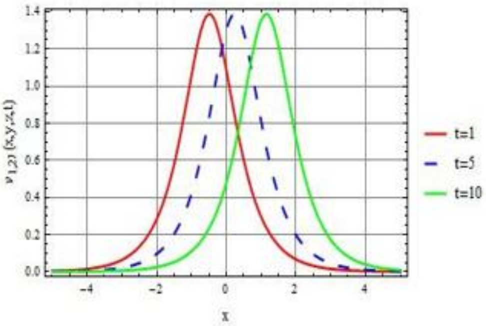

c) the time 2-D plot for t=1,5 and 10

Fig. 7. The 3-D visualization, contour plot, and 2-D graphical representation of $v_{1,27}(x, y, z)$ are presented for the parameter values $r = 3$, $p = 1.5$, $q = -2$, and $y = z = 1$

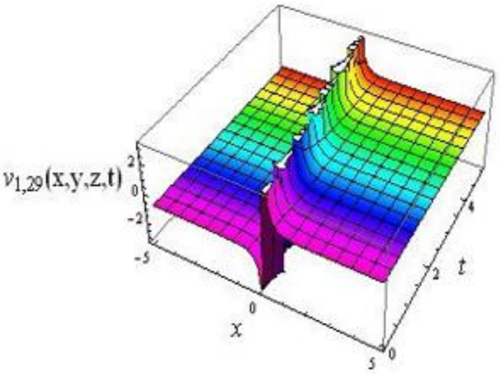

a) 3-D visualization

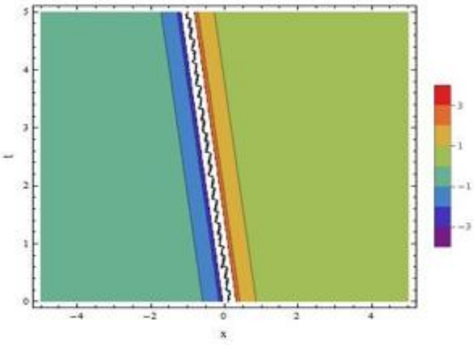

b) contour figure

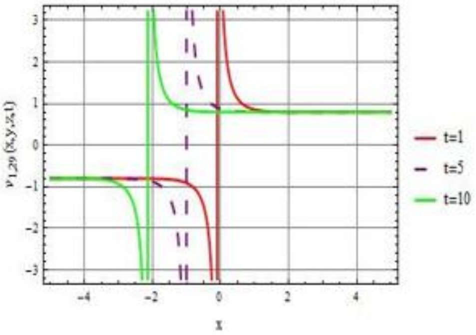

c) the time 2-D plot for t=1,5 and 10

Fig.8. The 3-D visualization, contour plot, and 2-D graphical representation of $v_{1,29}(x, y, z)$ are presented for the parameter values $r = 1.8$, $p = 1.5$, $q = -2$, and $y = z = 1$

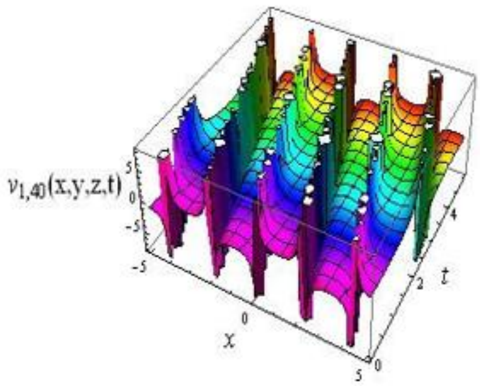

a) 3-D visualization

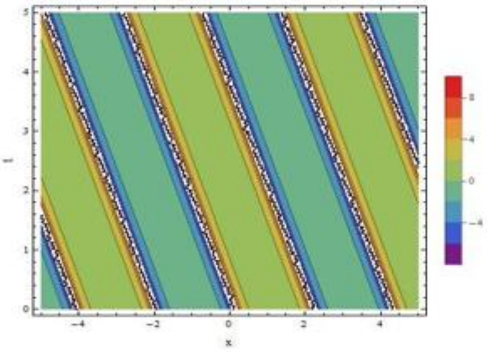

b) contour figure

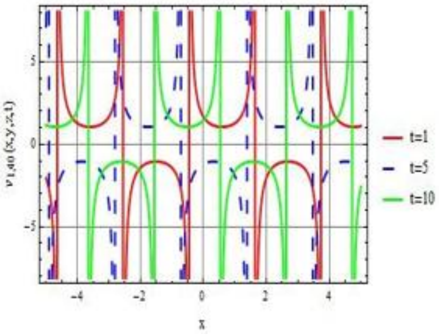

c) the time 2-D plot for t=1,5 and 10

Fig. 9. The 3-D visualization, contour plot, and 2-D graphical representation of $v_{1,40}(x, y, z)$ are presented for the parameter values $r = 1.8$, $p = 1.5$, $q = -2$, and $y = z = 1$

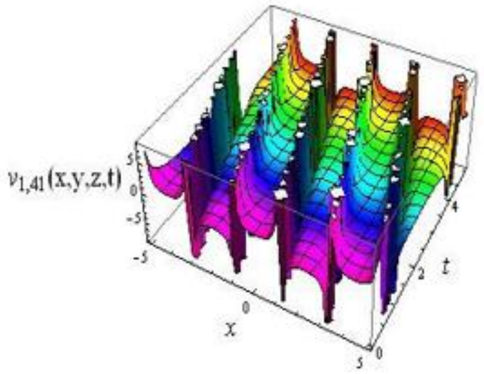

a) 3-D visualization

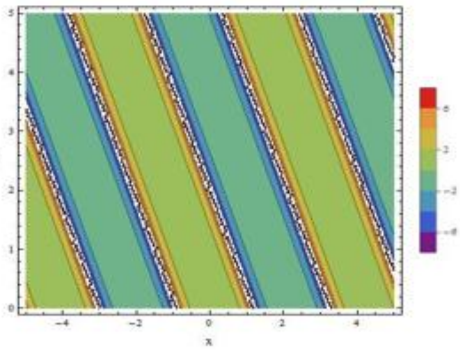

b) contour figure

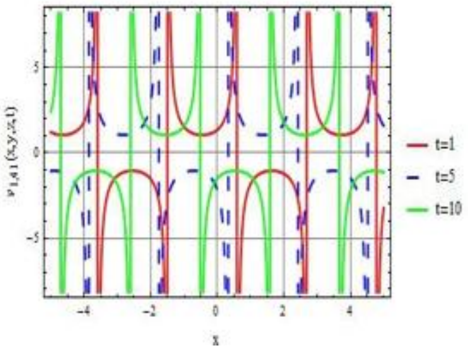

c) the time 2-D plot for t=1,5 and 10

Fig.10. The 3-D visualization, contour plot, and 2-D graphical representation of $v_{1,41}(x, y, z)$ are presented for the parameter values $r = 1.8$, $p = 1.5$, $q = -2$, and $y = z = 1$

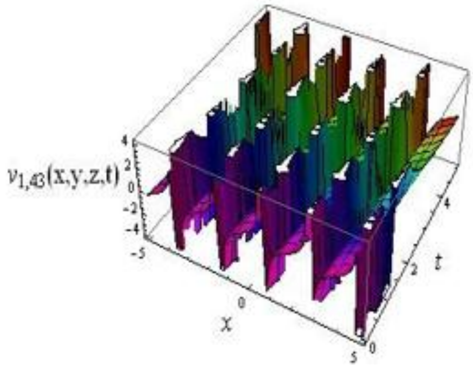

a) 3-D visualization

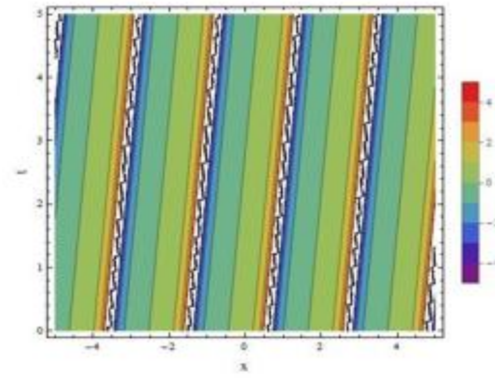

b) contour figure

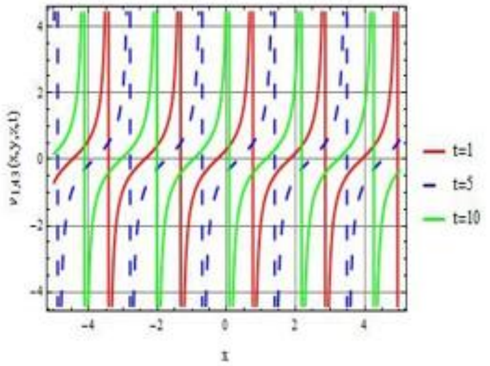

c) the time 2-D plot for t=1,5 and 10

Fig.11. The 3-D visualization, contour plot, and 2-D graphical representation of $v_{1,43}(x, y, z)$ are presented for the parameter values $r = 1.8$, $p = 1.5$, $q = 2$, and $y = z = 1$

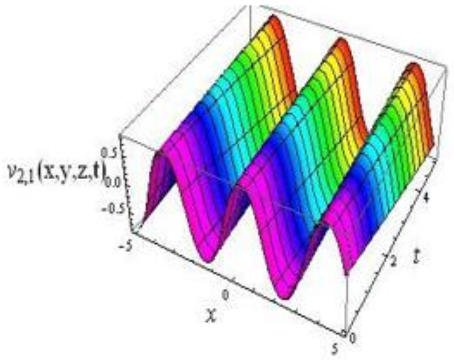

a) 3-D visualization

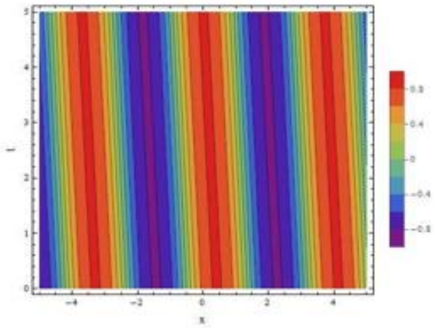

b) contour figure

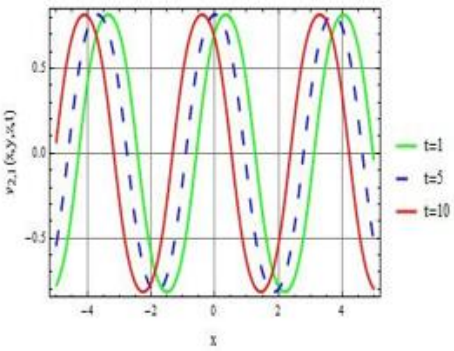

c) the time 2-D plot for t=1,5 and 10

Fig.12. The 3-D visualization, contour plot, and 2-D graphical representation of $v_{2,1}(x, y, z)$ are presented for the parameter values $k = 0.5$, $r = -1$, $p = 2$, $q = 2$, $y = 1$, and $z = 1$

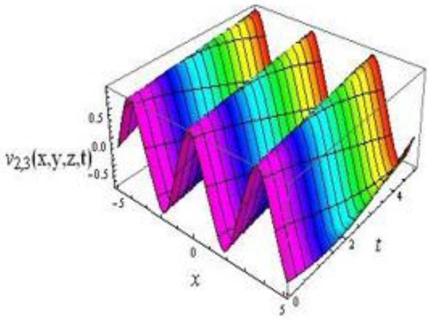

a) 3-D visualization

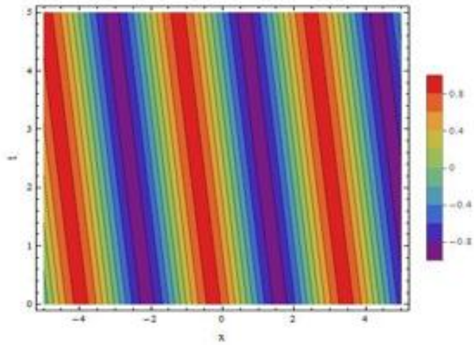

b) contour figure

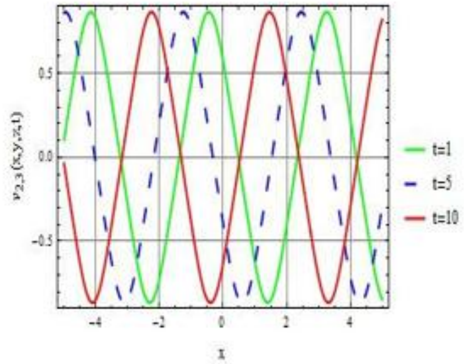

c) the time 2-D plot for t=1,5 and 10

Fig.13. The 3-D visualization, contour plot, and 2-D graphical representation of $v_{2,3}(x, y, z)$ are presented for the parameter values $k = 0.5$, $r = -1$, $p = 2$, $q = 1.5$, $y = 1$, and $z = 1$

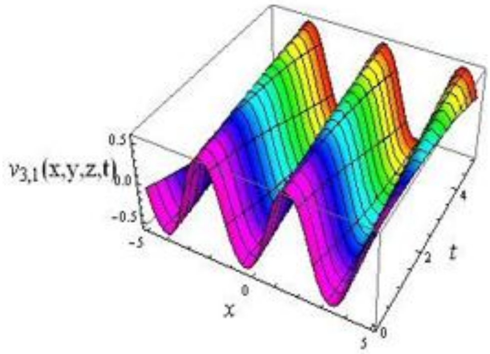

a) 3-D visualization

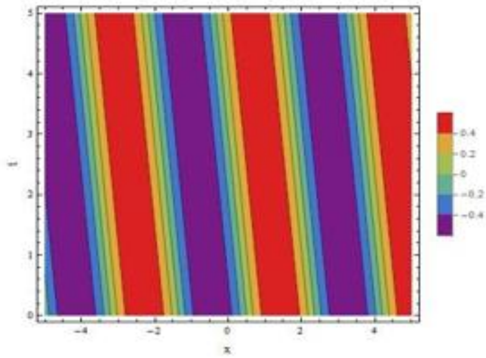

b) contour figure

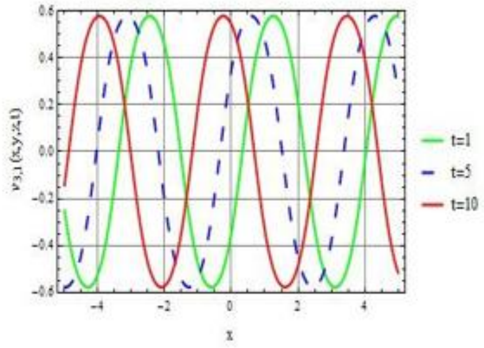

c) the time 2-D plot for t=1,5 and 10

Fig.14. The 3-D visualization, contour plot, and 2-D graphical representation of $v_{3,1}(x, y, z)$ are presented for the parameter values $k = 0.5$, $r = 1$, $p = 2$, $q = -2$, $y = 1$, and $z = 1$

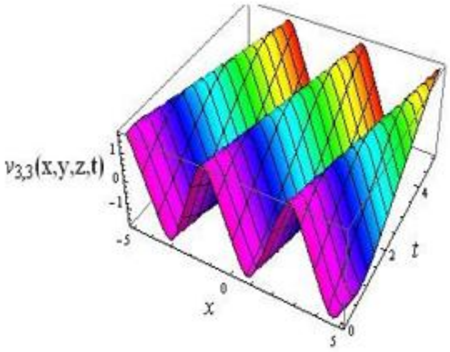

a) 3-D visualization

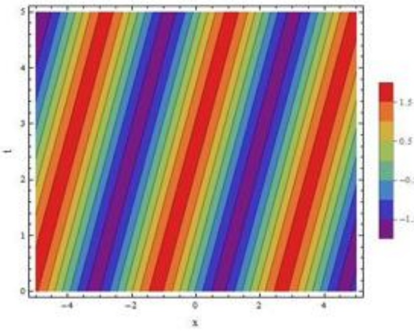

b) contour figure

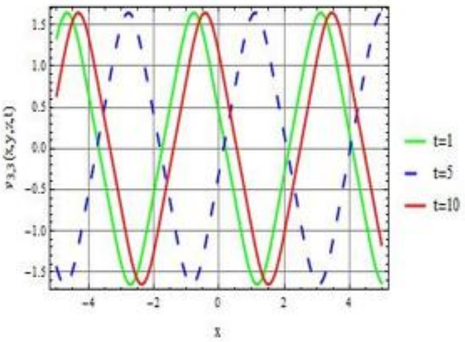

c) the time 2-D plot for t=1,5 and 10

Fig.15. The 3-D visualization, contour plot and 2-D graphical representation of $v_{3,3}(x, y, z)$ are presented for the parameter values $k = 0.6$, $r = 0.5$, $p = 2$, $q = 2$, and $y = z = 1$

5. CONCLUSION

The family of 3-D WBBM equations is efficiently solved in this work through the application of the generalized Jacobi elliptic function expansion technique. Through this method, the new periodic solutions are determined, which incorporates both solitary wave and shock wave solutions that have not been documented previously in the literature. These results give a greater understanding of the rich dynamic phenomena regulated by the family of 3-D WBBM equations, improving their applicability in fluid dynamics, nonlinear optics, plasma physics, and engineering. The obtained results have not been found in previous literature using this approach. To improve the physical description of the solutions several typical wave profiles are offered to provide a comprehensive analysis of the wave characteristics in 2-D, 3-D, and contour visualizations were generated using accurate parameters value with the help of Mathematica. Such graphical visualizations aid in our ability to more clearly understand and comprehend the system's inherent features. The objective of this approach is quite applicative and powerful to analyze various soliton solutions, therefore it may be additionally applicable to many other nonlinear evaluation equations. Future research direction should focus to apply these approaches to additional complicated nonlinear systems to determine their broader application. Furthermore, investigating the stability and interactions of the generated solutions under different initial conditions and parameter changes might provide additional information. Furthermore, incorporating physics-informed neural networks represents a promising avenue for validating these solutions in practical applications, with the potential to bridge the gap between theoretical mathematics and real-world implementations in fields such as fluid dynamics, plasma physics, and engineering systems.

REFERENCES

1. Qasim M, Yao F, Baber MZ, Younas U. Investigating the higher dimensional kadomtsev-petviashvili-sawada-kotera-ramani equation: Exploring the modulation instability, jacobi elliptic and soliton solutions. Physica Scripta. 2024.
2. Hamza A, Suhail M, Alsulami A, Mustafa A, Aldwoah K, Saber H. Exploring soliton solutions and chaotic dynamics in the (3+1)-dimensional wazwaz-benjamin-bona-mahony equation: A generalized rational exponential function approach. Fractal and Fractional. 2024:592.
3. Rahman Z, Ali MZ, Harun-Or-Roshid, Ullah MS. Analytical solutions of two space-time fractional nonlinear models using jacobi elliptic function expansion method. 2021.
4. Alam MN, Hafez MG, Akbar MA, Harun-Or Roshid. Exact traveling wave solutions to the (3+1)-dimensional mkdv-zk and the (2+1)-dimensional burgers equations via exp(-ϕ(ξ))-expansion method. Elsevier BV. 2015.
5. Hafez MG. Exact solutions to the (3+1)-dimensional coupled klein–gordon–zakharov equation using exp(-ϕ(ξ))-expansion method. Elsevier BV. 2016.
6. Akbar MA, Ali NHM, Zayed EME. A generalized and improved (G'/G)-expansion method for nonlinear evolution equations. Hindawi Publishing Corporation. 2012.
7. Alzaidy JF. The (G'/G)-expansion method and travelling wave solutions for some nonlinear pdes. Am J Math Anal. 2013;1(3):28–32.
8. Li X. Applications of F-expansion to periodic wave solutions for kdv equation.
9. Li BA, Wang ML. Applications of f-expansion method to the coupled kdv system. 2005.
10. Almatrafi M. Solitary wave solutions to a fractional model using the improved modified extended tanh-function method. Fractal and Fractional. 2023:252.
11. Zahran EHM, Khater MMA. Modified extended tanh-function method and its applications to the bogoyavlenskii equation. Applied Mathematical Modelling. 2016;40(3):1769–1775.
12. Kumar S, Mohan B. A novel and efficient method for obtaining Hirota's bilinear form for the nonlinear evolution equation in (n+1) dimensions. Partial Differential Equations in Applied Mathematics. 2022;5:100274.
13. Ma WX. Soliton solutions by means of Hirota bilinear forms. Partial Differential Equations in Applied Mathematics. 2022;5:100220.
14. Mahak N, Akram G. Extension of rational sine-cosine and rational sinh-cosh techniques to extract solutions for the perturbed nlse with kerr law nonlinearity. The European Physical Journal Plus. 2019;134.
15. Joseph S. Exact traveling wave doubly periodic solutions for generalized double sine-gordon equation. International Journal of Applied and Computational Mathematics. 2022;8.
16. Ray S. New analytical exact solutions of time fractional kdv–kzk equation by kudryashov methods. Chinese Physics B. 2016;25:040204.
17. Sadighi A, Ganji DD. Exact solutions of nonlinear diffusion equations by variational iteration method. Computers Mathematics with Applications. 2007;54:1112–1121.
18. Sahoo S, Ray S, Abdou M. New exact solutions for time-fractional kaup-kupershmidt equation using improved (G'/G)-expansion and extended (G'/G)-expansion methods. Alexandria Engineering Journal. 2020;59.
19. Naher H, Abdullah FA. New generalized and improved (G'/G)-expansion method for nonlinear evolution equations in mathematical physics. Journal of the Egyptian Mathematical Society. 2014;22(3):390–395.
20. Yang XF, Deng ZC, Wei Y. A riccati-bernoulli sub-ode method for nonlinear partial differential equations and its application. Advances in Difference Equations. 2015.
21. Kumar S, Kumar A, Wazwaz AM. New exact solitary wave solutions of the strain wave equation in microstructured solids via the generalized

exponential rational function method. European Physical Journal Plus. 2020;135.
22. Wazwaz AM. Exact soliton and kink solutions for new (3+1)-dimensional nonlinear modified equations of wave propagation. Open Engineering. 2017;7(1):169–174.
23. Javeed S, Imran T, Ahmad H, Tchier F, Zhao YH. New soliton solutions of modified (3+1)-d wazwaz–benjamin–bona–mahony and (2+1)-d cubic klein–gordon equations using first integral method. Open Physics. 2023;21.
24. Zayed EME, Abdelaziz MAM. The modified exp-function method and its applications to the generalized k (n, n) and bbm equations with variable coefficients. Iranian Journal of Science. 2014;36:359–365.
25. Hamza AE, Suhail M, Alsulami A, Mustafa A, Aldwoah K, Saber H. Exploring soliton solutions and chaotic dynamics in the (3+1)-dimensional wazwaz–benjamin–bona–mahony equation: A generalized rational exponential function approach. Fractal and Fractional. 2024;8(10).
26. Mamun AA, Ananna SN, An T, Asaduzzaman M, Rana MS. Sine-Gordon expansion method to construct the solitary wave solutions of a family of 3D fractional WBBM equations. Results in Physics. 2022;40:105845.
27. Ullah N, Asjad MI, Hussanan A, Akgül A, Alharbi WR, Algarni H, Yahia IS. Novel waves structures for two nonlinear partial differential equations arising in the nonlinear optics via sardar-subequation method. Alexandria Engineering Journal. 2023;71:105–113.
28. Demirbilek U. On the solitary wave solutions of different versions of fractional 3d-wazwaz-benjamin-bona-mahony equations. İstanbul Ticaret Üniversitesi Fen Bilimleri Dergisi. 2023;22.
29. Akram, Seadawy RA, Rizvi STR, Younis M, Althobaiti S, Sayed S. Traveling wave solutions for the fractional Wazwaz–Benjamin–Bona–Mahony model in arising shallow water waves. Results in Physics. 2021;20.
30. Siddique I, Mehdi KB, Jarad F, Elbrolosy ME, Elmandouh AA. Novel precise solutions and bifurcation of traveling wave solutions for the nonlinear fractional (3 + 1)-dimensional wbbm equation. International Journal of Modern Physics B. 2023;37(02):2350011.
31. Bilal M, Ahmad J, et al. New exact solitary wave solutions for the 3d-fwbbm model in arising shallow water waves by two analytical methods. Results in Physics. 2021;25:104230.
32. Ali A, Ahmad J, Javed S. Solitary wave solutions for the originating waves that propagate of the fractional wazwaz-benjamin-bona-mahony system. Alexandria Engineering Journal. 2023;69:121–133.
33. Ahmad J, Rani S, Turki NB, Shah NA. Novel resonant multi-soliton solutions of time fractional coupled nonlinear schrödinger equation in optical fiber via an analytical method. Results in Physics. 2023;52:106761.
34. Qasim M, Yao F, Baber MZ, Younas U. Investigating the higher dimensional Kadomtsev–Petviashvili–Sawada–Kotera–Ramani equation: exploring the modulation instability, Jacobi elliptic and soliton solutions. Physica Scripta. 2025;100(2):025215.
35. Farooq A, Khan MI, Nisar KS, Shah NA. A detailed analysis of the improved modified Korteweg-de Vries equation via the Jacobi elliptic function expansion method and the application of truncated M-fractional derivatives. Results in Physics. 2024;59:107604.
36. Khan MI, Asghar S, Sabi'u J. Jacobi elliptic function expansion method for the improved modified kortwedge-de vries equation. Optical and Quantum Electronics. 2022;54(11):734.
37. Khan MI, Khan A, Farooq A. Analyzing the Kuralay-II equation: bifurcation, chaos, and sensitivity insights through conformable derivative and Jacobi elliptic function expansion. Physica Scripta. 2024;99(9):095210.
38. Khan MI, Faridi WA, Murad MAS, Iqbal M, Myrzakulov R, Umurzakhova Z. The formation and propagation of soliton wave profiles for the Shynaray-IIA equation. acta mechanica et automatica. 2025;19(1).
39. El-Sabbagh M, Ali A. New generalized jacobi elliptic function expansion method. Communications in Nonlinear Science and Numerical Simulation. 2008;13:1758–1766.
40. Farooq A, Ma WX, Ishfaq M. Exploring exact solitary wave solutions of kuralay-ii equation based on the truncated m-fractional derivative using the jacobi elliptic function expansion method. Optical and Quantum Electronics. 2024;56.
41. Al-Muhiameed Z, Abdel-Salam E. Research article generalized jacobi elliptic function solution to a class of nonlinear schrodinger-type equations. Journal of Applied Mathematics. 2011;11.
42. Lai S, Lv X, Shuai M. The Jacobi elliptic function solutions to a generalized Benjamin–Bona–Mahony equation. Mathematical and computer Modelling. 2009;49(1-2):369–378.

Authors are thankful to Hohai University, Nanjing 21100, Jiangsu, P.R, China for supporting this research work.

Muhammad Ishfaq Khan: https://orcid.org/0009-0002-2160-9002

Kalim Ullah: https://orcid.org/0009-0006-6753-8552

DOI 10.2478/ama-2025-0049

AN INFLUENCE OF CROSS-SECTIONAL FEATURES ON THE STABILITY AND LOAD-CARRYING CAPACITY OF CARBON-EPOXY COMPOSITE STRUCTURES

Patryk RÓŻYŁO[*], **Kuba ROSŁANIEC**[*]

[*]Faculty of Mechanical Engineering, Department of Machine Design and Mechatronics, Lublin University of Technology,
Nadbystrzycka 36, 20-618 Lublin, Poland

p.rozylo@pollub.pl, kuba.roslaniec@pollub.edu.pl

received 08 April 2025, revised 21 August 2025, accepted 27 August 2025

Abstract: The paper aims experimental-numerical approaches to the behaviour of the compressed thin-walled composite profiles with closed sections. For this, thin-walled composite profiles made of carbon-epoxy composite from the autoclave technique. It was to analyse the effect of cross-section shape on the stability and fracture of composite structures. This was covered through a universal testing machine, an optical deformation measurement system, acoustic emission method as well as a microscope. Numerical simulations were carried out using the finite element method (based on progressive failure analysis). The research follows the project from the National Science Centre in Poland, Reg. No. 2021/41/B/ST8/00148.

Key words: numerical approach, experimental study, progressive failure analysis, buckling, fracture

1. INTRODUCTION

Thin-walled composite profiles belong to the group of load-carrying structures which have special features. They present low mass, at maintaining high mechanical resistance. These types of profiles can have an open or closed cross-sectional shape [1-3]. This kind of composite structure under loading is considered in many research groups [4-6]. It is taken at the isotropic features of the material kind. For these cases, approximation methods are employed, while in the case of numerical approaches the solution of a linear eigenproblem is used [7-8]. From a scientific point of view, it is important to evaluate the behaviour of thin-walled structures after stability lossing. Consequently, it is important to analyse the post-buckling behaviour for analysis of damages and changes in load-carrying capacity [9-11]. This can be supported by the acoustic emission method, while in the case of numerical simulations this is covered by damage initiation criteria, such as the Hashin one [12-13]. This enables to capture a force value at the first stage of damage occurrence [14]. Worth noticing, an in-depth analysis of the complex failure mechanism of the composite structure, where both experimental studies and numerical simulations (using, for example, progressive failure analysis) make it possible to assess the reduction load-carrying capacity [15-18]. Approaches for the composite type in the experiment can be reached using: universal testing machine, acoustic emission, optical deformation measurement system, while in the case of numerical simulations the finite element method (using advanced failure models) plays an important role [19-21]. This reflects, a composite type is analysed utilising different experimental and numerical approaches, but this does not cover the influence of the cross-section geometry on its behaviour under compression force.

Therefore, the paper focuses on a composite behaviour in the form of a thin-walled rectangular tube under compressive force at different dimensions of cross-sections.

2. THE SUBJECT OF STUDY

Additional novelty is the object of research in the form of thin-walled carbon-epoxy composite structures with varying strength and stiffness of the structure - manufactured within the framework of a project from the National Science Centre, Reg. No. 2021/41/B/ST8/00148. Thin-walled columns made of carbon-fiber epoxy composite (CFRP). The selected type of composite was determined on the basis of preliminary numerical simulations and experimental tests. The total number of specimens was equal to 9. Each specimen group collected three pieces at the following dimensions of a cross-section: A - 40x40 mm, B - 50x30 mm and C - 60x20 mm, Fig 1. The composite profiles had some common features/properties, such as: lay-up [0°/90°/0°/90°]s, properties, height of 200 mm, and the same wall-thickness the cross-section shapes' circuit.

The composite specimens were manufactured using an autoclave technique, and details of the manufacturing process [22]. With reference to the fundamental features of the cross-sections: the moment of inertia of the A-type square profile equals 58,033.51 mm4, of B-type rectangular profile equal 37,351.34 mm4 (in the first direction) and 78,715.68 mm4 (in the second direction), of C-type rectangular profile equal 19,149.18 mm4 (in the first direction) and 96,917.85 mm4 (in the second direction), while the moment of resistance (strength index) of the A-type profile equals 2,732.27 mm3, of B-type profile equal 2,299,96 mm3 (in the first direction) and 2,999.84 mm3 (in the second direction), of C-type profile equal 1,703.66 mm3 (in the first direction) and 3,102.36 mm3 (in the second direction).

The cross-sectional area for all three types of profiles was the same - 204.55 mm2.

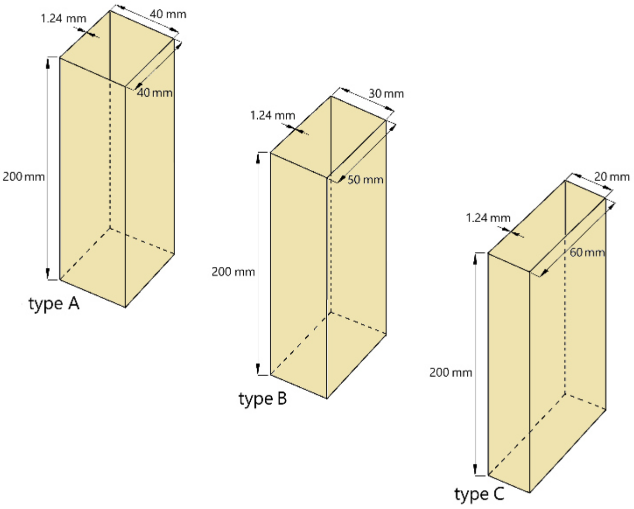

Fig. 1. Test specimens

3. EXPERIMENTAL AND NUMERICAL APPROACHES

The fundamental approach to the composite tubes was presented in [22]. In this tests were carried out at room temperature at constant value of displacement velocity of 2mm/min. The component behaviour was followed at different levels of loading, analysing a load-capacity reduction. At the post-buckling equilibrium paths, the value of the critical force was determined based on the straight intersection method [7] - taking into account the force-displacement curve (shortening of the structure). The non-contact optical digital image correlation system (Aramis 2D) for measuring the deformation in 2D coordinate system was used, Fig. 2 [23] (during the study, only the 2D version of the DIC system was available). The acoustic emission method was employed, within the framework of the use of the AMSY-5 [24] type apparatus and a piezoelectric sensor directly mounted to the test specimen captured results. This made it possible to register acoustic signals (such as energy, amplitude, etc.) in order to identify the damage-initiating force of composite structures. A digital microscope Keyence VHX-970F [25] with a mobile head was also used for damage analysis.

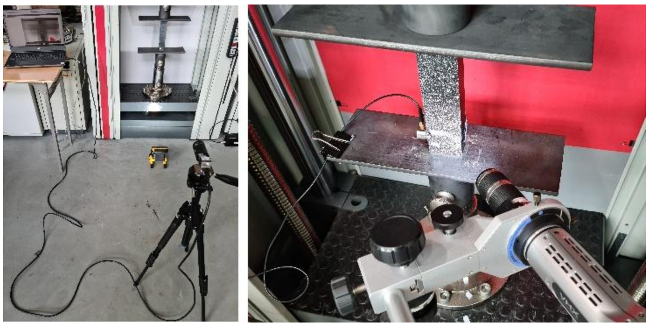

Fig. 2. Specimen in the Z100 Zwick electromechanical testing machine at DIC system

The DIC system included a high resolution camera of 4096 px × 3000 px. This enabled to capture 12Mpx images at frequency 25 Hz. The main objective of the experimental study was to determine the buckling force value, damage-initiation, and force at fracture. Buckling force were determined in accordance with the previously mentioned method of intersecting straight lines – using the post-buckling equilibrium paths [2]. The damage initiation was strongly related to the acoustic emission signal [9,10]. The forces values corresponding to the loss of load-carrying capacity were determined directly from the post-buckling equilibrium paths, as the maximum value [12].

For numerical simulations, the analysis of stability and load-carrying capacity phenomena were carried out using the finite element method in Abaqus. Consequently, the loss of stability was determined using a linear solution of the eigenproblem, while the fracture phenomenon was captured using a nonlinear analysis at a progressive fracture analysis model.

The solution of the linear eigenvalue problem was closely related to the equation [26]:

$$(K_0^{NM} + \lambda_i K_\Delta^{NM}) v_i^M = 0 \tag{1}$$

where: K_0^{NM} is the matrix stiffness (which includes the effects of the preloads P^N), K_Δ^{NM} refers the differential initial stress (and load stiffness matrix due to the incremental loading pattern Q^N), λ_i constitutes the eigenvalues, v_i^M is the buckling mode shapes (eigenvectors), ^{M} and ^{N} are degrees of freedom M and N (of the whole model), $_i$ refers to the $_i$th buckling mode. Furthermore, the buckling forces represent then $P^N + \lambda_i Q^N$.

It was possible to determine the value of the buckling force and the buckling form corresponding to this force - which was consequently implemented in a nonlinear analysis using the Newton-Raphson method [16]. Simulations of nonlinear stability were carried out considering the lowest numerically obtained form of buckling (corresponding to experimental tests), taking into account geometric imperfections with an amplitude of 0.05 of the wall thickness of the composite structure. Simulations considering the phenomenon of damage initiation and further damage evolution were carried out by using progressive fracture analysis [27] - where damage initiation represented by the Hashin criterion [28,29], and damage evolution expressed by the energy criterion. The damage initiation criterion enabled to determine a stress type (tensile or compressive) in the degradation of the composite components:

$$F_f^t = \left(\frac{\hat{\sigma}_{11}}{X^T}\right)^2 + \alpha\left(\frac{\hat{\tau}_{12}}{S^L}\right)^2 = 1, (\hat{\sigma}_{11} \geq 0), \tag{2}$$

$$F_f^c = \left(\frac{\hat{\sigma}_{11}}{X^C}\right), (\hat{\sigma}_{11} < 0), \tag{3}$$

$$F_m^t = \left(\frac{\hat{\sigma}_{22}}{Y^T}\right)^2 + \left(\frac{\hat{\tau}_{12}}{S^L}\right)^2 = 1, (\hat{\sigma}_{22} \geq 0), \tag{4}$$

$$F_m^c = \left(\frac{\hat{\sigma}_{22}}{2S^T}\right)^2 + \left[\left(\frac{Y^C}{2S^T}\right)^2 - 1\right]\frac{\hat{\sigma}_{22}}{Y^C} + \left(\frac{\hat{\tau}_{12}}{S^L}\right)^2 = 1, (\hat{\sigma}_{22} < 0) \tag{5}$$

where: X^T,X^C,Y^T,Y^C,S^L,S^T denotes the coefficients of the longitudinal tensile/compressive, transverse tensile/compressive, longitudinal/transverse shear strength; α represents the contribution of the shear stress; $\hat{\sigma}_{11}, \hat{\sigma}_{22}, \hat{\tau}_{12},$ represents the components of the effective stress tensor (which is used to evaluate the damage initiation criteria).

After the fulfillment of any one component of damage initiation, a phenomenon known as damage evolution begins during further loading of the structure. The damage evolution law is based on the fact that fracture energy is released during damage. It is necessary to determine the parameters responsible for the damage energy parameters (energy dissipation parameters due to the tension and compression of the fibers, as well as the tension and compression of the matrix) [27]. The numerical model was elaborated using Continuum Shell - SC8R (composite structure) and Shell - R3D4 (non-deformable plates that provide supports) finite elements. The continuum shell model takes into account the physical thickness of the composite material. This provides the ability to virtually design the number of plies relative to the physical thickness, taking into account the relative thickness of the ply. The Continuum Shell composite modeling technique reflects the physical wall thickness of the composite structure and simultaneously enables analysis of the structure's behavior - ply by ply. For the numerical model, the boundary conditions were reflected as accurately as possible. Between the non-deformable plate elements (where boundary conditions were defined) and the composite structure, contact interactions were defined in the normal and tangential directions (with a defined friction coefficient of 0.2). The material properties were consistent with the parameters determined experimentally and presented in previously-mentioned publication [22]. In the framework of numerical studies, the effect of mesh density on the accuracy of calculation results was analyzed [3] - on the basis of which it was estimated that the mesh that allows the most accurate representation of experimental results in the case of a composite structure was selected at the level of the previously mentioned size - 2mm. Regardless of the shape of the cross section (where the sum of the lengths of the edges creating the cross sections was constant), each numerical model had 10320 finite elements and 19802 computational nodes. The discrete model with boundary conditions is shown in Figure 3. The compression was realized by moving the upper plate.

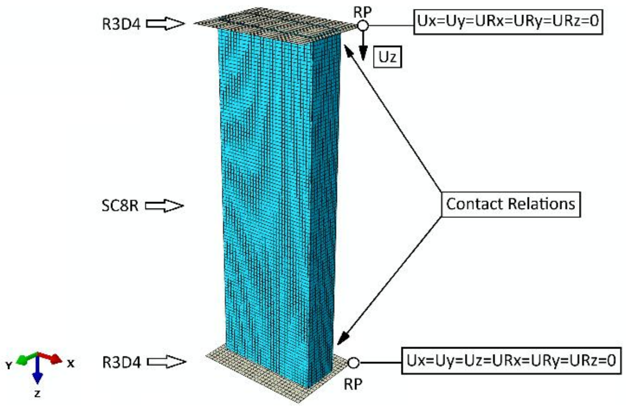

Fig. 3. Numerical model (with boundary conditions)

4. RESULTS

In the case of both experimental and FEM approaches the values of buckling forces and the corresponding buckling forms were determined at their eariler stage. In the case of experimental studies, the values of buckling forces were determined using the previously mentioned method of intersecting straight lines. The non-linear section of the force-shortening relationship was related to a specimen's response to the applied force.

Figure 4 presents only one determined buckling force value from each type of cross section. For the other specimens, the buckling force values were determined analogously (as presented in Table 1). The approximation ranges, representing lines of black color, were selected so as to make the correlation coefficient as high as possible [8]. In the case of numerical simulations, the buckling force values were determined by solving a linear eigenproblem (determined the buckling force value). Figure 5 presents a qualitative comparison of the forms of loss of stability, as well as shows the numerically obtained values of buckling forces. The results shown in Figure 5, recorded using the ARAMIS 2D system, show the relative deformation in the longitudinal direction, while FEM showed deformation in the framework of a linear eigenproblem. The results were compared only in terms of qualitative aspects, showing the same type of buckling.

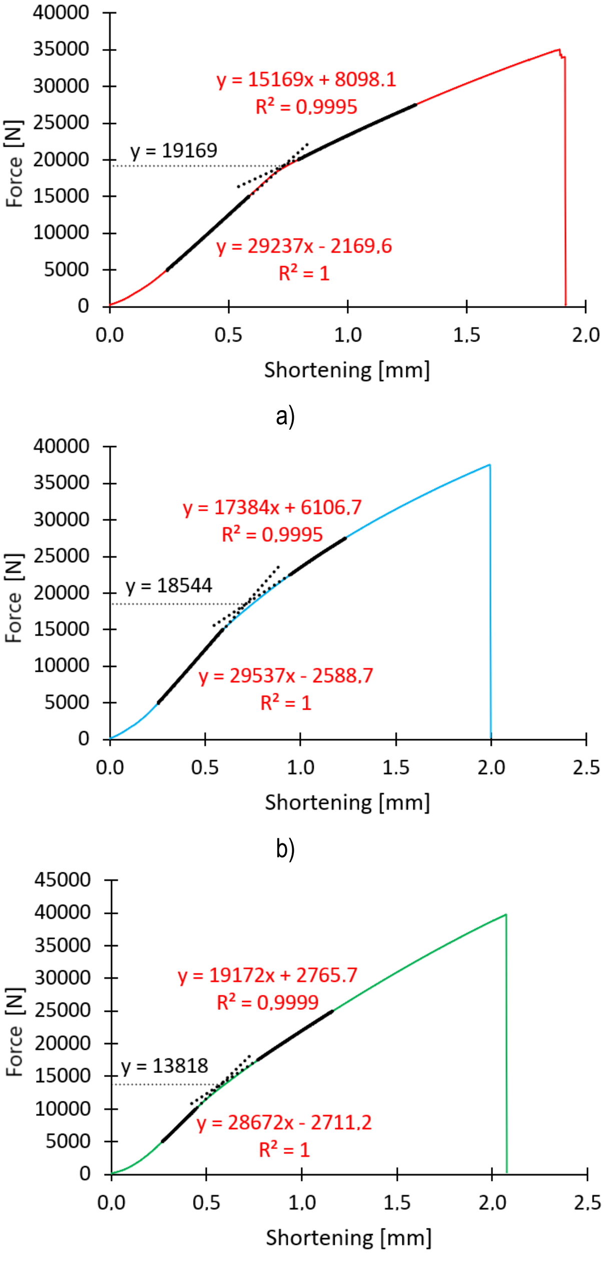

a)

b)

c)

Fig. 4. Force versus shortening: a) specimen A-1, b) specimen B-1, c) specimen C-1

Based on the buckling state analysis, very similar behaviour of composite structures was observed in terms of qualitative evaluation. In the case of type A and B structures, 4 half-waves were observed in the longitudinal direction of the composite columns, while in the case of type C structures, 3 half-waves occurred. The same situation was observed in the case of experimental tests and numerical simulations. Based on the conducted buckling state studies, the buckling force values for experimental tests and numerical simulations are summarized in Table 1.

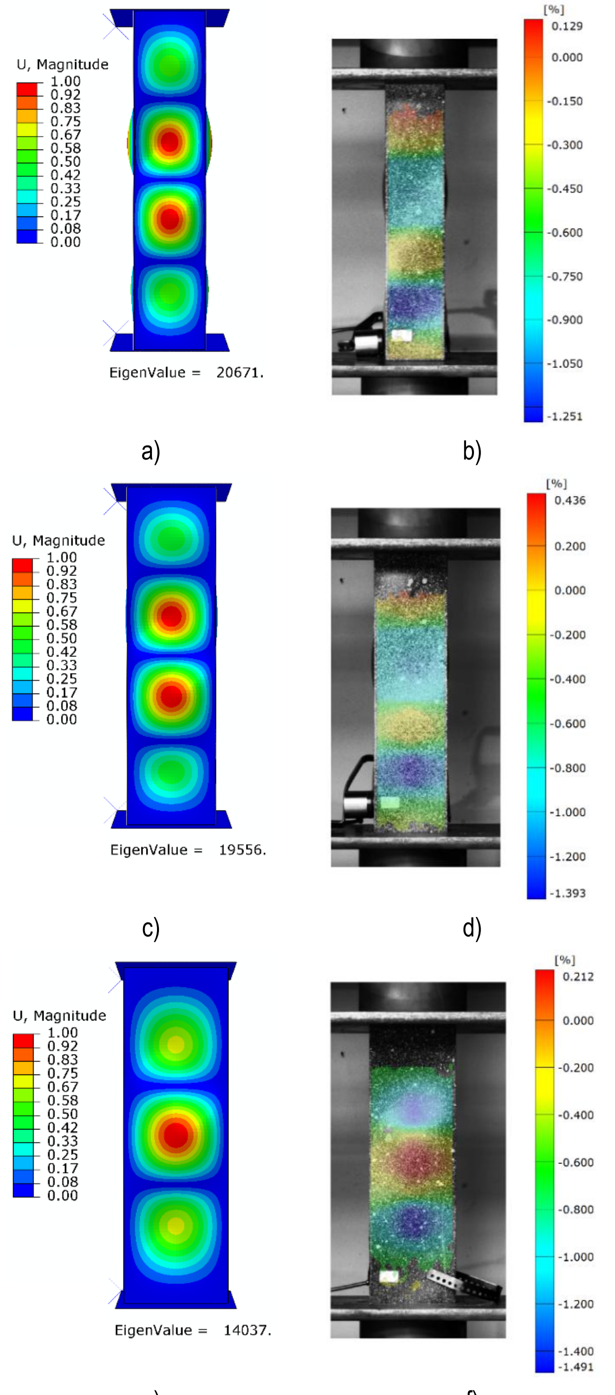

a) b)

c) d)

e) f)

Fig. 5. Buckling modes: a) specimen A (FEM), b) specimen A (EXP), c) specimen B (FEM), d) specimen B (EXP), e) specimen C (FEM), c) specimen C (EXP)

Tab. 1. Buckling force values

	1 (EXP)	2 (EXP)	3 (EXP)	EXP$_{avg}$	EXP$_{SD}$	FEM	FEM/ EXP$_{avg}$
A	19,169 N	18,512 N	19,002 N	18,894 N	279 N	20,671 N	1.09
B	18,544 N	18,892 N	18,771 N	18,736 N	144 N	19,556 N	1.04
C	13,818 N	13,352 N	13,284 N	13,485 N	237 N	14,037 N	1.04

Based on the study, it was observed that the buckling force values obtained in experiment and simulation were very similar. It was estimated that in the case of A-type structures, the buckling force value for FEM simulations relative to the average value from experimental tests was 1.09 times higher, and in the case of B- and C-type columns only 1.04 times higher. In addition, it was noted that the shape of the cross-section, has a significant impact on the loss of stability of the structure, where the ratio of buckling force in the case of A-type relative to C-type structures was 1.4 (experimental tests) and 1.47 (FEM simulations). For the analysis of the damage initiation phenomenon, acoustic emission signals were used to determine the value of the force at which the structure initiates the damage phenomenon. Figure 6 presents an example of post-buckling equilibrium paths for the B-type profile - where the energy signal (within the acoustic emission) was additionally compiled. This made it possible to determine the approximate values of damage-initiating forces, where the first significant "peak" of the acoustic emission signal determined the value of the force at which the structural damage process began. A significant increase in the acoustic emission signal indicated damage to the structure.

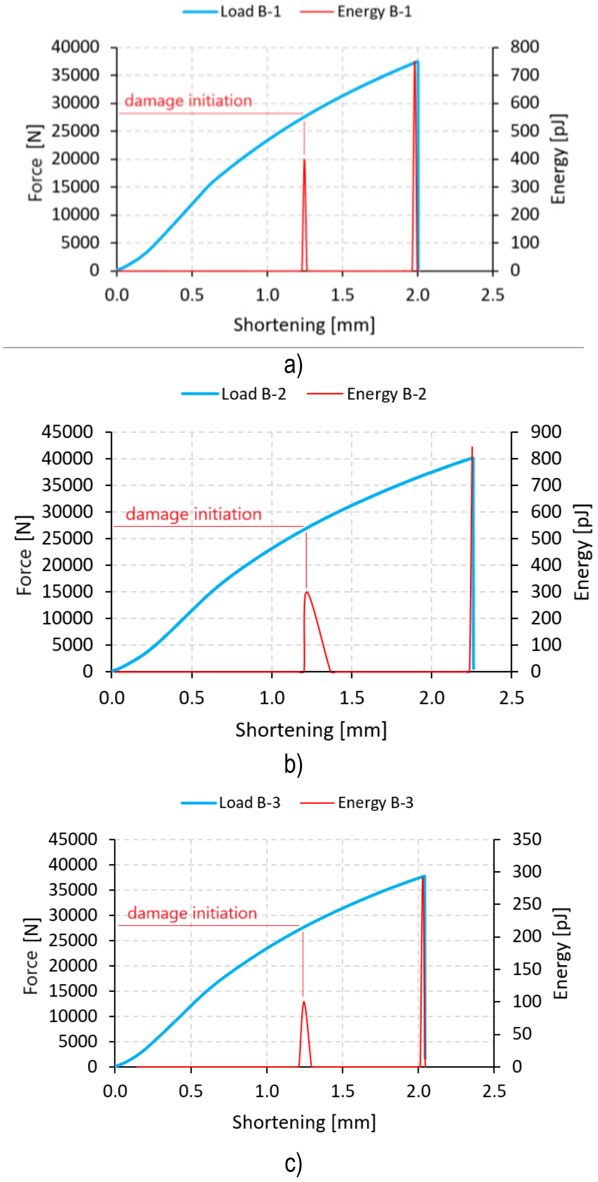

a)

b)

c)

Fig. 6. Force versus shortening at the damage initiation stage: a) specimen B-1, b) specimen B-2, c) specimen B-3

Simultaneously with the experimental studies, numerical simulations were carried out using Hashin's criterion. This criterion was selected for the different parameters of damage initiation and evolution of composite material damage. It was possible to independently assess damage to the fibers and matrix of the composite material. It was proved that the damage initiation in the composite occurred in the matrix due to tension (the HSNMTCRT parameter was fulfilled first). This followed the forms of buckling obtained by linear structural stability analysis. The damage regions covered the zones for the loss of structural stability, Fig. 7.

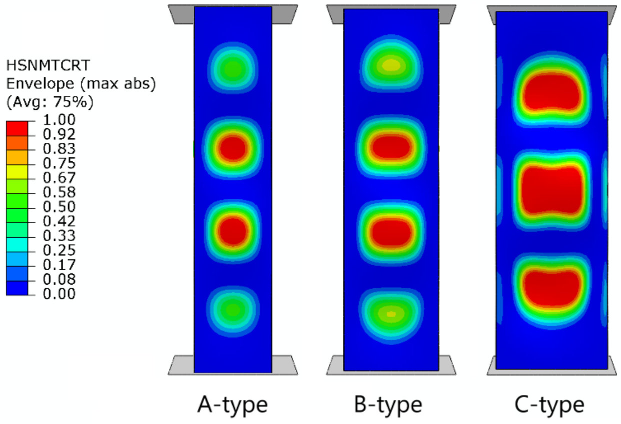

Fig. 7. Graphical representation of damage initiation for FEA simulations

Table 2 summarizes the force values corresponding to the damage initiation phenomenon for experimental tests and FEM simulations.

Tab. 2. Damage initiation force values

	1 (EXP)	2 (EXP)	3 (EXP)	EXP$_{avg}$	EXP$_{SD}$	FEM	FEM/ EXP$_{avg}$
A	20,234 N	23,557 N	21,042 N	21,611 N	1,415 N	24,694 N	1.14
B	27,537 N	26,916 N	27,615 N	27,356 N	312 N	28,679 N	1.05
C	31,081 N	30,128 N	30,304 N	30,504 N	414 N	31,074 N	1.02

It was estimated that in the case of A-type structures, the damage initiation force value for FEM simulations relative to the average value from experimental tests was 1.14 times higher, while in the case of B- and C-type columns only 1.05 and 1.02 times higher, respectively. Similar to the results of the buckling state, it was noted that the varied cross-sectional shape of the composite columns (cross-section A - 40x40 mm, B - 50x30 mm and C - 60x20 mm), has a significant impact on the damage initiation of the structure. In the case of C-type relative to A-type structures, the force value for the damage initiation was 1.41 (experimental tests) and 1.26 (FEM simulations).

The final stage was represented by the comparison of force-shortening relationships from experiment and simulation, Fig. 8. The characteristics of the FEM demonstrated higher mechanical resistance at the initial loading, due to the FEM model does not follow the differences in the composite features, related to the manufacturing.

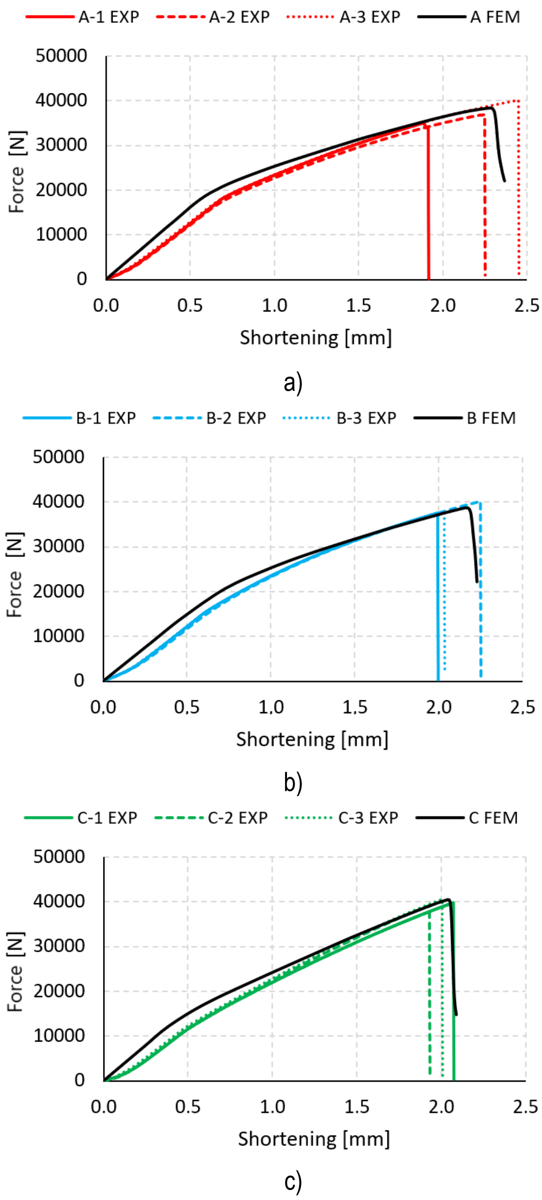

Fig. 8. Failure characteristics: a) specimen A-type, b) specimen B-type, c) specimen C-type

Post-buckling equilibrium paths made it possible to determine the values of fracture forces (maximum force values registered during the test trials). These values are summarized in Table 3.

Tab. 3. Fracture force values

	1 (EXP)	2 (EXP)	3 (EXP)	EXP$_{avg}$	EXP$_{SD}$	FEM	FEM/ EXP$_{avg}$
A	35,047 N	36,904 N	40,121 N	37,357 N	2,096 N	38,358 N	1.03
B	37,513 N	40,139 N	37,722 N	38,458 N	1,192 N	38,703 N	1.01
C	39,800 N	39,151 N	40,573 N	39,841 N	581 N	40,463 N	1.02

Based on the study, it was noted that the fracture force values from the both approaches were almost the same. It was estimated that in the case of A-type structures, the fracture force value for FEM simulations relative to the average value from experimental tests was 1.03 times higher, while in the case of B- and C-type columns only 1.01 and 1.02 times higher, respectively. Moreover, it was observed that the cross-section features, has a small influence on the component fracturing, while in the case of C-type relative to A-type structures it was equal to 1.07 (experimental tests) and 1.05 (FEM simulations). Based on the analysis of the results from the quantitative point of view, it was noted that there was a low effect of the cross-sectional shape of thin-walled composite columns on the values of fracture forces and load-carrying capacity. Furthermore, a qualitative comparison of the fracture phenomenon was performed - Figure 9.

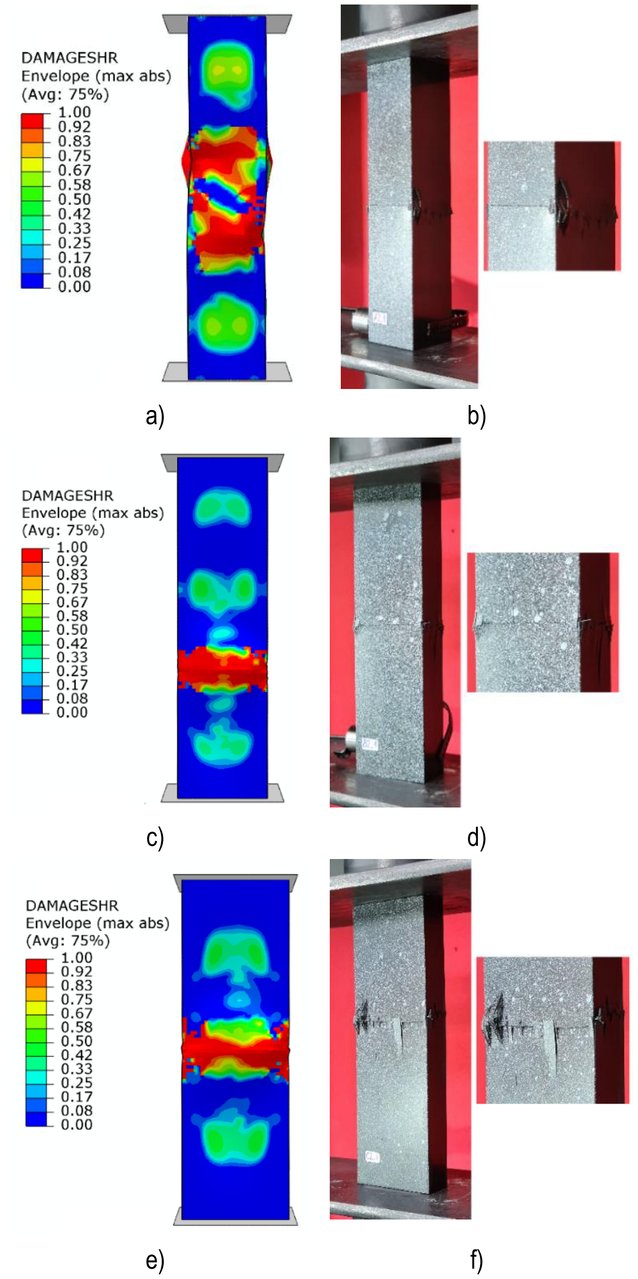

Fig. 9. Fracture modes: a) A specimen (FEM), b) A specimen (EXP), c) B specimen (FEM), d) B specimen (EXP), e) C specimen (FEM), c) C specimen (EXP)

In order to understand more detail the complex phenomenon of composite material fracture [30-34], the fracture of individual plies of the composite material was presented on the basis of numerical simulations carried out for each type of cross-section of the composite structure - Figure 10. Ply 1 was the ply located on the outside of the composite structure, while ply 8 was the inside (last) ply of the structure.

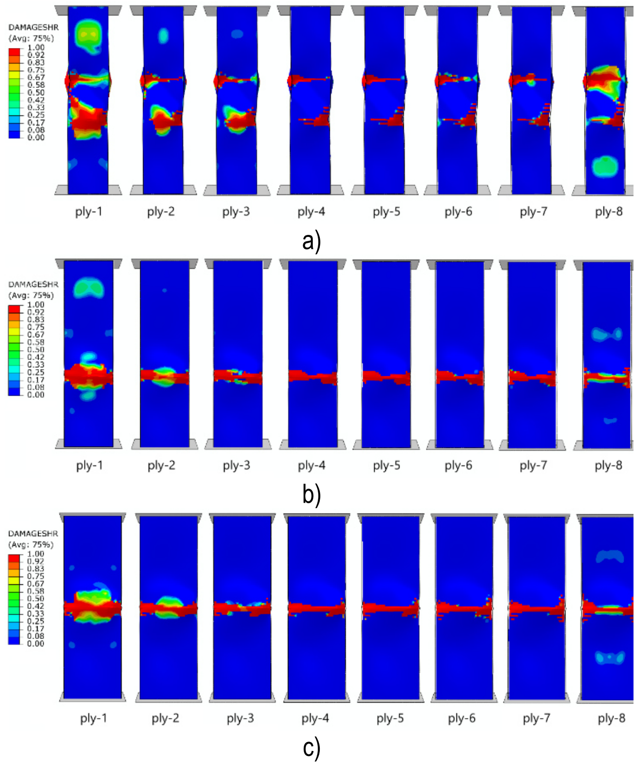

Fig. 10. The fracture stages - ply by ply: a) A-type, b) B-type, c) C-type

Based on the study, it was noted that the analysed structures with cross sections, regardless of the shape of the cross section, were characterised by a high reserve of load-carrying capacity - between the buckling and failure force. The failure phenomenon showed a complex character - where different forms of damage such as ply cracking and delamination occurred simultaneously. In the case of numerical simulations, it was observed that the failure phenomenon was significantly visible in the case of the outermost (extreme) plies of the composite material (such as, for example, plies 1 and 8) and noticeably less visible in the “middle” plies - which constitute the core of the structure. The outermost plies of the composite were the most susceptible to failure - which was confirmed by experimental studies, where complex forms of failure were visualized - in the area of the middle of the height of all structures. Both quantitatively and qualitatively, a satisfactory agreement was obtained between the results of experimental studies and FEM simulations. An interesting conclusion during the observation of the fracture phenomenon was primarily that the composite showed dominant forms of fracture in the area located around the mid-height of the structure. The above establishes the necessity of further research in the analysis of the fracture phenomenon using advanced FEM numerical models.

Additionally, it was decided to present the complex state of failure using an example of A-type structure – using a digital microscope (Figure 11 and 12). The analysis carried out using digital microscopy and recorded forms of damage was conducted to enable a qualitative assessment of the composite material damage. In each case, regardless of the test specimens, delamination and fracture of individual plies of this material were observed, which will be the subject of further and more detailed research.

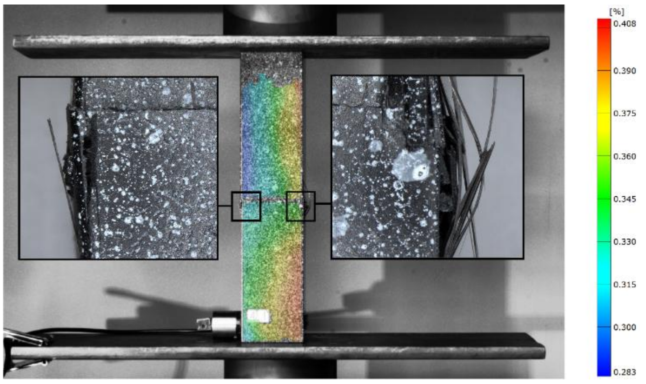

Fig. 11. The fracture phenomenon of A-type composite profile

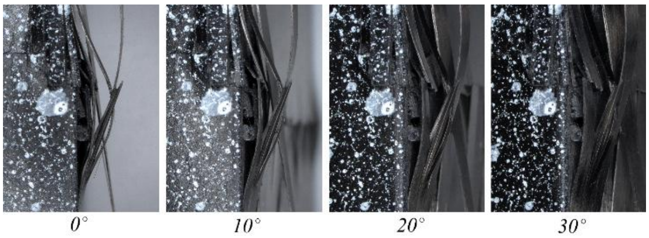

Fig. 12. The fracture phenomenon of A-type composite profile - detailed view of the failure form at orientation of the digital microscope head

Observations with the use of a digital microscope (at 20x magnification) made it possible to present in details of regions, indicating on the degradation complexity.

5. CONCLUSIONS

The present study was primarily conducted in order to determine the significance of the effect of the cross-sectional shape of composite structures on stability, damage initiation and failure phenomena - under axial compression. The research made it possible to extract important conclusions from the analysis of the buckling and post-buckling behavior of thin-walled structures with different cross-sectional shapes:

- The dimensions of the rectangular tube cross-section has a significant effect on buckling and damage initiation forces, while a minor effect on the load-carrying capacity of the structure;
- The failure/fracture phenomenon demonstrated a complex character, where, in the case of experimental studies, both fracture of the plies of the composite material and delamination were observed;
- The outer plies of the composite are most susceptible to damage occurrence;
- The composite profiles were characterised by a high reserve of load-capacity - between the buckling force and the fracture force there was a difference in values of two or more times.

Further research directions will take into account the development of advanced numerical models using FEM, such as the XFEM technique - for modeling the fracture of plies of composite material, or CZM for modeling the delamination phenomenon, in order to better represent the nature of the complex mechanism of failure. The findings of the study can be applied more comprehensively, e.g. in the aerospace and construction industries, where the force values obtained at buckling, damage initiation, and failure provide information about the load-carrying capacity of the analyzed structures. Knowledge of the load-carrying capacity of the investigated composite profiles when used as reinforcing/load-carrying structures is significant. In the future, it is also planned to use a passive thermography system, which would additionally enable the analysis of damage in the context of temperature increase observations at the moment of composite material structure degradation. It is important to model composite structures depending on their destination for industrial solutions – the most important issue is usually that these structures, after buckling, should have several times the load-carrying capacity before complete fracture.

REFERENCES

1. Banat D, Mania RJ. Failure assessment of thin-walled FML profiles during buckling and postbuckling response. Compos Part B Eng. 2017;112:278–89.
2. Różyło P, Rosłaniec K, Kuciej M. Buckling of Compressed Thin-Walled Composite Structures with Closed Sections. Advances in Science and Technology Research Journal. 2023;17(6):63-72.
3. Rozylo P, Rogala M, Pasnik J. Buckling Analysis of Thin-Walled Composite Structures with Rectangular Cross-Sections under Compressive Load. Materials. 2023;16:6835.
4. Li ZM, Qiao P. Buckling and postbuckling behavior of shear deformable anisotropic laminated beams with initial geometric imperfections subjected to axial compression. Engineering Structures. 2015;85: 277-292.
5. Bazant ZP, Cedolin L. Stability of structures. elastic, inelastic, fracture and damage theories. UK: Oxford University Press. 2010.
6. Singer J, Arbocz J, Weller T. Buckling experiments. Experimental methods in buckling of thin-walled structure. Basic concepts, columns, beams, and plates. New York: John Wiley & Sons Inc. 2002.
7. Kamarudin MNB, Ali JSM, Aabid A, Ibrahim YE. Buckling Analysis of a Thin-Walled Structure Using Finite Element and Design of Experiments Methods. Aerospace. 2022;9:541.
8. Paszkiewicz M, Kubiak T. Selected problems concerning determination of the buckling load of channel section beams and columns. Thin-Walled Struct. 2015;93:112–121.
9. Rozylo P, Debski H. Stability and load-carrying capacity of short composite Z-profiles under eccentric compression. Thin-Walled Struct. 2020;157:107019.
10. Różyło P, Dębski H. Failure study of compressed thin-walled composite columns with top-hat cross-section. Thin-Walled Structures. 2022;180:109869.
11. Li W, Cai H, Li C, Wang K, Fang L. Progressive failure of laminated composites with a hole under compressive loading based on micromechanics. Adv. Compos. Mater. 2014;23:477–490.
12. Rozylo P, Falkowicz K. Stability and failure analysis of compressed thin-walled composite structures with central cut-out, using three advanced independent damage models. Compos. Struct. 2021;273:114298.
13. Kubiak T, Samborski S, Teter A. Experimental investigation of failure process in compressed channel-section GFRP laminate columns assisted with the acoustic emission method. Compos. Struct. 2015;133:921–929.
14. Reddy JN, Pandey AK. A first-ply failure analysis of composite laminates. Comput. Struct. 1987;25:371–393.
15. Gliszczynski A, Kubiak T. Progressive failure analysis of thin-walled composite columns subjected to uniaxial compression. Compos. Struct. 2017;169:52–61.
16. Li Z, Cen S, Wu CJ, Shang Y, Li CF. High-performance geometric nonlinear analysis with the unsymmetric 4-node, 8-DOF plane element US-ATFQ4. Int. J. Numer. Meth. Eng. 2018;114:931–954.
17. Drozdziel M, Podolak P, Czapski P, Zgorniak P, Jakubczak P. Failure analysis of GFRP columns subjected to axial compression

manufactured under various curing-process conditions. Composite Structures. 2021;262:113342.

18. Czapski P, Kubiak T. Numerical and experimental investigations of the post-buckling behaviour of square cross-section composite tubes. Composite Structures. 2015;132:1160–1167.
19. Rozylo P. Stability and failure of compressed thin-walled composite columns using experimental tests and advanced numerical damage models. Int. J. Numer. Meth. Eng. 2021;122:5076–5099.
20. Rozylo P. Limit states of thin-walled composite structures with closed sections under axial compression. Composites Part B. 2024; 287:111813.
21. Podolak P, Drozdziel M, Czapski P, Kubiak T, Bienias J. The failure mode variation in post-buckled GFRP columns with different stacking sequences - Experimental damage analysis and numerical prediction. International Journal of Mechanical Sciences. 2021;210:106747.
22. Rozylo P, Smagowski W, Pasnik J. Experimental Research in the Aspect of Determining the Mechanical and Strength Properties of the Composite Material Made of Carbon-Epoxy Composite. Advances in Science and Technology Research Journal. 2023;17(2):232–246.
23. Wysmulski P. Non-linear analysis of the postbuckling behaviour of eccentrically compressed composite channel-section columns. Composite Structures. 2023;305:116446.
24. Samborski S, Rzeczkowski J, Korzec-Strzalka I. Experimental study of delamination process in elastically coupled laminates with the acoustic emission technique. Engineering Structures. 2024;300:117196.
25. Rozylo P. Failure analysis of beam composite elements subjected to three-point bending using advanced numerical damage models. Acta Mechanica et Automatica. 2023;17(1):133-144.
26. Rozylo P, Debski H. Stability and load carrying capacity of thin-walled composite columns with square cross-section under axial compression. Composite Structures. 2024;329:117795.
27. Lapczyk I, Hurtado JA. Progressive damage modeling in fiber-reinforced materials. Compos A Appl Sci Manuf. 2007;38:2333-2341.
28. Hashin Z, Rotem A. A Fatigue Failure Criterion for Fiber Reinforced Materials. Journal of Composite Materials. 1973;7(4):448–464.
29. Hashin Z. Failure Criteria for Unidirectional Fiber Composites. Journal of Applied Mechanics. 1980;47(2):329-334.
30. Benzeggagh ML, Kenane M. Measurement of mixed-mode delamination fracture toughness of unidirectional glass/epoxy composites with mixed-mode bending apparatus. Compos. Sci. Technol. 1996;56:439–449.
31. Turon A, Camanho PP, Costa J, Dávila CG. A damage model for the simulation of delamination in advanced composites under variable-mode loading. Mech. Mater. 2006;38(11):1072–1089.
32. Camanho PP, Davila CG, de Moura MF. Numerical simulation of mixed-mode progressive delamination in the composite materials. J. Compos. Mater. 2003;37(16):1415–1438.
33. Alhawamdeh M, Alajarmeh O, Aravinthan T, Shelley T, Schubel P, Kemp M, Zeng X. Modelling hollow pultruded FRP profiles under axial compression: Local buckling and progressive failure. Composite Structures. 2021;262:113650.
34. Ali HQ, Wagner HNR, Akalın C, Tabrizi IE, Hühne C, Yildiz M. Buckling and fracture analysis of thick and long composite cylinders with cutouts under axial Compression: An experimental and numerical campaign. Composite Structures. 2023;324:117530.

The research was conducted under project No. 2021/41/B/ST8/00148, financed by the National Science Centre, Poland. This research was funded in whole or in part by National Science Centre, Poland [2021/41/B/ST8/00148]. For the purpose of Open Access, the author has applied a CC-BY public copyright license to any Author Accepted Manuscript (AAM) version arising from this submission.

Patryk Różyło: https://orcid.org/0000-0003-1997-3235

Kuba Rosłaniec: https://orcid.org/0000-0002-4093-1702

DOI 10.2478/ama-2025-0050

DIGITALISATION OF PAINTING PATH TOPOGRAPHY FOR NUMERICAL MODELLING OF LOW-RELIEF SURFACES

Andrzej WERNER*, Bogusław HOŚCIŁO* , Piotr MROZEK, Krzysztof MOLSKI*****

*Faculty of Mechanical Engineering, Department of Materials and Production Engineering, Bialystok University of Technology, Poland
**Faculty of Mechanical Engineering, Department of Biomechatronics, Bialystok University of Technology, Poland
***SaMASZ Sp. z o.o., Zabludow, Poland

a.werner@pb.edu.pl, b.hoscilo@pb.edu.pl, p.mrozek@pb.edu.pl, krzysztof.molski@samasz.pl

received 15 July 2025, revised 28 July 2025, accepted 13 August 2025

Abstract: The methodology presented in this article involves the digitalization of painting path topography created using various brushes on different canvases. Measurements were conducted using a blue structured light scanner. Preliminary test scans were performed to determine the optimal digitalization parameters, including exposure time, number of exposures, and scanning resolution. A resolution of 0.08 mm was selected as the minimum point spacing, which was sufficient for both modelling and application use. This scanning process enabled the capture of surface deformations, including path fading and topographic variations arising from interactions between brush bristles, paint, and the canvas substrate—even in cases of partial paint coverage. The resulting 3D model was integrated into an application designed to replicate the glazing technique in painting.

Key words: reverse engineering, optical scanning, topography, painting path, canvas

1. INTRODUCTION

The digitalisation of 3D objects is the process of transforming real, three-dimensional physical objects into their digital representations in the form of three-dimensional (3D) models, containing data on shape, dimensions and often also surface texture and colour [1] [2]. In general, digitalisation techniques are divided into contact and non-contact methods [3]. Contact-based 3D digitalisation methods rely on the physical interaction of a measuring probe with the surface of an object to capture its geometry [4]. Unlike non-contact methods, these techniques require direct, point-by-point contact, which often provides high accuracy but at the cost of time and the inability to work with delicate objects. The most commonly used contact-based digitalisation methods involve coordinate measuring machines and measuring arms [5]. Non-contact digitalisation methods, on the other hand, are used to acquire digital data about the shape, texture, or structure of a physical object without any physical contact [6][7][8]. They are widely applied in fields such as museology, reverse engineering, archaeology, medicine, and industry [9][10][11]. There are various techniques for acquiring information about the geometry of a digitalised object. The most commonly used non-contact methods include 3D laser scanning, structured light scanning, photogrammetry, and computed tomography (CT) [12][13][14].

The digitalisation of low-height 3D objects (e.g. coins, reliefs, seals, PCBs, prints, or small archaeological artefacts) requires the selection of appropriate methods and equipment, as standard 3D techniques—such as photogrammetry or laser scanning—may have limitations when dealing with very flat forms [15][16]. Low-profile 3D objects, due to their delicate textures (e.g. reliefs, micro-surfaces), demand high measurement precision and high resolution. A distinct group includes objects with minimal height variations that extend over a relatively large surface area, such as canvases or painting paths. In such cases, the use of microscopic techniques (e.g. optical microscopes or micro-scanners) proves inefficient. The objects are too large for the measurement equipment, and the digitalisation process would be too time-consuming. Professional structured light scanners are a suitable solution in these situations [17]. Today, white and blue light scanners are commonly used. For the objects discussed in this paper, the use of blue light scanners is recommended [18]. These scanners offer greater resistance to ambient light (compared to white light), produce better results on challenging surfaces (e.g. dark, shiny, or metallic), and exhibit reduced optical scattering, resulting in higher scanning precision.

The research task described in this study was to develop a relatively fast and accurate method for preparing a numerical model of an object with small relative height differences. The topography of the canvas and the paths created by brush or spatula strokes—illuminated by directional light—give paintings a three-dimensional effect and influence the perception of the colour of transparent pigment applied to a textured surface. The technique of applying paint—typically oil paint—in thick layers that emphasise brush or spatula marks is known as impasto. Historically, the impasto technique evolved as a means of transforming the perception of art, gaining popularity with the Impressionists. It offered new opportunities for artistic expression, allowing artists to convey emotion and energy through texture. Pioneers of this technique included Vincent van Gogh and Claude Monet. Van Gogh's work Starry Night Over the Rhone exemplifies the impasto technique, where thick layers of paint bring the night sky to life. Such three-dimensional effects can be simulated in two-dimensional representations, most often through the use of chiaroscuro to imitate the structure and relief of brushstrokes [19][20]. Another important factor is the rheological properties of the oil paints used. For example, Van Gogh used two types of white in his paintings [21]. The authors of this study examined his works, identifying the characteristics of the paints he used and exploring how these materials contributed to the three-dimensionality of the painted surface.

In the development of a painting application intended to reproduce the Renaissance technique of glazed painting, the primary focus was on replicating the optical mixing of colours achieved through the use of natural pigments. However, the application of a glaze over a rough ground or an impasto base enables the creation of visually intriguing colour effects. To accurately transfer these effects into the digital realm, it was essential to study the topography of the canvas and the traces left by the paintbrush on such textured surfaces. Equally important was understanding the interaction between successive layers of brushstrokes applied on top of one another.

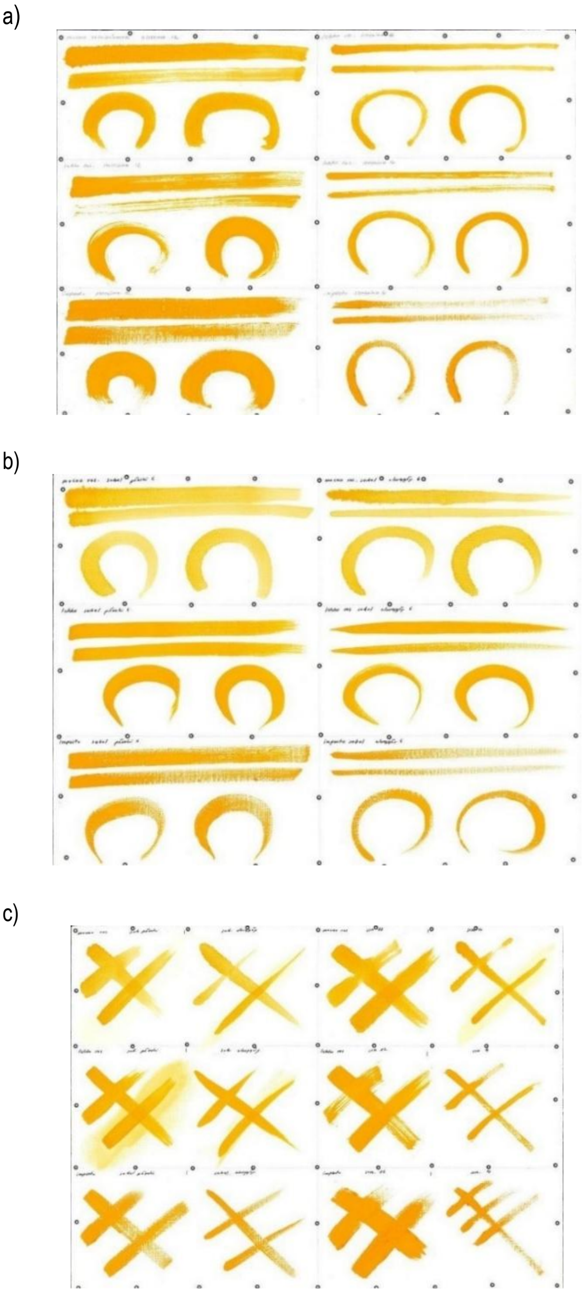

Fig. 1. Samples made on canvas ground:(a) single paths (brushes: natural bristle 4, 12), (b) single paths (brushes: sable flat, sable round), (c) crossing paths (brushes: sable flat, sable round)

2. DIGITALISATION OF CANVAS AND PAINTING PATHS

2.1. Research Material

The research material - canvases featuring painting paths created with various painting tools - was prepared by a professional artist with extensive experience in glaze painting.

The test samples were created based on the following assumptions:

1. preparation of canvas ground fragments,
2. application of brushstrokes using four types of brushes on linen canvas,
3. execution of paint strokes at four dilution levels (with maximum dilution defined as a 1:20 volume ratio of commercial paint to medium, and minimum dilution as 1:1),
4. use of four different paint application techniques:

- slowly in a straight line,
- slowly along a curve,
- quickly in a straight line,
- quickly along a curve.

Figure 1 presents selected samples prepared on the canvas ground. Figures 1a and 1b show single (straight and curved) brush paths applied at two different speeds. Figure 1c presents a sample containing intersecting, straight paint paths.

2.2. Measurement Platform

The digitalisation of the canvases and painting paths was carried out using an ATOS Core 200 scanner—a 3D scanner based on blue light technology.

Fig. 2. Measurement platform

The ATOS Core scanner (Fig. 2) uses a stereoscopic camera system operating on the principle of triangulation. The scanner projects a pattern of stripes onto the surface of the object. These

DOI 10.2478/ama-2025-0050

stripes are captured by two cameras, resulting in a phase shift based on the sinusoidal distribution of light intensity across the camera sensors. To achieve the highest sub-pixel accuracy, ATOS Core employs multiple phase shifts based on the heterodyne principle. Using optical transformation equations, independent 3D coordinates are automatically calculated for each camera pixel. The basic specifications of the scanner are presented in Table 1.

The projection technology developed by GOM is based on a narrow-spectrum blue LED light source. This enables precise measurement regardless of ambient lighting conditions. GOM's Blue Light Technology is characterised by an exceptionally long service life, minimal heat generation, and low operating costs.

Tab. 1. Technical data of the scanner

Measurement area	200 x 150 mm
Working distance	250 mm
Point spacing	0,08 mm
The device dimensions	206 x 205 x 64 mm
Working temperature	5 ° C do 40 ° C, without condensation

2.3. Measuring the Topography of the Canvas Ground

As part of the project, a sample of a linen canvas ground was prepared. The sample fit entirely within the measuring volume of the optical scanner. Preparation for scanning involved the application of reference markers, which enabled the automatic alignment and merging of individual scans during the digitalisation process. Figure 3 presents the canvas sample with the applied positioning markers.

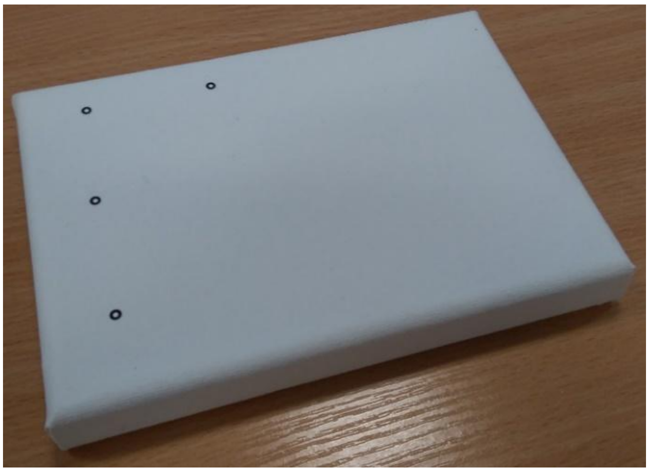

Fig. 3. Canvas ground with reference markers applied

2.3.1. Determination of the Scanning Parameters

Before scanning the topography of the canvas sample, it was necessary to determine the scanning parameters to ensure optimal final results. The parameters defined included:

- the exposure time of the scanned object,
- the number of exposures,
- the resolution of the scanner matrix.

The entire scanning process was carried out using GOM Scan software, which controls the scanner. Within the software interface, the exposure time is adjusted manually using a virtual knob displayed on the computer screen. The scanner control software analyses the image captured by the scanner's two cameras and provides feedback to the operator on the expected scan quality.

It is important to select an exposure time that prevents overexposure of the object. Overexposed areas are highlighted in red. Figure 4 illustrates a case of excessive exposure: the entire surface of the scanned canvas ground appears red in the scanner camera preview window (upper left corner of the figure). At this exposure setting, only the frame of the canvas ground was properly recorded.

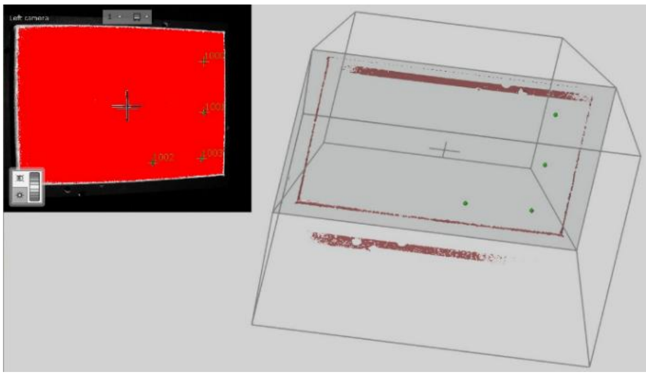

Fig. 4. Excessive exposure time of the scanned object

Therefore, the exposure time of the scanned object had to be shortened to eliminate the red-marked areas from the images captured by the cameras. This effect was achieved with an exposure time of 12 ms.

The scanner used allows for the selection of the number of exposures during a single scan. In this case, three options are available: one, two, or three exposures. The time ratio between successive exposures is 1:3:9. Multiple exposures are typically used for multicoloured objects, as each subsequent exposure is longer, improving scanning results across a wider colour range of the digitised object.

For the tested canvases, a trial was conducted using three exposure durations: 12 ms, 36 ms, and 108 ms. The observed percentages of measurement points for each exposure were as follows:

- 12 ms – 98% of measurement points observed,
- 36 ms – 2% of measurement points observed,
- 108 ms – 0% of measurement points observed.

Based on this information, the decision was made to eliminate the longest exposure time (108 ms), during which no measurement points were recorded.

The final scanning parameter selected was the scanner matrix resolution, which directly determines the number and spacing of the observed measurement points. The ATOS 200 scanner offers two scanning modes:

- Full Scan, which provides the scanner's maximum resolution of 5 MP, and
- Fast Scan, which sets the resolution to 2 MP.

Since the objective of the project was to accurately reproduce the topography of the scanned objects, all canvases samples were scanned using the maximum resolution setting.

In summary, the selected scanning parameters for the canvas ground samples were:

- basic exposure time: 12 ms,
- dual exposure settings: 12 ms and 36 ms,

- scanner resolution: maximum setting of 5 MP.

2.3.2. Determining the Topography of the Canvas

Once the scanning parameters had been established, the canvas sample was digitised. Four reference markers were applied to the canvas, enabling the automatic alignment and merging of individual scans into a unified dataset accurately representing the object's topography.

The digitised object was mounted on a rotary measuring table. The digitisation process involved acquiring five directional scans. The first scan was taken with the measuring table in the horizontal position. The table was then tilted by 30° along the horizontal axis. In this tilted position, four additional scans were performed, with the table rotated by 90° around its vertical axis between each scan.

As a result, point clouds were obtained that accurately captured the surface topography of the scanned sub-images (Fig. 5).

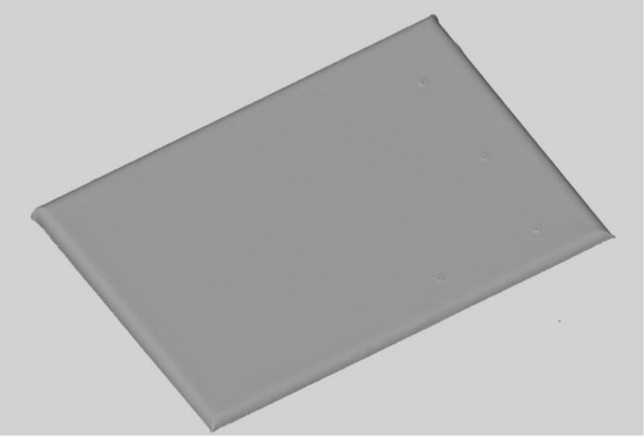

Fig. 5. Graphical representation of the canvas scanning results

The next stage of digitalisation involves converting the resulting point cloud into a triangular grid. During this process, called polygonisation, both filtering and unification of the scanning results take place. When the user initiates the polygonisation process, three levels of triangle mesh density can be selected (Fig. 6):

- Less details – provides a lower-quality representation of object details, resulting in the smallest file size,
- Standard – offers average mapping quality and a moderate file size,
- More details – delivers the highest level of detail, producing the largest file size.

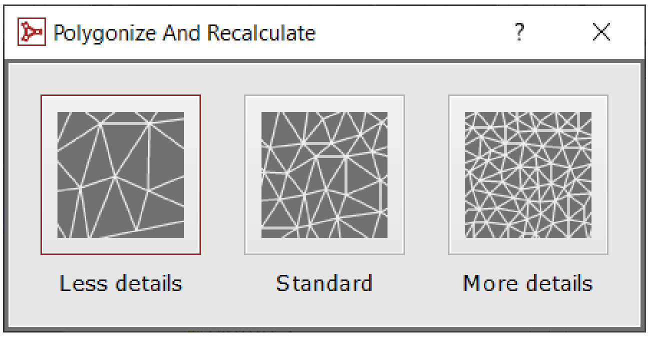

Fig. 6. Three modes of point cloud polygonisation

Figure 7 presents a graphical comparison of the three levels of detail achieved through the polygonisation process.

A quantitative summary of the polygonisation results is as follows:

- Less details – triangle mesh composed of 150,143 points,
- Standard – triangle mesh composed of 815,713 points,
- More details – triangle mesh composed of 1,863,953 points.

Given the project requirements, it was determined that the digitalisation should provide the most accurate representation of the surface topography. To meet this standard, the More details polygonisation mode was selected.

The resulting canvas topography scan was saved in STL format, a widely used standard in computer graphics for representing 3D geometry.

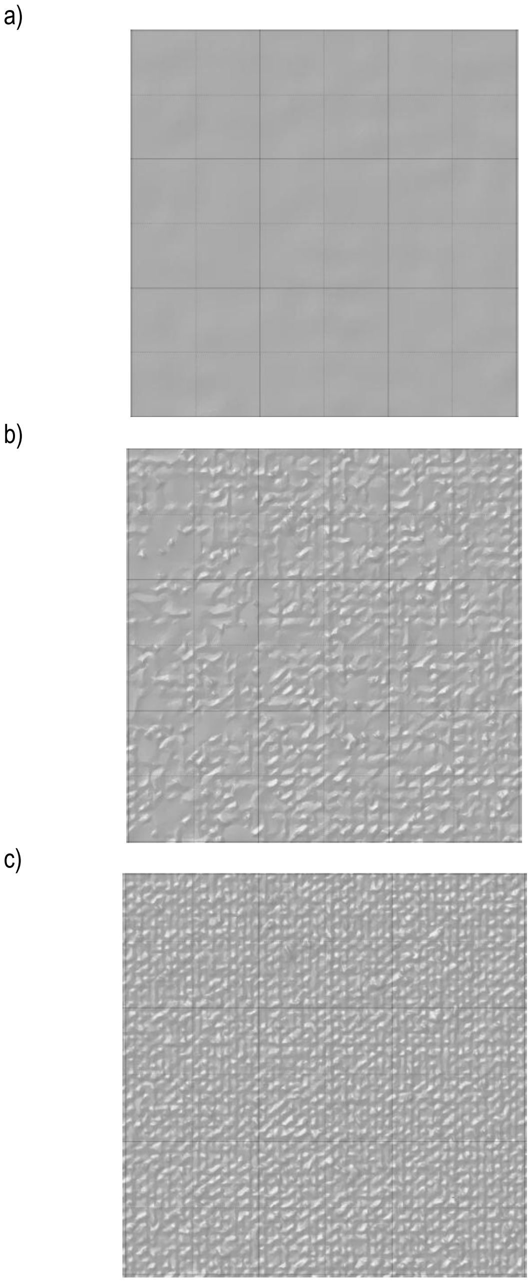

Fig. 7. Three levels of detail obtained during the polygonisation process: (a) Less details, (b) Standard, (c) More details

2.4. Scanning the Topography of Painting Tool Paths on a 3D Scanner – Linen Canvas

2.4.1. Selection of Sample Scanning Parameters

At this stage, selecting the number and duration of exposures during a single scan required detailed analysis. This was necessary due to two main factors:

- the samples were not monochromatic,
- the paint paths varied in shade due to differences in application speed and paint density.

Single-exposure scanning typically yields optimal results only for monochromatic objects. However, for the analysed samples, the scanning parameters had to be carefully adjusted to accurately capture both the underlying canvas texture and the variations in the paint paths.

As a result, the most advanced scanning option was selected—performing a single scan using three exposures. The exposure times were set in a ratio of 1:3:9, allowing the system to capture a wider range of shades and details, which is essential for scanning multicoloured or textured surfaces.

The first step in selecting digitalisation parameters was to set the shortest exposure time to prevent overexposure—this was verified by ensuring that no red zones appeared in the scanner camera preview (see Fig. 8).

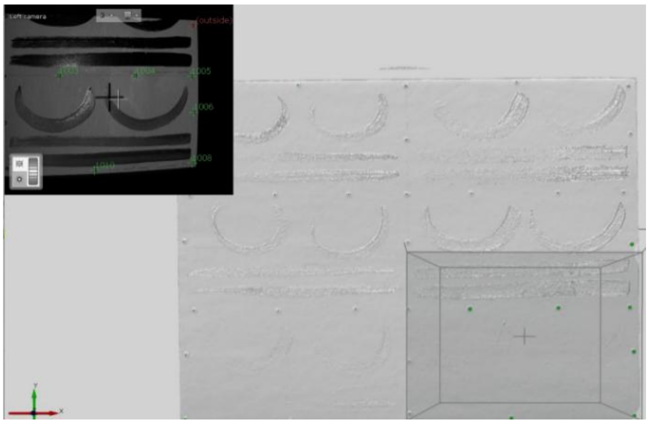

Fig. 8. Scanning result using the shortest exposure time, effectively eliminating overexposure of the scanned object

Using the selected exposure times, a series of sample scans were conducted and subsequently analysed. The results confirmed that the chosen exposure settings allowed for accurate reproduction of both the canvas and the painted paths on the samples. However, the initial images of the painting paths displayed several deficiencies, such as blank zones and ambiguous areas, which required correction.

To address this, it was decided that the digitisation of the painting samples would be performed in two separate scan series, each using different exposure settings. The first series, based on the predetermined exposure times, aimed to capture a comprehensive digital image of the entire sample - including both the canvas and the paint paths.

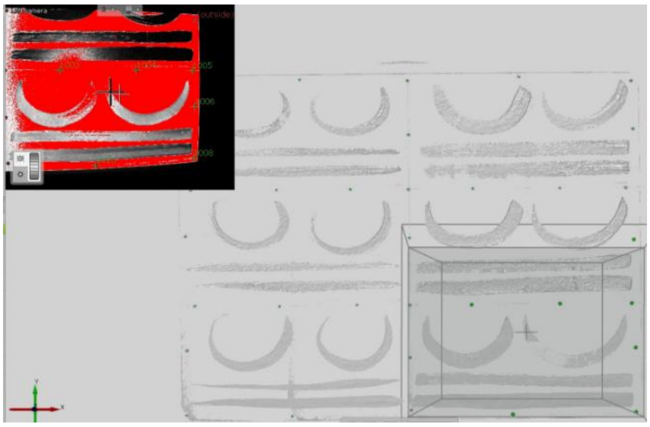

Fig. 9. Scanning effect with the shortest exposure time selected for the digitalisation of the painting paths

The second objective of the digitisation process was to isolate and accurately map the topography of the paint paths themselves. Therefore, a second series of scans was performed with specifically adjusted exposure settings. For this series, the minimum exposure time was deliberately selected to fully overexpose the canvas areas, as illustrated in Figure 9. These overexposed areas, highlighted in red in the scanner preview, are excluded from the digitalisation output.

Following a series of test scans, it became clear that the canvas was effectively removed from the digital data, leaving behind a highly accurate representation of the topography of the painted paths alone.

Summary of selected scanning parameters for painting path samples on canvas ground:

- basic (shortest) exposure time: 9.56 ms,
- 1st scan series *(digitisation of canvas and painting paths)*: single scan with three exposures at: 9.56 ms, 28.69 ms, 86.07 ms,
- 2nd scan series *(digitisation of painting paths only)*: single scan with three exposures at: 40.05 ms, 120.14 ms, 360.41 ms,
- maximum scanner resolution: 5 MP.

2.4.2. Determining the Topography of Painting Paths on a Canvas

The digitalisation procedure began with the application of reference markers. The positions of these reference points for each sample are shown in Figure 1. Following this, the object was mounted onto the rotating and tilting table of the optical scanner (see Figure 10).

The size of the samples significantly exceeded the measurement volume of the scanner. Therefore, digitising the entire object required multiple repositionings and settings adjustments. Additionally, since two series of scans with different exposure times were necessary, a total of 54 component scans were performed.

This process generated two separate point clouds: one representing the canvas along with the painting paths, and the other representing only the painting paths. Figure 11 illustrates the point cloud capturing the topography of the entire object.

Both point clouds were subsequently converted into triangular meshes. The resulting models, saved in STL format, are suitable for further processing in computer graphics applications.

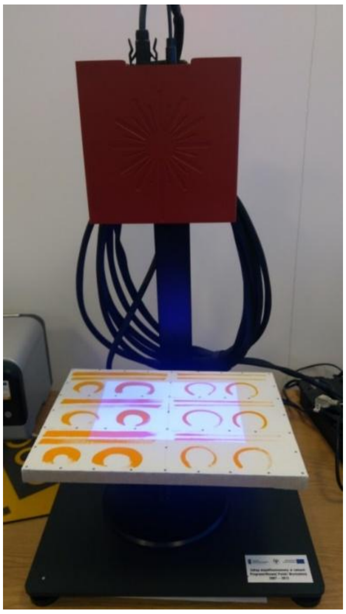

Fig. 10. Digitised sample of paint paths within the measurement area of the optical scanner

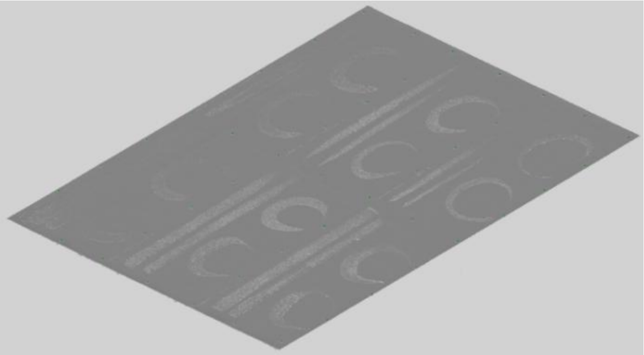

Fig. 11. Graphical representation of the scanning results showing the point cloud of the entire object's topography

Figure 12 presents a selected fragment of the results corresponding to one brush type and paint density. To facilitate comparison with the initial state, Fig. 12a shows a photograph of the scanned section of the sample. Fig. 12b displays the topography of the painting paths along with the surrounding canvas, while Fig. 12c depicts the topography of the painting paths alone.

a)

b)

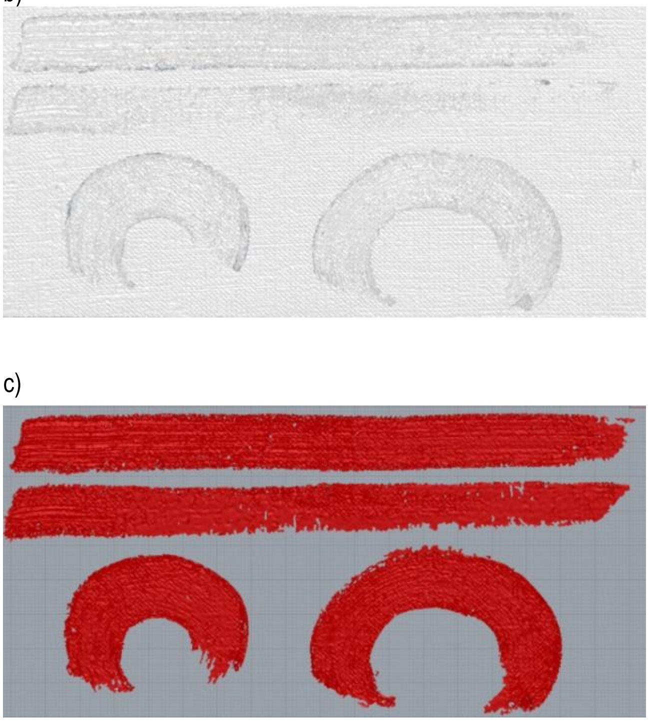

c)

Fig. 12. Example results of determining the topography of painting paths on a linen canvas: (a) photograph of a sample section, (b) topography including painting paths and surrounding canvas, (c) topography of the painting paths alone

3. SUMMARY

This paper presents a method for the digitalisation of painting paths and canvases. A unique challenge was the large surface area combined with low height of the objects, which made typical equipment designed for small-object digitisation unsuitable. As demonstrated, using a standard professional optical scanner required precise determination of critical scanning parameters and appropriate data processing.

The study shows that accurate selection of the number and duration of individual exposures enables selective data acquisition—either capturing the entire canvas or isolating just the paint paths—and allows for faithful reproduction of the scanned object's shapes.

The research involved close collaboration with a professional visual artist. This collaboration was essential because the resulting models of the canvas and painting paths were used to develop a computer application introducing users to the glazing painting technique.

The "Glaze" application, developed from this research, simulates two substrates commonly used in oil painting: board and canvas. For both substrates, the optical properties were modelled based on visible-light spectrograms obtained during scanning. The canvas also incorporates a two-dimensional representation of spatial texture derived from three-dimensional scanning. This texture realistically simulates brushstrokes and paint traces at varying levels of dilution.

Figure 13 presents sample paint strokes created with two different brushes—sable (left column) and hog (right column). The degree of paint dilution varies from impasto (first two rows) to glazing (bottom rows). On the right, crisscrossing brushstrokes illustrate the typical layering order used in the impasto technique.

Fig. 13. Paintbrush paths on the canvas as visualized in the *Glaze* application

REFERENCES

1. Ramos Barbero B, Santos Ureta E. Comparative study of different digitization techniques and their accuracy. Computer-Aided Design. 2011;43(2): 188–206. https://doi.org/10.1016/j.cad.2010.11.005
2. Piratelli-Filho A, Souza PHJ, Arencibia RV, Anwer N. Study of contact and non-contact measurement techniques applied to reverse engineering of complex freeform parts. International Journal of Mechanical Engineering and Automation. 2014;pp.10. https://hal.science/hal-01094272v1
3. Stojkic Z, Čuljak E, Šaravanja L. 3D Measurement - Comparison of CMM and 3D Scanner. 31ST DAAAM International Symposium On Intelligent Manufacturing And Automation. 2020. https://doi.org/10.2507/31st.daaam.proceedings.108
4. Zhuang Q, Wan N, Guo Y, Zhu G, Qian D. A state-of-the-art review on the research and application of on-machine measurement with a touch-trigger probe. Measurement. 2024; 224: 113923. https://doi.org/10.1016/j.measurement.2023.113923
5. Bastas A. Comparing the probing systems of coordinate measurement machine: Scanning probe versus touch-trigger probe. Measurement. 2020;156:107604. https://doi.org/10.1016/j.measurement.2020.107604
6. Adamopoulos E, Rinaudo F, Ardissono L. A Critical Comparison of 3D Digitization Techniques for Heritage Objects. ISPRS International Journal of Geo-Information. 2021; 10(1):10. https://doi.org/10.3390/ijgi10010010
7. Freeman Gebler O, Goudswaard M, Hicks B, et al. A comparison of structured light scanning and photogrammetry for the digitisation of physical prototypes. Proceedings of the Design Society. 2021;1:11-20. https://doi.org/10.1017/pds.2021.2
8. Verykokou S, Ioannidis C. An Overview on Image-Based and Scanner-Based 3D Modeling Technologies. Sensors (Basel). 2023;23(2):596. https://doi.org/10.3390/s23020596
9. Diara F. Structured-Light Scanning and Metrological Analysis for Archaeology: Quality Assessment of Artec 3D Solutions for Cuneiform Tablets. Heritage. 2023; 6(9):6016-6034. https://doi.org/10.3390/heritage6090317
10. Lunghi I, Vannini E, Dal Fovo A, Di Sarno V, Rocco A, Fontana R. A Performance Comparison of 3D Survey Instruments for Their Application in the Cultural Heritage Field. *Sensors*. 2024; 24(12):3876. https://doi.org/10.3390/s24123876
11. Creehan, KD, Bidanda, B. Reverse Engineering: A Review & Evaluation of Non-Contact Based Systems. In: Kamrani A, Nasr EA (eds) Rapid Prototyping. Manufacturing Systems Engineering Series. 2006;6:87-106. Springer. Boston. MA. https://doi.org/10.1007/0-387-23291-5_4
12. Geng J. Structured-light 3D surface imaging: a tutorial, Adv. Opt. Photon. 2011;3(2):128-160. https://doi.org/10.1364/AOP.3.000128
13. Remondino F, El-Hakim S. Image-based 3D Modelling: A Review. The Photogrammetric Record. 2006;21:269-291. https://doi.org/10.1111/j.1477-9730.2006.00383.x
14. Javaid M, Haleem A, Pratap Singh R, Suman R. Industrial perspectives of 3D scanning: Features, roles and it's analytical applications. Sensors International, 2021;2:100114. https://doi.org/10.1016/j.sintl.2021.100114
15. Liu J, Wang Y. 3D surface reconstruction of small height object based on thin structured light scanning. Micron. 2021;143:103022. https://doi.org/10.1016/j.micron.2021.103022
16. Wang Y, Chen J, Peng Y, Du Y. Design of thin-structured-light projection system for small-height measurement. Microsc Res Tech. 2022;85(3):1180-1193. https://doi.org/10.1002/jemt.23986
17. C. Park S, Chang M. Reverse engineering with a structured light system. Computers & Industrial Engineering. 2009;57(4):1377-1384. https://doi.org/10.1016/j.cie.2009.07.005
18. Martínez-Pellitero S, Cuesta E, Giganto S, Barreiro J. New procedure for qualification of structured light 3D scanners using an optical feature-based gauge. Optics and Lasers in Engineering. 2018;110:193-206. https://doi.org/10.1016/j.optlaseng.2018.06.002
19. Baxter W, Wendt J, Ming CL. IMPaSTo: a realistic, interactive model for paint. NPAR '04: Proceedings of the 3rd international symposium on Non-photorealistic animation and rendering. 2004:45–148. https://doi.org/10.1145/987657.987665
20. Annum GY. Artefactual Skills for Simulating Impasto Effect in Digital Painting: An Adobe Photoshop Solution. Art and Design Review. 2022;10:475-494. https://doi.org/10.4236/adr.2022.104038
21. Salvant Plisson J, de Viguerie L, Tahroucht L, Menu M, Ducouret G.Rheology of white paints: How Van Gogh achieved his famous impasto. Colloids and Surfaces A: Physicochemical and Engineering Aspects. 2014;458:134-141. https://doi.org/10.1016/j.colsurfa.2014.02.055

This work was carried out as part of the research project titled “Developing of glaze painting APP/graphic software with a colour palette based on historical pigments,” funded by the Intelligent Growth Operational Programme 2014–2020. Project number: POIR.01.01.01-00-1138/19.

Andrzej Werner: https://orcid.org/0000-0002-3768-5395

Bogusław Hościło: https://orcid.org/0000-0002-2525-5996

Piotr Mrozek: https://orcid.org/0000-0002-9788-6957

Krzysztof Molski: https://orcid.org/0000-0002-9196-7553

DOI 10.2478/ama-2025-0051

acta mechanica et automatica, vol.19 no.3 (2025)
Special Issue "New Trends in Biomedical Engineering"

MECHANO-RESPONSIVE POLYAMPHOLYTE HYDROGELS WITH STRAIN-STIFFENING PROPERTY FOR WOUND CLOSURE APPLICATIONS

Gustini GUSTINI*/, Kaprawi SAHIM**, Ida SRIYANTI***, Irmawan IRMAWAN******

*Faculty of Engineering, Doctoral Program of Mechanical Engineering, University of Sriwijaya,
Indralaya, South Sumatera, 30662, Indonesia
**Faculty of Engineering, Department of Mechanical Engineering, University of Sriwijaya,
Indralaya, South Sumatera, 30662, Indonesia
***Faculty of Education, Department of Physics Education, University of Sriwijaya,
Indralaya, South Sumatera, 30662, Indonesia
****Faculty of Engineering, Department of Electrical Engineering, University of Sriwijaya,
Indralaya, South Sumatera, 30662, Indonesia

gustini@unsri.ac.id, kaprawi@unsri.ac.id, ida_sriyanti@unsri.ac.id, irmawan@unsri.ac.id

received 02 October 2024, revised 04 June 2025, accepted 16 June 2025

Abstract: Strain-stiffening properties are the most applied in mechano-responsive hydrogels that respond to external mechanical forces. Wounds subjected to frequent deformations are difficult to treat because external mechanical forces can easily interfere with the healing process. The strain-stiffening property reduces the effect of external mechanical forces and acts as a damper response to these forces. Therefore, tough wound closure with stimuli-responsive strain-stiffening release properties for treating these wounds is highly desirable. In this study, we developed a strain-stiffening polyampholyte hydrogel that aims to accelerate wound closure as a damper of external mechanical forces. Self-assembly technique was used to fabricate a polyampholyte hydrogel. The differential modulus of the polyampholyte hydrogel exhibited strain-stiffening property. In addition, the mechanical stress applied to the polyampholyte hydrogel increased strain-stiffening penetration into the skin tissue. The strain-stiffening properties of the polyampholyte hydrogel also demonstrated an excellent damping of external mechanical forces to accelerate wound closure. The developed strain-stiffening hydrogel is promising for wound closure applications in wounds subjected to frequent deformations from external mechanical forces.

Key words: strain-stiffening property; self-assembly; differential modulus; polyampholyte hydrogel; wound closure

1. INTRODUCTION

Mechanical responsiveness plays an essential role in many biomechanical processes and is common in biological systems [1, 2]. Over the last two decades, significant effort has been made for developing biomimetic mechano-responsive hydrogels capable of altering their physical and chemical characteristics in response to external mechanical stimuli. In this study, a bioinspired hydrogel was developed to replicate tissue-like mechano-responsiveness, exhibiting strain-stiffening and stress-induced differential modulus adaptation. Biomimetic self-assembly endows the material with structural stability, biocompatibility, and enhanced mechanical performance in wound closure applications. Owing to the apparent combination of tissue resemblance and mechano-responsive capabilities, this type of hydrogel offers significant advantages in a wide range of biomedical applications. Based on preclinical research and clinical reports implicating mechanical tension effects, scar formation would be inhibited if mechanical forces were actively offset through stress shielding by activating mechano-responsiveness across the wound [3]. Mechano-responsive materials are also implicated in practically all physiological processes, such as homeostasis and development of organs and tissues [4-7]. It is widely recognized that mechano-responsive materials modulate skin and wound behavior [4, 8-10]. Mechano-responsive materials modulate skin and wound closure through mechanotransduction and extracellular matrix (ECM) remodeling pathways, particularly involving β-integrins. These mechanisms regulate cellular responses to mechanical stimuli, enhancing tissue repair and creating a supportive environment for wound closure. Mechano-responsive hydrogels are categorized into several groups based on properties that change in response to mechanical stimuli, such as viscosity, color, and strength. The most studied response properties in hydrogel systems include strain-stiffening, mechanochromism, self-healing, and shear thinning [1, 11-17]. Strain-stiffening is a mechanical response with a nonlinear force-extension relation. A material can exhibit strain-stiffening when stretched, and a positive strain causes an increase in stiffness along the strain direction [18, 19]. Strain-stiffening hydrogel mimics the physiological features of biological tissues, making them intriguing options for tissue scaffolds, artificial tissues, and wound closure [20-22]. However, if the external stimuli reach sufficiently high levels, it can lead to mechanical failure (fracture) and damage the skin [20]. Strain-stiffening synthetic materials consist of two or more separate networks with varying stiffnesses for synergizing firmness and softness [11, 23].

To the best of our knowledge, only a few studies have shown unique strain-stiffening properties for enhanced wound closure in synthetic materials as most synthetic materials exhibit negligible strain-stiffening properties. Previous research has resulted the development of wound dressings using polyisocyanopeptides that show strain-stiffening properties [21, 22]. The enhancement or acceleration of wound dressing techniques has been the topic of many recent studies. However, studies regarding the use of strain-stiffening properties of mechano-responsive materials for wound-closure applications are very few. Polyampholyte polymers, such as poly (SA-co-TMA), have been widely used as antifouling materials to facilitate wound dressing by enhancing skin re-epithelialization of wounds after injury [24]. Mixed-charge copolymers composed of 3-sulfopropyl methacrylate (SA) and [2-(methacryloyloxy)ethyl] trimethylammonium (TMA) exhibit precise charge balance, high hydration capacity, protein antifouling, and antibacterial activity through their polyampholyte nature. Mechanically, the incorporation with polytetrafluoroethylene (ePTFE) membranes provides high tensile strength, elasticity, fatigue resistance, and dimensional stability, making them suitable for dynamic and load-bearing wound environments.

Herein, we report the design and preparation of a self-assembly (SAM) technique to enhance the mechanical and mechano-responsive properties of TSC polyampholytes. The TSC polyampholyte constitutes a cationic monomer of a 2-(Acryloyloxy ethyl) trimethylammonium chloride (TMA) and two anionic monomers, 3-sulfopropyl methacrylate potassium salt (SA) and 2-carboxyethyl acrylate (CAA), where T, S, and C represents the TMA, SA, and CAA monomers, respectively, and the number represents the molar ratio that includes a cross-linking triethylene glycol dimethacrylate network. The influence of SAM technique on the phase structure, mechanical and mechano-responsive properties was examined. The characteristics of the TSC polyampholytes were studied in detail using IR. An SAM of the TSC polyampholyte hydrogel displayed strain-stiffening properties. In addition, the effects of the TSC polyampholyte hydrogel on mediating the cell fate was studied and optimized. The results indicated that the strain-stiffening property would aim in solving the problem of wound-closure in static or dynamic mechanical environments.

2. MATERIALS AND METHODS

2.1. Preparation of the TSC polyampholyte based on the SAM approach

A typical SAM approach was used for the synthesis of TSC. We synthesized a new type of polyampholyte hydrogel $T_1S_xC_{1-x}$ by one-step copolymerization of a cationic monomer of TMA and two anionic monomers, SA and CAA. In Milk Q water, 80 µL of a 15% sodium metabisulfite solution and 80 µL of a 40% ammonium persulfate solution were used to begin polymerization, which was slightly different from that used in a previous study [25]. The polymerization procedure was then performed for 1 h at 60°C, after which the gel was cooled for 1 h at room temperature. Following SAM, an 8 M sodium hydroxide (NaOH) aqueous solution was filtered to assemble the TSC building blocks to obtain TSC polyampholyte (SAM).

2.2. Sample Characterizations

Infrared spectroscopy (IR) was performed using a Vertex 70 series spectrophotometer (Bruker Optics, USA). This spectrometer was used to study the secondary structure of TSC polyampholyte with different ratios were referred to as $T_1S_0C_1$, $T_1C_{0.5}S_{0.5}$, and $T_1S_1C_0$ samples.

2.3. Mechanical Characterizations

A tensile machine (FGS-50E-H, Japan) was used to investigate the tensile properties of the TSC polyampholyte. Uniaxial tensile tests were performed in accordance with the ISO 37 Type 3 standard. The strain-stiffening of the material was used to determine the mechanical performance [25]. The differential modulus (k') of hydrogel was assessed according to the following equation (1) [26].

$$k' = \frac{\partial \sigma}{\partial \gamma} \tag{1}$$

Here, k' denotes the differential modulus, defined as a function of stress (σ) and strain (γ), for the same hydrogel.

2.4. In vitro Cell culture

The viability of human dermal fibroblasts-adult HDF-a was quantitatively verified by using cell counting kit (CCK-8, Dojindo, Japan) assay on days 3 and 7. The HDF-a cells were seeded in 21 well-cultured plates and then immersed in a CCK-8 reagent-mixed solution at 37°C for 2 h. Finally, viability of HDF-a cell was determined using a plate reader and absorbance was measured at 450 nm. The nuclei of HDF-a cells were stained with 4',6'-diamidino-2-phenyl-indol (DAPI, Sigma-Aldrich). For cell morphology and viability observation, the samples were stained using fluorescein diacetate (FDA, Sigma-Aldrich) staining assays and photographed after 7 days.

HDF-a cell migration was studied using an in vitro wound closure scratch assay. Firstly, seed the HDF-a cell suspension into each well with the silicone culture insert using 200 µm as a physical barrier. Afterwards, removal of the culture insert will engender a clean cell-free gap. Incubate the dishes for 24 hours at 37°C and 5% CO_2 to allow the cells to migrate into [27]. Finally, measurement of cell migration in the central gap area was measured using Image J software.

2.5. Statistical analysis

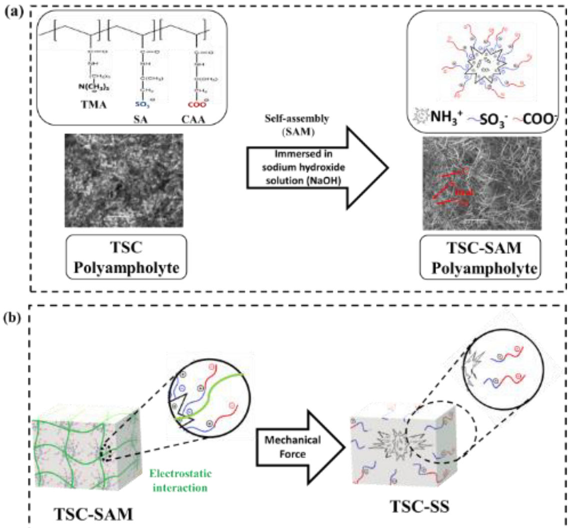

Scheme 1. Schematic Diagram Illustration (a) Preparation of TSC Polyampholyte hydrogel (b) Preparation of TSC-SS Polyampholyte under mechanical force (uniaxial stress)

All data were measured in five replicates (n = 5), unless specified otherwise, represented as the mean ± standard deviation. Statistical significance was indicated by (∗) for probability less than 0.05 ($P < 0.05$), (∗∗) for $P < 0.01$, (∗∗∗) for $P < 0.001$, and (∗∗∗∗) for $P < 0.0001$.

3. RESULT AND DISCUSSION

3.1. Preparation of the TSC polyampholyte based on the SAM approach

In this study, we used copolymerization to prepare TSC polyampholyte hydrogels. The positively charged T (TMA) is repulsive, whereas the negatively charged S (SA) and C (CAA) exert an attractive interaction. TSC polyampholytes were synthesized in three different types with varying numbers of S and C repeat units. In presence of S negatively charged, the $-SO_3^-$ strong anion (S) was exposed, thus increasing interaction with $-COO^-$ weak anion (C) on the TSC networks. After immersion in NaOH solution, negatively charged S and C interact with positively charged T to form structures in which S and C are located at the outer surface under physiological conditions. In presence of NaOH nanoparticles, the $-NH_3^+$ positively charged (T) was unexposed, thus preventing interaction with $-SO_3^-$ negatively charged (S) and $-COO^-$ negatively charged (C) on the TSC networks. This process, known as self-assembly (SAM) formation as shown in Fig. 1b, is depicted in Scheme 1a with an illustration. Thus, SEM imaging (Fig. 1) reveals that the self-assembly process promotes the formation of an interwoven fibrous network within the TSC polyampholyte hydrogel matrix, a feature that is lacking in the non-assembly control samples. These nanofibrillar structures result from the spontaneous organization of triblock copolymers into β-sheet-like domains, as further supported by FTIR analysis (Fig. 3).

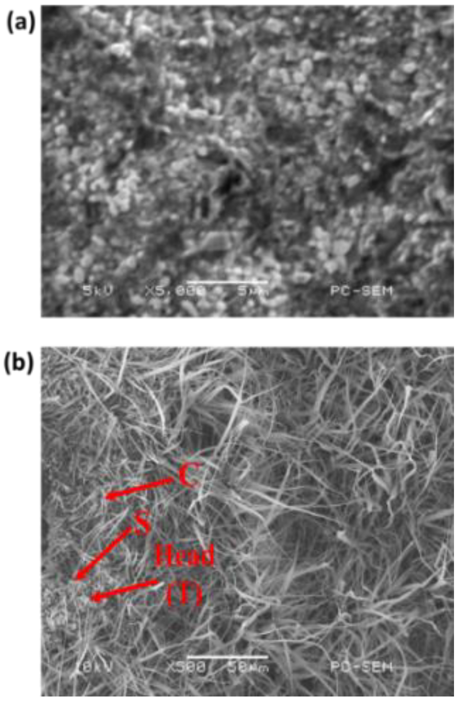

Fig. 1. Scanning electron microscopy (SEM) images of TSC polyampholyte hydrogel (a) before and (b) after self-assembly process

The C and S functional groups were protonated after immersion in aqueous 8 M NaOH. Mechanical force can weaken the electrostatic interaction between C and S, resulting in detachment from the complex in Scheme 1b.

The IR analysis results show that the absorption bands of the hydrogels are characteristic amide-I bands as shown in Fig. 2a-b below [28, 29].

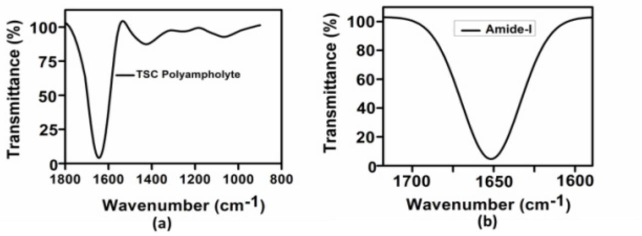

Fig. 2. Characterization of TSC polyampholyte (a) IR spectra of the TSC Polyampholyte the representative of the IR absorbance spectra of the TSC Polyampholyte (b) The amide-I band region (~1600-1700 cm^{-1})

The IR spectra in the amide-I band of TSC polyampholyte as shown in Fig. 3 with different ratios (Tab. 1). The amide-I induced pathogenic amyloid transitions that play an important role in immunological homeostasis during wound healing [30].

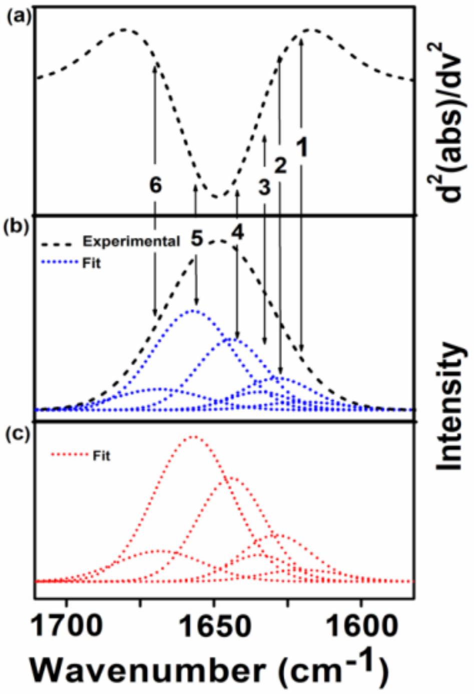

1	2	3	4	5	6
~1602 (Side chain)	~1611 (β-sheet)	~1623 (β-sheet)	~1635 (β-sheet)	~1656 (α-helix)	~1675 (β-turn)

Fig. 3. Spectra of protein secondary structure analysis (a) the IR absorbance spectra's second derivatives contained to the amide-I band (b) IR spectra in the amide-I were fitted by approximating the number and position, which experimental curve (▪▪▪) and simulated fits (···) (c) Result simulated fits are the six Gaussian band prof.

Tab. 1. Amide-I number and position (cm^{-1}) of TSC polyampholyte

TSC polyampholyte	**Amide-I number and position (cm^{-1})**					
	1	2	3	4	5	6
$T_1S_1C_0$	~1601 (Side chain)	~1602 (Side chain)	~1617 (β-sheet)	~1633 (β-sheet)	~1651 (α-helix)	~1664 (β-turn)
$T_1S_{0.5}C_{0.5}$	~1602 (Side chain)	~1611 (β-sheet)	~1623 (β-sheet)	~1635 (β-sheet)	~1656 (α-helix)	~1675 (β-turn)
$T_1S_0C_1$	~1602 (Side chain)	~1619 (Side chain)	~1631 (β-sheet)	~1650 (α-helix)	~1665 (β-turn)	~1680 (β-turn)

3.2. Preparation of the TSC polyampholyte based on the SAM approach

A uniaxial tensile test was performed to validate the increase in the mechanical performance of the TSC polyampholytes. The TSC polyampholytes ($T_1S_XC_{1-x}$) with different molar concentrations are referred to as $T_1S_1C_0$, $T_1S_{0.5}C_{0.5}$, and $T_1S_0C_1$. In this study, a variety of TSC polyampholytes were manufactured with different SC molar concentrations, using both self-assembly (SAM) and non-self-assembly (N-SAM) techniques. The TSC (SAM) with the SAM technique exhibits strain-stiffening as opposed to TSC (N-SAM) with no self-assembly. $T_1S_{0.5}C_{0.5}$ (SAM) exhibits an optimal differential modulus as shown in Fig. 4. The experimental results thus suggest that strain-stiffening properties enhance the mechanical performance and mechano-responsiveness of TSC polyampholyte.

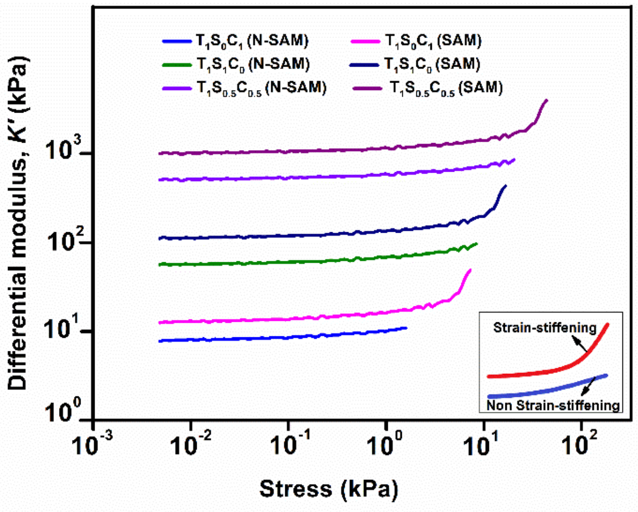

Fig. 4. Strain-stiffening curves of TSC polyampholyte

3.3. Strain-stiffening-mediated cell fate

Considering the results of the strain-stiffening analysis, it is possible to hypothesize that during tensile loading, cell bodies are pushed against the surroundings and contact each other, resulting in tensile resistance and strain-stiffening [25]. The current study reveals that the strain-stiffening property of tension may be considered to mediate cell fate. To evaluate the effect of strain-stiffening on the mediated cell fates, human dermal fibroblasts-adult (HDF-a) were cultured under controlled conditions, and no strain-stiffening (TSC-Non-SS) and strain-stiffening (TSC-SS) were calculated as Fig. 5. After 7 days of cultivation, HDF-a cells adhered well to the surface of the matrix. Strain-stiffening also guides the cell-cell-sensing process of cell adhesion [31]. Adhesion of cells (proliferation and differentiation) enhances with the strain-stiffening of TSC-SS as Fig. 5.

One interesting outcome was the effect of the TSC polyampholyte on the increase in HDF-a content. This effect can be explained by the strain-stiffening property of the TSC polyampholyte hydrogel. Strain-stiffening mediates cell spreading on the hydrogel matrix. Cell spreading of HDF-a cells enhances with the strain-stiffening of TSC polyampholyte (TSC-SS) as Fig. 6.

The results demonstrate that under tensile loading, cell bodies are compressed against their surrounding microenvironment, promoting cell-cell contact. This interaction enhances tensile resistance and increases cell stiffness. The resulting increase in stiffness induces strain-stiffening, a mechanical response that appears to critically influence cell fate determination.

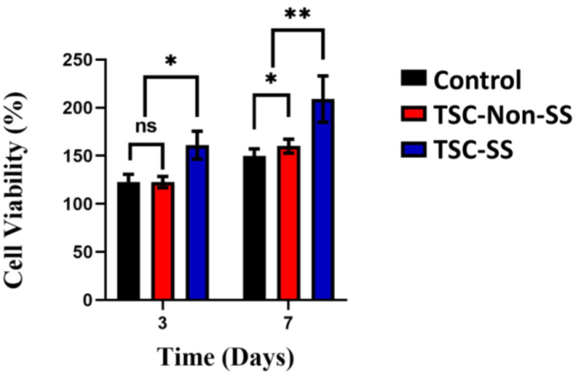

Fig. 5. The cell viability of HDF-a of the different culture plate (control), TSC-Non-SS polyampholyte and TSC-SS polyampholyte

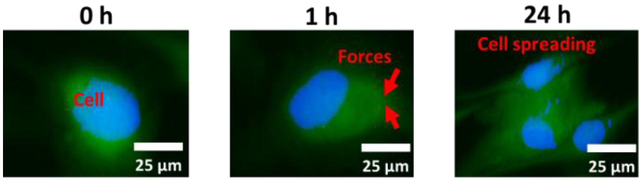

Fig. 6. The HDF-a cells spreading on strain-stiffening of TSC polyampholyte. Scale bar 25 µm

The strain-stiffening TSC could effectively mediate the cell migration than TSC-Non-SS and cultured plates after 24 hours treatment as Fig. 7.

TSC-SS demonstrated higher migrating activity, which could be represented as number of cells filling the central gap as Fig. 8. Furthermore, the strain-stiffening TSC could effectively mediate the cell fate of HDF-a to promote a general organizing principle during tissue development or regeneration. Overall, TSC-SS polyampholytes are promising for wound closure applications.

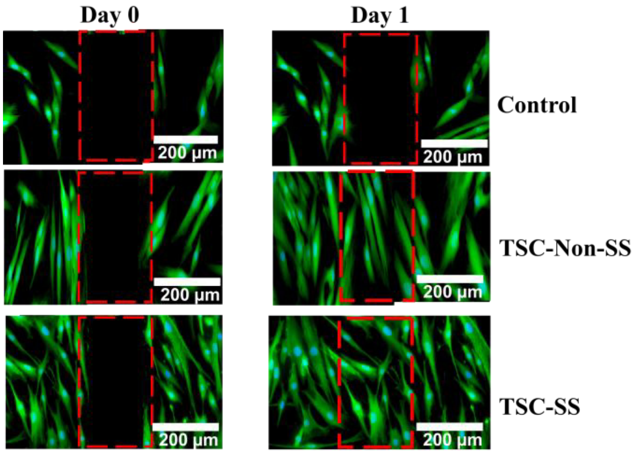

Fig.7. In vitro cell culture, strain-stiffening polyampholyte (TSC-SS), non-strain-stiffening polyampholyte (TSC-Non-SS) and control induce motility in HDF-a cells after 1 day. Scale bar = 200 µm

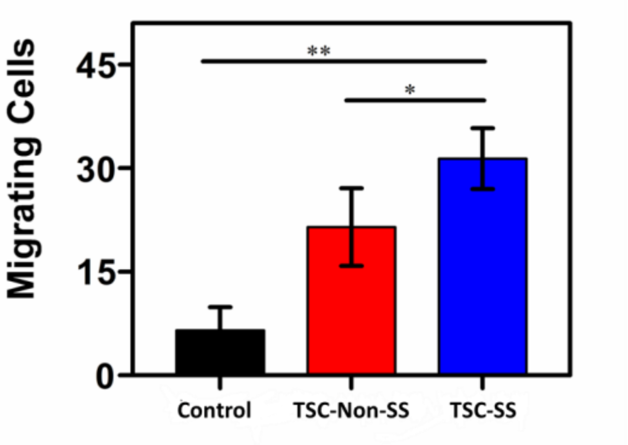

Fig. 8. Cell migration quantification of TSC polyampholyte

4. CONCLUSIONS

In this study, we developed mechano-responsive materials and a self-assembly (SAM) technique to evaluate the strain-stiffening property of TSC polyampholytes for wound closure applications. The TSC hydrogel has amide content, and its differential modulus, contributed to the excellent strain-stiffening property of the TSC polyampholyte. Therefore, strain-stiffening also guides mediated cell fate and is used to connect cells. In addition, the cell migration results indicated that the TSC-SS hydrogel took a shorter time to heal the wound than the TSC-non-SS hydrogel and significantly accelerated the wound closure process with less wound closure time. The strain-stiffening property is a damper response to external mechanical forces and promotes wound closure. Such tough strain-stiffening hydrogels hold great promise for treating wounds in static or dynamic mechanical environments.

REFERENCES

1. Chen J, Peng Q, Peng X, Han L, Wang X, Wang J, et al. Recent advances in mechano-responsive hydrogels for biomedical applications. ACS Appl Polym Mater. 2020;2(3):1092–107.
2. Lavrador P, Esteves MR, Gaspar VM, Mano JF. Stimuli-responsive nanocomposite hydrogels for biomedical applications. Adv Funct Mater. 2021;31(8):1–30.
3. Mascharak S, Griffin M, Chen K, Duoto B, Chinta M. Preventing Engrailed-1 activation in fibroblasts yields wound regeneration without scarring. Science (80-). 2021;372(6540):356.13-358.
4. Lin X, Bai Y, Zhou H, Yang L. Mechano-active biomaterials for tissue repair and regeneration. J Mater Sci Technol (Internet]. 2020;59(June):227-33.
Available from: https://doi.org/10.1016/j.jmst.2020.03.074
5. Panciera T, Azzolin L, Cordenonsi M, Piccolo S. Mechanobiology of YAP and TAZ in physiology and disease. Nat Rev Mol Cell Biol (Internet]. 2017;18(12): 758-70.
Available from: http://dx.doi.org/10.1038/nrm.2017.87
6. Armiger TJ, Lampi MC, Reinhart-King CA, Dahl KN. Determining mechanical features of modulated epithelial monolayers using subnuclear particle tracking. J Cell Sci. 2018;131(12):3–8.
7. Guilak F, Butler DL, Goldstein SA, Baaijens FP. Biomechanics and mechanobiology in functional tissue engineering. 2015;47(9):1933–40.
8. Wong VW, Akaishi S, Longaker MT, Gurtner GC. Pushing back: Wound mechanotransduction in repair and regeneration. J Invest Dermatol. 2011;131(11):2186–96.
9. Barnes LA, Marshall CD, Leavitt T, Hu MS, Moore AL, Gonzalez JG, et al. Mechanical forces in cutaneous wound healing: emerging therapies to minimize scar formation. Adv Wound Care. 2018;7(2): 47–56.
10. Aarabi S, Bhatt KA, Shi Y, Paterno J, Chang EI, Loh SA, et al. Mechanical load initiates hypertrophic scar formation through decreased cellular apoptosis. FASEB J. 2007;21(12):3250–61.
11. Zhang J, Keith AN, Sheiko SS, Wang X, Wang Z. To mimic mechanical properties of the skin by inducing oriented nanofiber microstructures in bottlebrush cellulose-graft-diblock copolymer elastomers. ACS Appl Mater Interfaces. 2021;13(2):3278–86.
12. Zhang W, Wu B, Sun S, Wu P. Skin-like mechanoresponsive self-healing ionic elastomer from supramolecular zwitterionic network. Nat Commun [Internet]. 2021;12(1).
Available from: http://dx.doi.org/10.1038/s41467-021-24382-4
13. Wang X-Y, Zhang J, Dong Y-B, Zhang Y, Yin J, Liu SH. Different structures modulated mechanochromism and aggregation-induced emission in a series of Gold (I) complexes [Internet]. Vol. 156, Dyes and Pigments. Elsevier Ltd; 2018. 74–81 hal. Available from: https://doi.org/10.1016/j.dyepig.2018.03.062
14. Norton AE, Abdolmaleki MK, Liang J, Sharma M, Golsby R, Zoller A, et al. Phase transformation induced mechanochromism in a platinum salt: a tale of two polymorphs. Chem Commun. 2020;56(70):10175–8.
15. Uman S, Dhand A, Burdick JA. Recent advances in shear-thinning and self-healing hydrogels for biomedical applications. J Appl Polym Sci. 2020;137(25):1–20.
16. Zandi N, Sani ES, Mostafavi E, Ibrahim DM, Saleh B, Shokrgozar MA, et al. Nanoengineered shear-thinning and bioprintable hydrogel as a versatile platform for biomedical applications. Biomaterials [Internet]. 2021;267:120476.
Available from: https://doi.org/10.1016/j.biomaterials.2020.120476
17. Seppala JE, Heo Y, Stutzman PE, Sieber JR, Snyder CR, Rice KD, et al. Characterization of clay composite ballistic witness materials. Time-, temperature-, and history-dependent properties. J Mater Sci. 2015;50(21):7048–57.
18. Ramos JRD, Travasso R, Carvalho J. Capillary network formation from dispersed endothelial cells: Influence of cell traction, cell adhesion, and extracellular matrix rigidity. Phys Rev E. 2018;97(1):1–11.
19. Van Oosten ASG, Vahabi M, Licup AJ, Sharma A, Galie PA, MacKintosh FC, et al. Uncoupling shear and uniaxial elastic moduli of semiflexible biopolymer networks: compression-softening and stretch-stiffening. Sci Rep. 2016;6(December 2015):1–9.
20. Op't Veld RC, Walboomers XF, Jansen JA, Wagener FADTG. Design considerations for hydrogel wound dressings: strategic and molecular advances. Tissue Eng - Part B Rev. 2020;26(3):230–48.
21. Op't Veld RC, Joosten L, van den Boomen OI, Boerman OC, Kouwer P, Middelkoop E, et al. Monitoring 111 In-labelled polyisocyanopeptide (PIC) hydrogel wound dressings in full-thickness wounds. Biomater Sci. 2019;7(7):3041–50.

22. op't Veld RC, van den Boomen OI, Lundvig DMS, Bronkhorst EM, Kouwer PHJ, Jansen JA, et al. Thermosensitive biomimetic polyisocyanopeptide hydrogels may facilitate wound repair. Biomaterials [Internet]. 2018;181:392–401.
Available from: https://doi.org/10.1016/j.biomaterials.2018.07.038
23. Keith AN, Vatankhah-Varnosfaderani M, Clair C, Fahimipour F, Dashtimoghadam E, Lallam A, et al. Bottlebrush bridge between soft gels and firm tissues. ACS Cent Sci. 2020;6(3):413–9.
24. Jhong JF, Venault A, Liu L, Zheng J, Chen SH, Higuchi A, et al. Introducing mixed-charge copolymers as wound dressing biomaterials. ACS Appl Mater Interfaces. 2014;6(12):9858–70.
25. Gustini, Lin WC. Characterizations of the strain-stiffening property and cytotoxicity in the self-assembled polyampholyte hydrogel. J Mech Sci Technol. 2022;36(5):2653–61.
26. Wang Y, Xu Z, Lovrak M, le Sage VAA, Zhang K, Guo X, et al. Biomimetic strain-stiffening self-assembled hydrogels. Angew Chemie - Int Ed. 2020;59(12):4830–4.
27. Riahi R, Yang Y, Zhang DD, Wong PK. Advances in wound-healing assays for probing collective cell migration. J Lab Autom. 2012;17(1):59–65.
28. Ji Y, Yang X, Ji Z, Zhu L, Ma N, Chen D, et al. DFT-calculated IR spectrum amide I, II, and III band contributions of N-methylacetamide fine components. ACS omega. 2020;5(15):8572-8.
29. Ghimire H, Venkataramani M, Bian Z, Liu Y, Perera AGU. ATR-FTIR spectral discrimination between normal and tumorous mouse models of lymphoma and melanoma from serum samples. Sci Rep [Internet]. 2017;7(1):1–9. Available from: http://dx.doi.org/10.1038/s41598-017-17027-4
30. Stapelfeldt K, Stamboroski S, Walter I, Suter N, Kowalik T, Michaelis M et al. Controlling the multiscale structure of nanofibrous fibrinogen scaffolds for wound healing. Nano Lett. 2019;19(9): 6554–63.
31. Das RK, Gocheva V, Hammink R, Zouani OF, Rowan AE. Stress-stiffening-mediated stem-cell commitment switch in soft responsive hydrogels. Nat Mater. 2016;15(3):318–25.

We are grateful to the all related institutions, especially Directorate General of Higher Education, Research, and Technology of the Republic of Indonesia for funding supports within State Contract No 090/E5/PG.02.00.PL/2024.

Gustini Gustini: https://orcid.org/0009-0002-8636-6857

Kaprawi Sahim: https://orcid.org/0000-0002-5297-5761

Ida Sriyanti: https://orcid.org/0000-0001-8011-8866

Irmawan Irmawan: https://orcid.org/0000-0002-6003-2333

PHASE VELOCITY OF QUASI SV, SH AND P-WAVES IN TRANSVERSELY ISOTROPIC MEDIUM

Prafulla Kumari PANDA*, Tapas Ranjan PANIGRAHI*

*Department of Mathematics, GIET University, Odisha, Gunupur, India

leenagics@gmail.com, tapas.infinity@gmail.com

received 23 January 2025, revised 12 June 2025, accepted 04 July 2025

Abstract: The current investigation is made to find the analytical solutions of the quasi- SV, SH and P-waves in an inhomogeneous transversely isotropic medium. The paper includes the heterogeneity as an exponential type in density as well as in Young's, and shear modulus with respect to the depth parameter z. Using the Hooke's law, stress-strain and strain-displacement relation in the equation of motion, the phase velocity of the above quasi waves can be evaluated. Again, with the help of analytic solution procedure, the equation of motion will convert to eigen value problem and subsequently the closed-form relation for the quasi velocities will formed. Using the numerical simulations and mathematical calculations, the propagation pattern has been studied. This present finding results the outcome of the heterogeneity constants for different velocities. Two-dimensional graphs have been plotted to show the prominent effect of phase velocity on the surface. The study on quasi wave's may be helpful geophysicists and civil engineers to overcome the problems related to earthquake.

Key words: quasi-waves, transversely isotropic, heterogeneity, Young's moduli, shear modulus

1. INTRODUCTION

In recent days, geologists have shown their greatest interest in anisotropic media, which comes under geophysics and various branches of engineering such as earthquake and petroleum engineering and soil dynamics. Watanabe [1] discussed the deposition of typical naturally occurring soils, such as flocculated clays, varied silts, or sands, in a process called sedimentation that occurs for a long period of time. The overburden may cause the soil medium to exhibit anisotroipic and heterogeneous deformability. Sometimes, due to a different source, i.e., an explosion or other related phenomena, the energy that propagates inside or on the Earth's surface is known as elastic waves. These waves propagate in different directions from the focus point (which is also known as the epicentre), through the body or interior of the surface, known as body waves, and on the surface, called surface waves. The magnitude of the waves can be recorded with the help of an instrument called a seismograph, which is basically kept near the epicenter. The frequency of body waves is higher in comparison to surface waves.

The seismic waves are basically divided into two categories, i.e., primary waves (P-waves) and secondary waves S-waves). Primary waves move faster among the seismic waves, which are also called compressional waves since the waves are perpendicular to the surface. However, the S-waves are called shear waves, where the seismic energy transverses to medium. The body's waves are sometimes called quasi-waves due to their polarization nature, in which waves are not exactly normal or parallel to the plane (energy propagation). Gibson [2] continues the study on the above quasi-waves to calculate the impact of the depth, orthotropy, and inhomogeneity, which lie on a surface of thickness 110 ft, upon a rigid base. t the same moment, Levin [3] discovered P-wave, SV-wave, and SH-wave velocities with the help of a cross-anisotropic medium.

Gazetas [4] explored the influence of transversely isotropic half-space on the surface of the medium. In the year 2019, Vishwakarma et al. [5] considered a fiber-reinforced viscoelastic medium and discussed the result of a shear horizontal wave under initial stress. The reference for this current work can be given to Singh et al. [6], Chaudhary et al. [7], Saha et al. [8], and Kaur et al. [9] for their advanced work towards seismic shear horizontal wave propagation. The reflection problems for the P-wave and SV-wave in a monoclinic medium at the free boundary were studied by Chattopadhyay et al. [10]. They also discussed that the incidence of the wave has a greater impact on the reflection coefficients. Wang et al. [11] and Zhang [12] have discussed the quasi SV, SH, and on P waves in a transversely isotropic medium. Reference can be given to Lu et al. ([13], [14]) for calculating traveltimes for quasi waves in transversely isotropic medium using fast sweeping method, which may be considered as an application to this current research.

Bullen [15] provided a comprehensive mathematical justification, supplemented by a heuristic proof and its subsequent validation. He further proposed an approximation for the Earth's internal density distribution, demonstrating that between depths of 413 km and 984 km, the density follows a quadratic variation with respect to depth. Beyond 984 km, extending towards the Earth's central core, Bullen approximated the density variation as a linear function of depth. He emphasized that it is reasonable to explore the behavior of wave profiles in geo-media exhibiting inhomogeneity represented as mathematical functions of depth. Numerous researchers have investigated such inhomogeneities, often modelling them as linear, quadratic, or exponential functions of the depth parameter. A limited number of studies also address quasi-wave propagation through heterogeneous substrata. In the following table, different inhomogeneity mathematical functions have been discussed. Different authors has been discussed about the quasi-wave velocities by considering various mathematical functions in terms of linear, quadratic, exponential and power law model in Young's moduli, shear modulus, and density. The following table-I has been created to give the idea of inhomogenity parameters used in varrious published works in reputed journals.

Tab. 1. Inhomogeneity table

1	$E = E_0 e^{az}$, a: Inhomogeneity parameter	Wang et. al 2010
2	$E = E_0(a + bz)^c$, $a, b,$ and c: Inhomogeneity parameters	Wang et. al 2012
3	$E = E_0 e^{nsinz}$,where $a, b,$ and c: Inhomogeneity parameters	Vishwakarma and Panigrahi 2021
4	$E = E_0(1 + \delta z)^n e^{\beta z}$, $\delta, \beta,$ and n: Inhomogeneity parameters	Kaur and Vishwakarma 2020
5	$E = E_0(a - \cos\gamma\, z)e^{\beta z}$, γ, β: Inhomogeneity parameters	Kaur and Vishwakarma 2020

Numerous researchers have made significant contributions to addressing the issues related to body waves in cross-anisotropic soils. However, no prior work has explored the scenario where the cross-anisotropic material exhibits inhomogeneity in Young's moduli, shear modulus, and density, characterized by the following exponential function i.e. the variation has been taken in the physical quantities like Young's and shear modulus and density of the surface is e^{ncosz}, where $n,\ z \in R$ of depth z. Generalized Hooke's law of elasticity and strain-displacement relationships along with equilibrium equations of motion have been used, which further reduces to eigenvalue problem whose spectral values reflect the wave velocities. A general analytical model for the velocities of P-wave, SH-wave and SV-wave in cross-anisotropic material has been proposed. Graphical illustrations have been presented to study the influence of each inhomogeneity parameter on wave velocity against the phase angle of wave. The study may be helpful for researchers or seismologists in the field of reflection and refraction problems in body waves, which will enrich the concept of the structure of the earth's interior. Recently, a number of researchers have conducted significant studies on reflection and refraction problems in elastic media. Among them, the contributions of Sahu et al. [16], Kumar and Paswan [17], Kumar et al. [18], and Paswan and Kumar [19] are noteworthy. These studies have explored the behavior of seismic waves at material interfaces under varying geological and anisotropic conditions.

2. GEOMETRY AND SOLUTIONS

The current article studies the seismic quasi-waves in the cross-anisotropic material, with detailed calculations for the quasi-wave velocities. The problem has been discussed with the help of the coordinate system (x, y, z), where x in the horizontal direction and z in the downward direction (positive direction), shown in Fig. 1. The stress-strain relationship is as follows:

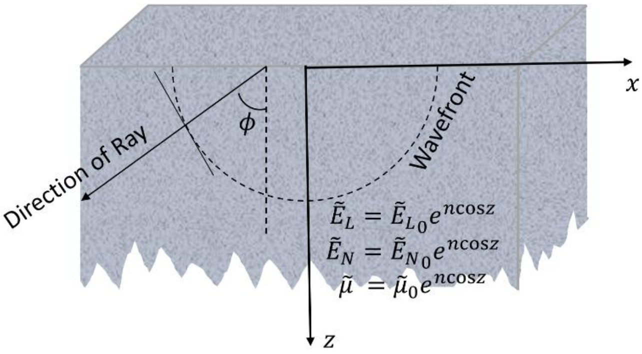

Fig. 1. Geometry of the problem

$$S_{xx} = \tilde{C}_{11}e_{xx} + (\tilde{C}_{11} - 2\tilde{C}_{66})e_{yy} + \tilde{C}_{13}e_{zz},\ S_{yy} = (\tilde{C}_{11} - 2\tilde{C}_{66})e_{xx} + \tilde{C}_{11}e_{yy} + \tilde{C}_{13}e_{zz}, S_{zz} = \tilde{C}_{13}e_{xx} + \tilde{C}_{13}e_{yy} + \tilde{C}_{33}e_{zz}, S_{yz} = \tilde{C}_{44}e_{yz}, S_{xz} = \tilde{C}_{44}x_{yz}, S_{xy} = \tilde{C}_{66}e_{xy}, \tag{1}$$

where

$$e_{xx} = \frac{\partial u_x}{\partial x}, e_{yy} = \frac{\partial u_y}{\partial y}, e_{zz} = \frac{\partial u_z}{\partial z}, e_{yz} = \frac{\partial u_y}{\partial z} + \frac{\partial u_z}{\partial y}, e_{xz} = \frac{\partial u_x}{\partial z} + \frac{\partial u_z}{\partial x}, e_{xy} = \frac{\partial u_x}{\partial y} + \frac{\partial u_y}{\partial x}.$$

The elastic constants may be represented as, $\tilde{E}_L,\ \tilde{E}_N,\ \tilde{\nu}_L, \tilde{\nu}_N,$ and $\tilde{\mu}$ as

$$\tilde{C}_{11} = \frac{\tilde{E}_L(1 - \frac{\tilde{E}_L}{\tilde{E}_N}\tilde{\nu}^2{}_N)}{(1+\tilde{\nu}_L)(1-\tilde{\nu}_L - 2\frac{\tilde{E}_L}{\tilde{E}_N}\tilde{\nu}^2{}_N)}, \tilde{C}_{13} = \frac{\tilde{E}_L\tilde{\nu}_N}{(1-\tilde{\nu}_L - 2\frac{\tilde{E}_L}{\tilde{E}_N}\tilde{\nu}^2{}_N)}, \tilde{C}_{33} = \frac{\tilde{E}_N(1-\tilde{\nu}_L)}{(1-\tilde{\nu}_L - 2\frac{\tilde{E}_L}{\tilde{E}_N}\tilde{\nu}^2{}_N)}, \tilde{C}_{44} = \tilde{\mu}, \tilde{C}_{66} = \frac{\tilde{E}_L}{2(1+\tilde{\nu}_L)}.$$

Assuming the inhomogeneity in the elastic parameters as

$$\tilde{E}_L = \tilde{E}_{L_0}e^{ncosz}, \tilde{E}_N = \tilde{E}_{N_0}e^{ncosz}, \mu = \tilde{\mu}_0 e^{ncosz}, \rho = \tilde{\rho}_0 e^{ncosz}, n, z \in R. \tag{2}$$

Where, n: inhomogeneity coefficient having no dimension. From above conditions, we have

$$\tilde{C}_{ij} = \tilde{C}_{ij}e^{ncosz}, \quad (i, j = 1,2, \ldots 6), \tag{3}$$

where

$$\tilde{C}_{11} = \frac{\tilde{E}_{L_0}(1 - \frac{\tilde{E}_{L0}}{\tilde{E}_{N_0}}\tilde{\nu}^2{}_N)}{(1+\tilde{\nu}_L)(1-\tilde{\nu}_L - 2\frac{\tilde{E}_{L0}}{\tilde{E}_{N_0}}\tilde{\nu}^2{}_N)}, \tilde{C}_{13} = \frac{\tilde{E}_{L_0}\tilde{\nu}_N}{(1-\tilde{\nu}_L - 2\frac{\tilde{E}_{L0}}{\tilde{E}_{N_0}}\tilde{\nu}^2{}_N)},$$

$$\tilde{C}_{33} = \frac{\tilde{E}_{N_0}(1-\tilde{\nu}_L)}{(1-\tilde{\nu}_L - 2\frac{\tilde{E}_{L0}}{\tilde{E}_{N_0}}\tilde{\nu}^2{}_N)}, \tilde{C}_{44} = \tilde{\mu}, \tilde{C}_{66} = \frac{\tilde{E}_{L0}}{2(1+\tilde{\nu}_L)}.$$

Biot's equation of motion as follows (Biot [20])

$$\frac{\partial S_{xx}}{\partial x} + \frac{\partial S_{xy}}{\partial y} + \frac{\partial S_{xz}}{\partial z} = \rho\frac{\partial^2 u_x}{\partial t^2}, \tag{4}$$

$$\frac{\partial S_{xy}}{\partial x} + \frac{\partial S_{yy}}{\partial y} + \frac{\partial S_{yz}}{\partial z} = \rho\frac{\partial^2 u_y}{\partial t^2}, \tag{5}$$

$$\frac{\partial S_{xz}}{\partial x} + \frac{\partial S_{yz}}{\partial y} + \frac{\partial S_{zz}}{\partial z} = \rho\frac{\partial^2 u_z}{\partial t^2}, \tag{6}$$

3. DERIVATION OF PHASE VELOCITY

The following equations has been derived by substituting the stress-strain, strain-displacement relationships and the inhomogeneities in the Biot's equation of motion.

$$[\tilde{C}_{11}\frac{\partial^2}{\partial x^2}+\ \tilde{C}_{66}\frac{\partial^2}{\partial y^2}+\tilde{C}_{44}\frac{\partial^2}{\partial z^2}-n\ sin\ z\tilde{C}_{44}\frac{\partial}{\partial z}]\ u_x\ +[\ \tilde{C}_{11}-\tilde{C}_{66}\ ]\frac{\partial^2 u_y}{\partial x\partial y}+\left[\left(\tilde{C}_{13}+\tilde{C}_{44}\right)\frac{\partial^2}{\partial x\partial z}-n\ sinz\ \tilde{C}_{44}\frac{\partial}{\partial x}\right]u_z=\rho_0\frac{\partial^2 u_x}{\partial t^2} \tag{7}$$

$$[\tilde{C}_{11}-C_{66}]\ \frac{\partial^2 u_x}{\partial x\partial y}\ [\tilde{C}_{66}\frac{\partial^2}{\partial x^2}+\tilde{C}_{11}\ \frac{\partial^2}{\partial y^2}+\ \tilde{C}_{44}\frac{\partial}{\partial z}-n\ sinz\ \tilde{C}_{44}\frac{\partial}{\partial z}]u_y+[(\tilde{C}_{13}+\ \tilde{C}_{44})\frac{\partial^2}{\partial y\partial z}-n\ sinzC_{44}\frac{\partial}{\partial y}]\ u_z=\rho_0\frac{\partial^2 u_y}{\partial t^2} \tag{8}$$

$$[\tilde{C}_{13}+\ \tilde{C}_{44})\frac{\partial^2}{\partial x\partial z}-n\ sinz\ \tilde{C}_{13}\frac{\partial}{\partial x}]u_x+[(\tilde{C}_{13}+\tilde{C}_{44})\frac{\partial^2}{\partial y\partial z}-n\ sinz\ \tilde{C}_{13}\frac{\partial}{\partial y}]u_y+[\tilde{C}_{44}\left(\frac{\partial^2}{\partial x^2}+\frac{\partial^2}{\partial y^2}\right)+\tilde{C}_{33}\frac{\partial^2}{\partial z^2}-n\ sinz\ \tilde{C}_{33}\frac{\partial}{\partial z}]\ u_z=\rho_0\frac{\partial^2 u_z}{\partial t^2} \tag{9}$$

The solutions for equations (7)-(9) can be considered as (Hu [21])

$$u_x=\widetilde{D}_1 g(x\ sin\emptyset+z\ cos\ \emptyset-Vt), \tag{10}$$

$$u_y=\widetilde{D}_2 g(x\ sin\ \emptyset+z\ cos\ \emptyset-Vt), \tag{11}$$

$$u_z=\widetilde{D}_3 g(x\ sin\ \emptyset+z\ cos\ \emptyset-Vt), \tag{12}$$

Where t=time. On putting the equations (10) - (12) in equations (7) - (9), we find

$$\left[\tilde{C}_{11}sin^2\emptyset+\ \tilde{C}_{44}cos^2\emptyset-n\ sin\ z\ \tilde{C}_{44}cos\ \emptyset-\rho_0 V^2\right]D_1+\left[\left(\tilde{C}_{13}+\tilde{C}_{44}\right)sin\ \emptyset cos\emptyset-acos\ z\tilde{C}_{44}sin\ \emptyset\right]D_3=0 \tag{13}$$

$$[\tilde{C}_{66}sin^2\emptyset+\tilde{C}_{44}cos^2\emptyset-n\ sin\ z\tilde{C}_{44}cos\ \emptyset-\rho_0 V^2]D_2=0 \tag{14}$$

$$[(\tilde{C}_{13}+\tilde{C}_{44})\sin\ \emptyset\ cos\emptyset-n\sin\ z\tilde{C}_{13}\sin\ \emptyset]D_1+[\tilde{C}_{44}sin^2\emptyset+\tilde{C}_{33}cos^2\emptyset-n\ sin\ z\tilde{C}_{33}cos\emptyset-\rho_0 V^2]D_3=0 \tag{15}$$

The above equations (13)-(15) can be written as follows

$$\begin{bmatrix} a_{11}-\rho_0 V^2 & 0 & a_{13} \\ 0 & a_{22}-\rho_0 V^2 & 0 \\ a_{31} & 0 & a_{33}-\rho_0 V^2 \end{bmatrix}\begin{bmatrix}\widetilde{D}_1\\ \widetilde{D}_2\\ \widetilde{D}_3\end{bmatrix}=\begin{bmatrix}0\\0\\0\end{bmatrix}$$

where

$$a_{11}=\tilde{C}_{11}sin^2\emptyset+\ \tilde{C}_{44}cos^2\emptyset-n\tilde{C}_{44}sin\ zcos\emptyset,$$

$$a_{13}=\left(\tilde{C}_{13}+\tilde{C}_{44}\right)sin\emptyset cos\emptyset-n\tilde{C}_{44}sin\ zsin\ \emptyset,$$

$$a_{22}=\tilde{C}_{66}sin^2\emptyset+\tilde{C}_{44}cos^2\emptyset-\ n\ \tilde{C}_{44}\sin\ z\ cos\emptyset,$$

$$a_{31}=\left(\tilde{C}_{13}+\tilde{C}_{44}\right)\sin\emptyset\cos\emptyset-n\tilde{C}_{13}\sin zsin\phi,$$

$$a_{33}=\tilde{C}_{44}sin^2\emptyset+\tilde{C}_{33}cos^2\emptyset-n\tilde{C}_{33}sin\ zcos\ \emptyset.$$

It gives rise to an eigenvalue problem for an in homogeneous cross-anisotropic medium and the solution of which gives the magnitude of velocities of three quasi-waves as (V_{SV},V_{SH},V_P) for an inhomogeneous cross-anisotropic medium

$$V_{SH}=\sqrt{\frac{\tilde{C}_{66}sin^2\emptyset+\ \tilde{C}_{44}cos\emptyset(cos\ \emptyset-nsin\ z)}{\rho_0}}$$

$$V_{SV}=\frac{1}{\sqrt{2\rho_0}}\sqrt{\tilde{A}_1-\sqrt{\tilde{A}^2{}_1+4\tilde{A}_2}} \tag{16}$$

$$V_P=\frac{1}{\sqrt{2\rho_0}}\sqrt{\tilde{A}_1+\sqrt{\tilde{A}^2{}_1+4\tilde{A}_2}}$$

where

$$\tilde{A}_1=\tilde{C}_{33}+\ \tilde{C}_{44}+sin^2\emptyset\left(\tilde{C}_{11}-\tilde{C}_{33}\right)$$

$$-n\ sin\ z\ cos\emptyset\left(\tilde{C}_{33}+\ \tilde{C}_{44}\right)$$

$$\tilde{A}_2=-\tilde{C}_{33}\tilde{C}_{44}cos^2\emptyset\ (n\ sinz-cos\ \emptyset)^2-\tilde{C}_{11}\tilde{C}_{44}sin^4\emptyset$$

$$+sin^2\emptyset\left[n^2 sin^2 z\tilde{C}_{13}\tilde{C}_{44}+cos\ \emptyset(cos\ \emptyset-n\ sin\ z)\left(\tilde{C}^2{}_{13}-\tilde{C}_{11}\tilde{C}_{33}+2\tilde{C}_{13}\tilde{C}_{44}\right)\right]$$

Equation (16) is the required velocities i.e SV, SH and P-waves.

4. PARTICULAR CASE

When $n\rightarrow 0$, equation (16) reduces to

$$V_{SH_0}=\sqrt{\frac{\tilde{C}_{66}sin^2\emptyset+\tilde{C}_{44}cos^2\emptyset}{\rho_0}}$$

$$V_{SV_0}=\frac{1}{\sqrt{2\rho_0}}\sqrt{\tilde{F}_1-\sqrt{\tilde{F}_1^2+4\tilde{F}_2}} \tag{17}$$

$$V_{P0}=\frac{1}{\sqrt{2\rho_0}}\sqrt{\tilde{F}_1+\sqrt{\tilde{F}_1^2+4\tilde{F}_2}}$$

where

$$\tilde{F}_1=\tilde{C}_{33}+\ \tilde{C}_{44}+sin^2\emptyset\left(\tilde{C}_{11}-\tilde{C}_{33}\right),\ \tilde{F}_2=-\tilde{C}_{33}\tilde{C}_{44}cos^4\emptyset\ -\tilde{C}_{11}\tilde{C}_{44}sin^4\emptyset+sin^2\emptyset\cos^2\emptyset\left(\tilde{C}^2{}_{13}-\tilde{C}_{11}\tilde{C}_{33}+2\tilde{C}_{13}\tilde{C}_{44}\right)$$

On reducing the inhomogeneity constants of eqn. (16) to zero, i.e., $n\rightarrow 0$, this model will reduce to the model designed by Daley and Hron [21] and Levin [22]), and the results match their results, which is given in eqn. (17).

5. NUMERICAL AND GRAPHICAL REPRESENTATION

In this section, the results of the inhomogeneity parameter n and the rigidity $\tilde{\mu}_0$ on the velocities of (V_{SV},V_{SH},V_P) waves have been discussed. On performing the numerical simulations, different graphs have been plotted for Eq. (16) and Eq. (17). The study was basically carried out to find the impact of the different parameters on varying the depth parameters $z=1\ m$ and $z=3\ m$. The comparison has been shown through graphs for these (V_{SV},V_{SH},V_P) waves.

The current investigation deals with two sets of graphs, i.e., Fig. 2 and Fig. 3. In Fig. 2, the study has been done for all three quasi-waves, i.e., V_{SV}-waves, V_{SH}-waves, and V_P-waves. The main intention is to find the influence of the inhomogeneity parameter n

(which varies as (n =-0.2, 0.0, 0.2) on the phase velocity of the (V_{SV}, V_{SH}, V_P) waves. Let us consider the first figure of Fig. 2, i.e., the V_{SV}-wave, in which it can be observed that the velocity decreases from 0 degrees to nearly 60-degree and then suddenly goes up and meets at the phase velocity 1.0. In the figure, it is clearly visible that the depth parameter has a significant effect on the phase velocity; the influence in the case of $z = 1\ m$ quite greater than that of $z = 3\ m$. Again, on considering the V_{SH}-wave, it has been found that on increasing the phase angle, the phase velocity seems constant up to 76-degree and then suddenly jerks up and down and meets at 1.0. Here, we can also say that the influence of the inhomogeneity parameter decreases with increasing depth. Finally, the last figure in Fig. 2 has been plotted for the V_P-wave for both the depth parameters $z = 1\ m$ and $z = 3\ m$. The study shows the increasing nature of the phase velocity for the increasing inhomogeneity parameters. The effects are visible to the naked eye, and for all three velocities, one can conclude that by increasing the inhomogeneity parameter n, the phase velocity decreases at a particular phase angle.

Figure 3 shows the effect of the rigidity ($\tilde{\mu}_0$) on the phase velocity of the three quasi-waves, i.e., V_{SV}-waves, V_{SH}-waves, and V_P-waves. Now taking the individual figures into the discussion, the first figure, V_{SV}-waves, which has been plotted for the parameter ($\tilde{\mu}_0$), gives the same effect as V_{SV}-wave varying for the inhomogeneity parameter n. Here, one can see that the first two curves, which have been plotted for ($\tilde{\mu}_0$ =1.0, 2.0), intersect at the phase angle nearly at 7 degrees. In the case of the V_{SH}-wave, the influence is quite significant in the case of the depth parameter $z = 1\ m$, in which the velocity remains constant up to 40 degrees and suddenly goes up to phase velocity 1.0. And the depth parameter $z = 3\ m$ produces a very negligible effect on the phase velocity, so the zoomed figure will help to recognize the pattern of the curves. Finally, the V_P-wave, which has been plotted for the increasing values of the parameter $\tilde{\mu}_0 = 1.0, 2.0, 3.0$, creates abnormal behavior for the depth parameter $z = 3\ m$, and for the depth parameter $z = 1\ m$, the curve first goes down, then moves up, and finally meets at 1.0.

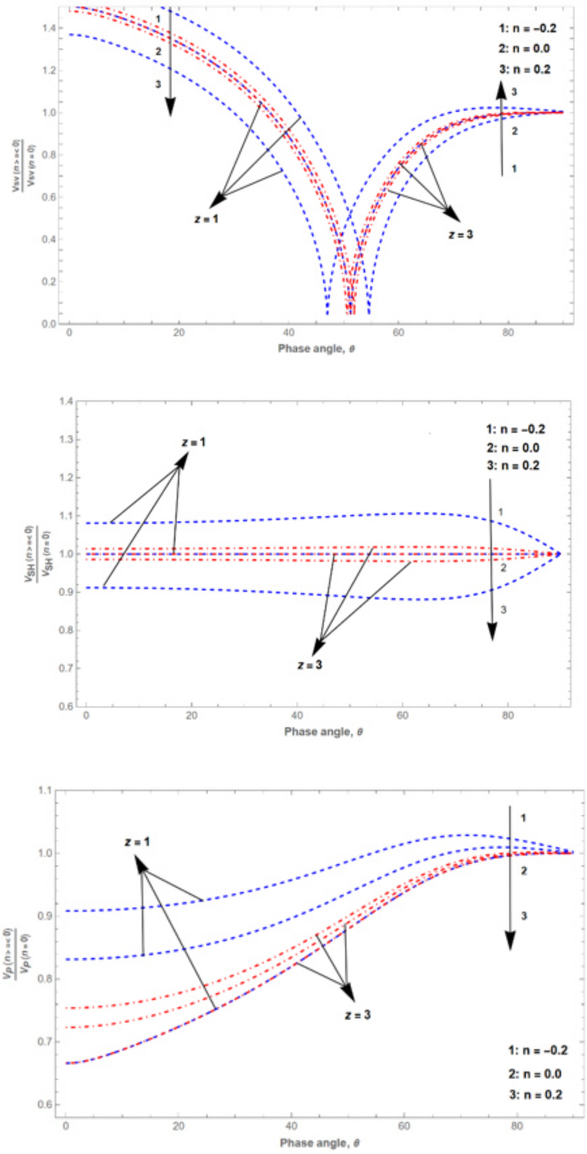

Fig. 2. Dimensionless phase velocity Vs. phase angle and to find impact of the inhomogeneity parameter n on the velocity of SV, SH, and P waves

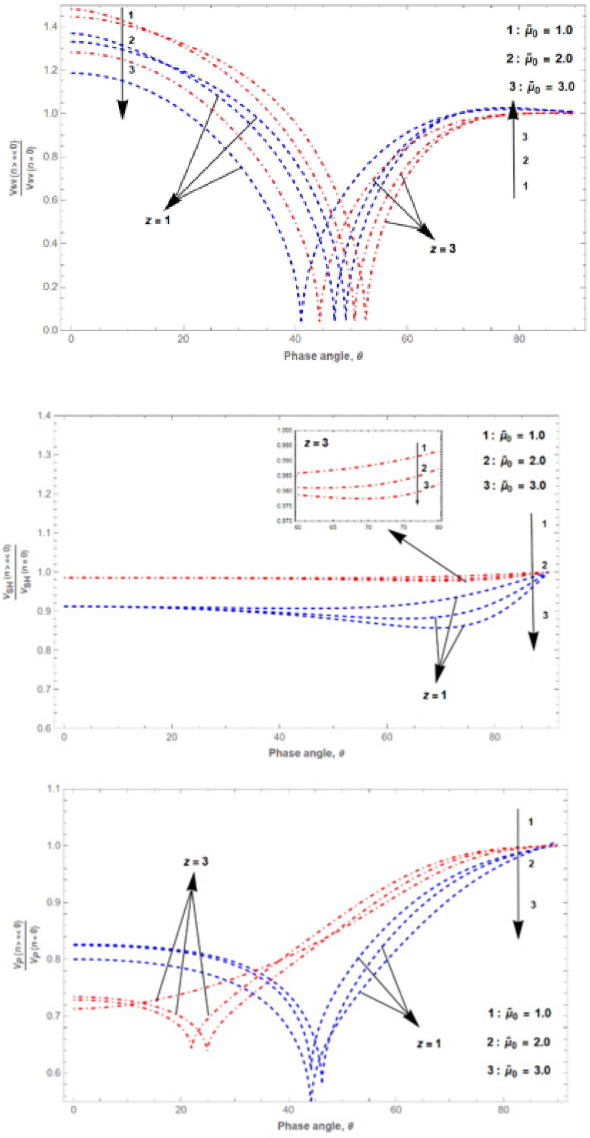

Fig. 3. Dimensionless phase velocity Vs. phase angle and to find impact of the inhomogeneity parameter $\tilde{\mu}_0$ on the velocity of SV, SH, and P waves

6. CONCLUSION

The current research work is helpful in finding a way to study the propagation behavior of body waves. The solution is carried out through a general analytical method for the three different waves, i.e., SV-wave, SH-wave, and P-wave, in a heterogeneous cross-anisotropic medium. The phase velocities of the three waves (SV, SH, and P) are obtained in closed form, as is the inhomogeneity, which is an exponential function with respect to the depth parameter z. The present study has been done for the depth of the Earth surface for $z = 1\ m$ and $z = 3\ m$. The following are the results of this current work:

Two figures i.e., fig. 2, and fig. 3 have been plotted to show the impacts of the inhomogeneity parameters n and $\tilde{\mu}_0$ on the phase velocity of the SV-waves, SH-waves, and P-waves. In Fig. 2, it has been found that for all the quasi-waves, the velocity is higher near the surface, and the velocity will be negligible while moving down and down. At an angle of 90 degrees, all the curves converge to meet at the same velocity at 1.0.

In fig. 3, which has been plotted for the parameter $\tilde{\mu}_0$, a similar type of result is found as in fig. 2. The only difference one can note is for the SH-wave, i.e., for the depth parameter $z = 3\ m$, the impact is quite negligible and can be observed through the zoomed figure, and for the P-wave, the abnormal behavior of the curves can be detected. The findings are valuable for developing simplified calculation methods to assess the effects of seismic waves on buildings, as highlighted in the works of Ha et al. [23] and Abdoun et al. [24]. Additionally, the results can aid in quantifying wave velocities from the source, which may contribute to predicting Earth's subsurface composition. Furthermore, this approach can assist in identifying oil traps and other economically significant geological formations. The study may be helpful to geologists to know the presence of different materials present inside the earth surface.

REFERENCES

1. Watanabe K, Payton RG. Green's function and its non-wave nature for SH-wave in inhomogeneous elastic solid. Int. J. Eng. Sci. 2004; 42: 2087-2106.
2. Gibson RE. The analytical method in soil mechanics. Geotechnique. 1974; 24:115-140.
3. Levin FK, Seismic velocities in transversely isotropic media. Geophysics. 1979; 44: 918-936.
4. Gazetas G. Stresses and displacements in cross-anisotropic soils. J Geotech Eng. 1982;108:532-553.
5. Vishwakarma SK, Panigrahi TR, Kaur R. SH-wave propagation in linearly varying fibre-reinforced viscoelastic composite structure under initial stress. Arab J Geosci. 2029;12:59.
6. Singh AK, Das A, Chattopadhyay A, Dhua S. Influence of magnetic effect, anisotropy, irregularity, initial stress and heterogeneity on propagation of SH-wave in an irregular prestressed magnetoelastic monoclinic sandwiched layer. Arab J Geosci.2017;10:284.
7. Chaudhary S, Sahu SA, Singhal A. On secular equation of SH waves propagating in pre-stressed and rotating piezo-composite structure with imperfect interface. J Intel Mat Syst Str. 2018; 29(10):2223–2235.
8. Saha S, Singh AK, Chattopadhyay A. On propagation behavior of SH-wave and Rayleigh-type wave in an initially stressed exponentially graded fiber-reinforced viscoelastic layered structure. Waves Random Complex Media. 2019; 31(3):1-29. https://doi.org/10.1080/17455030.2019.1599147
9. Kaur R, Vishwakarma SK, Panigrahi TR. Influence of irregular geologies and inhomogeneity on SH-wave propagation. Acta Mech. 2020;231:1821–1836.
10. Chattopadhyay A, Venkateswarlu RLK, Saha S. Reflection of quasi-P and quasi-SV waves at the free and rigid boundaries of a fibre-reinforced medium. Sadhana. 2002;27(6):613–630.
11. Wang CD, Wang WJ, Lin YT, Ruan ZW. Wave propagation in an inhomogeneous transversely isotropic material obeying the generalized power law. model Arch Appl Mech. 2012;82:919–936.
12. Zhang YH, Fu XD, Sheng Q, Leng XL, Study on elastic P-wave propagation law in unfavorable geologic structures with discontinuous deformation analysis method. Arab J Geosci. 2013; 6:4557–4564.
13. Lu Y, Zhang W, Zhang Y. Traveltime calculations for qP, qSV, and qSH waves in tilted transversely isotropic media using fast sweeping method with a Newton iterative solver, Geophysics. 2020; 0:1-89. https://doi.org/10.1190/geo2024-0093.1
14. Lu Y, Zhang W, Zhang J. Calculating traveltimes in 2D general tilted transversely isotropic media using fast sweeping method. Computers and Geosciences. 2024;193:105724. https://doi.org/10.1016/j.cageo.2024.105724
15. Bullen KE. The problem of the Earth's density Media. Bull Seismol Soc Am.1940; 30(3):235-250.
16. Sahu S A, Paswan B, Chattopadhyay A. Reflection and transmission of plane waves through isotropic medium sandwiched between two highly anisotropic half-spaces. Waves in Random and ComplexMedia. 2015; 26(1):42–67. https://doi.org/10.1080/17455030.2015.1102361
17. Kumar D, Paswan B. Mathematical Aspects of Reflection Phenomena at the Stress-Free Interface of Micropolar Transversely Isotropic Half-Space under Nonlocal Theory. Mech. Solids. 2024;59:1072–1082. https://doi.org/10.1134/S0025654423602276
18. Kumar D, Paswan B., Singh P. Reflection phenomena of plane wave at an initially stressed nonlocal triclinic half-space with stress-free interface. Appl. Phys. 2024; A:130:904. https://doi.org/10.1007/s00339-024-08045-x
19. Paswan B, Kumar D. Analytical study of the reflection and refraction phenomena of plane seismic waves at the interface of orthotropic material sandwiched between two highly anisotropic triclinic media under the initial stresses. Int J Geomath. 2024;15. https://doi.org/10.1007/s13137-024-00256-x
20. Biot MA. Mechanics of Incremental Deformation. John Willey and Sons. New York 1965.
21. Hu T. Assembly of an ultrasonic equipment and dynamic elastic properties of an anisotropic rock. Master Thesis. National Chiao-Tung University 1995.
22. Daley PF, Hron F. Reflection and transmission coefficients for transversely isotropic media. Bull Seismol Soc Am.1977;67:661-675.
23. Ha D, Adoun TH, O'Rourke MJ, Symans MD. Centrifuge modeling of earthquake effects on buried high- density polyethylene (HDPE) pipelines crossing Fault Zones. J Geotech Geoenviron Eng. 2008;134(10):1501–1515.
24. Abdoun TH, Ha D, O'Rourke MJ, SymansMD, O'Rourke TD, Palmer MC, Stewart HE. Factors influencing the behavior of buried pipelines subjected to earthquake faulting. Soil Dyn Earthq Eng. 2009; 29(3):415–427.

Prafulla Kumari Panda: https://orcid.org/0009-0000-5115-6425

Tapas Ranjan Panigrahi: https://orcid.org/0000-0001-8353-702X

DOI 10.2478/ama-2025-0053

SURFACE CHARACTERIZATION AND WEAR INVESTIGATION ON NI-DOPED CR-MO ALLOY STEEL IN GEAR APPLICATIONS

Hailemariam Nigus HAILU*, Daniel Tilahun REDDA**

*Mechanical Technology Faculty, Automotive Technology Department,
FDRE Technical and Vocational Training Institute, Ethiopia
**School of Mechanical and Industrial Engineering, Addis Ababa Institute of Technology, Addis Ababa University, Ethiopia

hailuqua@gmail.com, danieltredda@gmail.com

received 18 June 2025, revised 31 August 2025, accepted 01 September 2025

Abstract: This study carried out experimental rolling contact fatigue (RCF) tests on two types of materials: commercially available Cr-Mo alloy steel and 1.55% Ni-doped Cr-Mo alloy steel, using a twin-disc test rig. Micropitting was identified as the most prominent damage feature on the rolled surfaces of the disc samples during the gears' RCF tests. To investigate gear surface characteristics and wear behavior, RCF tests were conducted on both material types. The twin-disc test was designed to replicate asperity contact on mating gear flank surfaces, using low-speed cylindrical disc specimens and high-speed crowned disc specimens, ensuring a minimum effective contact area of 8.5 mm. After testing, surface morphology and topographical changes were examined using Scanning Electron Microscopy (SEM). The results revealed that 1.55% Ni-doped Cr-Mo alloy steel demonstrated superior resistance to contact fatigue failure compared to the commercially available Cr-Mo alloy steel, as evidenced by a lower micropitted area ratio, shallower pitted depth, and fewer pits. Specifically, the Ni-doped alloy exhibited a 5.66% lower micropitting area ratio under the same test conditions. Furthermore, prior studies support these findings, showing that the 1.55% Ni-doped steel performs better than the 2% Ni-doped alloys. Therefore, 1.55% Ni-doped Cr-Mo alloy steel is recommended for transmission gears to minimize RCF damage.

Keywords: Ni-doped, contact fatigue failure, RCF, twin-disc test rig, micropitting area ratio

1. INTRODUCTION

Contact fatigue can cause parts of rolling/sliding machines, like cam followers, bearings, and gears, to fail. The fatigue failure process of these components begins with the formation of microcracks between the contacting rolling elements due to the stress field below the surface, which eventually causes material removal, called RCF [1]. So far, the most common transmission problem is contact fatigue failure, which causes high friction and thus high energy consumption[2]. In some sensitive applications, gears are used to transmit high power/torque, which means more energy is spent to overcome friction and wear. Literature shows that 5.1% of fuel energy is used for friction and wear, of which only gears consume 55% of fuel energy [3]. Besides, further research is currently underway to improve transmission performance to reduce maintenance costs significantly. Due to the service life and performance of power transmission gearboxes, RCF testing is very important for the development of new materials that can operate at high rolling speeds [4, 5].

In this case, the gearbox gear with non-conformal rolling/sliding contact due to the contact pressure between the tooth surfaces on the gear tooth flanks can easily reach a pressure of up to 1 GPa Hertz. Therefore, near these surfaces, there are three main failure mechanisms caused by these conditions. These are excessive wear, scuffing, and rolling contact fatigue. Rolling contact fatigue is divided into subsurface RCF and surface RCF [6]. As shown in multiple literature studies, various methods and analyses have been developed to study the RCF of rolling/sliding components [7-11]. These studies were established to define different testing methods. Three types of tests have been identified as benchmarks [12], including accelerated testing [13], long-term tests [11], and full-scale rig tests [10]. As a result, this study is a long-term experiment. Verifying the material qualities of new alloy steel gear material using gear samples necessitates several costly and time-consuming test processes and tracking records. To replicate the contact between the teeth of the two gears' flanks, the contact state of the gears is switched to two test rollers (discs) [14].

During the RCF test, the slide-to-roll ratio (SRR) simulates a specific point on teeth with an equivalent SRR during actual gear meshing. Pure rolling simulates the point of contact with a pitch line. The teeth of gears usually have pits at the root or tip. Two rollers can be used to simulate the RCF of mating transmission gears. It is easy to observe experiments with continuous motion, slip, and sliding, and oil thickness.[15]. Accordingly, Fig. 1 schematically illustrates how the Hertzian contact pressure between the two test roller specimens simulates the two gear teeth in the RCF test.

The RCF twin-disc test bench uses a disc-shaped sampling roller with a built-in temperature-controlled lubrication system, contact load, and a predefined period of fixed speed rotation. The machine uses two disc-shaped rollers, powered by a separate AC motor. The test result of such an experimental test is the same as the actual application of the transmission gear mechanism [16].

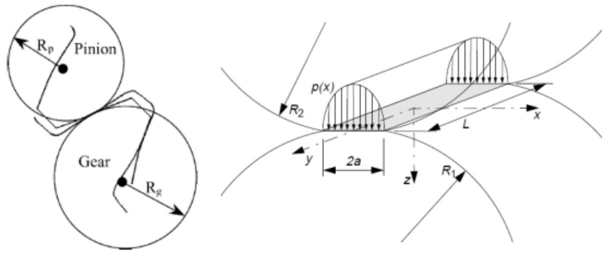

a) b)

Fig. 1. Cylinders simulate two gear teeth in an RCF test (a), and Hertzian contact between two rollers(b) [15]

Damage of RCF transmission gear is a very complex issue because many parameters are considered when commencing to simulate using by twin discs test rig. Material type, surface profile, load, lubrication, and SRR are a few of the factors taken into account in RCF test working conditions [17]. The RCF damage is mainly caused by micro-cracks, and small cracks protruding from the surface can damage the transmission gear. And, visible gray or frost on the surface is exhibited and usually named as frost gray/micropitting [18, 19]. Repeated stress and plastic deformation are affected by many factors, such as load, speed, temperature, surface quality, heat treatment, and lubrication properties. Research studies have shown that micro-pitting can cause considerable surface damage and even catastrophic damage [20].

The tooth contact fatigue test, also known as the gear contact fatigue test, is a type of gear performance test that is primarily used to assess lifetime, pitting, and spalling. When transmission gears are made of alloyed steels with sufficient hardness to obtain microstructures consisting mainly of tempered martensite, the gears have optimal resistance to micro-pitting. As the residual stress in the case-hardened gear reduces the toughness, strength, and residual compressive stress by more than 30%, the micropitting resistance is reduced [21].

In the RCF test, in addition to design factors, surface topography also stimulates friction and wear between the rolling/sliding surfaces of gear teeth [22]. There are various gear manufacturing and finishing approaches. In terms of efficiency, ultra-super finish gears are more powerful than ground gears. As the surface moves in, the conformity between the mating bodies is improved. During the running-in phase, the more aggressive roughness will plastically deform, and the surface will become smoother. This situation has changed drastically due to multiple conditions [23]. It is commonly recognized that proper running-in can increase the lifespan of parts like gears [24]. Real surfaces initially make contact at the points of asperities when they come into touch [25]. Despite applying the normal load, extremely high pressure is created around micro-contacts, and the plastic deformation of asperities in the contacting bodies' surface results in the production of a very small area known as the true effective contact area [26].

2. MATERIALS, GEOMETRY, METHODOLOGY AND CONDITIONS

2.1. Materials

The high-speed and low-speed samples were made from commercially available Cr-Mo alloy steel and a newly developed Ni-doped Cr-Mo alloy steel. The chemical composition of alloy steel, both newly created and commercially accessible, is depicted in Tab. 1. Commercially available and newly developed samples were manufactured using the same process, which included melting in an argon atmosphere vacuum, hot forging, applying Ni content (for the newly developed material), rolling the forged material to the desired shape, normalizing, heat treatment (tempering, quenching, and nitriding), and surface finishing.

Tab.1. Chemical composition of commercially available (Cr-Mo) and newly developed Ni-doped Cr-Mo alloy (Cr-Mo-1.55 Ni)

	Chemical composition mass (%)									
	C	P	S	Si	Mn	Cr	Ni	Mo	Cu	Bal
Cr-Mo	0.21	0.002	0.003	0.25	0.65	1.15	0.22	0.21	0.18	97.12
Cr-Mo-1.55 Ni	0.18	0.002	0.003	0.24	0.65	1.13	1.55	0.21	0.18	95.85

2.2. Geometry

To achieve the least effective contact area, the high-speed specimens in this investigation were crowned-shaped discs, while the low-speed specimens were cylindrical-shaped discs. Cylindrical and crowned disk samples with the same surface polish and hardness were employed in the sample preparation procedure. A tribologically compatible disc-on-disc test is used in gear RCF testing to minimize the time and expense involved in producing complex gear geometries. Consequently, disc specimens with outer and inner diameters of 70 and 45 mm, respectively, and a thickness of 28 mm were produced. The high-speed disc geometry is altered in this experiment so that the 8.5 mm effective contact surface is crowned on both sides by 3 degrees (30). The test discs' measurements in Fig. 2 were modified for greater clarity from [27].

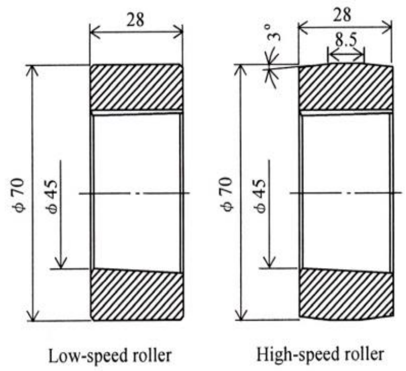

Fig. 2. Dimension of test discs [27]

2.3. Methodology

Analytical models struggle to accurately predict micropitting due to its asperity level impact on the specimen's metallurgy, surface roughness, lubrication properties, applied stresses, and tooth shape [20]. Research suggests using rolling pairs of discs in loaded contact to replicate transmission gears, reducing costs and time-consuming preparation of spacemen's equipment, and assessing contact fatigue capabilities of different gear materials [28-31]. The fact that disc specimens are more durable than gears is acknowledged by researchers, who employ disc specimen studies to assess the surface fatigue performance of various materials. Therefore, an experimental test with disc samples is the most effective method for determining the micropitting area ratio of a transmission gear [32].

The modified RCF twin-disc test equipment was used in Ethiopia for experimental testing, positioning specimens on separate shafts powered by AC motors. The design and development were optimized according to the test sample's standard specification, resulting in a contact pressure of [27]. According to the literature, lubricating the disc-to-disc contact region required applying one drop of water or transmission oil every three seconds [33]. Additionally, lubricant temperature is a crucial test parameter that affects its viscosity. An induction system is used to maintain the required temperature, ensuring the oil temperature doesn't exceed 150°C. [34].

Therefore, as shown in Tab.2, the severely saturated SAE 90 grade was used in this study's modified twin-disc test setup, and the controlled lubricant temperature ranged from 80 to 90 °C.

Tab. 2. SAE90 lubricant property

Parameter	Value
Kinematic viscosity @40 °C	155
Kinematic viscosity @100 °C	15.5
Density	7.28 lbs/gal
Specific gravity	0.875

2.4. Contact Load Conditions and Parameters

A step load stage procedure was used for the experimental tests, which involved progressively raising the normal load applied up to 8.2 KN and reaching a maximum Hertzian contact pressure of 1.5 GPa. Tab. 3 provides a summary of the experimental tests. Four distinct load levels (K3, K6, K8, and K9) are seen in the usual load on the rollers (disks). The reference makes it apparent that these loads are broken down into sub-levels [6]. Almost ten million (107) load cycles are required for high-speed discs to finish the test, with each load phase taking several minutes to hours. Furthermore, low-speed discs required about 5 million load cycles to operate. At every load stage change, the sole lubricating oil was changed. Nevertheless, there was no change in the lubricating oil between load sub-stages. Following each disruption, the test bench's discs were removed, cleaned, weighed, and measured before being replaced with a fresh test specimen. The SRR, which is displayed in Tab. 4, is the crucial parameter throughout the run-in and RCF testing. SRR is the ratio of sliding and rolling velocity in a twin-disc device, with rolling velocity corresponding to lubricant entrainment as indicated in equation (1). It affects RCF testing, with higher SRR resulting in greater pitting, as calculated using Equation 1 [35]. The study suggests that surfaces with negative SRR values are more susceptible to micropitting due to their maturity [36].

$$SRR = \frac{u_s}{u_r} = 2 \times \left(\frac{|u_1 - u_2|}{u_1 + u_2}\right) \tag{1}$$

where: u_s —sliding speed, u_r —Mean rolling speed, u_1 —Surface speed of body 1 (m/s), u_2 —Surface speed of body 2 (m/s)

Slip between the contact surfaces is another factor that influences the rolling contact's lifespan. Keep in mind that the slip of Entity 1 is provided by Eq. 2. The surface's durability depends on the presence and severity of slippage, with positive slip preventing contact fatigue cracks and negative slip increasing surface wear and decreasing initial load cycles.

$$s_1 = \frac{u_1 - u_2}{u_1} \tag{2}$$

Tab. 3. Parameters during the run-in and RCF Experiment

Test Stages	Description	High-speed disc(rpm)	Low-speed disc (rpm)	Slip ratio	SRR
K3, K6, k8 & k9	Run-in & RCF	2800	1400	-1 & 0.5	0.66

Tab.4. Load stages on RCF Experiment

Load stage	Normal force (N)	Hertzian pressure (Mpa)	Half pressure width (mm)	Load sub-stage	No_Cyles for high speed *10^3	No_Cyles for low speed *10^3	Time need (hr)	Oil To
K3	1090.8	514	0.159	K3-1	20	10	7.15’	80
				K3-2	60	30	21.428’	
				K3-3	100	50	35.714’	
K6	3749.7	953	0.295	K6-1	200	100	71.428’	90
				K6-2	800	400	4.762hr	
				K6-3	1880	940	11.191hr	
K8	6513.131	1256	0.388	K8-1	200	100	71.428’	90
				K8-2	800	400	4.762hr	
				K8-3	1880	940	11.191hr	
K9	8184.95	1408	0.435	K9-1	2880	1440	17.143 hrs	90
Total					8820	= 4,410	52.5 hrs	

3. RESULT AND DISCUSSION

RCF experimental testing on Cr-Mo and Ni-doped Cr-Mo alloy steels was conducted under identical conditions to ensure gear damage robustness. The experiment showed damage in wear mass, surface topography, and surface morphology. Following a successful experimental test, evaluate the cutoff samples' surfaces using an optical microscope and an electron microscope (SEM) to determine their surface characterization. As a result, low-speed samples typically experience rapid RCF failure because of negative SRR. Micropitted area (Ap), Micropitted depth, and the corresponding diameter of the pitted surface were used to explain the RCF failure and disclose RCF damage, as confirmed by research studies.

3.1. Surface characterization

Purposefully, the material's tribological properties can be obtained by the methodical assessment of damaged surfaces. Both the high-speed and low-speed disc samples were measured and examined in this work following the completion of the RCF test. Using SEM and OM micrographs, examine the damaged samples by viewing and post-processing the micrographs of the discs' damaged surfaces. Additionally, MountainsMap® software for SEM and OM imaging was used to calculate the textural characteristics in the micrographs. After analysis, the textural parameters were presented as the mean of several scales and magnification data. Using leveling filter techniques, the SEM image's cylindrical characteristic is eliminated. Consequently, the cylinder feature was eliminated from the SEM and OM micrographs using a third-order polynomial function.

Fig. 3 (a) and (b) revealed the reconnoitered damaged surface texture of the Cr-Mo alloy steel disc samples. Surface roughness was used to measure the surface maps of the Cr-Mo alloy steels' high-speed and low-speed discs. At both high and low speeds, the surface map of the Cr-Mo alloy steel's Root Mean Square (RMS) surface roughness (Sq) is acceptab.. The two surface maps show that the low-speed disc's surface roughness is marginally higher than the high-speed discs.

Fig. 4 (a) and (b) examine surface maps of RMS surface roughness (Sq) for high-speed and low-speed discs of Ni-doped Cr-Mo alloy steel materials. Results show that Ni-doped Cr-Mo alloy steel has lower surface roughness than Cr-Mo alloy steel, indicating a positive correlation between surface damage and root mean surface roughness texture. The area with more damage increases with surface RMS roughness.

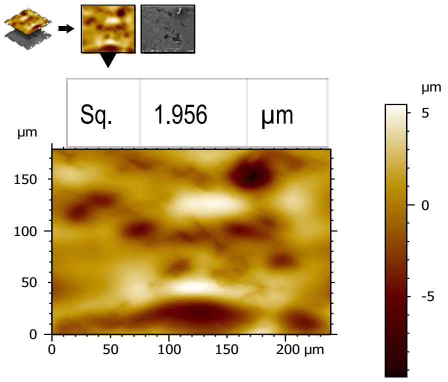

a)

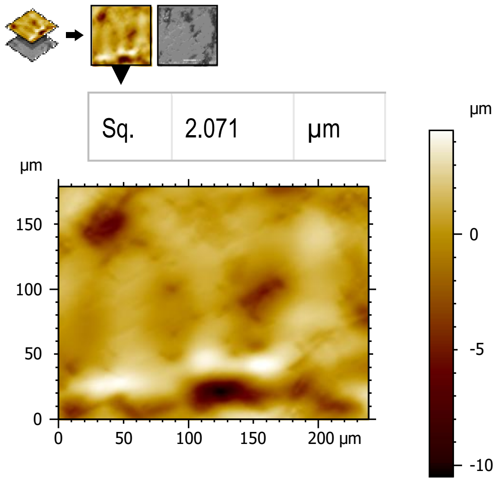

b)

Fig. 3. High-speed disc Surface map of Cr-Mo alloy steel (a) , and low-speed disc (b)

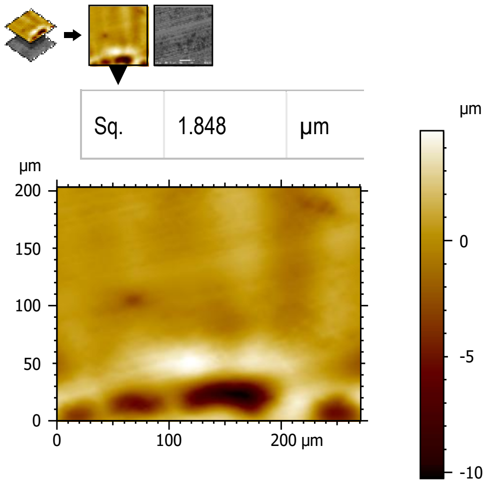

a)

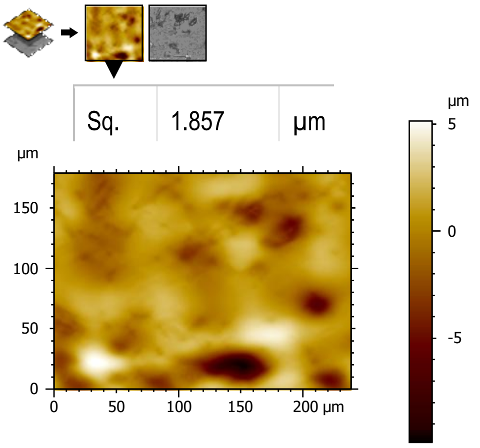

b)

Fig. 4. Surface map of Ni-doped Cr-Mo alloy steel (a), and high-speed disc after low-speed disc (b)

3.2. Surface Morphology

Following the RCF testing, a small sample of the tested disc specimens was extracted from the twin-disc test bench, cleaned with an ultrasonic cleaner, and dried with hot air. The extracted sample discs were then analyzed by SEM at various magnifications and scales (200 µm, 100 µm, 50 µm, 20 µm, and 10 µm). Additionally, a small piece of the examined disc is extracted for optical microscope (OM) purposes in this investigation.

OM and SEM micrographs of the high-speed and low-speed disks of Cr-Mo and Ni-doped Cr-Mo alloy steels were displayed in Fig. 5 to 8. Among the several SEM micrographs of high-speed and low-speed discs of Cr-Mo alloy steel materials, Fig. 5 (a) & (b) and Fig. 6 (a) & (b) show SEM micrographs of 50 µm scale and 500 magnifications. It is evident from both micrographs that pits are already present. Following a run-in, mated bodies that are subjected to rolling or sliding motion experience significant plastic deformation [35, 37]. After 10 million stress cycles, the damaged area of the Cr-Mo alloy steel is visible in Fig. 5, high-speed disk micrographs. Consequently, some surface micropits are visible. The Cr-Mo alloy steel of low-speed disk SEM micrographs at about 5 million stress cycles is similarly shown in Fig. 6. When the disk is viewed under high magnification, minute pits are apparent.

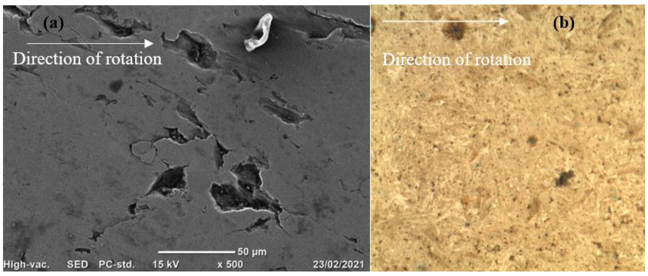

Fig. 5. High-speed Cr-Mo alloy steel after RCF test, (a) SEM Micrograph and (b) OM Micrograph

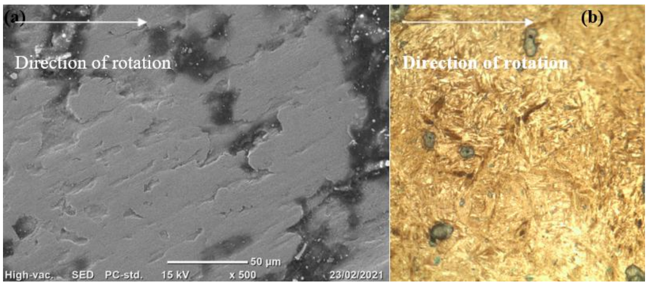

Fig. 6. Low-speed Cr-Mo alloy steel after RCF test, (a) SEM Micrograph, and (b) OM Micrograph

SEM micrographs of 50 µm scale and 500 magnifications were also shown in Fig. 7 and 8, which were SEM micrographs of high-speed and low-speed discs of Ni-doped Cr-Mo alloy steel. After 10 million stress cycles for the high-speed disc and 5 million stress cycles for the low-speed disc, the pitted section of the Ni-doped Cr-Mo alloy steel of the high-speed disc micrographs is shown in Fig. 7 (a) and (b). Micropits are therefore visible on both surfaces. Similarly, low-speed disk SEM micrographs of the Ni-doped Cr-Mo alloy steel at almost 5 million stress cycles are shown in Fig. 8. When viewing the disk at high magnification, it is understandable that micro pits are visible.

This study uses MountanMap® software to compute micropitting variables like pitted depth, equivalent diameter, and roundness from SEM micrographs. The factors are determined by shifting the micrograph to topography, converting it to a 3D image, and determining pit factors. A micro pit is defined as a surface imperfection with a depth more than 1 µm and a diameter between 10-50 µm below the surface's mean plane [38, 39]. In this study, damaged surfaces with a pitted depth greater than or equal to 1 µm, an equivalent diameter between 10–40 µm are regarded as micropitting. Else if the values are beyond the stated values, it is considered small pitting.

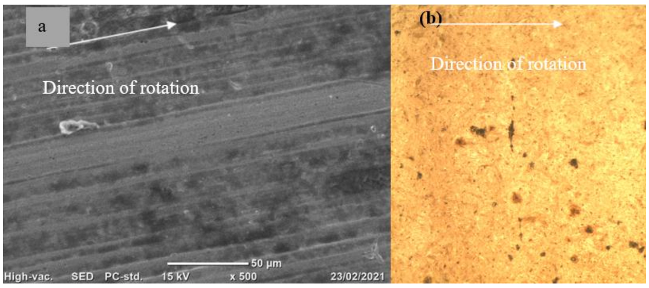

Fig. 7. High-speed Ni-doped Cr-Mo alloy steel after RCF test (a) SEM Micrograph, and (b) OM Micrograph

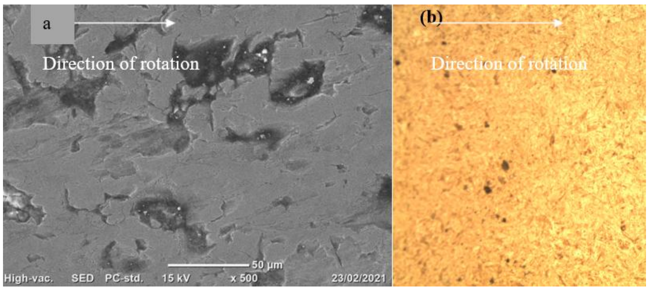

Fig. 8. Low-speed Ni-doped Cr-Mo alloy steel after RCF, (a) SEM Micrograph, and (b) OM Micrograph

Fig. 9, 10, 11, and 12 show histograms of micropitting metrics such as pitted depth, pitted equivalent diameter, and pitted roundness for the two candidate materials at high and low speeds. Fig. demonstrate micron-level depths ranging from -1.0 µm to -10 µm, with equivalent pit diameters ranging from 10-40 µm, indicating pitting at both the micro and macro levels. As the fatigue cycle progresses, the macro-scale depth and equivalent diameter rise. However, at both high and low speeds of Cr-Mo alloy steel material, pits of considerable depth (up to 12 µm) and equivalent diameter (up to 50 µm) are seen, as shown in Fig. 11 (a) and (b) and 12 (a) and (b). Fig. 9 (a) and (b), Fig. 10 (a) and (b), Fig. 11, and Fig. 12 show that surface damage is more severe in Fig. 12 (a) and (b). Since certain pits in Fig. 12 (a) and (b) appear deeper than pits in another identical image.

Similarly, Fig. 9 (c), 10 (c), 11 (c), and 12 (c) depict the morphology of the micro pits in the candidate materials. If the micro pits are circular, the value becomes one. As seen in the Figures, the closer the pits are to one, the more circular the shape; the further apart from one, the less circular the shape. Another factor used to distinguish between micropitted and macropitted areas is the establishment of a link between micropitting depth and equivalent diameter. Fig. 9 (d), 10 (d), 11, and 12 (d) show a link between pit depth and equivalent diameter. In this study, a pit is said to be a macro pit if the diameter of the pit exceeds 50. In Fig. 12 (d), the pitted depth of the Cr-Mo alloy low-speed disc pit is limited to 10 µm. Although the maximum pit depth of a low-speed disc with 12 µm (see Fig. 12 (b), it is much deeper than that of a high-speed disc.

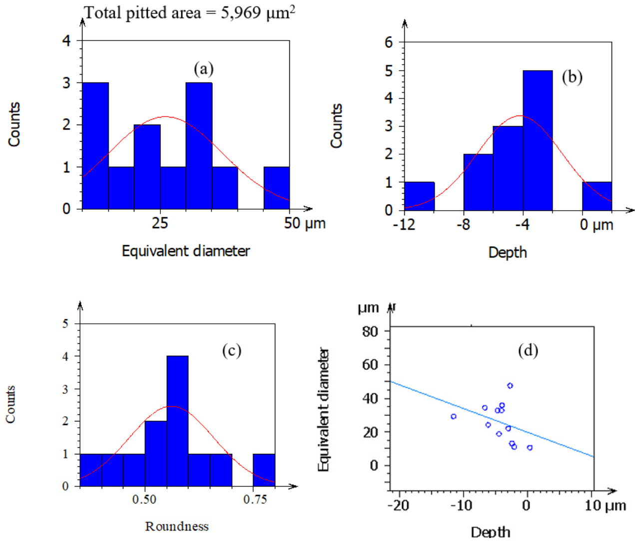

Fig. 9. Ni-doped Cr-Mo alloy steel of low-speed micropits (a) equivalent diameter, (b) depth, (c) shape, (d) correlation b/n micropits depth and micropits equivalent diameter

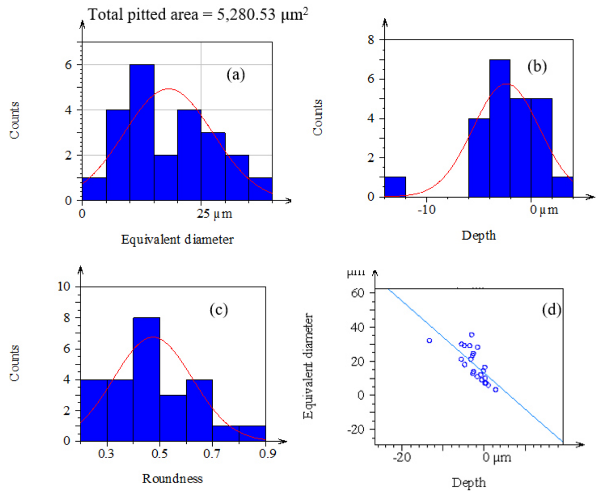

Fig. 10. Ni-doped Cr-Mo alloy steel of high-speed micropits (a) equivalent diameter, (b) depth, (c) shape, (d) correlation b/n micropits depth and micropits equivalent diameter

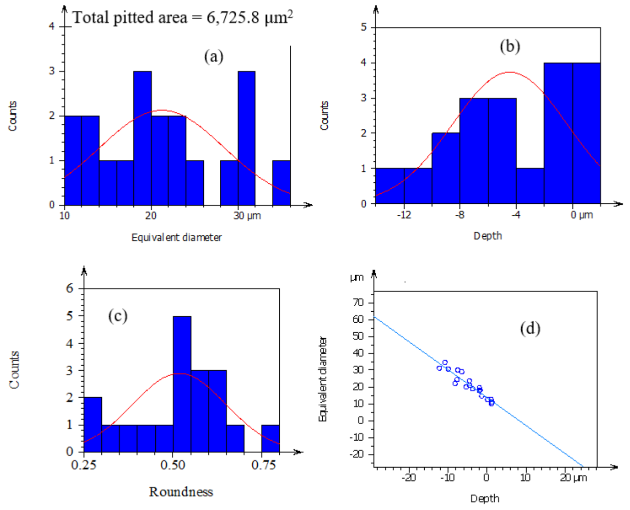

Fig. 11. Cr-Mo alloy steel of low-speed micropits (a) equivalent diameter, (b) depth, (c) shape, (d) correlation b/n micropit depth and micropit equivalent diameter

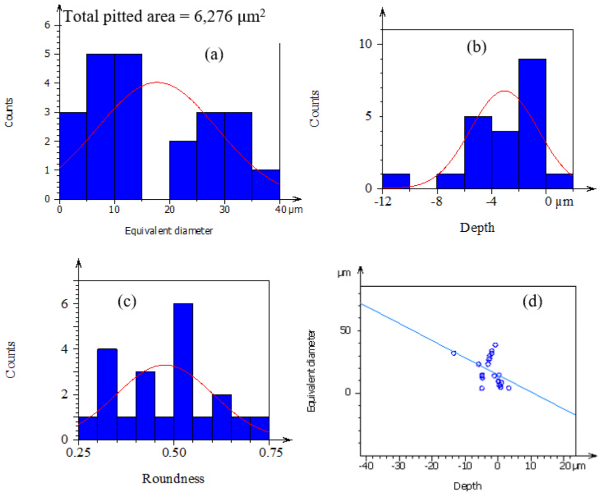

Fig. 12. Cr-Mo alloy steel of high-speed micropits of (a) equivalent diameter, (b) depth, (c) shape, (d) correlation b/n micropit depth and micropit equivalent diameter

Fig. 13 to 16 show rainbow topography scale photographs, with the blue (watershed segmentation) area representing the pitted area and the reddish area representing the undamaged area. The damage component is given as a percentage of the micro pitting area ratio (AP), which is likewise shown on the upper side of Fig. 13 to 16. The percentage of the Micropitted area can be calculated by dividing the total pitted area by the whole surface scanned by the SEM. The overall picture area for all potential materials is 120,000 µm². Fig. 14 displays a bigger micropitting area ratio of 5.66%, whereas Fig. 16 shows a lower ratio of 5.23%.

To create novel alloy steel for power transmission gears, this study generally investigates the effects of adding Ni content in varying amounts to the current Cr-Mo alloy steel. The findings then continue to show that a Ni-content of 1.55% has good resistance to fatigue failure. Studies with a higher Ni-content (2% Ni) alteration than the candidates in this investigation provided further support for these findings.

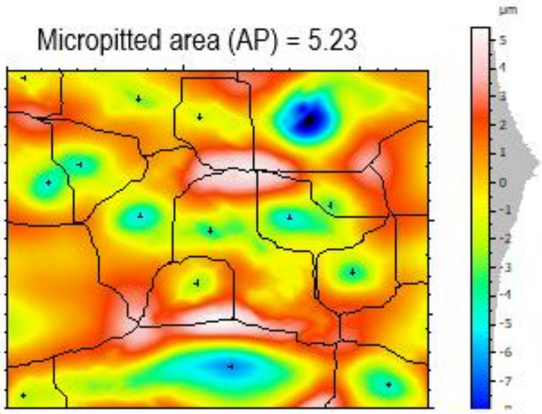

Fig.13. Evaluation of Surface damage of Cr-Mo alloy high-speed disc

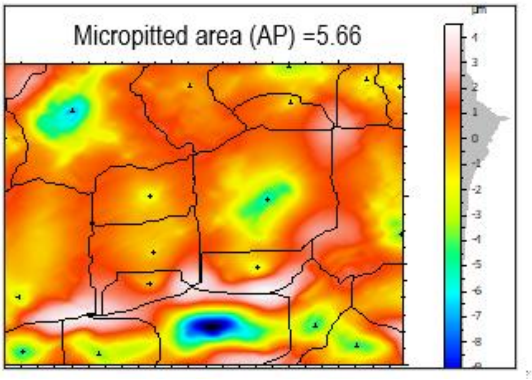

Fig. 14. Evaluation of Surface damage of Cr-Mo alloy low-speed disc

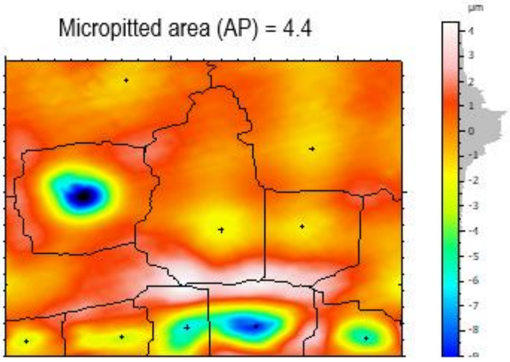

Fig. 15. Evaluation of Surface damage of Ni-doped Cr-Mo alloy steel of high-speed disc

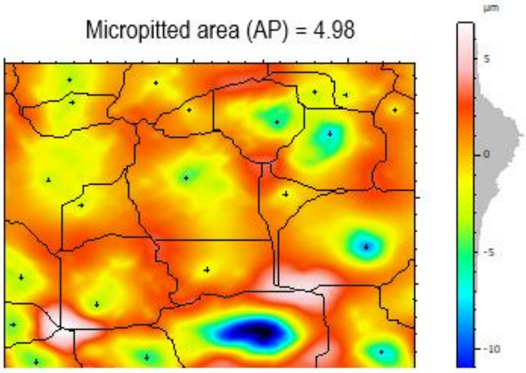

Fig. 16. Evaluation of Surface damage of Ni-doped Cr-Mo alloy steel of low-speed disc

4. CONCLUSIONS

The assessment of Cr-Mo and Ni-doped Cr-Mo alloy steels in high-speed and low-speed disc specimens has been experimentally investigated in this work. Every alloy steel candidate sample came from the same batch that was manufactured, heat-treated, and had the same surface polish. A twin-disc test rig was used to examine the rolling contact fatigue of the candidate materials. Following that, SEM was used to evaluate the damaged area of the tested disc samples at different places using varying scales and magnifications. It was easy to examine the damage that occurred on both of the candidate materials with pitted characteristics using the micrographs that were acquired from OM and SEM, and the following conclusions were reached:

– Damage resistance has a Positive correlation with root mean surface roughness (Sq) and surface damage. As a result, Ni-doped Cr-Mo alloy steels have less Sq compared with Cr-Mo alloy steel.
– In comparison to Cr-Mo alloy steels, Ni-doped Cr-Mo alloy steel has a higher resistance to micropitting in terms of pitted diameter, pitted depth, and micropitted area ratio.
– The Ni-doped Cr-Mo alloy steel is the preferred material for transmission gears and withstands rolling fatigue failure.

REFERENCES

1. Borgaonkar A, Syed I. Effect of coatings on rolling contact fatigue and tribological parameters of rolling/sliding contacts under dry/lubricated conditions: a review. Sādhanā. 2020;45(1):30.
2. Prajapati DK, Tiwari M. Assessment of topography parameters during running-in and subsequent rolling contact fatigue tests. Journal of Tribology. 2019;141(5).
3. Holmberg K, Kivikytö-Reponen P, Härkisaari P, Valtonen K, Erdemir A. Global energy consumption due to friction and wear in the mining industry. Tribology International. 2017;115:116-39.
4. Bodini I, Sansoni G, Lancini M, Pasinetti S, Docchio F. A novel optical apparatus for the study of rolling contact wear/fatigue based on a high-speed camera and multiple-source laser illumination. Review of Scientific Instruments. 2016;87(8):083701.
5. Li W, Deng S, Liu B. Experimental study on the influence of different carburized layer depth on gear contact fatigue strength. Engineering Failure Analysis. 2020;107:104225.
6. Brandao JA, Martins R, Seabra JH, Castro MJ. Surface damage prediction during an FZG gear micropitting test. Proceedings of the Institution of Mechanical Engineers, Part J: Journal of Engineering Tribology. 2012;226(12):1051-73.
7. Kaneta M, Murakami Y. Effects of oil hydraulic pressure on surface crack growth in rolling/sliding contact. Tribology international. 1987;20(4):210-7.
8. Tyfour W, Beynon J, Kapoor A. The steady state wear behaviour of pearlitic rail steel under dry rolling-sliding contact conditions. Wear. 1995;180(1-2):79-89.
9. Santa J, Cuervo P, Christoforou P, Harmon M, Beagles A, Toro A, et al. Twin disc assessment of wear regime transitions and rolling contact fatigue in R400HT–E8 pairs. Wear. 2019;432:102916.
10. Stock R, Pippan R. Rail grade dependent damage behaviour–Characteristics and damage formation hypothesis. Wear. 2014;314(1-2):44-50.
11. Eadie DT, Elvidge D, Oldknow K, Stock R, Pointner P, Kalousek J, et al. The effects of top of rail friction modifier on wear and rolling contact fatigue: Full-scale rail–wheel test rig evaluation, analysis and modelling. Wear. 2008;265(9-10):1222-30.
12. Santa J, Christoforou P, Cuervo P, Toro A, Beagles A, Lewis R. Evaluation of rolling contact fatigue of rail materials in twin disc tests. 2018.
13. Fletcher D, Beynon J. The influence of lubricant type on rolling contact fatigue of pearlitic rail steel. Tribology Series. 36: Elsevier; 1999. p. 299-310.
14. Britton W, Clarke A, Evans H. A Novel Method for Automatic Detection of Incipient Micropitting in Ground Surfaces. Tribology International. 2021:106959.
15. Aslantaş K, Taşgetiren S. A study of spur gear pitting formation and life prediction. Wear. 2004;257(11):1167-75.
16. Tokuda M, Nagafuchi M, Tsushima N, Muro H. Observations of the peeling mode of failure and surface-originated flaking from a ring-to-ring rolling contact fatigue test rig. Rolling Contact Fatigue Testing of Bearing Steels: ASTM International; 1982.
17. Gohritz A. Ermittlung der Zahnflankentragfähigkeit mittlerer und großer Getriebe durch Analogieversuche: Rheinisch-Westfälische Technische Hochschule Aachen; 1982.
18. Ariura Y, Ueno T, Nakanishi T. An investigation of surface failure of

surface-hardened gears by scanning electron microscopy observations. Wear. 1983;87(3):305-16.
19. Snidle R, Evans H, Alanou M. Gears: elastohydrodynamic lubrication and durability. Proceedings of the Institution of Mechanical Engineers, Part C: Journal of Mechanical Engineering Science. 2000;214(1): 39-50.
20. Keller J, Olson R, Michaud M. Case Study of ISO/TS 6336-22 Micropitting Method. National Renewable Energy Lab.(NREL), Golden, CO (United States); 2020.
21. Errichello R. Morphology of micropitting. Gear technology. 2012;4: 74-81.
22. Mallipeddi D, Norell M, Sosa M, Nyborg L. Influence of running-in on surface characteristics of efficiency tested ground gears. Tribology International. 2017;115:45-58.
23. Hutt S, Clarke A, Evans H. Generation of Acoustic Emission from the running-in and subsequent micropitting of a mixed-elastohydrodynamic contact. Tribology International. 2018;119: 270-80.
24. Zhou Y, Zuo X, Zhu H, Fan Y. System dependence of running-in attractor derived from lubricated sliding contact of steel alloys 52100 and 1045. Journal of Tribology. 2018;140(5).
25. Menezes PL, Nosonovsky M, Ingole SP, Kailas SV, Lovell MR. Tribology for scientists and engineers: Springer; 2013.
26. Bhushan B. Introduction to tribology: John Wiley&Sons; 2013.
27. Redda DT, Nakanishi T, Deng G. Surface Durability of Developed Cr-Mo-Si Steel under Rolling-Sliding Contact. Journal of Advanced Mechanical Design, Systems, and Manufacturing. 2008;2(2):214-21.
28. Wilkinson C, Olver A. The durability of gear and disc specimens—part i: The effect of some novel materials and surface treatments. Tribology transactions. 1999;42(3):503-10.
29. Wilkinson C, Olver A. The Durability of Gear and Disc Specimens—Part II: Post Failure Examination and Gear-Disc Correlation. Tribology transactions. 1999;42(3):610-8.
30. Niemman G, Winter H. Maschinenelemente Band II Getriebe allgemein, Zahnradgetriebe-Grundlagen, Stirnradgetriebe. Springer-Verlag; 1985.
31. Flamand L, Berthe D, Godet M. Simulation of Hertzian contacts found in spur gears with a high performance disk machine. 1981.
32. Kleemola J, Lehtovaara A. Experimental simulation of gear contact along the line of action. Tribology International. 2009;42(10):1453-9.
33. Gao N, Dwyer-Joyce R, Grieve D. Disc machine testing to assess the life of surface-damaged railway track. Proceedings of the Institution of Mechanical Engineers, Part F: Journal of Rail and Rapid Transit. 2001;215(4):261-75.
34. Le M, Ville F, Kleber X, Buffière J-Y, Cavoret J, Sainte-Catherine M-C, et al. Rolling contact fatigue crack propagation in nitrided alloyed steels. Proceedings of the Institution of Mechanical Engineers, Part J: Journal of Engineering Tribology. 2017;231(9):1192-208.
35. Rabaso P, Gauthier T, Diaby M, Ville F. Rolling contact fatigue: experimental study of the influence of sliding, load, and material properties on the resistance to micropitting of steel discs. Tribology transactions. 2013;56(2):203-14.
36. Terrin A, Meneghetti G. A comparison of rolling contact fatigue behaviour of 17NiCrMo6-4 case-hardened disc specimens and gears. Fatigue & Fracture of Engineering Materials & Structures. 2018;41(11):2321-37.
37. Jeng Y-R, Lin Z-W, Shyu S-H. Changes of surface topography during running-in process. J Trib. 2004;126(3):620-5.
38. Roy S, Ooi GTC, Sundararajan S. Effect of retained austenite on micropitting behavior of carburized AISI 8620 steel under boundary lubrication. Materialia. 2018;3:192-201.
39. Roy S, White D, Sundararajan S. Correlation between evolution of surface roughness parameters and micropitting of carburized steel under boundary lubrication condition. Surface and Coatings Technology. 2018;350:445-52.

Hailemariam Nigus Hailu: https://orcid.org/0000-0001-6644-645X

CAUSES OF ERRORS IN ESTIMATING THE CHARACTERISTIC FREQUENCIES OF ANTIRESONANT CONVEYORS

Jerzy MICHALCZYK*, Marek GAJOWY*, Krzysztof MICHALCZYK**

*Faculty of Mechanical Engineering and Robotics, Department of Mechanics and Vibroacoustics,
AGH University of Krakow,al. Mickiewicza 30, 30-059 Kraków, Poland
**Faculty of Mechanical Engineering and Robotics, Department of Machine Design and Maintenance,
AGH University of Krakow,al. Mickiewicza 30, 30-059 Kraków, Poland

michalcz@agh.edu.pl, mgajowy@agh.edu.pl, kmichal@agh.edu.pl

received 07 September 2024, revised 01 July 2025, accepted 13 August 2025

Abstract: This paper demonstrates the unsuitability of relations and diagrams known from literature for antiresonant machines, in terms of determining the position of resonances of dynamic elimination systems. Correct formulas were derived and a nomogram for designers was built based on them. The effect of the actual number of degrees of freedom on the natural frequencies of machines with a design based on the dynam-ic eliminator principle is presented. The effect of the spring mass on the antiresonance frequency explicit to the natural frequency of the eliminator was pointed out, and correct relations for its consideration were derived. The experimental and numerical studies carried out in this paper have confirmed that including the effect of spring inertia in analytical calculations improves the accuracy of the results obtained. Furthermore, it was shown that the actual way in which the ends of the leaf springs are attached can significantly affect the natural frequency of the system. The factors discussed and analysed in this paper are omitted in conventional vibrating machine calculations, resulting in an overestimation of the natural frequencies determined from them.

Keywords: dynamic damper, characteristic frequencies, self-synchronisation, reduced mass, flat spring

1. INTRODUCTION

Antiresonant vibratory conveyors (Base – Excited Conveyors), shown in Fig.1, owe their rapidly increasing popularity to their two main advantages:

- Negligible, theoretically equal to zero, value of dynamic forces transferred to the ground during operation, resulting from the Frahm dynamic eliminator effect used in their construction, with the trough as the properly tuned eliminator mass [1], and
- Lower, compared to currently used over-resonant machines, required excitation force of vibrators, which induces vibrations of only a light transport trough, which does not require significant bending rigidity, as it is ensured by a massive body of the machine, and which is not burdened by significant masses of the drive system attached to this body.

These conveyors are becoming more and more widely used to transport loose materials [2], where dynamic forces transmitted to the ground by super-resonant conveyors are a significant disadvantage. For example, this is the case in mineral raw material processing plants, where flimsy buildings of processing stations, made of reinforced concrete, usually contain a considerable number of vibratory machines accumulated: conveyors, screens, dewatering centrifuges, etc., leading to intensive spread of floor vibrations, covering the majority of operation sites, endangering the health of operators and sometimes leading to building damage.

The antiresonance phenomenon is widely described in existing literature [3, 4]. Authors of [5] pointed out, that it is possible to determine the resonance frequencies of the structure under ideal boundary conditions, based on the experimentally determined antiresonance frequencies for structure under arbitrary boundary conditions. Renault et al. [6] proposed extension of linear concepts about antiresonances to the nonlinear cases of vibrating systems. The influence of transported material mass fluctuation has been analysed in [7], where authors presented nonlinear dynamic model of antiresonant vibrating machine.

Fig. 1. VIBRAflex II Sanitary Antiresonant Vibratory Conveyor – PFI, which dynamic and discret model is presented in Fig. 2

The widespread use of antiresonant machines such as conveyors [8] or vibrating screens [9, 10] requires accurate and reliable methods of calculation, in which the correct determination of the antiresonant frequency and resonant frequency of the system plays a fundamental role. The development of anti-resonance vibration isolation methods is also important because more accurate computational models can be used both in the design of new systems and in the optimisation of the existing ones [11].

Due to the fact that there are a number of erroneous traditions in this field, usually resulting from misinterpretation, but also from the incompleteness of the dynamic elimination theory, this paper presents the basic mistakes made in this field, and the addition to Frahm's theory and other phenomena to the extent required in the design of antiresonant machines.

2. THEORETICAL FOUNDATIONS OF ANTIRESONANT CONVEYOR OPERATION - DYNAMIC ELIMINATOR THEORY [12], [13]

Antiresonant machines operate on the basis of the dynamic eliminator scheme [14], where the body of the machine, resiliently located and set in motion by a set of inertial vibrators, constitutes the protected object, while the transport trough, connected to the body by a set of springs, constitutes the mass of the eliminator. Let us denote the mass and the elastic and damping coefficients of the body spring elements by *M, K, C,* respectively, and the mass of the trough and the elastic and damping coefficients of the springs by m_e, k_e, c_e.

The operating principle of this system involves proper tuning of the eliminator [1]. The force in the eliminator spring (or spring system, in the case of a conveyor) reaches an amplitude and phase that counteracts the excitation force. For conveyors, this excitation force is the resultant force from the vibrators. When tuned correctly, the protected system (the machine body) nearly stops vibrating. This means it no longer transmits dynamic forces to the ground. Meanwhile, vibrations of the eliminator (the trough) enable the vibratory transport process.

Since this phenomenon occurs only in a narrow range of excitation frequencies [15] around the eliminator's natural frequency (1)

$$f_n = \frac{1}{2\pi}\sqrt{k_e/m_e} \tag{1}$$

(the so-called partial frequency, as it is not the vibration frequency of a combined system), wherein this frequency is closely surrounded by the resonant frequencies of the system on both sides. „The excitation and natural frequencies of the eliminator are subject to various interferences. Therefore, accurately determining these frequencies is essential for the machine's practical usability. These values significantly depend on precisely defined suspension parameters of the machine, including mass distribution, suspension stiffness and damping [1].

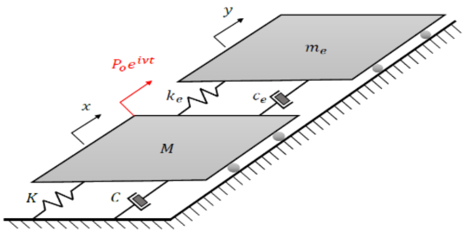

Fig. 2. Diagram of the dynamic vibration eliminator: *M* – protected mass, m_e – eliminator mass, *K*, *C* – constants of elasticity and damping of support elements of protected mass, k_e, c_e – constants of elasticity and damping of elastic elements of the eliminator, $P_o e^{ivt}$ – harmonic excitation force

Let us denote the absolute displacements of the masses *M* and m_e in the vibrations of the direction of the system by *x* and *y*, respectively, while the amplitude and frequency of the excitation force by P_o and *v* (Fig. 2.)

The dynamic equations of motion of both masses are described by the following relationships :

$$\begin{gathered} M\ddot{x} + C\dot{x} + Kx + c_e(\dot{x}-\dot{y}) + k_e(x-y) = P_o e^{ivt} \\ m_e\ddot{y} - c_e(\dot{x}-\dot{y}) - k_e(x-y) = 0 \end{gathered} \tag{2}$$

The solution to the system of equations is predicted to be :

$$\begin{gathered} x = Ae^{ivt},\ \dot{x} = ivAe^{ivt},\ \ \ddot{x} = -v^2Ae^{ivt} \\ y = Be^{ivt},\ \dot{y} = ivBe^{ivt},\ \ \ddot{y} = -v^2Be^{ivt} \end{gathered} \tag{3}$$

here *A* and *B* – vibrations amplitudes of the protected mass and the vibration eliminator and *i* – imaginary unit

Substituting the expected forms of the solutions of (3) into (2) resulted in the following relations:

$$\begin{gathered} M(-v^2Ae^{ivt}) + CivAe^{ivt} + KAe^{ivt} + c_e(ivAe^{ivt} - ivBe^{ivt}) + \\ +k_e(Ae^{ivt} - Be^{ivt}) = P_o e^{ivt} \\ m_e(-v^2Be^{ivt}) - c_e(ivAe^{ivt} - ivBe^{ivt}) - k_e(Ae^{ivt} - Be^{ivt}) = 0 \end{gathered} \tag{4}$$

Equations (4) can be represented in matrix form (5).

$$\begin{bmatrix} -Mv^2 + (C+c_e)iv + (K+k_e) & -c_eiv - k_e \\ -c_eiv - k_e & -m_ev^2 + c_eiv + k_e \end{bmatrix} \cdot \\ \cdot \begin{bmatrix} Ae^{ivt} \\ Be^{ivt} \end{bmatrix} = \begin{bmatrix} P_o e^{ivt} \\ 0 \end{bmatrix} \tag{5}$$

After solving the matrix system (5), absolute amplitudes of the form (6) and (7) were obtained for quasi-stationary values of *v*.

$$|A| = \frac{\sqrt{(P_oc_ev)^2+(-P_om_ev^2+P_ok_e)^2}}{\sqrt{\begin{gathered}(Km_ev^2-Kk_e+k_eMv^2+k_em_ev^2-Mm_ev^4+Cc_ev^2)^2 \\ +([Cm_e+c_eM+c_em_e]v^3-Ck_ev-c_eKv)^2\end{gathered}}} \tag{6}$$

$$|B| = \frac{\sqrt{(P_oc_ev)^2+(P_ok_e)^2}}{\sqrt{\begin{gathered}(Km_ev^2-Kk_e+k_eMv^2+k_em_ev^2-Mm_ev^4+Cc_ev^2)^2 \\ +([Cm_e+c_eM+c_em_e]v^3-Ck_ev-c_eKv)^2\end{gathered}}} \tag{7}$$

The partial frequency of the undamped vibrations of the protected system {*M, K, C*} is ω_o (8)

$$\omega_o = \sqrt{K/M} \tag{8}$$

and of the eliminator is ω_n (9)

$$\omega_n = \sqrt{k_e/m_e} \tag{9}$$

(Since the frequency ω_n (9) is at the same time an antiresonant frequency ω_a, i.e., one at which body vibrations in the undamped system disappear, therefore, both designations are equivalent).

After assuming the coefficient values (Tab.1), an amplitude-phase diagram of the type shown in Fig. 3 can be obtained, on which the vibration amplitudes of the basic system without eliminator are usually plotted for comparison.

As can be seen in Fig. 3, the vibration amplitude *A* of the protected mass *M* will be close to zero (red curve) at the antiresonant frequency (10).

$$v = \omega_n \overset{\text{def}}{=} \omega_a = \sqrt{k_e/m_e} \tag{10}$$

This condition is a condition for dynamic elimination of vibrations by means of an additional attached mechanical system – the dynamic eliminator.

Graphs such as these are common in the literature and reproduce the position of the resonance frequencies for weakly damped systems quite faithfully, but they completely deform the vibration amplitudes, which results from the real excitation nature, depending on the square of the excitation frequency *v*. To make them more realistic, one can, for example, substitute the force amplitude P_o in equations (6), (7) with the expression $P_o \cdot (v/\omega_n)^2$. However, the route discussed below is much easier in order to determine the resonance frequencies of the system.

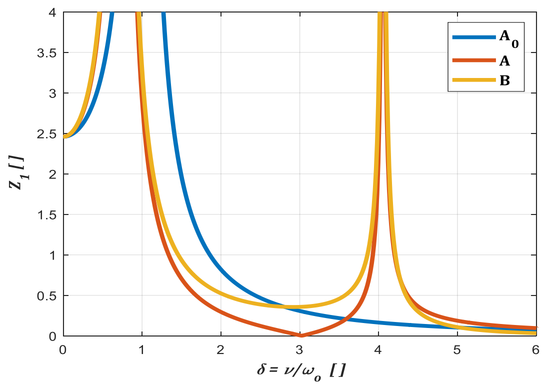

Fig. 3. Plot of dimensionless amplitudes z_1 for absolute displacements of the protected system *A*, the vibration eliminator *B*, and the system without the eliminator A_o, as a function of the ratio *δ* for the excitation frequency *v* to the partial frequency of the eliminator ω_n, equal to the antiresonant frequency (10) of the system, where z_1 – the ratio of amplitudes to the value of static deflection of the protected mass

Tab. 1. Parameters of the dynamic model from Fig. 2

Parameter	*Value*	*Unit*
M	600	kg
m_e	450	kg
K	719.387	N/m
k_e	4.963.770	N/m
C	142	Ns/m
c_e	298	Ns/m
P	14.450	N

3. NOMOGRAMS FOR DETERMINATION OF RESONANCE FREQUENCIES

Around the resonance frequency (10) on its left and right sides there is an antiresonance zone, i.e. a region of frequencies for which vibrations of the protected mass *M* are the lowest. The values of amplitudes increase as one moves away from the antiresonant frequency, towards the resonance frequency forming a peculiar zone (Fig. 3. red graph). The width of the interval between the resonance frequencies is important for the safety of the system operation. The wider it is, the higher the operational safety, and therefore the more resistant the mechanical system is to various interferences of its operation. To precisely determine the safe operating range — which is not the subject of this study — it is necessary not only to determine the width of the antiresonant zone, but also to define the acceptable vibration amplitude limits, which requires a detailed analysis of each specific case and the corresponding identification of a safe operating frequency band. The primary objective for the designer of antiresonant machines should be to estimate the antiresonant frequency as accurately as possible and ensure that the system operates in its vicinity.

To determine the distance on the axis between the values of the natural frequency in a simple way, based on the solution of the damped linear system, we assumed $c_e = C \approx 0$. When equating the denominator of the expression (6) or (7) to zero with the damping neglected yields the expression (11), which allows to determine the resonant frequencies of the system, limiting the antiresonant zone:

$$(K + k_e - M\nu^2)(k_e - m_e\nu^2) - {k_e}^2 = 0 \tag{11}$$

Dividing the above equation by k_e, K, and making further transformations and simplifications, we finally obtain the form (12).

To solve this equation efficiently, the assumption of equality of the partial frequencies of the eliminator and the protected mass (13) is used in the literature [12].

$$\left(1+\frac{k_e}{K}-\frac{\nu^2}{\frac{K}{M}}\right)\left(1-\frac{\nu^2}{\frac{k_e}{m_e}}\right)-\frac{k_e}{K}=0 \tag{12}$$

$$\frac{k_e}{m_e}=\frac{K}{M}=\omega_n^2 \ \text{or} \ \frac{k_e}{K}=\frac{m_e}{M} \tag{13}$$

Using the notation (14) we obtain the final form of the foregoing equation for this case (15):

$$\frac{m_e}{M}=\mu \tag{14}$$

$$\left(1+\mu-\frac{\nu^2}{\omega_n^2}\right)\left(1-\frac{\nu^2}{\omega_n^2}\right)-\mu=0 \tag{15}$$

The roots of this equation are the following values:

$$\left(\frac{\nu}{\omega_n}\right)^2=\left(1+\frac{\mu}{2}\right)\mp\sqrt{\mu+\frac{\mu^2}{4}} \tag{16}$$

The obtained dependence of the antiresonant zone width on the mass ratio only is shown in the graph in Fig. 4. The value of $v/\omega_n = 1$ for $m_e / M = \mu = 0$ in Fig. 4 indicates that no eliminator mass was applied ($m_e = 0$). In this case, the resonant frequency is singular and determined solely by the main suspension. Attaching an eliminator mass on an additional suspension with a partial frequency equal to the partial frequency of the main suspension results in the emergence of two resonant frequencies, which appear on the graph on either side of the antiresonant frequency. This antiresonant frequency corresponds simultaneously to the partial frequency of the eliminator and the main mass. As a result, two curves are formed, representing the natural frequencies for a given μ value. When the eliminator mass increases, the mass ratio μ increases as well, leading to a greater separation between the antiresonant frequency and the two resonant frequencies. In case (13), the differences between the lower and upper resonances relative to the antiresonant frequency are practically identical.

As can be seen in Fig. 4, the ratio of eliminator mass to main mass cannot be too low, as this reduces the antiresonant zone, and thus the system may be subjected to increased amplitudes when operating with a non-uniform load or other disturbances that may shift the operating point to a frequency close to the resonance frequency.

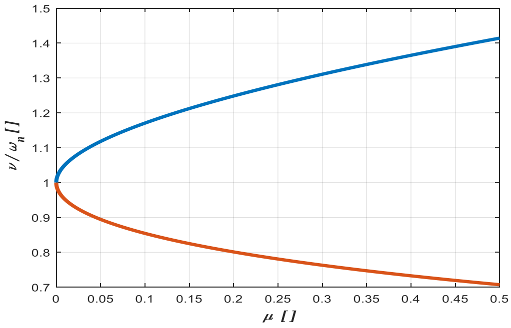

Fig. 4. Graph showing the ratio of the resonance frequencies to the antiresonance frequency v/ω_n of the analysed system, compared to the ratio of masses $m_e/M = \mu$ in the equality of partial frequencies of the protected and eliminator masses

Unfortunately, this solution does not cover the case of antiresonant machines, since they do not satisfy the equality condition (13) of the partial frequencies of the object and the eliminator. Although a change in the support stiffness of the protected system *K* does not affect the existence and location of the antiresonant point, it does affect the location of the target natural frequencies of the main mass-eliminator system.) The aforementioned assumption (13) means only that a special case is considered when the protected mass is excited in its partial resonance. Having considered that, further conclusions based on this assumption would only apply to such a case, which obviously does not occur in soft-based antiresonant conveyor systems. This fact will be considered further on, where dependencies on the position of the resonance frequencies of the main mass – eliminator system will be derived, useful for analysing the operation of antiresonant conveyors.

4. EXTENSION OF THE METHOD FOR DETERMINING THE RESONANT FREQUENCIES PRESENTS THE CASE OF SYSTEMS IN WHICH THE MAIN MASS IS TUNED SUPER-RESONANTLY

To derive relations that define the location of resonance frequencies of the main mass–eliminator system in the general case involving the partial tuning of the main mass below the excitation force frequency, we will make the following additional assumption: we assume that the ratio of the antiresonance frequency (10) to the frequency of body oscillation on its spring suspension system (8) is represented by (17).

$$\frac{\omega_n}{\omega_o} = \Delta \qquad (17)$$

In this case, we get (18)

$$\frac{k_e}{m_e} = \Delta^2 \frac{K}{M} \qquad (18)$$

therefore (19) and (20)

$$\frac{k_e}{K} = \Delta^2 \mu \qquad (19)$$

$$\frac{K}{M} = \frac{\omega_n^2}{\Delta^2} \qquad (20)$$

Inserting (18), (19), and (20) into (12), we obtain:

$$\left(1 + \Delta^2\mu - \frac{\Delta^2 \nu^2}{\omega_n^2}\right)\left(1 - \frac{\nu^2}{\omega_n^2}\right) - \Delta^2\mu = 0 \qquad (21)$$

Transforming this expression by extracting the ratio ν/ω_n, we obtain the equation to determine the resonance frequencies at any tuning of the main system:

$$\left(\left(\frac{\nu}{\omega_n}\right)^2\right)^2 \Delta^2 - \left(\frac{\nu}{\omega_n}\right)^2 (1 + \Delta^2(1+\mu)) + 1 = 0 \qquad (22)$$

The roots of this equation are as follows.

$$\frac{\nu}{\omega_n} = \sqrt{\frac{[1+\Delta^2(1+\mu)] \pm \sqrt{[1+\Delta^2(1+\mu)]^2 - 4\Delta^2}}{2\Delta^2}} \qquad (23)$$

Graphs showing the ratios of the upper and lower frequencies of the system to the antiresonance frequency $\omega_a = \omega_n$ are shown in Fig. 5 for a typical operating range of antiresonant machines and, comparatively, for $\Delta = 1$.

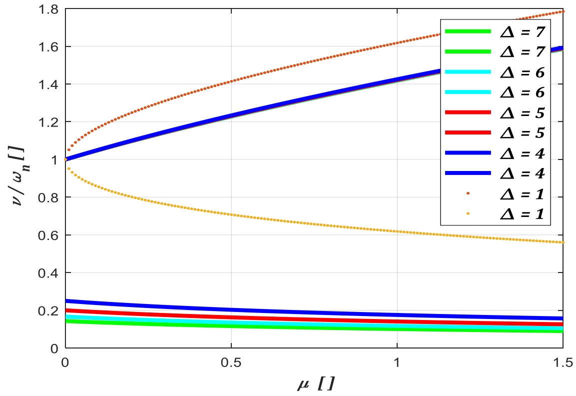

Fig. 5. Graphs showing the ratio of the upper and lower resonance frequency to ωn as a function of the mass ratio μ, depending on the value of the parameter Δ. Note: upper frequency graphs for Δ>>1 values (Δ = 4 to 7) coincide approximately on the graph

Comparison of the diagrams for $\Delta = 1$ and those corresponding to typical super-resonant tunings of the protected system $\Delta = 4$ to 7, leads to the conclusion that the nature of the two relations is different, wherein the super-resonant tuning of the main mass causes a downward shift of the resonant frequencies surrounding the antiresonant zone, causing a significant approximation of the upper resonant frequency to the operating frequency $\nu = \omega_n$, which increases the danger of accidental entry of the system into the near-resonant state.

To provide a better illustration of the effect of the parameter Δ (17) on the ratio of the resonance frequency to the antiresonance frequency, a graph, shown in Fig. 6, was prepared presenting four values of the parameter μ (14). These diagrams prove that for machines with bodies operating in the typical super-resonance regime, the main effect on widening the antiresonance zone is to increase the eliminator-to-body mass ratio, and for a fixed value of this ratio, it is advantageous to increase the parameter Δ, which, however, almost exclusively decreases the lower resonance frequency, leaving the upper resonance frequency, located relatively close to the excitation frequency, almost unchanged, much lower than the one resulting from the graphs for $\Delta = 1$ (Fig. 4).

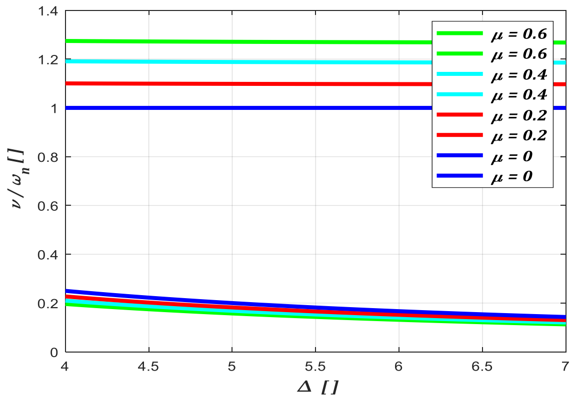

Fig. 6. Plots of the ratios of the upper and lower frequency of the system to the antiresonance frequency ωn as a function of Δ

5. THE EFFECT OF THE ACTUAL NUMBER OF DEGREES OF FREEDOM IN A SYSTEM ON ITS CHARACTERISTIC FREQUENCIES

Although the theoretical analysis cited above allows the position of resonant frequencies to be determined with respect to the antiresonant frequency, which is the intended operating frequency of the system, this analysis does not take into account the fact that the actual system of an antiresonant conveyor has a much greater number of degrees of freedom, as shown in Fig. 5 on the example of a machine with a flat layout [16].

In particular, the actual system has the possibility and the specified frequency of the swinging motion α in the machine plane of symmetry, resulting in the actual lower limit of operating speed fluctuation possibly not corresponding to the lower resonant frequency of the eliminator considered earlier. These phenomena will be investigated during the modal analysis using the simulation model shown in Fig. 7.

5.1. Discrete dynamic model of an antiresonant conveyor

To perform a dynamic and modal analysis of the antiresonant conveyor, its discrete model formulated in [16] was used, with 6 degrees of freedom $\{ x, y, \alpha, f, \varphi_1, \varphi_2 \}$, as shown in Fig. 7. The model consists of two masses, i.e. the mass of the body M_k and the mass of the trough M_r, acting as a dynamic eliminator in this model, and two inertial vibrators with individual induction drive.

The body was spring-supported on helical springs fixed to the ground, while the conveyor trough was supported on spring rails fixed to the body. Counter-rotating inertial vibrators are the source of the resultant excitation force acting on the body at an angle β to the horizontal. The vibrators were mounted in such a way that the symmetrical segment connecting the centers of the vibrator bearings intersected the center of mass of the body and the trough. The following values of constants [SI] were assumed in the Tab. 2. and came from the literature [16].

Tab. 2. Parameters of the dynamic model from Fig. 7

Parameter	*Value*	*Unit*
M_r	1000	kg
M_k	2500	kg
J_k	12200	kgm^2
J_r	5000	kgm^2
k_y	2328000	N/m
k_x	1164000	N/m
k_f	10962000	N/m
b_y	0 *	Ns/m
b_x	0 *	Ns/m
b_f	0 *	Ns/m
L	2	m
L_r	1.92	m
H	0.48	m
h_r	1.1	m
β	30	deg

To analyse the motion of the system, in the static equilibrium state of the machine without a feed, an absolute central system was assumed in relation to the body of the machine, with the axes x, y, body rotation angle α, relative displacement of the trough relative to the body f and the absolute angles of rotation of the vibrators φ_1 and φ_2.

The set of equations describing the motion of the machine can be expressed in matrix form:

$$\boldsymbol{M} \cdot \ddot{\boldsymbol{q}} = \boldsymbol{Q} \tag{24}$$

where

$$\ddot{q} = \frac{d^2}{dt^2}[x, y, \alpha, f, \phi_1, \phi_2]^T$$

The form of the mass matrix **M** and the vector of free expressions **Q** can be found in [2]. An approximate linearised form of these relations is used below to perform a modal analysis of the system.

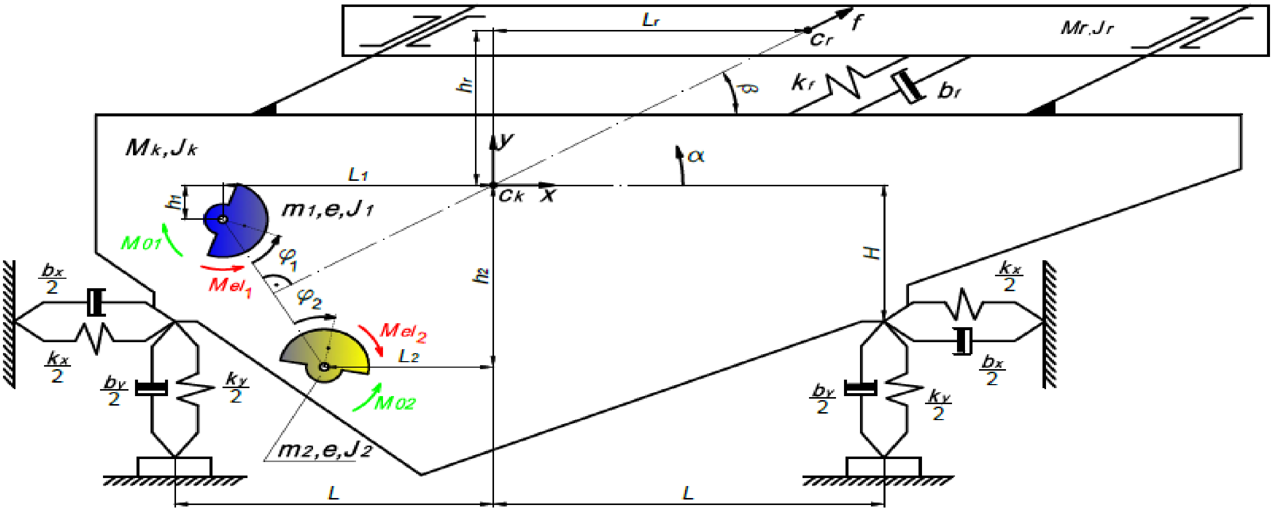

Fig. 7. Discrete model of an antiresonant vibratory conveyor shown in Fig. 2

5.2. Linearisation of a Nonlinear System

Due to the low energy dissipation in the springs, mainly from material and structural damping, it is possible to analyse the natural vibrations of the system as undamped. The remaining nonlinearities of the machine model without feed are related to the effect of body vibrations on the vibrator motion and to the Coriolis acceleration in the compound motion of the trough. The dimension-to-mass ratios in typical vibratory machine designs generally allow the motion of the vibrator to be neglected in the natural vibration analysis and its mass to be focused on the rotation axis [12]. Similarly, when analysing the Coriolis acceleration value, it can be neglected compared to the other acceleration components for typical machine dimension ratios.

By doing so, the dynamic equation (24) can be reduced to the form (25)

$$\boldsymbol{M} \cdot \ddot{\boldsymbol{q}} + \boldsymbol{K} \cdot \boldsymbol{q} = \boldsymbol{0} \tag{25}$$

in which: **0** – zero vector, **M** – mass matrix, **K** – elasticity matrix,

$$\boldsymbol{q} = \boldsymbol{q_0} \cdot sin(\omega t + \gamma) \tag{26}$$

where:

q₀ – vector of coordinate amplitudes: *x, y, α, f*,
ω – natural frequency,
γ – vibration phase angle.

Therefore, we obtain the matrix equation (27).

$$(\boldsymbol{K} - \omega^2 \cdot \boldsymbol{M}) \cdot \boldsymbol{q} = \boldsymbol{0} \tag{27}$$

The existence of a non-zero solution to this equation is possible if the matrix$(\boldsymbol{K} - \omega^2 \cdot \boldsymbol{M})$is singular, i.e.

$$det(\boldsymbol{K} - \omega^2 \cdot \boldsymbol{M}) = 0 \tag{28}$$

The relation (24) is a 4th degree equation on ω^2 and leads to the determination of 4 natural frequencies (not necessarily different). We reject negative frequencies as physically meaningless.

After considering the form of the mass and elasticity matrices, we obtain:

$$(\boldsymbol{K} - \omega^2 \cdot \boldsymbol{M}) = \begin{bmatrix} a_{11} & a_{12} & a_{13} & a_{14} \\ a_{21} & a_{22} & a_{23} & a_{24} \\ a_{31} & a_{32} & a_{33} & a_{34} \\ a_{41} & a_{42} & a_{43} & a_{44} \end{bmatrix} \tag{29}$$

where

$$a_{11} = k_x - (M_k + M_r)\omega^2$$
$$a_{12} = a_{21} = 0$$
$$a_{13} = a_{31} = k_x H + h_r M_r \omega^2$$
$$a_{14} = a_{41} = -M_r \omega^2 \, cos(\beta)$$
$$a_{22} = k_y - (M_k + M_r)\omega^2$$
$$a_{23} = a_{32} = -L_r M_r \omega^2$$
$$a_{24} = a_{42} = -M_r \omega^2 \, sin(\beta)$$
$$a_{33} = k_x H^2 + k_y L^2 - (J_k + J_r + M_r L_r^2 + M_r h_r^2)\omega^2$$
$$a_{34} = a_{43} = [-M_r L_r \, sin(\beta) + M_r h_r \, cos(\beta)]\omega^2$$
$$a_{44} = -M_r \omega^2 + k_f$$

After substituting the previously assumed numerical values and equating the determinant of the matrix (29) to zero, we obtain the following solution of equation (28) in the form of 4 natural frequencies:

f_1 = 2.61 Hz, f_2 = 3.47 Hz, f_3 = 4.41 Hz, f_4 = 19.84 Hz.

5.3. Forms of natural vibrations

Zeroing the principal matrix determinant means that the equations are linearly dependent, therefore it is not possible to obtain specific values of the amplitudes. By substituting a given natural frequency into the matrix, it is possible to determine the corresponding vibration form, that is, the ratio of amplitudes of individual coordinates. For specific values of vibration frequency, vibration forms were obtained in the form (30)

$$\boldsymbol{q_0} = \begin{bmatrix} A \\ B \\ C \\ D \end{bmatrix} \tag{30}$$

Calculation of the vibration form for a given natural frequency:

$$(\boldsymbol{K} - \omega^2 \cdot \boldsymbol{M}) \cdot \boldsymbol{q_0} = (\boldsymbol{K} - \omega^2 \cdot \boldsymbol{M}) \cdot \begin{bmatrix} A \\ B \\ C \\ D \end{bmatrix} = \begin{bmatrix} 0 \\ 0 \\ 0 \\ 0 \end{bmatrix} \tag{31}$$

The form of the vibration related to the relative displacement amplitude *f* was obtained using the LU matrix decomposition.

For f_1 = 2.61 Hz

$$\begin{bmatrix} A \\ B \\ C \\ D \end{bmatrix} = \begin{bmatrix} 48.32 \\ -4.43 \\ -12.10 \\ 1 \end{bmatrix} \cdot D \tag{32}$$

Proceeding similarly for the other frequencies, the following was obtained in Tab. 3.

Tab. 3. The form of the vibration

	f_2 = 3.47 Hz	**f_3 = 4.41 Hz**	**f_4 = 19.84 Hz**
$\begin{bmatrix} A \\ B \\ C \\ D \end{bmatrix} =$	$\begin{bmatrix} 18.22 \\ 12.51 \\ 8.80 \\ 1 \end{bmatrix} \cdot D$	$\begin{bmatrix} -10.75 \\ 45.26 \\ -11.10 \\ 1 \end{bmatrix} \cdot D$	$\begin{bmatrix} -0.25 \\ -0.15 \\ -0.00014 \\ 1 \end{bmatrix} \cdot D$

The form of the foregoing vibration forms indicates that the successive frequencies correspond approximately, respectively, to: horizontal vibrations of the entire machine, co-phase vibrations close to vibrations with lower frequency of the machine as an eliminator, angular vibrations of the machine and reciprocating vibrations of the trough and the body in the operating direction. The last form, which corresponds to the highest natural frequency, has the nature of an upper resonant frequency of the Frahm system.

If based on machine parameters we determine the value of the ratio of the trough mass to the body mass $\mu = 0.4$ and based on the relations (23) derived for the Frahm's model we calculate the value of the upper resonance frequency f_u and the lower resonance frequency f_l. Using formulas (10), (18), (23) and values from Tab. 2.:

$$\Delta^2 = \frac{k_f M_k}{M_r k_{xy}} \tag{33}$$

where equivalent stiffness coefficient k_{xy} is (34)

$$k_{xy} = \sqrt{(k_x \cdot \cos\alpha)^2 + \left(k_y \cdot \sin\alpha\right)^2} \tag{34}$$

and finaly

$$\nu_{u,l} = \sqrt{\frac{[1+\Delta^2(1+\mu)] \pm \sqrt{[1+\Delta^2(1+\mu)]^2 - 4\Delta^2}}{2\Delta^2}} \cdot \sqrt{\frac{k_f}{M_r}} \left[\frac{rad}{s}\right] \tag{35}$$

We obtain the following frequencies: f_u = 19,83 Hz and f_l = 3,32 Hz, respectively. The higher value is in satisfactory agreement with f_4 of the machine, while the lower value reproduces f_2 of the machine with an error of 4,3%. More importantly, the lower limit of the antiresonant zone does not correspond to f_l, since the resonant region f_3 of the machine, corresponding in the real machine to its angular vibration, is closer to the antiresonant frequency.

6. SPRING WEIGHT REDUCED TO TROUGH

In the case of antiresonant machines, the high stiffness of the spring system means that the mass of the springs is significant, accounting for about 1/4 of the trough mass, and should not be ignored when determining the antiresonant frequency. Since the spring is a deformable system, its mass "belonging" to the trough should be determined by determining the reduced mass. The lack of adequate values of reduction factors for springs in the literature makes it necessary to determine them.

To do so, assuming in line with reality that the first bending frequency of the spring positioned in its outermost points is many times higher than the operating frequency of the machine, to determine the deformation form f of the spring, we can assume that it is caused by the static application of force S in the operating direction – Fig. 8.

Let us denote by mj the mass of the active part of the spring. Taking advantage of the symmetry of the system, which leads to zero bending moment for w=l/2 , let us write the equation of the deflection line of the lower half of the spring, i.e. for the range w=0 to l/2 in the form (36):

$$EJ\frac{d^2 f}{dw^2} = S(l/2 - w) \tag{36}$$

The solution to this equation (36) with boundary conditions (37) is (38)

$$f(0) = 0,\ \frac{df}{dw}(0) = 0 \tag{37}$$

$$f(w) = \frac{S}{EJ} \cdot \left[\left(\frac{l}{2}\right) \cdot \frac{w^2}{2} - \frac{w^3}{6}\right] \tag{38}$$

Therefore, (39) were obtained.

$$f\left(\frac{l}{2}\right) = \frac{A}{2} = \frac{S}{3EJ}\left(\frac{l}{2}\right)^3 \tag{39}$$

where *A=f(l)* denotes the total amplitude of the relative displacement of both ends of the spring, equal to the vibration amplitude of the trough relative to the body in the direction *f*.

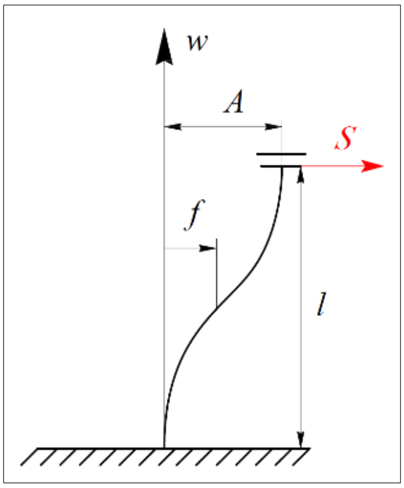

Fig. 8. Continuous spring model (flat spring during deformation)

By determining the *S* value from relation (39) and substituting it in equation (38) we obtain the deflection line of the lower half of the spring depending on *A* (40):

$$f_I(w) = \frac{3}{(l/2)^3} \cdot \left[\left(\frac{l}{2}\right) \cdot \frac{w^2}{2} - \frac{w^3}{6}\right]\frac{A}{2}, \tag{40}$$

for

$w = 0$ to $l/2$

Using the antisymmetry of the deformation form of the upper and lower spring halves, the displacements of the upper part can be written in the form (41).

$$f_{II}(w) = \left\{1 - \frac{3}{2(l/2)^3} \cdot \left[\left(\frac{l}{2}\right) \cdot \frac{(l-w)^2}{2} - \frac{(l-w)^3}{6}\right]\right\} A, \quad \text{for } w = \frac{l}{2} \text{ to } l \tag{41}$$

Between the time course of deflection *f(t)* and the speed course $\dot{f}(t)$ for harmonic vibrations, there is a relation of the velocity amplitude being equal to the displacement amplitude multiplied by the angular frequency of vibrations ω.

Therefore, the square of the velocity amplitude of the point of the spring with deflection *f* is $f^2\omega^2$. This allows us to present the maximum kinetic energy of the mass reduced to the trough as (42)

$$E_{m_{zr}} = \frac{1}{2} m_{zr} A^2 \omega^2 \tag{42}$$

And the spring:

$$E_{m_{zr}} = \frac{1}{2}\int_0^l f(w)^2 \omega^2\, \bar{m}\, dw \tag{43}$$

where

$$\bar{m} = \frac{m_i}{l} \tag{44}$$

DOI 10.2478/ama-2025-0054

By comparing the two expressions (42) and (43) for kinetic energy, the second of which is the sum of both parts of the spring, it is possible*,* after calculating the integral and dividing by $A^2\omega^2/2$, to determine the reduced mass of the spring (45) which is connected with the trough and that produces the same inertial resistance at the attachment point as the tip of the spring.

$$m_{zr} = \frac{m_i}{A^2 l}\left\{\int_0^{l/2} [f_I(w)]^2\, dw + \int_{l/2}^{l} [f_{II}(w)]^2\, dw\right\}$$
$$= \frac{13}{35} m_i \qquad (45)$$

Correct determination of the antiresonant frequency of the system requires adding the determined fraction of the mass of the active spring part to the mass of the trough (and, of course, the total mass of the grip parts associated with the trough).

6.1. Experimental and numerical study of the frequency of bending vibrations

6.1.1. An experimental model and Identification of system parameters and experimental determination of the first natural frequency

To check the accuracy of the calculation model taking into account the mass of the flat springs (Equation (45)), an experiment was carried out to determine the first natural frequency of bending vibrations of the system shown in Fig. 9. This system reflects the typical method of attaching flat springs in vibrating conveyors, such as the one shown in Fig. 1. attached by screws E, washers F and nuts G and pressure plates D to distancing bodies B. Figure 9a shows the basic dimensions of the elements of the analysed system. Figure 9b shows the system of Figure 9a attached by means of a vice to the anchored in the foundation. The vibrations of the free end of the system were induced by its deflection and release. Vibration recording was performed using a vibration analyzer KSD-400 from SENSOR equipped with a miniature accelerometer 352C22 from PCB PIEZOTRONICS with a mass of 0.5 g. The accelerometer was glued to one of the flat springs, as shown in Fig. 9b. The sampling frequency was 4.096 Hz. Due to analog integration, the vibration velocity was measured over time.

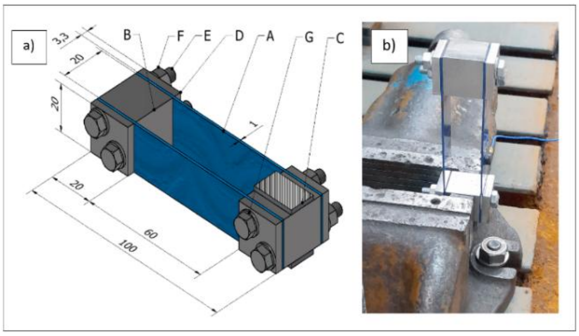

Fig. 9. Scheme of the elastic support system, (a) A – flat spring, B – distancing mass, C – mounting washers in the vice jaws, D – pressure plates, E – screws M5x40, F – nuts, G – washers; (b) the system attached to the foundation with a vice

The results of free vibration tests of the system are shown in Fig.10. The time course of the vibration velocity decay is shown in Fig.10a. The results of the FFT analysis are presented on Fig. 10b. The natural frequency obtained from the experiments was 85,3 Hz.

In order to determine the actual elastic-inertial properties of the system, additional tests were carried out:

- three-point bending flexural tests of each of both flat springs, in order to determine their individual bending stiffnesses EJsi ;
- testing of the transverse stiffness kf of the entire system;
- measurement of the masses of system elements.

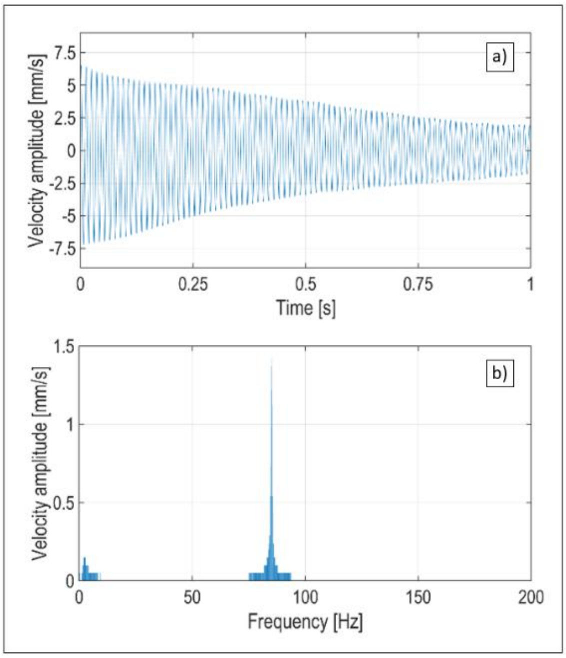

Fig. 10. Time course of vibration velocity (a), FFT analysis results (b)

The values of the bending stiffness EJs1 and EJs2 of the used springs and the transverse stiffness kf of the entire system were experimentally tested using the MTS ACUMEN 3 testing machine, equipped with a 250 N force sensor. The traverse shift velocity in all tests was 0.5 mm/s. In the three-point bending flexural tests, the distance between the supports was 70 mm. Figure 11 shows a stand for three-point bending flexural tests and a graph of the lateral force versus the deflection arrow for one of the springs, along with a 1st degree polynomial approximating this course. Approximations of the experimental results were performed in the MATLAB software environment. The values of the slope coefficients of the linear approximating functions were 48.7078 N/mm and 48.4407 N/mm respectively, while the coefficients of determination were 0.9991 R-squared and 0.9992 R-squared respectively. Based on these values and the known relations, the bending stiffness values of the two springs were determined, which were EJs1 = 348058 Nmm2 and EJs2 = 346149 Nmm2 respectively. Figure 12 shows the entire system subjected to transverse load (Fig. 12a) and the relationship between transverse force and stiffness kf of the system along with a function that approximates stiffness (Fig. 12b). The approximate stiffness value was 30.4068 N/mm, with a coefficient of determination of 0.9967.

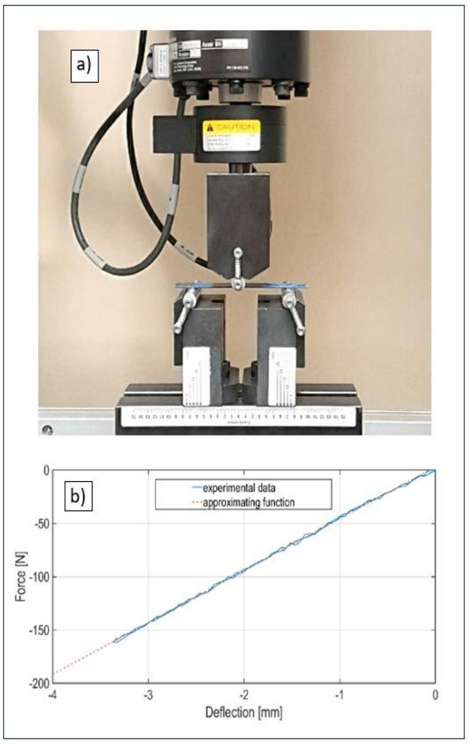

Fig. 11. An experimental determination of the transverse stiffness of flat springs: (a) view of the station, (b) force-displacement diagram for one of the spring

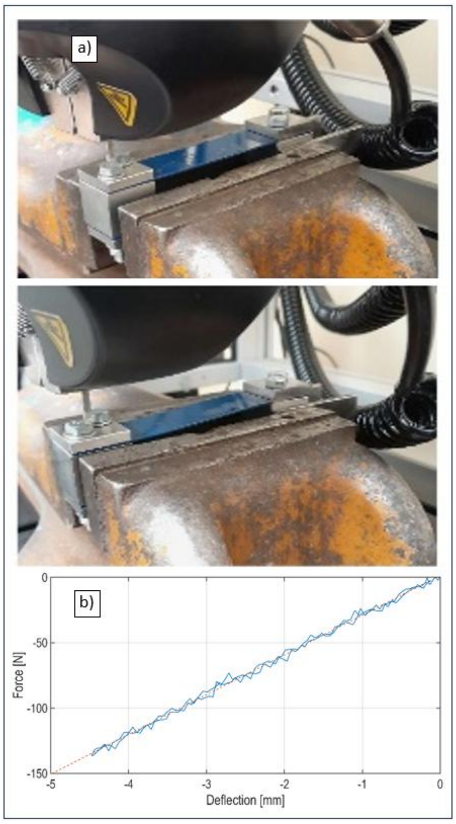

Fig. 12. Experimental determination of the stiffness of the entire system (a) before and after the load, (b) the relationship between the transverse force and the stiffness kf of the system

The information contained in Tab. 4 with the following notations was obtained from the analysis.

Tab. 4. Geometric and physical parameters of flat springs and other components of the test system (Fig. 9) - mass values are given with an accuracy of 0.01 g

Parameter		*Value*	*Unit*	*Meaning*
l_c	=	0.1	m	total length of the spring
l	=	0.06	m	active length of the spring
b	=	0.02	m	spring width
h	=	0.001	m	spring thickness
m_r	=	0.00948	kg	mass of the active part of a single spring
m_{zr}	=	0.00352	kg	reduced mass of a single spring (45)
m_d	=	0.09609	kg	vibrating mass B + D + E
m_z	=	0.10314	kg	total weight reduced
EJ_{s1}	=	348058	Nmm²	spring stiffness no. 1
EJ_{s2}	=	346149	Nmm²	spring stiffness no. 2

6.1.2. The 1st natural frequency – a continuous and discrete model

The impulse excitation was used to perform a modal analysis, i.e. the appearance of a short-term high force acting across the springs. The appearance of this force causes the excitation of resonance vibrations. These vibrations also include the first form of natural vibrations, which is related to the deformation of the springs of mass m_r and the oscillations of the mass m_d, which is the sum of the masses of the non-deformable parts (distancing mass (B), screws and washers (E)). The behaviour of the vibrating system with the first mode of natural vibrations from Fig. 9 shows not only the continuous model (Fig. 13a), but also the discrete model (Fig. 13b), which simplifies the behaviour of the system for the translational movement of the mass m_z (due to the identical displacement of the mounting points of the flat springs). The mass m_z is the reduced mass of the vibrating elements, i.e. masses of the deformed springs m_r and the nondeformable vibrating parts m_d. Using formula (45), the reduced mass m_z was obtained in the form (46).

$$m_z = m_d + 2 \cdot m_{zr} = m_d + 2 \cdot \frac{13}{35} m_r \tag{46}$$

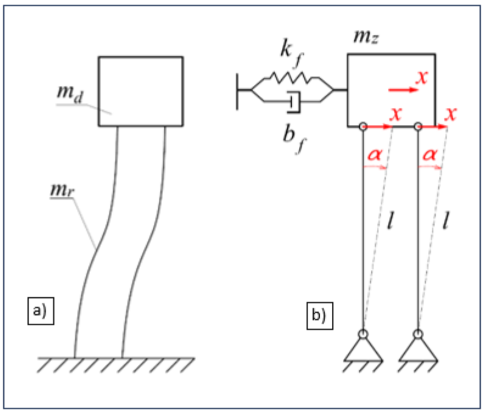

Fig. 13. Continuous model of the tested system showing the first natural frequency (a), discrete equivalent model of the tested system for the first natural frequency (b)

In this case, the replacement suspension system was a spring and damper package with stiffness and damping coefficients k_f and b_f, respectively, attached to the support and the reduced mass m_z parallel to the direction of vibration.

The elasticity of a single flat spring used in the experiment was calculated from the Eq. (47), which takes into account the constant moment of inertia (48) of the cross-section *b* x *h* of the spring bar shown in Fig. 9a and Tab. 4.

$$k_{f\,i} = \frac{12EJ_{si}}{l^3} \tag{47}$$

where

$$J = \frac{bh^3}{12} \tag{48}$$

The energy absorption coefficient ψ for flat steel springs is equal to 0.04 [17], which means that the viscous damping coefficient of the spring is so small that its impact on the vibration frequency is negligible. After taking into account the parallel connection of flat springs and the discrete model, the doubled elasticity k_f and the first natural frequency of undamped vibrations (doubled damping coefficient $b_f \approx 0$) in the form (49) were obtained.

$$f = \frac{\sqrt{\frac{\sum_{i=1}^{2} k_{f\,i}}{m_z} - \left(\frac{\sum_{i=1}^{2} b_{f\,i}}{2m_z}\right)^2}}{2\pi} \approx \frac{\sqrt{\frac{\sum_{i=1}^{2} k_{f\,i}}{m_z}}}{2\pi} \approx 97.33\ Hz \tag{49}$$

Frequency not taking into account the spring mass calculated from the Eq. (50)

$$f = \frac{\sqrt{\frac{\sum_{i=1}^{2} k_{f\,i}}{m_d} - \left(\frac{\sum_{i=1}^{2} b_{f\,i}}{2m_d}\right)^2}}{2\pi} \approx \frac{\sqrt{\frac{\sum_{i=1}^{2} k_{f\,i}}{m_d}}}{2\pi} \approx 100.83\ Hz \tag{50}$$

6.1.3. The 1st natural frequency – a numerical model

FEM software is usually used as a tool to check the accuracy of analytical calculations carried out in the conveyor design process. Modal analyses are most often used to determine the natural frequency of the system. The results of such an analysis, performed in the ANSYS software environment, are presented below. The inertial and elastic parameters of the solid model were determined on the basis of experimental data presented in Tab. 4. Due to differences in the geometry of the real elements and the solid model (e.g. modelling the threaded part of the screws in the form of a cylinder, omitting chamfers, etc.), appropriate density values were assigned to individual elements in the solid model so that their masses were consistent with those measured experimentally. The Poisson number for all elements was assumed to be 0.3, and the Young's modulus of springs was assumed to be 208262.1 MPa, which is the average of the values determined on the basis of experiments. For the remaining elements, a value of Young's modulus representative for carbon steels was assumed, equal to 200000 MPa. In order to obtain a high-quality FE mesh, the selected elements were divided into smaller volumes and then the requirement for compliance of common nodes was imposed within these elements. All parts of the system have been discretised using higher-order finite elements exhibiting quadratic displacement behavior. Springs have been discretised using quadratic 20-node hexahedral elements, which generally give more accurate results than tetrahedral-shaped elements and are also more reliable in terms of the skewness parameter [18, 19]. To obtain reliable results from the FEM analyses, in addition to analysing the quality of the FE mesh, an additional analysis of the influence of the density of the spring modelling mesh was performed. Modal analyses were performed with three finite element mesh settings in the spring thickness direction *b*: with one, two, and three finite element layers. The models obtained in this way are shown in Fig. 14. In Figure 14, the boundary condition of the restraint on the surface of the mounting plate on the FEM model is additionally marked in yellow. Table 4 lists the number of nodes in individual system models, the results of the FE mesh quality analysis (average skewness and average orthogonal quality), and the results of the impact of the FE mesh density on the natural frequency value obtained in the modal analysis.

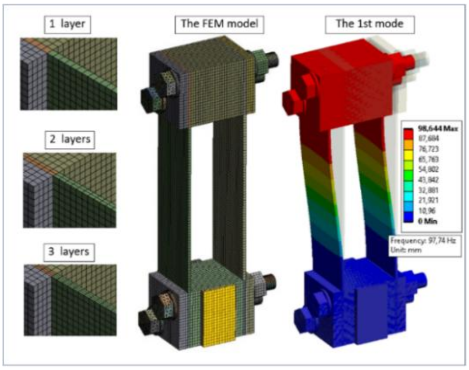

Fig. 14. The results of the modal analysis performed in the ANSYS environment - the first form of vibration from Fig. 8 and 9 - the simulation result is 97,74 Hz (Tab.4) for three finite element layers on flat springs

The difference between the results (Tab. 5.) obtained for models with 3 and 2 layers was approximately 0.06%, indicating the high accuracy of the results. These results are in good agreement with the result of the formula (49) taking into account the mass of the spring (97.33 Hz). The difference between the pattern result and the 3-layer FEM result was approximately 0.4%.

6.1.4. Comparison of analysis results

In the comparative analysis, the reference value with which the remaining results were compared is the frequency of the first form of vibration obtained from the experimental analysis, which was 85.3 Hz. As shown in Table 6, the result of the theoretical analysis of 97.33 Hz, taking into account the reduced mass of flat springs (49), is closest to the value obtained from the experimental test. The difference in values and the relative error of 14.10% may result from assembly errors and measurement errors when determining the active length of the flat spring.

Tab. 5. Parameters of modal analysis

Number of layers in thickness h	1	2	3
Total number of nodes / number of nodes of one spring	379514/ 15629	397475/ 24586	415436/ 33543
Average Skewness parameter	0.24776	0.23940	0.23175
Average Orthogonal Quality	0.87048	0.87567	0.88043
The 1st natural frequency	98.01 Hz	97.80 Hz	97.74 Hz

Tab. 6. Comparison of the frequency results of the first form of bending vibrations

A type of modal analysis	f [Hz]	ε [%] *
theoretical without taking into account the mass of flat springs	100.83	18.21
theoretical taking into account the mass of flat springs	97.33	14.10
numerical	97.74	14.58
experimental	85.30	0

* ε - the relative difference between a specific value and the value obtained from experiment

The active length should be counted from the place where the spring is attached, taking into account the chamfers of the spacer mass (B) and the pressing washers (D) from Fig. 9. The theoretical method does not take into account their deformability, which could occur under real conditions. Failure to take into account the mass of the springs (50) with the result of 100.83 Hz leads to even greater errors in frequency estimation at the level of 18.21%. The numerical analysis gave a result very close to the theoretical value, taking into account the reduced spring mass. Both of these methods assume tight adhesion of the springs and spacer masses to each other, and hence the active length in both methods is identical. In fact, due to the slight deformability of the handles, the active length can be greater and the elasticity of the springs can decrease with the cube of the active length of the spring (45).

7. CONCLUSIONS

Achieving high mobility properties of conveyors operating on the basis of Frahm's principle of dynamic elimination requires high accuracy in determining both the position of the antiresonant point and the resonance frequency of the system. Relationships based on the classical Frahm damping theory lead to results that are far from real in this regard. This paper presents correct derived formulas and a nomogram built for designers based on them. The effect was shown that the actual number of degrees of freedom in machines constructed using the dynamic eliminator principle has on frequencies limiting the antiresonance zone. The effect of the spring mass on the antiresonance frequency was also pointed out, and correct relations for its consideration were derived. The issues discussed do not exhaust the possible causes of unsatisfactory running properties of antiresonance type conveyors. Many significant errors may also result from a simplified mathematical description of the vibrating system, not including the phenomenon of self-synchronisation of vibrators [7] or even the construction of a system that does not guarantee the possibility of obtaining the exciting force along a straight line [20], which is the cause of the component of the direct transfer of the exciting force to the ground.

REFERENCES

1. Czubak P, Gajowy M. Influence of selected physical parameters on vibroinsulation of base-exited vibratory conveyors. Open Engineering. 2022 Jan 1;12(1):382–93. Available from: https://doi.org/10.1515/eng-2022-0033
2. Surówka W, Czubak P. Transport properties of the new vibratory conveyor at operations in the resonance zone. Open Engineering. 2021 Jan 1;11(1):1214–22. Available from: https://doi.org/10.1515/eng-2021-0122
3. Sun JQ, Jolly MR, Norris MA. Passive, Adaptive and Active Tuned Vibration Absorbers—A Survey. Journal of Mechanical Design. 1995 Jun 1;117(B):234–42. Available from: https://doi.org/10.1115/1.2836462
4. Ibrahim RA. Recent advances in nonlinear passive vibration isolators. Journal of Sound and Vibration. 2008 Jul;314(3-5):371–452. Available from: https://doi.org/10.1016/j.jsv.2008.01.014
5. Wahl F, Schmidt G, Forrai L. On The Significance Of Antiresonance Frequencies In Experimental Structural Analysis. Journal of Sound and Vibration. 1999 Jan;219(3):379–94. Available from: https://doi.org/10.1006/jsvi.1998.1831
6. Renault A, Thomas O, Mahé H. Numerical antiresonance continuation of structural systems. Mechanical Systems and Signal Processing. 2018 Jul 27;116:963–84. Available from: https://doi.org/10.1016/j.ymssp.2018.07.005
7. Li X, Shen T. Dynamic performance analysis of nonlinear anti-resonance vibrating machine with the fluctuation of material mass. Journal of Vibroengineering. 2016 Mar 31;18(2):978–88. Available from: https://doi.org/10.21595/jve.2016.16559
8. Cieplok G. Self-synchronization of drive vibrators of an antiresonance vibratory conveyor. Journal of Theoretical and Applied Mechanics. 2023 Sep 18;61(4):501–11. Available from https://doi.org/10.15632/jtam-pl/170840
9. Li Y, Ren T, Meng X, Zhang M, Zhao P. Experimental and theoretical investigation on synchronization of a vibration system flexibly driven by two motors. Proceedings of the Institution of Mechanical Engineers Part C Journal of Mechanical Engineering Science. 2020 Feb 25;234(13):2550–62. Available from: https://doi.org/10.1177/0954406220907930
10. Peng H, Hou Y, Fang P, Zou M, Zhang Z. Synchronization analysis of the anti-resonance system with three exciters. Applied Mathematical Modelling. 2021 Apr 13;97:96–112. Available from: https://doi.org/10.1016/j.apm.2021.03.055
11. Richiedei D, Tamellin I, Trevisani A. Beyond the Tuned Mass Damper: a Comparative Study of Passive Approaches to Vibration Absorption Through Antiresonance Assignment. Archives of Computational Methods in Engineering. 2021 Apr 28; 29. Available from: https://doi.org/10.1007/s11831-021-09583-w
12. Den Hartog, JP. Mechnical vibrations [in Polish]. PWN. Warszawa; 1971.
13. Frahm H. Device for Damping Vibrations of Bodies. 1909, US Patent No. 989958.
14. Michalczyk J, Gajowy M. Operational properties of vibratory conveyors of the antiresonance type. Archives of Mining Sciences. 2018, 63(2):301–319.
15. Klemiato M, Czubak P. Control of the transport direction and velocity of the two-way reversible vibratory conveyor. Arch Appl Mech. 2019 Jan 4;89(7):1359–73. Available from: https://doi.org/10.1007/s00419-018-01507-8
16. Gajowy M. Analysis of the dynamic properties of vibrating conveyors operating on the basis of the phenomenon of dynamic vibration elimination [in Polish]. Doctoral dissertation, Faculty of Mechanical Engineering and Robotics, AGH University of Science and Technology, Kraków, Poland. 2017
17. Michalczyk J. Vibration machines, dynamic calculations, vibrations, noise [in Polish]. WNT; 2011
18. Burkhart TA, Andrews DM, Dunning CE. Finite element modeling mesh quality, energy balance and validation methods: A review with recommendations associated with the modeling of bone tissue. J Biomech. 2013;46(9):1477–1488. Available from: https://doi.org/10.1016/j.jbiomech.2013.03.022
19. Ruggiero A, D'Amato R, Affatato S. Comparison of meshing strategies in THR finite element modelling. Materials. 2019 Jul 23;12(14):2332. Available from: https://doi.org/10.3390/ma12142332
20. Sturm M. Two-mass linear vibratory conveyor with reduced vibration transmission to the ground. Vibroengineering Procedia. 2017 Sep 19;13:20-3. Available from: https://doi.org/10.21595/vp.2017.19066

This work is financed by AGH University of Krakow, Faculty of Mechanical Engineering and Robotics, research program No. 16.16.130.942.

Jerzy Michalczyk: https://orcid.org/0009-0006-1968-7561

Marek Gajowy: https://orcid.org/0000-0001-6326-2364

Krzysztof Michalczyk: https://orcid.org/0000-0002-1024-5947

DOI 10.2478/ama-2025-0055

EFFECT OF THE END COIL SHAPE OF THE HELICAL COMPRESSION SPRING ON ITS STIFFNESS AND DISTRIBUTION OF TRANSVERSE REACTIONS DURING AXIAL LOADING

Robert BARAN*, Krzysztof MICHALCZYK*, Mariusz WARZECHA*

*Faculty of Mechanical Engineering and Robotics, Department of Machine Design and Maintenance,
AGH University of Krakow, al. Mickiewicza 30, 30-059 Krakow, Poland

rbaran@agh.edu.pl, kmichal@agh.edu.pl, mwarzech@agh.edu.pl

received 10 February 2025, revised 18 July 2025, accepted 13 August 2025

Abstract: This paper investigates the effect of ground end coils on axial stiffness, as well as the magnitude and direction of transverse reactions occurring during axial compression of a coil spring. As shown, conventional relationships for calculating axial stiffness can significantly overestimate its value, especially for springs with a small number of active coils. Transverse reaction forces during axial compression of a spring can reach high values. The paper shows that these forces can exceed more than 30% of the axial force caused by the compression of the spring. There are no relations in the available literature to estimate the effect of spring geometry on the value and direction of the transverse reaction generated during axial compression of the spring. On the basis of experimental studies of axial compression of springs, a numerical model with high accuracy was developed - the average difference between the experimental results and the results of the numerical model was 2.7%. The model took into account friction between coils, large deformations and carefully studied material parameters. Using the developed numerical model, a total of 245 numerical analyses were carried out, based on which new relationships were developed to accurately calculate axial stiffness, lateral reaction force and its angle. The new relationship for calculating axial stiffness shows better agreement with the results of numerical analyses than all the relationships found in the literature to date. The average difference between the results of this relation and the results of the numerical analyses carried out did not exceed 2%. A new relation has been proposed for determining the value of the transverse reaction occurring in axial compression of springs. This relation also shows high agreement with the results of numerical analyses. In addition, a new relation has been proposed to determine the direction of the transverse reaction force.

Key words: helical compression spring, coil spring, axial stiffness, end coils, transverse reaction, spring design

1. INTRODUCTION

Helical compression springs are widely used in mechanical engineering. The primary functions of springs are absorbing energy and mitigating shocks, applying a definite force or torque, supporting moving masses, isolating vibrations, indicating or controlling load or torque and providing an elastic pivot or guide [1]. Consequently, they find widespread application in vehicle suspensions, such as those in cars [2], railway bogies [3, 4], vibratory conveyors [5], internal combustion engine valves [6], and vibration absorbers [7]. Springs operate under static and dynamic conditions and are subject to buckling. In specialized applications, these performance characteristics must be determined with high precision. This necessitates precise design, including a meticulously shaped coil configuration. In the paper [8] a method for modeling helical irregular polymer structures and determining their stiffness and stresses in a numerical and experimental way is presented, showing the possibilities of numerical methods in geometry modeling. Most designers still rely on basic helical structures, which have not been thoroughly studied. One aspect of spring construction that remains insufficiently studied is the end coil, whose shape influences the spring's stiffness and the distribution of transverse forces resulting from axial compression [9]. However, the precise extent to which the shape of the end coil influences the spring's stiffness, and the distribution of transverse forces has not yet been thoroughly evaluated. The motivation for conducting research in this area arises from the occurrence of spring failure [10, 11, 12], especially damage in the form of coil fractures near the inactive coil [13, 14]. In paper [10], using FEM analysis of an automotive barrel spring, the stress distribution of on its surface was investigated in the area around a modelled failure in the form of a blind hole. In paper [11], a numerical analysis of a torsion spring made of round wire was carried out, indicating the locations of possible fatigue cracks initiated by defects created by machining. This is also related to both axial and transverse stiffness, which significantly affects load transmission [15, 16], and is directly linked to the transverse forces generated by compression [17].

The inaccuracy in determining the stiffness of a spring arises from at least four factors, which include dimensional inaccuracies in the geometric parameters of the spring, such as the wire diameter d, the mean coil diameter D, the number of active coils n_a (which decreases during compression), and errors in estimating the modulus of rigidity G [18]. Additionally, a smaller influence on the spring's characteristics is attributed to the helix angle γ, which can be neglected for springs with angles smaller than 10 degrees, or even 15 degrees (resulting in an error of only 2.5%) [1]. Wahl indicates that the parameters mentioned earlier, as well as the shape of the end coil, have a greater influence on stiffness than the helix angle. Therefore, deviations in the helix angle along the entire length of the spring have an even smaller effect. The paper [12] also highlights the problem of non-uniformity of pitch and wire diameter, but also hardness, which affect the stiffness characteristics of the spring. Further factors mentioned in the literature include errors in the perpendicularity of the spring axis to the support surfaces [18], the type of end coil used [19], and the transition between inactive and active coils associated with it [20]. The latter factor can significantly contribute to nonlinearities, especially if the progressive transition zone is large [21]. The way the spring is assembled also affects its characteristics, i.e., whether the spring ends are fixed or free to rotate [1], which also leads to variations in the detailed formulas for axial stiffness [18]. The continuous change in structural parameters D, n_a, and γ during spring deformation results in the development of nonlinearities in the spring's characteristics [18]. During compression, nonlinearity initially arises from factors such as the non-parallelism of the spring ends, the lack of perpendicularity between the spring axis and the support surfaces, load eccentricity, and errors in the contact of the inactive coils. In the final stage, nonlinearity is caused by the non-simultaneous blocking of active coils. For this reason, it is recommended to calculate the axial stiffness within the central range of the spring's characteristics, i.e., for forces within 0.3 to 0.7 of the spring's blocking force F_n [18]. Additionally, the process of loading and unloading a compressed spring exhibits hysteresis [22], which means that stiffness may not necessarily have the same value in both loading directions.

Differences in the value of axial stiffness also result from the development of transverse forces during compression. In [9], the causes of transverse forces were presented, including spring asymmetry, load misalignment, buckling, stresses, variable wire diameter, and pitch variation. When these factors are significant, larger transverse forces are generated, which reduce the axial force and, consequently, the axial stiffness of the spring. The highest transverse forces occur in conical springs [9]. The issue of axial force transfer is addressed by recommending the use of a fractional total number of coils. In this configuration, the ground ends of the spring are arranged in opposite directions, preventing load misalignment [18]. Springs typically have one inactive coil on each end, but for long springs and under variable loads, 2 or 2.5 inactive coils are used to improve spring stability [18, 23]. Conventionally, the boundary between active and inactive coils is considered to be the point where coil contact begins in the unloaded state. However, this point is movable during compression, and it has been shown that part of the inactive coils primarily experiences torsional stresses [24]. For this reason, it cannot be assumed that the entire inactive coil does not contribute to the spring's stiffness. The EN 13906-2013 (E) standard [25] does not acknowledge this fact, adhering to the conventional boundary principle. This applies to supported coils, as defined in the ISO 2162-2:1993(E) standard [26]. For springs with open-ground ends, the inactive coil begins at the start of the ground surface, whereas open-unground springs lack an inactive coil. Such springs require specialized mounts using, for example, elastomer inserts [27]. In such cases, the boundary between inactive and active coils may be where the spring exits the fixture, although this depends on the degrees of freedom provided by the fixture. Transitional coils, which lie between inactive and active coils, are also identified [20]. This distinction arises from a pitch difference compared to the active section, which increases nonlinearly. It has been shown that the length of the transitional coil influences the magnitude of transverse forces and, consequently, axial stiffness [20]. The lack of standardized methods for defining the boundary between spring coils causes discrepancies in measurement results compared to the basic formula for the spring rate k provided in EN 13906-2013 (E) [21]. The full formula, which accounts for the helix angle, is not widely used, as helix angles typically do not exceed 10°, and spring indices greater than 10° result in minimal calculation errors [28]. One way to improve formula accuracy is by adding a correction factor to the number of active coils. The first proposal was made by Vogt [29], who suggested adding 0.5 to the number of active coils. Later, Paredes [30] proposed a correction of 0.35 and introduced a version that adjusts both the number of coils and the spring height, achieving an error of less than 0.2 compared to experimental force measurements. Additionally, Paredes demonstrated that the relationship in EN 13906-2013 (E) provides sufficient accuracy for springs with more than five active coils. In [28], formulas were developed to calculate the axial deflection of springs with rectangular, square, circular, annular, and elliptical wire cross-sections. The study analyzed stress contributions from axial force, shear force, bending, and torsional moments. It also presented formulas proposed by Wahl, Timoshenko, Ancker, and Goodier. The results were compared with finite element analyses performed in ANSYS, showing that the Ancker and Goodier analytical formula yielded the most accurate results. The formulas by Yıldırım and Timoshenko take the helix angle into account [31]. A similar assumption is made in the Krużelecki and Życzkowski formula [32], which provides results comparable to those of Timoshenko. In [33], Hiroyuki's formula was introduced, which incorporates material constants E and G, as well as the tangent of the helix angle. In [31], a more accurate formula than those of Timoshenko and Hiroyuki was proposed, though it is highly complex, incorporating parameters such as wire inclination κ, spring wire length L_0, and Poisson's ratio ν. Liu and Kim [24] proposed adding spiral ends to the active coils of helical springs, modeling the torsional stresses occurring in the end coil. They supported their findings with finite element simulations. Using Castigliano's theorem, they derived a correction factor for the end coil, which should be multiplied by the classical formula to account for its effects.

The aim of the study is to determine the effect of varying the contact length between coils on the axial stiffness and transverse force resulting from the axial compression of springs with ground and supported end coils, as specified in ISO 2162-2: 1993 (E) [26]. The research will be conducted using a tensile testing machine and numerical methods. Additionally, the results for axial stiffness will be compared with commonly used formulas, and empirical equations will be proposed to predict the axial stiffness and transverse reaction forces. This study's main novelty lies in its comprehensive quantification of how end-coil geometry significantly affects not only axial stiffness but also the magnitude and direction of transverse reaction forces — areas previously lacking precise analytical relationships in the literature. From an industrial standpoint, the new relationships enable more reliable spring design, particularly in suspension systems, vibration absorbers, and conveyor mechanisms — applications where unaccounted transverse reactions can lead to misalignment, fatigue fracture, or operational instability. Ultimately, the improved predictive accuracy supports enhanced performance, safety, and longevity of springs in automotive, rail, and industrial machinery contexts, enabling engineers to design with tighter tolerances and fewer prototypes.

2. ANALYTICAL METHODS

In the literature, several formulas for determining axial stiffness are distinguished, some of which were mentioned in the introduction. The most commonly used formula for the axial stiffness k_N is the equation (1) provided in the EN 13906-2013 (E) standard [25], which does not take the helix angle γ into account.

$$k_N = \frac{G \cdot d^4}{8 \cdot D^3 \cdot n_a} \tag{1}$$

where G represents the modulus of rigidity, d is the nominal diameter of wire, D is the mean diameter of coil, n_a represents the number of active coils.

Among the methods that increase the accuracy of axial stiffness calculations for springs, the most popular and straightforward ones were selected, which, after preliminary analysis, yield results that differ from each other.

As mentioned in the introduction, Vogt [29], in order to account for the influence of the inactive coils, proposed increasing the number of active coils by 0.5. On the other hand, Paredes [30] verified this and introduced an increase of 0.35 in the number of active coils. This value is named as correcting number of active coils n_{cor}, which is used in formula (2), describing Vogt (V) or Paredes (P) method.

$$k_{V,P} = \frac{G \cdot d^4}{8 \cdot D^3 \cdot (n_a + n_{cor})} \tag{2}$$

A more accurate method compared to equation (1), which takes the helix angle γ into account, is the formula (3) proposed by Krużelecki and Życzkowski [32], which slightly changes the value of the axial stiffness compared to equation (1).

$$k_K = \frac{C_{t0}}{H_a} = \frac{E \cdot I \cdot sin(\gamma)}{R_0^2 \cdot (1 + \nu \cdot cos^2(\gamma)) \cdot H_a} \tag{3}$$

where C_{t0} represents the initial compression stiffness, R_0 is the initial spring radius, ν represents Poisson's ratio, E is the Young modulus, I represents axial moment of inertia of spring wire, γ represents helix angle and H_a is the height of unloaded active coils.

In the publication [28] Yıldırım proposed equation (4), which takes into account the shear stiffness C_b, compression stiffness C_t, bending stiffness D_b and torsion stiffness D_t, expressed by equations (5-8), respectively.

$$k_Y = \left(\frac{1}{4} C d n \pi \left(\cos(\gamma)\left(\frac{4}{C_b} + \frac{C^2 d^2}{D_t}\right) + \sin(\gamma)\tan(\gamma)\left(\frac{4}{C_t} + \frac{C^2 d^2}{D_b}\right)\right)\right)^{-1} \tag{4}$$

$$C_b = \frac{G \pi d^2}{4 \vartheta},\ \vartheta = 1{,}1\ or\ \vartheta = \frac{7 + 6\nu}{6(1 + \nu)} \tag{5}$$

$$C_t = 2(1 + \nu) \cdot \frac{G \pi d^2}{4} \tag{6}$$

$$D_b = 2(1 + \nu) \cdot \frac{G \pi d^4}{64} \tag{7}$$

$$D_t = \frac{G \pi d^4}{32} \tag{8}$$

Another method accounting for the inactive coils was presented by Liu and Kim in their publication [24], where they introduced the concept of end coils above the ground surface. The number of these coils should be added to the active coils and placed in the denominator of the ratio, with the numerator being the number of active coils. This is represented by equation (9).

$$k_{LK} = k_N \cdot \left(\frac{n_a}{x_n + x_{end}}\right) \tag{9}$$

where x_n is the number of coils from the bottom to a certain point of the spring and x_{end} is the number of effective coils at the bottom [19].

The presented formulas will be compared during the numerical analysis stage, aiming to find the smallest mean absolute percentage error (MAPE) in order to identify the methods that provide results closest to reality and to propose a new method.

3. MECHANICAL TESTS

3.1. Stiffness experimental tests settings

The spring compression tests were carried out using an HT-2402 testing machine from Hung Ta Instrument Co., Ltd., Taiwan, equipped with a CL16md 5kN load cell from ZEPWN, Poland, of the precision class 0.5 according to ISO 376 (Fig. 1) [15]. The results were recorded using dedicated software. The test sample consisted of 18 sets of springs with squared and ground end-coils, each containing 3 identical springs in terms of their parameters. In total, this amounted to 54 springs. The spring sets (Fig. 2) differed in the spring index C, which was 5 or 7, the number of active coils n_a, which was 2.5, 2.75, or 3, and the contact length of the end coils s, which was 0 (point contact), 0.25, or 0.5. The contact length s was defined as the quotient of the length of the contact line between the end coils on one side of the spring and the length of one coil of wire. It was determined by inserting a 0.07 mm thick plate of feeler gauge until it locked in place. Then, using a protractor with a resolution of 1 degree, the angle of the arc from the end of the spring to the locking point of the slotted gauge plate was measured. The pitch P of the springs equaled 10 mm for all springs.

Fig. 1. The testing machine used to spring axial stiffness researches

The springs were supplied by a company specializing in custom-made springs. They were manufactured in accordance with the EN 13906-1:2013 standard [25]. The springs were made from 55CrSi FD Becrosi 26 spring steel, which complies with the EN-10270-2 standard [25]. The wire diameter d was nominally 5 mm with upper and lower deviations equal to respectively: +0.008 mm and -0.010 mm. The main material properties of this steel include a modulus of elasticity in tension *E* of 206 GPa, a modulus of elasticity in shear *G* of 79.5 GPa, and an ultimate tensile strength R_m of 1800 MPa. The first technological process involved coiling the springs. Next, the springs were tempered at 220°C for 15 minutes, after which the end coils were ground to ¾ of the circumference. Finally, the same heat treatment was applied again [15].

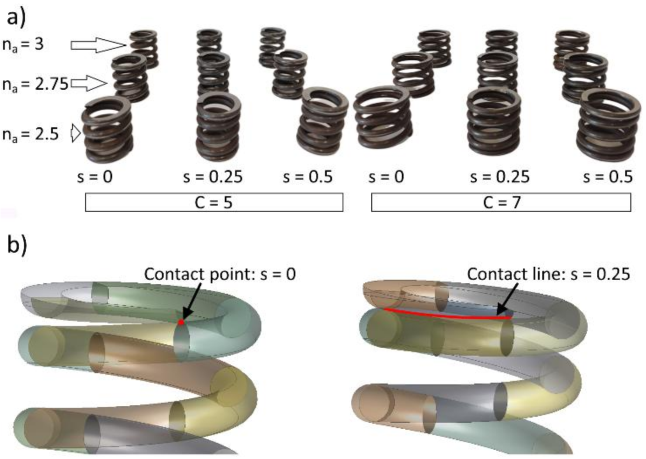

Fig. 2. Samples of springs (a) used to axial stiffness researches; (b) graphical representation of contact length for two example lengths s = 0 and s = 0.25

The springs were measured in terms of height using an electronic caliper and the number of coils in contact using a protractor with an accuracy of 1 degree. The reference point was the theoretical height, calculated as the product of the pitch *P* and the number of coils *n*, while for the contacts, the measurement corresponded to the order specifications. The springs that were closest to the benchmark geometry were considered as reference specimens for validating the numerical model. These were precisely replicated, and their measured axial stiffness became the benchmark for calculating the accuracy of the numerical model. The axial stiffness *k* in the bench tests was calculated according to Eq. (10). The maximum deflection for each spring was half of the theoretical spring gap, and the minimum reading point was 20% of the maximum deflection. Therefore, the maximum deflections for the springs with 2.5, 2.75, and 3 coils were 6.25 mm, 6.875 mm and 7.5 mm, respectively.

$$k = \frac{F_{max} - F_{min}}{s_{max} - s_{min}} \tag{10}$$

where F_{max}, F_{min} – force, s_{max}, s_{min} – deflections for the maximum and minimum measuring point, respectively.

3.2. Results and initial analyses

The results of the axial stiffness tests are presented in the form of a scatter plot (Fig. 3), with error bars indicating the variability range of the 3 measured samples. The variability was minimal, indicating repeatability of the results. When comparing the springs in terms of contact size, an increase in axial stiffness was observed for the 0.25 coil contact, which requires further investigation. These changes are particularly significant for the shortest spring with a spring index *C* = 5, where the ratio of the data spread to the mean was equal 11.2%. For the same number of coils but with a spring index *C* = 7, this ratio was 4.3%. A higher spring index also results in greater stiffness for point or quarter-coil contacts, although this effect is less apparent than for the springs with smaller index. It was decided to extend studies with a numerical model to highlight specific trends in the changes.

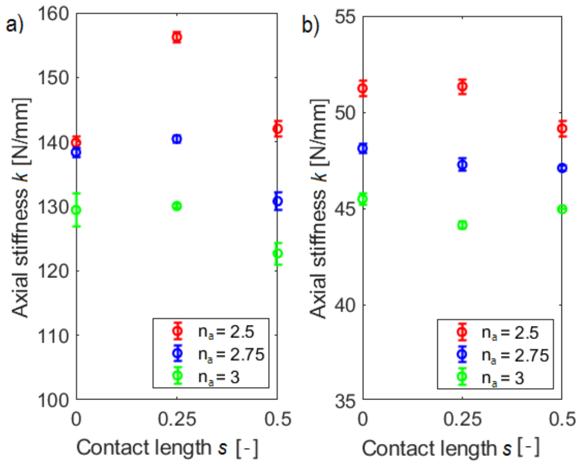

Fig. 3. Axial stiffness *k* for different numbers of active coils n_a depending on the contact length per one side of spring *s* for a) *C* = 5, b) *C* = 7

4. NUMERICAL TESTS

4.1. Material research

To build a more accurate numerical model, measurements of Young's modulus *E*, Kirchhoff's modulus *G*, and the coefficient of friction for the material from which the spring wire was made were performed. The measurement of Young's modulus *E* was conducted for two samples of straight wire with a diameter of 5 mm, sourced from the same spring manufacturer. The tests were carried out on the same testing machine equipped with load cell CL16md 5kN and a ZEPWN CL 25D-R B50 L30 extensometer, with resolution of 1 μm (Fig. 4). Tension was carried out under crosshead control at a speed of 1 mm/min, with the length of the entire specimen between the grips being approximately 180 mm. As a result of the measurement, elongations and stresses in the wire cross-section were obtained, as shown in Table 1.

Tab. 1. Results of Young's Modulus *E* measurement

Wire number	Initial wire length L_0 [mm]	Elongation L_1 [mm]	Elongation L_2 [mm]	Stress σ_1 [MPa]	Stress σ_2 [MPa]	Young's modulus [MPa]
1	60.23	0.031	0.207	120	720	205330
2	60.82	0.031	0.211	120	720	202733
Average Young's modulus *E*						204031

Young's modulus was calculated according to the relationship given in ASTM E111 – 04, based on the values given in Tab.1. The increase in force divided by the original cross-section of the specimen corresponds to the difference in stress σ_2 and σ_1, while the increase in strain corresponds to the quotient of the difference in elongation L_2 and L_1 and the original measurement length L_0. Averaged over the two measurements, the value of Young's modulus was 204031 MPa.

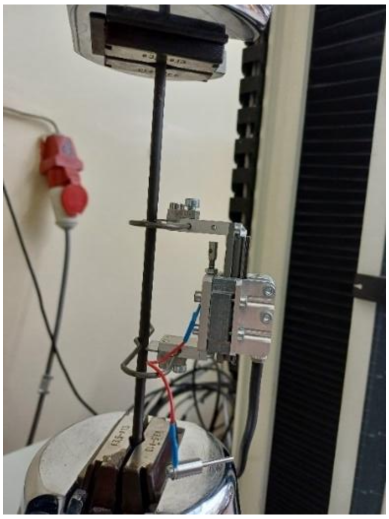

Fig. 4. Young's modulus measurement station

The next stage involved measuring the shear modulus *G*. The measurement was conducted using the same testing machine, but with an extension for twisting rods (Fig. 5). To secure the rod in the extension, it was bent, leaving a section *L* equal to 112 mm. To avoid damaging the samples, the measurement was repeated 14 times on the same rod, with the traverse displacement of the testing machine set to 20 mm. The first 3 results were excluded due to significant deviation, and the average force was calculated to be 118.6 N, with a coefficient of variation of 0.6%. The calculations based on formula (11), resulted in a shear modulus *G* value of 80,550 MPa.

Fig. 5. Kirchhoff's transverse elasticity modulus *G* measurement station

$$G = \frac{32 \cdot F \cdot R_g \cdot L}{\varphi \cdot \pi \cdot d^4} \tag{11}$$

where: F – force measured by the sensor of the testing machine, R_g – radius of the gear wheel of the attachment, L – twisted wire length, φ – wire twist angle obtained by measuring the axial displacement of the testing machine crosshead, d – wire diameter.

The final key material property is the coefficient of friction μ. Two coefficients were distinguished - one larger for the ground surface in contact with the machine supports and a smaller one for the contact between the wires. The friction coefficient between the contacting wires was measured using a constructed bench based on an inclined plane (Fig. 6). There is currently no international standard that specifically addresses the measurement of the coefficient of friction between round steel bars. A straight spring wire was fixed, and the shortest spring was placed on it, with the measurement repeated 6 times for 3 samples of the same spring on two inner sides of the springs, giving 36 results. This way, point contact was achieved between 4 coils and the wire. The flat surface was raised until the spring began to slide. As a result of the data analysis, 6 values significantly deviating from the average were discarded, resulting in 30 values, which were used to calculate the average coefficient of friction. The range of variation of the friction angle spread from 0.153 to 0.186.

Fig. 6. Measurement of the friction coefficient for steel-steel friction pair

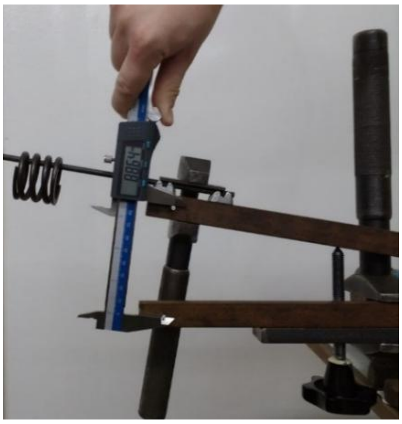

Using geometric relations, the friction coefficient was calculated as the tangent of the friction angle. Average value of measured friction coefficient was equal to approximately 0.18. The result was considered to be determined with sufficient accuracy, also confirmed by literature [34]. This parameter also depends on pressure force [34]. For the ground surfaces, it was assumed that the friction coefficient would be much higher than for smooth surfaces, and in the numerical analyses, it was taken as 0.5. This value is also one of possible for steel to steel pair [34] and steel to aluminium pair [35]. Under actual operating conditions of helical compression springs, the friction forces between the spring's ends and the supports should be greater than the transverse reaction forces. Otherwise, there would be abrasion of the ground wire surface, which would increase the risk of wire fracture and could also result in a loss of support stability. If it is anticipated that the transverse forces may be greater than the frictional forces, then the support of such a spring is strengthened by shaped end protection, e.g. in the form of pins or cylinders centering the spring end coils. Such solutions are used, for example, in vibrating machinery and in railway bogies. Therefore, the adopted value for the friction coefficient, ensuring no slippage between the analysed spring models and their supports, ensured at the same time a correct representation of the actual working conditions of this type of spring.

4.2. Numerical model

The numerical simulations were performed based on the finite element method using Ansys Workbench software, specifically the SpaceClaim, Design Modeler, and Static Structural modules. Each model was created using a script described in the publication [21].

By transforming the formulas presented there, the radius of the arc aligning the pitch between the applied and active coils was calculated in Matlab. By inserting this radius, the spring helix angle γ, spring index C, and wire diameter d into the program's algorithm, a code was generated that could be input into SpaceClaim. In this software, the spring ends were cut to ¾ of the circumference. Then, in the Design Modeler module, the spring was splitted along its axial planes, dividing each coil into four equal parts and creating the contact surfaces needed for the next stage of model construction. Two supports in the form of rings, with a thickness of $0.2d$ and diameters slightly different from the inner and outer diameters of the spring, were also added. An example of a spring modeled in Design Modeler is shown in Figure 7a.

The mesh shown in Figure 7b was divided into several parts due to the geometric irregularities of the model. For the regular part of the spring, the sweep method was applied using quadratic elements, i.e., second-order hexahedron elements, with a size of 1 mm in the radial direction and 2 mm along the length. For the last ground coils, the tetrahedrons patch conforming quadratic method was used, i.e., second order tetrahedral elements, of 1 mm size. For the supports, the sweep method was applied with a single element along the length, of 2.5 mm size, and the face meshing option was used to align elements on the end surfaces. The applied finite element mesh has an average skewness value of 0.237, orthogonal quality of 0.797 and aspect ratio of 2.112 for the tested models. The values defining that the model is satisfactory are skewness less than 0.25 - excellent, orthogonal quality more than 0.7 is very good, aspect ratio close to 1 is excellent [36, 37]. An attempt was made to refine the tetrahedrons patch conforming quadratic mesh with 0.75 mm size using contact sizing 0.4 mm between contacted coils, but for the spring with $C = 5$, $n_a = 2.5$, and $s = 0.5$, the axial stiffness value differed by less than 0.04%. For this reason, further refinement of the mesh was abandoned, as it was concluded that the first mesh provides sufficiently accurate results for this study.

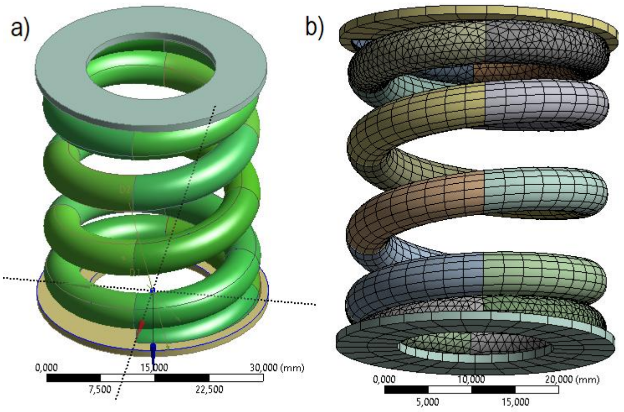

Fig. 7. Spring with parameters $C = 5$, $d = 5$ mm, $n_a = 2.5$, $s = 0.25$ with supports a) modeled in the Design Modeler module of Ansys Workbench software, b) mesh used to stiffness calculation modeled in Static Structural module

It was necessary to standardize at least some of the contact parameters to ensure that the results did not rely on program-controlled parameters. The following contact properties were defined:

- frictional, coefficient: 0.18 between coils and 0.5 between planed coils and supports,
- behavior: symmetric,
- trim contact: program controlled,
- formulation: Augmented Lagrange,
- small sliding: on,
- detection method: on Gauss point,
- penetration tolerance value: 0.01 mm,
- elastic slip tolerance: program controlled,
- normal stiffness factor: 1,
- update stiffness: program controlled,
- stabilization damping factor: 0,
- pinball region radius: 0.2 mm,
- interface treatment: adjust to touch between contacted parts and add offset ramped effect between uncontacted coils.

The spring was loaded with axial displacement through the upper support in the same proportion as in the actual testing. Additionally, all its degrees of freedom were constrained, except for the axial displacement. The lower support was fixed and served as the surface for measuring the reaction force. These settings were maintained for all numerical simulations. Numerical solid models of springs were developed based on measured dimensions of real samples. Springs with spring indices $C = 5$ and $C = 7$, active coils of 2.5 and 3, and all lengths of contacting coils were used. Material properties were assumed to be in accordance with the measurements taken. Table 2 presents a comparison of the stiffness of the idealized model springs, with geometries closest to the theoretical ideal, and the stiffness calculated using the finite element model. The relative error, its range, and the mean absolute percentage error (MAPE) were determined. The data range shown in Tab. 2 is defined as the span between the minimum and the maximum values of the differences between experimental and numerical results across all data points for specified number of active coils. It is a significant parameter, because it shows how much the numerical model deviates from experimental results across the dataset.

Tab. 2. Comparison of experimental data with numerical results.¥

Spring index C	Active coils n_a	Contact length per ending s	Experimental stiffness k [N/mm]	FEM stiffness k_{FEM} [N/mm]	Error [%]	Data range [%]	MAPE [%]
5	2.5	0	140.8	143.6	-2.0	8.7	3.6
		0.25	155.9	148.5	6.7		
		0.5	142.2	139.0	2.2		
	3	0	128.0	121.4	5.1	2.2	3.7
		0.25	130.0	126.0	3.1		
		0.5	121.2	117.7	2.9		
7	2.5	0	51.4	51.8	-0.8	6.1	2.3
		0.25	51.6	49.9	3.3		
		0.5	49.5	50.9	-2.8		
	3	0	45.2	44.3	1.9	1.6	1.2
		0.25	43.9	43.8	0.4		
		0.5	45.0	44.3	1.4		

According to the comparison (Tab. 2), the average MAPE was around 2.7%, and the range of data did not exceed 9%. These are the values that were considered sufficient with regard to the compatibility of the numerical model with experimental results, qualifying the model as suitable for the target set of numerical simulations. It should be noted that larger discrepancies were observed in springs with 2.5 active coils, with the largest discrepancies occurring in the spring with an index $C = 5$.

In the next phase of the study, standard material data according to the EN 10270-2 standard were applied, i.e., $E = 206$ GPa, $G = 79.5$ GPa [25]. It was decided that the springs would have a wire diameter of $d = 1$ mm and would differ in spring indices $C = 4, 8, 12$; spring angles $\gamma = 5°, 10°, 15°$; numbers of active coils $n_a = 1, 1.25, 1.75, 2.5, 3.5$; and end coil contact lengths $s = 0, 0.25, 0.5, 1$. In total, 180 numerical models of springs were created. In the further part of the study, due to the need for additional data, the simulation test was expanded for springs with $C = 8$, using active coils $n_a = 1.5, 2, 2.25, 2.75, 3, 3.25, 3.75, 4, 4.25, 4.5, 4.75, 5$, maintaining contact $s = 0$ and helix angle $\gamma = 5°, 10°, 15°$ (for $\gamma = 10°$ and $n_a = 1.5, 2, 2.75$, tests were made for all contacts). These studies aimed to supplement the distribution of transverse reaction forces occurring during axial compression. To supplement the data when determining the value of the transverse reaction angle it was also added additional simulations for C = 8, $\gamma = 10°$, $n_a = 1, 1.25, 1.5, 1.75$ and $s = 0.125, 0.375, 0.625, 0.75, 0.875$. The front surfaces of all springs were ground to a value of ¾ circumference as in the experimental tests. Including the extended simulation cases, a total of 245 simulations were performed.

The mesh and contact parameters were appropriately rescaled, in line with the reduction of wire diameter from 5 mm to 1 mm. In the case of determining the penetration contact, the value was set to 0.002 mm. However, in about half of the cases, this value prevented calculations from being performed, so it was gradually increased until the calculations were feasible, but no more than 0.3 mm, with the program-controlled option applied in a few cases.

4.3. Results and discussion of the experiments

4.3.1. Axial stiffness

An example plot of the force-displacement curve for a spring with $C = 4$, $n_a = 1$, $\gamma = 10°$ and $s = 0.5$, obtained from numerical simulation is shown in Figure 8. It can be noticed that, nonlinearity of force-displacement curve is negligible.

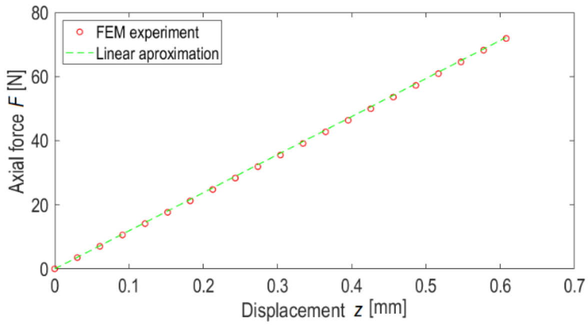

Fig. 8. Force-displacement curve for a spring with C = 4, na = 1, γ = 10° for coil contact length s = 0.5

The results of the axial stiffness tests were too extensive to be presented in full in this publication. Therefore, they were aggregated, and the trends in stiffness changes were analyzed. Data analysis began by examining the correlation of the output variable, i.e., numerical axial stiffness *k*, with the input independent variables *C*, n_a, γ, and *s*, for the primary set of 180 springs. The results of the correlation analyses are presented in Figures 9–12 along with the correlation coefficients.

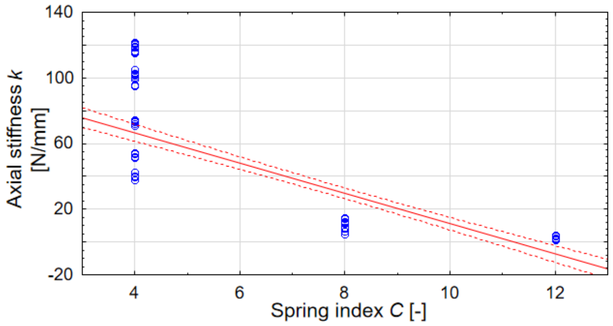

Fig. 9. Correlation plot of axial stiffness *k* versus spring index *C* with coefficient $r = -0.81$

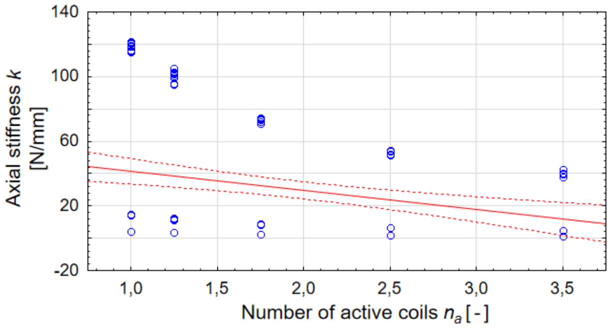

Fig. 10. Correlation plot of axial stiffness *k* versus number of active coils n_a with coefficient $r = -0.29$

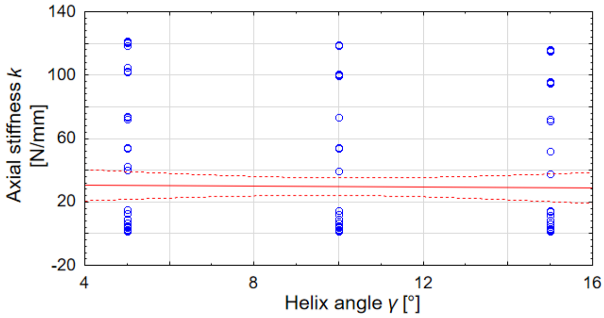

Fig. 11. Correlation plot of axial stiffness *k* versus helix angle γ with coefficient $r = -0.02$

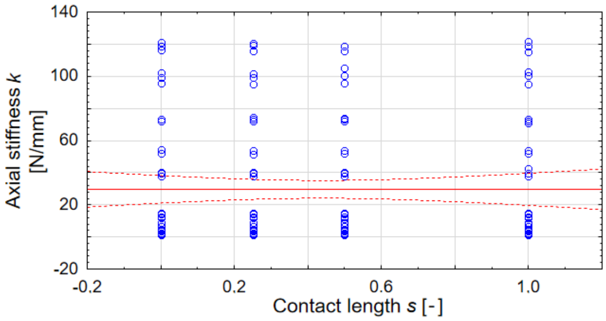

Fig. 12. Correlation plot of axial stiffness *k* versus contact length per one ending *s* with coefficient $r = -0.0002$

The analysis conducted on the given sample revealed that the axial stiffness is primarily influenced by the input variables used in the classical formula from the standard, namely the spring index C and the number of active coils n_a. The spring angle γ, included in many more precise formulas, has a significantly smaller effect, while the spring end coil contact length has practically no influence. However, this conclusion needs to be verified for specific spring geometries. To this end, the coefficient of variation was calculated for each of the contact configurations of the coils within the same number of active coils. The coefficient of variation, expressed as a percentage, represents the ratio of the standard deviation to the mean value of the sample. The results are presented in Table 3, with coefficients color-coded for clarity.

Tab. 3. Coefficient of variation of springs axial stiffness depending on spring angle, number of active coils and spring index

Spring index C	Active coils n_a	Helix angle γ		
		5°	10°	15°
4	1	1.12%	0.25%	0.40%
	1.25	1.38%	0.62%	0.30%
	1.75	1.17%	0.30%	0.59%
	2.5	0.49%	0.51%	0.21%
	3.5	2.82%	0.20%	0.12%
8	1	0.23%	0.33%	0.13%
	1.25	0.81%	0.04%	0.22%
	1.75	0.64%	0.36%	0.31%
	2.5	0.34%	0.28%	0.10%
	3.5	0.14%	0.13%	0.17%
12	1	0.48%	0.42%	0.30%
	1.25	0.29%	0.33%	0.38%
	1.75	0.35%	0.17%	0.92%
	2.5	0.35%	0.20%	0.13%
	3.5	0.13%	0.22%	0.22%

The highest coefficients of variation were obtained for $C = 4$ and $\gamma = 5°$. This aligns with the results from experimental studies for $C = 5$, where variations in stiffness due to changes in the terminal coil contact length were also evident. For $C = 12$ the stiffness variability coefficient did not surpass 1%. For $C = 8$, the coefficient exceeded 0.5% only twice, to values of 0.81% and 0.64%. In general, it is accepted that a feature is statistically significant if the coefficient of variation exceeds 10%. This threshold was not reached. The vast majority of spring sets showed no change in stiffness due to changes in the spring end coil contact length, allowing the conclusion that this factor is insignificant, except for small angles and small spring indices. Therefore, for further calculations, the stiffness value for point contact ($s = 0$) will be used.

Figure 13 illustrates the change in axial stiffness for springs with point contact and a spring index of $C = 8$, depending on the number of coils and the spring angle. This confirms the minimal effect of the spring angle on axial stiffness. Additionally, all variability patterns exhibit the same trend: the greater the number of coils, the lower the stiffness. This reflects the fundamental relationship provided in EN 13906-1:2013(E).

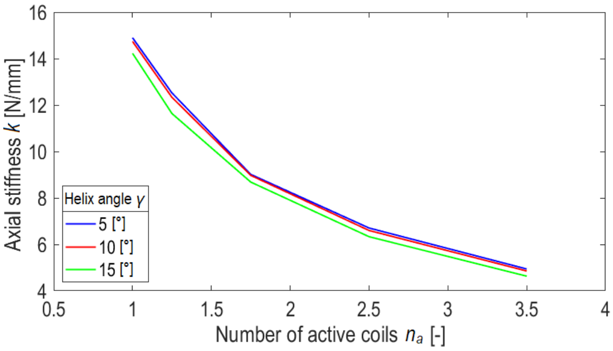

Fig. 13. Axial stiffness for index $C = 8$, point contact ($s = 0$) for spring angles of 5, 10 and 15 degrees

A general overview of the results for point contact of the terminal coils is visualized in Figure 14, created using Matlab. The three axes represent the influence of the spring index C and the number of active coils n_a on axial stiffness k. The most significant changes in stiffness are observed for low spring indices and small numbers of active coils.

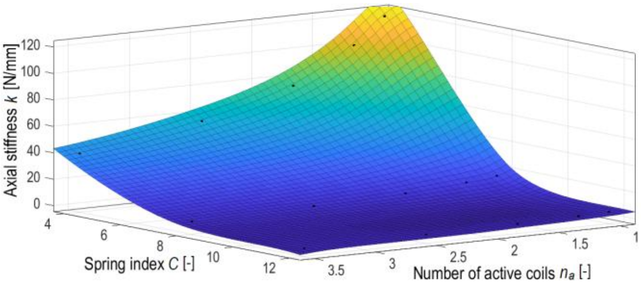

Fig. 14. Axial stiffness distribution depending on the spring index C and the number of active coils n_a for the point contact of end coils

Fitting functions to the data visualized in Figure 14 proved challenging. Consequently, the applicability of formulas described in Section 2 was analyzed, highlighting differences for the batch of springs with $C = 8$, $\gamma = 5°$, and $s = 0$. The plot given in Fig. 15 indicates that the formulas by Paredes and Liu & Kim, which introduce an equivalent number of active coils, most closely align with the simulation results. Similar results are provided by the formulas from EN 13906-1:2013(E), Yıldırım, and Krużelecki, though they deviate from the FEM results. The Vogt correction produced values close to the simulation outcomes for springs with more than 2.5 active coils. The greater the number of active coils, the more accurate all formulas become.

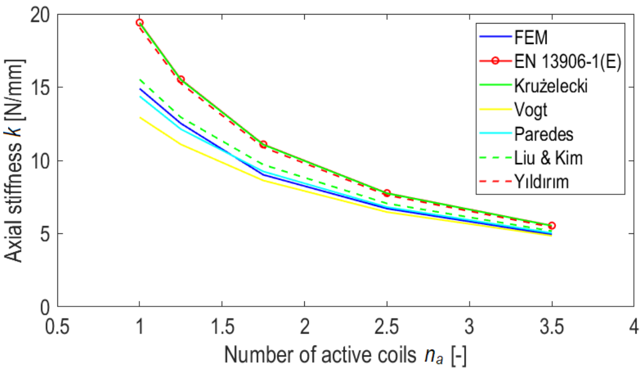

Fig. 15. Axial stiffness k for the index $C = 8$, angle $\gamma = 5°$, point contact ($s = 0$) in comparison with selected analytical methods

A decision was made to derive a new formula based on the most commonly used equation from EN 13906-1:2013(E). To accomplish this, the ratio χ (Equation 12) between the axial stiffness value obtained using FEM (k_{FEM}) and the value calculated using the standard formula (k_N) was computed.

$$\chi = \frac{k_{FEM}}{k_N} \tag{12}$$

Then, the average value of χ was calculated for each number of coils, i.e. for 4 measurements of axial stiffness depending on the contact length. Using the Curve Fitting Tool in Matlab, a power function (13) was fitted to the χ coefficient, which tends to 1. In this way, it was not avoided that the stiffness was significantly higher than the value obtained from the formula in spring norm [25]. This assumption was made because in the vast majority of FEM data, the axial stiffness was lower than the value calculated from the standard formula. The function was made dependent only on the number of active coils. The results of fitting the function (13) to the calculated χ coefficients are given in Table 4.

$$\chi = 1 - (a \cdot n_a^b)^{-1} \tag{13}$$

Tab. 4. The values of coefficient *a* and *b* of equation (13) depending on the spring index *C* and helix angle *γ* together with the given R-square parameter

C	γ [°]	a	b	R²
4	5	4.550	0.6462	0.8685
	10	4.328	0.5942	0.9889
	15	3.946	0.4576	0.9917
8	5	4.409	0.5350	0.9164
	10	4.168	0.4938	0.9726
	15	3.701	0.3970	0.9961
12	5	4.393	0.5183	0.9021
	10	4.055	0.4600	0.9751
	15	3.587	0.3937	0.9910

Fitting with the function Eq. (13) appeared to be sufficiently accurate obtaining the lowest R-square of 0.8685, and an average of about 0.956. All data was regular and therefore was used for determining the description of parameters *a* and *b* with respect to the spring angle *γ*. In Matlab, attempts were made to fit various forms of the function, for example, giving high accuracies (of the order of R-square equals 1) Gaussian or Power options, but it was difficult to produce a generalized form describing all the data with high accuracy. The Rational form also gave good results, but contained three parameters. It was decided to use the linear form Eq. (14) and (15) with two parameters to keep the formula as simple as possible.

The values of the parameters k_1, k_2, m_1, m_2 are given in Table 5, and the finished formulas are described in equations (16) and (17).

$$a = k_1 \cdot \gamma + k_2 \tag{14}$$

$$b = m_1 \cdot \gamma + m_2 \tag{15}$$

The average values of *a* and *b* were then approximated by equations (16) and (17) which parameters were the average value of k_1 k_2, m_1, m_2 in terms of spring index (Tab. 5), determining the R-square of the model. The results of the approximation are recorded in Table 6.

$$a = -0.071 \cdot \gamma + 4.833 \tag{16}$$

$$b = -0.015 \cdot \gamma + 0.650 \tag{17}$$

Tab. 5. The values of coefficient k_1 k_2, m_1, m_2 of equations (14) and (15) depending on the spring index with the given R-square parameter

C	k_1	k_2	R²	m_1	m_2	R²
4	-0.060	4.879	0.9771	-0.019	0.755	0.9371
8	-0.071	4.801	0.9672	-0.014	0.613	0.9487
12	-0.081	4.818	0.9914	-0.012	0.582	0.9986
Av.	-0.071	4.833	0.9786	-0.015	0.650	0.9615

Tab. 6. Comparison of parameters *a* and *b* calculated using equations (16) and (17) with the target values

C	γ [°]	a	a (16)	b	b (17)
4	5	4.550	4.478	0.6462	0.575
	10	4.328	4.123	0.5942	0.5
	15	3.946	3.768	0.4576	0.425
8	5	4.409	4.478	0.5350	0.575
	10	4.168	4.123	0.4938	0.5
	15	3.701	3.768	0.3970	0.425
12	5	4.393	4.478	0.5183	0.575
	10	4.055	4.123	0.4600	0.5
	15	3.587	3.768	0.3937	0.425
		R²	0.9786	R²	0.9615

The calculated R² values mean that it is possible to approximate these values with the given formula. Other attempts have not yielded a better value in terms of R². The final form of the formula for the axial stiffness k_χ dependent on the k_N formula (1) derived from [25] has the form Eq. (18).The developed correction factor reflects the effect of the number of active coils n_a and the helix angle *γ* given in degrees.

$$k_\chi = k_N \cdot \left(1 - \frac{1}{(4.83 - 0.071 \cdot \gamma) \cdot n_a^{(0.65 - 0.015 \cdot \gamma)}}\right) \tag{18}$$

The formula (18) allows to calculate with high accuracy (above 90%) the axial stiffness of steel springs with an index from 4 to 20, number of active coils from 1 to 5 and helix angle from 5° to 20°. This was checked on a random selection of 6 springs with the mentioned sizes of these parameters obtaining MAPE equal to 2%. Table 7 compares the determined formula (18) with those described in Chapter 2. The mean absolute percentage error (MAPE) was calculated for a sample of 180 springs, which served as a measure for the comparison of results.

It is showed that the most accurate method is the one with a correction calculated in a power-law manner (18), achieving a MAPE of 1.38%. The least accurate was the formula commonly used described by Eq. (1). Among the known methods, the Paredes method (2) is the most accurate, with a MAPE of 3.62%.

Tab. 7. Comparison of the accuracy of selected methods for calculating the axial stiffness of compression springs

Axial stiffness formula	Mean absolute percentage error (MAPE)
EN 13906-1:2013(E) norm (1)	23.40%
Vogt (1934) (2)	5.91%
Paredes (2016) (2)	3.62%
Krużelecki and Życzkowski (1990) (3)	22.17%
Yıldırım (2016) (4)	18.95%
Liu and Kim (2009) (5)	13.93%
k_X (18)	1.38%

Table 8 shows a comparison of the two most accurate methods and method (1) [25] with the actual axial stiffness values obtained from the experiment performed, described in Chapter 3.

Tab. 8. Comparison of axial stiffness values calculated using the most accurate methods and the commonly used Eq. (1) with bench test results

Spring index C	Active coils n_a	Contacting coils per ending s	Experimental mean stiffness [N/mm]	k_N (1)	k_X (18)	k_P (2)
				Error to experimental value [%]		
5	2.5	0	139.9	-15	1	-1
		0.25	156.3	-3	12	10
		0.5	142.0	-13	3	1
	2.75	0	138.4	-6	8	6
		0.25	140.5	-4	10	7
		0.5	130.8	-12	3	1
	3	0	129.4	-4	10	7
		0.25	130.0	-3	10	8
		0.5	122.7	-9	5	2
MAPE [%]				**8**	**7**	**5**
Gap [%]				**12**	**10**	**11**
7	2.5	0	51.2	-15	1	-1
		0.25	51.3	-14	1	0
		0.5	49.2	-19	-4	-5
	2.75	0	48.1	-11	3	2
		0.25	47.3	-13	1	0
		0.5	47.1	-13	1	-1
	3	0	45.5	-8	5	4
		0.25	44.1	-11	2	1
		0.5	45.0	-9	4	3
MAPE [%]				**13**	**2**	**2**
Gap [%]				**12**	**9**	**8**

Table 8 indicates that the compared formulas are more accurate for larger spring index. Formula (18) achieved a MAPE for $C = 5$ of 7%, and 2% for $C = 7$. The smallest mean absolute percentage error (MAPE) was shown by the Paredes formula (2) – 5% and 2%, respectively. For $C = 5$ and contact $s = 0.25$, the better accuracy of formula (1) is noted. Due to the fact that the new formulas proposed in the article are subject to numerical simulation error, their accuracy is comparable to commonly used methods. This means that they can be used alternatively. In addition, the real springs were not made with high precision. The methodology used to determine the correction to formula (1) can be successfully applied to determine more accurate formulas on the basis of extensive stand tests. This task is feasible, but the cost of implementation may exceed the expected result. These errors are based on various material and geometric deviations. Therefore, extensive bench testing could only statistically determine an accurate method.

4.3.2. Transverse reaction value Influence of geometrical parameters on spring response in the transverse direction

The numerical compression simulations conducted on the initial set of 180 spring models allowed conclusions to be drawn regarding the influence of individual geometric parameters on the transverse reaction force exerted by the spring on the support. Based on these analyses, the value of the relative transverse reaction R_{rel} was determined. This quantity was defined as the ratio of the transverse reaction force of the spring to its axial reaction force during axial compression, under conditions where the displacements of the supports in transverse directions were constrained:

$$R_{rel} = \frac{\sqrt{R_x^2+R_y^2}}{|R_z|} \tag{19}$$

where R_x and R_y are the numerically determined components of the transverse reaction. The angle formed by the resultant vector of the transverse reaction with the X-axis, which marks the start of the spring wire, was also determined. The results of 180 simulations investigating the influence of geometric parameters on the relative transverse reaction value are illustrated by the surface plots shown in Fig. 16.

The surface plots shown in Fig. 16 reveal a significant variation in relative transverse reactions R_{rel}, ranging from values close to zero to those exceeding 0.3. These plots also demonstrate the low degree of correlation between R_{rel} and the contact length s. This is consistent with the correlation analysis performed earlier, performed analogously to point 4.3.1 for axial stiffness. This analysis showed that: the correlation coefficient r of the transverse reaction value generated during axial compression with the spring index C equals -0.52, with the number of active coils n_a equals -0.03, with the helix angle γ 0.56 and with the contact length s -0.02. Therefore, the reaction value depends most on the spring index and helix angle. Additionally, the plots indicate that the maximum R_{rel} values occurred at an active coil count of $n_a = 1.75$, regardless of the spring index C. To determine the relationship between R_{rel} and the number of active coils n_a, further 45 analyses were conducted by extending the range of active coil counts to: 1, 1.25, 1.5, 1.75, 2, 2.25, 2.5, 2.75, 3, 3.25, 3.5, 3.75, 4, 4.25, 4.5 and 5. Based on observations indicating a minor influence of the contact length s and the spring index C on the variation of R_{rel}, subsequent analyses were limited to springs with $s = 0$ and $C = 8$. The total number of numerical analyses carried out was therefore 225. Fig. 17 presents the results of the relationship between relative transverse reaction R_{rel} and the number of active coils n_a for helix angle values γ: 5°, 10° and 15°.

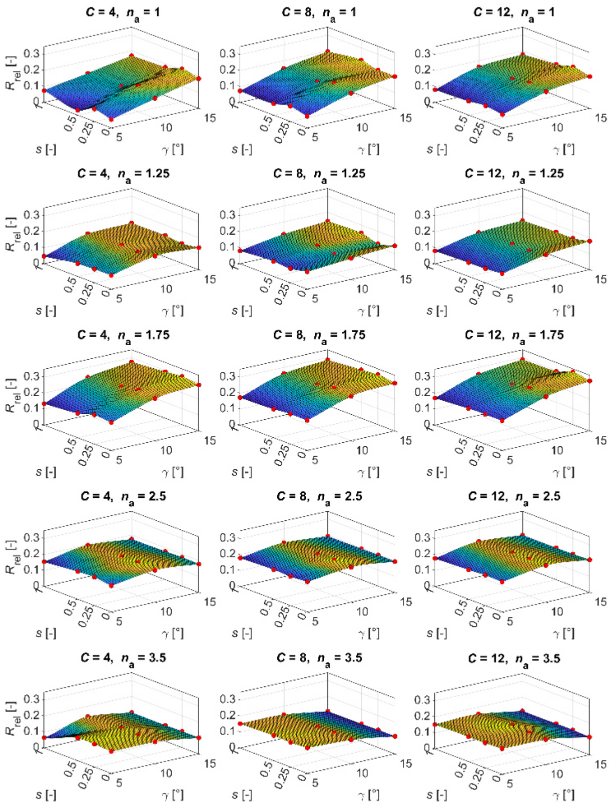

Fig. 16. Plots of the R_{rel} dependency on the contact length and the helix pitch angle for springs with a given spring index C and number of active coils n_a

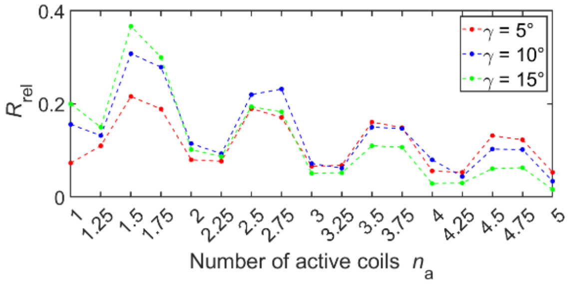

Fig. 17. Plots of the R_{rel} dependency on the number of active coils n_a for helix pitch angles γ: 5°, 10°, 15°, for springs with $C = 8$ oraz $s = 0$

The presented plots clearly show that the highest R_{rel} values occur for springs with partial coil numbers of 0.5 and 0.75, whereas the lowest relative transverse reaction values are observed for springs with fractional coil numbers of 0 and 0.25. This observation provides an important insight for the spring designers, as it enables the deliberate selection of the active number of coils, which should be chosen not only based on the required axial stiffness but also considering the desired transverse reaction value.

The presented results were utilized to develop a generalized approximation model capable of estimating R_{rel} values depending on the number of active coils for springs with any spring index C and helix angle γ.

Given the pattern of R_{rel} variations shown in Fig. 17, resembling a damped sinusoid, functions composed of the product of a decaying nonlinear function representing the mean value trend and combinations of trigonometric functions were tested. Among all the tested functions, the best fit was achieved with the function of the form:

$$R_{rel} = c_1 e^{c_2 n_a} \cdot (c_3 - c_4 \cos(2\pi n_a) - \sin(2\pi n_a)) \qquad (20)$$

Fig. 18 shows the preliminary approximation functions (continuous lines) along with the input data (dots), while Table 9 provides the values of the obtained coefficients c_i and the corresponding coefficients of determination.

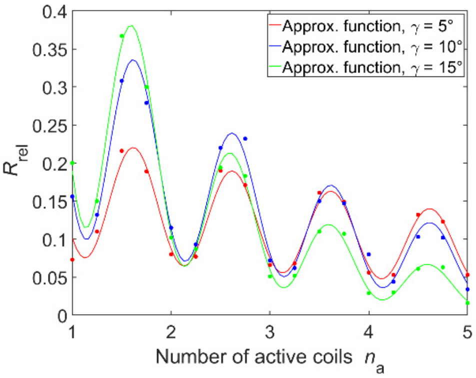

Fig. 18. Preliminary approximation plots of R_{rel} as a function of the number of active coils n_a for helix pitch angles of 5° 10° and 15°, for springs with $C = 8$ and $s = 0$

Tab. 9. The values of the function coefficients Eq. (20), along with the coefficients of determination

γ [°]	c_1	c_2	c_3	c_4	R-square
5	0.0685	-0.1508	2.7048	1.2563	0.9862
10	0.1660	-0.3381	2.1928	0.8522	0.9853
15	0.2731	-0.5805	2.1819	0.9409	0.9948

To achieve a simple and easily applicable relationship, the values of coefficients c_3 and c_4 have been fixed. Each value was set to the average of all values for the different angles γ: c_3 = 2.3598 and c_4 = 1.0165. Based on this assumption, another approximation was performed to determine the corresponding values of coefficients c_1 and c_2. The results are presented in Table 10.

Tab. 10. The approximation results with fixed values of coefficients c_3 and c_4

γ [°]	c_1	c_2	c_3	c_4	R-square
5	0.0787	-0.1529	2.3598	1.0165	0.9760
10	0.1541	-0.3385			0.9796
15	0.2502	-0.5745			0.9934

The final step was to determine the approximation functions for the dependencies $c_1(\gamma)$ and $c_2(\gamma)$ based on the data presented in Table 10. The aim was to find the simplest possible functions that ensure a coefficient of determination not less than 0.99. Ultimately, the approximation of the dependency of coefficient c_1 on the helix pitch angle γ was performed using a linear function, while c_2 was approximated using a power function:

$$c_1(\gamma) = 0.0162\gamma \qquad (21a)$$

$$c_2(\gamma) = -0.0199\gamma^{1.24} \qquad (21b)$$

The coefficients of determination for both approximations were 0.9920 for c_1 and 0.9988 for c_2, respectively. A graphical representation of the correspondence between input data and approximation functions is shown in Fig.19.

By substituting equations (21a) and (21b) into Eq.(20), we obtain, after transformations, the final relationship which allows to determine the value of R_{rel} as a function of the number of active coils n_a and the helix angle γ:

$$R_{rel} = \frac{0.0231\gamma}{e^{0.0199 n_a \gamma^{1.24}}} \cdot (1.66 - \cos(2\pi n_a - 0.777)) \qquad (22)$$

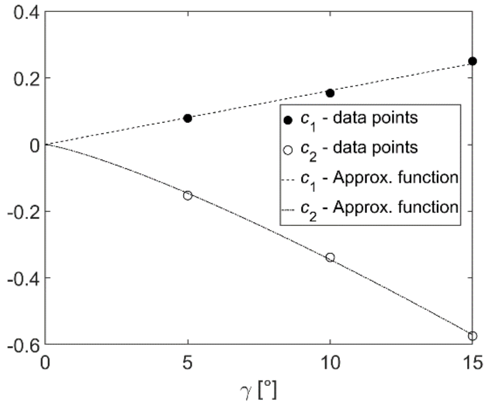

Fig. 19. Approximation plots of coefficients c_1 and c_2 along with the data for springs with $C = 8$ and $s = 0$

The analysis of the compliance of Eq. (22) with the results of FEM analyses was performed for a full set of 225 geometric spring models. This analysis showed that:

- Only in 6 cases out of 225, the absolute value of the difference between the R_{rel} determined from the FEM analyses (denoted hereafter as R_{relF}) and the result of Eq. (22) (denoted hereafter as R_{relA}) exceeded the value of 0.05;
- In 75 cases out of 225, the absolute value of the difference between R_{relF} a R_{relA} was within the range between 0.01 and 0.05;
- In the remaining 144 cases, the value of $|R_{relF} - R_{relA}|$ did not exceed 0.01.

A graphical interpretation of the results obtained is shown in Fig.19, where the vertical axis represents the number of cases with a given difference value $R_{relF} - R_{relA}$, while the horizontal axis shows the values of the obtained differences rounded to two decimal places.

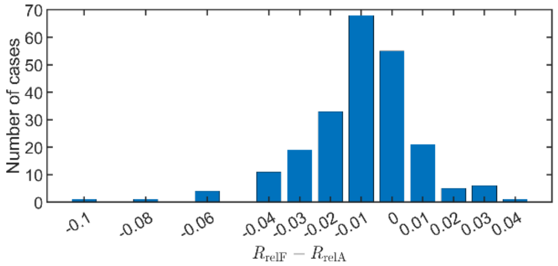

Fig. 20. Distribution of the number of particular cases with specific values of difference $R_{relF} - R_{relA}$

It can be seen in Fig. 20 that the absolute value of $R_{relF} - R_{relA}$ difference exceeded 0.06, only in 2 cases. All of them refer to springs with index $C = 4$ and helix angle $\gamma = 5°$. It should be noted that the average value of relative transverse reaction R_{rel} for the set of 225 tested spring models was equal to 0.16, while the average value of $R_{relF} - R_{relA}$ difference was only 0.0095, thus it is only about 5.9% of the average R_{rel} value. The performed analysis indicates the high accuracy of the proposed Eq. (22) over a wide range of variation in the geometric parameters of springs.

4.3.3. Transverse reaction angle

As shown in section 4.3.2, the value of the transverse reaction generated by the spring during axial compression can reach significant levels. These reactions may be substantial enough that neglecting them during the design of the system in which the spring operates would lead to an oversimplification. One possible solution in such cases is to arrange the springs so that their transverse reactions cancel each other out. For this to be feasible, the designer must have knowledge of the direction of the transverse force to correctly determine the spring assembly. Precise determination of this direction may require simulations or experimental testing. However, the ability to approximate it using a simple relation at an early stage of the design process can be highly beneficial, potentially reducing the number of iterations during the design phase. Based on the analyses conducted, such a relation is presented in this section.

To determine the direction of the transverse reaction, the angle ψ was defined as the angle between the mentioned direction and the X-axis. The reaction angle ψ was calculated relative to the X-axis, as the arcus cosine of the reaction value on the X-axis to the resultant reaction value R_{rel}. Additionally, the sign of the transverse reaction was included to account for its orientation. For instance, angles of 135° and −45° represent the same direction but opposite orientations. The direction of the resultant reaction was determined based on the plus or minus signs of the reactions on the X and Y-axes. This is illustrated in Fig. 21. The analysis was based on all 225 conducted studies. Similarly to previous analyses, correlations between variables were first examined. The correlation coefficient r of angle with the spring index was −0.005, with the number of active coils −0.179, with the spring angle −0.004, and with end coil contact length −0.063. Thus, it is evident that the direction of the transverse reaction is independent of these parameters.

The results are presented in Table 11. The values provided in the table are accurate to within +/-3°. For the parameters $C = 4$ and $\gamma = 5°$, which occur simultaneously, deviations from the general trend were observed. These cases were excluded, as previously noted, as challenging spring geometries whose behavior is best evaluated experimentally or numerically.

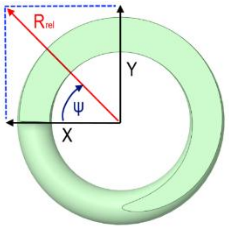

Fig. 21. The coordinate system used to determine the transverse reaction angle R_{rel}. Top view of the spring

Analyzing Table 11, it was found that the different configurations of the partial number of coils and contact lengths yielded the same values of angle ψ, regardless of the number of coils, helix angle and spring index. In order to describe the course of changes in more detail, 20 additional analyses were carried out for spring models with C = 8, γ = 10°, n_a = 1, 1.25, 1.5, 1.75 and contact lengths s = 0.125, 0.375, 0.625, 0.75, 0.875. All the values of angle ψ obtained from the FEM analyses are shown in Fig. 22, along with linear approximation functions. Based on these data, equation (23) was derived, describing the course of change of angle ψ as a function of contact length s and the partial number of active coils n_p.

Tab. 11. Results of the transverse reaction angle ψ test due to axial compression – basic 225 results

Active coils n_a	**Contact length s**	**Angle of reaction ψ [°]**	**Active coils n_a**	**Contact length s**	**Angle of reaction ψ [°]**
1	0	90	**2.25**	0	315
1	0.25	180	**2.5**	0	0
1	0.5	270	**2.5**	0.25	90
1	1	90	**2.5**	0.5	180
1.25	0	315	**2.5**	1	0
1.25	0.25	45	**2.75**	0	45
1.25	0.5	135	**3**	0	90
1.25	1	315	**3.25**	0	315
1.5	0	0	**3.5**	0	0
1.5	0.25	90	**3.5**	0.25	90
1.5	0.5	180	**3.5**	0.5	180
1.5	1	0	**3.5**	1	0
1.75	0	45	**3.75**	0	45
1.75	0.25	135	**4**	0	90
1.75	0.5	225	**4.25**	0	315
1.75	1	45	**4.5**	0	0
2	0	90	**4.75**	0	45

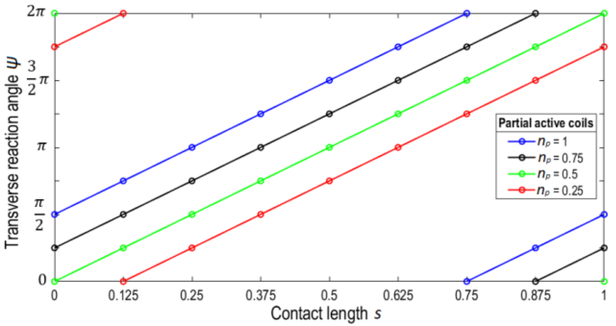

Fig. 22. Graph of functions describing the dependence of the transverse reaction angle ψ on the contact length s and the partial number of active coils n_p

$$\psi = \pi \cdot (2 \cdot s + n_p - 0.5) \tag{23}$$

where: n_p – partial number of active coils. When the number of active coils is an integer, assume that n_p = 1.

The relationship (23) is valid only for the values of the partial number of active coils listed in Fig. 22, since, as additional tests not included here have shown that in other cases this relationship may not give satisfactory results.

5. CONCLUSIONS

This article presents an in depth analysis of the changes in axial stiffness, the transverse reaction from axial compression and the angle of this reaction. Also presented is a comprehensive modeling process of spring work in the Static Structural module of Ansys Workbench software, supported by bench tests. The prepared numerical model achieved an accuracy of about 2.7% (MAPE), which allows us to unequivocally confirm the sufficient effectiveness of the use of the finite element method for modeling the basic characteristics of the spring's work.

As a result of numerical experiments of the axial stiffness, it was found that the size of the contact of the end coils does not significantly affect the axial stiffness variance except for the index C = 4 and the spring angle γ = 5° at the same time. A formula (18) was drawn up to calculate the axial stiffness with satisfactory accuracy with a mean absolute percentage error (MAPE) of less than 2% for numerical simulations and from 2 to 7% for real tests. The proposed equation (18) can be used to calculate the axial stiffness of typical coil springs encountered in industry, with an index between 4 and 20 and a helix angle between 5° and 20°, as it gives the most accurate results in this regard among all verified computational models available in the existing literature with respect to the numerical analyses performed. This is especially true for short springs with a small number of active coils. The consistency of formula (18) with the results of numerical analyses was verified only for springs with the number of active coils from 1 to 5. However, as the number of active coils increases, the value of the correction factor in parentheses in Eq. (18) approaches unity. It follows that relation (18) can be used for springs with any number of active coils, not less than 1. It was also pointed out that the Paredes method proposed in 2016 achieves very good agreement at a similar MAPE level of 2 to 5%. The construction of an accurate formula can only be based on bench tests on a large sample of springs.

Numerical studies have made it possible to address an issue not addressed in the previous literature, which is the occurrence of transverse reaction, generated during axial compression of the spring. The numerical studies carried out in this paper allowed to formulate new relations in this regard. The relation (22) proposed in Section 4.3.2 is easy to apply and allows to estimate the value of the transverse reaction force arising in axial compression of the spring. Numerical studies have shown that this force can exceed up to 30% of the value of the axial force. In engineering practice, it is important to know not only the values of transverse reaction forces when springs are axially loaded, but also the directions of their action. This allows for an informed selection of the orientation of springs in machine support systems, in order to achieve adequate stability of a given system. In this paper, an analysis of the dependence of the direction of the transverse reaction on the shape of the end coils and on the number of active coils was carried out. This analysis made it possible to propose a new relation (23) to determine this angle. The values of the angle turned out to be reproducible for all springs depending on the partial number of active coils and the number of contacting coils with an accuracy of +/-3°. This rule was not observed for small spring index C < 5 and simultaneously occurring spring angle γ < 10°, which is due to the large curvatures and the close position of the coils relative to each other. The map produced and the formula describing it are simple enough to give results with the same accuracy as the input data (+/-3°). These results are an important input for simplifying the design of compression springs and their installation, since they cover the most commonly used geometries, i.e. with faces ground to ¾ of the circumference, commonly occurring spring angles and spring indexes.

REFERENCES

1. Wahl AM. Mechanical Springs. Penton Publishing Company; 1944. Available from: http://hdl.handle.net/2027/uc1.$b76475
2. Goodarzi A, Khajepour A. Vehicle Suspension System Technology and Design. Morgan & Claypool Publisher; 2017. Available from: https://link.springer.com/book/10.1007/978-3-031-01494-9
3. Okamoto I. Railway Technology Today 5. Japan Railway and Transport. 1998;18. Available from: https://www.ejrcf.or.jp/jrtr/jrtr18/pdf/f52_technology.pdf
4. Lee CM, Goverdovskiy VN. A multi-stage high-speed railroad vibration isolation system with 'negative' stiffness. Journal of Sound and Vibration. 2012;331(4): 914–921. Available from: https://doi.org/10.1016/j.jsv.2011.09.014
5. Cieplok G, Wójcik K. Conditions for self-synchronization of inertial vibrators of vibratory conveyors in general motion. Journal of Theoretical and Applied Mechanics. 2020;58(2): 513–524. Available from: https://doi.org/10.15632/jtam-pl/119023.
6. Yu ZW, Xu XL. Failure Analysis on Diesel-Engine Valve Springs. J. Fail. Anal. and Preven. 2009;9: 329–334. Available from: https://doi.org/10.1007/s11668-009-9247-9
7. Vazquez-Gonzalez B., Silva-Navarro G. Evaluation of the Autoparametric Pendulum Vibration Absorber for a Duffing System. Shock and Vibration. 2008;15(3–4): 355–368. Available from: https://doi.org/10.1155/2008/827129
8. Cimolai G, Dayyani I, Qin Q. Multi-objective shape optimization of large strain 3D helical structures for mechanical metamaterials. Materials & Design. 2022;215. Available from:https://doi.org/10.1016/j.matdes.2022.110444
9. Bobade RS, Yadav SK. Lateral Forces in the Helical Compression Spring. International Journal for Research in Applied Science & Engineering Technology. 2017;5(12): 2589-2593. Available from: https://www.researchgate.net/publication/342782816_Lateral_Forces_in_the_Helical_Compression_Spring
10. Arslan E, Genel K. Failure analysis of automotive helical spring. Engineering Failure Analysis. 2023;153. Available from: https://doi.org/10.1016/ j.engfailanal.2023.107569
11. Liu L et al. Failure analysis and finite element assessment of a torsional spring. Engineering Failure Analysis. 2023;146. Available from: https://doi.org/ 10.1016/j.engfailanal.2023.107096
12. Yetgin A et al. Failure analysis of a helical compression spring with relatively low spring index. Engineering Failure Analysis. 2024;165. Available from: https://doi.org/10.1016/j.engfailanal.2024.108798
13. Zhou C et al. An Investigation of Abnormal Vibration – Induced Coil Spring Failure in Metro Vehicles. Engineering Failure Analysis. 2020;108. Available from: https://doi.org/10.1016/j.engfailanal.2019.104238
14. Kumbhalkar MA, Bhope DV, Vanalkar AV, Chaoji PP. Failure Analysis of Primary Suspension Spring of Rail Road Vehicle, J Fail. Anal. and Preven. 2018;18: 1447–1460. Available from: https://doi.org/10.1007/s11668-018-0542-1
15. Baran R, Michalczyk K, Warzecha M. Experimental analysis of transverse stiffness distribution of helical compression springs, Acta Mechanica et Automatica. 2023;17(1):95-103. Available from: https://doi.org/10.2478/ama-2023-0011
16. Dragoni E, Strozzi A. Measuring the load eccentricity in helical compression springs. Strain. 1989;25(3):89-94. Available from: https://doi.org/10.1111/j.1475-1305.1989.tb00699.x
17. Polish Committee for Standardization. Railway applications - suspension components - helical suspension springs, steel, EN 13298:2003. PKN; 2003.
18. Branowski B. Sprężyny metalowe. Wydawnictwo Naukowe PWN; 1997.
19. Grajnert J et al. Izolacja drgań w maszynach i pojazdach. Oficyna Wydawnicza Politechniki Wrocławskiej; 1995: 62-67.
20. Libermann K. Optimierung von Schraubendruckfedern. Seminar Kaltgeformte Federn - Vortrag 10. Technische Akademie Esslingen. Ostfildern-Nellingen; 2006. Available from: https://www.db-thueringen.de/servlets/MCRFileNodeServlet/dbt_derivate_00010614/TAE2006_L.pdf
21. Michalczyk K, Warzecha M, Baran R. A new method for generating virtual models of nonlinear helical springs based on a rigorous mathematical model. Applied Computer Science. 2023;19(2): 96–111. Available from: https://doi.org/10.35784/acs-2023-17
22. Meissner M, Schrocht HJ. Metallfedern. Grundlagen, Werkstoffe, Berechnung, Gestaltung und Rechnereinsatz. Springer Berlin Heidelberg; 2007. Available from: https://link.springer.com/book/10.1007/978-3-642-39123-1
23. Dragoni E. Counting the coils in cylindrical helical compression springs: A clarification note. Proceedings of the Institution of Mechanical Engineers, Part L: Journal of Materials: Design and Applications. 2024;239(7):1399-1404. Available from: https://doi.org/10.1177/14644207241290958
24. Liu H, Kim D. Effects of end Coils on the Natural Frequency of Automotive Engine Valve Springs. International Journal of Automotive Technology. 2009;10(4): 413–420. Available from: https://doi.org/10.1007/s12239-009-0047-8
25. Polish Committee for Standardization. Cylindrical helical springs made from round wire and bar - calculation and design - part 1: compression springs. EN 13906-1:2013(E). PKN; 2013.
26. Polish Committee for Standardization. Technical product documentation - springs - part 2: Presentation of data for cylindrical helical compression springs. ISO 2162-2:1993(E). PKN; 1993.
27. Michalczyk K, Sikora W. Analysis of the influence of parameters of elastomeric layer in shock-absorbing holder of helical spring on its dynamic and static properties. [in:] Awrejcewicz J et al. Engineering dynamics and life sciences. DSTA. 2017: 355-364. Available from: https://doi.org/10.34658/9788393531240
28. Yıldırım V. Exact Determination of the Global Tip Deflection of both Close-Coiled and Open-Coiled Cylindrical Helical Compression Springs having Arbitrary Doubly-Symmetric Cross-Sections. Interna-tional Journal of Mechanical Sciences. 2016;115–116: 280–298. Available from: https://doi.org/10.1016/j.ijmecsci.2016.06.022
29. Vogt RF. Number of active coils in helical springs. Transactions of the American Society of Mechanical Engineers. 1934;56(4): 467-476. Available from: https://cybra.lodz.pl/Content/6327/RP_56_4.pdf
30. Paredes M. Enhanced Formulae for Determining Both Free Length and Rate of Cylindrical Compression Springs. Journal of Mechanical Design. 2016;138(2). Available from: https://doi.org/10.1115/1.4032094
31. Huang Z, Xiao F, Zhu R, Rao Ch, Huang M, Zhao Z, Yin H. Formula of Cylindrical Spring Stiffness for Nonlinear Large Deformation and Its FEM Verification. Wiley Advances in Mathematical Physics. 2024. Available from: https://doi.org/10.1155/2024/3763892
32. Krużelecki J, Życzkowski M. On the concept of an equivalent column in the stability problem of compressed helical springs. Ingenieur - Archiv. 1990;60: 367-377. Available from: https://doi.org/10.1007/BF00542566
33. Kato H, Suzuki H. Nonlinear deflection analysis of helical spring in elastic–perfect plastic material: Application to the plastic extension of piano wire spring. Mechanics of Materials. 2021;160. Available from: https://doi.org/10.1016/j.mechmat.2021.103971
34. Pijper RJM, Slot HM. Friction coefficient for steel to steel contact surfaces in air and seawater. Journal of Physics: Conference Series. 2020;1669. Available from: https://doi:10.1088/1742-6596/1669/1/012002
35. Javadi M, Tajdari M. Experimental investigation of the friction coefficient between aluminium and steel. Materials Science-Poland. 2006;24(2/1). Available from: https://www.researchgate.net/publication/252733277_Experimental_investigation_of_the_friction_coefficient_between_aluminium_and_steel
36. Fatchurrohman N, Chia ST. Performance of hybrid nano-micro reinforced mg metal matrix composites brake calliper: simulation approach. IOP Conf. Series: Materials Science and Engineering. 2017;257. Available from: https://doi.org/10.1088/1757-899X/257/1/012060
37. Özgün. Ansys Mesh Metrics Explained. Mechead – engineering, analysis, design; 2023. Available from: https://www.mechead.com/mesh-quality-checking-ansys-workbench/

This work is supported by AGH University of Science and Technology under research program No. 16.16.130.942

Robert Baran: https://orcid.org/0000-0002-0711-230X

Krzysztof Michalczyk: https://orcid.org/0000-0002-1024-5947

Mariusz Warzecha: https://orcid.org/0000-0002-7417-1561

DOI 10.2478/ama-2025-0056

acta mechanica et automatica, vol.19 no.3 (2025)
Special Issue "Techniki Komputerowe w Inżynierii TKI2024"

COMPUTER SIMULATION IN THE DESIGN OF TOOLS AND THE STAMPING PROCESS OF NON-TYPICAL SHAPED DRAWPIECES - A CASE STUDY

Piotr Danielczyk[*], **Ireneusz WRÓBEL**[**]

[*]Faculty of Mechanical Engineering and Computer Science, University of Bielsko-Biala, ul. Willowa 2, 43-309 Bielsko-Biała,
Dział Badań i Rozwoju, Polmotors sp z o.o., Mazańcowice 57, 43-391 Mazańcowice
[**] Faculty of Mechanical Engineering and Computer Science, University of Bielsko-Biala, ul. Willowa 2, 43-309 Bielsko-Biała,
Dział Badań i Rozwoju, Polmotors sp z o.o., Mazańcowice 57, 43-391 Mazańcowice

pdanielczyk@ubb.edu.pl, pdanielczyk@polmotors.com.pl, iwrobel@ubb.edu.pl, iwrobel@polmotors.com.pl

received 08 February 2025, revised 16 July 2025, accepted 07 September 2025

Abstract: The paper presents a hot stamping technology of body components in modern passenger cars. The technology guarantees obtaining lightweight drawpieces with high mechanical parameters, which results in a significant reduction in the weight of passenger car bodies, particularly those with an electric drive. The Finite Element Method was used to simulate hot stamping of a large-size drawpiece with an atypical shape. The results of these simulations and experimental tests of a drawpiece have been presented and discussed. Relevant conclusions have been formulated.

Key words: hot stamping, FEM simulations, manganese-boron steel, Usibor 2000, MBW-K1900

1. INTRODUCTION

It is desirable that body structures of new generation cars, especially electric ones, have the lowest mass possible [1]. In order to achieve a significant mass reduction, load-bearing components of automotive bodies have been produced for several years using hot stamping technology [2,3]. The components are manufactured from well-hardened manganese-boron steels, such as Usibor 2000 and MBW-K1900 [4-6]. Hot stamping is a process which consists of plastic forming and quenching of a blank heated to the austenitisation temperature in a stamping die. This is illustrated in Fig.1.

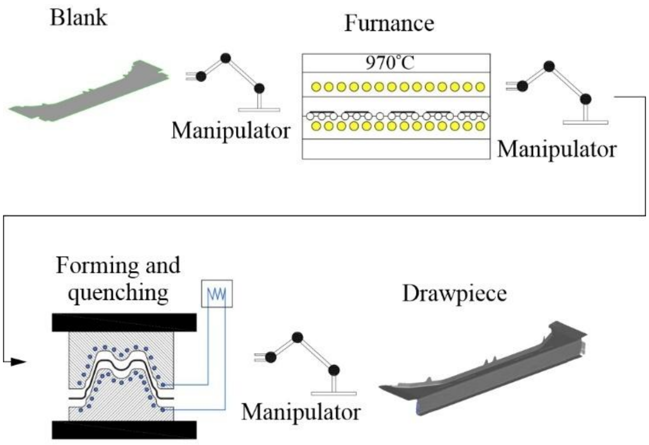

Fig. 1. Hot stamping process

After the hot stamping process, the steel structure is a martensitic and can achieve tensile strength reaching 1900 MPa and Vickers hardness exceeding 400HV. This represents a new quality in the production of high-strength drawpieces. Moreover, the technology enables the production of drawpieces with zones of varying thicknesses, and thus with different mechanical properties in these zones [7,8].

The development of a technological process for the production of drawpieces using the hot stamping technology requires each time an individual approach. Although similar products can be distinguished within the group of drawpieces produced using this technology, such as door reinforcement beams, thresholds, A- and B-pillars, etc., the design of the die for each drawpiece is different. This is due to the required distribution of cooling channels in the die, punches and binders, the expected kinematics of the tool as well as the conditions of the process itself. The specificity of a hot stamping process means that the detail should remain in a fixed position throughout the entire process and be formed in a single cycle of the press slider movement.

This paper presents steps leading to the development of a hot stamping technology for the rear beam connecting the side members of a passenger car (Fig.2). The beam, with dimensions of 1600 mm x 270 mm x 150 mm, classified as a large-size drawpiece is manufactured from a 1.6 mm thick sheet of MBW-K1900 steel, without coatings. The steel is supplied with the following properties:

- yield strength $R_{p0.2}$ = 300÷500 MPa
- yield strength R_m = 450÷650 MPa
- elongation A_{80} = 16%.

After the hot stamping process (forming and quenching), a drawpiece manufactured from this steel exhibits a martensitic structure, which in turn guarantees the strength limit R_m within the range of 1400÷1900 MPa and Vickers hardness of *HV*>400

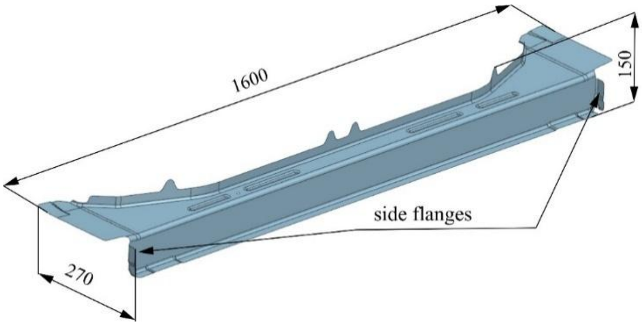

Fig. 2. Passenger car beam

The analysed drawpiece has an non-typical shape in the form of a side flange bent transverse to the main stamping direction (Fig.3). This is an uncommon situation in typical hot-stamped drawpieces, which makes stamping from the main direction difficult. The situation is different in cold stamping processes where stamping from different directions is a common practice. Cam units are then used to change the direction of the tool operation, or the products are rotated on specially designed turntables. In hot stamping processes, such solutions have not yet been used.

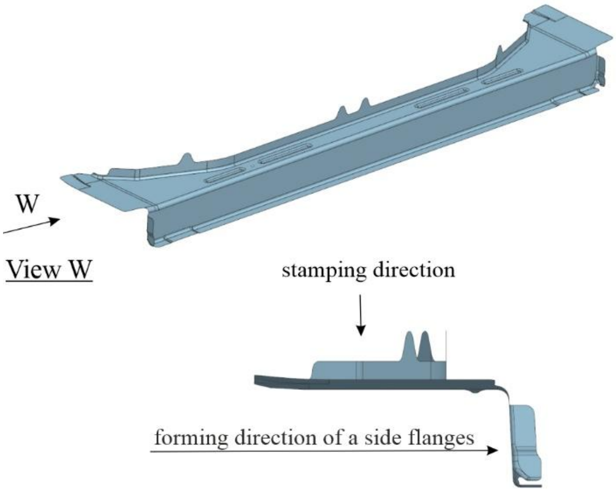

Fig. 3. Stamping directions

The development of assumptions for the design of a stamping die with a complex shape requires a series of computer simulations of the stamping process and tool cooling, in addition to the assessment of the product feasibility [9-11]. Simulations will consider the factors that can affect the stamping process itself and the quality of the final product. In particular, the temperature distribution in the drawpiece and tool will be assessed as well, maximum temperature values, and the proportion of martensite in the drawpiece. A drive system for dies and punches operating from the direction other than the main one will be developed. An actuator will be selected to ensure the appropriate slide speed, stroke and the force required for the formation of side flanges. The simulation of the thermal expansion of dies and punches will facilitate the assessment of the correct selection of tool clearances. This is significant especially when stamping large-size products where drawpiece jamming in the tool is possible. This is caused by thermal shrinkage and hardening stresses that occur during the process [12].

Stamping process of the discussed drawpiece according to the developed technology will be verified in real conditions in the hot stamping process. The quality of the obtained drawpieces will be verified in laboratory tests which will include:

- testing mechanical properties and hardness of a drawpiece by non-destructive and destructive methods,
- hydrogen embrittlement tests,
- evaluation of the microstructure of steel after pressing and quenching,
- testing shape and dimensional accuracy of the finished drawpieces.

2. SIMULATION OF THE STAMPING PROCESS

Simulation of the stamping process was performed using Autoform software. A thermomechanical analysis is carried out throughout the simulation until a steady state is achieved. The effectiveness of the cooling system is determined by monitoring the temperature of the drawpiece and the temperature on the working surfaces of the tools. The temperature of the drawpieces at the end of the process should not exceed 250°C. This, together with a minimum cooling rate of approximately 27°C/s for MBW-K1900 steel [13], guarantees the desired martensitic structure of the drawpiece.

Computer-aided design models of the tools were prepared for the simulation of the process. Based on a three-dimensional model of the drawpiece, working surfaces of the die, binders, and punches were obtained, as illustrated in Fig.4.

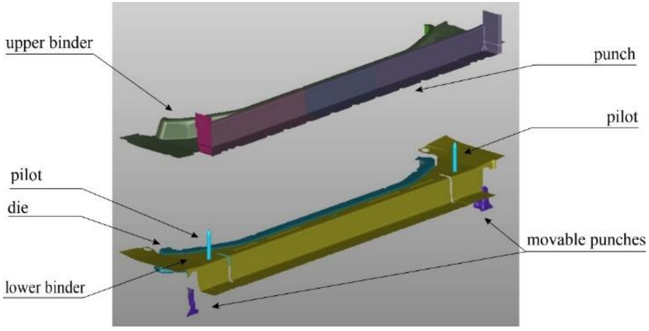

Fig. 4. Tools working surfaces

Prior to the simulation of the stamping process, tool kinematics and basic process parameters, including tool stroke and stamping speed were selected. Firstly, a correctly cut blank is positioned on the upper surface of the die and the lower binder, and the stamping process is initiated (Fig.5a). The application of the upper binder serves to secure the blank while the punches simultaneously initiate the formation of the initial bottom flange (see Fig.5b). Next, the die and lower binder, mounted on gas springs, move downwards, together with the closed upper binder and punches, forming the top flange (Fig.5c). Afterwards, dies designed for this purpose, attached to sliders with actuators, form the side flanges (Fig.5d). After closing the tool, the press pressure is increased (for improvement of heat exchange between the stamping die and the tool) and the quenching process is initiated. At the end of this stage, the press tool is opened and the tools take their initial position.

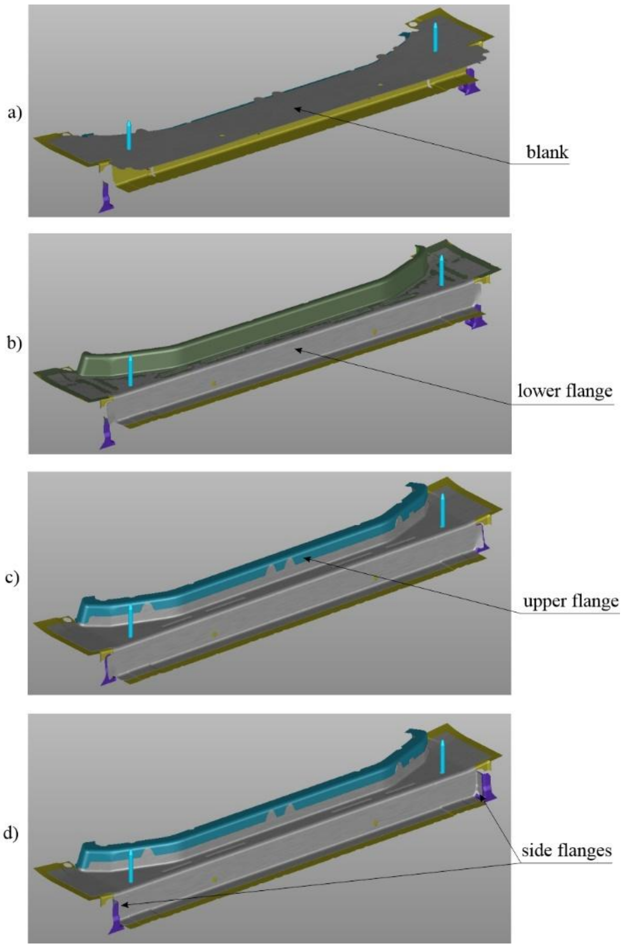

Fig. 5. Stages of drawpieces forming

Once the tool kinematics had been established, the parameters related to the cooling process of the die could be determined. In the actual tool, the cooling channels are drilled into individual sections of the tool. In order to simulate the cooling process, the position of the centre lines of the channels was planned and the appropriate diameters were assigned (Fig.6).

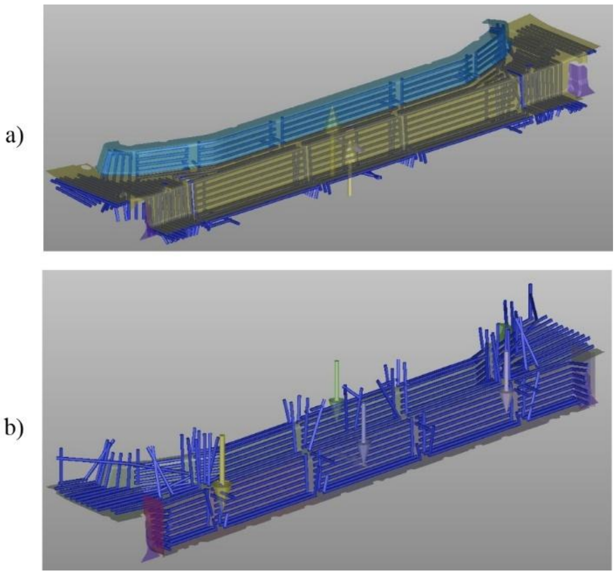

Fig. 7. Distribution of cooling channels a) in the upper part of the tool b) in the lower part of the tool

At this point, it is necessary to note a certain aspect related to the modelling of tool cooling channels in the AutoForm package. The latest version of the software does not yet allow the modelling of cooling channels for tools operating in a direction other than the main stamping direction which is a requirement for the designed process (a punch for bending side flanges). The software only permits the assumption of a constant temperature (an initial value of 80°C was assumed for the analyses) on the surface in question. This also serves to illustrate the innovative nature of the proposed solution with a movable punch. Accordingly, simulations of the cooling process of punches for bending side flanges will be carried out after the preliminary design of the tool in the Simcenter FloEFD thermal-fluid analysis module.

The geometric models of the tools and cooling channels were supplemented with the material properties of the drawpiece. In accordance with the design assumptions and with reference to the experience of tool manufacturers, considering suggestions provided by the sheet metal manufacturer, the following was assumed for the process:

- the initial temperature of the blank 810 °C,
- heat transfer coefficient from the tool to the cooling medium 15 mW/mm^{2}K,
- the temperature of cooling medium 20 °C.

It was assumed that the maximum value of the heat transfer coefficient from the blank to the tools would be 3.5 mW/mm^{2}K. This is the value for a tool pressure of 100 MPa. For lower pressures, the heat transfer coefficient decreases. In such cases, the value corrected by the scaling factor (Fig.7) determined by the supplier of the stamping sheet is adopted for the calculations.

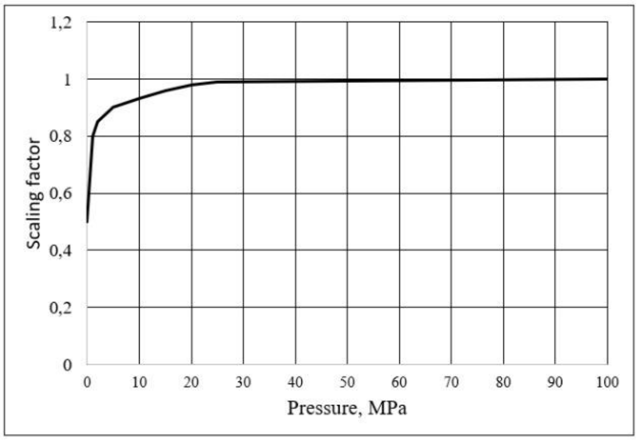

Fig. 7. Scaling factor of the pressure

The simulation of tool heating and cooling is performed in an iterative manner. The convergence criterion of the computational process is the state at which the differences in tool temperature in subsequent iterations are no greater than 2°C. In the case under discussion, four complete cycles were required, with the Quick Numerical Cycling option enabled. This method enables a notable reduction in the number of cycles required to stabilise the temperature of the drawpiece and the tool. Instead of starting the analysis with the ambient temperature for the tools, the tool initial temperature is estimated for the first cycle, enhancing the overall efficiency of the analysis.

DOI 10.2478/ama-2025-0056

The calculations provided a number of results describing the course of the stamping process. Primarily, the FLD (Forming Limit Diagram) was subjected to analysis. The results shown in Fig.8 do not indicate any product feasibility issues. No regions susceptible to cracking were noticed.

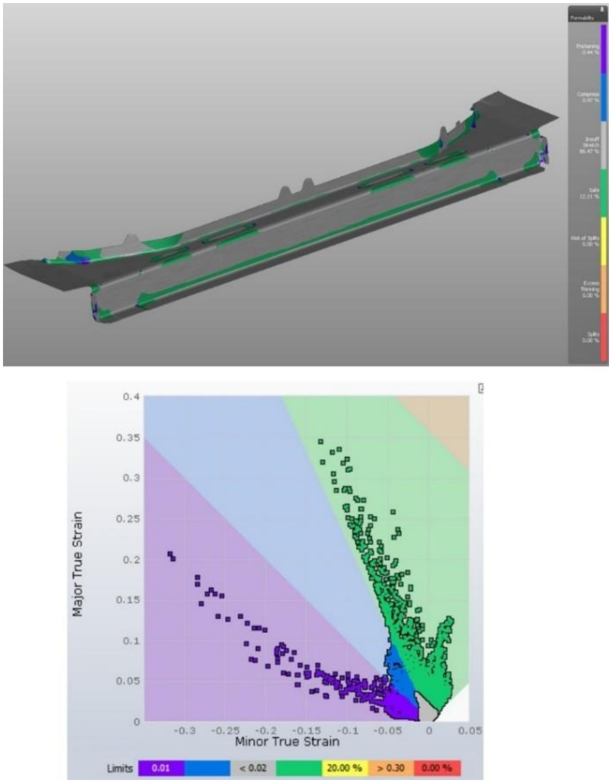

Fig. 8. Distribution of cooling channels a) in the upper part of the tool b) in the lower part of the tool

The next figure (Fig.9) shows the temperature distribution of the drawpiece at the end of the quenching process. It can be seen that the maximum temperature does not exceed 248°C and is lower than the required temperature. It is also worth noting that over almost the entire surface of the finished drawpiece, these temperatures are only slightly higher than 180°C. The two places with significantly higher drawpiece temperatures are where the lifting devices are to be located in the tool. Their function is to lift the drawpiece after the quenching process to a position where it can be picked up by the robot arm. Inside the die tools, during the quenching process, the top surfaces of the lifting devices are positioned approximately 0.5mm below the surface of the die and are therefore not involved in the intense heat exchange between the die and the drawpiece.

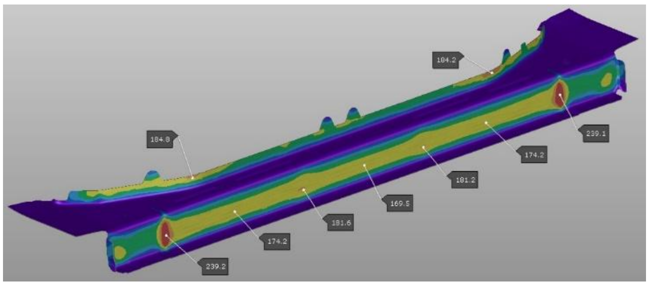

Fig. 9. Temperature distribution in the drawpiece

Fig.10 shows the temperature distribution on the working surfaces of the tools. As can be seen, the highest temperatures only slightly exceed 100°C, which means that the process will be able to run continuously, without the need for additional time to allow the tools to cool down.

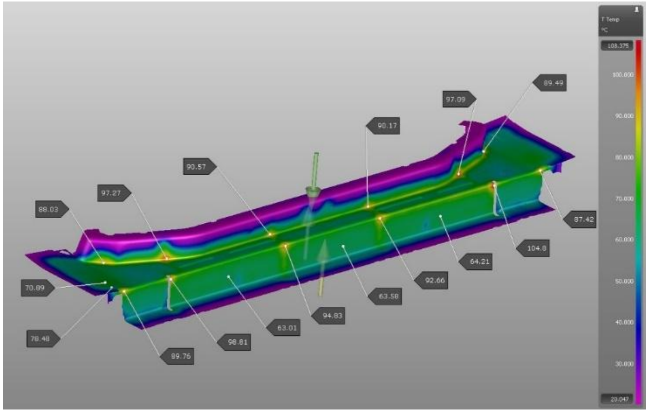

Fig. 10. Temperature distribution in tools

The predicted martensite distribution in the drawpiece (Fig.11) guarantees a product with the required material properties.

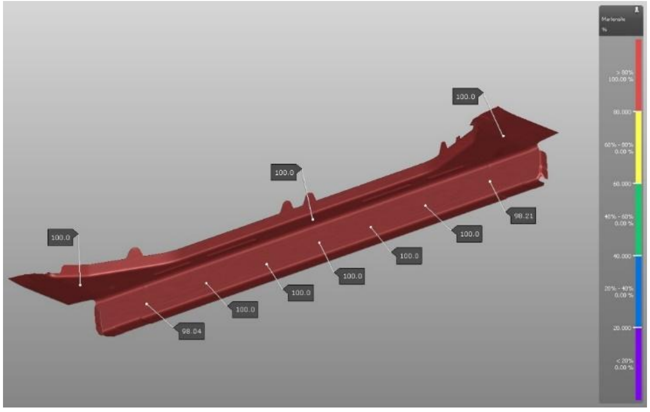

Fig. 11. Share of martensite in the drawpiece

Based on the results of the simulations, a 3D model of the tool was made. It is a two-cavity die, the main components of which are a lower plate (ribbed cast iron) with a die, lower binder and a system of punches working in a direction other than the main stamping direction (Fig.12a), and an upper plate (ribbed cast iron) with an upper binder and forming punches (Fig.12b).

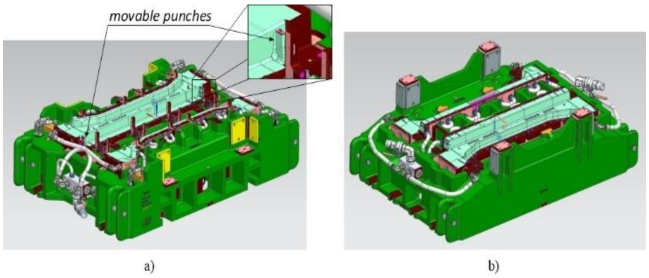

a) b)

Fig. 12. Parts of the tool a) lower part of the tool, b) upper part of the tool

Two punch units are built into the tool, for forming flanges in a direction other than the stamping direction (Fig.13).

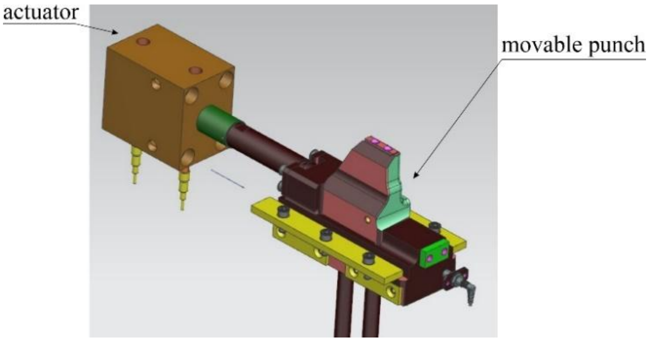

Fig. 13. Movable punch

3. COOLING SIMULATION OF MOVABLE PUNCHES

A special cooling system with drilled channels (Fig.14) was designed for the moving punch system, as for the other parts of the tool, with a separate coolant supply system.

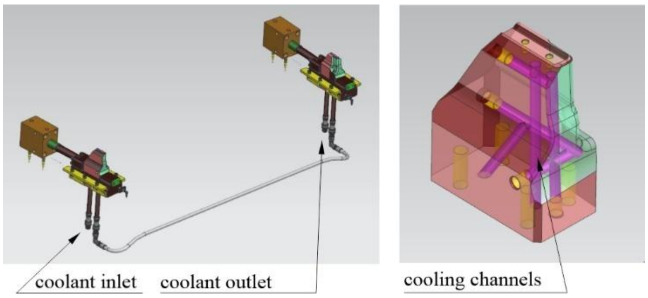

Fig. 14. Cooling water supply system for stamps

As mentioned above, when analysing the stamping process in the AutoForm package, it is not possible to simulate cooling of the tools operating in a direction other than the stamping direction. For this reason, the cooling system for the moving punches was analysed in the FloEFD thermal-fluid calculation system. Fig.15 shows a model of the system with the computational domain of the cooling fluid highlighted.

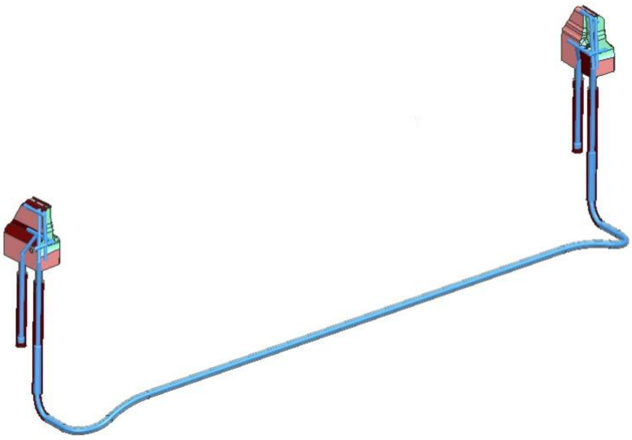

Fig. 15. 3D model of the coolant domain

The geometric model thus prepared was discretised. The dimensions of the mesh in the discrete model were selected in an iterative manner. In successive iterations, the size of the finite elements was reduced and the effect on the results obtained (temperatures and velocities) was examined. If the results did not change significantly (more than 2%) in the next iteration, it was assumed that the finite element dimensions from the previous iteration were optimal. Fig. 16 shows, in an example section, a mesh discretising the volume of the punch and coolant adopted for the calculations. The computational model of the die consisted of 1427330 cells, of which 468882 elements represented the coolant volume.

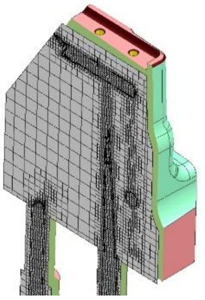

Fig. 16. FEM mesh of the punch model

No simulation of the stamping process is performed during the heat-flow analysis. It is therefore necessary to determine the heat flux density that the drawpiece gives off to the top and bottom of the tool during the forming and quenching processes. Then, the temperature of the drawpiece decreases from the initial temperature of t_2=*810°C* (before the forming process), to the final temperature of t_1=180°C (after the quenching process). Knowing the forming and quenching time *T*=14 s, the mass of the drawpiece *m*=4 kg, and the specific heat of the steel *c*=0.46 kJ/(kg°K), it is possible to calculate the heat flux $\dot{Q}$, transferred to the tool:

$$\dot{Q} = \frac{c\cdot m(t_2-t_1)}{T} \tag{1}$$

For the beam described, the flux is $\dot{Q} = 83\ \mathrm{kW}$. Assuming that the heat is transferred uniformly to the top and bottom of the tool, a heat flux density of $\dot{q} = 130\ \mathrm{kW/m^2}$ was obtained (Fig.17). The cooling system on the inlet side was supplied with the medium at 20°C and the flow rate of 6 l/min (0.0001 m^3/s). Open channels were assumed to be on the outlet side of the medium. Free convection with the ambient temperature of 40°C was taken into account.

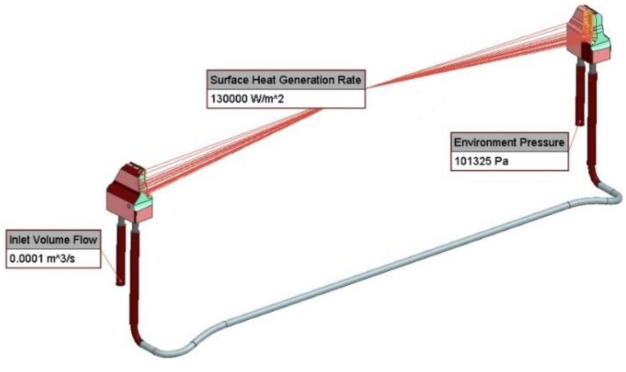

Fig. 17. Analysis boundary conditions

To evaluate the effectiveness of the proposed cooling system, the temperature of the working surfaces of the tools was tested. Fig.18 shows the temperature distribution on the working surface of the moving punches. As can be seen, the temperatures are around 74°C, which is slightly lower than the 80°C initially assumed. It can therefore be concluded that the cooling system for the moving punches was correctly designed.

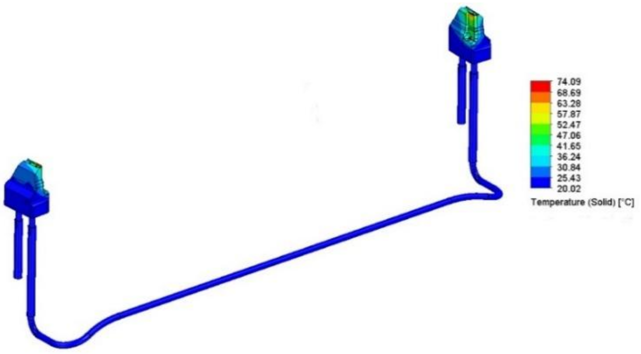

Fig. 18. Temperature distribution in moving punches

4. PROBLEM OF PRODUCT JAMMING. ANALYSIS OF THERMAL SHRINKAGE OF THE DRAWPIECE AND TOOLS

The problem associated with large-size drawpieces jamming in the tool after quenching is relatively common. Shrinkage and quenching stresses can cause problems when removing the drawpiece from the die tools. The value of the force exerted by the drawpiece on the die after cooling to the final process temperature is significant and exceeds 40 kN (Fig.19).

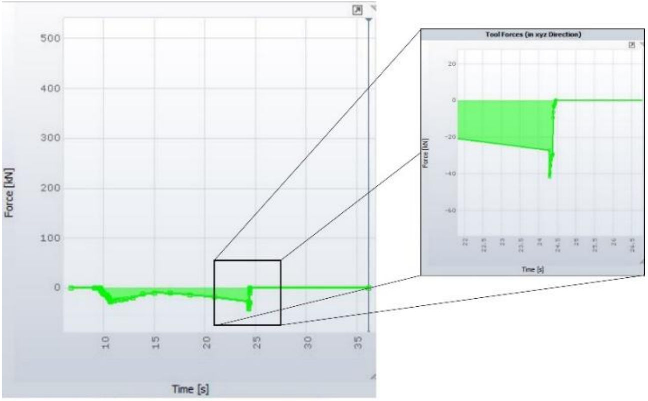

Fig. 19. The force of the drawpiece on the die

In the example described, jamming is eliminated in two ways. Firstly, based on the simulation results (Fig.20), a tool is made with a dimension that compensates for the shrinkage of the drawpieces. It is worth noting that the magnitude of this shrinkage along the beam is approximately 0.8 mm, which is half the thickness of the drawpiece. During the beam production, stamping conditions change and, within the limits agreed with the supplier, the material changes. This can result in the tool being insufficiently adjusted and the die continuing to jam. This phenomenon is going to be eliminated by the use of movable punches (retracted after hardening).

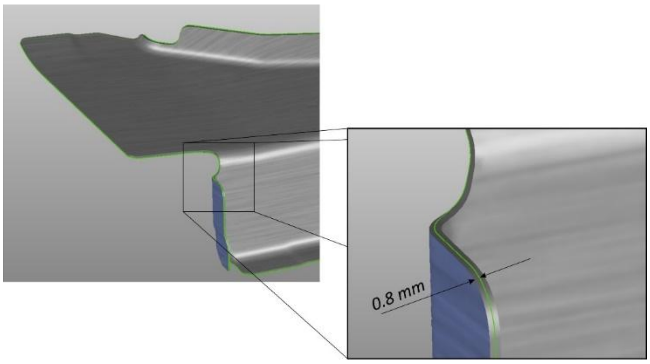

Fig. 20. Drawpiece deformation after hardening (in relation to nominal shape)

Thermal expansion of dies and punches can also be the cause of a drawpiece jamming and problems with correct tool operation. For this reason, a thermo-mechanical analysis was carried out for the lower and upper part of the tool and their deformations were determined. Simplified 3D models of the tools were developed for this analysis. These simplifications consisted in removing from the model all parts whose influence on the load and strength of the die is negligible. For reasons of symmetry, half of the top and half of the bottom of the tool were calculated (Fig.21). The models prepared this way were analysed using the finite element method in the Simcenter package.

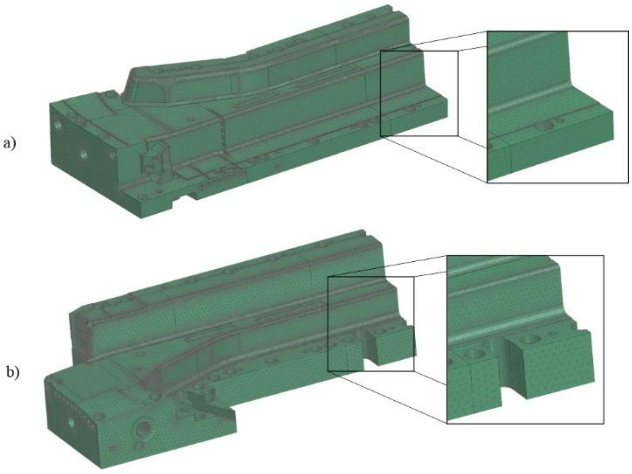

Fig. 21. FEM model for calculating the expansion of a) the lower part of the tools b) the upper part of the tools

The upper part of the die and lower part of the die were loaded with a heat flux $\dot{q} = 130\ \mathrm{kW/m^2}$ determined by analysing the flow through the moving punch system. The temperature in the cooling channels was assumed to be 20°C. The model was supported on the lower and upper surfaces of the dies where the die is in contact with the press bed. In addition, symmetry conditions were assumed in the model (Fig. 22). Material data was added. (base material is GG25 cast iron, working parts are CR7V steel).

The problem was completed in two stages. First, the thermal analysis problem was solved and the temperature distribution in the tool was determined. This was followed by a static analysis under the temperature load obtained from the previous analysis. As a result of the calculations, deformation values were determined for the lower and upper parts of the tool (Fig.23 and 24) due to their thermal expansion. These values do not exceed 0.07 mm for the lower part of the tool and a maximum of 0.024 mm for the upper part of the tool. These deformations are very small and do not affect the stamping process, in particular the jamming and the dimensional accuracy of the drawpieces. It is worth mentioning that the minimum value of the clearance between the moving parts of the stamping tool (dies, punches and binders) is assumed to be 0.4 mm, i.e. many times greater than the deformation values determined.

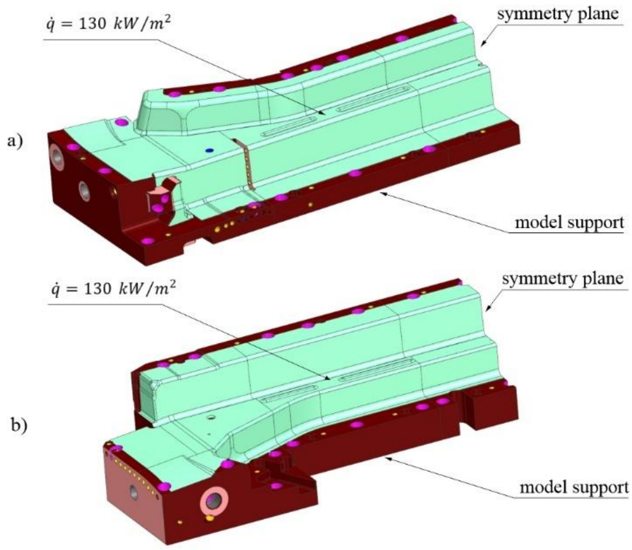

Fig. 22. Boundary conditions for the analysis of (a) the lower part of the tool (b) the upper part of the tool

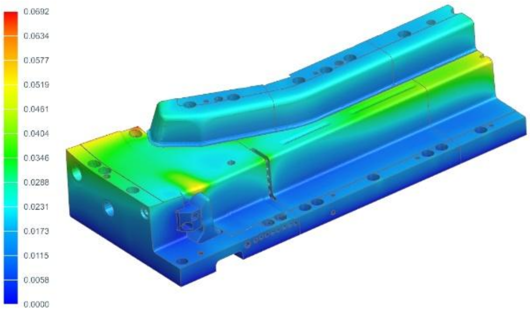

Fig. 23. Deformation in the lower part of the tool

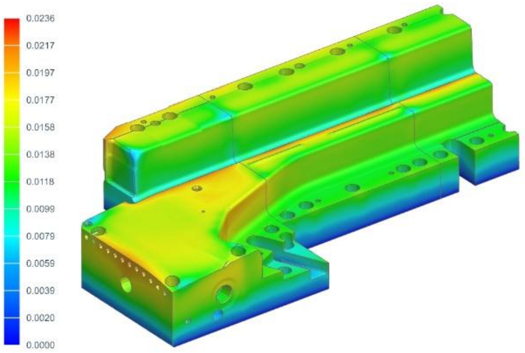

Fig. 24. Deformation in the upper part of the tool

5. TESTING OF MANUFACTURED PARTS

In accordance with the described project, a stamping die was made (Fig.25) and mounted on an experimental stamping line. In order to assess the correct performance of the stamping die, a test batch of 150 drawpieces was prepared (Fig.26). Mechanical parameters were then measured using both non-destructive and destructive testing methods. Non-destructive testing was carried out on 20 randomly selected drawpieces and 5 drawpieces were chosen for destructive testing.

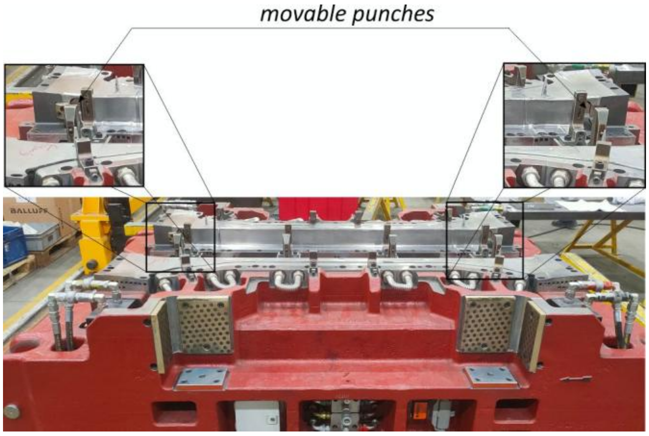

Fig. 25. Stamping die (lower part)

Fig. 26. Photo of a sample of a drawpiece

5.1. Non-destructive testing - measurement of mechanical properties of the drawpiece

The 3MA (*Micromagnetic Multiparameter Microstructure and Stress Analysis*) instrument from the Fraunhofer Institute [14] was used to measure basic mechanical parameters of the drawpiece, such as yield strength Rm and hardness in Vickers degrees. Measurements were taken at 10 control points as shown in Fig. 27.

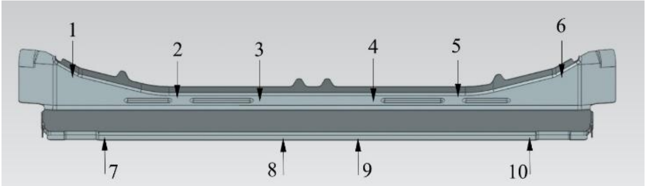

Fig. 27. Position of the measurement points on the drawpiece

Analysing the obtained results (Tab. 1, Tab. 2), it can be concluded that for each of the drawpieces, the required mechanical parameters were achieved at each measurement point. Hardness exceeded the required value of 400 HV and the strength limit was within the expected range of 1400÷1900 MPa.

Tab. 1. Results of strength limit measurements R_m, MPa

		Measurement point number									
		1	**2**	**3**	**4**	**5**	**6**	**7**	**8**	**9**	**10**
Drawpiece number	**W1**	1747	1712	1700	1762	1795	1800	1732	1776	1745	1766
	W2	1712	1703	1757	1784	1779	1746	1708	1743	1723	1785
	W3	1719	1731	1701	1745	1781	1708	1719	1761	1738	1777
	W4	1770	1739	1779	1711	1767	1747	1779	1773	1710	1764
	W5	1757	1771	1720	1709	1711	1701	1739	1780	1732	1799
	W6	1792	1734	1758	1778	1746	1728	1703	1751	1700	1717
	W7	1742	1751	1740	1786	1757	1702	1709	1744	1759	1729
	W8	1789	1774	1799	1717	1771	1709	1700	1799	1743	1729
	W9	1735	1724	1705	1713	1795	1758	1775	1730	1750	1745
	W10	1764	1755	1773	1755	1764	1787	1720	1720	1759	1773
	W11	1715	1770	1731	1720	1790	1758	1715	1771	1742	1755
	W12	1728	1779	1745	1703	1784	1737	1704	1704	1729	1781
	W13	1721	1753	1776	1740	1717	1714	1782	1740	1755	1726
	W14	1742	1732	1718	1704	1761	1734	1730	1769	1797	1743
	W15	1755	1747	1757	1800	1765	1724	1783	1792	1795	1742
	W16	1777	1750	1733	1717	1756	1787	1771	1789	1774	1756
	W17	1726	1790	1760	1769	1717	1741	1707	1785	1709	1771
	W18	1741	1789	1789	1700	1708	1731	1767	1758	1742	1765
	W19	1707	1797	1800	1800	1772	1735	1717	1793	1716	1731
	W20	1775	1727	1711	1795	1700	1758	1738	1742	1787	1764

Tab. 2. Results of *HV* hardness measurements

		Measurement point number									
		1	**2**	**3**	**4**	**5**	**6**	**7**	**8**	**9**	**10**
Drawpiece number	**W1**	591	584	604	616	583	613	598	585	610	590
	W2	586	612	584	614	582	605	598	597	595	612
	W3	619	594	615	614	613	612	594	605	613	582
	W4	592	581	605	609	619	599	615	602	593	584
	W5	599	599	620	599	616	590	587	601	598	580
	W6	590	617	596	609	587	607	613	616	615	583
	W7	607	613	612	609	593	603	599	589	593	607
	W8	600	600	606	592	598	615	582	604	587	601
	W9	598	590	606	593	597	595	618	607	598	580
	W10	601	598	610	595	595	580	589	587	618	583
	W11	583	606	582	593	610	602	605	615	588	601
	W12	614	597	607	598	597	615	604	590	615	616
	W13	617	582	618	583	585	593	596	582	587	601
	W14	594	611	613	607	599	596	596	603	606	580
	W15	592	581	595	615	585	605	618	618	591	607
	W16	603	595	593	604	585	613	600	612	582	610
	W17	610	618	580	611	594	611	595	608	615	600
	W18	605	587	612	589	613	607	608	583	608	597
	W19	594	602	599	603	603	609	612	588	619	609
	W20	615	606	612	596	588	598	590	592	608	614

5.2. Destructive testing

5.2.1. Tensile test

Paddle samples with a gauge length of 50 mm were cut from the flat areas of the test drawpieces using a plasma cutter. These samples were then elongated on WDW-300S testing machine from TEST Lab. During the test, the yield point and ultimate strength were determined. Fig.28 shows a photograph of a selected sample after the test, and Fig.29 shows the results of the measurements.

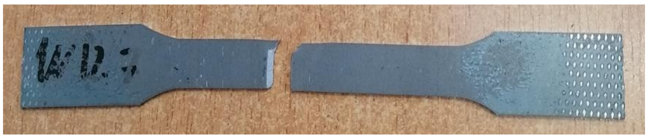

Fig. 28. Photo of a sample

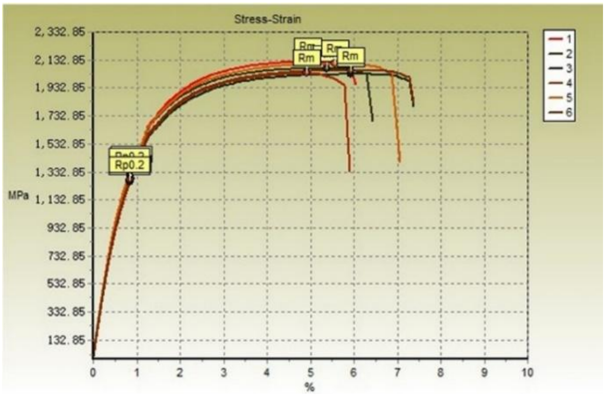

Fig. 29. The results of the tensile tests

The report of these measurements (Tab. 3) confirms the production of drawpieces with the required mechanical parameters.

Tab. 3. Tensile test results

Sample number	Yield strength Rp02, MPa	Tensile strength Rm, MPa
1	1355	1851
2	1316	1873
3	1262	1830
4	1284	1838
5	1336	1804
6	1279	1858

5.2.2. Vickers hardness measurement and microstructure analysis

Vickers hardness tests and microstructure analysis after the hardening process require special preparation. Samples for microstructure analysis were cut from selected areas on the drawpiece using a water-abrasive cutter (Fig.30).

Fig. 30. Locations where samples were taken for testing

Next, the prepared material was positioned with a metallographic pin and then embedded in phenolic resin. In the next step, the samples were ground with diamond discs and polished using diamond suspensions with grain sizes of 9 µm and 3 µm and oxide suspensions with grain sizes of 0.05 µm (Fig.31).

Fig. 31. Locations where samples were taken for testing

Examples of Vickers hardness results are shown in Tab. 4. As can be seen, the obtained values for the tested samples exceed the 400HV value which is considered to be required.

Tab. 4. Results of *HV* hardness measurements

Measurement number	Imprint/value	
1	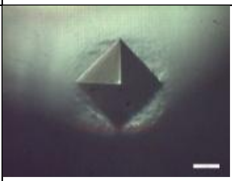	579.1
2	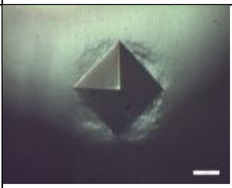	538.7
3	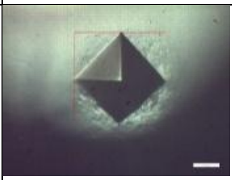	533.4
4	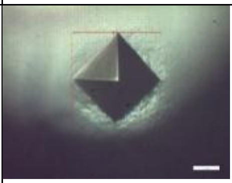	561.9
5	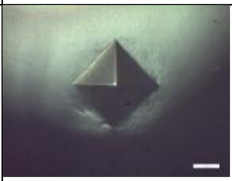	573.3
6	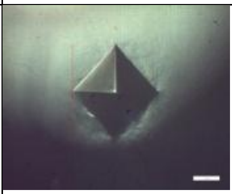	583.6

In the subsequent phase of the experiment, the samples that had been previously prepared were etched in a solution of 4% Nital-4 acid. The structure was then examined at 50x magnification using a microscope of the AmScope ME1200TC-5M Inverted Trinocular Metallurgical Microscope + 5MP Camera type. Fig.32 shows an example of a photograph taken using this microscope.

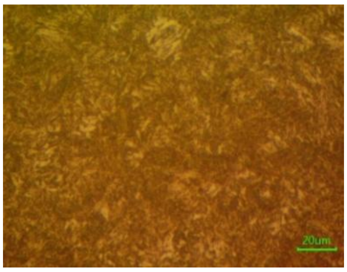

Fig. 32. Microstructure photograph of the sample

The resulting structure is a martensitic structure, which is a required outcome of the hot stamping process. It is distinguished by high mechanical properties and was observed in all samples obtained from each of the measurement areas.

5.2.3. Hydrogen embrittlement test

Hydrogen embrittlement occurring during the hot stamping process can lead to uncontrolled cracking of body drawpieces during normal automotive operation. A simple workshop test of a material resistance to hydrogen embrittlement is four-point bending of samples taken from the drawpiece. Such a sample, rectangular with the dimensions of 110 x 25, is placed in a special tool [14]. The punch of the tool is tightened with a screw so that the deflection of the sample induces a stress equal to 80% of the tensile strength limit. The sample is left in the tool for 300 hours and next visual inspection is performed. Table 5 presents the photographs of the tests performed. None of the tested samples showed cracks or scratches on the surface, which could mean the onset of cracking. Therefore, it can be concluded that the samples passed the four-point bending test.

Tab. 5. Results of four-point bending test

Sample	During study	After completion of the study
1		
2		
3		
4		

5.2.4. Measuring the shape-dimensional accuracy of a drawpiece

To check the shape-dimensional accuracy of the manufactured drawpieces, we first analysed the requirements defined in the technical documentation. For the drawpiece in question, the shape and dimensional accuracy was to be within ±0.5mm at the adjacent surfaces and ±1.2mm in other areas. Based on this analysis, a measurement plan was drawn up and five parts were randomly selected and measured on the CMM (Coordinate Measuring Machine). Fig. 33 shows an example of the measurement report.

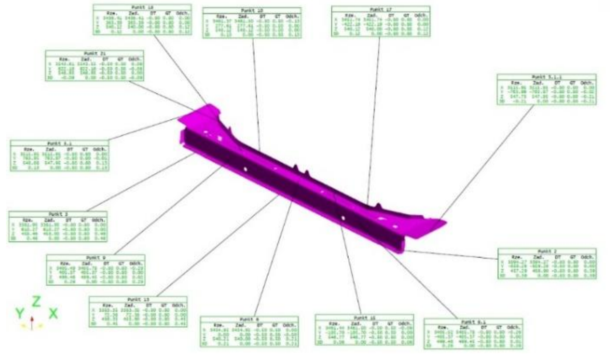

Fig. 33. Example measurement report

It was found that at none of the measurement points, the assumed tolerances of the drawpiece production were exceeded, particularly on the adjacent surfaces significant for the assembly of the drawpieces.

6. SUMMARY

The design of a hot stamping tool with an innovative arrangement of punches operating in a direction other than the stamping direction was performed in several stages. Computer simulations constituted a significant part of the overall process. Their results include a lot of information concerning stamping and quenching processes. These include the FLD diagram, the temperature distribution on the drawpiece surface and the working surfaces of the tools, as well as the predicted distribution of martensite in the drawpiece. The evaluation confirmed that there were no risks associated with the feasibility of the detail or its quality following the stamping process. The martensitic structure guarantees the strength limit R_m=1400÷1900 MPa for the whole product and Vickers hardness of HV>400. The maximum temperature of the drawpiece does not exceed 248°C, which is lower than the required value of 250°C. The temperature distributions on the working surfaces of the tools at the end of the stamping process slightly exceed 100°C, which has a beneficial effect on the duration of the whole process. The image from the thermal imaging camera monitoring the stamping process (Fig.34) confirms the results obtained during the simulation. The obtained temperature distribution and values are similar.

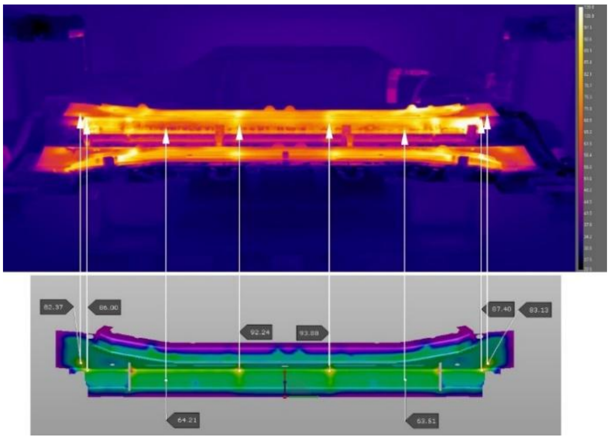

Fig. 33. The image from the thermal camera

Based on the results of the simulations of the stamping process, the force exerted by the drawpiece on the die after cooling to the final process temperature (approximately 40 kN) was determined. This elevated force value can be attributed to the shrinkage along the beam of 0.8 mm, which is half the thickness of the sheet. The problem of drawpiece jamming was successfully eliminated through the implementation of an appropriate correction of the working surfaces of the tool, using the controlled moving punches (withdrawn after the hardening process) and the strategic selection of tool kinematics. Furthermore, the thermal expansion of dies and punches was determined through the solution of thermomechanical analysis problems with the NX Simcenter package. This investigation concluded that the potential risks associated with the incorrect adoption of tool clearances were not present.

In conclusion, it should be stated that the possibilities offered by modern packages supporting the work of the designer of hot stamping dies, significantly shorten the time of preparation of the test series of drawpieces, and in turn have a positive impact on the financial aspect of the preparation of production processes.

Measurements of the finished drawpieces from the test series showed that all required parameters were met. Thus:

- the drawpiece material has a strength limit Rm in the range of 1400÷1900 MPa,
- the hardness of the drawpiece after hardening is greater than the required 400 HV,
- the material of the drawpiece after hardening has a martensitic structure,
- the drawpieces passed the hydrogen embrittlement test,
- the beams produced have the required shape-dimensional accuracy.

REFERENCES

1. Directive (EU) 2019/1161 of the European Parliament and of the Council of 20 June 2019 amending Directive 2009/33/EC on the promotion of clean and energy-efficient road transport vehicles. Off J Eur Union. 2019;L 188:116-130
2. Karbasian H, Tekkaya AE. A review on hot stamping. J Mater Process Technol. 2010;210(15):2103-18. doi:10.1016/j.jmatprotec.2010.07.019
3. Jeswiet J, Geiger M, Engel U, Kleiner M, Schikorra M, Duflou J, et al. Metal forming progress since 2000. CIRP J Manuf Sci Technol. 2008;1(1):2-17. doi:10.1016/j.cirpj.2008.06.005
4. Huang G, Tihay K, Sriram S, Weber B, Dietsch P, Cornette D. Fracture characterization of AHSS using two different experimental methods. IOP Conf Ser Mater Sci Eng. 2016;418:012080. doi:10.1088/1757-899X/418/1/012080
5. Turetta A, Bruschi S, Ghiotti A. Investigation of 22MnB5 formability in hot stamping operations. J Mater Process Technol. 2006;177 (1-3):396-400. doi:10.1016/j.jmatprotec.2006.04.041
6. Horvath CD. Advanced steels for lightweight automotive structures. In: Mallick PK, editor. Materials, design and manufacturing for lightweight vehicles. Cambridge: Woodhead Publishing; 2010. p. 35-78. doi:10.1533/9781845697822.1.35
7. Feuser P, Schweiker T, Merklein M. Partially hot-formed parts from 22MnB5—process window, material characteristics and component test results. In: Proceedings of the 10th International Conference on Technology of Plasticity; 2011 Sep 25-30; Aachen, Germany. Aachen: ICTP; 2011: 408-13.
8. Palmieri ME, Lorusso DV, Tricarico L. Investigation of material properties of tailored press hardening parts using numerical and physical simulation. Procedia Manuf. 2020;50:104-9. doi:10.1016/j.promfg.2020.08.019
9. Chen X, Xiao N, Li D, Li G, Sun G. The finite element analysis of austenite decomposition during continuous cooling in 22MnB5 steel. Model Simul Mater Sci Eng. 2014;22(6):065005. doi:10.1088/0965-0393/22/6/065005
10. Liu H, Xing Z, Bao J, Song B. Investigation of the hot-stamping process for advanced high-strength steel sheet by numerical simulation. J Mater Eng Perform. 2010;19(3):325-34. doi:10.1007/s11665-009-9510-y

11. Kim H, Park JK, Lee MG. Phase transformation-based finite element modeling to predict strength and deformation of press-hardened tubular automotive part. Int J Adv Manuf Technol. 2014;70 (9-12):1787-801. doi:10.1007/s00170-013-5424-9
12. Wróbel I. Numerical and experimental analysis of hardening distortions of drawpieces produced in hot stamping process. Metals (Basel). 2021;11(3):457. doi:10.3390/met11030457
13. Palmieri ME, Tricarico L. Comparison of flow behaviors at high temperature of two press hardening boron steels with different hardenability. Metals (Basel). 2022;12(11):1935. doi:10.3390/met12111935
14. Wróbel I, Danielczyk P. Control system for automated technological process of hot stamping—a case study. Materials (Basel). 2023;16(10):3658. doi:10.3390/ma16103658

Piotr Danielczyk: https://orcid.org/0000-0002-7622-3150

Ireneusz Wróbel: https://orcid.org/0000-0002-7587-0217

DOI 10.2478/ama-2025-0057

CONTROL OF FREE CONVECTION BY FLEXIBLE FINS IN A SQUARE CAVITY CONTAINING A HEATED TRIANGULAR BLOCK

Said AZZI*, Belkacem BELKACEM*, Mohamed BOUZIT, Mohamed BOUHAFS*,**
Atika BENCHERIF, Imadeddine DEHIMI***

*Laboratory of Industrial Production and Maintenance Engineering, Institute of Maintenance and Industrial Safety,
University of Oran2 Mohamed Ben Ahmed, BP 1015 El M'naouer, 31000 Oran, Algeria
**Laboratory of Maritime Sciences and Engineering LSIM Faculty of Mechanical Engineering,
University of Science and Technology of Oran, Mohamed Boudiaf, El Mnaouar, BP 1505, 31000 Oran, Algeria

azzi.said@univ-oran2.dz, belkacem.belkacem@univ-oran2.dz, mohamed.bouzit@univ-usto.dz, bouhafs.mohamed@univ-oran2.dz,
atika.bencherif@univ-usto.dz, dehimi.imadeddine@univ-oran2.dz

received 06 January 2025, revised 17 September 2025, accepted 18 September 2025

Abstract: This study investigated the role of fin flexibility to control the fluid flow on natural convection heat transfer within a square cavity containing a heated triangular block. Two flexible fins, attached to the cavity's cold vertical walls, interact with an incompressible fluid under varying Rayleigh numbers (Ra) and elasticity modulus (Et), highlighting how these parameters affect thermal and fluid dynamics and the interaction between the top and the bottom regions of the cavity. The novelty of this study is to create passive control over the flexible fins to control the fluid flow and creating a separation between the top region or the bottom region using these mentioned parameters. Using the Arbitrary Lagrangian-Eulerian (ALE) technique, the fluid-structure interaction (FSI) model captured the bending response of the fins and the resulting convective heat transfer. Results indicated that lower fin rigidity (low Et) significantly enhanced thermal mixing and heat transfer due to increased fluid flow, driven by the bending of the fins at higher Ra. Hence, the top and the bottom regions of the cavity interacted with each other. Conversely, higher Et values restricted fluid circulation, maintaining thermal stratification and reducing heat transfer efficiency and separated these regions. This study provides insights into controlling and optimizing heat transfer in systems with flexible structures, with potential applications in thermal management and energy-efficient design.

Keywords: natural convection, FSI, heat transfer, square cavity, FEM

1. INTRODUCTION

The interest of researchers and engineers in studying heat transfer and fluid flow during natural, forced and mixed convection in enclosed geometries came from the crucial necessity for enhanced performance in various energy-related applications. Some of these applications include air conditioning [1], [2], drying processes [3], stenotic artery [4],geothermal reservoir utilization [5], cooling of electronics [6-8], thermal insulations [9], nuclear reactor operations [10]. There have been different studies for convection heat transfer for a variety of geometries and cavities such as square cavities, rectangular cavities, circular cavities and more [11-16].

In cooling systems, Fluid-structure interaction (FSI) has proven to be highly effective in enhancing heat transfer within cooling systems by disrupting thermal boundary layers through the use of obstacles. This approach has garnered significant interest, particularly in scenarios where fluid dynamics interact with flexible structures or membranes [17]. S.A.M. Mehryan et al [18] investigated the natural convection behavior of a square cavity containing a heated thin flexible plate which encountered a large deformation, the perpendicular side of the cavity were assumed to be cold and the horizontal walls was assumed to be adiabatic and the heated flexible thin plate was isothermal and fixed in the center of the cavity with a variation in inclination angles, the finite element method was adopted with the arbitrary lagrangian-Eulerian to solve this system. The results shown that the heat transfer and the fluid flow affected by the location of the inclination angle and the fixed point. Also, the increase in Rayleigh number with the low elasticity of the flexible thin plate gives better results than a rigid thin plate in terms of heat transfer and it was confirmed by the visualization of the Nusselt number graph. Afraz Hussain Majeed et al. [19] numerically analyzed natural convection and energy storage in Casson fluids within enclosures containing cylinders and wavy surfaces. Using a Galerkin finite element approach with an LBB-stable element, Newton's method, and PARDISO solver, the study explored how geometry and parameters such as Rayleigh, Hartmann, Lewis numbers, and β affect flow, heat, and mass transfer. Results showed that higher Rayleigh numbers enhance concentration gradients, while increased Hartmann numbers suppress convection, offering insights into optimizing thermal storage systems. Habibis Saleh et al [20] studied numerically the contribution of two flexible fins attached on the left heated wall interact with the fluid towards the natural convection in an open square cavity, the right wall is in contact with ambient air, the rest of the walls are insulated, the movement of the end of the upper elastic fin was followed using the trigonometry function. The results showed that an increase in Rayleigh number increase the fluid velocity and made a strong fluid circulation, the identical oscillating fins permitted better fluid circulation at the left hot wall. Also, the maximum point of the heat transfer enhancements reached at the extreme amplitude tip configuration for the highest flexibility. Afraz Hussain Majeed et al. [21] numerically investigated convective thermal flow in a vertical enclosure with sinusoidal walls filled with nanofluid. This study aimed to focus on how magnetic field, oscillation and concentration particles alter heat transfer. By using the finite element method with an LBB-stable element, the study showed that lower nanoparticle volume fractions enhanced kinetic energy and Nusselt number, while higher Hartmann numbers reduced temperature and velocity highlighting optimal conditions for energy-efficient thermal management. Ahmadreza B et al [15] studied the natural convection to analyze the heat transfer rate of a circular enclosure divided in two parts, one of them is cold and the other is hot, where the fluid structure interaction is inside it, the middle wall transport the heat that goes from the hot part to the cold part, they considered the middle wall flexible. They noticed that increasing the Rayleigh number increased the flow of fluid which makes the middle wall experience a significant stress and get deformed. Therefore, these remarks let them to conclude that the dominant mechanism was the convective heat transfer, and the opposite, in low values of Rayleigh number the plate distortion and the power produced by the vortex was almost negligible. Mixed convection heat transfer in a vented cavity was investigated numerically by Md. Azizul Hakim et al [22]. This study employed a flexible flow modulator subjected to external oscillations, with air as the working fluid. The numerical simulations utilized a combination of the Galerkin finite element method and the Arbitrary Lagrangian-Eulerian (ALE) method. The focus was on evaluating the impact of various dynamic parameters, including the amplitude and period of oscillation, as well as the flexibility of the modulator, on the flow field, heat transfer performance, thermal field, thermal oscillations, and induced flow. The findings revealed that interaction with a more flexible modulator generated vortices closer to the heater wall near the modulator, whereas stiffer modulators caused the vortices to move away. Furthermore, as the modulators flexibility increased, the thermal boundary layers became thinner, leading to enhanced heat transfer. H. Saleh et al [23] studied the impact of a flexible fin on the unsteady convective flow within a square enclosure consisting of a porous layer and a vertical fluid layer, the fin connected in the left of heated wall. The Brinkman-Forchheimer-extended Darcy flow model was used in the porous layer. The computational system was solved using the finite element method and the governing equations were written by the aid of the Arbitrary Lagran-gian-Eulerian (ALE) formulation in the fluid and structure domains. The oscillation of the fin affected the area beneath the fin more significantly than the area above or in the center. Additionally, the positioning of the fin tip altered both the quantity and position of the flow circulation core which showed the impact of the position variation of the fin. Mufeng Chen et al [24] analyzed numerical and experimental methods to investigate the R-B natural convection of a TSMF with an immersed nonmagnetic particle and an external magnetic field. The results showed that an increase in Ra number increases the Nu number with low magnetic field values, in the meanwhile, the same increasing in Nu number achieved by using highest variations of external magnetic field with the lowest variations in the Ra number. Khalil Khanafer et al [25] investigated numerically phenomena of transport inside a solar porous collector where there was inside an isothermal cylinder positioning in the center of the enclosure for different parameters. The results showed that an increasing in the heat transfer caused by an increasing in the Rayleigh number and the effective thermal conductivity. Moreover, heat transfer was higher when there was a cylinder. Mohammad Ghalambaz et al [26] studied the heat transfer and fluid flow of dilatants liquids and pseudo-plastic in a square cavity that has a thin hot plate in it. The outcomes results revealed that increasing in Rayleigh number increases the buoyancy forces that lead to higher heat transfer. In addition, when they used longer flexible plate, the heat transfer reduced significantly. Bader Alshuraiaan et al [27] numerically investigated the applied effects on lid driven trapezoidal cavity by a hybrid nanofluid in addition of a flexible wall. Different Reynolds numbers along with volume fraction of the hybrid nanofluid was used in this study which showed that using a flexible wall has significantly increased the heat transfer rate. Those previous studies showed the importance of the fluid structure interaction and their effects on increasing the heat transfer.

In the present study, we focused on controlling fluid dynamics by utilizing deformable fins that bend in response to increasing Rayleigh numbers. This deformation created an opening between the top and bottom of the cavity or established a separation between these two regions, this could be useful in many industrial applications especially in thermal management field, microfluidic devices with deformable boundaries. Therefore, this investigation highlighted the effect of these combinations on the fluid flow and heat transfer performances.

2. MODELING APPROACH

The geometry in the present study that shown in Fig. 1, is a square cavity containing a heated triangular block from the bottom and adiabatic wall from the top base of it with two flexible fins separately attached in the cold vertical walls of the cavity, the top and bottom walls of the cavity are considered to be thermally insulated. The cavity filled with an incompressible fluid. The natural convection produced a buoyancy force that make the two flexible fins to bend. The no-slip boundary condition is imposed on all the cavity walls, the triangular structure, and the two flexible fins.

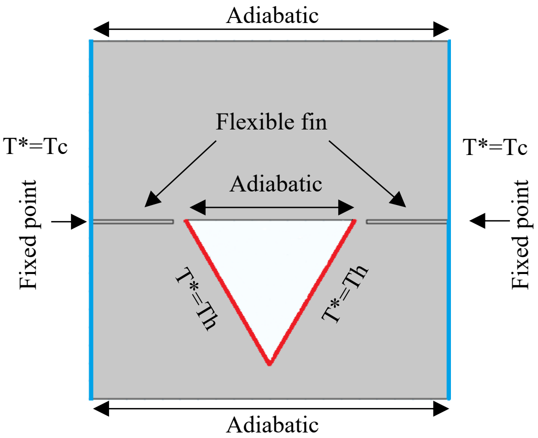

Fig. 1. Physical 2D model of our study

2.1. Mathematical Equations

The temperature variations were assumed to be minimal. Also, the thermo physical properties and temperature was considered to be independent of each other, but not for the case of variation of the density liquid where it’s was not neglected and solved by using the Boussinesq model. Additionally, the technique of ‘’Arbitrary Lagrangian-Eulerian’’ (ALE) is employed besides of utilizing the assumptions mentioned earlier, the equations governing the thermal characteristics and hydrodynamics of the problem are presented below [17], [28]:

Continuity equation:

$$\nabla^*.u^* = 0 \tag{1}$$

Momentum equations:

$$\rho_f\left[\frac{\partial u^*}{\partial t} + (u^* - w^*)\nabla^* u^*\right] - \nabla^*.[-P^*I + \mu(\nabla^* u^* + (\nabla^* u^*)^{tr})] - \rho_f \beta g(T^* - T_c^*) = 0 \tag{2}$$

The energy equation for the fluid is defined in the Eq. (3) as:

$$(\rho c_p)_f\left[\frac{\partial T^*}{\partial t} + (u^* - w^*).\nabla^* T^*\right] - k_f \nabla^{*2} T^* = 0 \tag{3}$$

For elastic structure domain, the energy equation for the fins can be written in Eq. (4) as:

$$(\rho c_p)_f \frac{\partial T^*}{\partial t} - k_s \nabla^{*^2} T^* = 0 \tag{4}$$

where, u^* represents the velocity vector, w^* shows the moving mesh velocity vector, and P represents the pressure filed, g is the gravity vector. k_f and k_s signifies thermal conductivity of the fluid and the solid respectively.

To define the stress tensor of Eq. (5) we applied the Neo-Hookean solid model:

$$\sigma^* = J^{-1} F S F^{tr} | F = (I + \nabla^* d_s^*), J = det(F) \& S = \partial W_s / \partial \varepsilon \tag{5}$$

$$W_s = \frac{1}{2} l(J^{-1} I_1 - 3) - l Ln(J) + \frac{1}{2}\lambda(Ln(J))^2 \left| \begin{matrix} l = \frac{E}{2(\nu+1)} \\ \lambda = \frac{E\nu}{(\nu+1)(-2\nu+1)} \end{matrix} \right. \tag{6}$$

$$\varepsilon = \frac{1}{2}\left(\nabla^* d_s^* + \nabla^* d_s^{*tr} + \nabla^* d_s^{*tr} \nabla^* d_s^*\right) \tag{7}$$

The boundary conditions applicable to the external walls Eq. (8) and Eq. (9), and the two flexible fins interface Eq. (10) are defined as follow:

At the hot wall:

$$T^* = T_h^*, u^* = v^* = 0 \tag{8}$$

At the cold wall

$$T^* = T_c^*, u^* = v^* = 0 \tag{9}$$

At the interface of the flexible fin:

$$k_f \left.\frac{\partial y}{\partial x}\right|_f = k_s \left.\frac{\partial y}{\partial x}\right|_s \cdot \tag{10}$$

Also, Prandtl numbers and the Rayleigh and the Elasticity modulus are introduced as:

$$Ra = \frac{\rho_0^2 c_p g \beta \Delta T d^3}{\mu_B k} \cdot \tag{11}$$

Prandtl number:

$$Pr = \frac{c_p \mu_B}{k} \cdot \tag{12}$$

Elasticity modulus

$$E\tau = \frac{E \cdot 2R^{*2}}{\rho_f {\alpha_f}^2} \cdot \tag{13}$$

To quantify the heat transfer between the two flexible fins and the fluid, the nusselt number has been used as follows in the Eq. (14) and Eq. (15):

$$Nu_f = -\frac{\partial \theta}{\partial X} \cdot \tag{14}$$

$$Nu_s = -k_r \frac{\partial \theta}{\partial X}. \tag{15}$$

The average Nusselt number on the wall is given by Eq. (16) as follows:

$$\overline{Nu} = \int_0^{s_1} Nu_f\, dy + \int_{s_1}^{s_2} Nu_s\, dy + \int_{s_2}^{1} Nu_f\, dy \left| \begin{matrix} s_1 = \frac{1}{2} - \frac{t_{fin}}{2} \\ s_2 = \frac{1}{2} + \frac{t_{fin}}{2} \end{matrix} \right. \tag{16}$$

2.2. Numerical Method

In our study we employed the technique of Arbitrary Lagrangian-Eulerian (ALE) combined with finite element method (FEM) to solve the non-linear governing equations. The finite element method and the details approach are discussed in reference [29]. In our work, Gaussian quadrature, based on FEM, gives smooth solutions within the internal sub-domains. A fully coupled approach integrates the structure, heat, mesh displacements and momentum, resulting in a large matrix of coefficients, which is solved at each time step using the method of Newton.

2.3. Validation

To make sure that this current study has accurate results, a validation results have been made with another study that made the same numerical technique as shown as in figure 2 and 3. [30]

2.4. Grid Study

Tab. 1. The average Nusselt number for variety of elements number

Number of elements	1112	8139	12172	54685	54981
Average Nusselt number	4,3988	4,8061	4,8905	4,9829	4,9829

After several tests of meshing, we choose 54685 number of elements since the value of average Nusselt number didn't change after this number.

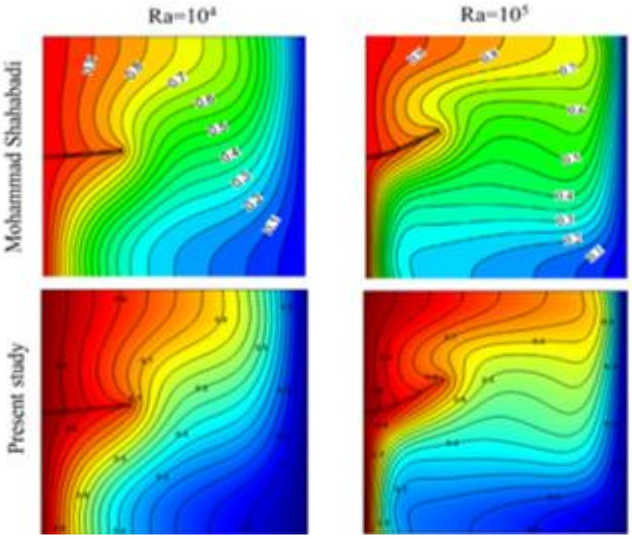

Fig. 2. Comparison of the results of the contours of isotherms when Pr = 10 and Et = 10^{10} between the present study and the study of Mohammad Shahabady et al.

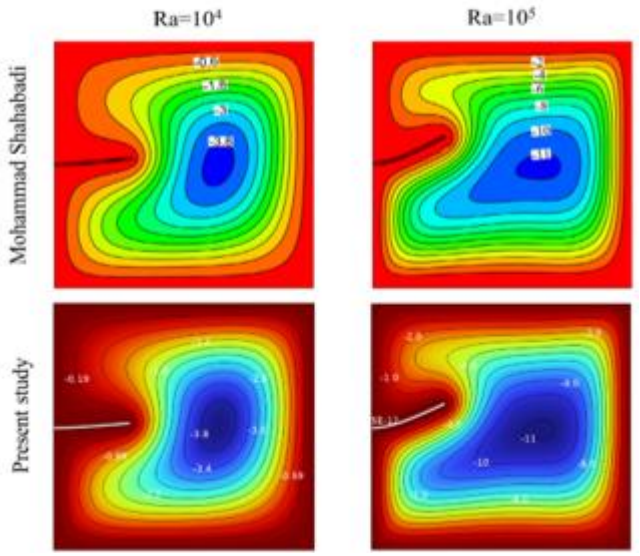

Fig. 3. Comparison of the results of the streamlines when Pr = 10 and Et = 10^{10} between the present work and the work of Mohammad Shahabady et al.

3. RESULTS AND DISCUSSION

The aim of this study is to examines the effects of the fin elasticity with the variation of Ra on thermal behavior and the dynamic of the fluid in a cavity that contain a heated triangular shape. A simulation was performed to visualize the impact of the fins and the Rayleigh number as a control parameter. The range values for the Rayleigh number were ($10^3 \leq Ra \leq 10^6$) to perform moderate to strong buoyancy regimes, elasticity modulus ($5\times10^9 \leq Et \leq 10^{11}$) to cover practical materials used in microdevices, polymers and thin fins in electronic systems, Pr=7.1. In the next following, the obtained results were presented in a qualitative way by the streamlines and the contours in figures (4-5). The temperature profiles as well as the velocity profiles for different regions via the cutlines L1, L2, L3, L4 in figures (7-14). The average Nusselt number in function of Ra in figure 15. These lines likely correspond to critical locations where temperature gradients can reveal the thermal behavior and where velocity reveal the streamlines variations across different sections of the cavity.

Figure 4 depict the effect of the Rayleigh number on the velocity streamlines when the elasticity modulus of the fins was equal to 5×10^9 and 10^{11} respectively. For low value of Rayleigh number which is 10^3 there was no effect on the fins and the fluid motion was nearly negligible due to the lack of significant thermal exchange, the streamlines were separated between the top and bottom parts of the cavity for both values of the elasticity modulus. The remarkable change started when the Rayleigh number reached the value of 10^5 for Et = 5×10^9, we noticed that the two fins started to bend indicating that the hydrodynamic forces started to exerts on the fins, but not for the case when the elasticity modulus was equal to 10^{11} where the fin acted as a fixed obstacle at this value, the fluid remained separated between the two parts of the cavity in both cases. At a Rayleigh number of 10^6, we observed that when the fins flexibility was 5×10^9, the fins bended more prominently, nearly touching the cavity walls. This created a wider passage, allowing significant fluid flow and interaction between the upper and lower regions of the cavity caused by the significant effect of hydrodynamic forces on the fins at this value. In contrast, when the fins flexibility was 10^{11}, this passage did not exist despite the high Rayleigh number, as the fins was not affected by the increased Rayleigh number, and thus, do not bend due to fixed behavior of the fins as previously mentioned.

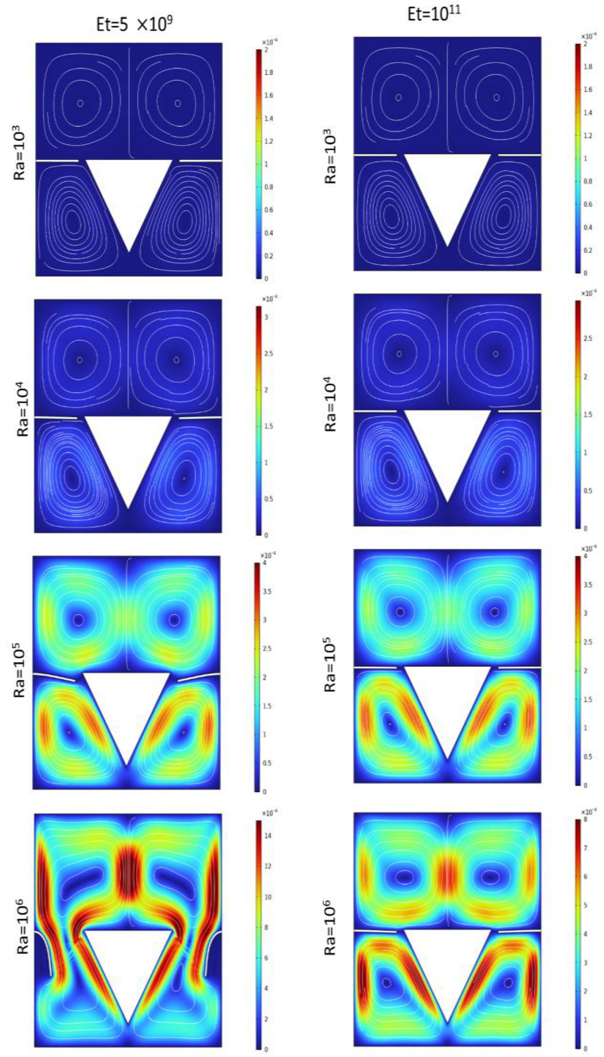

Fig. 4. Streamlines of the velocity when Et=5×10^9 and Et=10^{11} for different Rayleigh numbers

In Figure 5 that represent the effects of the Rayleigh number (Ra) on the isotherm contours within the cavity under two distinct elasticity modulus for the fins 5×10^9 and 10^{11}.

For Et=5×10^9: at low Ra values, there is minimal thermal convection within the cavity, resulting in non-uniform isotherms that indicate limited fluid motion and minimal temperature gradients. As Ra increases to 10^4, slight changes in the isotherms appear, indicating slight convective flow. However, the fins remain mostly unaffected due to low buoyancy forces. At Ra=10^5, stronger buoyancy forces cause the fins to bend slightly, significantly impacting the isotherms, fluid motion enhanced.

At the highest Ra=10^6, intense convection results in more distorted isotherms and efficient heat transfer between the upper and lower parts of the cavity. The fin flexibility allows the isotherms to converge near the fins, showing that heat transfer is intensified by the fluid mixing caused by fin deformation.

For Et=10^{11} we noticed that across all Ra values, the fins remain largely rigid due to the high elasticity modulus, resisting deformation. Consequently, the isotherm contours indicate limited fluid mixing between the upper and lower cavity regions, even as Ra increases.

As Ra grows, the isotherms show increased thermal gradients, but the rigid fins restrict flow interaction, maintaining a relatively stable boundary between the upper and lower sections.

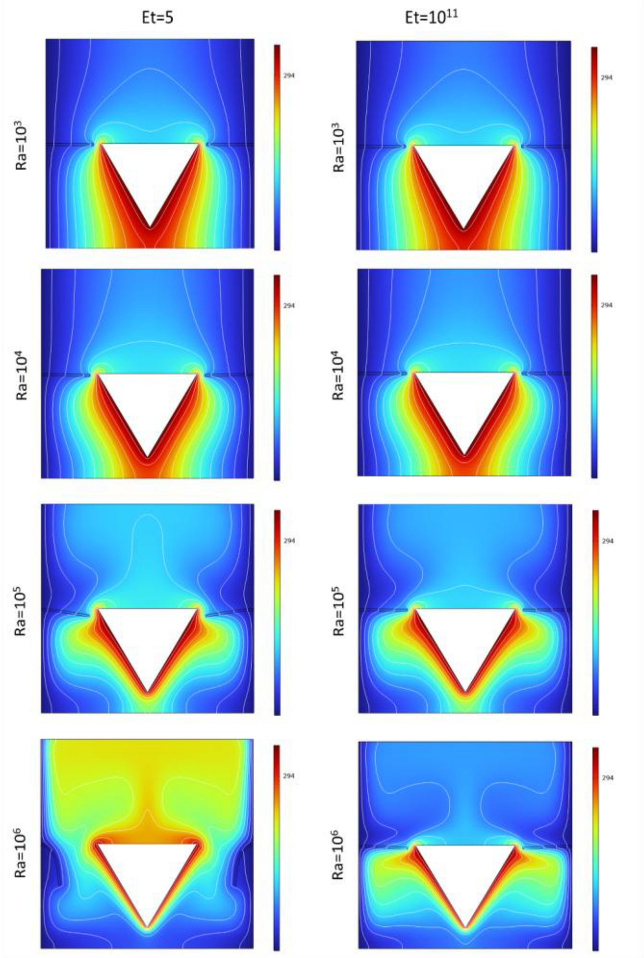

Fig. 5. Isotherms for Et=5×10^9 and Et=10^{11} for different Rayleigh numbers

Figure 6 illustrated the cutlines (L1, L2, L3, and L4) used to measure the velocity profiles and the temperature variations within specific areas of the cavity.

In figures 7-10, at Et=5×10^9 the temperature profiles along the cutlines showed more pronounced variations, indicating significant heat transfer across different regions of the cavity. In figure 7, along the L1 cutline, there was minimal change when the value of the Rayleigh number was low for both elasticity modulus. At Ra=10^6 when Et=5×10^9: the fin bended downward, leading to temperature increases in the region between the fin and the triangular structure (from 0.01 arc length (m) to 0.02 arc length (m)). This area exhibited higher temperatures compared to the case where Et=1011 for the same value of the Rayleigh number, which indicated the heat transfer in this area.

Similarly in figure 8, along the L2 cutline which intersects the fin, a comparable pattern was observed.

In figure 9, at the L3 cutline, variations also occurred at Ra=10^6, specifically, at Et=5×10^9, the temperature near the vertical walls of the cavity was lower compared to when Et=10^{11}, this reduction is due to the fin opening at Ra=10^6, allowing heat to dissipate more from this area. In contrast, when the fin remained closed, the heat remained concentrated in the lower region.

In figure 10 for the L4 cutline (upper part), an increase in temperature was observed at Ra=10^6 for Et=5×10^9 which indicated that there is a heat dissipation from the lower region to the upper region. In contrast, at the same Rayleigh number but with Et=10^{11}, the temperature was lower due to the high rigidity of the fin which made the fin to be closed, thus, restricted heat dissipation from the lower part to the upper part in this region.

These observations align with the earlier findings on fin flexibility at these elasticity values, indicating that more flexible fins improve mixing and thermal distribution, especially at higher Rayleigh numbers.

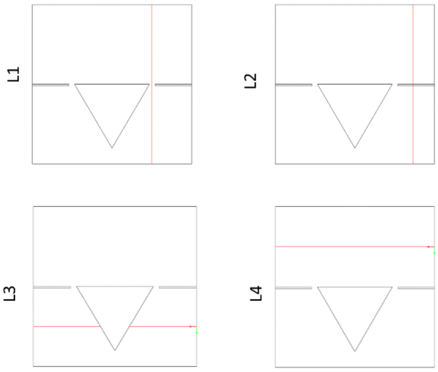

Fig. 6. Cutlines for different regions of the cavity

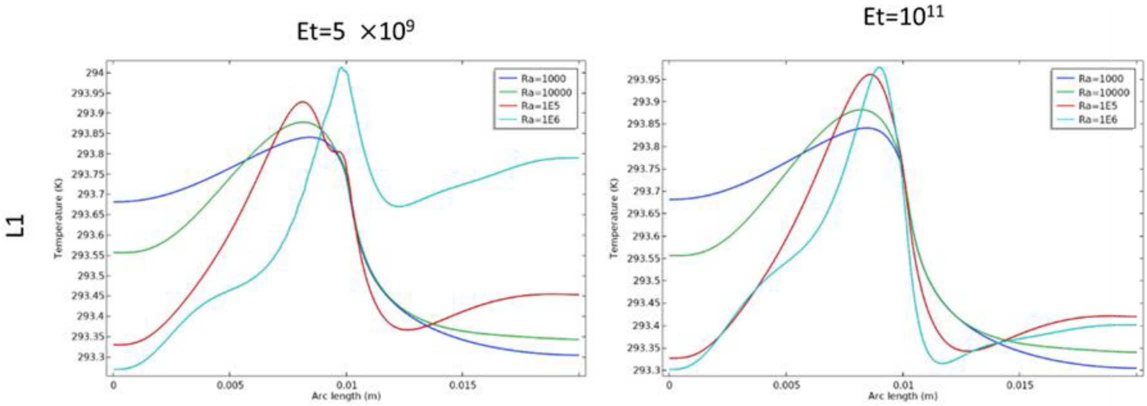

Fig. 7. Temperature profiles in the region L1 for multiples Rayleigh numbers and Et=5×10^9, Et=10^{11}

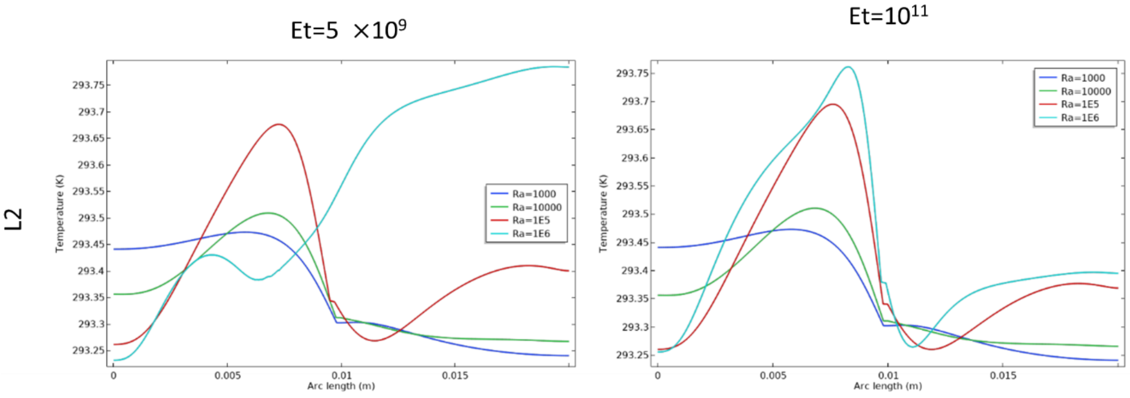

Fig. 8. Temperature profiles in L2 cutline for variating Rayleigh numbers and Et=5×10^9, Et=10^{11}

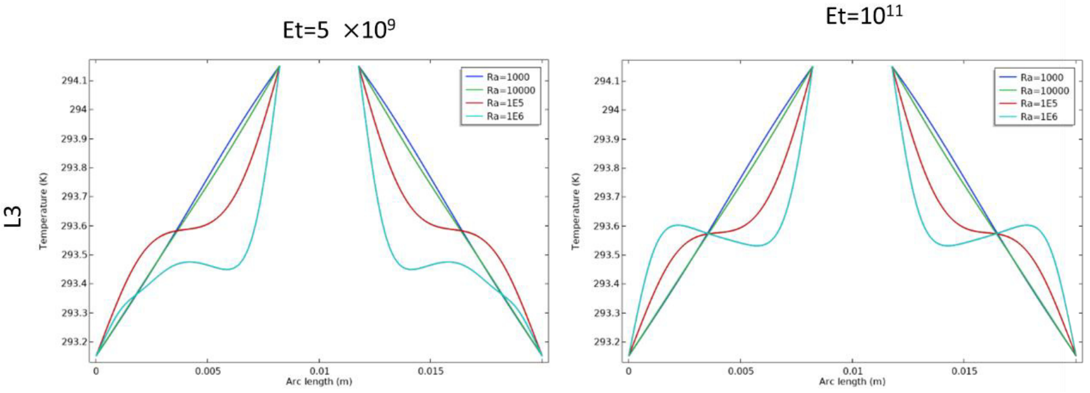

Fig. 9. Temperature profiles in L3 cutline for different Rayleigh numbers and Et=5×10^9, Et=10^{11}

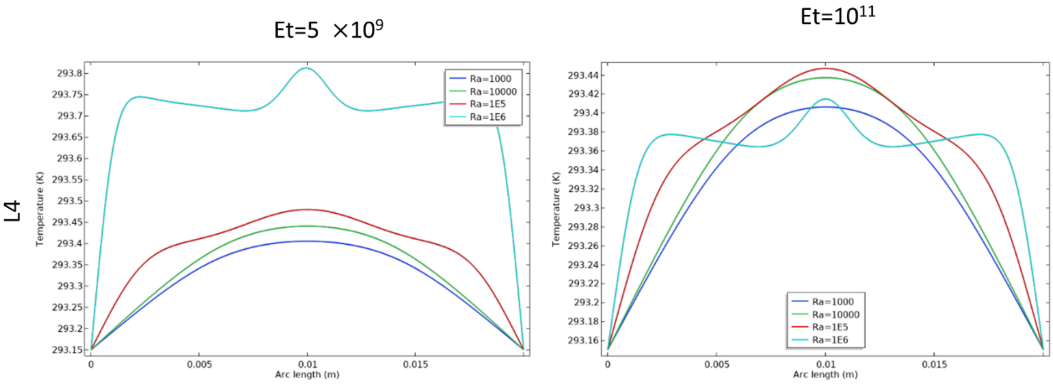

Fig. 10. Temperature profiles in L4 cutline where Et=5×10^9, 10^{11} for different Ra

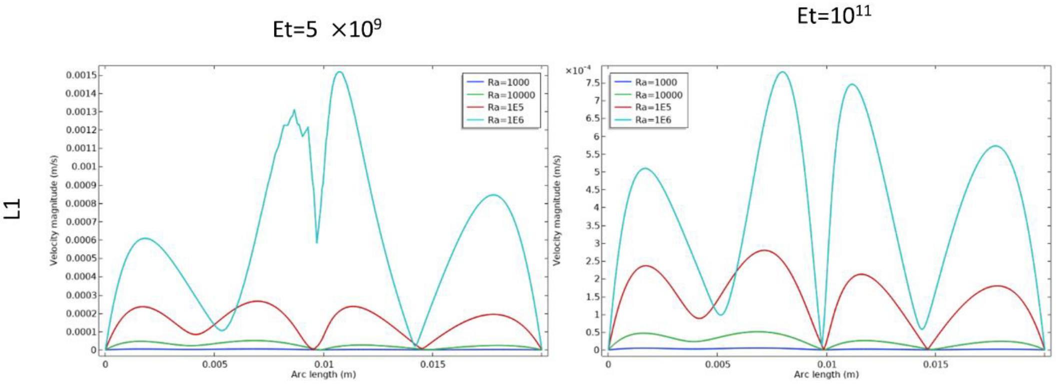

Fig. 11. Velocity profiles in cutline L1 for different Rayleigh numbers and Et=5×10^9, Et=10^{11}

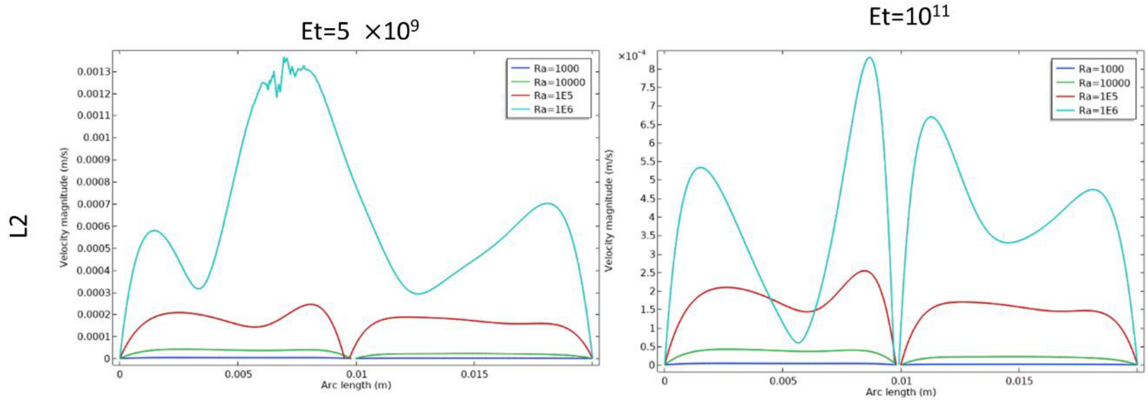

Fig. 12. Velocity profiles in cutline L2 for different Rayleigh numbers and Et=5×10^9, Et=10^{11}

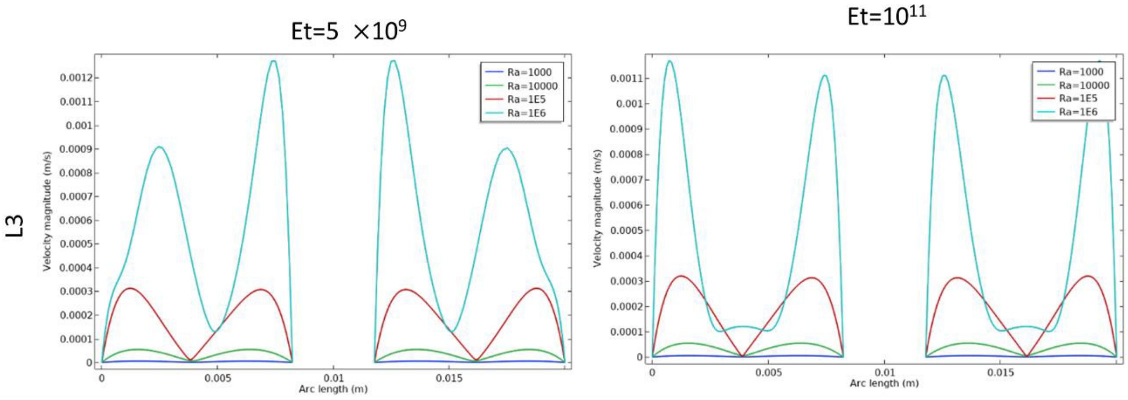

Fig. 13. Velocity profiles in cutline L3 for different Rayleigh numbers and Et=5×10^9, Et=10^{11}

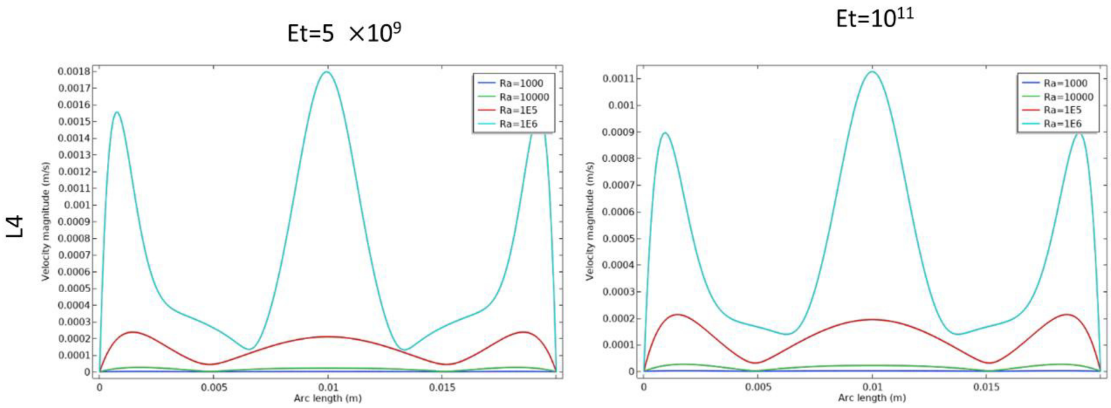

Fig. 14. Velocity profiles in cutline L4 for different Rayleigh numbers and Et=5×10^9, Et=10^{11}

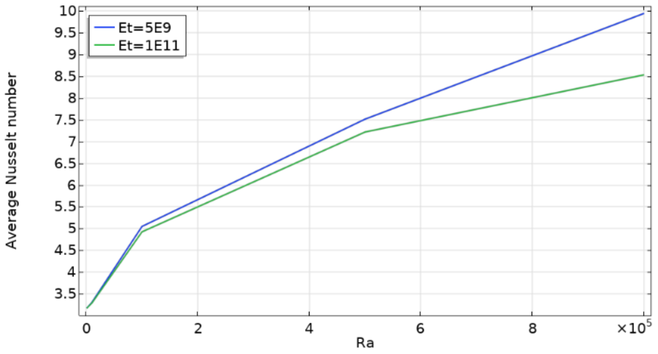

Fig. 15. Variation of the average Nusselt number as a function of Ra for different Et values

In figures 11-14 depict the velocity profiles in different areas of the enclosure according to the cutlines L1, L2, L3, L4 for different values of Ra where Et=5×10^9, Et=10^{11} respectively. The velocity profiles across the cutlines L1, L2 provide a higher fluid motion within the cavity at Et=5×10^9 compared to Et=10^{11} and the same observations in L3, L4 in specifics areas. As the Rayleigh number increased, the profiles show higher peak velocities, indicating stronger convective flows due to the enhanced buoyancy forces. The high rigidity of the fins limits their deformation, maintaining a more rigid structure that hinders the fluid movement between the top and bottom regions. Even at higher Rayleigh numbers, the velocities values remain subdued, showing limited convective mixing. The lower peak velocities values in these profiles confirm that the fins rigidity prevents the cavity from achieving the mixing fluid between the upper and lower parts of the cavity that seen in the flexible fin case.

In figure 11, along L1 cutline, a significant change in the velocity speed as mentioned earlier when Et=5×10^9. Also, at Ra=10^6 when Et=5×10^9 the fin bended downward which created an opening between the upper and lower parts of the regions. Additionally, a vibrating curve appeared between (0.007 arc length (m) and 0.01 arc length (m)) in the same parameter's values which can be attributed to the downward bending of the fin and the resulting opening, in the other hand, the curve goes smoothly between (0.01 arc length (m) and 0.013 arc length (m)) as the fin didn't bend upward.

In Figure 12, similar results are observed along the L2 cutline that intersects the fin.

In figure 13, along L3 cutline where it intersects the bottom of the triangular, at (Ra=10^6, Et=5×10^9), there is an increase in velocity motion near the vertical edges of the cavity compared to Et=10^{11} due to the opening that has been created by the bending of the fins.

In Figure 14, along L4 cutline, a slight increase is observed in middle of the cavity, while a significant increase occurs near the vertical edges.

Figure 15 represent the average Nusselt number variation as a function of the Rayleigh number (Ra) for variating values of elasticity modulus (Et) of the fins.

Effect of increasing Ra : As Ra increased, the average Nusselt number also increased for all elasticity values, indicating enhanced heat transfer. Higher Ra values induce greater buoyancy forces, intensifying fluid motion and thus increasing thermal exchange within the cavity.

Influence of the fin elasticity Et: for lower Et, the average Nusselt number shows a steeper increase with Ra compared to higher Et values. This suggests that flexible fins enhance convection by bending more significantly with increasing Ra, allowing fluid of the hot and cold regions to mix more effectively. Conversely, at higher Et values, the fins remain largely rigid, limiting fluid interaction between the regions of the cavity. As a result, the heat transfer enhancement due to convection is lower, even at high Ra values.

4. CONCLUSION

This work highlights the critical role of fin flexibility in promoting thermal interaction between the upper and lower regions of an enclosed cavity. Flexible fins facilitate fluid circulation between these areas, particularly at higher Ra values, as fin deformation opens channels that allow hot and cold fluid regions to mix. This dynamic interaction reduces thermal stratification, leading to significantly higher heat transfer rates. Conversely, rigid fins restrict the passage of fluid between the bottom and upper of the cavity, resulting in a stable thermal boundary that limits convective heat transfer. These findings underscore the importance of fin flexibility to control and create an open and a close passage of the fluid which can lead to achieve enhancement thermal mixing, which can be advantageous in designing heat transfer systems were minimizing thermal gradients and maximizing energy efficiency are priorities as well as in devices like microfluidic and biomedical devices requiring localized thermal control.

This numerical study is limited to 2d simulations with laminar flow. For this reason, future contributions has the possibilities to investigate and analyses 3D simulations, turbulent flows with different types of fluids, different flexible structural shapes.

Nomenclature

s	the second Piola–Kirchhoff stress tensor
d_s	vector of displacement
g	gravitational acceleration (m/s^2);
Pr	Prandtl number
T	non-dimensional form of temperature
u	velocity in a vector form
y	cartesian coordinate in y direction
T*	temperature (K)
w	the vector of moving coordinate velocity
L*	height and width of the cavity
x	cartesian coordinate in x direction
cp	specific heat capacity at constant pressure (J/kg.K);
E_T	non-dimensional form of the elasticity modulus
Ra	Rayleigh number
F_v	vector of body force
P	fluid pressure
k	thermal conductivity (W/(m.K));
E	dimensional form of young's modulus (N/m^2)
t	dimensional time
t_b	thickness of flexible baffle

Greek symbols

σ	the field of the tensor of stress
μ	fluid's dynamic viscosity
ρ_R	the ratio of fluid to solid-structure density
α	coefficient of thermal diffusivity
τ	dimensionless time
ρ	density
ν	Poisson's ratio
β	coefficient of the volumetric thermal expansion

REFERENCES

1. Yamamoto T, Ozaki A, Keigo Aratsu, Fukui R. Energy simulation and CFD coupled analysis for the optimal operation of combined convection and radiant air conditioning considering dehumidification. Heliyon. 2023 Jul 1;9(7):e18092–2.
2. Liu X, Wang H, Li Z, Zhao J, Li C, Xie D. Effectiveness of natural ventilation through single-sided window opening in air-conditioning rooms. Energy and Buildings. 2024 May 10;314:114260–0.
3. Anuma O, Ndukwu MC, Usoh G, Sam EO, Akpan G, Oriaku L, et al. Energy and exergy analysis of a natural convection solar greenhouse drier with insulated opaque walls for drying aromatic yellow pepper. Renewable Energy [Internet]. 2024 Aug 8;233:121141. Available from: https://www.sciencedirect.com/science/article/abs/pii/S0960148124012096?via%3Dihub
4. Majeed AH, Jan AZ, Alamri AM, AlQahtani SA, Ali MR, Hendy AS. Recent developments in the Darcy-Forchheimer model of magnetized tetra hybrid nanofluid activation energy/joule heating in a stenotic artery. Case Studies in Thermal Engineering. 2024 Apr 30;59: 104346–6.
5. Zhang L, Luo G, Wang S. The effects of fractures on porous flow and heat transfer in a reservoir of a U-shaped closed geothermal system. Applied Thermal Engineering. 2024 Mar 2;246:122852–2.
6. Teertstra PM, Yovanovich M, Culham JR. Modeling of natural convection in electronic enclosures. J Electron Packag. 2006; 128(2):157–65. Available from: http://dx.doi.org/10.1115/1.2188953
7. Mng'ang'a J. Effects of Ohmic heating, induced magnetic field and Newtonian heating on magnetohydrodynamic generalized Couette flow of Jeffrey nanofluid between two parallel horizontal plates with convective cooling. International Journal of Thermofluids. 2023 Nov;20:100402.

8. Bouchenafa R, Saim R, Abboudi S. Numerical study of forced convection in a turbulent heat sink made of several rows of blocks of square form. Heat and Mass Transfer. 2015 Jan 23;51(9):1301–11.
9. Villasmil W, Fischer LJ, Worlitschek J. A review and evaluation of thermal insulation materials and methods for thermal energy storage systems. Renewable and Sustainable Energy Reviews. 2019 Apr;103:71–84.
10. Freile R, Tano M, Ragusa J. Lattice Boltzmann Solidification Modeling of Forced Convection Internal Flows Applied to Gen-Iv Nuclear Reactor Coolants. 2023 Jan 1;
11. Acharya N, Chamkha AJ. On the magnetohydrodynamic Al2O3-water nanofluid flow through parallel fins enclosed inside a partially heated hexagonal cavity. International Communications in Heat and Mass Transfer. 2022 Mar;132:105885.
12. Rahimi A, Saee AD, Kasaeipoor A, Malekshah EH. A comprehensive review on natural convection flow and heat transfer. 2019 Mar 4;29(3):834–77.
13. Biswas N, Mahapatra PS, Manna NK. Buoyancy-driven fluid and energy flow in protruded heater enclosure. Meccanica. 2016 Jan 28;51(9):2159–84.
14. Biswas N, Mandal DK, Manna NK, Gorla R SR, Chamkha AJ. Hybridized nanofluidic convection in umbrella-shaped porous thermal systems with identical heating and cooling surfaces. International Journal of Numerical Methods for Heat & Fluid Flow. 2023 Jun 7;33(9):3164–201.
15. Shahrestani AB, Alshuraiaan B, Izadi M. Combined natural convection-FSI inside a circular enclosure divided by a movable barrier. International Communications in Heat and Mass Transfer. 2021 Jul;126:105426.
16. Majeed AH, Mahmood R, Liu D, Ali MR, Hendy AS, Zhao B, et al. Flow and heat transfer analysis over a pair of heated bluff bodies in a channel: Characteristics of non-linear rheological models. Case Studies in Thermal Engineering. 2023 Nov 30;53:103827–7.
17. Sabbar WA, Ismael MA, Almudhaffar M. Fluid-structure interaction of mixed convection in a cavity-channel assembly of flexible wall. International Journal of Mechanical Sciences. 2018 Dec 1;149:73–83.
18. Mehryan SAM, Alsabery A, Modir A, Izadpanahi E, Ghalambaz M. Fluid-structure interaction of a hot flexible thin plate inside an enclosure. International Journal of Thermal Sciences. 2020 Mar 5;153:106340–0.
19. Majeed AH, Liu D, Ali AR, Alotaibi H, Yin ZJ, Yi RH. Numerical simulations of energy storage performance in a close configuration: A Galerkin finite element-based computation. Alexandria Engineering Journal. 2024 Jun 21;104:56–65.
20. Saleh H, Naganthran K, Hashim I, Ghalambaz M, Nazar R. Role of fluid-structure interaction in free convection in square open cavity with double flexible oscillating fins. Alexandria Engineering Journal. 2021 Aug 22;61(2):1217–34.
21. Majeed AH, Mahmood R, Liu D, Zhang Y, Zhang JY, Ren HY, et al. Effects of oscillation on convective thermal flow in a vertical enclosure filled by nanofluid particles. Case Studies in Thermal Engineering. 2024 Sep 1;61:105133–3.
22. Hakim MA, Ahad AI, Karim AU, Saha S, Hasan MN. Fluid structure interaction and heat transfer enhancement with dynamic flexible flow modulator. International Communications in Heat and Mass Transfer. 2022 Mar 19;134:105983–3.
23. Saleh H, Hashim I, E. Jamesahar, M. Ghalambaz. Effects of flexible fin on natural convection in enclosure partially-filled with porous medium. Alexandria Engineering Journal. 2020 Jul 6;59(5):3515–29.
24. Chen M, Niu X, Yu P, Wang Y, Khan A, Yamasaki H, et al. Effect of fluid-particle interaction on 2D Rayleigh-Bénard laminar convection of a temperature-sensitive magnetic fluid. International Journal of Thermal Sciences. 2023 Nov 10;197:108752–2.
25. Khanafer K, Vafai K. Effect of a circular cylinder and flexible wall on natural convective heat transfer characteristics in a cavity filled with a porous medium. Applied Thermal Engineering. 2020 Nov;181:115989.
26. Ghalambaz M, Mehryan SAM, Feeoj RK, Hajjar A, Hashim I, Mahani RB. Free convective heat transfer of a non-Newtonian fluid in a cavity containing a thin flexible heater plate: an Eulerian–Lagrangian approach. Journal of Thermal Analysis and Calorimetry. 2020 Nov 27;147(2):1809–24.
27. Alshuraiaan B, Pop I. Numerical simulation of mixed convection in a lid-driven trapezoidal cavity with flexible bottom wall and filled with a hybrid nanofluid, Eur. Phys. J. Plus; May 2021. Available from: https://doi.org/10.1140/epjp/s13360-021-01349-4.
28. Afrasiab Raisi, Arvin I. A numerical study of the effect of fluid-structure interaction on transient natural convection in an air-filled square cavity. 2018 Jun 1;128:1–14.
29. Donea J, Huerta A. Finite Element Methods for Flow Problems. 2003.
30. Shahabadi M, Mehryan SAM, Ghalambaz M, Ismael M. Controlling the natural convection of a non-Newtonian fluid using a flexible fin. Applied Mathematical Modelling. 2020 Nov 24;92:669–86.

Said Azzi: https://orcid.org/0009-0005-8836-4136

Belkacem Belkacem: https://orcid.org/0000-0002-5318-8647

Mohamed Bouzit: https://orcid.org/0000-0002-1417-7291

Mohamed Bouhafs: https://orcid.org/0000-0002-8911-7015

Atika Bencherif: https://orcid.org/0000-0002-6126-0434

Imadeddine Dehimi: https://orcid.org/0009-0006-1005-6923

DESIGN AND SIMULATION OF MULTIBAND MICROSTRIP PATCH ANTENNA FOR WIRELESS APPLICATIONS USING HFSS

Rajeshwar B.*, Krishnanaik VANKDOTH*, Anvesh THATIKONDA*

*Department of Electronics and Communication Engineering, Chaitanya Deemed to be University,
Hyderabad, Telangana 500075, India

rajeshwar713@gmail.com, krishnanaik.ece@gmail.com, thatikondaanvesh@gmail.com

received 29 May 2025, revised 25 August 2025, accepted 07 September 2025

Abstract: This paper presents the design and simulation of a multiband microstrip patch antenna optimized for modern wireless applications such as IoT devices, WLAN (2.4/5 GHz), WiMAX, and sub-6 GHz 5G systems. The novelty of this work lies in the integration of artificial neural networks (ANNs) with HFSS simulations, enabling rapid geometry prediction and reducing optimization iterations by nearly 50% compared to conventional design approaches. The proposed antenna, implemented on an FR-4 substrate with strategically placed L-shaped slots, achieves well-defined resonances at 2.4 GHz, 3.6 GHz, and 5.8 GHz. Simulation results show return loss (S_{11}) better than –15 dB, VSWR < 2, and peak gains of 7–8 dBi, with stable broadside radiation patterns across all bands. A parametric study demonstrates the influence of slot dimensions and substrate parameters on multiband behavior, while a comparative analysis highlights performance advantages over existing designs. These results confirm that the ANN-assisted HFSS workflow provides an efficient methodology for realizing compact, high-performance antennas suitable for multistandard wireless communication platforms.

Key words: multiband antenna, microstrip patch, WiMAX, WLAN, neural network, HFSS simulation, return loss, VSWR, gain

1. INTRODUCTION

The rapid proliferation of wireless communication technologies and the growing demand for seamless, always-on connectivity have significantly accelerated the development of compact, cost-effective, and high-performance antenna systems. Modern wireless devices are expected to support a wide array of communication protocols—such as Wi-Fi (2.4/5 GHz), Bluetooth, LTE, and the rapidly evolving 5G and beyond (B5G/6G) standards—within a limited form factor. In this context, traditional single-band antennas fall short, as they lack the versatility required to operate across multiple frequency bands simultaneously. Multiband antennas address this limitation by enabling a single radiating element to function over several distinct frequency ranges. This capability not only reduces the number of individual antennas needed in a device but also simplifies system integration, lowers manufacturing costs, and conserves valuable PCB real estate—an increasingly critical factor in miniaturized wireless systems. Among the various antenna types explored for multiband operation, microstrip patch antennas have emerged as a preferred choice for wireless and mobile applications. Their planar profile, ease of integration with printed circuit boards, mechanical robustness, and low fabrication costs make them ideal for compact devices. Structurally, a typical microstrip antenna comprises a metallic radiating patch printed on one side of a dielectric substrate, with a ground plane on the opposite side. While conventional rectangular or circular patches inherently support only a single resonant frequency, a multitude of design modifications can be employed to facilitate multiband behavior. Common strategies include introducing slots of various shapes (e.g., U-shaped, E-shaped, or fractal slots) into the patch to create additional resonant modes [13–15]. Parasitic elements, either co-planar or stacked above/below the main patch, are also effective in generating multiple frequency bands through electromagnetic coupling [12,16]. Additionally, the use of defected ground structures (DGS), split-ring resonators (SRRs), or multi-layered configurations can further enhance bandwidth and frequency agility [14,15].

In recent years, artificial intelligence (AI) and machine learning (ML) techniques have been increasingly applied to antenna design, offering new pathways for performance prediction and optimization [5–7,17–22]. For example, Lahiani et al. [1] and Djermane & Talbi [5] demonstrated the potential of artificial neural networks (ANNs) for rapid patch antenna parameter estimation, while Lo et al. [6] and Zang et al. [7] showed that AI can enhance broadband and RF circuit optimization. More recent works [17–22] explored AI-driven design for IoT and 5G applications; however, these studies often remain restricted to single- or dual-band configurations and do not explicitly integrate ANN prediction with full-wave EM simulators for multiband operation. In contrast, the present research integrates an ANN-based geometry prediction model with HFSS-driven optimization, trained on more than 1000 simulation samples, to achieve accurate and efficient design of a compact multiband patch antenna resonating at 2.4 GHz, 3.6 GHz, and 5.8 GHz. This hybrid approach reduces simulation iterations by nearly 50%, providing both computational efficiency and practical utility. The design targets well-defined resonances with S_{11} < –15 dB, VSWR < 2, and directive gain of 7–8 dBi, making it suitable for deployment in IoT devices, WLAN access points, vehicular systems, and sub-6 GHz 5G platforms. Ansys HFSS (High Frequency Structure Simulator) serves as the primary electromagnetic simulation tool in this study. HFSS offers full-wave 3D simulation capabilities based on the finite element method (FEM), providing highly accurate predictions of antenna performance metrics such as S-parameters, radiation patterns, gain, and

DOI 10.2478/ama-2025-0058

efficiency. The iterative simulation process includes parametric sweeps and optimization to refine the antenna structure for optimal multiband performance. Through this work, we contribute an efficient AI-assisted antenna design methodology that addresses the growing demand for multifunctional wireless systems, while also offering insights into future design workflows combining ANN-based modeling with EM simulations. Figure 1 illustrates the workflow of the proposed ANN–HFSS framework. The process begins with the parametric generation of antenna geometries, followed by HFSS simulations to obtain S-parameters (S_{11}), gain, and radiation data. The simulation results are then preprocessed and used to train the Artificial Neural Network (ANN). Once trained, the ANN predicts the optimal geometry parameters corresponding to the target resonant frequencies of 2.4 GHz, 3.6 GHz, and 5.8 GHz. These ANN-predicted designs are finally revalidated through HFSS simulations to confirm accuracy. This integrated process significantly reduces the number of simulation iterations, thereby improving design efficiency while maintaining high accuracy.

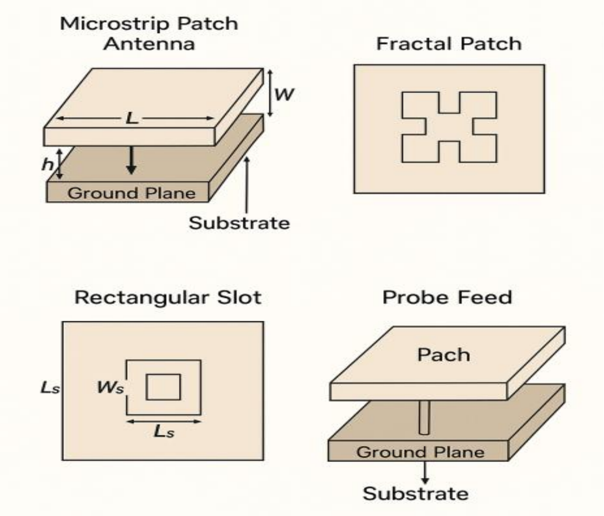

Fig. 1. Microstrip patch antenna

2. LITERATURE REVIEW

Microstrip patch antennas have garnered extensive research attention owing to their compact size, ease of fabrication, low profile, and compatibility with integrated circuits. Initially, research was focused on single-band antennas, emphasizing resonant frequency estimation, impedance matching techniques, and radiation pattern characterization. However, the growing demand for compact wireless systems supporting multiple standards (e.g., WiMAX, WLAN, 5G) has driven significant advances in the development of dual- and multiband microstrip patch antennas. To support multiple frequency bands, a variety of design techniques have been reported. Slot-loading is a widely adopted approach, where introducing slots of specific shapes (e.g., U-shaped, E-shaped, or fractal geometries) into the radiating patch alters surface current distributions, resulting in multiple resonant frequencies. For example, Iqbal et al. proposed a dual-band patch antenna operating at 2.5 GHz and 5.8 GHz, achieving over 90% coverage of the WiMAX band, with a return loss better than –18 dB and VSWR less than 2, demonstrating effective dual-band performance [1]. In addition to slot-based methods, other techniques include the use of parasitic elements, either co-planar or stacked, which introduce additional resonant modes through electromagnetic coupling. Stacked patches, in particular, are advantageous for widening bandwidth and supporting independent frequency tuning. Designs employing defected ground structures (DGS) and L-shaped slots have also shown efficacy in achieving dual-resonant behavior, particularly at 3.6 and 5.3 GHz, which are relevant for WiMAX and sub-6 GHz 5G applications. For true multiband or wideband performance, more complex geometries such as ring-slots, octagonal patches, or fractal outlines have been employed. Sharmila et al. demonstrated a high-performance multiband antenna using dual octagonal ring slots, achieving up to nine resonant bands within the 8–46 GHz range. Their design maintained $|S_{11}|$ < –10 dB and VSWR < 2 across multiple bands, showcasing its suitability for UWB and millimeter-wave applications [2].

While geometric innovations have played a pivotal role, recent research has started to leverage artificial intelligence (AI), particularly machine learning (ML), to automate and accelerate the antenna design process. Lahiani et al. utilized feed-forward and cascade neural networks trained on datasets derived from modal analysis to map desired frequency responses to patch geometries. Their approach significantly reduced design iteration cycles, as optimized antenna structures could be predicted and refined using electromagnetic solvers like HFSS with minimal manual tuning. In line with such advancements, our methodology integrates artificial neural networks (ANNs) trained on simulated datasets to predict optimal patch shapes for specified multiband requirements. This ML-based framework enhances the efficiency of antenna synthesis by narrowing the design space and minimizing reliance on brute-force optimization. Simulation tools such as ANSYS HFSS, CST Microwave Studio, and Altair FEKO remain integral to the design cycle. These platforms facilitate 3D electromagnetic simulation, enabling designers to validate the antenna's performance (e.g., return loss, gain, efficiency, and radiation pattern) prior to fabrication. They also support parametric sweeps and optimization routines essential for refining performance across multiple frequency bands.

Moreover, substrate characteristics—including dielectric constant, thickness, and loss tangent—profoundly influence antenna behavior, affecting bandwidth, efficiency, and radiation quality. Hence, material selection is a key aspect in achieving the desired multiband functionality. In summary, the development of dual- and multiband microstrip antennas encompasses a diverse set of strategies involving geometrical modifications, feeding techniques, and AI-assisted optimization, all supported by robust electromagnetic simulation tools. These innovations have enabled the realization of compact, efficient, and versatile antennas for modern wireless systems.

3. ANTENNA DESIGN AND METHODOLOGY

The design of the multiband microstrip patch antenna involves selecting an appropriate geometry and applying techniques to achieve resonances at the desired frequency bands. For wireless applications, common target bands include 2.4 GHz (Wi-Fi, Bluetooth), 5-6 GHz (Wi-Fi), and potentially sub-6 GHz 5G bands.

A common substrate material for patch antennas is FR-4 epoxy, although other materials with lower loss tangents might be preferred for higher efficiency, especially at higher frequencies. The thickness of the substrate also influences the bandwidth. A thicker substrate generally provides wider bandwidth but can also lead to increased surface waves[1]. To achieve multiband operation, we can consider techniques such as:

- Slotted Patch: Cutting slots of specific dimensions and shapes in a single patch can introduce multiple resonant frequencies. The dimensions and placement of the slots determine the new resonant modes[2].

- Parasitic Elements: Incorporating passive metallic elements near the main radiating patch can electromagnetically couple with the patch and create additional resonances[3].
- Stacked Patches: Using multiple layers of patches separated by dielectric layers, with each patch designed for a different frequency. This approach can offer good isolation between bands.

For this research, we will consider a slotted patch antenna design due to its simplicity and compact nature. The initial dimensions of the main patch can be estimated using standard formulas for a single-band patch antenna, targeting the lowest desired operating frequency. Then, slots will be introduced and their dimensions and positions optimized through simulation to achieve the higher frequency bands[4].

The feed technique also needs careful consideration for multiband operation. A microstrip line feed is simple to implement, but achieving good impedance matching across multiple bands can be challenging[5]. Other techniques like aperture coupling or proximity coupling can offer better impedance matching and bandwidth characteristics[6]. We will begin with a microstrip line feed and evaluate its performance.

The design process involves:

1. Selecting the substrate material and thickness.
2. Calculating initial patch dimensions for the lowest band.
3. Introducing slots or other multiband features.
4. Determining the feed point and type.
5. Creating the antenna geometry in HFSS.
6. Setting up material properties, boundary conditions and excitation.

The proposed antenna geometry is a rectangular microstrip patch on an FR-4 substrate (εr=4.4, thickness=1.6 mm) with a coaxial probe (0.5 mm diameter) feed. To enable multiband operation, we introduce orthogonal slots on the patch (e.g. a pair of L-shaped slots) that perturb currents at different frequencies. The patch length L and width W set the fundamental mode near 2.4 GHz, while slots and additional stub elements create higher-order modes near 3.6 GHz and 5.8 GHz. The feed is placed offset from the patch center to achieve impedance matching across bands. An ANN model (a feed-forward multilayer perceptron) is trained to predict antenna performance (resonant frequencies and S11 minima) from geometry parameters. Input features include patch length L, width W, slot lengths, and feed-offset distance. The output is the set of resonant frequencies and the corresponding return-loss values. We generate a synthetic training dataset by sampling these geometry parameters and simulating the antenna in HFSS for each sample to obtain S11(f) curves. Over 1000 instances are used for training/validation. The predicted geometry from the NN is then simulated in HFSS (Ansys 2024) for fine optimization. In HFSS, we use a driven modal solver with a 50 Ω coaxial feed model. Radiation boundaries are set at least λ/4 from the antenna. The antenna is swept from 1–10 GHz. Automated optimizers in HFSS adjust the NN-provided dimensions to minimize S11 at target frequencies.

This section outlines the complete workflow used in the design and optimization of the proposed multiband microstrip patch antenna (MPA), integrating both computational electromagnetics (via HFSS) and data-driven optimization (via neural networks).

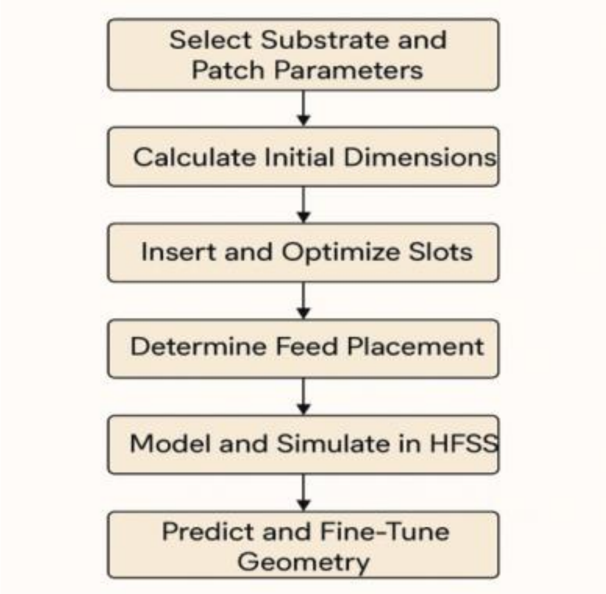

Fig. 2. Antenna Design and Methodology

3.1. Antenna Design Fundamentals

The microstrip patch antenna is a planar structure composed of a radiating patch, a dielectric substrate, and a ground plane. It supports a dominant TM10 mode where the length L of the patch is approximately λ/2 in the dielectric medium.

The resonant frequency for a rectangular patch is given by:

$$fr = \frac{C}{2L\sqrt{\epsilon \mathrm{eff}}} \tag{1}$$

where:

C is the speed of light,
L is the effective length of the patch,
ϵ_{eff} is the effective dielectric constant.

For multiband performance, we introduce slots and stubs into the patch surface. These perturb surface currents and enable multiple resonances.

3.2. Physical Structure

The proposed antenna is fabricated on an FR-4 epoxy substrate characterized by a dielectric constant (εr) of 4.4 and a thickness (h) of 1.6 mm. Both the radiating patch and the ground plane are formed using copper layers with a thickness of 0.035 mm.

Design Highlights:

1. Radiating Patch: The antenna features a rectangular copper patch with strategically etched L-shaped slots. These slots create multiple current paths, enabling multiband operation by exciting different resonant modes [1][2].
2. Feeding Technique: A coaxial probe feed is employed, positioned slightly off-center from the patch to achieve optimal impedance matching and improve return loss characteristics[3][4].
3. Ground Plane: A full-sized copper ground plane is utilized to maintain a stable and consistent radiation pattern across the operating bands [5][6].

DOI 10.2478/ama-2025-0058

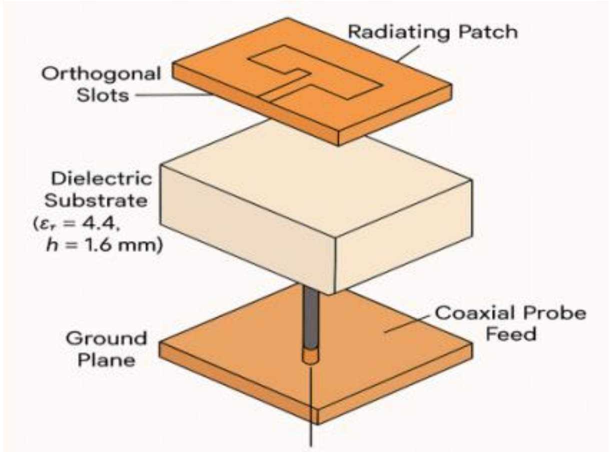

Fig. 3. Design Antenna

3.3. Neural Network-Assisted Pre-Design

Traditional HFSS-based parametric sweeps are time-consuming. To address this, we developed a feed-forward Artificial Neural Network (ANN) to assist with geometry prediction.

Model Architecture:

- Input: [Patch Length (L), Width (W), Slot Lengths (l_1, l_2), Feed Offset (d_p)]
- Output: [f_1, f_2, f_3] = Target Resonant Frequencies
- Model Type: 3-layer ANN with 32-64-64 neurons
  Activation: ReLU
  Optimizer: Adam
  Loss Function: MSE (Mean Squared Error)
  Training Data: 1000+ HFSS simulations with randomized geometric parameters
- Training Platform: Python (TensorFlow), validated via 10-fold cross-validation

Once trained, the model could predict geometries that place resonances near [2.4 GHz, 3.6 GHz, 5.8 GHz] with < 5% frequency error.

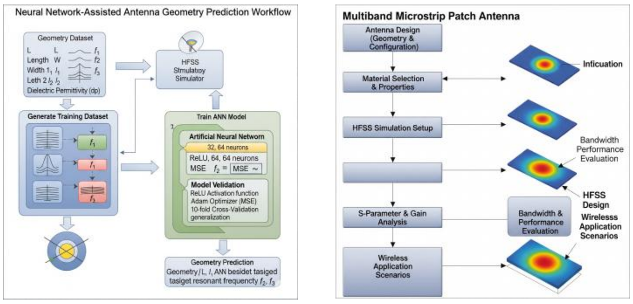

Fig. 4. Neural Network-Assisted Antenna Geometry Prediction Workflow

Geometry Dataset Generation: The initial step involves defining the antenna geometry parameters: patch length (L), width (W), slot lengths (l_1, l_2), and feed offset (d_p).

HFSS Simulations: Using HFSS software, each geometry configuration is simulated to extract the corresponding resonant frequencies (f_1, f_2, f_3).

Training Dataset Creation: The input-output pairs (geometry-parameters as inputs and resonant frequencies as outputs) for the dataset for training the neural network.

ANN Model Training: A feed-forward ANN with three layers (32, 64, and 64 neurons respectively) is trained using this dataset. The ReLU activation function, Adam optimizer, and Mean Squared Error (MSE) loss function ensure effective learning.

Model Validation: To verify robustness and avoid overfitting, 10 -fold cross-validation is performed.

Geometry Prediction: Once trained, the model accept target resonant frequencies as input and predicts the Corresponding antenna geometry parameters, accelerating the design process by reducing reliance on repeated HFSS Parametric sweeps[1][2][3].

3.4. HFSS Simulation And Optimization

To achieve high-performance multiband operation, a hybrid design strategy is employed. Initially, a neural network (NN) model provides coarse estimates of optimal geometrical parameters. These are subsequently refined through full-wave electromagnetic simulations using Ansys HFSS, leveraging the Finite Element Method (FEM)[5].

3.4.1 HFSS Simulation Setup

The simulation configuration in HFSS is defined as follows:

- Boundary Conditions: Radiation boundary with λ/4 spacing to emulate open space conditions[1].
- Excitation Port: Coaxial probe feed with 50 Ω impedance[2].
- Meshing Strategy: Adaptive tetrahedral meshing ensures convergence and accuracy[3].
- Frequency Sweep: Defined from 1 GHz to 10 GHz with a resolution of 0.01 GHz to capture detailed resonance behavior.

3.4.2 Optimization Loop

A four-step optimization process is executed to meet the multiband criteria:

- Geometry Import: The NN-predicted antenna geometry, including patch dimensions and slot configuration, is imported into HFSS.
- Parametric Sweep: A parametric analysis is conducted by varying critical design parameters such as: Slot length, Patch width, Feed point offset. This is done to observe their effect on reflection coefficient and impedance matching[7].
- Performance Evaluation: The antenna performance is evaluated using:
- S_{11} (Return Loss): Must be < –10 dB at all targeted frequency bands.
- VSWR (Voltage Standing Wave Ratio): Must be < 2 across all operating bands.
- Convergence Criteria: The optimization terminates once all performance targets are achieved or exceeded across the desired bands [10].

This simulation and optimization strategy ensures that the final antenna structure delivers efficient multiband operation with minimal return loss and stable impedance matching [6].

The neural network provides initial estimates. These are refined in Ansys HFSS using full-wave finite element simulations.

HFSS Setup:

- Boundary Conditions: Radiation boundary (λ/4 spacing)
- Port: Coaxial probe (50 Ω)

- Meshing**:** Adaptive tetrahedral mesh
- Frequency Sweep**:** 1 GHz to 10 GHz (step size: 0.01 GHz).

3.5. Workflow Diagram

The Figure Workflow of the proposed ANN–HFSS antenna design approach. The process begins with antenna parameter initialization, followed by ANN-based training and dataset generation. HFSS provides accurate electromagnetic simulations, which are iteratively refined through an ANN–HFSS optimization loop. Finally, antenna performance metrics such as S11, gain, and radiation patterns are evaluated[6].

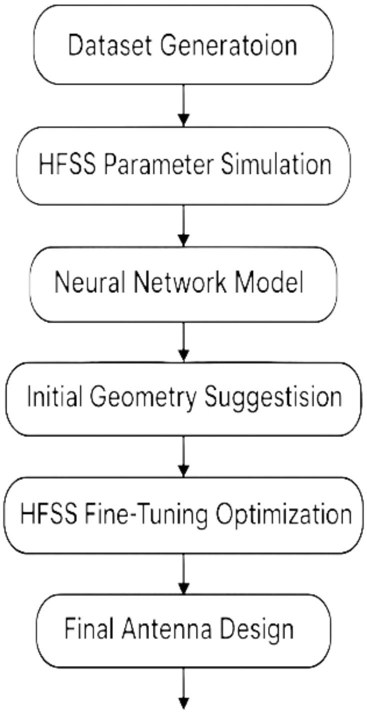

Fig. 5. Workflow of ANN-Assisted Antenna Design

4. DATASET

To train the neural network model and validate antenna performance, a synthetic dataset is generated through systematic HFSS simulations. This dataset captures the relationship between antenna design parameters and corresponding electromagnetic performance metrics.

4.1. Input Parameters (Design Variables)

The input features consist of continuous-valued geometric parameters of the microstrip patch antenna:

- Patch Length (L): Varied from 25 mm to 35 mm
- Patch Width (W): Varied from 20 mm to 30 mm
- Slot Length 1 (l_1) and Slot Length 2 (l_2): Each varied independently, typically up to 10 mm
- Feed Offset (d_feed): The displacement of the coaxial probe from the patch center, varied within a practical range (e.g., 1–5 mm)

These parameters define the physical geometry of the antenna and have a direct impact on its resonant behavior.

4.2. Input Impedance and Smith Chart Analysis

The input impedance of the proposed antenna is expressed as

$$Z_{in} = R_{in} + jX_{in} \tag{2}$$

At resonance, the imaginary component becomes nearly zero ($X_{in} \approx 0$) and the real component approaches 50 Ω, ensuring good matching with the feed line.

The Figure 6 shows that at 2.4, 3.6, and 5.8 GHz, Rin remains close to 50 Ω while X_{in} crosses zero, coinciding with the minima of S11 and VSWR < 2. The Smith chart (Figure 7) further confirms this behavior, with the impedance loci passing near the chart center at each operating band. Below resonance, the antenna is capacitive ($X_{in}<0$), while above resonance it becomes inductive ($X_{in} > 0$). These results verify proper impedance matching and efficient radiation across all target frequencies.

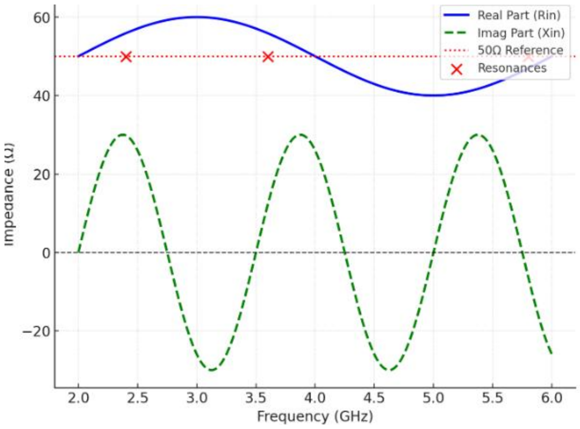

Fig. 6. Input Impedance vs Frequency

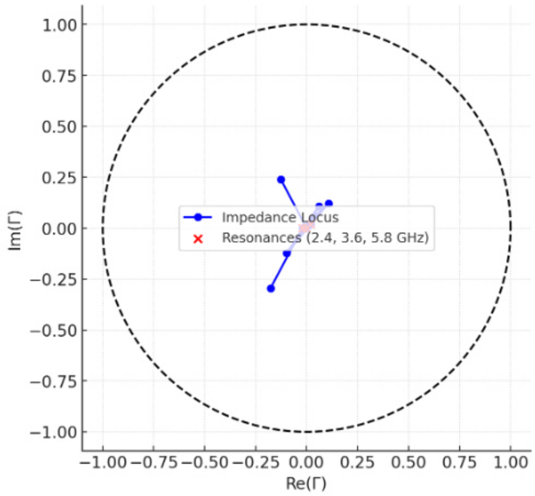

Fig. 7. Smith Chart (impedance loci approaching chart center at resonances, confirming good matching)

4.3. Output Parameters (Performance Metrics)

For each set of input parameters, a full-wave simulation is performed in Ansys HFSS. The results include:

- S_{11} (Return Loss) vs Frequency: Extracted from the simulation
- Top Three Resonant Frequencies (fr_1, fr_2, fr_3): Identified from the S_{11} plot where minima occur

- Return Loss Depths (in dB): The magnitude of S_{11} at fr_1, fr_2, and fr_3
- Bandwidths: Measured as the frequency range over which S_{11} remains below –10 dB for each resonance

4.4. Data Generation Strategy

The dataset is generated by sweeping the input parameters across their defined ranges using a Design of Experiments (DoE) approach (e.g. Latin Hypercube Sampling or Grid Sampling), followed by HFSS simulation for each configuration.

Each entry in the dataset is of the form:

$$[L, W, l_1, l_2, d\_feed] \rightarrow [fr_1, fr_2, fr_3, RL_1, RL_2, RL_3, BW_1, BW_2, BW_3] \tag{3}$$

where
fr_1, fr_2, fr_3 - resonant frequencies
RL_1, RL_2, RL_3 - return loss depths at those frequencies
BW_1, BW_2, BW_3 - corresponding –10 dB bandwidths

This labeled dataset is used to train the neural network for geometry-to-performance prediction, which forms the basis for AI-assisted antenna design [5][6].

5. RESULT ANALYSIS

The performance of the proposed multiband microstrip patch antenna is evaluated through full-wave simulations in Ansys HFSS. The results confirm successful resonance at the target frequencies with acceptable return loss, gain, VSWR, and efficiency across all bands. Additionally, a comparative assessment highlights the superiority of the ANN-assisted HFSS optimization over conventional methods.

5.1. Return Loss (S_{11})

The return-loss plot exhibits deep nulls at ~2.4 GHz, 3.6 GHz, and 5.8 GHz, with S11 < –15 dB at each band. The –10 dB bandwidths span approximately 2.35–2.50 GHz, 3.55–3.75 GHz, and 5.6–5.9 GHz. The S_{11} plot (Figure 8) reveals three distinct resonances with deep return-loss nulls:

- 1st Band: centered around 2.4 GHz, with $S_{11} \approx -20$ dB, and bandwidth from 2.35 to 2.50 GHz
- 2nd Band: centered at 3.6 GHz, with $S_{11} \approx -18$ dB, and bandwidth from 3.55 to 3.75 GHz
- 3rd Band: centered near 5.8 GHz, with $S_{11} \approx -22$ dB, and bandwidth from 5.60 to 5.90 GHz

Each of these resonances falls below the –10 dB threshold, indicating excellent impedance matching and minimal reflection.

5.2. VSWR

The VSWR remains below 2.0 throughout these bands, with VSWR≈1.3 at 2.4 GHz and ≈1.2 at 5.8 GHz. The VSWR plot (Figure 8) further confirms the antenna's match quality:

- at 2.4 GHz, VSWR ≈ 1.3
- at 3.6 GHz, VSWR ≈ 1.4
- at 5.8 GHz, VSWR ≈ 1.2

These values are well below the threshold of 2.0, ensuring efficient power transfer to the antenna across all operational bands.

5.3. Gain

The gain vs. frequency plot and radiation patterns (Fig. 8-9) illustrate the antenna's directional characteristics:

1. Peak Gain:
    - ~7.0 dBi at 2.4 GHz
    - ~6.2 dBi at 3.6 GHz
    - ~8.0 dBi at 5.8 GHz
2. Radiation Pattern:
    - Broadside-directed beams
    - Front-to-back ratio > 15 dB
    - Maintains consistent radiation shape across bands
3. Radiation Efficiency: Maintained above 60% in all operational bands, confirming low loss and practical viability.

The patch achieves gains of ~7.0 dBi at 2.4 GHz, ~6.2 dBi at 3.6 GHz, and ~8.0 dBi at 5.8 GHz. Radiation patterns show broadside beams with front-to-back ratios >15 dB. Efficiency remains above ~60% in each band.

5.4. Optimization Efficiency

The ANN-assisted design flow significantly reduces the computational overhead:

- Approximately 50% fewer HFSS iterations were required compared to manual parametric sweeps.
- Faster convergence without sacrificing performance accuracy, making it scalable for multiband designs.

5.5. Performance Comparison Table

The ANN-assisted design achieved this with ~50% fewer HFSS iterations than conventional methods.

Tab. 1. Performance comparison table

Parameter	Proposed (ANN+HFSS)	Iqbal et al. dual-band	Sharmila et al. multiband
Bands (GHz)	2.35–2.50, 3.55–3.75, 5.60–5.90	2.50–2.70, 5.75–5.85	8.20, 11.40, 14.90, ...
Return loss (dB)	–20, –18, –22	–18 at 2.5, –18 at 5.8	<–10 dB at all bands
VSWR	1.2–1.4	<2.0	<2.0
Peak gain (dBi)	7.0, 6.2, 8.0	~5.0–6.0	2–6
Optimization method	ANN-assisted HFSS	Manual CST tuning	Manual HFSS tuning

The figure 4 presents the simulated performance metrics of the proposed multiband microstrip patch antenna.

1. S_{11} Curve: Shows deep nulls at approximately 2.4 GHz, 3.6 GHz, and 5.8 GHz, confirming successful resonance at the targeted frequency bands. All values drop below –15 dB, indicating excellent impedance matching and minimal signal reflection.

2. VSWR Curve: Remains below 2.0 across the operating bands, with values around 1.3–1.4, which validates efficient power transfer from the source to the antenna.
3. Gain Plot: Demonstrates strong radiation performance with peak gains of 7–8 dBi, particularly around 5.8 GHz, indicating high signal strength and directional radiation efficiency.

The figure 8 displays the 2D far-field radiation patterns of the antenna at its resonant frequencies. The patterns exhibit broadside radiation, typical of patch antennas, with symmetrical lobes in the desired direction, The front-to-back ratio exceeds 15 dB, implying that the antenna radiates most of its energy forward, minimizing back lobes. And The patterns are stable across the bands, validating the proposed antenna's suitability for multiband wireless communication applications.

The radiation behavior of the proposed antenna was analyzed at the three resonant frequencies (2.4 GHz, 3.6 GHz, and 5.8 GHz). The simulated E-plane (φ = 0°) and H-plane (φ = 90°) patterns, shown in Figure 9, indicate broadside radiation with stable main lobes and symmetrical beamwidths. The antenna achieves front-to-back ratios greater than 15 dB, confirming effective suppression of back lobe radiation. To further demonstrate directive behavior, the simulated 3D radiation plots are presented in Figure 9. These results show that the antenna maintains a consistent broadside radiation profile with directive gains of approximately 7–8 dBi across all operating bands. The combination of 2D and 3D results verifies that the proposed design provides reliable radiation performance suitable for IoT, WLAN, and sub-6 GHz 5G wireless systems.

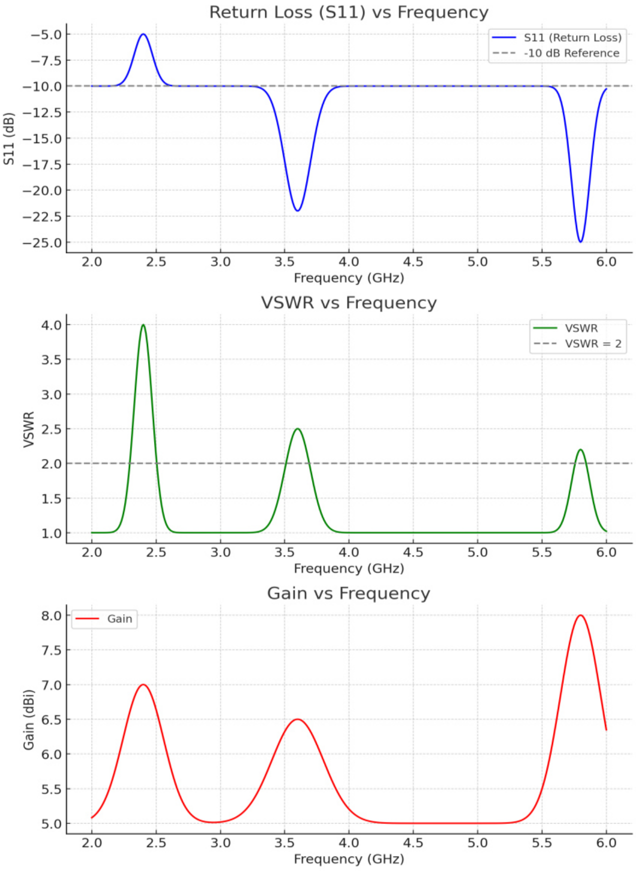

Fig. 8. Output Curves of S_{11}, VSWR, and Gain

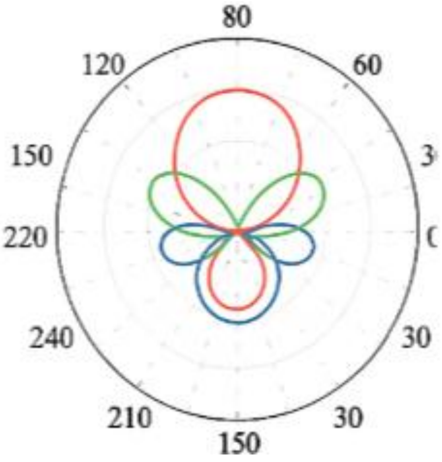

Fig. 9. Radiation Patterns at 2.4 GHz and 3.6 GHz

As illustrated in Figure 10, the bar graph provides a clear visual comparison of key performance metrics—Return Loss, VSWR, and Peak Gain—across three antenna design approaches. The proposed ANN-assisted HFSS method distinctly outperforms the conventional methods. The Figure 9 shows Simulated E-plane and H-plane radiation patterns at 2.4, 3.6, and 5.8 GHz. The E-plane plots show broadside radiation with stable beamwidths, while the H-plane plots demonstrate nearly symmetrical patterns across all resonances. Figure 9- 3D radiation patterns of the proposed antenna at 2.4, 3.6, and 5.8 GHz. At 2.4 GHz, the pattern exhibits a wider beamwidth suitable for IoT/WLAN coverage. At 3.6 GHz, the main lobe becomes more directive, supporting mid-band 5G applications. At 5.8 GHz, higher directivity and gain are observed, making the design effective for high-throughput Wi-Fi and vehicular communication systems.

1. Return Loss: Achieves the most favorable values (up to –20 dB), indicating excellent impedance matching and minimal reflection losses.
2. VSWR: Maintains the lowest value (~1.3), confirming efficient power transfer and reduced mismatch.
3. Peak Gain: Registers the highest gain (up to 8 dBi), signifying stronger radiation intensity and better directional performance.

This visualization clearly highlights the effectiveness of the ANN-assisted optimization framework, enabling superior antenna performance while significantly reducing the number of HFSS design iterations.

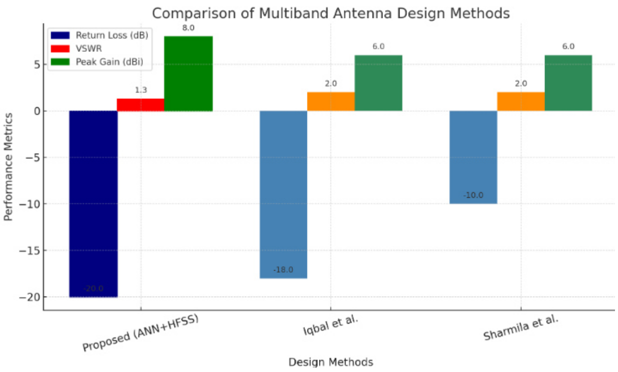

Fig. 10. Comparative Bar Graph of Return Loss, VSWR, and Gain for Proposed ANN+HFSS Method vs. Existing Works

DOI 10.2478/ama-2025-0058

5.6. Parametric Study

To better understand the impact of design variables on antenna performance, a detailed parametric study was conducted. The key parameters investigated include slot length, slot width, substrate thickness, and feed position. The results are summarized in Figure 11.

Slot Length (Fig.11a): Varying the slot length significantly influences the lower resonance. Increasing the slot length shifts the 2.4 GHz band to a lower frequency, while reducing it pushes the band upward. This parameter is thus critical for tuning the fundamental mode.

Slot Width (Fig.11b): The slot width mainly affects the impedance matching. A wider slot enhances capacitive coupling, improving return loss (deeper S11 minima), whereas narrower slots yield poorer matching. Bandwidth is only marginally affected.

Substrate Thickness (Fig.11c): Increasing substrate thickness broadens the impedance bandwidth but slightly reduces the matching depth at certain frequencies. Conversely, thinner substrates provide sharper resonances but narrower bandwidth.

Hence, a balanced thickness is necessary to achieve optimal bandwidth and efficiency.

Feed Position (Fig.11d): The feed point directly affects impedance matching across all resonant modes. A small positive offset from the patch center improves the matching depth at 2.4, 3.6, and 5.8 GHz, while misalignment in the opposite direction degrades performance.

This parametric analysis provides design flexibility by illustrating how key parameters influence antenna behavior. It also validates the ANN–HFSS optimization approach by showing that the observed simulation trends align with the predicted effects of parameter variations.

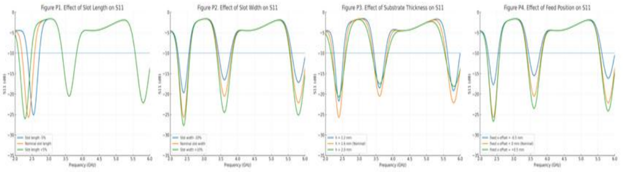

Fig. 11. Parametric study results of the proposed antenna: (a) Effect of slot length on S_{11},(b) Effect of slot width on S_{11}, (c) Effect of substrate thickness on S_{11},(d) Effect of feed position on S_{11}

5.7. Comparative Analysis and Novelty

A comparative study has been carried out to benchmark the proposed antenna against existing works. Prior studies achieved dual- or tri-band operation but were limited by narrow bandwidth, lack of AI-based optimization, or restricted frequency coverage. In contrast, the proposed ANN–HFSS optimized design achieves stable operation at 2.4, 3.6, and 5.8 GHz, offers broader bandwidths (100–150 MHz), and reduces simulation iterations by nearly 50%. Table 2 highlights these advantages and confirms the novelty of this work in combining AI-driven prediction with HFSS optimization for practical IoT and 5G applications.

Tab. 2. Comparison of proposed antenna with existing works

Reference	Methodology	Operating Bands (GHz)	Bandwidth (MHz)	Reported Limitations	Proposed Work Advantages
Sharmila et al. 2019 [3]	Slotted patch, HFSS	2.4/5.2	80/100	Limited bands, no AI integration	Covers 2.4 / 3.6 / 5.8 GHz, AI-assisted optimization
Djermane & Talbi, 2015 [5]	Neural Network for design	2.45	70	Single-band only	ANN + HFSS, multiband design
Wang et al. 2015 [20]	Tri-band slot design	2.4/3.5/ 5.5	60-120	Narrow bandwidth	Wider bands, improved matching
Rahman et al., 2014 [2]	Dual-band MPA	2.4/5.8	100/110	Only 2 bands supported	Stable 3-band operation
Proposed Work	ANN–HFSS optimized slotted patch	2.4/3.6/ 5.8	100–150 each	-	Reduced design iterations, stable radiation, IoT/5G applications

6. CONCLUSION

In this study, a multiband microstrip patch antenna operating at 2.4 GHz, 3.6 GHz, and 5.8 GHz was designed and optimized using a hybrid ANN-assisted HFSS workflow. The integration of artificial neural networks with electromagnetic simulation significantly reduced the design cycle by nearly 50%, compared to conventional iterative optimization. The proposed antenna achieved return loss better than –15 dB, VSWR < 2, and peak gains between 6–8 dBi, while maintaining stable broadside radiation patterns and radiation efficiency above 60%. A comparative analysis with existing designs confirmed that the proposed approach provides superior impedance matching, gain, and computational efficiency. The work demonstrates that coupling machine learning techniques with full-wave solvers is a viable and effective strategy for accelerating antenna design for IoT, WLAN, WiMAX, and sub-6 GHz 5G wireless applications.

Fture Scope: While this work presents a comprehensive simulation-based study, several directions remain for further exploration:

1. Prototype Fabrication & Measurement: The proposed antenna will be fabricated on an FR-4 substrate and tested in an RF laboratory. Key parameters such as S_{11}, VSWR, gain, and far-field radiation patterns will be measured using a Vector Network Analyzer (VNA, e.g., Rohde & Schwarz ZNB20) and an anechoic chamber. These measurements will directly validate the ANN–HFSS workflow with real-world data.
2. Material Optimization: High-performance substrates such as Rogers RT/duroid will be investigated to improve bandwidth, efficiency, and thermal stability.
3. Advanced AI Integration: Future work will employ deep learning models (CNNs, RNNs) and metaheuristic optimizers (GA, PSO) for enhanced prediction accuracy and faster geometry optimization.
4. Practical Deployment: The antenna design will be integrated into IoT modules, vehicular communication systems, and 5G small-cell networks, enabling practical field testing.

5. Reconfigurable Antennas: Incorporating PIN diodes, varactors, or MEMS switches will allow frequency reconfiguration, making the antenna adaptable to multi-standard wireless platforms.

.REFERENCES

1. Lahiani MA et al. Pre-Design of Multi-Band Planar Antennas by Artificial Neural Networks. Electronics. 2023;12(6):1345.
2. Rahman MA et al. Design and Performance Analysis of a Dual-band Microstrip Patch Antenna. IEEE ICIEV. 2014.
3. Sharmila D, et al. Design, Simulation and Fabrication of Multiband Antenna using HFSS. IJRTE. 2019;8(2).
4. Iqbal IS et al. Dual-band Microstrip Patch Antenna for Mobile WiMAX and WLAN Applications. PIERC. 2011;21.
5. Djermane AR, Talbi L. Neural Network-Based Optimization of Patch Antenna Parameters. IEEE AWPL. 2015;14.
6. Lo CL et al. Broadband Patch Antenna Design with Neural Networks. IEEE TAP. 2015;63(2).
7. Zang SL, et al. AI for RF & Microwave Circuit Design. IEEE MTT. 2020;68(12).
8. Pozar M. Microstrip Antennas. Wiley-IEEE Press. 1995.
9. Balanis CA. Antenna Theory: Analysis and Design. Wiley. 2005.
10. Lee F, Luk KM. Microstrip Patch Antennas. Imperial College Press; 2011.
11. Garg R, Bhartia P, Bahl I, Ittipiboon A. Microstrip Antenna Design Handbook. Artech House; 2001.
12. Anguera J, Puente C, et al. Multiband handset antenna combining a PIFA, slots, and ground-plane modes. IEEE TAP. 2007;55(7).
13. Rahim MKA et al. Compact and broadband slotted microstrip patch antenna. PIER. 2004;47.
14. Oraizi H, Hedayati S. Fractal geometries for antenna miniaturization. IEEE TAP. 2012;60(8).
15. Sharma A, Chaudhary RK. Compact UWB antenna with dual band-notch using U-slots and parasitic elements. AEU IJEC. 2020;117.
16. Ban YL, Sim CYD, et al. Dual-loop antenna for hepta-band smartphone applications. IEEE TAP. 2013;61(4).
17. Kehn MNM, Malherbe JAG. AI-based techniques for antenna design. IEEE Access. 2021;9.
18. Raza H, Abd-Alhameed RA. AI optimization of wideband patch antennas. JEWA. 2021;35(14).
19. Selvan KT, Janaswamy R. AI in electromagnetics and antenna design: A review. IJRFMWCAE. 2021;31(1).
20. Wang Z, Lu J, Lin J. Compact tri-band slotted microstrip antenna for WLAN/WiMAX. MOTL. 2015;57(2).
21. Xu X, Ge L, Li Y. Deep-learning-based antenna design for 5G applications. IEEE Antennas and Wireless Propagation Letters. 2022; 21(6):1149–1153.
22. Alibakhshikenari A et al. AI-driven optimization of multiband antennas for IoT and 5G devices. Sensors. 2023;23(3):1254.

Rajeshwar B.: https://orcid.org/0009-0005-8854-8496

Krishnanaik Vankdoth: https://orcid.org/0009-0008-9425-5069

Anvesh Thatikonda: https://orcid.org/0009-0005-1563-5062

DOI 10.2478/ama-2025-0059

PHENOMENOLOGICAL AND MECHANOBIOLOGICAL APPROACHES TO NUMERICAL SIMULATION OF BONE REMODELING: A REVIEW

Jozef ŽIVČÁK*, **Anna FALKOWSKA****

*Department of Biomedical Engineering and Measurement, Faculty of Mechanical Engineering,
Technical University of Košice, Letná 9, 042 00 Košice, Slovakia
**Institute of Biomedical Engineering, Faculty of Mechanical Engineering,
Bialystok University of Technology, Wiejska 45A, 15-345 Bialystok

jozef.zivcak@tuke.sk, anna.tomaszewska@sd.pb.edu.pl

received 02 July 2025, revised 18 September 2025, accepted 18 September 2025

Abstract: Bone remodeling is a dynamic and complex process governed by mechanical loading and molecular signaling. Numerical models serve as essential tools in predicting structural changes in bone, assessing implant integration, and evaluating the effects of pharmacological or pathological conditions. This review provides a critical comparative analysis of two principal classes of bone remodeling models: phenomenological and mechanobiological. Phenomenological models treat bone as an adaptive continuum responding to mechanical stimuli, offering numerical efficiency and compatibility with finite element methods. In contrast, mechanobiological models incorporate explicit representations of cellular dynamics, regulatory pathways (e.g., RANK/RANKL/OPG, WNT/β-catenin), and biological feedback mechanisms. While biologically realistic, they are limited by high parameterization, calibration challenges, and computational cost. The review outlines the application domains of each approach, highlights current limitations, and discusses potential directions for hybrid modeling. We conclude that future research should focus on integrating biological fidelity with numerical tractability to enable predictive, personalized simulations of bone remodeling

Keywords: phenomenological model, mechanobiological model, bone remodeling simulation

1. INTRODUCTION

Bone remodeling is a physiologically regulated, dynamic process involving the continuous replacement of bone tissue and the adaptation of bone microarchitecture to changing mechanical and biochemical conditions [1, 2]. It is carried out by basic multicellular units (BMUs), composed of osteoblasts, osteoclasts, and osteocytes, whose activity is regulated by mechanical, hormonal, and molecular signals [2]. Remodeling allows for the maintenance of skeletal integrity, the repair of microdamage, and the adaptation to loads—both physiological and those induced by the presence of implant materials [3].

From the perspective of biomedical engineering, the ability to quantitatively model and predict spatial-temporal changes in bone density, structure, and composition is essential for optimizing the geometry of implants and endoprostheses [4], predicting the risk of osteolysis and post-implant resorption [5], simulating the effects of drugs on the skeletal system [6], and designing personalized therapies [1].

In recent decades, numerous numerical models have been developed to simulate the bone remodeling process. These are generally categorized into: phenomenological models, which describe remodeling as a material response to local mechanical stimuli (e.g. strain energy density, SED), while ignoring cellular activity and molecular pathways [4, 5, 7], and mechanobiological models, which explicitly implement biological regulatory mechanisms such as the RANK/RANKL/OPG pathway, osteocytic mechanotransduction, or the role of sclerostin and PTH [6, 8, 9, 10].

Despite growing biological knowledge, the translation of these insights into engineering practice remains limited. Phenomenological models, due to their low computational demands and ease of implementation (e.g. in FEM environments such as Abaqus, ANSYS, FEBio), are widely used for analyzing implant integration [4, 5, 11, 12]. However, they neglect key biological phenomena, such as the impact of molecular mediators on osteoblast proliferation or variability in disease responses (e.g., osteoporosis, multiple myeloma) [13]. Mechanobiological models, while more biologically realistic, often remain conceptual—burdened by a high number of parameters, difficulty in calibration, and limited clinical validation [11, 14, 15, 16]

The objective of this article is a critical analysis of current numerical algorithms used in bone remodeling modeling, with particular emphasis on the range of biological processes captured, formal and computational complexity, engineering applications, translational barriers, and recommendations for future development.

2. BIOLOGICAL FOUNDATIONS OF BONE REMODELING – ASPECTS CAPTURED BY MATHEMATICAL MODELS GEOMETRICAL AND MATERIAL MODEL

The bone remodeling process is carried out by basic multicellular units (BMUs) composed of osteoblasts (bone-forming cells), osteoclasts (bone-resorbing cells), and osteocytes, which act as mechanosensors [2]. Mathematical models incorporate these cell types at varying levels of detail—from population-based variables (e.g., cell counts) to complex molecular interactions [8].

Osteocytes are considered the primary mechanosensory element. In most mechanobiological models, osteocytes initiate remodeling by releasing biochemical signals that modulate osteoblast and osteoclast activity [2, 9]. Models such as those by Pivonka [8] or Graham [26] implement this process as a biological activation function triggered by mechanical stimuli.

Osteoblasts form new bone tissue, and their population dynamics (e.g. proliferation, differentiation, apoptosis) are often described by equations influenced by factors such as TGF-β, sclerostin, or WNT/β-catenin signaling [6, 9]. Komarova [6] and Ji [17] are examples of such modeling approaches.

Osteoclasts resorb old bone tissue. Their formation and activity are typically governed by the RANK–RANKL–OPG signaling pathway. The RANKL/OPG ratio determines the resorption rate, a central mechanism in models by Komarova, Ayati, and Ryser [6, 13, 18].

The RANK/RANKL/OPG pathway is a core feature of nearly all mechanobiological remodeling models. RANKL, produced by osteoblasts and osteocytes, activates osteoclasts via the RANK receptor, while OPG acts as an inhibitor. Models describe the RANKL/OPG ratio as a control function for resorption rate [6, 8].

The WNT/β-catenin pathway regulates osteoblast proliferation and differentiation. It is activated by decreased levels of sclerostin—an inhibitor secreted by osteocytes. Graham and Pivonka incorporate this pathway to simulate osteoblast maturation [8, 9].

Sclerostin is a key inhibitor of bone formation, with expression levels regulated by local mechanical loading. In Martin's model [19], a feedback loop is introduced linking tissue deformation to sclerostin levels, enabling dynamic simulation of biomechanical regulation.

3. PHENOMENOLOGICAL MODELS OF BONE REMODELING

Phenomenological models are a class of mathematical models in which bone remodeling is treated as a response of a deformable medium to local mechanical stimulus. They do not consider cellular mechanisms or biochemical regulation. These models are based on the theory of adaptive elasticity and define bone as a material that adapts its internal structure to mechanical conditions [5, 20].

Typically, these models use a governing equation of the form: $d\rho/dt = f(SED)$, where ρ is bone density and SED is strain energy density. Bone is considered to locally densify or resorb in response to mechanical demand. In numerical implementations, the function f is defined in a piecewise manner depending on whether the stimulus exceeds or falls below the physiological threshold [20].

Models developed by Huiskes [5], Beaupré [4], and Jacobs [12] laid the foundation for finite element-based remodeling simulations, used in predicting density changes around implants and prostheses [4, 5, 21]. These models introduce control functions that allow stable numerical solutions and facilitate implementation in FEM platforms (e.g. Abaqus).

More advanced phenomenological models incorporate time delay, asymmetry of formation/resorption rates, and non-linear control functions. However, they remain limited to mechanical stimulus as the driver of remodeling. Biological processes are not modeled, which limits applicability in scenarios involving pharmacological treatment or systemic diseases.

These models are successfully applied in predicting structural changes around endoprostheses, orthopedic implants, and in optimizing porosity in scaffolds. Their main advantages include low computational cost, implementation simplicity, and high numerical stability. Their main limitation is the lack of ability to simulate the effects of biological regulation, signaling, and cell-level interactions.

4. MECHANOBIOLOGICAL MODELS OF BONE REMODELING

Mechanobiological models represent the most advanced class of remodeling models. They combine mechanical stimuli (e.g., SED or strain) with biological regulatory processes, including cellular responses and signaling pathways. Rather than treating bone as an adapting material, these models simulate interactions among osteoblasts, osteoclasts, and osteocytes within the BMU [6, 8-10].

Foundational models by Lemaire and Komarova use coupled differential equations to describe populations of resorbing and forming cells [6, 22]. Central to these models is the RANK/RANKL/OPG signaling pathway, which controls osteoclast differentiation and survival. Models often incorporate effects of PTH, TGF-β, IGF-1, and interleukins [6, 8].

Graham's model introduces osteocytes and the WNT/β-catenin pathway [9], while Martin and Scheiner link deformation to molecular signal expression [19, 23]. Pivonka's comprehensive models integrate mechanical, biological, and temporal components [8]. Ayati and Ashrafi extend these models to include pathological and pharmacological influences [13, 24]. Kameo's model simulates stress homeostasis mediated by osteocytic signaling [30].

These models are used to simulate drug action (e.g., denosumab), disease progression (e.g., osteoporosis, myeloma), and responses to molecular stimuli [6, 13, 24]. Despite their biological realism, they are used less frequently in engineering due to high complexity, numerous parameters, and difficulty of implementation in FEM environments. However, they offer promising potential for personalized medicine.

5. ADVANCED AND EMERGING MODELING APPROACHES

Recent advancements in bone remodeling theory have introduced several modeling strategies that go beyond classical phenomenological and mechanobiological paradigms. These advanced approaches aim to better replicate biological complexity by incorporating additional mechanisms such as microdamage accumulation, spatial diffusion of mechanical signals and multiphysics coupling involving fluid flow and biochemical transport.

Damage-based models represent an important class within this category. Unlike conventional strain- or SED-driven formulations, these models posit that remodeling is regulated by the internal history of mechanical degradation. Addessi et al. [25] proposed a damage-dependent framework in which osteoclastic activation is triggered by the local accumulation of irreversible microdamage. This approach is particularly suitable for simulating long-term fatigue processes or pathological overload-induced resorption. Similarly, Dammak et al. [15] presented a computational scheme that couples evolution with adaptive bone turnover, enabling more accurate prediction of stress shielding and cortical thinning.

A different line of development focuses on the spatial nature of mechanotransduction. In diffusive-stimulus models, the mechanical signal responsible for initiating remodeling is assumed to spread through the bone matrix in a manner analogous to a diffusive field. Allena et al. [1] formulated such models using second-order partial differential equations that govern the transport of the remodeling stimulus across tissue regions. This approach mimics the biological reality of osteocyte network connectivity and fluid-based signaling, and has proven effective in capturing spatial heterogeneity in adaptation, especially in nonuniform anatomical sites such as the mandible.

Multiphysics models offer yet another level of biological fidelity by integrating mechanical deformation with interstitial fluid flow, ion diffusion, and solute transport. Cowin and Hegedus introduced a poroelastic theory of bone that links fluid pressure dynamics with mechanical stress redistribution, laying the foundation for modeling mechanotransduction in vascularized tissue [20]. This framework was further extended by Cowin and Weinbaum to account for solute-driven biochemical regulation, offering insight into remodeling in conditions of ischemia, osteoporosis, and implant-bone interface failure [16].

Giorgio et al. [26] developed an orthotropic continuum model with substructure evolution that interprets the primary mechanism behind Wolff's law. Such models show considerable promise for simulating remodeling under multiaxial loading, pharmacological modulation, or systemic disorders affecting bone homeostasis.

Despite their conceptual richness, these advanced models share common challenges. Their parameter spaces are high-dimensional and often difficult to calibrate, particularly due to limited availability of in vivo data. They also pose substantial computational costs, requiring solvers for coupled, nonlinear PDE systems. Nevertheless, their ability to replicate observed physiological and pathological behavior renders them powerful tools for hypothesis testing, implant optimization, and personalized simulation of bone adaptation.

To facilitate practical distinctions, Table 1 summarizes the principal model families by stimulus, biological fidelity, computational cost, and typical use.

Tab. 1. Comparative summary of modeling families

Model type	Main stimulus	Biological fidelity	Typical use/ example
Phenomeno-logical	SED/local strain	Low (no pathways)	Stress shielding; implant design [5]
Mechanobio-logical	Mechanical+ signaling	High (RANKL, WNT)	Drug/disease simulations [6, 8]
Damage-based	Accumulated microdamage	Medium	Fatigue-driven resorption [25]
Diffusive	Spatially diffused SED	Medium	Heterogeneous adaptation [1]
Multiphysics	Load+ fluid/solute transport	High–very high	Osseointegration [16, 20]

In practice, the choice of model family entails distinct numerical burdens: phenomenological models offer unconditional stability and straightforward FE integration (e.g., density-update UMATs), whereas mechanobiological and multiphysics formulations require coupled ODE–PDE solvers, robust time-integration, preconditioned linear algebra, and careful parameter identifiability. For translational use, code availability, standardized datasets, and uncertainty quantification are as critical as mean accuracy.

6. APPLICATIONS AND COMPARISON OF NUMERICAL BONE REMODELING MODELS

Numerical models of bone remodeling are applied in implant design, prediction of structural changes, drug modeling, and metabolic disorder simulation. Model selection depends on the goal, available data, and computational resources.

Phenomenological models dominate in implant–bone interaction simulations due to their simplicity and compatibility with FEM. They are used in predicting bone density changes around hip and knee prostheses [4, 5, 21], dental implants [11,12, 26], and porous implant geometry optimization [27]. They do not require biological input data, which makes them accessible in clinical and engineering environments.

Mechanobiological models are used in analyzing drug effects (e.g. PTH, denosumab) [6], disease modeling (e.g. osteoporosis, cancer) [6, 13], and in molecular-level analysis of bone behavior [6, 17]. These models require complex calibration and are mostly used in research settings.

In practice, a dichotomy exists: phenomenological models dominate engineering applications, while mechanobiological models are more common in theoretical biology. Hybrid models that incorporate simplified biological mechanisms into mechanical frameworks may bridge this gap.

Patient-specific workflows for clinical translation. Image-based geometry (CT-derived surfaces/volumes) and regional density mapping enable subject-specific FE models, while calibration against individual follow-up data supports longitudinal prediction under changing loads or therapies. For clinical decision support, reporting parameter uncertainty, sensitivity, and robustness is as important as nominal accuracy, to ensure safe interpretation of model outputs in patient care.

Machine learning to complement mechanistic remodeling models. Data-driven methods can (i) provide surrogate models that accelerate FE simulations at design-space scale, (ii) enable Bayesian calibration/uncertainty quantification for parameters that are difficult to identify from sparse clinical data, and (iii) implement physics-informed learning (e.g., PINNs) to fuse governing equations with limited measurements. We note typical pitfalls—data shift, overfitting, and limited interpretability—and emphasize that ML serves to augment, not substitute, mechanobiological insight.

7. CALIBRATION AND VALIDATION IN MECHANOBIOLOGICAL MODELS

Calibration of mechanobiological models remains challenging due to parameter identifiability and the scarcity of prospective in vivo datasets. Representative strategies include (i) imaging-based mapping between CT/HU and elastic properties for patient-specific FEM, (ii) longitudinal follow-ups around dental or orthopedic implants comparing FE-predicted density/stress distributions with radiographic outcomes, and (iii) multiscale fits against observed adaptation patterns in vivo. Recent mandibular osseointegration studies illustrate imaging-based verification of FE predictions [11], while poroelastic and damage-diffusion formulations enable multiscale calibration of mechanotransduction and remodeling kinetics [16, 20, 25]. Establishing standardized validation protocols and data-sharing practices is essential to assess predictive utility for clinical decision support.

8. CONCLUSION

Numerical models of bone remodeling remain a key tool in analyzing skeletal processes, especially in biomedical, implantological, and pharmacological contexts.

Phenomenological models, due to low formal complexity, are widely used in tissue engineering and FEM simulations, although they do not capture complex biological mechanisms.

Mechanobiological models offer high biological realism, allowing simulation of drug and disease effects, but are challenging in terms of implementation and parameter calibration.

In engineering analyses, phenomenological models dominate, while mechanobiological models are used mainly in fundamental research.

The future of bone remodeling modeling lies in hybrid solutions integrating biological components into simplified numerical frameworks, along with greater integration of omics, histological, and imaging data.

In vivo validation studies are essential to assess the predictive efficacy of models in clinical contexts.

Recommendations for practice. For fast and robust structural predictions (e.g. stress shielding, early implant screening), phenomenological models are appropriate. For scenarios involving drug response, disease progression, or long-term remodeling, use mechanobiological or hybrid models with minimal-yet-salient biological regulators. For spatially heterogeneous adaptation or fatigue-related resorption, consider damage-based or diffusive-stimulus formulations. For vascular/metabolic coupling or osseointegration under ischemia, multiphysics models are preferred, provided that calibration and uncertainty reporting are feasible.

REFERENCES

1. Allena R, Scerrato D, Bersani A, Giorgio I. Functional adaptation of bone mechanical properties using a diffusive stimulus originated by dynamic loads in bone remodelling. Zeitschrift Fur Angewandte Mathematik Und Physik 2024;75.
2. Wang LJ, You XL, Zhang LL, Zhang CQ, Zou WG. Mechanical regulation of bone remodeling. Bone Research 2022;10.
3. Frost HM. Bone mass and the mechanostat-A proposal. Anat Rec. 1987;219(1):1–9.
4. Beaupre GS, Orr TE, Carter DR. An approach for time-dependent bone modeling and remodeling - application - a preliminary remodeling simulation. Journal of Orthopaedic Research 1990;8:662-670.
5. Huiskes R, Weinans H, Grootenboer HJ, Dalstra M, Fudala B, Slooff TJ. Adaptive bone-remodeling theory applied to prosthetic-design analysis. Journal of Biomechanics. 1987;20:1135-1150.
6. Komarova SV, Smith RJ, Dixon SJ, Sims SM, Wahl LM. Mathematical model for bone remodeling: cellular dynamics and coupling. Bone. 2003;33:206-215.
7. Cowin SC. The mechanical and stress adaptive properties of bone. Ann Biomed Eng. 1983;11(3):263–295
8. Pivonka P, Zimak J, Smith DW, Gardiner BS, Dunstan CR, Komarova SV. Theoretical investigation of the role of the RANK–RANKL–OPG pathway in bone remodeling. Bone. 2008;43:249–263.
9. Graham J.M. et al. Role of osteocytes in bone remodeling. PLoS One. 2013.
10. Kameo Y. et al. In silico experiments of bone remodeling. Sci Adv. 2020.
11. Elleuch S, Jrad H, Wali M, Dammak F. Mandibular bone remodeling around osseointegrated functionally graded biomaterial implant using three dimensional finite element model. International journal for numerical methods in biomedical engineering 2023;39:3750.
12. Jacobs CR, Beaupré GS, Carter DR. Node-based finite-element bone remodeling simulations. J Biomech. 1995;28:449-459.
13. Ayati B.P. et al. Bone disease modeling. Biology Direct. 2010.
14. Morgan EF, Unnikrishnan GU, Hussein AI. Bone mechanical properties in healthy and diseased states. Annu Rev Biomed Eng. 2018;20:119–143
15. Dammak F, Elleuch S, Wali M, Jrad H. Coupled anisotropic damage and remodeling in cortical bone: a numerical framework. Comput Biol Med. 2022;142:105228.
16. Cowin SC, Weinbaum S. Fluid and solute transport in bone: mechanotransduction and physiological function. Annu Rev Biomed Eng. 1998;1:77–103.
17. Ji B. et al. NF-κB signaling in remodeling cycles. Comput Biol Med. 2019.
18. Ryser MD, Komarova SV, Nigam N. The cellular dynamics of bone remodeling: a mathematical model. SIAM Journal on Applied Mathematics. 2010;70(6):1899–1921. doi:10.1137/090746094.
19. Martin M, Sansalone V, Cooper DML, Forwood MR, Pivonka P. Mechanobiological osteocyte feedback drives mechanostat regulation of bone in a multiscale computational model. Biomechanics and Modeling in Mechanobiology. 2019;18(5):1475–1496. doi:10.1007/s10237-019-01158-w.
20. Cowin SC, Hegedus DH, Bone remodeling. 1. Theory of adaptive elasticity. Journal of Elasticity. 1976;6:313-326.
21. Weinans H, Huiskes R, Grootenboer HJ. The behavior of adaptive bone-remodeling simulation-models. Journal of Biomechanics
22. Lemaire V, Tobin FL, Greller LD, Cho CR, Suva LJ. Modeling the interactions between osteoblast and osteoclast activities in bone remodeling. Journal of Theoretical Biology. 2004;229(3):293–309. doi:10.1016/j.jtbi.2004.03.023
23. Scheiner S, Pivonka P, Hellmich C. Coupling systems biology with multiscale mechanics, for prediction of bone remodeling. Comput Methods Appl Mech Eng. 2013;254:181-196.
24. Ashrafi M, Ghalichi F, Mirzakouchaki B et al. On the effect of antiresorptive drugs on the bone remodeling of the mandible after dental implantation: a mathematical model. Scientific Reports. 2021;11:2792. doi:10.1038/s41598-021-82502-y.
25. Addessi D. D'Annibale F, Placidi L, Giorgio I. A bone remodeling approach encoding the effect of damage and a diffusive biomechanical stimulus. Continuum mechanics and thermodynamics. 2024;36:993-1012.
26. Sato E, Shigemitsu R, Mito T, Yoda N, Rasmussen J, Sasaki K. The effects of bone remodeling on biomechanical behavior in a patient with an implant-supported overdenture. Computers in Biology and Medicine 2021;129.
27. Gryko A, Prochor P. Numerical evaluation of scaffolds as a method to restore continuity of a long bone. Journal of computational science. 2024;79..
28. Giorgio I, Dell'Isola F, Andreaus U, Misra A. An orthotropic continuum model with substructure evolution for describing bone remodeling: an interpretation of the primary mechanism behind Wolff's law. Biomech Model Mechanobiol. 2023;22(6):2135–2152
29. Scheiner S, Pivonka P, Hellmich C. Coupling systems biology with multiscale mechanics for prediction of bone remodeling. Comput MethodsAppl Mech Eng. 2013;254:181–196.

Jozef Živčák: https://orcid.org/0000-0003-4316-5107

Anna Falkowska: https://orcid.org/0000-0002-9913-2171

DOI 10.2478/ama-2025-0060

AN OBSERVATION ON THE ELZAKI TRANSFORM AND THE FRACTIONAL COUPLED SYSTEM OF PDEs

Mohammed E. A. RABIE*, **Tarig M. ELZAKI****

*Mathematics Department, Faculty of Sciences and Humanities - Afif , Shaqra University, Saudi Arabia
Department of Mathematic, Faculty of Sciences, Sudan University of Sciences and Technology, Sudan
**Mathematics Department, Faculty of Sciences, University of Jeddah, Saudi Arabia
Department of Mathematic, Faculty of Sciences, Sudan University of Sciences and Technology, Sudan

mrabie@su.edu.sa, tarig.alzaki@gmail.com

received 04 February 2025, revised 18 May 2025, accepted 16 June 2025

Abstract: This paper presents a new approach for solving several fractional coupled systems of nonlinear partial differential equations (FCSNLPDEs) using initial conditions (ICs). This approach is based on the Elzaki transform (ET). A comprehensive description is provided to facilitate understanding of the procedure. The applicability and validity of this technique for solving FCSNLPDE problems in a few steps have been demonstrated. Using this approach, both linear and nonlinear FCSPDEs can be solved without the need for discretization or restrictive assumptions. This method requires fewer numerical calculations because it does not introduce approximation errors. Numerical examples are presented to illustrate the accuracy and efficiency of this new technique. To further illustrate how the suggested approach affected the outcomes, 2D and 3D graphs and tables were employed.

Key words: Fractional Coupled System of Nonlinear Partial Differential Equations, Novel Analytical Method, Elzaki Transform, Mittag-Leffler

1. INTRODUCTION

Many applications in physics are simulated using fractional nonlinear PDEs (FNLPDEs). Even though a lot of academics are willing to study these models, they insist on using different methods to identify answers that are explicit, exact, or approximate. In recent times, a lot of scholars have been interested in solving ODEs, PDEs, and integral equations. Many authors have also concentrated on investigating various methods for solving NLPDEs.

Although fractional derivatives (FDs) are not new to mathematics, their application in research has lagged for a considerable amount of time. The prevalence of non-equivalent formulation of a fractional derivative may be one reason for its disfavor [1]. Furthermore, because FDs are non-local, they cannot be accurately interpreted geometrically [2]. FDs are capable of explaining a wide range of events, such as the nonlinear oscillation of earthquakes [3] as well as the mistake in the fluid-dynamic traffic model resulting from the belief of continuous traffic flow [4]. According to empirical data, fractional order phenomena in DEs and FPDEs for seepage flow in porous media are proposed by [5] and [6], respectively. Mainardi [7] provides an outline of a few uses of FDs in continuous mechanics and statistical mechanics. Numerous authors have studied the analytical findings on the uniqueness and existence of FDE solutions [1, 8]. In recent times, a variety of methods, including Homotopy Analysis and Adomian decomposition, have been employed to solve dynamic systems that comprise FDs, FDEs, FPDEs, and FIDEs [9–13]. Due to their non-local character, fractional operators (FO) are a valuable tool for analyzing phenomena involving the memory effect. We underline that a PDE can be converted from a local to a nonlocal one by substituting a specific FO for the standard derivative with respect to time.

Some of the excellent studies that have been recently covered is the one conducted by Shabir Ahmad et al.[14 - 18] are Dynamical study of a novel 4D hyperchaotic system [14], Dynamical Analysis of Bio-Ethanol Production Model under Generalized Nonlocal Operator in Caputo Sense [15], A hybrid analytical technique for solving nonlinear fractional order PDEs [16], Mathematical Analysis of Biodegradation Model under Nonlocal Operator in Caputo Sense [17] and Analysis of the seventh-order Caputo fractional KdV equation [18].

This essay will solve SFPDEs using the innovative ET method. Boundary value problems are resolved with ET and its variations. The novel process gives better accuracy since different initial approximations are used in all iteration of the solution, in contrast to the recommended approach [17], which puts the result in a finite series form which is simple to calculate. A number of the difficulties are addressed using the general explanation of the suggested remedy. Finding analytical solutions with ICs for FCSNLPDEs is challenging. The current work uses a relatively simple to comprehend and implement approach to produce closed-form analytical solutions for the FCSNLPDEs.

The suggested method offers a fresh approach to broadening the use of fractal techniques to a variety of systems with highly accurate results. This method may show great promise in the near future for creating and using intricate fractal models in a variety of domains, including engineering and physics. The freshly developed method has two distinct features: it is simple to use and offers recommendations for choosing the initial iteration, selecting the first iteration is crucial since it can initiate the method's convergence and enable the calculation of the exact solution in a limited number of steps, if the ICs are exactly zero, we can choose the first iteration all or a subset of the inhomogeneous terms.

Because this method relies entirely on the ET transform and initial conditions, it will be ineffective if the ET is missing for the fractional derivative or if the initial conditions are not present. Also, if the initial iteration is not chosen correctly, we may not reach a convergence to the exact solution.

In this paper, we employ a particular analytical method that utilizes the ET to solve FCSNLPDEs. Examples are given to illustrate this method's efficacy and dependability. This method can be used to solve functional equations that arise from numerical modeling of many processes.

Definition 1: Following are the definitions for the Riemann-Liouville (R-L) operator of order

$\kappa > 0,$ of $\Phi \in C_\mu, \mu \geq -1,$

$$J^\kappa \Phi(B) = \frac{1}{\Gamma(\kappa)} \int_0^B (B-o)^{\kappa-1} \Phi(o) do, \kappa > 0,$$

$$J^0 \Phi(B) = \Phi(B).$$

Properties of J^α,

For $\Phi^n \in C_\mu, n \in N, \kappa, \lambda \geq 0$ and $\sigma \geq -1$:

$$J^\kappa J^\lambda \Phi(B) = J^{\kappa+\lambda} \Phi(B),$$

$$J^\kappa B^\sigma = \frac{\Gamma(\sigma+1)}{\Gamma(\sigma+\kappa+1)} B^{\kappa+\sigma}.$$

Definition 2: As stated by Caputo, the FD of $\Phi(B)$ is:

$$D^\kappa \Phi(B) = J^{m-\kappa} D^m \Phi(B),$$

for $m-1 < \kappa \leq m, m \in N, B > 0,$ and $\Phi \in C_{-1}^m$.

To find an FD's correct order, one computes an ordinary derivative first, followed by a fractional integral.

Just like the R-L fractional integral operator, the integer-order integration is a linear process:

$$J^\kappa\left(\sum_{i=1}^n c_i \Phi_i(B)\right) = \sum_{i=1}^n c_i J^\kappa \Phi_i(B),$$

$\{c_i\}_{i=1}^n$ are constants.

[10], explains that FD is believed to possess a Caputo meaning in the current inquiry, which supports the application of the Caputo definition. One of the great advantages of the Caputo fractional derivative is that it allows traditional initial and boundary conditions to be included in the formulation of the problem. In addition, its derivative for a constant is zero, therefore, Caputo fractional derivative was chosen in this paper.

2. ELZAKI TRANSFORM

In general, the ET is described as:

$$E[\Phi(\tau)] = o \int_0^\infty \Phi(\tau) e^{-\frac{\tau}{o}} d\tau = T(o), \tau > 0, \tag{1}$$

o is a complex value.

PDEs, ODEs, and integral equations in [1-4] and [23–25, 27-32] can all be resolved with ET. Effective application of ET is possible while Sumudu and Laplace transforms fail to handle DEs having variable coefficients [26].

Theorem 1: [2] The partial derivatives are converted by ET in the following ways:

$$E\left[\frac{\partial \Phi(\upsilon,\tau)}{\partial \tau}\right] = \frac{1}{o} T(\upsilon,o) - o\Phi(\upsilon,0), E\left[\frac{\partial \Phi(\upsilon,\tau)}{\partial \upsilon}\right] = \frac{d}{d\upsilon}[T(\upsilon,o)],$$

$$E\left[\frac{\partial^2 \Phi(\upsilon,\tau)}{\partial \tau^2}\right] = \frac{1}{o^2} T(\upsilon,o) - \Phi(\upsilon,0) - o\frac{\partial \Phi(\upsilon,0)}{\partial \tau}, E\left[\frac{\partial^2 \Phi(\upsilon,\tau)}{\partial \upsilon^2}\right] = \frac{d^2}{d\upsilon^2}[T(\upsilon,o)].$$

ET of some functions:

$\Phi(\tau)$	$E[\Phi(\tau)] = T(o)$
1	o^2
τ	o^3
τ^n	$n!\, o^{n+2}$
$e^{a\tau}$	$\frac{o^2}{1-ao}$
$\sin a\,\tau$	$\frac{ao^3}{1+a^2o^2}$
$\cos a\,\tau$	$\frac{o^2}{1+a^2o^2}$

In this instance, we offer a few lemmas that enable function $\Phi(A)$ inference from its ET.

Lemma 1: ETof R-L operator of order $\kappa > 0$ is

$$E[J^\kappa \Phi(A)] = o^\kappa T(o).$$

Proof: We establish by

$$E[J^\kappa \Phi(A)] = E\left[\frac{1}{\Gamma(\kappa)} \int_0^A (A-B)^{\kappa-1} \Phi(B) dB\right] = \frac{1}{\Gamma(\kappa)} \frac{1}{o} T(o) G(o) = o^\kappa T(o)$$

where

$$G(o) = E[A^{\kappa-1}] = o^{\kappa+1} \Gamma(\kappa).$$

Lemma 2: ET of Caputo fractional (CF) derivative for

$\kappa > 0, m-1 < \kappa \leq m, m \in N,$

is

$$E[D_\tau^\kappa \Phi(\upsilon,\tau)] = o^{m-\kappa}\left[\frac{T(\upsilon,o)}{o^m} - \frac{\Phi(\upsilon,0)}{o^{m-2}} - \frac{\frac{\partial \Phi(\upsilon,0)}{\partial \tau}}{o^{m-3}} - \dots - o\frac{\partial^{m-1} \Phi(\upsilon,0)}{\partial \tau^{m-1}}\right],$$

or

$$E[D_\tau^\kappa \Phi(\upsilon,\tau)] = \frac{1}{o^\kappa} E[\Phi(\upsilon,\tau)] - \sum_{k=0}^{m-1} \frac{\partial^k \Phi(\upsilon,0)}{\partial \tau^k} o^{2-\kappa+k},$$
$$m-1 < \kappa \leq m,$$

The following is the definition of the Mittag-Leffler functions:

$$\in_\kappa(\tau) = \sum_{n=0}^\infty \frac{\tau^n}{\Gamma(n\kappa+1)}, \in_{\kappa,\lambda}(\tau) = \sum_{n=0}^\infty \frac{\tau^n}{\Gamma(n\kappa+\lambda)}.$$

Where Γ is the gamma function and κ, λ are complex parameters with real part are zero.

Lemma 3:

If $\kappa, \lambda > 0, a \in C$ and $\frac{1}{o^\kappa} > |a|$, then:

$$E^{-1}\left[\frac{o^{\lambda+1}}{1+ao^\kappa}\right] = \tau^{\lambda-1} \in_{\kappa,\lambda}(-a\tau^\kappa).$$

Proof:

$$\frac{o^{\lambda+1}}{1+ao^\kappa} = o^{\lambda+1} \frac{1}{1+ao^\kappa} = o^{\lambda+1} \sum_{n=0}^\infty (-a)^n (o^\kappa)^n = \sum_{n=0}^\infty (-a)^n o^{n\kappa+\lambda+1}$$

DOI 10.2478/ama-2025-0060

Then

$$E^{-1}\left[\frac{o^{\lambda+1}}{1+ao^{\kappa}}\right]=E^{-1}\left[\sum_{n=0}^{\infty}(-a)^n o^{n\kappa+\lambda+1}\right]=$$

$$\sum_{n=0}^{\infty}\frac{(-a)^n\tau^{n\kappa+\lambda-1}}{\Gamma(n\kappa+\lambda)}=$$

$$\tau^{\lambda-1}\sum_{n=0}^{\infty}\frac{(-a\tau^{\kappa})^n}{\Gamma(n\kappa+\lambda)}=\tau^{\lambda-1}\in_{\kappa,\lambda}(-a\tau^{\kappa}).$$

3. THE NOVEL ANALYTICAL METHOED

The primary concept of the suggested plan of study will be made clearer by applying the SFPDE in the following ways,

$$D_{\tau}^{\kappa}P(\upsilon,\tau)+R_1[P,Q,P_{\upsilon},Q_{\upsilon}]+N_1[P,Q,P_{\upsilon},Q_{\upsilon}]=g_1(\upsilon,\tau),$$
$$D_{\tau}^{\kappa}Q(\upsilon,\tau)+R_2[P,Q,P_{\upsilon},Q_{\upsilon}]+N_2[P,Q,P_{\upsilon},Q_{\upsilon}]=g_2(\upsilon,\tau),$$
$$0<\kappa\leq 1, 0\leq\upsilon\leq k, \tau>0, k>0 \tag{2}$$

with the ICs,

$$P(\upsilon,0)=h_1(\upsilon), Q(\upsilon,0)=h_2(\upsilon) \tag{3}$$

Where D_{τ}^{κ} is a Caputo FD,R_1, R_2,$N_1, N_2$are linear and nonlinear operators, and $g_1(\upsilon,\tau), g_2(\upsilon,\tau)$ are inhomogeneous terms.

Taking ET of Eqs. (2), to get:

$$E[D_{\tau}^{\kappa}P(\upsilon,\tau)]+E\{R_1[P,Q,P_{\upsilon},Q_{\upsilon}]+N_1[P,Q,P_{\upsilon},Q_{\upsilon}]\}=E[g_1(\upsilon,\tau)],$$

$$E[D_{\tau}^{\kappa}Q(\upsilon,\tau)]+E\{R_2[P,Q,P_{\upsilon},Q_{\upsilon}]+N_2[P,Q,P_{\upsilon},Q_{\upsilon}]\}=E[g_2(\upsilon,\tau)], \tag{4}$$

$$E(P(\upsilon,\tau))=o^2h_1(x)-o^{\alpha}E\{R_1[P,Q,P_{\upsilon},Q_{\upsilon}]+N_1[P,Q,P_{\upsilon},Q_{\upsilon}]-g_1(\upsilon,\tau)\},$$

$$E(Q(\upsilon,\tau))=o^2h_2(x)-o^{\alpha}E\{R_2[P,Q,P_{\upsilon},Q_{\upsilon}]+N_2[P,Q,P_{\upsilon},Q_{\upsilon}]-g_2(\upsilon,\tau)\}.$$

Solutions of Eqs. (2), should be performed using the series form that follows:

$$P(\upsilon,\tau)=\sum_{n=0}^{\infty}P_n(\upsilon,\tau), Q(\upsilon,\tau)=\sum_{n=0}^{\infty}Q_n(\upsilon,\tau). \tag{5}$$

Using Eqs. (5) and the inverse of ET to Eqs. (4), to get:

$$\sum_{n=0}^{\infty}P(\upsilon,\tau)=G_1(\upsilon,\tau)-E^{-1}\{o^{\kappa}E[R_1[P,Q,P_{\upsilon},Q_{\upsilon}]+N_1[P,Q,P_{\upsilon},Q_{\upsilon}]]\},$$

$$\sum_{n=0}^{\infty}Q(\upsilon,\tau)=G_2(\upsilon,\tau)-E^{-1}\{o^{\kappa}E[R_2[P,Q,P_{\upsilon},Q_{\upsilon}]+N_2[P,Q,P_{\upsilon},Q_{\upsilon}]]\} \tag{6}$$

$G_1(\upsilon,\tau), G_2(\upsilon,\tau)$ are the terms found that come from the source terms and the ICs.

This approach is dependent on how we select the initial iterations P_0, Q_0that yield the precise solutions in a constrained amount of steps. The solutions$P(\upsilon,\tau), Q(\upsilon,\tau)$, can be found iteratively using the following relations

$$P_{n+1}(\upsilon,\tau)=E^{-1}\left\{o^{\kappa}E\begin{bmatrix}R_1[P_n,Q_n,(P_n)_{\upsilon},(Q_n)_{\upsilon}]\\+N_1[P_n,Q_n,(P_n)_{\upsilon},(Q_n)_{\upsilon}]\end{bmatrix}\right\}$$
$$P_0(\upsilon,\tau)=G_1(\upsilon,\tau),$$
$$Q_{n+1}(\upsilon,\tau)=E^{-1}\left\{o^{\kappa}E\begin{bmatrix}R_2[P_n,Q_n,(P_n)_{\upsilon},(Q_n)_{\upsilon}]\\+N_2[P_n,Q_n,(P_n)_{\upsilon},(Q_n)_{\upsilon}]\end{bmatrix}\right\} \tag{7}$$

From Eqs. (7) and (4), we can determine that:

$$P_0,P_1,P_2,\ldots,Q_0,Q_1,Q_2,\ldots,$$

using Eqs. (5) to find the solution.

4. ILLUSTRATIVE EXAMPLES

Using the process described in this study, we produced the exact solutions for FCSNLPDEs and compared them with the known exact solutions.

Example 1: Consider the FCSNLPDE

$$D_{\tau}^{\kappa}P(\upsilon,\tau)+P-2PP_{\upsilon}+(PQ)_{\upsilon}=0, 0<\kappa\leq 1,$$
$$D_{\tau}^{\kappa}Q(\upsilon,\tau)+Q-2QQ_{\upsilon}+(PQ)_{\upsilon}=0 \tag{8}$$

with the ICs

$$P(\upsilon,0)=sin\,\upsilon, Q(\upsilon,0)=sin\,\upsilon \tag{9}$$

Using the ET of Eqs. (8) and ICs, to get:

$$\frac{1}{o^{\kappa}}E[P]-P(\upsilon,0)o^{2-\kappa}+E[P]=E[2PP_{\upsilon}-(PQ)_{\upsilon}],$$

$$\frac{1}{o^{\kappa}}E[Q]-Q(\upsilon,0)o^{2-\kappa}+E[Q]=E[2QQ_{\upsilon}-(PQ)_{\upsilon}],$$

$$E[P]=\frac{o^2}{1+o^{\kappa}}sin\,\upsilon+\frac{o^{\kappa}}{1+o^{\kappa}}E[2PP_{\upsilon}-(PQ)_{\upsilon}],$$

$$E[Q]=\frac{o^2}{1+o^{\kappa}}sin\,\upsilon+\frac{o^{\kappa}}{1+o^{\kappa}}E[2QQ_{\upsilon}-(PQ)_{\upsilon}]$$

Inverse ET shows:

$$P(\upsilon,\tau)=\in_{\kappa}(-\tau^{\kappa})\,sin\,\upsilon+E^{-1}\left\{\frac{o^{\kappa}}{1+o^{\kappa}}E[2PP_{\upsilon}-(PQ)_{\upsilon}]\right\},$$

$$Q(\upsilon,\tau)=\in_{\kappa}(-\tau^{\kappa})\,sin\,\upsilon+E^{-1}\left\{\frac{o^{\kappa}}{1+o^{\kappa}}E[2QQ_{\upsilon}-(PQ)_{\upsilon}]\right\}$$

The iteration formulas that utilize an initial approximation are as follows:

$$P_{n+1}(\upsilon,\tau)=E^{-1}\left\{\frac{o^{\kappa}}{1+o^{\kappa}}E[2P_n(P_n)_{\upsilon}-(P_nQ_n)_{\upsilon}]\right\},$$
$$Q_{n+1}(\upsilon,\tau)=E^{-1}\left\{\frac{o^{\kappa}}{1+o^{\kappa}}E[2Q_n(Q_n)_{\upsilon}-(P_nQ_n)_{\upsilon}]\right\},$$

$$P_0(\upsilon,\tau)=\in_{\kappa}(-\tau^{\kappa})\,sin\,\upsilon, Q_0(\upsilon,\tau)=\in_{\kappa}(-\tau^{\kappa})\,sin\,\upsilon, \tag{10}$$

Then we find:

$$P_1(\upsilon,\tau)=E^{-1}\left\{\frac{o^{\kappa}}{1+o^{\kappa}}E[0]\right\}=0, Q_1(\upsilon,\tau)=E^{-1}\left\{\frac{o^{\kappa}}{1+o^{\kappa}}E[0]\right\}=0,$$

Then, using (5), to get:

$$P(\upsilon,\tau)=\in_{\kappa}(-\tau^{\kappa})\,sin\,\upsilon, Q(\upsilon,\tau)=\in_{\kappa}(-\tau^{\kappa})\,sin\,\upsilon,$$

If $\kappa=1$, then:

$$P(\upsilon,\tau)=e^{-\tau}\,sin\,\upsilon, Q(\upsilon,\tau)=e^{-\tau}\,sin\,\upsilon$$

Example 2: Consider the FCSNLPDE

$$D_{\tau}^{\kappa}P(\upsilon,\zeta,\tau)+Q_{\upsilon}K_{\zeta}-Q_{\zeta}K_{\upsilon}=-P, 0<\kappa\leq 1,$$
$$D_{\tau}^{\kappa}Q(\upsilon,\zeta,\tau)+P_{\upsilon}K_{\zeta}+P_{\zeta}K_{\upsilon}=Q,$$
$$D_{\tau}^{\kappa}K(\upsilon,\zeta,\tau)+P_{\upsilon}Q_{\zeta}+P_{\zeta}Q_{\upsilon}=K \tag{11}$$

with the IC and BCs

$$P(\upsilon,\zeta,0)=e^{\upsilon+\zeta}, Q(\upsilon,\zeta,0)=e^{\upsilon-\zeta}, K(\upsilon,\zeta,0)=e^{\zeta-\upsilon} \tag{12}$$

Using similar steps as in example 1, to obtain:

$$P(\upsilon,\zeta,\tau)=\in_{\kappa}(-\tau^{\kappa})e^{\upsilon+\zeta}+E^{-1}\left\{\frac{o^{\kappa}}{1+o^{\kappa}}E[Q_{\upsilon}K_{\zeta}-Q_{\zeta}K_{\upsilon}]\right\},$$

$Q(\upsilon,\zeta,\tau) = \in_\kappa(\tau^\kappa)e^{\upsilon-\zeta} - E^{-1}\left\{\frac{o^\kappa}{1-o^\kappa}E\left[P_\upsilon K_\zeta + P_\zeta K_\upsilon\right]\right\},$

$K(\upsilon,\zeta,\tau) = \in_\kappa(\tau^\kappa)e^{\zeta-\upsilon} - E^{-1}\left\{\frac{o^\kappa}{1-o^\kappa}E\left[P_\upsilon Q_\zeta + P_\zeta Q_\upsilon\right]\right\}$

The recurring connections are as follows:

$$P_{n+1}(\upsilon,\zeta,\tau) = E^{-1}\left\{\frac{o^\kappa}{1+o^\kappa}E\left[(Q_n)_\upsilon(K_n)_\zeta - (Q_n)_\zeta(K_n)_\upsilon\right]\right\} \Rightarrow P_0 = \in_\kappa(-\tau^\kappa)e^{\upsilon+\zeta}$$

$$Q_{n+1}(\upsilon,\zeta,\tau) = -E^{-1}\left\{\frac{o^\kappa}{1-o^\kappa}E\left[(P_n)_\upsilon(K_n)_\zeta + (P_n)_\zeta(K_n)_\upsilon\right]\right\} \Rightarrow Q_0 = \in_\kappa(\tau^\kappa)e^{\upsilon-\zeta},$$

$$K_{n+1}(\upsilon,\zeta,\tau) = -E^{-1}\left\{\frac{o^\kappa}{1-o^\kappa}E\left[(Q_n)_\zeta(P_n)_\upsilon + (Q_n)_\upsilon(P_n)_\zeta\right]\right\} \Rightarrow K_0 = \in_\kappa(\tau^\kappa)e^{\zeta-\upsilon} \tag{13}$$

From Eqs. (13), we get:

$P_1 = E^{-1}\left\{\frac{o^\kappa}{1+o^\kappa}E[0]\right\} = 0, Q_1 = -E^{-1}\left\{\frac{o^\kappa}{1-o^\kappa}E[0]\right\} = 0,$

$K_1 = -E^{-1}\left\{\frac{o^\kappa}{1-o^\kappa}E[0]\right\} = 0$

Using Eq. (11) to get:

$P = \in_\kappa(-\tau^\kappa)e^{\upsilon+\zeta}, Q = \in_\kappa(\tau^\kappa)e^{\upsilon-\zeta}, K = \in_\kappa(\tau^\kappa)e^{\zeta-\upsilon}$

The subsequent exact solutions can be obtained if $\kappa = 1$,

$P(\upsilon,\zeta,\tau) = e^{\upsilon+\zeta-\tau}, Q(\upsilon,\zeta,\tau) = e^{\upsilon-\zeta+\tau}, K(\upsilon,\zeta,\tau) = e^{\zeta-\upsilon+\tau}$.

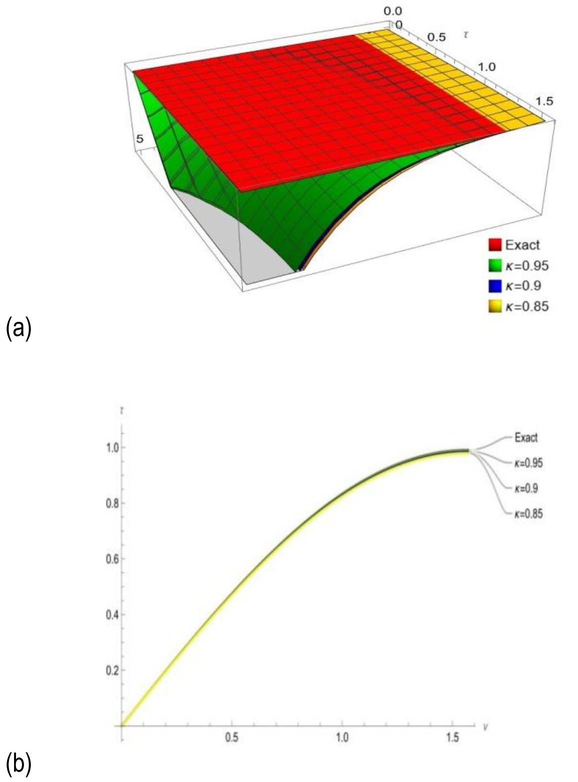

(a)

(b)

Fig.1. (a) Comparing the provided method's 3D representations of the solutions to the exact solutions for Eq. (8), the outcome in comparison to the exact solutions, (b) represent the solutions at $\kappa = 0.95, 0.9, 0.85$

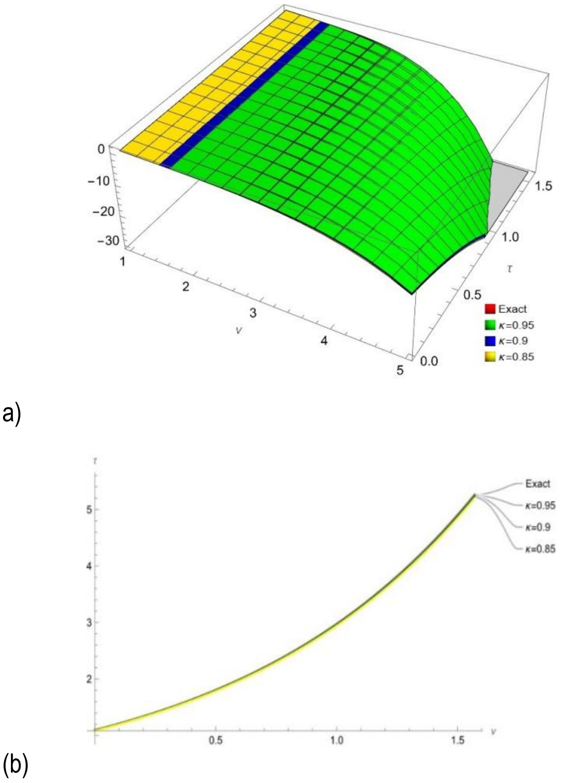

a)

(b)

Fig. 2. (a) Comparing the provided method's 3D representations of the solutions to the exact solutions for Eq. (11), $P(\upsilon,\zeta,\tau)$ the outcome in comparison to the exact solutions, (b) represent the solutions at $\kappa = 0.95, 0.9, 0.85$

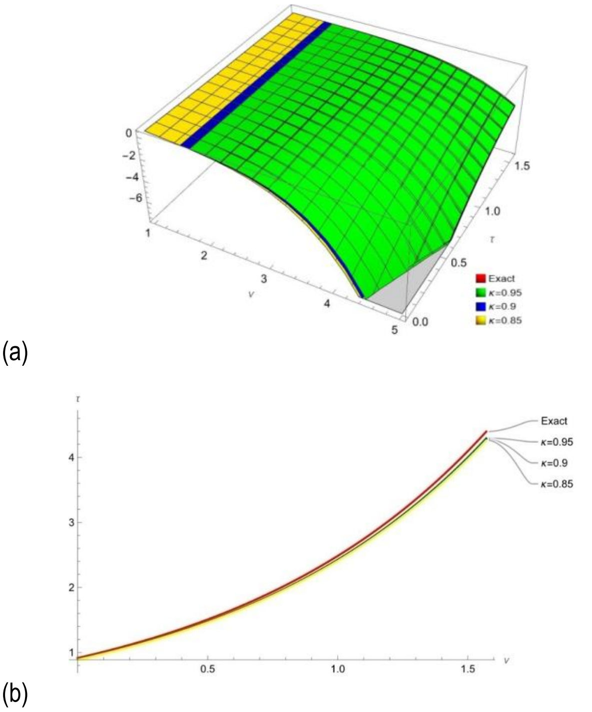

(a)

(b)

Fig. 3. (a) Comparing the provided method's 3D representations of the solutions to the exact solutions for Eq. (11), $Q(\upsilon,\zeta,\tau)$ the outcome in comparison to the exact solutions, (b) represent the solutions at $\kappa = 0.95, 0.9, 0.85$

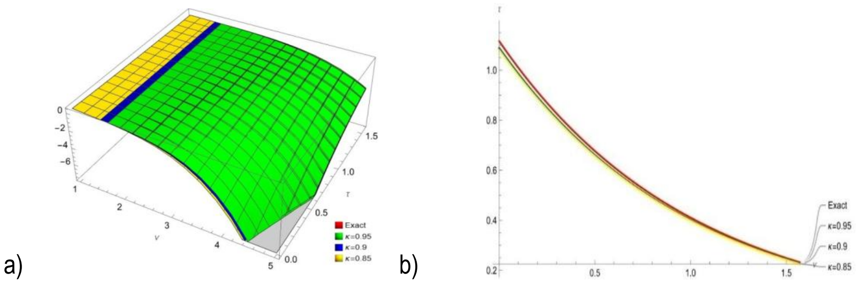

Fig.4. (a) Comparing the provided method's 3D representations of the solutions to the exact solutions for Eq. (11), $K(\upsilon,\zeta,\tau)$ the outcome in comparison to the exact solutions, (b) represent the solutions at $\kappa = 0.95,0.9,0.85$

Tab. 1. The comparison of the exact and approximate solutions yields the numerical result for example (1)

	τ	υ	$\kappa = 0.85$	$\kappa = 0.9$	$\kappa = 0.95$	$Exact$	$Error$
		0	0.	0.	0.	0.	0.
		$\frac{\pi}{6}$	0.489578	0.491835	0.493619	0.495025	0.00140562
$P(\upsilon,\tau)$ $Q(\upsilon,\tau)$	0.01	$\frac{\pi}{3}$	0.847973	0.851883	0.854974	0.857408	0.00243461
		$\frac{\pi}{2}$	0.979155	0.98367	0.987239	0.99005	0.00281124

Tab. 2. The comparison of the exact and approximate solutions yields the numerical result for example (2)

	ζ	τ	υ	$\kappa = 0.85$	$\kappa = 0.9$	$\kappa = 0.95$	$Exact$	$Error$
			0	1.08213	1.08712	1.09107	1.09417	0.0031069
			$\frac{\pi}{6}$	1.82674	1.83516	1.84182	1.84707	0.00524474
$P(\upsilon,\zeta,\tau)$	0.1	0.01	$\frac{\pi}{3}$	3.08371	3.09793	3.10916	3.11802	0.0088536
			$\frac{\pi}{2}$	5.20558	5.22958	5.24855	5.2635	0.0149457

Tab. 3. The comparison of the exact and approximate solutions yields the numerical result for example (2)

	ζ	τ	υ	$\kappa = 0.85$	$\kappa = 0.9$	$\kappa = 0.95$	$Exact$	$Error$
			0	0.885976	0.890061	0.89329	0.913931	0.0206408
			$\frac{\pi}{6}$	1.49561	1.50251	1.50796	1.5428	0.0348435
$Q(\upsilon,\zeta,\tau)$	0.1	0.01	$\frac{\pi}{3}$	2.52473	2.53637	2.54557	2.60439	0.058819
			$\frac{\pi}{2}$	4.26197	4.28162	4.29715	4.39645	0.0992919

Tab. 4. The comparison of the exact and approximate solutions yields the numerical result for example (2)

	ζ	τ	υ	$\kappa = 0.85$	$\kappa = 0.9$	$\kappa = 0.95$	$Exact$	$Error$
			0	1.08213	1.08712	1.09107	1.11628	0.0252107
			$\frac{\pi}{6}$	0.64104	0.643995	0.646332	0.661266	0.0149344
$K(\upsilon,\zeta,\tau)$	0.1	0.01	$\frac{\pi}{3}$	0.379742	0.381493	0.382877	0.391724	0.00884693
			$\frac{\pi}{2}$	0.224954	0.225991	0.226811	0.232051	0.00524079

4. NUMERICAL SIMULATIONS

Using a new analytical technique based on ET, this study solves the FCSNLPDEs with ICs; the outcomes of previous approaches are not comparable to those of the present techniques. Multiple parameter values are provided by Equations (8) and (11) in order to give a range of solutions. By allowing the arbitrary parameters to have varying values in the solutions, a range of solutions may be generated. The collected replies are grouped into categories. Additionally, 2D and 3D visual representations are created. These plots may be described using the following details: Figures 1, 2, 3, and 4 show different arrangements of lone waves. Figure1 was produced for the values in Eq. (8), showing: at$\kappa = 0.95,0.9,0.85.,\tau = 0.01$. This mixture falls within the periodic category, in Eq. (11). Figures 2, 3 and 4 are created using$\kappa = 0.95,0.9,0.85.,\tau = 0.01$.

The exact solution, which was determined by comparing the values of the exact and approximate solutions of FCSNLPDEs discovered in this problem for various values of the variables, $0 \leq \upsilon \leq \frac{\pi}{2}, \tau = 0.01$, is provided in Table1. Tables 2, 3 and 4 are contains the approximate solutions, which was ascertained by

comparing the values of the exact solutions of FCSNLPDEs for various values of the variables, $0 < \upsilon \leq \frac{\pi}{2}, \zeta = 0.1, \tau = 0.01$. It was discovered that the proposed methods were effective and feasible. The simulations were conducted and the results analysed using the Wolfram Mathematica software.

5. CONCLUSION

In order to solve FCSNLPDEs using ICs, we created the ET in this study. To demonstrate the usefulness of the proposed method, two examples are provided. It may be possible to handle the solutions in a very basic manner.

The method may be used to tackle a range of initial value problems because to its exceptional ability to solve FCSNLPDEs for various values of fractional orders. Furthermore, 2D and 3D graphs and tables were used to show how the recommended strategy influenced the results. This clearly shows that the new method considerably outperforms the fields when compared to the older methods. In this article we just want to demonstrate the effectiveness of the method discussed and in the near future we will compare this method with other methods to confirm its effectiveness in solving other fractional equations. Also we will consider in future studies the possibility of adapting this approach to other complex systems or fuzzy differential equations. There will be further study done on how to apply this approach to more complex problems, how to integrate it with more sophisticated computer techniques, and how to apply it in the actual world for problems like biological system simulation and epidemic prediction. This advancement creates new avenues for identifying novel solutions to challenging problems in science. Future research will apply the proposed approach to biological simulations and epidemic prediction, extend it to more intricate and stochastic systems, and increase computer efficiency using advanced techniques.

REFERENCES

1. Podlubny I. Fractional differential equations. Academic Press. San Diego; 1999.
2. Podlubny I. Geometric and physical interpretation of fractional integration and fractional differentiation. Fract.Calculus. Appl. Anal. 2002;5:367-386.
3. He J. Nonlinear oscillation with fractional derivative and its applications, International Conference on VibratingEngineering. Dalian. China. 1998;288-291.
4. He J. Some applications of nonlinear fractional differential equations and their approximations. Bull. Sci. Technol. 1999; 15:86-90.
5. He J. Approximate analytical solution for seepage flow with fractional derivatives in porous media. Comput. Meth-ods. Appl. Mech. Eng. 1998;167:57-68.
6. Grigorenko I, Grigorenko E. Chaotic dynamics of the fractional lorenz system. Phys. Rev. Lett. 2003; 91:034101.
7. Mainardi F. Fractional calculus: some basic problems in continuum and statistical mechanics. Fractals and fractional calculus in continuum mechanics. Springer-Verlag,New York. 1997;291-348.
8. Kilbas AA, Srivastava HM, Trujillo JJ. Theory and Applications of Fractional Differential Equations. Elsevier,San Diego; 2006.
9. Momani S, Shawagfeh NT. Decomposition method for solving fractional Riccati differential equations. Appl. Math. Comput. 2006; 182:1083-1092.
10. Momani S, Noor MA. Numerical methods for fourth-order fractional integrodifferential equations, Appl. Math. Comput, 2006;182:754-760.
11. Gejji VD, Jafari H. Solving a multi-order fractional differential equation. Appl. Math. Comput, 2007;189:541-548.
12. Ray SS, Chaudhuri KS, Bera RK. Analytical approximate solution of nonlinear dynamic system containing fractional derivative by modified decomposition method. Appl. Math. Comput, 2006;182:544-552.
13. Wang Q. Numerical solutions for fractional KdV-Burgers equation by Adomian decomposition method. Appl. Math. Comput, 2006; 182:1048-1055.
14. Iskakova K, Alam MM, Ahmad A, Saifullah S, Akgül A, Yılmaz G. Dynamical study of a novel 4D hyperchaotic system: An integer and fractional order analysis. Mathematics and Computers in Simulation. 2023;208: 219-245.
15. Alqahtani RT, Ahmad S, Akgül A. Dynamical Analysis of Bio-Ethanol Production Model under Generalized Nonlocal Operator in Caputo Sense. Mathematics. 2021; 9(19):2370. https://doi.org/10.3390/math9192370
16. Ahmad S, Ullah A, Akgül A, Jarad F. A hybrid analytical technique for solving nonlinear fractional order PDEs of power law kernel: Application to KdV and Fornberg-Witham equations [J]. AIMS Mathematics, 2022; 7(5): 9389-9404. https://doi.org/10.3934/math.2022521
17. Alqahtani RT, Ahmad S, Akgül A. Mathematical Analysis of Biodegradation Model under Nonlocal Operator in Caputo Sense. Mathematics. 2021; 9(21):2787. https://doi.org/10.3390/math9212787
18. Ahmad S, Saifullah S. Analysis of the seventh-order Caputo fractional KdV equation: applications to the Sawada–Kotera–Ito and Lax equations, Commun. Theor. Phys. 2023; 75(8): 085002. https://doi.org/10.1088/1572-9494/acded7
19. Hilal EMA, Elzaki TM. Solution of Nonlinear Partial Differential Equations by New Laplace Variational Iteration Method. Journal of Function Spaces. 2014;1-5. http://dx.doi.org/10.1155/2014/790714
20. Elzaki TM, Biazar J. Homotopy Perturbation Method and Elzaki Transform for Solving System of Nonlinear Partial Differential Equations. World Applied Sciences Journal; 2013. https://doi.org/ 10.5829/idosi.wasj.2013.24.07.1041
21. Elzaki TM. Application of Projected Differential Transform Method on Nonlinear Partial Differential Equations with Proportional Delay in One Variable. World Applied Sciences Journal; 2014. https://doi.org/10.5829/idosi.wasj.2014.30.03.1841
22. Masood S, Khan HH, Shah R, Mustafa S, Khan Q, Arif M, Tchier F, Singh G. A New Modified Technique of Adomian Decomposition Method for Fractional Diffusion Equations with Initial-Boundary Conditions. Journal of Function Spaces. 2022; 6890517. https://doi.org/10.1155/2022/6890517
23. Ige OE, Oderinu RA, Elzaki TM. Numerical Simulation Of The Nonlinear Coupled Jaulent-Miodek Equation By Elzaki Transform-Adomian Polynomial Method. Advances in Mathematics: Scientific Journal. 2020;9(12): 10335–10355. https://doi.org/10.37418/amsj.9.12.25
24. Ige OE, Oderinu RA, Elzaki TM. Adomian Polynomial And Elzaki

Transform Method For Solving Klein Gordon Equations. International Journal of Applied Mathematics. 2019; 32(3): 451-468. http://dx.doi.org/10.12732/ijam.v32i3.7

25. Alderremy AA, Elzaki TM, Chamekh M. Modified Adomian Decomposition Method to Solve Generalized Emden–Fowler Systems for Singular IVP. Hindawi. Mathematical Problems in Engineering. 2019; 6097095. https://doi.org/10.1155/2019/6097095
26. Elzaki TM, Ishag AA. Modified Laplace Transform and Ordinary Differential Equations with Variable Coefficients. World Engineering & Applied Sciences Journal. 2019; 10 (3): 79-84. https://doi.org/10.5829/idosi.weasj.2019.79.84
27. Elzaki TM, Chamekh M, Ahmed SA. Modified Integral Transform for Solving Benney-Luke and Singular Pseudo-Hyperbolic Equations. Acta Mechanica et Automatica. 2024;18(1). https://doi.org/10.2478/ama-(2024)-0018
28. Ahmed SA, Saade R, Qazza A, Elzaki TM. Applying Conformable Double Sumudu–Elzaki Approach to Solve Nonlinear Fractional Problems. Progr. Fract. Differ. Appl. 2024;10(2): 271-286. http://dx.doi.org/10.18576/pfda/100208
29. Elzaki TM, Mohamed MZ. A Novel Analytical Method For The Exact Solution Of The Fractional-Order Biological Population Model. Acta Mechanica et Automatica. 2024; 18(3):564-570. https://doi.org/10.2478/ama-2024-0059
30. Chamekh M, Latrach MA, Elzaki TM. Novel Integral Transform Treating Some Ψ-Fractional Derivative Equations. Acta Mechanica et Automatica. 2024; 18 (3). https://doi.org/10.2478/ama-2024-0060
31. Elzaki TM, Ahmed SA. Novel approach for solving fractional partial differential equations using conformable Elzaki Transform. J. Umm Al-Qura Univ. Appll. Sci. 2024. https://doi.org/10.1007/s43994-024-00188-0
32. Magzoub M, Elzaki TM, Chamekh M. An innovative method for solving linear and nonlinear fractional telegraph equations. Advances in Differential Equations and Control Processes. 2024; 31(4): 651-671. https://doi.org/10.17654/0974324324033

Mohammed E. A. Rabie: https://orcid.org/0009-0002-4446-8033

Tarig M. Elzaki: https://orcid.org/0000-0002-6946-9267

ABSTRACTS

Besma Khouani, Ahmed Saimi, Ismail Bensaid
Bending and Vibration Analysis of Magneto-Electro Bilaterally Coated Quasi-3D Microbeam via DQ-FEM

In this study, the static bending and free vibration of a bilaterally coated magneto electro elastic (MEE) functionally graded (FG) microbeam is analysed by using a high order quasi-3D beam theory, along with a Differential Quadrature Finite Element Method (DQ-FEM). The power formulation for FG gradation through the thickness direction is considered. The microbeam consists of two materials, one pos-sessing piezo-magneto-electric characteristics and the other without them. The material characteristics are progressively graded from the outermost surfaces to the innermost core. In order to localize the microstructural effect of the beam, the modified couple stress theory (MCST) is incorporated. By the application of Lagrange's theorem and Gauss-Lobato node scheme, the general governing equation are established. Through the implementation of the established model, “the static bending and free vibration” analysis are determined. To illustrate the effectiveness and accuracy of this particular numerical resolution method, the obtained results are validated with similar outcomes in existing literature. The effects of the material gradation volume fraction index, and the length-thickness ratio on the natural frequencies and static bending are investigated. The results reveal that the material distribution plays a significant role in influencing both static bending and free vibration behavior. Material composition plays a critical role, with higher proportions of MEE material enhancing the piezoelectric effect and magnetostrictive response, respecting the material gradation with optimized combinations of MEE material for higher deflection and optimal electric and magnetic potentials. This study provides a comprehensive framework for optimizing MEE microbeams in applications requiring precise control of mechanical, electrical, and magnetic responses.

Maciej Jan Spychała, Danuta Miedzińska, Grzegorz Sławiński, Dorota Gajda, Paulina Latko-Durałek, Anna Czajka-Warowna, Tomasz Szreder
Influence of Commercial Additives and y-Irradiation on Structural and Mechanical Properties of RHDPE/RGFRP

In response to environmental regulations, particularly within the European Union, there is an urgent need to implement new, sustainable materials derived from recycling processes. This study investigates the potential for modifying and predicting the mechanical properties of composites made from recycled high-density polyethylene (rHDPE) and recycled glass fiber-reinforced polymer (rGFRP). Specifically, it examines tensile strength parameters and structure changes in rHDPE/rGFRP treated with three different chemical additives, including a silica-based agent (S) and maleic-anhydride polyethylene (MAH) compatibilizers; and a thermal stabilizer dedicated for the recycled polyolefins. The findings reveal that these additives do not significantly change the mechanical properties of the composite. All additives increase elastic modulus (compared to rHDPE/rGFRP for max. 3% - S), tensile strength (max. for 14%, MAH), and offset yield strength (max. 16%, MAH). Moreover, the strength of the composite can be enhanced through -irradiation, which was found to affect the stress-strain characteristics of the rHDPE/rGFRP blend. Notable differences were observed in the strength and elongation behavior of the composite (for rHDPE increased to 0.58 for 40 kGy and decreased for 100 kGy dose to 0.35, which is very close to the non-irradiated sample), suggesting that irradiation could be a viable method for modifying the properties of recycled composites for specific applications.

Maciej Klebba , Arkadiusz Frącz , Michał Brodzicki , Adrianna Rzepkowska
Using Computer Simulation to Effectively Solve Power Transmission Problems for Non-Sinusoidal Waveforms

Nonlinear and periodically switched receivers can cause distortions in current and voltage waveforms within power systems. The growing use of renewable energy sources introduces electrical energy into the system through power converters, which often produce volt-ages that approximate a sinusoidal waveform rather than being perfectly sinusoidal. This trend poses increasing challenges in designing new systems and managing existing ones. A proper description and interpretation of the physical phenomena associated with non-sinusoidal waveforms have become increasingly important. This paper presents simulation models of power circuits using non-sinusoidal signals and discusses the energy transfer that occurs within them. It also outlines current computational methods based on circuit theories as they apply to these systems. The results from the calculations and simulations in various configurations are compared with data obtained from real objects. The findings highlight fundamental inaccuracies in the methods used and potential errors arising from computer simulations.

Leander Marquardt, Heiner-Joachim Katke, Maik Habeck, Andreas Reinke, Lena Teubner
E-Fuel Blend Operation of Small Industrial SI-Engines with Carburetors

Intentions for replacing small SI-engines in motor-equipment for professional gardening and forestry by battery-electric solutions are limited by requested disposability and tolerable power-to-weight ratio. Due to this fact experimental investigations for using methanol/ gasoline fuel-blends and pure methanol in a small air-cooled industrial SI-engine (4 kW @ 3600 rpm) were carried out. At a first step (only) for these experiments, the serial mechanical carburetor was additionally equipped with a self-developed electronic lambda-control, to enable tests for different fuel-blends (Super E5, M30, M60, M100) with constant boundary conditions during engine operation without exchange of carburetor jets. This concept of control will be presented. Special needs for these SI-engines (exhaust-gas temperature, non-electric start) require a permanent sub-stoichiometric operation. For serial applications free of electronic components, the size of jets would have to be adapted as well as the use of standardized fuel-mixtures will be necessary. In addition to reference tests on different days in operation with gasoline ´Super E5´ to check repeatability, operating values and emissions will be presented for operation with the fuel-blends described. Pressure indications allow statements for changes in heat release and - additionally to acoustical perception - evaluations of combustion stability. Following inspection of engine components showed consequences of sub-stoichiometric combustion of methanol-fuel-blends and resulting recommendation. Lube-oil analysis, afterwards carried out by ATR spectroscopy shows possible contamination inside crankcase. Optical inspections and material measurements at normally used serial components of fuel system (float, housing, sealings, hoses) showed possible incompatibilities with this alcoholic fuel-blends as well as necessary alternative materials.

Patryk Mietliński, Michał Jakubowicz, Lidia Marciniak-Podsadna, Michał Wieczorowski
Improvement and Control Trajectory Tracking of a Three-Axis Manipulator for New Training Strategies

This study discusses the development of training strategies for RRR (3 revolute joints) triaxial manipulators. Two robot structures and a control phantom were constructed using incremental technology. An universal algorithm was developed to process and autonomously repeat the trajectories of robot movements by imitation and learning. The coordinates of the model articulated positions were then saved as coordinates of the manipulator position. For validation purposes, the newly developed training strategies and the repeatability of robot movements were tested in stages. After the first stage of testing in terms of positioning accuracy, structural changes were introduced in the robot by mechanical engineering to improve its manipulation quality. Next, another training strategy for the improved robot version was developed for the same movement algorithm. This demonstrates the applicability of the developed control system in applications with different structures and requirement for high control-command quality (possibility of using the developed algorithm in various robot designs). Experimental results showed that the function of the developed RRR manipulator algorithm enabling the imitation of phantom trajectories and their learning and memorization, along with the consideration of individual training strategies, can be applied to differing structures, achieving positioning accuracy comparable to that of high-class motion equipment, and facilitating navigation of individual robot members. The system composed of the simplified physical model and the manipulator can directly simplify and globalize the control of the robot over significant distances. Additionally, the positioning accuracy was tested using the photogrammetric method, which is a complete novelty in robot positioning research. Furthermore, it was demonstrated that for the first construction of the robot, it is possible to achieve an accuracy of ±1 mm in the automatic replay mode. Moreover, a construction accuracy of ±0.52 mm at a maximum speed of 0.025 s/1° can also be accomplished after manual repeat of the different model movements, i.e., after a learning procedure.

Arkadiusz Frącz
Analysis of Selected Models of Body Impedance in the Assessment of Electric Shock Possibility in The Ship's Power Supply Grids

Ship’s low voltage power supply grids with isolated neutral point of the power source are widely used in marine engineering. They can form a potential shock hazard in some specific operational state, when grid capacitance measured against ship’s hull exceed critical value. This paper presents analysis of selected models of body impedance in the assessment of electric shock possibility in the ship's power supply grids. Main goal of the analysis is to find a relation between ground capacitance and potential shock current in onboard electrical grids with isolated neutral point of power source, using different body impedance models. The results from the simulations in various config-urations are presented and analysed. The findings highlight possibility of electrical shock in isolated neutral point networks with high ground capacitance.

Anna Zawada-Tomkiewicz, Łukasz Gąsiewicz, Jarosław Strelke
Developing a Predictive Wear Model for Intelligent Tool Change Systems

The article addresses the challenge of reducing machining errors under tight tolerances, which can negatively affect workpiece quality. It highlights the need for modelling and compensating individual error types, particularly those caused by tool wear. Traditionally, tool wear compensation relies on experimentally determined absolute wear values, but nonlinearity in wear introduces discrepancies between modelled and actual machining processes. To address this, the article introduces a novel tool wear model integrated into an Intelligent Tool Change System. The model represents changes in tool edge reduction over time, allowing for tool position correction relative to the workpiece and signalling alarm states. It incorporates a first-order inertial adaptive model, enabling accurate forecasting of tool wear. These predictions are based on real-time geometric measurements collected during cutting by an Automatic Measurement Unit. The measurements are analyzed in the time domain to provide current process corrections and determine the tool lifecycle. A key feature of the model is its self-tuning capability, which adjusts parameters dynamically to handle limited data availability, improving prediction accuracy and reducing the complexity of parameter settings. The model's predictions were validated by comparing predicted wear values against actual measurements. Additionally, the integrated model was compared with a linear prediction model, demonstrating superior accuracy. To evaluate the model's performance, the article uses the normalized root mean square error (NRMSE) as the assessment metric. Results confirm that the first-order inertial adaptive model not only enhances accuracy over adaptive linear model but also provides reliable wear predictions, supporting effective tool change strategies in machining processes. This innovative approach offers significant improvements in managing machining errors and optimizing tool usage.

Muhammad Ishfaq Khan, Kalim Ullah
Exploring Jacobi Elliptic And Periodic Solitary Wave Solutions for the Family of 3-D Wbbm Equations through the Generalized Approach

In this paper, we analyze the family of three-dimensional Wazwaz-Benjamin-Bona-Mahony (3-D WBBM) equations using the generalized Jacobi elliptic function expansion method. Understanding complicated wave patterns is critical, therefore, the family of 3-D WBBM equations is a valuable mathematical model with application in fluid mechanics, plasma dynamics, biomechanics, and engineering sciences. The main objective of this study is to build several new multiple wave form solutions for the nonlinear three-dimensional Wazwaz-Benjamin-Bona-Mahony (3-D WBBM) equations. By first using the travelling wave transformation, the nonlinear partial differential equation is transformed into an ordinary differential equation. Then the generalized Jacobi elliptic function expansion method is used to execute a finite series expansion of degree n. Due to this analytical method, we obtained numerous new exact solutions, including periodic solutions in Jacobi elliptic function forms and their corresponding Solitary and shock wave solutions in a limit convergence sense when the modulus parameter m approaches 1 and 0. These results are particularly useful for nonlinear science and mathematical physics professionals, since they provide important insights into the structure and evolution of nonlinear waves in a variety of physical circumstances. To improve the physical description of the solutions, several typical wave profiles are offered to provide a comprehensive analysis of the wave characteristics of the solutions in 2-D, 3-D, and contour visualizations were generated using accurate parameters value with the help of Mathematica. Moreover, by generating novel and accurate propagating soliton waveform solutions, the generalized Jacobi elliptic function expansion methods highlight its importance in uncovering key aspects of the model behaviours as well as suggesting potential applications in the study of water waves**.**

Patryk Różyło, Kuba Rosłaniec
An Influence of Cross-Sectional Features on the Stability and Load-Carrying Capacity of Carbon-Epoxy Composite Structures

The paper aims experimental-numerical approaches to the behaviour of the compressed thin-walled composite profiles with closed sections. For this, thin-walled composite profiles made of carbon-epoxy composite from the autoclave technique. It was to analyse the effect of cross-section shape on the stability and fracture of composite structures. This was covered through a universal testing machine, an optical deformation measurement system, acoustic emission method as well as a microscope. Numerical simulations were carried out using the finite element method (based on progressive failure analysis). The research follows the project from the National Science Centre in Poland, Reg. No. 2021/41/B/ST8/00148.

Andrzej Werner, Bogusław Hościło , Piotr Mrozek, Krzysztof Molski
Digitalisation of Painting Path Topography for Numerical Modelling of Low-Relief Surfaces

The methodology presented in this article involves the digitalization of painting path topography created using various brushes on different canvases. Measurements were conducted using a blue structured light scanner. Preliminary test scans were performed to determine the optimal digitalization parameters, including exposure time, number of exposures, and scanning resolution. A resolution of 0.08 mm was selected as the minimum point spacing, which was sufficient for both modelling and application use. This scanning process enabled the capture of surface deformations, including path fading and topographic variations arising from interactions between brush bristles, paint, and the canvas substrate-even in cases of partial paint coverage. The resulting 3D model was integrated into an application designed to replicate the glazing technique in painting.

Gustini Gustini, Kaprawi Sahim, Ida Sriyanti, Irmawan Irmawan
Mechano-Responsive Polyampholyte Hydrogels with Strain-Stiffening Property for Wound Closure Applications

Strain-stiffening properties are the most applied in mechano-responsive hydrogels that respond to external mechanical forces. Wounds subjected to frequent deformations are difficult to treat because external mechanical forces can easily interfere with the healing process. The strain-stiffening property reduces the effect of external mechanical forces and acts as a damper response to these forces. Therefore, tough wound closure with stimuli-responsive strain-stiffening release properties for treating these wounds is highly desirable. In this study, we developed a strain-stiffening polyampholyte hydrogel that aims to accelerate wound closure as a damper of external mechanical forces. Self-assembly technique was used to fabricate a polyampholyte hydrogel. The differential modulus of the polyampholyte hydrogel exhibited strain-stiffening property. In addition, the mechanical stress applied to the polyampholyte hydrogel increased strain-stiffening penetration into the skin tissue. The strain-stiffening properties of the polyampholyte hydrogel also demonstrated an excellent damping of external mechanical forces to accelerate wound closure. The developed strain-stiffening hydrogel is promising for wound closure applications in wounds subjected to frequent deformations from external mechanical forces.

Prafulla Kumari Panda, Tapas Ranjan Panigrahi
Phase Velocity of Quasi SV, SH and P-waves in Transversely Isotropic Medium

The current investigation is made to find the analytical solutions of the quasi- SV, SH and P-waves in an inhomogeneous transversely isotropic medium. The paper includes the heterogeneity as an exponential type in density as well as in Young's, and shear modulus with respect to the depth parameter z. Using the Hooke's law, stress-strain and strain-displacement relation in the equation of motion, the phase velocity of the above quasi waves can be evaluated. Again, with the help of analytic solution procedure, the equation of motion will convert to eigen value problem and subsequently the closed-form relation for the quasi velocities will formed. Using the numerical simulations and mathematical calculations, the propagation pattern has been studied. This present finding results the outcome of the heterogeneity constants for different velocities. Two-dimensional graphs have been plotted to show the prominent effect of phase velocity on the surface. The study on quasi wave's may be helpful geophysicists and civil engineers to overcome the problems related to earthquake.

Hailemariam Nigus Hailu, Daniel Tilahun Redda
Surface Characterization and Wear Investigation on Ni-Doped Cr-Mo Alloy Steel in Gear Applications

This study carried out experimental rolling contact fatigue (RCF) tests on two types of materials: commercially available Cr-Mo alloy steel and 1.55% Ni-doped Cr-Mo alloy steel, using a twin-disc test rig. Micropitting was identified as the most prominent damage feature on the rolled surfaces of the disc samples during the gears' RCF tests. To investigate gear surface characteristics and wear behavior, RCF tests were conducted on both material types. The twin-disc test was designed to replicate asperity contact on mating gear flank surfaces, using low-speed cylindrical disc specimens and high-speed crowned disc specimens, ensuring a minimum effective contact area of 8.5 mm. After testing, surface morphology and topographical changes were examined using Scanning Electron Microscopy (SEM). The results revealed that 1.55% Ni-doped Cr-Mo alloy steel demonstrated superior resistance to contact fatigue failure compared to the commercially available Cr-Mo alloy steel, as evidenced by a lower micropitted area ratio, shallower pitted depth, and fewer pits. Specifically, the Ni-doped alloy exhibited a 5.66% lower micropitting area ratio under the same test conditions. Furthermore, prior studies support these findings, showing that the 1.55% Ni-doped steel performs better than the 2% Ni-doped alloys. Therefore, 1.55% Ni-doped Cr-Mo alloy steel is recommended for transmission gears to minimize RCF damage.

Jerzy Michalczyk, Marek Gajowy, Krzysztof Michalczyk
Causes of Errors in Estimating the Characteristic Frequencies of Antiresonant Conveyors

This paper demonstrates the unsuitability of relations and diagrams known from literature for antiresonant machines, in terms of determining the position of resonances of dynamic elimination systems. Correct formulas were derived and a nomogram for designers was built based on them. The effect of the actual number of degrees of freedom on the natural frequencies of machines with a design based on the dynam-ic eliminator principle is presented. The effect of the spring mass on the antiresonance frequency explicit to the natural frequency of the eliminator was pointed out, and correct relations for its consideration were derived. The experimental and numerical studies carried out in this paper have confirmed that including the effect of spring inertia in analytical calculations improves the accuracy of the results obtained. Furthermore, it was shown that the actual way in which the ends of the leaf springs are attached can significantly affect the natural frequency of the system. The factors discussed and analysed in this paper are omitted in conventional vibrating machine calculations, resulting in an overestimation of the natural frequencies determined from them.

Robert Baran, Krzysztof Michalczyk, Mariusz Warzecha
Effect of the End Coil Shape of the Helical Compression Spring on its Stiffness and Distribution of Transverse Reactions during Axial Loading

This paper investigates the effect of ground end coils on axial stiffness, as well as the magnitude and direction of transverse reactions occurring during axial compression of a coil spring. As shown, conventional relationships for calculating axial stiffness can significantly overestimate its value, especially for springs with a small number of active coils. Transverse reaction forces during axial compression of a spring can reach high values. The paper shows that these forces can exceed more than 30% of the axial force caused by the compression of the spring. There are no relations in the available literature to estimate the effect of spring geometry on the value and direction of the transverse reaction generated during axial compression of the spring. On the basis of experimental studies of axial compression of springs, a numerical model with high accuracy was developed - the average difference between the experimental results and the results of the numerical model was 2.7%. The model took into account friction between coils, large deformations and carefully studied material parameters. Using the developed numerical model, a total of 245 numerical analyses were carried out, based on which new relationships were developed to accurately calculate axial stiffness, lateral reaction force and its angle. The new relationship for calculating axial stiffness shows better agreement with the results of numerical analyses than all the relationships found in the literature to date. The average difference between the results of this relation and the results of the numerical analyses carried out did not exceed 2%. A new relation has been proposed for determining the value of the transverse reaction occurring in axial compression of springs. This relation also shows high agreement with the results of numerical analyses. In addition, a new relation has been proposed to determine the direction of the transverse reaction force.

Piotr Danielczyk, Ireneusz Wróbel
Computer Simulation in the Design of Tools and the Stamping Process of Non-Typical Shaped Drawpieces – a Case Study

The paper presents a hot stamping technology of body components in modern passenger cars. The technology guarantees obtaining lightweight drawpieces with high mechanical parameters, which results in a significant reduction in the weight of passenger car bodies, particularly those with an electric drive. The Finite Element Method was used to simulate hot stamping of a large-size drawpiece with an atypical shape. The results of these simulations and experimental tests of a drawpiece have been presented and discussed. Relevant conclusions have been formulated.

Said Azzi, Belkacem Belkacem, Mohamed Bouzit, Mohamed Bouhafs, Atika Bencherif, Imadeddine Dehimi
Control of Free Convection by Flexible Fins in a Square Cavity Containing a Heated Triangular Block

This study investigated the role of fin flexibility to control the fluid flow on natural convection heat transfer within a square cavity containing a heated triangular block. Two flexible fins, attached to the cavity's cold vertical walls, interact with an incompressible fluid under varying Rayleigh numbers (Ra) and elasticity modulus (Et), highlighting how these parameters affect thermal and fluid dynamics and the interaction between the top and the bottom regions of the cavity. The novelty of this study is to create passive control over the flexible fins to control the fluid flow and creating a separation between the top region or the bottom region using these mentioned parameters. Using the Arbitrary Lagrangian-Eulerian (ALE) technique, the fluid-structure interaction (FSI) model captured the bending response of the fins and the resulting convective heat transfer. Results indicated that lower fin rigidity (low Et) significantly enhanced thermal mixing and heat transfer due to increased fluid flow, driven by the bending of the fins at higher Ra. Hence, the top and the bottom regions of the cavity interacted with each other. Conversely, higher Et values restricted fluid circulation, maintaining thermal stratification and reducing heat transfer efficiency and separated these regions. This study provides insights into controlling and optimizing heat transfer in systems with flexible structures, with potential applications in thermal management and energy-efficient design.

Rajeshwar B., Krishnanaik Vankdoth, Anvesh Thatikonda
Design and Simulation of Multiband Microstrip Patch Antenna for Wireless Applications using HFSS

This paper presents the design and simulation of a multiband microstrip patch antenna optimized for modern wireless applications such as IoT devices, WLAN (2.4/5 GHz), WiMAX, and sub-6 GHz 5G systems. The novelty of this work lies in the integration of artificial neural networks (ANNs) with HFSS simulations, enabling rapid geometry prediction and reducing optimization iterations by nearly 50% compared to conventional design approaches. The proposed antenna, implemented on an FR-4 substrate with strategically placed L-shaped slots, achieves well-defined resonances at 2.4 GHz, 3.6 GHz, and 5.8 GHz. Simulation results show return loss (S_{11}) better than –15 dB, VSWR < 2, and peak gains of 7–8 dBi, with stable broadside radiation patterns across all bands. A parametric study demonstrates the influence of slot dimensions and substrate parameters on multiband behavior, while a comparative analysis highlights performance advantages over existing designs. These results confirm that the ANN-assisted HFSS workflow provides an efficient methodology for realizing compact, high-performance antennas suitable for multistandard wireless communication platforms.

Jozef Živčák, Anna Falkowska
Phenomenological And Mechanobiological Approaches To Numerical Simulation Of Bone Remodeling: a Review

Bone remodeling is a dynamic and complex process governed by mechanical loading and molecular signaling. Numerical models serve as essential tools in predicting structural changes in bone, assessing implant integration, and evaluating the effects of pharmacological or pathological conditions. This review provides a critical comparative analysis of two principal classes of bone remodeling models: phenomenological and mechanobiological. Phenomenological models treat bone as an adaptive continuum responding to mechanical stimuli, offering numerical efficiency and compatibility with finite element methods. In contrast, mechanobiological models incorporate explicit representations of cellular dynamics, regulatory pathways (e.g., RANK/RANKL/OPG, WNT/β-catenin), and biological feedback mechanisms. While biologically realistic, they are limited by high parameterization, calibration challenges, and computational cost. The review outlines the application domains of each approach, highlights current limitations, and discusses potential directions for hybrid modeling. We conclude that future research should focus on integrating biological fidelity with numerical tractability to enable predictive, personalized simulations of bone remodeling.

Mohammed E. A. Rabie, Tarig M. Elzaki
An Observation on The Elzaki Transform and The Fractional Coupled System of PDEs

This paper presents a new approach for solving several fractional coupled systems of nonlinear partial differential equations (FCSNLPDEs) using initial conditions (ICs). This approach is based on the Elzaki transform (ET). A comprehensive description is provided to facilitate understanding of the procedure. The applicability and validity of this technique for solving FCSNLPDE problems in a few steps have been demonstrated. Using this approach, both linear and nonlinear FCSPDEs can be solved without the need for discretization or restrictive assumptions. This method requires fewer numerical calculations because it does not introduce approximation errors. Numerical examples are presented to illustrate the accuracy and efficiency of this new technique. To further illustrate how the suggested approach affected the outcomes, 2D and 3D graphs and tables were employed.

Faculty of Mechanical Engineering

BIALYSTOK UNIVERSITY OF TECHNOLOGY

ACTA MECHANICA
ET AUTOMATICA

online available at https://www.amajournal.com/